Complexity

Applications in Science and Engineering for Modelling, Analysis and Control of Chaos

Lead Guest Editor: Zhouchao Wei
Guest Editors: Karthikeyan Rajagopal and Yongjian Liu

Applications in Science and Engineering for Modelling, Analysis and Control of Chaos

Complexity

Applications in Science and Engineering for Modelling, Analysis and Control of Chaos

Lead Guest Editor: Zhouchao Wei
Guest Editors: Karthikeyan Rajagopal and Yongjian Liu

Contents

Contents

Hindawi
Complexity
Volume 2021, Article ID 8845553, 14 pages
https://doi.org/10.1155/2021/8845553

Research Article

Robust Synchronization of Class Chaotic Systems Using Novel Time-Varying Gain Disturbance Observer-Based Sliding Mode Control

Yang Wang, Zhen Wang, and Lingyun Kong

School of Science, Xijing University, Xi'an, China

Correspondence should be addressed to Yang Wang; 2013100280@mail.nwpu.edu.cn

Received 16 August 2020; Revised 19 September 2020; Accepted 2 April 2021; Published 21 April 2021

Academic Editor: Hassan Zargarzadeh

For synchronization of a class of chaotic systems in the presence of nonvanishing uncertainties, a novel time-varying gain observer-based sliding mode control is proposed. First, a novel time-varying gain disturbance observer (TVGDO) is developed to estimate the uncertainties. Then, by using the output of TVGDO to modify sliding mode control (SMC), a new TVGDO-based SMC scheme is developed. Although the observation and control precision of conventional fixed gain disturbance observer-based control (FGDOC) for chaotic systems can be guaranteed by a high observer gain, the undesirable spike problem may be caused by the high gain if the initial values of estimate and true states are not equal. The most attractive feature of this work is that the newly proposed TVGDO can eliminate the spike problem by developing a time-varying gain scheme. Finally, the effectiveness of the proposed method is demonstrated by the numerical simulation.

1. Introduction

In the past decades, with the development of theoretical analysis methods of chaos, many chaos systems such as the Lorenz system [1], Rossler system [2], and Chen system [3] have been wildly studied. These theoretical advancements of chaotic systems have been influentially applicated in many fields, such as power electrical systems [4, 5], robotics [6], lasers [7], and secure communications [8]. Among these applications, to achieve the desired chaotic characteristic, the high-precision synchronization problem is the key problem that must be solved. The objective of synchronization control between the master and slave chaotic systems can be achieved when the instantaneous states of the two systems become identical. Note that unmodeling dynamic, environmental disturbance, and uncertainty parameters usually exist in the slave chaotic systems [9]. These uncertainties can greatly affect the synchronization performance. To improve the robustness of chaos synchronization in allusion to uncertainties, many modern robust control theories have been applied to design synchronization controllers, including H_∞ robust control [10, 11], adaptive control [12, 13], neural network control [14, 15], observer-based control [16, 17], and sliding mode control (SMC) [18–22]. Among these schemes in [10–22], due to its advantage of low sensitivity to uncertainties and fast dynamic response, SMC is a good candidate to achieve high-precision synchronization in the presence of uncertainties. In [18, 19], the authors adopted the linear sliding mode surface to design a synchronization controller for chaotic systems. In [20, 21], the terminal sliding mode method was investigated to guarantee the fast finite-time synchronization of uncertain chaotic systems. In [22], to establish invariance of the system with uncertainties from the initial time instant, the integral sliding mode control scheme was investigated to design the synchronization controller. However, the robustness of these conventional SMC schemes in [18–22] is guaranteed by using the discontinuous control terms. The discontinuous terms can bring an undesirable chattering problem.

It is well known that the chattering problem may affect the synchronization precision and cause the instability of the closed-loop system [23–25]. Thus, research on chattering-

free SMC synchronization scheme has the important practical and theoretical significance. Based on observer techniques, the chattering problem of conventional SMC can be eliminated by using the estimation of uncertainties to replace the discontinuous control terms of SMC. In [26, 27], the authors adopted the high-order sliding mode (HOSM) observers to estimate the uncertainties of the chaotic system. However, the HOSM observer used in [26, 27] must know the upper bound of uncertainties in advance. Since the characteristics of uncertainties are complex, it is difficult to know the upper bound. In [28–30], the SMC schemes were proposed by employing the disturbance observer (DO) to estimate the uncertainties in chaotic systems. In [31], the authors adopted the estimation of extended state observer (ESO) to modify the conventional SMC. Unlike HOSM observer in [26, 27], the DO and ESO in [28–31] does not require the upper bound of uncertainties.

For the DO-based and ESO-based SMC schemes in [28–31], to guarantee the observation and control precision, the observer gains of DO and ESO should be chosen as the high gains. However, the undesirable spike problem can be caused by the high observer gains when the initial values of estimate and true states are not equal. The spike problem may cause the saturation of control input and even the instability. Actually, it is difficult to obtain the initial values of state in advance for the most of practical systems. Thus, the DO-based and ESO-based SMC schemes in [28–31] may not work well in many practical situations.

In this study, a new time-varying gain disturbance observer (TVGDO) is proposed to estimate the lumped uncertainties of the chaotic system. And then, a novel TVGDO-based SMC scheme is designed based on the output of TVGDO. The main contributions of this study lie in the following aspects:

(1) Compared with conventional DO and ESO used in the uncertain chaotic systems, the most attractive feature of the proposed TVGDO is that the spike problem can be eliminated on the condition of the initial values of estimate and true states are not equal.

(2) The proposed TVGDO-based SMC is spike-free and chattering-free. And the TVGDO-based SMC can guarantee the synchronization without using the upper bound information of uncertainties.

The remaining parts of this study are as follows. In Section 2, the synchronization control model, the design objective, and the motivation of this study are expounded. The main results are presented in Section 3. In Section 3.1, a novel observer TVGDO is developed, and the stability proof of TVGDO is presented. In Section 3.2, the spike-free characteristic of TVGDO is analyzed. In Section 3.3, a TVGDO-based SMC scheme is proposed, and the stability of the proposed controller is also obtained. In Section 4, a simulation verifies the effectiveness of both TVGDO and the proposed TVGDO-based SMC. In Section 5, the conclusion of the whole study is presented.

Notations. The following notations will be used in this study: t denotes the time and the initial time is 0. Let $\|\cdot\|$ denote the Euclidean norm of a vector and its induced norm of a matrix.

2. Problem Formulation

2.1. System Description. In this study, the dynamic of the master chaotic system is described as follows [12]:

$$\begin{cases} \dot{x}_{m1} = f_{m1}(\mathbf{X}_m, t), \\ \dot{x}_{m2} = f_{m2}(\mathbf{X}_m, t), \\ \vdots \\ \dot{x}_{mn} = f_{mn}(\mathbf{X}_m, t), \end{cases} \tag{1}$$

where $x_{mi}\,(i = 1, 2, \ldots, n)$ represents the states of the master system, $X_m = [\, x_{m1} \;\; x_{m2} \;\; \ldots \;\; x_{mn} \,]^T$ is the state vector, and $f_{mi}(X_m, t)$, $(i = 1, 2, \ldots, n)$ is the nonlinear function and determines the chaotic characteristic.

The slave chaotic system is given as follows [12]:

$$\begin{cases} \dot{x}_{s1} = f_{s1}(\mathbf{X}_s, t) + \Delta f_{s1}(\mathbf{X}_s, t) + u_1(t) + d_1(t), \\ \dot{x}_{s2} = f_{s2}(\mathbf{X}_s, t) + \Delta f_{s2}(\mathbf{X}_s, t) + u_2(t) + d_2(t), \\ \vdots \\ \dot{x}_{sn} = f_{sn}(\mathbf{X}_s, t) + \Delta f_{sn}(\mathbf{X}_s, t) + u_n(t) + d_n(t), \end{cases} \tag{2}$$

where $x_{si}\,(i = 1, 2, \ldots, n)$ represents the states of the slave system, $\mathbf{X}_s = [\, x_{s1} \;\; x_{s2} \;\; \ldots \;\; x_{sn} \,]^T$ is the state vector, $f_{si}(\mathbf{X}_s, t)\,(i = 1, 2, \ldots, n)$ is the nonlinear function, $u_i(t)\,(i = 1, 2, \ldots, n)$ is the control input, and $\Delta f_{si}(\mathbf{X}_s, t)$ and $d_i(t)\,(i = 1, 2, \ldots, n)$ are the bounded uncertainty and disturbance, respectively. Like the conventional SMC, the uncertainties considered in this study are matched uncertainties, which imply that the uncertainties and control inputs exist in the same channel. It is assumed that all states of systems (1) and (2) are measured and noise-free.

The synchronization errors are defined as follows:

$$\begin{aligned} &e_i = x_{si} - x_{mi}, \quad (i = 1, 2, \ldots, n), \\ &\overline{e} = [\, x_{s1} - x_{m1} \;\; x_{s2} - x_{m2} \;\; \ldots \;\; x_{sn} - x_{mn} \,]^T. \end{aligned} \tag{3}$$

Note that if the following condition is satisfied, then the objective of synchronization is realized:

$$\|\overline{e}\| \longrightarrow 0. \tag{4}$$

Considering (1) and (2), for $i = 1, 2, \ldots, n$, the error dynamics can be obtained as

$$\dot{e}_i = \overline{F}_i(\mathbf{X}_m, \mathbf{X}_s, t) + u_i(t) + D_i(t), \tag{5}$$

where

$$\begin{aligned} \overline{F}_i(\mathbf{X}_m, \mathbf{X}_s, t) &= f_{si}(\mathbf{X}_s, t) - f_{mi}(\mathbf{X}_m, t), \\ D_i &= \Delta f_{si}(\mathbf{X}_s, t) + d_i(t), \end{aligned} \tag{6}$$

where D_i denotes the lumped uncertainties.

The following Assumption is assumed to be valid throughout this study.

Assumption 1. The lumped uncertainties $D_i\,(i = 1, 2, \ldots, n)$ is differentiable and satisfies $|D_i| \le D_{i\max}$ and $|\dot{D}_i(t)| \le D^d_{i\max}$, where $D_{i\max}$ and $D^d_{i\max}$ are the unknown positive constants.

2.2. Problem Description and Purposes of This Study. To satisfy condition (4), like [32], a simple sliding mode surface vector can be chosen as

$$\mathbf{s} = \mathbf{c}\overline{e}, \tag{7}$$

where

$$\begin{aligned} \mathbf{s} &= \begin{bmatrix} s_1 & s_2 & \ldots & s_n \end{bmatrix}^T, \\ \mathbf{c} &= \operatorname{diag}\begin{pmatrix} c_1 & c_2 & \ldots & c_n \end{pmatrix}, \end{aligned} \tag{8}$$

where $c_i\,(i = 1, 2, \ldots, n)$ is a positive constant.

Then, calculating the time derivative of $s_i\,(i = 1, 2, \ldots, n)$ along the trajectories of (5) and (7), we have

$$\dot{s}_i = c_i\left(\overline{F}_i\left(\mathbf{X}_m, \mathbf{X}_s, t\right) + D_i + u_i(t)\right). \tag{9}$$

To guarantee the sliding mode surface s_i converge to zero, it is necessary to design a robust scheme to suppress the lumped uncertainties D_i.

Then, the conventional sliding mode controller (SMC) can be designed as

$$u_i(t) = \left(c_i\right)^{-1}\left(-\overline{F}_i\left(\mathbf{X}_m, \mathbf{X}_s, t\right) - k_{\mathrm{SMC}i}\operatorname{sign}\left(s_i\right)\right), \tag{10}$$

where $\operatorname{sign}(\cdot)$ denotes the signum function, and $k_{\mathrm{SMC}i}$ is a positive constant.

Substituting (10) into (9), we have $\dot{s}_i = -(k_{\mathrm{SMC}i} - D_i)\operatorname{sign}(s_i)$. Then, we can know that $s_i\dot{s}_i < 0$ if $k_{\mathrm{SMC}i} > D_i$ and $s_i \ne 0$. Thus, the uncertainty D_i can be suppressed by the discontinuous switch item $k_{\mathrm{SMC}i}\operatorname{sign}(s_i)$. However, the constant k_{SMCi} must be selected as the upper bound of D_i, which is difficult to be obtained in advance. And the discontinuous term $k_{SMCi}\operatorname{sign}(s_i)$ brings undesirable chattering problem.

Recently, to avoid using the upper bound of D_i and solve the chattering problem, some observer-based SMC schemes have been developed in [28–31].

In [26–28], the disturbance observer (DO) is designed to estimate nonvanishing disturbances and model uncertainties in the chaotic system. For the uncertainties $D_i\,(i = 1, 2, \ldots, n)$, the DO can be designed by using the method in [28–30]:

$$\begin{cases} \dot{Z}_{\mathrm{DO}i} = c_i\left(\overline{F}_i\left(\mathbf{X}_m, \mathbf{X}_s, t\right) + \widehat{D}_{\mathrm{DO}i} + u_i(t)\right), \\ \widehat{D}_{\mathrm{DO}i} = -k_{\mathrm{DO}i}\left(Z_{\mathrm{DO}i} - s_i\right), \end{cases} \tag{11}$$

where $Z_{\mathrm{DO}i}$ is the estimate state of DO, $k_{\mathrm{DO}i}$ is the positive observer gain, and $\widehat{D}_{\mathrm{DO}i}$ is the estimation of D_i. Then, the DO-based SMC can be designed as

$$u_i(t) = -\overline{F}_i\left(\mathbf{X}_m, \mathbf{X}_s, t\right) - \varepsilon_{\mathrm{DO}i}s_i - \sigma_{\mathrm{DO}i}\left|s_i\right|^{\gamma_{\mathrm{DO}i}}\operatorname{sign}\left(s_i\right) - \widehat{D}_{\mathrm{DO}i}, \tag{12}$$

where $\varepsilon_{\mathrm{DO}i}$, $\sigma_{\mathrm{DO}i}$, and $\gamma_{\mathrm{DO}i}$ are the positive constants, $0 < \gamma_{\mathrm{DO}i} < 1$. The DO (11) can guarantee the estimate error converge to the following region:

$$\left|\widehat{D}_{\mathrm{DO}i} - D_i\right| \longrightarrow \frac{D^d_{i\max}}{\left(k_{\mathrm{DO}i}c_i\right)}, \quad \text{if } t \longrightarrow \infty, \tag{13}$$

where the constant $D_{d\max}$ is defined in Assumption 1. From (13), to achieve the high observation precision, the observer gain $k_{\mathrm{DO}i}$ should be large enough. However, from (11), it is clear that the initial value $\widehat{D}_{\mathrm{DO}i}(0)$ may be very large if $k_{\mathrm{DO}i}$ is a high gain and the initial estimate state error $Z_{\mathrm{DO}i}(0) - s_i(0) \ne 0$. Actually, the initial values of true state $s_i(0)$ cannot be known in advance for most of the cases. Thus, the initial estimate state error $Z_{\mathrm{DO}i}(0) - s_i(0)$ maybe not equal to 0 and even a large value. The large value $\widehat{D}_{\mathrm{DO}i}(0)$ may lead to a large overshoot control input $u_i(t)$ (see (12)). Then, the large overshoot $u_i(t)$ may reduce the dynamic performance of synchronization and even lead to the instability, and this is the undesirable spike problem of DO.

In [31], the extended state observer (ESO) is developed to estimate the uncertainties and chaotic nonlinear function. The uncertainties $D_i\,(i = 1, 2, \ldots, n)$ also can be estimated by using the method in [31]:

$$\begin{cases} \dot{Z}_{\mathrm{ESO}i} = c_i\left(\overline{F}_i\left(\mathbf{X}_m, \mathbf{X}_s, t\right) + \widehat{D}_{\mathrm{ESO}i} + u_i(t) - 2k_{\mathrm{ESO}i}\left(Z_{\mathrm{ESO}i} - s_i\right)\right), \\ \dot{\widehat{D}}_{\mathrm{ESO}i} = -k^2_{\mathrm{ESO}i}c_i\left(Z_{\mathrm{ESO}i} - s_i\right), \end{cases} \tag{14}$$

where $Z_{\mathrm{ESO}i}$ is the estimated state of ESO, $\widehat{D}_{\mathrm{ESO}i}$ is an estimation of D_i, and $k_{\mathrm{ESO}i}$ is the observer gain of ESO. Then, the ESO-based SMC can be designed as

$$\begin{aligned} u_i(t) = &-\overline{F}_i\left(X_m, X_s, t\right) - \varepsilon_{\mathrm{ESO}i}s_i - \sigma_{\mathrm{ESO}i}\left|s_i\right|^{\gamma_{\mathrm{ESO}i}}\operatorname{sign}\left(s_i\right) \\ &- \widehat{D}_{\mathrm{ESO}i}, \end{aligned} \tag{15}$$

where $\varepsilon_{\mathrm{ESO}i}$, $\sigma_{\mathrm{ESO}i}$, and $\gamma_{\mathrm{ESO}i}$ are the positive constants, $0 < \gamma_{\mathrm{ESO}i} < 1$. The ESO can guarantee the estimate error converge to following region:

$$\left|\widehat{D}_{\mathrm{ESO}i} - D_i\right| \longrightarrow \frac{D^d_{i\max}}{\left(k_{\mathrm{ESO}i}c_i\right)}, \quad \text{if } t \longrightarrow \infty. \tag{16}$$

Define the estimate error vector $\mathbf{h} = \begin{bmatrix} Z_{\mathrm{ESO}i} - s_i & \widehat{D}_{\mathrm{ESO}i} - D_i \end{bmatrix}^T$. From ESO (14), we have

$$\dot{\mathbf{h}} = \mathbf{A}_h\mathbf{h} + \mathbf{\Delta}, \tag{17}$$

where

$$\begin{aligned} \mathbf{A}_h &= c_i\begin{bmatrix} -2k_{\mathrm{ESO}i} & 1 \\ -k^2_{\mathrm{ESO}i} & 0 \end{bmatrix}, \\ \mathbf{\Delta} &= \begin{bmatrix} 0 \\ \dot{D}_i \end{bmatrix}. \end{aligned} \tag{18}$$

The solution to the differential equation (17) can be easily obtained as

$$\mathbf{h} = \mathbf{e}^{\mathbf{A}_h t}\mathbf{h}(0) + \int_0^t \mathbf{e}^{\mathbf{A}_h (t-\tau)}\dot{D}_i(\tau)\mathrm{d}\tau, \tag{19}$$

where e is the e constant. Let $\begin{bmatrix} * & 20\overline{h}_1 & \overline{h}_2 \end{bmatrix}^T = \int_0^t \mathbf{e}^{\mathbf{A}_h (t-\tau)}\dot{D}_i(\tau)\mathrm{d}\tau$. Expanding $e^{\mathbf{A}_h t}\mathbf{h}(0)$, the estimate error can be rewritten as

$$\begin{aligned}\widehat{D}_{\mathrm{ESO}i} - D_i = &-\left(k_{\mathrm{ESO}i}c_i\right)^2 t e^{-k_{\mathrm{ESO}i}c_i t}\left(Z_{\mathrm{ESO}i}(0) - s_i(0)\right) \\ &+ \left(k_{\mathrm{ESO}i}c_i t + 1\right)e^{-k_{\mathrm{ESO}i}c_i t}\left(\widehat{D}_{\mathrm{ESO}i}(0) - D_i(0)\right) + \overline{h}_2.\end{aligned} \tag{20}$$

For the small time $t = 1/(k_{\mathrm{ESO}i}c_i)$, we have

$$\begin{aligned}\widehat{D}_{\mathrm{ESO}i} = &-k_{\mathrm{ESO}i}c_i\left(Z_{\mathrm{ESO}i}(0) - s_i(0)\right)e^{-1} \\ &+ 2e^{-1}\left(\widehat{D}_{\mathrm{ESO}i}(0) - D_i(0)\right) + D_i \\ &+ \overline{h}_2, \quad \text{if } t = \frac{1}{\left(k_{\mathrm{ESO}i}c_i\right)}.\end{aligned} \tag{21}$$

It can be known that $(k_{\mathrm{ESO}i}c_i)(Z_{\mathrm{ESO}i}(0) - s_i(0))$ is a very large value if $k_{\mathrm{ESO}i}$ is a high gain and $Z_{\mathrm{ESO}i}(0) - s_i(0) \neq 0$. Thus, the undesirable spike problem also exists in ESO.

2.2.1. Motivation of This Study. From the previous discussion, an undesirable spike problem can be caused by the high observer gain in ESO and DO if the initial values of estimate and true states are not equal. Thus, if the initial value of true states is unknown, to avoid the spike problem, the ESO-based and DO-based controller cannot adopt the high observer gains to guarantee the control precision. Actually, the initial value of true states cannot be known in advance in most of cases. This motivates the research topic of this study, that is, for the chaotic system in the presence of uncertainties, designing a new TVGDO and TVGDO-based SMC schemes not only can guarantee high control precision but also eliminate the undesirable spike problem.

3. Main Result

3.1. Observer Design and Stability Analysis. In this section, a novel time-varying gain disturbance observer (TVGDO) will be proposed. The TVGDO can guarantee the high precision and avoid the undesirable spike problem even if the initial values of estimate and true states are not equal.

The expression of TVGDO and the stability analysis are given in the following Theorem.

Theorem 1. *Taking the master and slave chaotic systems (1) and (2) into consideration, for the uncertainties $D_i(i = 1, 2, \ldots, n)$, the TVGDO (22) is constructed.*

$$\begin{cases} \dot{Z}_i = c_i\left(\overline{F}_i(\mathbf{X}_m, \mathbf{X}_s, t) + \widehat{D}_i + u_i(t)\right), \\ \widehat{D}_i = -k_i(t)\left(Z_i - s_i\right) + \int_0^t \dot{k}_i(\tau)\left(Z_i - s_i\right)\mathrm{d}\tau, \\ k_i(t) = \eta_{i1}\left(1 - e^{-\eta_{i2}t}\right), \\ \dot{k}_i(\tau) = \eta_{i1}\eta_{i2}e^{-\eta_{i2}\tau}, \end{cases} \tag{22}$$

where η_{i1} and η_{i2} are the positive constants, and $k_i(t)$ is a nonnegative time-varying gain. Assumption 1 is valid. The estimate error of TVGDO is defined as $\overline{D}_i = \widehat{D}_i - D_i$. Then, the estimate error $\overline{D}_i$ will converge to the following region:

$$\left|\overline{D}_i\right| \leq \frac{D_{i\max}^d}{\left(\eta_{i1}c_i\right)}, \quad \text{if } t \longrightarrow \infty. \tag{23}$$

Proof. The estimate error of TVGDO is defined as $\overline{D}_i = \widehat{D}_i - D_i(i = 1, 2, \ldots, n)$. Differentiating $\overline{D}_i$ gives

$$\dot{\overline{D}}_i = \dot{\widehat{D}}_i - \dot{D}_i. \tag{24}$$

Considering (9) and (22), (24) can be rewritten as

$$\begin{aligned}\dot{\overline{D}}_i &= -\dot{k}_i(t)\left(Z_i - s_i\right) - k_i(t)\left(\dot{Z}_i - \dot{s}_i\right) + \dot{k}_i(t)\left(Z_i - s_i\right) - \dot{D}_i \\ &= -k_i(t)\left(\dot{Z}_i - \dot{s}_i\right) - \dot{D}_i \\ &= -k_i(t)\left(c_i\left(\overline{F}_i(\mathbf{X}_m, \mathbf{X}_s, t) + \widehat{D}_i + u_i(t)\right) - c_i\left(\overline{F}_i(\mathbf{X}_m, \mathbf{X}_s, t) + D_i + u_i(t)\right)\right) - \dot{D}_i \\ &= -k_i(t)c_i\left(\widehat{D}_i - D_i\right) - \dot{D}_i \\ &= -k_i(t)c_i\overline{D}_i - \dot{D}_i.\end{aligned} \tag{25}$$

Construct the Lyapunov function J_i as

$$J_i = \overline{D}_i^2/2 \tag{26}$$

Then, calculating the time derivative of J_i along the trajectory of (25), we get

$$\dot{J}_i = \overline{D}_i\dot{\overline{D}}_i = -k_i(t)c_i\left|\overline{D}_i\right|^2 - \dot{D}_i\overline{D}_i. \tag{27}$$

Considering Assumption 1, we have

$$\begin{aligned}\dot{J}_i \leq &-k_i(t)c_i\left|\overline{D}_i\right|^2 + D_{i\max}^d\left|\overline{D}_i\right| = -2k_i(t)c_iJ_i \\ &+ \sqrt{2}D_{i\max}^d J_i^{1/2}, \quad \text{if } t \geq 0.\end{aligned} \tag{28}$$

Since $k_i(t) \geq 0$, from (28), it can be known that

$$\dot{J}_i \leq \sqrt{2}D_{i\max}^d J_i^{1/2}, \quad \text{if } t \geq 0. \tag{29}$$

Then, we have

$$J_i^{-1/2}\dot{J}_i \le \sqrt{2}D_{i\max}^d, \quad \text{if } t \ge 0. \tag{30}$$

Integrating (30) gives

$$2J_i^{1/2} \le \sqrt{2}D_{i\max}^d t + 2J_i^{1/2}(0), \quad \text{if } t \ge 0. \tag{31}$$

From the expression of $k_i(t)$, it can be known that the following condition can be satisfied in an arbitrary finite time t_{if}:

$$k_i(t) \ge k_i\left(t_{if}\right) > 0, \quad \text{if } t \ge t_{if}. \tag{32}$$

Combining (28) and (32), we have

$$\dot{J}_i \le -2k_i(t)c_iJ_i + \sqrt{2}D_{i\max}^d J_i^{1/2}, \quad \text{if } t \ge t_{if}. \tag{33}$$

From (31), for an arbitrary finite time t_{if}, it is clear that $J_i^{1/2}(t_{if})$ is bounded. If $J_i^{1/2} > D_{i\max}^d/(\sqrt{2}\,k_i(t)c_i)$, it also can be known from (33) that $\dot{J}_i < 0$. Then, we have

$$J_i^{1/2} \le \frac{D_{i\max}^d}{(\sqrt{2}\,k_i(t)c_i)}, \quad \text{if } t \longrightarrow \infty. \tag{34}$$

Consider $\lim_{t\longrightarrow\infty} k_i(t) = \eta_{i1}$; then, we have

$$J_i^{1/2} \le \frac{D_{i\max}^d}{(\sqrt{2}\,\eta_{i1}c_i)}, \quad \text{if } t \longrightarrow \infty. \tag{35}$$

From (35) and $\sqrt{2}J_i^{1/2} = |\overline{D}_i|$, we have

$$|\overline{D}_i| \le \frac{D_{i\max}^d}{(\eta_{i1}c_i)}, \quad \text{if } t \longrightarrow \infty. \tag{36}$$

The proof is finished.

3.2. The Spike-Free Characteristic Analysis. Let $\int_0^t k_i(\tau)\,c_i\mathrm{d}\tau = k_{iS}(t)$. Considering (22) and solving the differential equation (25), the solution of estimate error $\overline{D}_i$ in time domain can be easily obtained as

$$\overline{D}_i = e^{-k_{iS}(t)}\left(\widehat{D}_i(0) - D_i(0) - \int_0^t \dot{D}_i(\tau)e^{k_{iS}(\tau)}\mathrm{d}\tau\right), \tag{37}$$

where e is the e constant. Substituting the detailed expression of $\widehat{D}_i(0)$ into (37), we have

$$\begin{aligned}\overline{D}_i &= e^{-k_{iS}(t)}\left(\widehat{D}_i(0) - D_i(0)\right) - e^{-k_{iS}(t)}\int_0^t \dot{D}_i(\tau)e^{k_{iS}(\tau)}\mathrm{d}\tau \\ &= e^{-k_{iS}(t)}\left(-k_i(0)\left(Z_i(0) - s_i(0)\right) + \int_0^0 \dot{k}_i(\tau)\left(Z_i - s_i\right)\mathrm{d}\tau - D_i(0)\right) - e^{-k_{iS}(t)}\int_0^t \dot{D}_i(\tau)e^{k_{iS}(\tau)}\mathrm{d}\tau.\end{aligned} \tag{38}$$

From the previous discussion in Section 2.2, it can be known that the undesirable spike problem is caused by the spike term $k_{\mathrm{DO}i}(Z_{\mathrm{DO}i}(0) - s_i(0))$ in DO (11) or the spike term $(k_{\mathrm{ESO}i}c_i)(Z_{\mathrm{ESO}i}(0) - s_i(0))$ in ESO (14). Since $k_i(0)(Z_i(0) - s_i(0)) = 0$ and $\int_0^0 \dot{k}_i(\tau)(Z_i - s_i)\mathrm{d}\tau = 0$, it is clear that the expression of $\overline{D}_i$ in (38) does not contain any spike term. Thus, the spike problem is avoided in the TVGDO.

Remark 1. It can be known from (26) that a small enough estimate error can be guaranteed by choosing η_{i1} reasonably. Thus, the proposed TVGDO not only can eliminate the undesirable spike problem but also can guarantee high observation precision.

3.3. Observer-Based Controller Design and Stability Analysis. Then, a novel TVGDO-based sliding mode controller will be developed in this section. The expression of the proposed controller and the stability analysis are given in the following Theorem.

Theorem 2. *Taking the master and slave chaotic systems (1) and (2) into consideration, for $i = 1, 2, \ldots, n$, the TVGDO-based sliding mode controller is constructed as*

$$u_i(t) = -\overline{F}_i(\mathbf{X}_m, \mathbf{X}_s, t) - \varepsilon_i s_i - \sigma_i|s_i|^{\gamma_i}\mathrm{sign}(s_i) - \widehat{D}_i, \tag{39}$$

where the sliding mode surface s_i is defined in (7). ε_i, σ_i, and γ_i are the positive constants. $0 < \gamma_i < 1$. $\widehat{D}_i$ is given in TVGDO (22). Assumption 1 is valid. The synchronization error e_i can converge to following small region:

$$|e_i| \le \min\left\{\frac{\left(D_{i\max}^d/(\varepsilon_i\eta_{i1}c_i)\right)}{c_i}, \frac{\left(D_{i\max}^d/(\sigma_i\eta_{i1}c_i)\right)^{1/\gamma_i}}{c_i}\right\}, \quad \text{if } t \longrightarrow \infty. \tag{40}$$

Proof. Construct the Lyapunov function $P_i\,(i = 1, 2, \ldots, n)$ as

$$P_i = \frac{s_i^2}{2}. \tag{41}$$

Then, calculating the time derivative of P_i along the trajectory of (9), we get

$$P_i = s_i\dot{s}_i = s_i\left(c_i\left(\overline{F}_i(\mathbf{X}_m, \mathbf{X}_s, t) + D_i + u_i(t)\right)\right). \tag{42}$$

Substituting the control input (39) into (42), we have

$$\begin{aligned}\dot{P}_i &= c_is_i\left(D_i - \varepsilon_is_i - \sigma_i|s_i|^{\gamma_i}\mathrm{sign}(s_i) - \widehat{D}_i\right) \\ &= c_i\left(-\varepsilon_is_i^2 - \sigma_i|s_i|^{\gamma_i+1} - \left(\widehat{D}_i - D_i\right)s_i\right) \\ &= -\varepsilon_ic_is_i^2 - \sigma_ic_i|s_i|^{\gamma_i+1} - c_i\overline{D}_is_i \\ &\le -2\varepsilon_ic_iP_i - 2^{(\gamma_i+1/2)}\sigma_ic_iP_i^{(\gamma_i+1/2)} + c_i\sqrt{2}|\overline{D}_i|P_i^{1/2},\end{aligned} \tag{43}$$

where the estimate error $\overline{D}_i = \widehat{D}_i - D_i$.

From (43), we know that e_i affected the estimate error $\overline{D}_i$. Thus, the following proof will consist of two steps. In the first step, it will be proved that e_i will not escape to infinity in arbitrary finite time (before $\overline{D}_i$ converges to a neighborhood of zero). In the second step, it will be proved that e_i will converge to a neighborhood of zero after $\overline{D}_i$ converges to a small neighborhood of zero.

Step 1. From (31) in Theorem 1, we have known that the estimate error $\overline{D}_i$ is bounded as

$$2J_i^{1/2} \le \sqrt{2}D_{i\max}^d t + 2J_i^{1/2}(0), \quad \text{if } t \ge 0. \tag{44}$$

For the arbitrary finite time $t \le t_s$, it can be known that

$$\left|\overline{D}_i\right| \le D_{i\max}^d t + \sqrt{2}J_i^{1/2}(0) \le D_{i\max}^d(t_s) + \sqrt{2}J_i^{1/2}(0), \quad \text{if } t \le t_s. \tag{45}$$

Let the positive constant $D_{Pi} = D_{i\max}^d(t_s) + \sqrt{2}J_i^{1/2}(0)$. Then, combining (43) with (45), we have

$$\begin{aligned} \dot{P}_i &\le -2\varepsilon_i c_i P_i + c_i\sqrt{2}D_{Pi}P_i^{1/2} \\ &\le P_i^{1/2}\left(-2\varepsilon_i c_i P_i^{1/2} + c_i\sqrt{2}\,D_{Pi}\right), \quad \text{if } t \le t_s, \end{aligned} \tag{46}$$

$$\begin{aligned} \dot{P}_i &\le -2^{(\gamma_i+1/2)}\sigma_i c_i P_i^{(\gamma_i+1/2)} + c_i\sqrt{2}D_{Pi}P_i^{1/2} \\ &= P_i^{1/2}\left(-2^{(\gamma_i+1/2)}\sigma_i c_i P_i^{(\gamma_i/2)} + c_i\sqrt{2}\,D_{Pi}\right), \quad \text{if } t \le t_s. \end{aligned} \tag{47}$$

From (46) and (47), we can know that $\dot{P}_i < 0$ if $P_i > (D_{Pi}/(2^{(\gamma_i/2)}\sigma_i))^{(\gamma_i/2)}$ or $P_i > (D_{Pi}/(\sqrt{2}\,\varepsilon_i))^2$. Thus, for $t \le t_s$, P_i will not escape to infinity and is bounded as

$$\left|P_i\right| \le \max\left\{\left(\frac{D_{Pi}}{\left(2^{(\gamma_i/2)}\sigma_i\right)}\right)^{(2/\gamma_i)}, \left(\frac{D_{Pi}}{\left(\sqrt{2}\,\varepsilon_i\right)}\right)^2\right\}, \quad \text{if } t \le t_s. \tag{48}$$

Let the constant $P_{i\max} = \max\{(D_{Pi}/(2^{(\gamma_i/2)}\sigma_i))^{(2/\gamma_i)}, (D_{Pi}/(\sqrt{2}\,\varepsilon_i))^2\}$. Then, we can know that e_i will not escape to infinity and is bounded as $|e_i| \le \sqrt{2P_{i\max}}/c_i$ if $t \le t_s$.

Step 2. From (43), we have

$$\begin{aligned} \dot{P}_i &\le -\sqrt{2}c_i P_i^{1/2}\left(\sqrt{2}\,\varepsilon_i P_i^{1/2} - \left|\overline{D}_i\right|\right), \\ \dot{P}_i &\le -\sqrt{2}c_i P_i^{1/2}\left(2^{(\gamma_i/2)}\sigma_i P_i^{(\gamma_i/2)} - \left|\overline{D}_i\right|\right). \end{aligned} \tag{49}$$

Then, we can know that

$$\dot{P}_i < 0, \quad \text{if } \sqrt{2}\varepsilon_i P_i^{1/2} > \left|\overline{D}_i\right| \ge 0, \tag{50}$$

$$\dot{P}_i < 0, \quad \text{if } 2^{(\gamma_i/2)}\sigma_i P_i^{(\gamma_i/2)} > \left|\overline{D}_i\right| \ge 0. \tag{51}$$

According to (50) and (51), we have

$$P_i \le \left(\frac{\left|\overline{D}_i\right|}{\left(\sqrt{2}\,\varepsilon_i\right)}\right)^2, \quad \text{if } t \longrightarrow \infty, \tag{52}$$

$$P_i \le \left(\frac{\left|\overline{D}_i\right|}{\left(2^{(\gamma_i/2)}\sigma_i\right)}\right)^{(2/\gamma_i)}, \quad \text{if } t \longrightarrow \infty. \tag{53}$$

From Theorem 1, it can be known that the estimate error $\overline{D}_i$ is bounded as

$$\left|\overline{D}_i\right| \le \frac{D_{i\max}^d}{(\eta_{i1}c_i)}, \quad \text{if } t \longrightarrow \infty. \tag{54}$$

Combining (52)–(54), we have

$$P_i \le \min\left\{\left(\frac{D_{i\max}^d}{(\sqrt{2}\,\varepsilon_i\eta_{i1}c_i)}\right)^2, \left(\frac{D_{i\max}^d}{\left(2^{(\gamma_i/2)}\sigma_i\eta_{i1}c_i\right)}\right)^{(2/\gamma_i)}\right\}, \quad \text{if } t \longrightarrow \infty. \tag{55}$$

From (55), it can be known that s_i will converge to following region:

$$\left|s_i\right| \le \min\left\{\left(\frac{D_{i\max}^d}{(\varepsilon_i\eta_{i1}c_i)}\right), \left(\frac{D_{i\max}^d}{(\sigma_i\eta_{i1}c_i)}\right)^{(1/\gamma_i)}\right\}, \quad \text{if } t \longrightarrow \infty. \tag{56}$$

Then, the synchronization error will converge to following small region:

$$\left|e_i\right| \le \min\left\{\frac{\left(D_{i\max}^d/(\varepsilon_i\eta_{i1}c_i)\right)}{c_i}, \frac{\left(D_{i\max}^d/(\sigma_i\eta_{i1}c_i)\right)^{(1/\gamma_i)}}{c_i}\right\}, \quad \text{if } t \longrightarrow \infty. \tag{57}$$

The proof is finished.

Remark 2. It can be known from (57) that, if large enough observer parameter η_{i1} and the control parameters σ_i, ε_i, and c_i are chosen, then the convergence region of synchronization error will be small enough. It means that the synchronization error can be made arbitrarily small through adjusting parameters properly.

4. Simulation Results

In this section, to illustrate the effectiveness of the proposed methods, the mathematical simulation is presented. The master and slave chaotic systems are selected as the three-dimensional chaotic systems given in [32]. Thus, for systems (1) and (2), we select $n = 3$. The chaotic nonlinear function and uncertainties are chosen as

$$\begin{cases} f_{m1}(X_m,t) = \dfrac{40}{14}x_{m1} - x_{m2}x_{m3} + 10, \\ f_{m2}(X_m,t) = -10x_{m2} + x_{m1}x_{m3}, \\ f_{m3}(X_m,t) = -4x_{m3} + x_{m1}x_{m2}, \\ f_{s1}(X_s,t) = \dfrac{40}{14}x_{s1} - x_{s2}x_{s3} + 10, \\ f_{s2}(X_s,t) = -10x_{s2} + x_{s1}x_{s3}, \\ f_{s3}(X_s,t) = -4x_{s3} + x_{s1}x_{s2}, \\ \Delta f_{s1}(X_s,t) = 3\%x_{s1} + 5\%x_{s2}, \\ \Delta f_{s2}(X_s,t) = 2\%x_{s1} + 7\%x_{s2} + 3\%x_{s3}, \\ \Delta f_{s3}(X_s,t) = -2\%x_{s1} + 3\%x_{s2} + 6\%x_{s3}, \\ d_1(t) = 60\ \cos\left(\dfrac{t}{5}\right) + 20, \\ d_2(t) = 50\ \cos\left(\dfrac{t}{5}\right) + 20, \\ d_3(t) = 40\ \cos\left(\dfrac{u}{5}\right) + 10. \end{cases} \tag{58}$$

The initial system states are set as $x_{m1}(0) = 4$, $x_{m2}(0) = 3.5$, $x_{m3}(0) = 2.5$, and $x_{s1}(0) = x_{s2}(0) = x_{s3}(0) = 0$. The simulation method is chosen as the fixed step Dormand–Prince method. The step size of simulation is set as 0.001s. Let $u_i(t) = 0\,(i = 1, 2, 3)$, and the chaotic behavior of the master system (1) is shown in Figure 1.

For the comparison, the proposed TVGDO-based SMC (46), DO-based SMC (12), and ESO-based SMC (15) are considered in this section.

Case 1. (Initial values of estimate and true states are equal). In this case, the SMC parameters of the three methods are selected as $c_i = 1$, $\varepsilon_{\mathrm{DO}i} = 2$, $\varepsilon_{\mathrm{ESO}i} = 0.5$, $\varepsilon_i = 0.5$, $\sigma_{\mathrm{DO}i} = 12$, $\sigma_{\mathrm{ESO}i} = 7$, $\sigma_i = 2$, and $\gamma_{\mathrm{DO}i} = \gamma_{\mathrm{ESO}i} = \gamma_i = 0.7\,(i = 1, 2, 3)$. Then, it can be known that the initial values of sliding mode surface are $s_1(0) = -4$, $s_2(0) = -3.5$, and $s_3(0) = -2.5$. The observer gains of DO and ESO are chosen as $k_{\mathrm{DO}i} = 50$ and $k_{\mathrm{ESO}i} = 50\,(i = 1, 2, 3)$, respectively. The time-varying parameters are chosen as $\eta_{i1} = 50$ and $\eta_{i1} = 25\,(i = 1, 2, 3)$. Thus, the observer gain of TVGDO $k_i(t)\,(i = 1, 2, 3)$ is close to 50. And, in this case, we consider that the initial value of sliding mode surface $s_i(0)\,(i = 1, 2, 3)$ is known. Then, the initial values of estimate states in DO, ESO, and TVGDO can be chosen as

$$\begin{cases} Z_{\mathrm{DO1}} = s_1(0) = -4, \\ Z_{\mathrm{DO2}} = s_2(0) = -3.5, \\ Z_{\mathrm{DO3}} = s_3(0) = -2.5, \\ Z_{\mathrm{ESO1}} = s_1(0) = -4, \\ Z_{\mathrm{ESO2}} = s_2(0) = -3.5, \\ Z_{\mathrm{ESO3}} = s_3(0) = -2.5, \\ Z_1 = s_1(0) = -4, \\ Z_2 = s_2(0) = -3.5, \\ Z_3 = s_3(0) = -2.5. \end{cases} \tag{59}$$

Thus, for DO, ESO, and TVGDO, the initial values of estimate and true states are equal. Figures 2–5 show the simulation results for Case1. From Figure 2, it is clear that the DO-based SMC, ESO-based SMC, and proposed TVGDO-based SMC all can guarantee the synchronization errors that converge to a small neighborhood of zero. Figure 3 shows that DO, ESO, and TVGDO can ensure the estimation errors converge to a small neighborhood of zero. From Figure 4, it is clear that the control inputs of the three observer-based sling mode controllers are chattering-free. Thus, the undesirable chattering problem in conventional SMC can be solved by employing these observer-based schemes. Figure 5 shows the time-varying observer gains of proposed TVGDO. Thus, the results in Case 1 proved that the control parameters used in Case 1 for the three methods can achieve a similar good performance when the initial values of estimate and true states are equal.

Case 2. (The initial values of estimate and true states are not equal). From the simulation result of Case 1, we have known that the three methods can achieve a similar control performance under the control parameters chosen in Case 1. To ensure the fairness of comparison, the control parameters are selected, the same parameters as in Case 1. And, in this case, we consider that the initial value $s_i(0)\,(i = 1, 2, 3)$ is unknown. The initial values of estimate states of DO, ESO, and TVGDO are chosen as

$$\begin{cases} Z_{\mathrm{DO1}} = 0 \neq s_1(0), \\ Z_{\mathrm{DO2}} = 0 \neq s_2(0), \\ Z_{\mathrm{DO3}} = 0 \neq s_3(0), \\ Z_{\mathrm{ESO1}} = 0 \neq s_1(0), \\ Z_{\mathrm{ESO2}} = 0 \neq s_2(0), \\ Z_{\mathrm{ESO3}} = 0 \neq s_3(0) \\ Z_1 = 0 \neq s_1(0), \\ Z_2 = 0 \neq s_2(0), \\ Z_3 = 0 \neq s_3(0). \end{cases} \tag{60}$$

Thus, for DO, ESO, and TVGDO, the initial values of estimate and true states are not equal.

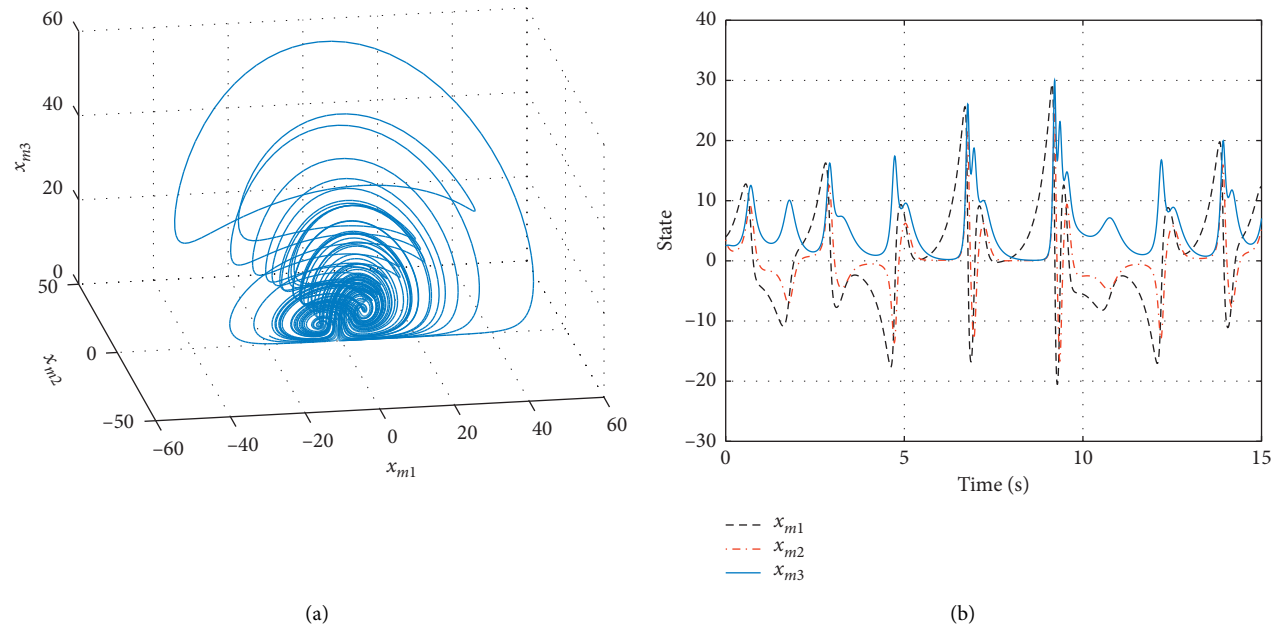

FIGURE 1: Chaotic behavior of the system without the control input. (a) Phase portrait of the system. (b) System states x_1 and x_2.

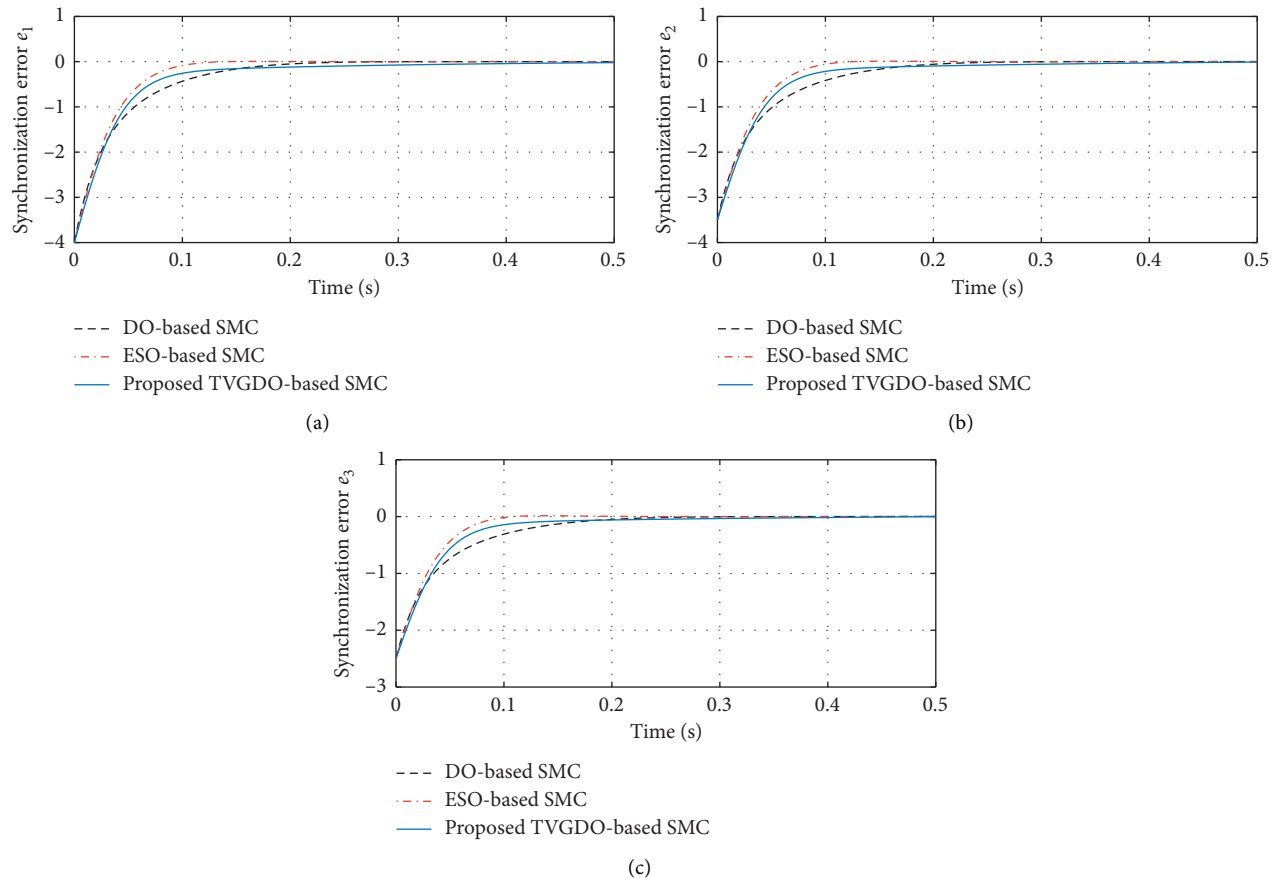

FIGURE 2: Synchronization error (Case 1).

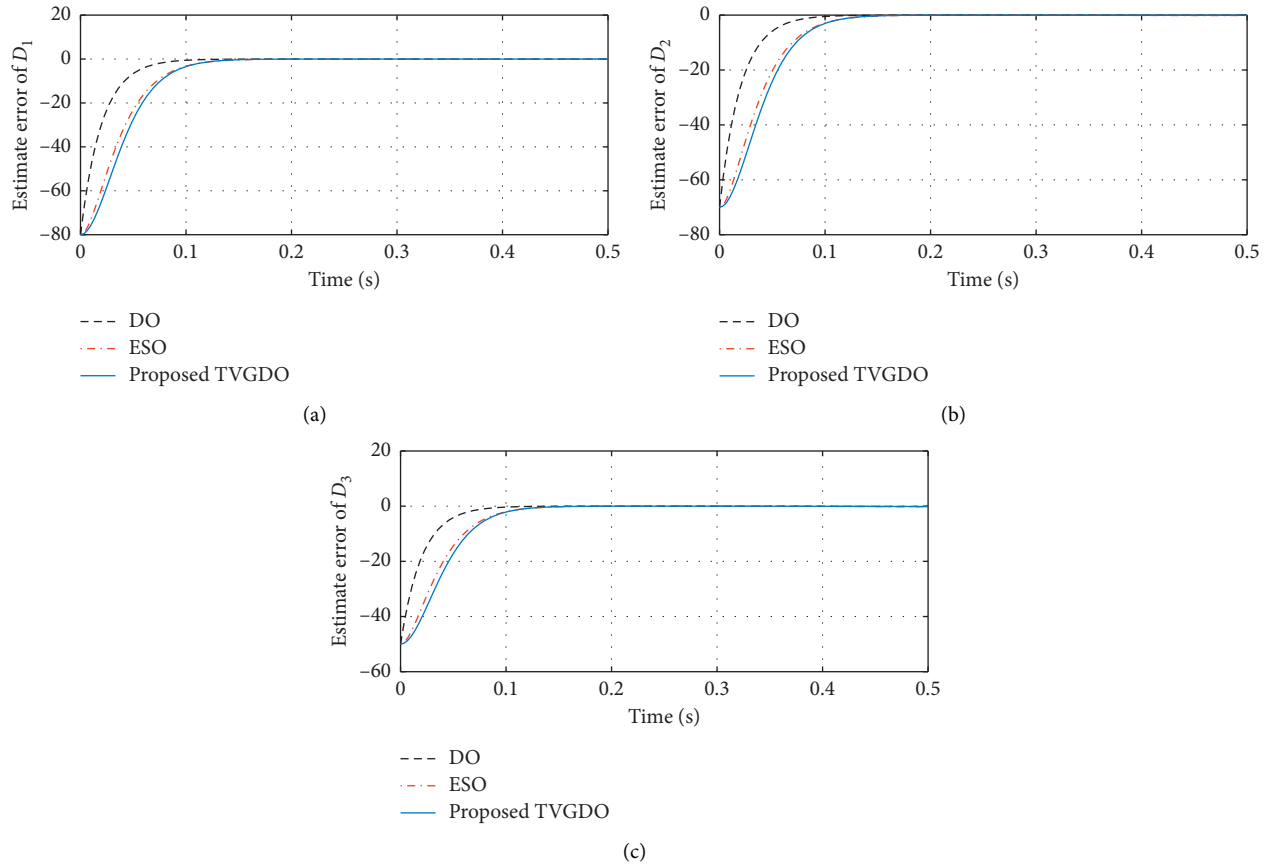

Figure 3: Estimate error (Case 1).

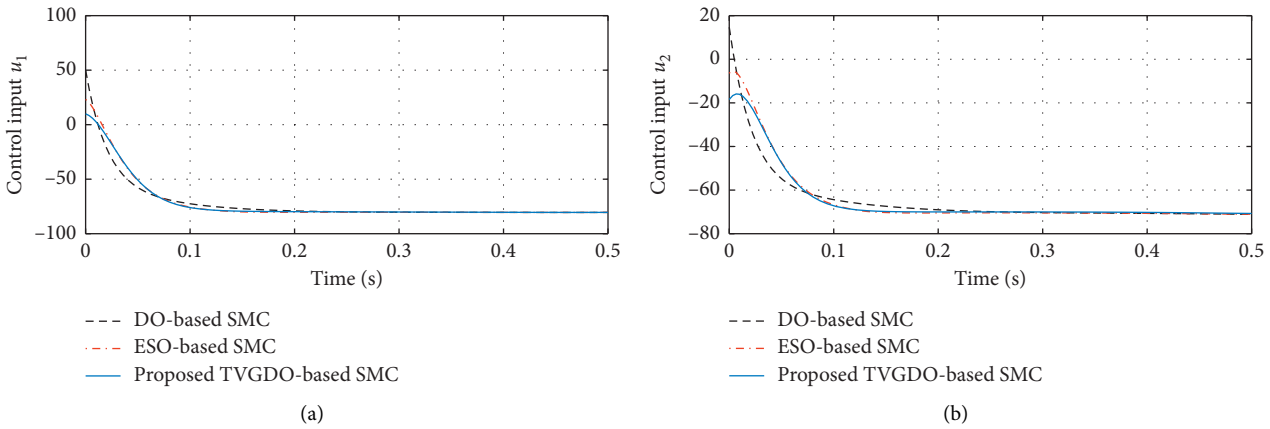

Figure 4: Continued.

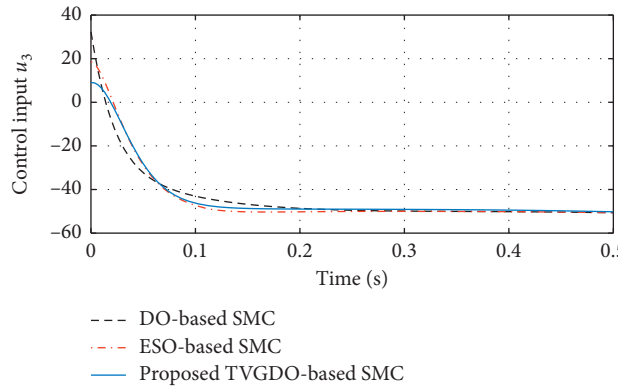

(c)

Figure 4: Control input (Case 1).

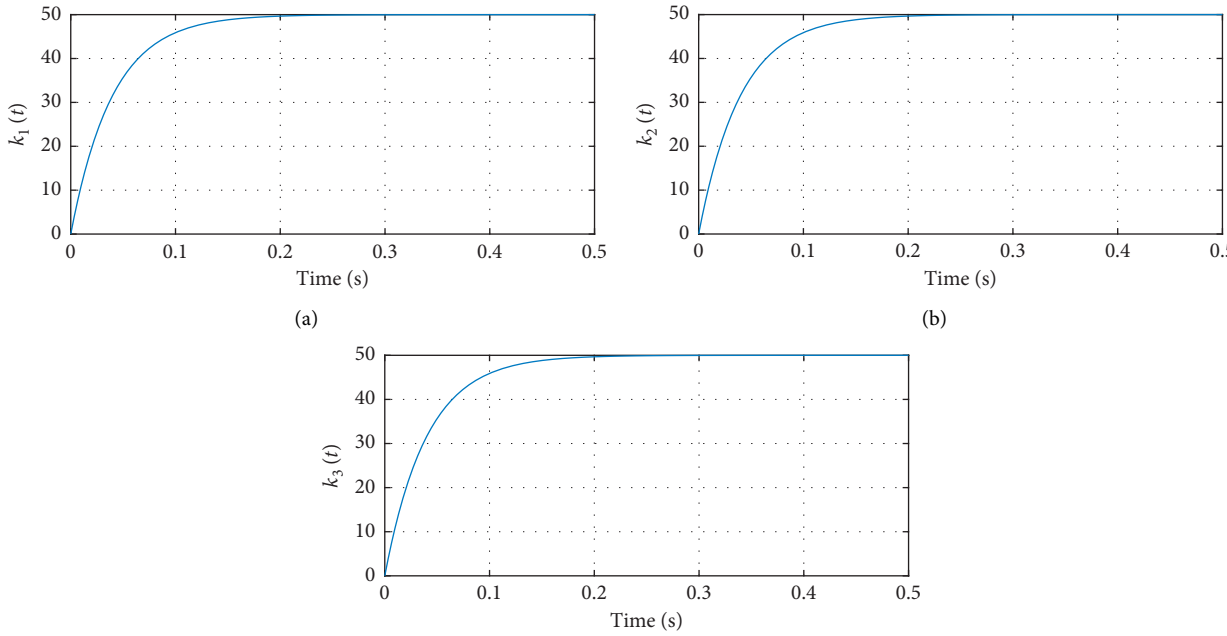

(c)

Figure 5: Observer gain of TVGDO (Case 1).

Figures 6–8 show the simulation results for Case 2. From Figure 6, for DO-based SMC and ESO-based SMC, the undesirable large overshoot of synchronization errors can be observed. And the proposed TVGDO-based SMC can achieve the faster convergence rate than the DO-based and ESO-based schemes. As mentioned before in Section 2.2, the reason is that the spike problem of DO and ESO can be caused by choosing a large observer gain if the initial values of estimate and true states are not equal. Then, the spike output values of observer are transmitted into the control inputs to lead the large overshoot of synchronization errors. The undesirable spike phenomenon of DO and ESO can be observed from Figure 7. Figure 8 shows the undesirable large spike control inputs of DO-based SMC and ESO-based SMC. From Figures 6–8, it is clear that the undesirable spike phenomenon is eliminated in the proposed TVGDO and TVGDO-based SMC. An excellent control performance which is similar to Case 1 still can be guaranteed by the proposed controller and observer. Thus, the spike problem is avoided by the proposed scheme of this study.

According to the simulation results, the following can be concluded:

(1) For conventional ESO and DO, an undesirable spike problem can be caused if the initial values of estimate and true states are not equal. The proposed TVGDO can eliminate the undesirable spike problem (Figures 2–4 and 6–8).

(2) Since the uncertainties have been estimated by proposed TVGDO, the TVGDO-SMC has no

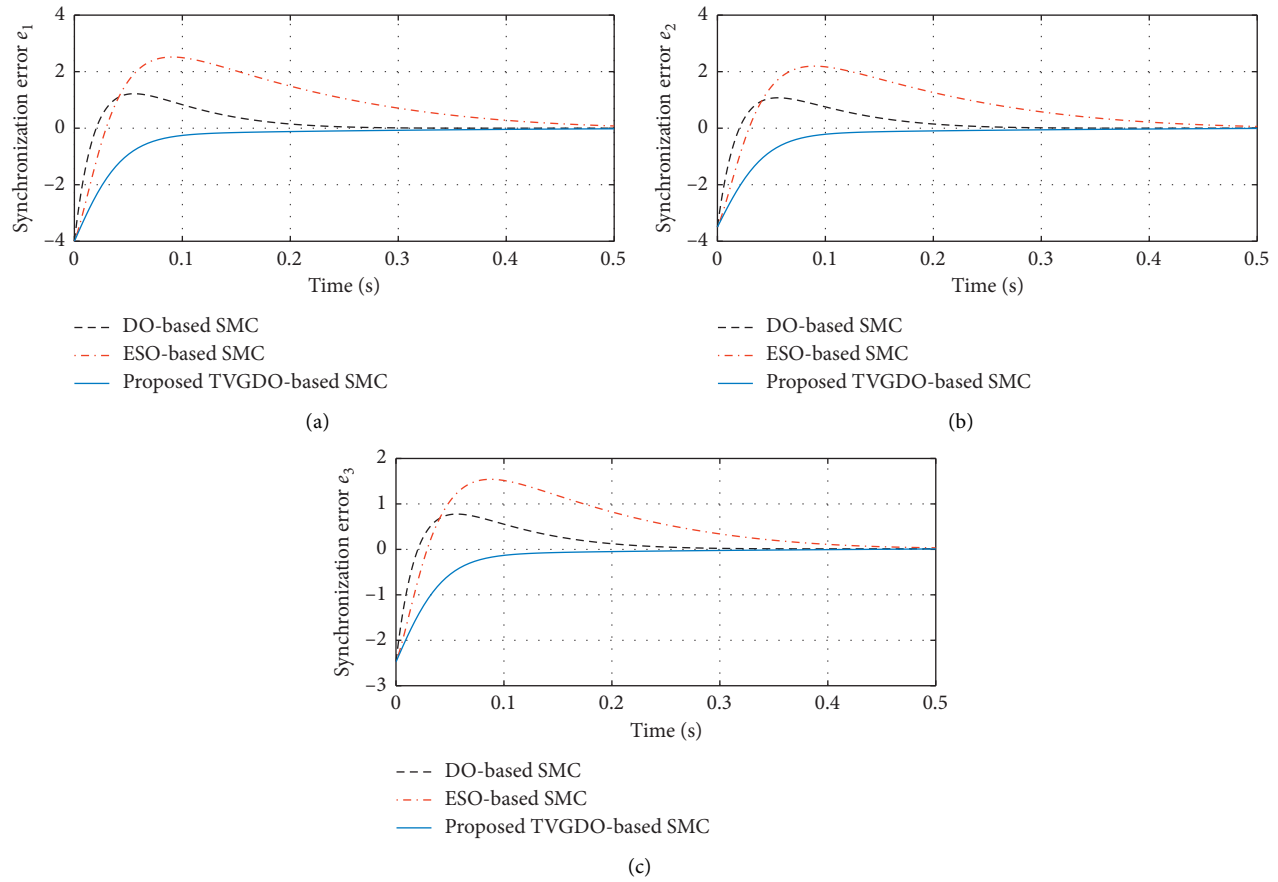

Figure 6: Synchronization error (Case 2).

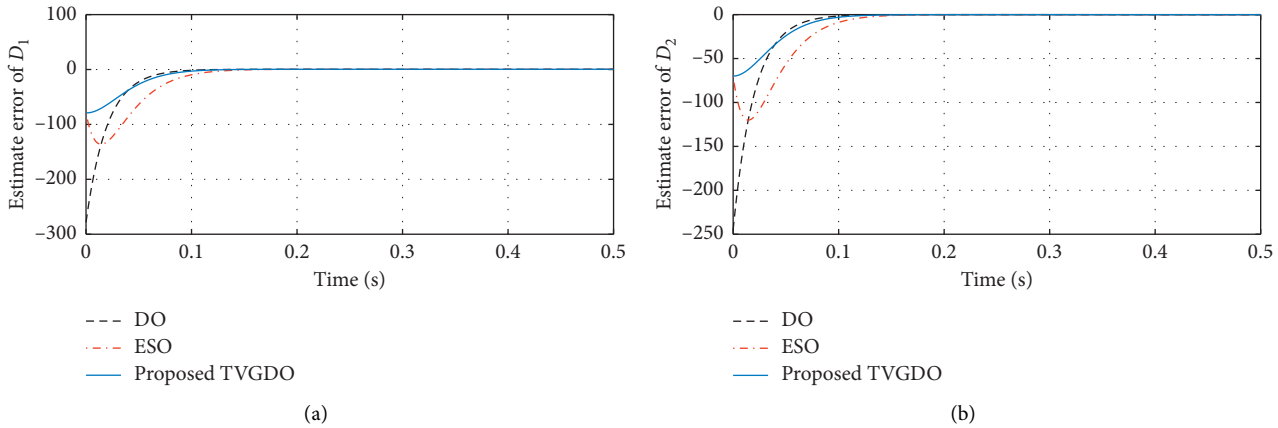

Figure 7: Continued.

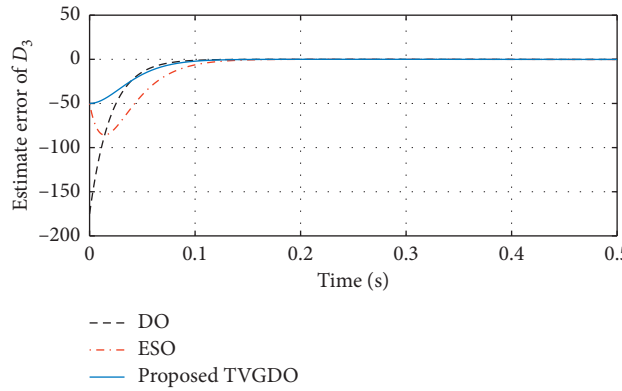

(c)

Figure 7: Estimate error (Case 2).

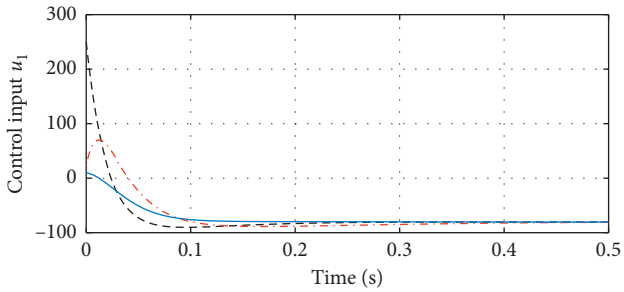

(a)

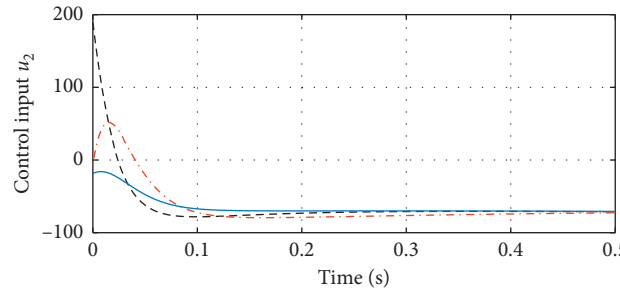

(b)

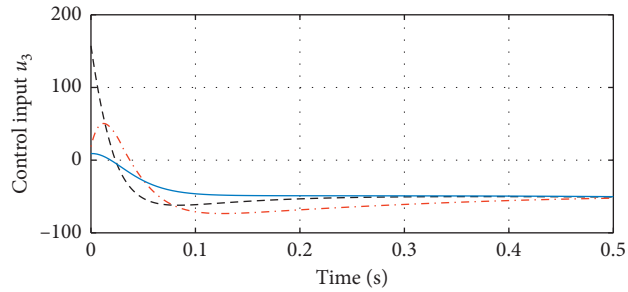

(c)

Figure 8: Control input (Case 2).

discontinuous control term. Thus, the chattering problem in conventional SMC is solved (Figures 4 and 8). And, unlike the conventional SMC, the proposed controller does not need the upper bound of uncertainties.

5. Conclusion

(1) In this study, a novel TVGDO was proposed to estimate the lumped uncertainties and disturbances in the slave chaotic system, which can solve the spike problem in the conventional DO and ESO on the condition of the initial values of estimate and true states are not equal. Moreover, the proposed TVGDO does not need to know the upper bound of uncertainties in advance.

(2) Subsequently, a novel TVGDO-based SMC was proposed to synchronize the chaotic systems. The newly proposed SMC scheme has several advantages over existing SMC. First, the spike problem in the observer-based SMC such as the DO-based and ESO-based SMC is solved by the proposed controller. Second, the chattering problem in the conventional SMC also is avoided in the proposed method. Third, unlike the conventional SMC, the proposed method requires no information on the uncertainties.

(3) Finally, mathematical simulation result illustrated the effectiveness of the TVGDO and the proposed TVGDO-based SMC.

Data Availability

The data used to support the findings of this study are available from the corresponding author upon request.

Conflicts of Interest

The authors declare that there are no conflicts of interest.

Acknowledgments

This work was supported by the Natural Science Basic Research Program of Shaanxi (2021JQ-880, 2021JM-533, and 2020JM-646), the Innovation Capability Support Program of Shaanxi (2018GHJD-21), the Science and Technology Program of Xi'an (2019218414GXRC020CG021-GXYD20.3), and the Fund of Excellent Doctoral Innovation of Xi'an University of Technology and the Scientific Research Foundation of Xijing University (XJ200202).

References

[1] E. N. Lorenz, "Deterministic nonperiodic flow," *Journal of the Atmospheric Sciences*, vol. 20, no. 2, pp. 130–141, 1963.

[2] O. E. Rössler, "An equation for continuous chaos," *Physics Letters A*, vol. 57, no. 5, pp. 397-398, 1976.

[3] J. Lü, G. Chen, D. Cheng, and S. Celikovsky, "Bridge the gap between the Lorenz system and the chen system," *International Journal of Bifurcation and Chaos*, vol. 12, no. 12, pp. 2917–2926, 2002.

[4] K. Koubaâ and M. Feki, "Quasi-periodicity, chaos and co-existence in the time delay controlled two-cell DC-DC buck converter," *International Journal of Bifurcation and Chaos*, vol. 24, no. 10, p. 1450124, 2014.

[5] B. Robert, M. Feki, and H. H. C. Iu, "Control of a pwm inverter using proportional plus extended time-delayed feedback," *International Journal of Bifurcation and Chaos*, vol. 16, no. 1, pp. 113–128, 2006.

[6] J. Oliveira, P. M. Oliveira, J. Boaventura-Cunha, and T. Pinho, "Chaos-based grey wolf optimizer for higher order sliding mode position control of a robotic manipulator," *Nonlinear Dynamics*, vol. 90, no. 2, pp. 1353–1362, 2017.

[7] T. Malica, G. Bouchez, D. Wolfersberger, and M. Sciamanna, "Spatiotemporal complexity of chaos in a phase-conjugate feedback laser system," *Optics Letters*, vol. 45, no. 4, pp. 819–822, 2020.

[8] S. Liu, N. Jiang, A. Zhao, Y. Zhang, and K. Qiu, "Secure optical communication based on cluster chaos synchronization in semiconductor lasers network," *IEEE Access*, vol. 8, pp. 11872–11879, 2020.

[9] H. Zhang, T. Ma, G. B. Huang et al., "Robust global exponential synchronization of uncertain chaotic delayed neural networks via dual-stage impulsive control," *IEEE Transactions on Systems, Man, and Cybernetics, Part B (Cybernetics)*, vol. 40, no. 3, pp. 831–844, 2009.

[10] V. Vesely, A. Ilka, L. Korosi, and M. Ernek, "Master-slave H-Infinity robust controller design for synchronization of chaotic systems," *Modeling, Identification and Control: A Norwegian Research Bulletin*, vol. 40, no. 1, pp. 41–50, 2019.

[11] X. Li, Z. Liu, Z. Qiu, Y. Qi, and S. Yuan, "Event-triggered H ∞ synchronization control for switched master-slave systems subject to stochastic cyber attacks and quantization," *Optimal Control Applications and Methods*, vol. 41, no. 2, pp. 690–708, 2020.

[12] X. Chen, J. H. Park, J. Cao, and J. Qiu, "Adaptive synchronization of multiple uncertain coupled chaotic systems via sliding mode control," *Neurocomputing*, vol. 273, pp. 9–21, 2018.

[13] I. Ahmad and M. Shafiq, "Oscillation free robust adaptive synchronization of chaotic systems with parametric uncertainties," *Transactions of the Institute of Measurement and Control*, vol. 42, no. 11, pp. 1977–1996, 2020.

[14] Z. Peng, D. Wang, H. Zhang et al., "Distributed neural network control for adaptive synchronization of uncertain dynamical multiagent systems," *IEEE Transactions on Neural Networks and Learning Systems*, vol. 25, no. 8, pp. 1508–1519, 2013.

[15] C. Mou, C.-s. Jiang, J. Bin, and Q.-x. Wu, "Sliding mode synchronization controller design with neural network for uncertain chaotic systems," *Chaos, Solitons & Fractals*, vol. 39, no. 4, pp. 1856–1863, 2009.

[16] R. Sakthivel, R. Sakthivel, O.-M. Kwon, P. Selvaraj, and S. M. Anthoni, "Observer-based robust synchronization of fractional-order multi-weighted complex dynamical networks," *Nonlinear Dynamics*, vol. 98, no. 2, pp. 1231–1246, 2019.

[17] T. Wang, J. Ge, T. Li et al., "Observer-based H_∞ control for synchronization in delayed neural networks under multiple disturbances," *International Journal of Control, Automation and Systems*, vol. 18, no. 8, pp. 1–12, 2020.

[18] H. Zhang, X.-K. Ma, and W.-Z. Liu, "Synchronization of chaotic systems with parametric uncertainty using active sliding mode control," *Chaos, Solitons & Fractals*, vol. 21, no. 5, pp. 1249–1257, 2004.

[19] S. Vaidyanathan, S. Sampath, and A. T. Azar, "Global chaos synchronisation of identical chaotic systems via novel sliding mode control method and its application to Zhu system," *International Journal of Modelling, Identification and Control*, vol. 23, no. 1, pp. 92–100, 2015.

[20] A. Zhou and J. Lei, "Research on a novel kind of robust terminal sliding mode synchronization of chaotic systems," *Optik*, vol. 131, pp. 527–538, 2017.

[21] Y. Gao, J. Ren, and M. Zhao, "Projective lag synchronization of second-order chaotic systems via modified terminal sliding mode control," *IMA Journal of Mathematical Control and Information*, vol. 34, no. 3, pp. 1045–1059, 2017.

[22] S. Vaidyanathan and A. Rhif, "A novel four-leaf chaotic system, its control and synchronisation via integral sliding mode control," *International Journal of Modelling, Identification and Control*, vol. 28, no. 1, pp. 28–39, 2017.

[23] S. Lin and W. Zhang, "Chattering reduced sliding mode control for a class of chaotic systems," *Nonlinear Dynamics*, vol. 93, no. 4, pp. 2273–2282, 2018.

[24] H.-T. Yau and C.-L. Chen, "Chattering-free fuzzy sliding-mode control strategy for uncertain chaotic systems," *Chaos, Solitons & Fractals*, vol. 30, no. 3, pp. 709–718, 2006.

[25] M. P. Aghababa and M. E. Akbari, "A chattering-free robust adaptive sliding mode controller for synchronization of two different chaotic systems with unknown uncertainties and external disturbances," *Applied Mathematics and Computation*, vol. 218, no. 9, pp. 5757–5768, 2012.

[26] J. Luo, S. Qu, Z. Xiong, E. Appiagyei, and L. Zhao, "Observer-based finite-time modified projective synchronization of multiple uncertain chaotic systems and applications to secure communication using DNA encoding," *IEEE Access*, vol. 7, pp. 65527–65543, 2019.

[27] X.-T. Tran and H.-J. Kang, "A novel observer-based finite-time control method for modified function projective synchronization of uncertain chaotic (hyperchaotic) systems," *Nonlinear Dynamics*, vol. 80, no. 1-2, pp. 905–916, 2015.

[28] D. Qian, H. Ding, S. G. Lee et al., "Suppression of chaotic behaviors in a complex biological system by disturbance observer-based derivative-integral terminal sliding mode," *IEEE/CAA Journal of Automatica Sinica*, vol. 7, no. 1, pp. 126–135, 2019.

[29] F. Shiravani and M. H. Shafiei, "Robust output regulation via sliding mode control and disturbance observer: application in a forced Van Der Pol chaotic oscillator," *Journal of Dynamic Systems, Measurement, and Control*, vol. 139, no. 9, 2017.

[30] Y. Zhao, X. Li, and P. Duan, "Observer-based sliding mode control for synchronization of delayed chaotic neural networks with unknown disturbance," *Neural Networks*, vol. 117, pp. 268–273, 2019.

[31] F. Abu Khadra, "Tracking control of chaotic systems via optimized active disturbance rejection control," *Mathematical Problems in Engineering*, vol. 2018, Article ID 4698953, 10 pages, 2018.

[32] X. Xi, S. Mobayen, H. Ren, and S. Jafari, "Robust finite-time synchronization of a class of chaotic systems via adaptive global sliding mode control," *Journal of Vibration and Control*, vol. 24, no. 17, pp. 3842–3854, 2018.

Hindawi
Complexity
Volume 2021, Article ID 6618435, 7 pages
https://doi.org/10.1155/2021/6618435

Research Article

Synchronization of a Hyperchaotic Finance System

Huangen Chen,[1] **Lu Yu**,[2] **Yilin Wang**,[3] **and Miaomei Guo**[4]

[1]*School of Business Administration, Southwestern University of Finance and Economics, Chengdu, Sichuan 610074, China*
[2]*School of International Business, Southwestern University of Finance and Economics, Chengdu, Sichuan 610074, China*
[3]*Business School, Guangzhou College of Technology and Business, Guangzhou, China*
[4]*School of Finance and Trade, Wenzhou Business College, Wenzhou, Zhejiang 325035, China*

Correspondence should be addressed to Miaomei Guo; 20209189@wzbc.edu.cn

Received 2 October 2020; Revised 28 February 2021; Accepted 18 March 2021; Published 30 March 2021

Academic Editor: Karthikeyan Rajagopal

In this article, we propose a series of control strategies to synchronize two chaotic financial systems. Due to the characteristics of chaotic systems, the system is very sensitive to its initial values. Thus, the behaviour of two systems with different initial values will be completely different. In order to realize the synchronization of two financial chaotic systems, we designed a series of controls including controllers to realize global asymptotic synchronization and controllers to realize global exponential synchronization to make the two systems fully synchronized. We provide mathematical proofs to show that the designed controls are effective. Numerical methods are used to verify the effectiveness of the controls.

1. Introduction

In recent years, it has been found that there exists chaos in many engineering systems and scientific systems such as chemistry models and ecology models. For example, Lorentz chaotic system family [1–3], Rössler chaotic system [4], and Chua's chaotic circuit [5] have great applications in the field of natural science and engineering. More complex multidimensional, multiscroll, and multiwing chaotic systems have also been studied [6–8]. The dynamic behaviours of chaotic systems with time-delay have also been studied extensively [9–11]. Chaos in many financial systems has also been considered in the literature [12–15]. These models show that the interactions of financial factors can lead to complex phenomena that are difficult to estimate. An important characteristic of chaotic systems is their extreme sensitivity to initial conditions. In chaotic systems, very small initial state differences will lead to great differences in systematic trajectories. Another characteristic of chaotic systems is their global boundedness. The global boundedness of a variety of chaotic systems has been studied in the literature [16–19].

In recent years, the work of Ott, Grebogi, and Yorke (OGY method) [20] has pioneered the academic research of chaos control. Chaos leads to irregular and unpredictable situation. Therefore, eliminating or completely suppressing chaos in nonlinear dynamic systems has practical application value. A variety of control strategies were used to suppress chaos in the literature [21, 22]. Pecora and Carrol [23, 24] have carried out pioneering work on chaos synchronization. In recent years, chaos synchronization has been extensively studied [7, 25–27]. Synchronization of chaotic systems has been studied extensively in recent years. Mu et al. investigated route to broadband optical chaos generation and synchronization using dual-path optically injected semiconductor lasers [28]. Lü et al. studied a new synchronization tracking technique for uncertain discrete network with spatiotemporal chaos behaviours [29]. Lai et al. analysed the synchronization control of an unusual chaotic system with exponential term and coexisting attractors [30]. Yadav et al. studied difference synchronization among three chaotic systems [31]. Zheng et al. studied a hybrid model for construction of digital chaos and local synchronization [32].

In this paper, we consider the chaotic system proposed in [33]. The system presented in [33] is based on a system of differential equations which describes the interactions

between elements in the financial system. The interactions between these elements trigged chaos. Chaos phenomenon will bring unpredictable risks to the financial system. Thus, it is very important to control the system. In this paper, we propose a series of control laws to achieve the synchronization of the system. Our study provides insight into hedging risks in the financial system. The purpose of this article is to apply feedback to controls to this financial model to realize the synchronization of the chaotic system. Furthermore, we adopt the Lyapunov direct method to prove our results. We also use numerical simulations to verify the effectiveness of the designed controls.

The rest of this paper is organized as follows. In Section 2, we present the preliminary of this paper, where the idea of chaos synchronization is outlined. Then, in Section 3, we design control laws for the hyperchaotic financial model. Under such control laws, two systems of the model with different initial conditions are synchronized. We use mathematical analysis to prove the effectiveness of the control laws and use numerical simulation to show the applications of the designed control laws. Conclusions are drawn in Section 4.

2. Preliminary

Tong et al. [33] proposed a hyperchaotic financial system, which is described by the following system of differential equations:

$$\begin{aligned}\dot{x} &= z + (y - a)x + w,\\ \dot{y} &= 1 - by - x^2,\\ \dot{z} &= -x - cz,\\ \dot{w} &= -0.05xz + rw,\end{aligned} \tag{1}$$

where the dot denotes differentiation with respect to time t. System (1) displays complicated dynamical behaviours. As shown in Figure 1, for $a = 0.9$, $b = 0.1$, $c = 1$, and $r = -0.6$, the trajectory of system is a chaotic attractor. By calculating the Lyapunov exponent of system (1), we find that the system has Lyapunov exponents 0.828, 0.046, −0.582, and −0.976. Since the system has two positive Lyapunov exponents, the system is hyperchaotic.

Next, we assume that there are two hyperchaotic financial systems including a drive system with subscript d and a receiving system with subscript r. For system (1), the drive system is given by

$$\begin{aligned}\dot{x}_d &= z_d + (y_d - a)x_d + w_d,\\ \dot{y}_d &= 1 - by_d - x_d^2,\\ \dot{z}_d &= -x_d - cz_d,\\ \dot{w}_d &= -0.05x_dz_d + rw_d.\end{aligned} \tag{2}$$

The corresponding receiving system is obtained as

$$\begin{aligned}\dot{x}_r &= z_r + (y_r - a)x_r + w_r + u_1,\\ \dot{y}_r &= 1 - by_r - x_r^2 + u_2,\\ \dot{z}_r &= -x_r - cz_r + u_3,\\ \dot{w}_r &= -0.05x_rz_r + rw_r + u_4,\end{aligned} \tag{3}$$

where u_1, u_2, u_3, and u_4 are nonlinear controllers to be designed such that drive system (2) and driven system (3) can be synchronized. For this purpose, we obtain the error dynamical system by subtracting equation (2) from equation (3). Thus, the error system is obtained as

$$\begin{aligned}\dot{e}_x &= z_r + (y_r - a)x_r + w_r - (z_d + (y_d - a)x_d + w_d) + u_1,\\ \dot{e}_y &= 1 - by_r - x_r^2 - \left(1 - by_d - x_d^2\right) + u_2,\\ \dot{e}_z &= -x_r - cz_r - (-x_d - cz_d) + u_3,\\ \dot{e}_w &= -0.05x_rz_r + rw_r - (-0.05x_dz_d + rw_d) + u_4,\end{aligned} \tag{4}$$

where $e_x = x_r - x_d$, $e_y = y_r - y_d$, $e_z = z_r - z_d$, and $e_w = w_r - w_d$.

Equation (4) can be simplified as

$$\begin{aligned}\dot{e}_x &= e_z + e_w - ae_x + y_rx_r - y_dx_d + u_1,\\ \dot{e}_y &= -be_y - x_r^2 + x_d^2 + u_2,\\ \dot{e}_z &= -e_x - ce_z + u_3,\\ \dot{e}_w &= re_w - 0.05x_rz_r + 0.05x_dz_d + u_4.\end{aligned} \tag{5}$$

When there is no control, i.e., $u_1 = 0$, $u_2 = 0$, $u_3 = 0$, and $u_4 = 0$ if the two hyperchaotic finance systems have different initial conditions, i.e.,

$$[x_d(t_0),\ y_d(t_0), z_d(t_0), w_d(t_0)] \neq t\,[x_r(t_0),\ y_r(t_0), z_r(t_0), w_r(t_0)]. \tag{6}$$

The trajectories of the two hyperchaotic systems are quite different.

In this work, our aim is to establish appropriate control laws u_1, u_2, u_3, and u_4 such that the drive hyperchaotic financial system (2) and the receiving hyperchaotic system (3) are synchronized. That is, to say, we need

$$\lim_{t \longrightarrow \infty} \mathbf{e}(t) = 0, \tag{7}$$

where $\mathbf{e}(t) = [e_1, e_2, e_3, e_4]^T$.

3. Synchronization Scheme

In this section, we will design a series of control strategies to synchronization two hyperechaotic systems with different initial conditions.

Definition 1. $\forall$ initial condition of drive system (2) $x_d(t_0)$, $y_d(t_0), z_d(t_0)$, and $w_d(t_0) \in R^4$ and the corresponding initial condition of receiving system (3) $x_r(t_0)$, $y_r(t_0), z_r(t_0)$, and $w_r(t_0) \in R^4$, if the zero solution of error system (4) is locally asymptotically stable, then we say

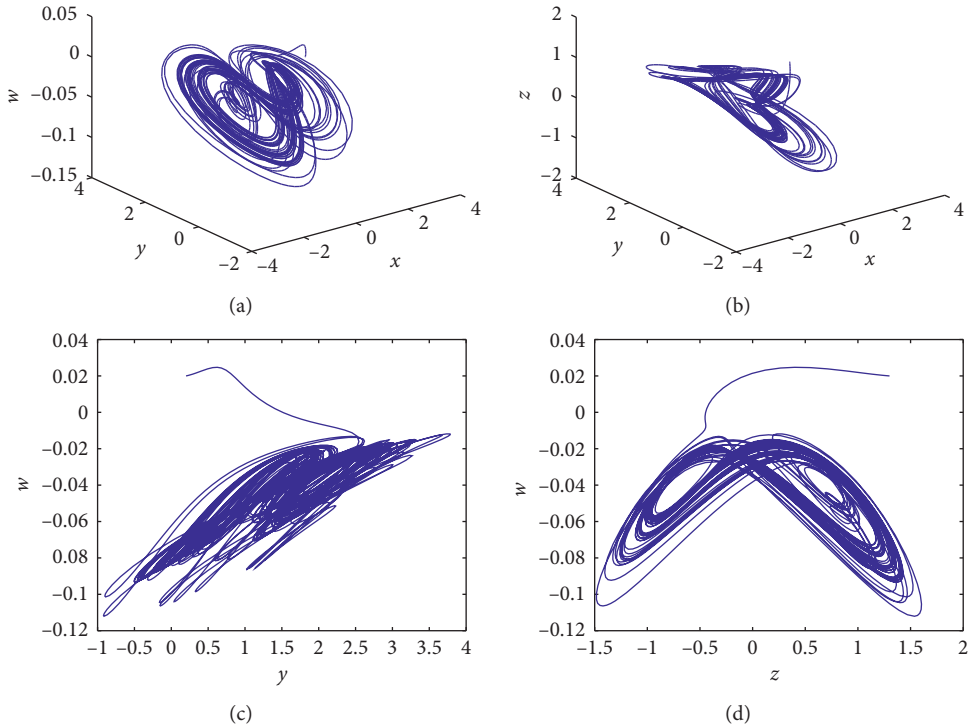

FIGURE 1: Simulation results of system (1) when $a = 0.9$, $b = 0.1$, $c = 1$, and $r = -0.6$ (a) in the x-y-w space, (b) in the x-y-z space, (c) projected on the y-w plane, and (d) projected on the z-w plane.

that drive system (2) and receiving system (18) are locally asymptotically synchronized.

Theorem 1. *For any arbitrary initial conditions, drive system (2) and receiving system (3) are globally asymptotically synchronized by the following control law:*

$$\begin{aligned} u_1 &= -y_r x_r + y_d x_d, \\ u_2 &= x_r^2 - x_d^2, \\ u_3 &= 0, \\ u_4 &= 0.05 x_r z_r - 0.05 x_d z_d. \end{aligned} \tag{8}$$

Proof. Under control law (6), we linearize system (4) at the equilibrium (0,0,0,0) to obtain

$$\begin{bmatrix} -a & 0 & 1 & 1 \\ 0 & -b & 0 & 0 \\ -1 & 0 & -c & 0 \\ 0 & 0 & 0 & r \end{bmatrix}. \tag{9}$$

Matrix (7) has the eigenvalues $\lambda_1 = r$, $\lambda_2 = -b$, $\lambda_3 = -(a/2) - (c/2) + (\sqrt{a^2 - 2ac + c^2 - 4}/2)$, $\lambda_4 = -(a/2) - (c/2) - (\sqrt{a^2 - 2ac + c^2 - 4}/2)$. It can be seen that all these eigenvalues are negative. Therefore, the zero solution of system (4) is locally asymptotically stable. Hence, drive system (2) and driven system (3) are locally asymptotically synchronized with the control law (6). The proof is complete.

In the following, we use numerical simulations to verify that the designed control law (6) is effective. In Figure 2, we plot the time history of error system (4). As shown in the simulation results, the zero solution of system (4) is stable.

Next, we investigate the global exponential synchronization of drive system (2) and the corresponding receiving system (3). □

Definition 2. $\forall$ initial condition of drive system (2) $x_d(t_0)$, $y_d(t_0)$, $z_d(t_0)$ and $w_d(t_0) \in R^4$, and the corresponding initial condition of receiving system (3) $x_r(t_0)$, $y_r(t_0)$, $z_r(t_0)$ and $w_r(t_0) \in R^4$, if the zero solution of error system (4) satisfies the inequality

$$e_x^2(t) + e_y^2(t) + e_z^2(t) + e_w^2(t) \leq \beta(e(t_0))e^{-\mu t}, \tag{10}$$

where $\beta(e(t_0))$ is a constant depending on $e(t_0)$ and $\mu > 0$, then the zero solution of (4) is globally, exponentially stable, that is, system (2) and system (3) are globally, exponentially synchronized.

Theorem 2. *For any arbitrary initial conditions, the drive system (2) and the receiving system (3) are globally exponentially synchronized under the following control law:*

$$\begin{aligned} u_1 &= -y_r x_r + y_d x_d - e_w, \\ u_2 &= x_r^2 - x_d^2, \\ u_3 &= 0, \\ u_4 &= 0.05 x_r z_r - 0.05 x_d z_d. \end{aligned} \tag{11}$$

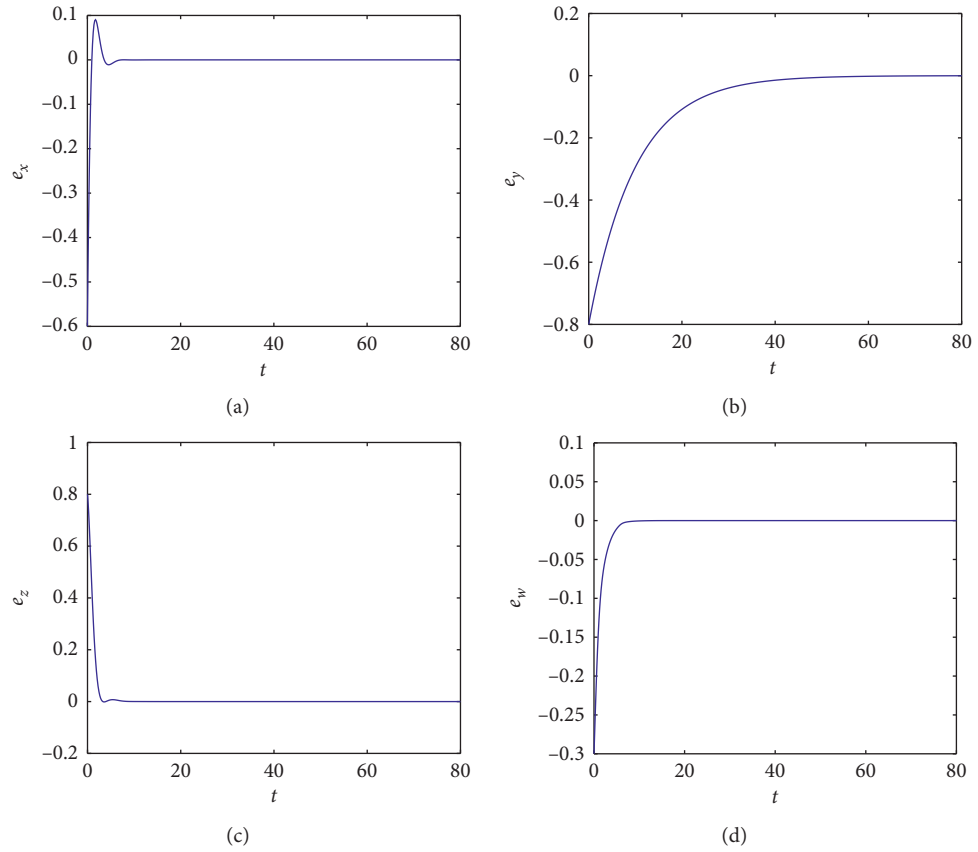

Figure 2: Time history of error system (4) under the control law given in Theorem 1. The values of parameters are the same as those in Figure 1.

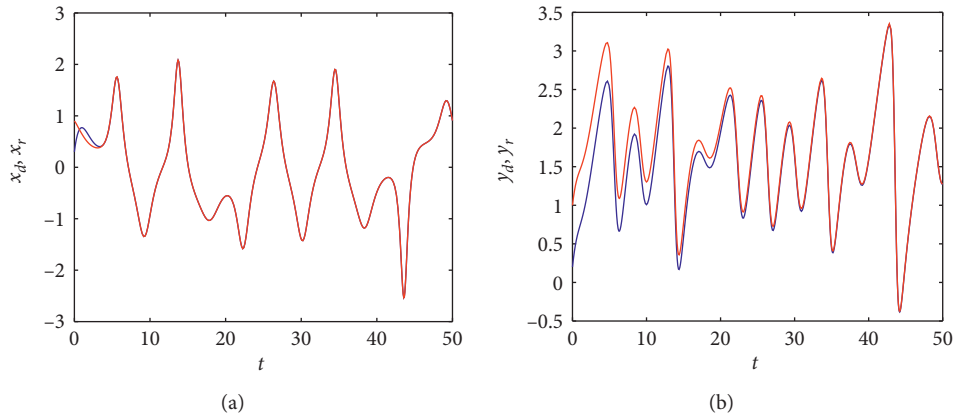

Figure 3: Continued.

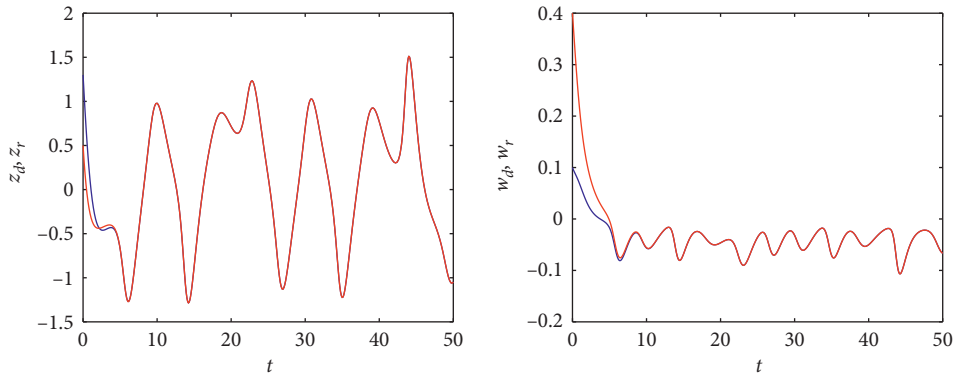

Figure 3: Time histories of drive system (2) (blue curve) and driven system (3) (red curve) under the control law given in Theorem 2.

Proof. For system (4), we design positive definite, radially unbounded Lyapunov function

$$V = e_x^2 + e_y^2 + e_z^2 + e_z^2. \tag{12}$$

We then calculate the derivative of V along the trajectory of system (4) with control law (8). Then, we have

$$\begin{aligned}\frac{dV}{dt} &= 2e_x\dot{e}_x + 2e_y\dot{e}_y + 2e_z\dot{e}_z + 2e_w\dot{e}_w = 2e_x\left(e_z - ae_x\right) + 2e_y\left(-be_y\right) + 2e_z\left(-e_x - ce_z\right) + 2e_w\left(re_w\right)\\ &= 2e_xe_z - 2ae_x^2 - 2be_y^2 - 2e_xe_z - 2ce_z^2 + 2re_w^2\\ &= -2ae_x^2 - 2be_y^2 - 2ce_z^2 + 2re_w^2\\ &= \begin{bmatrix} e_x \\ e_y \\ e_z \\ e_w \end{bmatrix}^T \begin{bmatrix} -2a & 0 & 0 & 0 \\ 0 & -2b & 0 & 0 \\ 0 & 0 & -2c & 0 \\ 0 & 0 & 0 & 2r \end{bmatrix} \begin{bmatrix} e_x \\ e_y \\ e_z \\ e_w \end{bmatrix}.\end{aligned} \tag{13}$$

Therefore, the zero solution of (4) is globally, exponentially stable, and thus systems (2) and (3) are globally, exponentially synchronized.

Now, we use numerical method to verify that the control law proposed in Theorem 2 is correct. In Figure 3, we plot the time histories of both drive system (2) and receiving system (3) in the same figure. Here, the time history of system (2) is plotted using blue curve, and the time history of the receiving system is plotted using red curve. As shown in Figure 3, the control strategy proposed in Theorem 2 is effective.

The chaos in the financial system makes it difficult to predict, which poses a challenge to the analysis of the system. By designing chaos synchronization schemes, two chaotic financial systems can behave synchronously and are beneficial to the control and early warning of financial risks. Specifically, on the one hand, synchronized financial systems are controllable. On the other hand, since the behaviours of the drive system and the driven systems are synchronized, we can use the drive system to predict the behaviours of the driven systems to forecast potential financial risks. □

4. Conclusions

In this work, we investigate the synchronization of a financial hyperchaotic system. Through studying the properties of the model, we design appropriate control strategies to synchronize the two such financial systems with different initial conditions. We provide mathematical proofs showing the effectiveness of the control law. Moreover, we conduct numerical simulations to confirm that the designed control strategies are effective and applicable. Therefore, the controls proposed in this paper provide methods for achieving synchronous chaotic systems. This is a major contribution of

this work because the chaotic behaviour of a financial system creates uncertainty and unpredictable risk. In contrast, a synchronized financial system can be predicted, and thus the risk is hedged. In short, this study provides insights into the risk management of chaotic financial systems.

The method to realize chaotic synchronization is not unique. In this work, we only design a few synchronization methods for the system. In our future work, we will design more strategies to achieve synchronizations for a variety of chaotic systems. Surely, this method could also be implemented in other fields such as supply chain management, especially the application mentioned in studies [34–36].

Data Availability

No data were used to support this study.

Conflicts of Interest

The authors declare that they have no conflicts of interest.

References

[1] E. N. Lorenz, "Deterministic nonperiodic flow," *Journal of the Atmospheric Sciences*, vol. 20, no. 2, pp. 130–141, 1963.

[2] G. Chen and T. Ueta, "Yet another chaotic attractor," *International Journal of Bifurcation and Chaos*, vol. 09, no. 7, pp. 1465-1466, 1999.

[3] J. Lü and G. Chen, "A new chaotic attractor coined," *International Journal of Bifurcation and Chaos*, vol. 12, no. 3, pp. 659–661, 2002.

[4] O. E. Rössler, "An equation for continuous chaos," *Physics Letters A*, vol. 57, no. 5, pp. 397-398, 1976.

[5] L. Chua, M. Komuro, and T. Matsumoto, "The double scroll family," *IEEE Transactions on Circuits and Systems*, vol. 33, no. 11, pp. 1072–1118, 1986.

[6] F. Xu, P. Yu, and X. Liao, "Global analysis on n-scroll chaotic attractors of modified Chua's circuit," *International Journal of Bifurcation and Chaos*, vol. 19, no. 1, pp. 135–157, 2009.

[7] F. Xu, P. Yu, and X. Liao, "Synchronization and stabilization of multi-scroll integer and fractional order chaotic attractors generated using trigonometric functions," *International Journal of Bifurcation and Chaos*, vol. 23, no. 8, p. 1350145, 2013.

[8] F. Xu, "A class of integer order and fractional order hyperchaotic systems via the Chen system," *International Journal of Bifurcation and Chaos*, vol. 26, no. 6, p. 1650109, 2016.

[9] P. Yu and F. Xu, "A common phenomenon in chaotic systems linked by time delay," *International Journal of Bifurcation and Chaos*, vol. 16, no. 12, pp. 3727–3736, 2006.

[10] M. Jiang, Y. Shen, J. Jian, and X. Liao, "Stability, bifurcation and a new chaos in the logistic differential equation with delay," *Physics Letters A*, vol. 350, no. 3-4, pp. 221–227, 2006.

[11] S. Wang, S. He, A. Yousefpour, H. Jahanshahi, R. Repnik, and M. Perc, "Chaos and complexity in a fractional-order financial system with time delays," *Chaos, Solitons and Fractals*, vol. 131, p. 109521, 2020.

[12] J.-H. Ma and Y.-S. Chen, "Study for the bifurcation topological structure and the global complicated character of a kind of nonlinear finance system (i)," *Applied Mathematics and Mechanics*, vol. 22, no. 11, pp. 1240–1251, 2001.

[13] J.-H. Ma and Y.-S. Chen, "Study for the bifurcation topological structure and the global complicated character of a kind of nonlinear finance system (ii)," *Applied Mathematics and Mechanics*, vol. 22, no. 12, pp. 1375–1382, 2001.

[14] F. Xu, Y. Lai, and X.-B. Shu, "Chaos in integer order and fractional order financial systems and their synchronization," *Chaos, Solitons & Fractals*, vol. 117, pp. 125–136, 2018.

[15] F. Zhang, G. Yang, Y. Zhang, X. Liao, and G. Zhang, "Qualitative Study of a 4D Chaos Financial System," *Complexity*, vol. 2018, Article ID 3789873, , 2018.

[16] G. A. Leonov, "Bounds for attractors and the existence of homoclinic orbits in the Lorenz system," *Journal of Applied Mathematics and Mechanics*, vol. 65, no. 1, pp. 19–32, 2001.

[17] F. Zhang, X. Liao, and G. Zhang, "On the global boundedness of the Lü system," *Applied Mathematics and Computation*, vol. 284, pp. 332–339, 2016.

[18] F. Zhang and G. Zhang, "Dynamics of a low-order atmospheric circulation chaotic model," *Optik*, vol. 127, no. 8, pp. 4105–4108, 2016.

[19] F. Zhang, R. Chen, and X. Chen, "Analysis of a Generalized Lorenz–Stenflo Equation," *Complexity*, vol. 2017, Article ID 7520590, , 2017.

[20] E. Ott, C. Grebogi, and J. A. Yorke, "Controlling chaos," *Physical Review Letters*, vol. 64, no. 11, pp. 1196–1199, 1990.

[21] L. Chen and G. Chen, "Controlling chaos in an economic model," *Physica A: Statistical Mechanics and Its Applications*, vol. 374, no. 1, pp. 349–358, 2007.

[22] K. B. Kim, J. B. Park, Y. H. Choi, and G. Chen, "Control of chaotic dynamical systems using radial basis function network approximators," *Information Sciences*, vol. 130, no. 1-4, pp. 165–183, 2000.

[23] L. M. Pecora and T. L. Carroll, "Synchronization in chaotic systems," *Physical Review Letters*, vol. 64, no. 8, pp. 821–824, 1990.

[24] T. L. Carroll and L. M. Pecora, "Synchronizing chaotic circuits," *IEEE Transactions on Circuits and Systems*, vol. 38, no. 4, pp. 453–456, 1991.

[25] X. Wu, G. Chen, and J. Cai, "Chaos synchronization of the master-slave generalized Lorenz systems via linear state error feedback control," *Physica D: Nonlinear Phenomena*, vol. 229, no. 1, pp. 52–80, 2007.

[26] F. Xu and P. Yu, "Global stabilization and synchronization of n-scroll chaotic attractors in a modified Chua's circuit with hyperbolic tangent function," *International Journal of Bifurcation and Chaos*, vol. 19, no. 8, pp. 2563–2572, 2009.

[27] C. Liu, Z. Yang, D. Sun, X. Liu, and W. Liu, "Synchronization of chaotic systems with time delays via periodically intermittent control," *Journal of Circuits, Systems and Computers*, vol. 26, no. 9, p. 1750139, 2017.

[28] P. Mu, W. Pan, L. Yan, B. Luo, and X. Zou, "Route to broadband optical chaos generation and synchronization using dual-path optically injected semiconductor lasers," *Optik*, vol. 124, no. 21, pp. 4867–4872, 2013.

[29] L. Lü, L. Chen, S. Bai, and G. Li, "A new synchronization tracking technique for uncertain discrete network with spatiotemporal chaos behaviors," *Physica A Statistical Mechanics and its Applications*, vol. 460, pp. 314–325, 2016.

[30] Q. Lai, A. Akgul, M. Varan, J. Kengne, and A. Turan Erguzel, "Dynamic analysis and synchronization control of an unusual chaotic system with exponential term and coexisting attractors," *Chinese Journal of Physics*, vol. 56, no. 6, pp. 2837–2851, 2018.

[31] V. K. Yadav, V. K. Shukla, and S. Das, "Difference synchronization among three chaotic systems with exponential term and its chaos control," *Chaos, Solitons and Fractals*, vol. 124, pp. 36–51, 2019.

[32] J. Zheng, H. Hu, H. Ming, and Y. Zhang, "Design of a hybrid model for construction of digital chaos and local synchronization," *Applied Mathematics and Computation*, vol. 392, p. 125673, 2021.
[33] X.-J. Tong, M. Zhang, Z. Wang, Y. Liu, and J. Ma, "An image encryption scheme based on a new hyperchaotic finance system," *Optik*, vol. 126, no. 20, pp. 2445–2452, 2015.
[34] J. Li, L. Yi, V. Shi, and X. Chen, "Supplier encroachment strategy in the presence of retail strategic inventory: centralization or decentralization?" *Omega*, vol. 98, p. 102213, 2021.
[35] P. He, Z. Wang, V. Shi, and Y. Liao, "The direct and cross effects in a supply chain with consumers sensitive to both carbon emissions and delivery time," *European Journal of Operational Research*, vol. 292, no. 1, pp. 172–183, 2021.
[36] F. Wang, A. Diabat, and L. Wu, "Supply chain coordination with competing suppliers under price-sensitive stochastic demand," *International Journal of Production Economics*, vol. 234, p. 108020, 2021.

Hindawi
Complexity
Volume 2021, Article ID 6402459, 15 pages
https://doi.org/10.1155/2021/6402459

Research Article

Further Study on Dynamics for a Fractional-Order Competitor-Competitor-Mutualist Lotka–Volterra System

Bingnan Tang

Business School, Jiangsu University of Technology, Changzhou 213001, China

Correspondence should be addressed to Bingnan Tang; regales1988@sina.com

Received 11 June 2020; Accepted 28 January 2021; Published 22 February 2021

Academic Editor: Karthikeyan Rajagopal

On the basis of the previous publications, a new fractional-order prey-predator model is set up. Firstly, we discuss the existence, uniqueness, and nonnegativity for the involved fractional-order prey-predator model. Secondly, by analyzing the characteristic equation of the considered fractional-order Lotka–Volterra model and regarding the delay as bifurcation variable, we set up a new sufficient criterion to guarantee the stability behavior and the appearance of Hopf bifurcation for the addressed fractional-order Lotka–Volterra system. Thirdly, we perform the computer simulations with Matlab software to substantiate the rationalisation of the analysis conclusions. The obtained results play an important role in maintaining the balance of population in natural world.

1. Introduction

For a long time, the dynamic characteristics of interaction between predator population and prey population has been a central issue in ecology and biomathematics due to its general appearance and potential importance [1]. General speaking, the interaction between predator population and prey population includes four cases: competition, predation, mutualism, and parasitism [2]. During the past few decades, a great deal of valuable research fruits on dynamical behavior of the above four-type predator-prey models has been covered. For example, Alidousti and Ghafari [3] investigated the Hopf bifurcation and limit cycle of the fractional-order predator-prey model; Sasmal and Takeuchi [4] studied the stability behavior of all equilibria, bifurcation nature, global features, and multistability of a predator-prey model; Ryu and Ko [5] discussed the asymptotic peculiarity for positive solutions for a prey-predator model; Guo et al. [6] proved the appearance of traveling waves in a prey-predator system. Zhang et al. [7] revealed the effect of the fear factor on the periodic solution of a prey-predator model. As for concrete works, we refer the readers to [8–25].

In real life, any biological or environmental coefficients will change with time. So, the parameters in predator-prey models are usually not fixed constants. They are often functions with respect to time. In particular, the influence of a periodically varying environment on the dynamics of predator-prey models plays a vital role in maintaining population balance. Furthermore, the capture of the prey from the predator throughout its past time has an important effect on the present birth rate of the predator [26, 27]. Thus, it is of importance to establish the various type predator-prey models with periodic coefficients. Based on this idea, in 2010, Lv et al. [27] established the predator-prey model involving periodic coefficients as follows:

$$\begin{cases} \dot{u}_1(t) = u_1(t)\left[\gamma_1(t) - \alpha_{11}(t)u_1\left(t-\sigma_{11}(t)\right) - \alpha_{12}(t)u_2\left(t-\sigma_{12}(t)\right) + \alpha_{13}(t)u_3\left(t-\sigma_{13}(t)\right)\right], \\ \dot{u}_2(t) = u_2(t)\left[\gamma_2(t) - \alpha_{21}(t)u_1\left(t-\sigma_{21}(t)\right) - \alpha_{22}(t)u_2\left(t-\sigma_{22}(t)\right) + \alpha_{23}(t)u_3\left(t-\sigma_{23}(t)\right)\right], \\ \dot{u}_3(t) = u_3(t)\left[\gamma_3(t) + \alpha_{31}(t)u_1\left(t-\sigma_{31}(t)\right) + \alpha_{32}(t)u_2\left(t-\sigma_{32}(t)\right) - \alpha_{33}(t)u_3\left(t-\sigma_{33}(t)\right)\right], \end{cases} \tag{1}$$

where $u_1(t)$ and $u_2(t)$ stand for the densities of competing species at time t, $u_3(t)$ stands for the density of cooperating species at time t, And $\gamma_l, \alpha_{lk} \in C(R, [0,\infty))$ and $\sigma_{lk} \in C(R,R)$ denote ψ-periodic function ($\psi > 0$). The parameter $\sigma_{lk}(t) \geq 0 (l,k = 1,2,3)$ is the delay. Applying the fixed point theory and constructing Lyapunov functions, Lv et al. [27] set up the condition to ensure the global stability of periodic solutions for model (1). For details, one can see [27].

To reveal the Hopf bifurcation nature of model (1), Xu [26] assumes that all biological and environmental coefficients remain constants and only the feedback time delays of all species $u_i (i = 1,2,3)$ to the growth of the species themselves exist and are same [26]. Then, model (1) is rewritten as the following form:

$$\begin{cases} \dot{u}_1(t) = u_1(t)\left[\gamma_1 - \alpha_{11}u_1(t-\sigma) - \alpha_{12}u_2(t) + \alpha_{13}u_3(t)\right], \\ \dot{u}_2(t) = u_2(t)\left[\gamma_2 - \alpha_{21}u_1(t) - \alpha_{22}u_2(t-\sigma) + \alpha_{23}u_3(t)\right], \\ \dot{u}_3(t) = u_3(t)\left[\gamma_3 + \alpha_{31}u_1(t) + \alpha_{32}u_2(t) - \alpha_{33}u_3(t-\sigma)\right]. \end{cases} \tag{2}$$

With the Hopf bifurcation theory, normal form theory, and center manifold principle, Xu [26] obtained a sufficient condition to guarantee the stability behavior and the appearance for bifurcation phenomenon of model (2). Also, they have derived the concrete expression to find the nature of bifurcation periodic solution.

However, the mentioned works above are only restricted to the integer-order differential systems. Recently, the dynamics of fractional-order dynamical models has attracted great attention of many authors due to their extensive application in numerous areas, such as electromagnetic waves, medicine, mechanics, network science, biology, and finance [28–30]. Many scholars argue that fractional calculus is a powerful tool to depict real phenomena of the object world due to its owned hereditary and memory properties of various practical dynamical models [31]. In recent several decades, fractional calculus has attracted more and more attention from a large number of researchers in various fields. In particular, a great deal of interesting fruits on various dynamical natures of prey-predator systems has sprung up. For instance, Mondal et al. [32] derived the condition to ensure the stability behavior for a class of fractional-order prey-predator system; El-Saka et al. [33] analyzed the local stability and bifurcation of fractional-order predator-prey models; Li et al. [34] dealt with the dynamical property of the solutions and global asymptotic stability for a class of fractional-order prey-predator system. For more relational publications, one can see [35–37]. Here, we particularly emphasize that the study on Hopf bifurcation for fractional-order dynamical models starts relatively late. Up to now, only a few literatures have been published. For example, Alidousti [38] investigated the bifurcation phenomenon of a fractional-order predator-prey model; Huang et al. [30] proposed a novel control technique of bifurcation for a fractional-order prey-predator model with delays; Xu et al. [39] revealed the effect of two delays on bifurcation for fractional-order neural networks. Xiao et al. [40] put up PD control way for Hopf bifurcations of fractional-order networks. As for more related literatures, one can see [41–44].

In terms of the above analysis, we think that it is meaningful for us to study the dynamics (especially Hopf bifurcation) of fractional-order prey-predator models. Based on the previous predator-prey model (2) and assuming that the feedback time delays of all species $u_i (i = 1,2,3)$ to the growth of the species themselves and other species exists are same, then we propose the following fractional-order competitor-competitor-mutualist Lotka–Volterra system:

$$\begin{cases} \dfrac{\mathrm{d}^{\varrho}u_1(t)}{\mathrm{d}t^{\varrho}} = u_1(t)\left[\gamma_1 - \alpha_{11}u_1(t-\sigma) - \alpha_{12}u_2(t-\sigma) + \alpha_{13}u_3(t-\sigma)\right], \\ \dfrac{\mathrm{d}^{\varrho}u_2(t)}{\mathrm{d}t^{\varrho}} = u_2(t)\left[\gamma_2 - \alpha_{21}u_1(t-\sigma) - \alpha_{22}u_2(t-\sigma) + \alpha_{23}u_3(t-\sigma)\right], \\ \dfrac{\mathrm{d}^{\varrho}u_3(t)}{\mathrm{d}t^{\varrho}} = u_3(t)\left[\gamma_3 + \alpha_{31}u_1(t-\sigma) + \alpha_{32}u_2(t-\sigma) - \alpha_{33}u_3(t-\sigma)\right], \end{cases} \tag{3}$$

where $u_1(t)$ and $u_2(t)$ stand for the densities of competing population and $u_3(t)$ stands for the density of cooperating population, $\gamma_l, \alpha_{lk} \in CR, [0,\infty) (l,k = 1,2,3)$, the parameter $\sigma \geq 0$ is the feedback time delay of different species, and $\varrho \in (0,1]$ is a constant. For more concrete meaning of coefficients for system (3), see [26, 27].

The initial condition of system (3) takes the form

$$\begin{cases} u_1(\vartheta) = u_{1\vartheta}, & -\sigma \leq \vartheta \leq t_0, \\ u_2(\vartheta) = u_{2\vartheta}, & -\sigma \leq \vartheta \leq t_0, \\ u_3(\vartheta) = u_{3\vartheta}, & -\sigma \leq \vartheta \leq t_0, \end{cases} \tag{4}$$

where $t_0 > 0$ is a constant. The key object of this work focuses on existence, uniqueness, nonnegativity, stability, and bifurcation phenomenon of model (3). Different from the methodology in [26, 27], in this paper, we will mainly discuss the various dynamics by applying fractional-order differential equation theory. Due to the introduction of fractional order, various dynamical behaviors of the predator-prey model (3) are different from the integer-order case. We think that it is necessary to reveal the effect of time delay, parameters of system, and fractional order on dynamics such as the stability and Hopt bifurcation. Thus, this study has significance in theory and practice.

We plan the structure of this manuscript as follows. Section 2 gives some related knowledge about fractional-order dynamical systems. Section 3 discusses the existence,

uniqueness, nonnegativity, local stability, and Hopf bifurcation of model (3). Section 4 gives an example to support the effectiveness of the obtained key conclusions. Section 6 ends our work.

2. Basic Knowledge

In this part, we present several related definitions and lemmas on fractional-order dynamical systems that will be applied in the later proof. Let R_+ represent the set of all nonnegative real numbers.

Definition 1. (see [45]). Define Caputo fractional-order derivative as follows:

$$\mathscr{D}^{\varrho}h(w) = \frac{1}{\Gamma(n-\varrho)}\int_{w_0}^{w}\frac{h^{(l)}(s)}{(w-s)^{w-l+1}}\mathrm{d}s, \tag{5}$$

where $h(w) \in ([w_0,\infty), R), \Gamma(s) = \int_0^{\infty} w^{s-1}e^{-w}\mathrm{d}w$, $w \geq w_0$, and $l \in Z^+, l-1 \leq \varrho < l$.

The Laplace transform of Caputo fractional-order derivative is defined as follows:

$$\mathscr{L}\{\mathscr{D}^{\varrho}h(t);s\} = s^{\varrho}\mathscr{H}(s) - \sum_{j=0}^{m-1} s^{\varrho-j-1}h^{(j)}(0), \quad m-1 \leq \varrho < m \in Z^+, \tag{6}$$

where $\mathscr{H}(s) = \mathscr{L}\{h(t)\}$. Especially, if $h^{(j)}(0) = 0, j = 1,2,\ldots,m$, then $\mathscr{L}\{\mathscr{H}^{\varrho}h(t);s\} = s^{\varrho}\mathscr{H}(s)$.

Definition 2 (see [46]). (v_{1*}, v_{2*}, v_{3*}) is called an equilibrium point of model (3) provided that the following system

$$\begin{cases} v_{1*}(\gamma_1 - \alpha_{11}v_{1*} - \alpha_{12}v_{2*} + \alpha_{13}v_{3*}) = 0, \\ v_{2*}(\gamma_2 - \alpha_{21}v_{1*} - \alpha_{22}v_{2*} + \alpha_{23}v_{3*}) = 0, \\ v_{3*}(\gamma_3 + \alpha_{31}v_{1*} + \alpha_{32}v_{2*} - \alpha_{33}v_{3*}) = 0, \end{cases} \tag{7}$$

holds.

Lemma 1 (see [47]). *Given the following system*

$$\frac{\mathrm{d}^{\varrho}v(t)}{\mathrm{d}t^{\varrho}} = h(t,v(t)), \quad v(t_0) = v_{t_0}, \quad t_0 > 0, \tag{8}$$

where $\varrho \in (0,1t, nhq: h[t_0,\infty) \times \Lambda \longrightarrow R_+^n, \Lambda \subset R_+^n$. *If* $h(t,v)$ *satisfies the local Lipschitz condition with respect to* v, *then model (3) possesses a unique solution defined on* $[t_0,\infty)$.

Lemma 2 (see [48]). *Suppose that* $\varrho \in (0,1), h(t) \in C[\gamma,\delta]$ *and* $\mathscr{D}^{\varrho}h(t) \in C[\gamma,\delta]$, *where* $\gamma,\delta \in R$. *If* $\mathscr{D}^{\varrho}h(t) \geq 0, t \in [\gamma,\delta]$, *then* $h(t)$ *is a nondecreasing function* $\forall t \in [\gamma,\delta]$. *If* $\mathscr{D}^{\varrho}h(t) \leq 0, t \in [\gamma,\delta]$, *then* $h(t)$ *is a nonincreasing function* $\forall t \in [\gamma,\delta]$.

Lemma 3 (see [49, 50]). *For a given fractional-order model,*

$$\frac{\mathrm{d}^{\varrho}v(t)}{\mathrm{d}t^{\varrho}} = g(t,v(t)), \quad v(0) = v_0, \tag{9}$$

where $\varrho \in (0,1]$ *and* $g(t,v(t))$: $R_+ \times R^m \longrightarrow R^m$, *the equilibrium point of model (9) is locally asymptotically stable if all eigenvalues* ς *of* $(\partial g(t,v)/\partial v)$ *evaluated near the equilibrium point satisfy* $|\arg(\varsigma)| > ((\varrho\pi)/2)$.

Lemma 4 (see [51]). *For given m-dimensional fractional-order system,*

$$\begin{cases} \dfrac{\mathrm{d}^{\varrho_1}\mathscr{V}_1(t)}{\mathrm{d}t^{\varrho_1}} = l_{11}\mathscr{V}_1(t-\sigma_{11}) + l_{12}\mathscr{V}_2(t-\sigma_{12}) + \cdots + l_{1m}\mathscr{V}_m(t-\sigma_{1m}), \\ \dfrac{\mathrm{d}^{\varrho_2}\mathscr{V}_2(t)}{\mathrm{d}t^{\varrho_2}} = l_{21}\mathscr{V}_1(t-\sigma_{21}) + l_{22}\mathscr{V}_2(t-\sigma_{22}) + \cdots + l_{2m}\mathscr{V}_m(t-\sigma_{2m}), \\ \vdots \\ \dfrac{\mathrm{d}^{\varrho_m}\mathscr{V}_m(t)}{\mathrm{d}t^{\varrho_m}} = l_{m1}\mathscr{V}_1(t-\sigma_{m1}) + l_{m2}\mathscr{V}_2(t-\sigma_{m2}) + \cdots + l_{mm}\mathscr{V}_m(t-\sigma_{mm}), \end{cases} \tag{10}$$

where $0 < \varrho_i < 1\,(i = 1,2,\ldots,m)$, *the initial values* $\mathscr{V}_i(t) = \varphi_i(t) \in C[-\max_{i,l}\sigma_{il}, 0]$, *and* $t \in [-\max_{i,l}\sigma_{il}, 0]$, $i,l = 1,2,\ldots,m$. *Denote*

$$\Delta(\chi) = \begin{bmatrix} \chi^{\varrho_1} - l_{11}e^{-\chi\sigma_{11}} & -l_{12}e^{-\chi\sigma_{12}} & \cdots & -l_{1m}e^{-\chi\sigma_{1m}} \\ -l_{21}e^{-\chi\sigma_{12}} & \chi^{\varrho_2} - l_{22}e^{-\chi\sigma_{22}} & \cdots & -l_{2m}e^{-\chi\sigma_{2m}} \\ \vdots & \vdots & \ddots & \vdots \\ -l_{m1}e^{-\chi\sigma_{m1}} & -l_{m2}e^{-\chi\sigma_{m2}} & \cdots & \chi^{\varrho_m} - l_{mm}e^{-\chi\sigma_{mm}} \end{bmatrix}, \tag{11}$$

and then, the zero solution of equation (10) is Lyapunov asymptotically stable if all roots of $\det(\Delta(\chi)) = 0$ *possess negative real parts.*

3. Main Results

3.1. Existence and Uniqueness

Theorem 1. *Let* $\Theta = \{(u_1, u_2, u_3) \in R^3 : \max\{|u_1|, |u_2|, |u_3|\} < \mathcal{Q}\}$, *where* $\mathcal{Q}$ *is a positive constant. Then, for every* $U_{t_0} = (u_{1t_0}, u_{2t_0}, u_{3t_0}) \in \Theta$ *and for every* $t \geq t_0$, *there exists a unique solution* $U(t) \in \Theta$ *of system (3) with initial value* U_{t_0}.

Proof. We discuss this issue for model (3) in $\Theta \times [t_0, t^*]$, where $t^* < +\infty$. Let $U = (u_1, u_2, u_3)$ and $\widetilde{U} = (\widetilde{u}_1, \widetilde{u}_2, \widetilde{u}_3)$, and define the following mapping: $L(U) = (L_1(U), L_2(U), L_3(U))$, where

$$\begin{cases} L_1(U) = u_1(t)[\gamma_1 - \alpha_{11}u_1(t-\sigma) - \alpha_{12}u_2(t-\sigma) + \alpha_{13}u_3(t-\sigma)], \\ L_2[U] = u_2[t][\gamma_2 - \alpha_{21}u_1(t-\sigma) - \alpha_{22}u_2(t-\sigma) + \alpha_{23}u_3(t-\sigma)], \\ L_3(U) = u_3(t)[\gamma_3 + \alpha_{31}u_1(t-\sigma) + \alpha_{32}u_2(t-\sigma) - \alpha_{33}u_3(t-\sigma)]. \end{cases} \tag{12}$$

For arbitrary $U, \widetilde{U} \in \Theta, t_1, t_2 \in R, t_1, t_2 \geq t_0$, one has

$$\begin{aligned}
&\|L(U) - L(\widetilde{U})\| \\
&= |L_1(U) - L_1(\widetilde{U})| + |L_2(U) - L_2(\widetilde{U})| + |L_3(U) - L_3(\widetilde{U})| \\
&= |u_1(t_1)[\gamma_1 - \alpha_{11}u_1(t_1-\sigma) - \alpha_{12}u_2(t_1-\sigma) + \alpha_{13}u_3(t_1-\sigma)] \\
&\quad - u_1(t_2)[\gamma_1 - \alpha_{11}u_1(t_2-\sigma) - \alpha_{12}u_2(t_2-\sigma) + \alpha_{13}u_3(t_2-\sigma)]| \\
&\quad + |u_2(t_1)[\gamma_2 - \alpha_{21}u_1(t_1-\sigma) - \alpha_{22}u_2(t_1-\sigma) + \alpha_{23}u_3(t_1-\sigma)] \\
&\quad - u_2(t_2)[\gamma_2 - \alpha_{21}u_1(t_2-\sigma) - \alpha_{22}u_2(t_2-\sigma) + \alpha_{23}u_3(t_2-\sigma)]| \\
&\quad + |u_3(t_1)[\gamma_3 + \alpha_{31}u_1(t_1-\sigma) + \alpha_{32}u_2(t_1-\sigma) - \alpha_{33}u_3(t_1-\sigma)] \\
&\quad - u_3(t_2)[\gamma_3 + \alpha_{31}u_1(t_2-\sigma) + \alpha_{32}u_2(t_2-\sigma) - \alpha_{33}u_3(t_2-\sigma)]| \\
&\leq |u_1(t_1) - u_1(t_2)||\gamma_1 - \alpha_{11}u_1(t_1-\sigma) - \alpha_{12}u_2(t_1-\sigma) + \alpha_{13}u_3(t_1-\sigma)| \\
&\quad + \max\{|u_1(t_1)|, |u_1(t_2)|\}|[\gamma_1 - \alpha_{11}u_1(t_1-\sigma) - \alpha_{12}u_2(t_1-\sigma) + \alpha_{13}u_3(t_1-\sigma)] \\
&\quad - [\gamma_1 - \alpha_{11}u_1(t_2-\sigma) - \alpha_{12}u_2(t_2-\sigma) + \alpha_{13}u_3(t_2-\sigma)]| \\
&\quad + |u_2(t_1) - u_2(t_2)||\gamma_2 - \alpha_{21}u_1(t_1-\sigma) - \alpha_{22}u_2(t_1-\sigma) + \alpha_{23}u_3(t_1-\sigma)| \\
&\quad + \max\{|u_2(t_1)|, |u_2(t_2)|\}|[\gamma_2 - \alpha_{21}u_1(t_1-\sigma) - \alpha_{22}u_2(t_1-\sigma) + \alpha_{23}u_3(t_1-\sigma)] \\
&\quad - [\gamma_2 - \alpha_{21}u_1(t_2-\sigma) - \alpha_{22}u_2(t_2-\sigma) + \alpha_{23}u_3(t_2-\sigma)]| \\
&\quad + |u_3(t_1) - u_3(t_2)||\gamma_3 + \alpha_{31}u_1(t_1-\sigma) + \alpha_{32}u_2(t_1-\sigma) - \alpha_{33}u_3(t_1-\sigma)| \\
&\quad + \max\{|u_3(t_1)|, |u_3(t_2)|\}|[\gamma_3 + \alpha_{31}u_1(t_1-\sigma) + \alpha_{32}u_2(t_1-\sigma) - \alpha_{33}u_3(t_1-\sigma)] \\
&\quad - [\gamma_3 + \alpha_{31}u_1(t_2-\sigma) + \alpha_{32}u_2(t_2-\sigma) - \alpha_{33}u_3(t_2-\sigma)]| \\
&\leq |u_1(t_1) - u_1(t_2)|(\gamma_1 + \alpha_{11}\mathcal{Q} + \alpha_{12}\mathcal{Q} + \alpha_{13}\mathcal{Q}) \\
&\quad + \mathcal{Q}\alpha_{11}|u_1(t_1-\sigma) - u_1(t_2-\sigma)| + \mathcal{Q}\alpha_{12}|u_2(t_1-\sigma) - u_2(t_2-\sigma)| \\
&\quad + \mathcal{Q}\alpha_{13}|u_3(t_1-\sigma) - u_3(t_2-\sigma)| \\
&\quad + |u_2(t_1) - u_2(t_2)|(\gamma_2 + \alpha_{21}\mathcal{Q} + \alpha_{22}\mathcal{Q} + \alpha_{23}\mathcal{Q}) \\
&\quad + \mathcal{Q}\alpha_{21}|u_1(t_1-\sigma) - u_1(t_2-\sigma)| + \mathcal{Q}\alpha_{22}|u_2(t_1-\sigma) - u_2(t_2-\sigma)| \\
&\quad + \mathcal{Q}\alpha_{23}|u_3(t_1-\sigma) - u_3(t_2-\sigma)| \\
&\quad + |u_3(t_1) - u_3(t_2)|(\gamma_3 + \alpha_{31}\mathcal{Q} + \alpha_{32}\mathcal{Q} + \alpha_{33}\mathcal{Q}) \\
&\quad + \mathcal{Q}\alpha_{31}|u_1(t_1-\sigma) - u_1(t_2-\sigma)| + \mathcal{Q}\alpha_{32}|u_2(t_1-\sigma) - u_2(t_2-\sigma)| \\
&\quad + \mathcal{Q}\alpha_{33}|u_3(t_1-\sigma) - u_3(t_2-\sigma)| \\
&\leq L_1|u_1(t_1) - u_1(t_2)| + L_2|u_2(t_1) - u_2(t_2)| + L_3|u_3(t_1) - u_3(t_2)|,
\end{aligned} \tag{13}$$

where

$$\begin{cases} L_1 = \gamma_1 + \mathcal{Q}\left(2\alpha_{11} + \alpha_{21} + \alpha_{31} + \alpha_{12} + \alpha_{13}\right), \\ L_2 = \gamma_2 + \mathcal{Q}\left(2\alpha_{21} + \alpha_{22} + \alpha_{32} + \alpha_{22} + \alpha_{23}\right), \\ L_3 = \gamma_3 + \mathcal{Q}\left(2\alpha_{31} + \alpha_{23} + \alpha_{33} + \alpha_{32} + \alpha_{33}\right). \end{cases} \tag{14}$$

It follows from (13) that

$$\|L(U) - L(\widetilde{U})\| \le LU - \widetilde{U}|, \tag{15}$$

where

$$L = \max\{L_1, L_2, L_3\}. \tag{16}$$

In view of Lemma 1, one can conclude that Theorem 1 is true. We finish the proof. □

3.2. Nonnegativity. Denote $\Theta_+ = \{(u_1, u_2, u_3) \in \Theta: u_1,\ u_2,\ u_3 \in R_+\}$.

Theorem 2. *Each solution of model (3) that begins with Θ_+ remains nonnegative.*

Proof. Our object is to prove that $u_i(t) \ge 0\,(i = 1, 2, 3) \forall t \ge t_0$. Let $U(t_0) = (u_1(t_0), u_1(t_0), u_1(t_0)) \in \Theta_+$ be the initial value of system (3). Assume that $\exists$ is a constant and $t_0 \le t < \rho$ such that

$$\begin{cases} u_i(t) = 0, \quad t_0 \le t < \rho, \\ u_i(\rho) = 0, \\ u_i(\rho^+) < 0, \end{cases} \tag{17}$$

where $i = 1, 2, 3$. In view of system (3), one has

$$\begin{cases} \dfrac{\mathrm{d}^{\varrho} u_1(t)}{\mathrm{d}t^{\varrho}}|_{u_i=0} = 0, \\ \dfrac{\mathrm{d}^{\varrho} u_2(t)}{\mathrm{d}t^{\varrho}}|_{u_i=0} = 0, \\ \dfrac{\mathrm{d}^{\varrho} u_3(t)}{\mathrm{d}t^{\varrho}}|_{u_i=0} = 0, \end{cases} \tag{18}$$

where $i = 1, 2, 3$. By Lemma 2, one knows that $u_i(\rho^+) = 0\,(i = 1, 2, 3)$, which contradicts $u_i(\rho^+) < 0\,(i = 1, 2, 3)$ in (17). Thus, one can conclude that $u_i(t) \ge 0 \forall t \ge t_0$. The proof is complete. □

3.3. Stability and Hopf Bifurcation. In the section, we shall focus on the local stability and the appearance of Hopf bifurcation of system (3). Consider the biological implication of system (3); we only seek the sufficient condition to guarantee the local stability of the positive equilibrium and the emergence of Hopf bifurcations of system (3).

Clearly, system (3) has a unique positive equilibrium $U_0(u_1^*, u_2^*, u_3^*)$ provided that the following condition

$$(\mathscr{M}_1)\mathrm{sign}\{\mathscr{A}\} = \mathrm{sign}\{\mathscr{A}_1\} = \mathrm{sign}\{\mathscr{A}_2\} = \mathrm{sign}\{\mathscr{A}_3\}, \tag{19}$$

is satisfied, where

$$\begin{cases} \mathscr{A} = \det\begin{bmatrix} \alpha_{11}\alpha_{12} - \alpha_{13} & \alpha_{21}\alpha_{22} - \alpha_{23} & \alpha_{31}\alpha_{31} - \alpha_{33} \end{bmatrix} \ne 0, \\ \mathscr{A}_1 = \det\begin{bmatrix} \gamma_1 & \alpha_{12} & -\alpha_{13} \\ \gamma_2 & \alpha_{22} & -\alpha_{23} \\ -\gamma_3 & \alpha_{31} & -\alpha_{33} \end{bmatrix}, \\ \mathscr{A}_2 = \det\begin{bmatrix} \alpha_{11} & \gamma_1 & -\alpha_{13} \\ \alpha_{21} & \gamma_2 & -\alpha_{23} \\ \alpha_{31} & -\gamma_3 & -\alpha_{33} \end{bmatrix}, \\ \mathscr{A}_3 = \det\begin{bmatrix} \alpha_{11} & \alpha_{12} & \gamma_1 \\ \alpha_{21} & \alpha_{22} & \gamma_2 \\ \alpha_{31} & \alpha_{31} & -\gamma_3 \end{bmatrix}, \end{cases}$$

$$\begin{aligned} u_1^* &= \frac{\mathscr{A}_1}{\mathscr{A}}, \\ u_2^* &= \frac{\mathscr{A}_2}{\mathscr{A}}, \\ u_3^* &= \frac{\mathscr{A}_3}{\mathscr{A}}. \end{aligned} \tag{20}$$

The linear system of equation (3) near $U_0(u_1^*, u_2^*, u_3^*)$ takes

$$\begin{cases} \dfrac{\mathrm{d}^{\varrho} u_1(t)}{\mathrm{d}t^{\varrho}} = a_{11}u_1(t-\sigma) + a_{12}u_2(t-\sigma) + a_{13}u_3(t-\sigma), \\ \dfrac{\mathrm{d}^{\varrho} u_2(t)}{\mathrm{d}t^{\varrho}} = a_{21}u_1(t-\sigma) + a_{22}u_2(t-\sigma) + a_{23}u_3(t-\sigma), \\ \dfrac{\mathrm{d}^{\varrho} u_3(t)}{\mathrm{d}t^{\varrho}} = a_{31}u_1(t-\sigma) + a_{32}u_2(t-\sigma) + a_{33}u_3(t-\sigma), \end{cases} \tag{21}$$

where

$$\begin{cases} a_{11} = -u_{1*}\alpha_{11}, a_{12} = -u_{1*}\alpha_{12}, a_{13} = u_{1*}\alpha_{13}, \\ a_{21} = -u_{2*}\alpha_{21}, a_{22} = -u_{2*}\alpha_{22}, a_{23} = u_{2*}\alpha_{23}, \\ a_{31} = u_{3*}\alpha_{31}, a_{32} = u_{3*}\alpha_{32}, a_{33} = -u_{3*}\alpha_{33}. \end{cases} \tag{22}$$

The characteristic equation of equation (21) is computed as follows:

$$\det\begin{bmatrix} s^{\varrho}-a_{11}e^{-s\sigma} & -a_{12}e^{-s\sigma} & -a_{13}e^{-s\sigma} \\ -a_{21}e^{-s\sigma} & s^{\varrho}-a_{22}e^{-s\sigma} & -a_{23}e^{-s\sigma} \\ -a_{31}e^{-s\sigma} & -a_{32}e^{-s\sigma} & s^{\varrho}-a_{33}e^{-s\sigma} \end{bmatrix}=0, \tag{23}$$

which leads to

$$s^{3\varrho}+b_1s^{2\varrho}e^{-s\sigma}+b_2s^{\varrho}e^{-2s\sigma}+b_3e^{-3s\sigma}=0, \tag{24}$$

where

$$\begin{cases} b_1=-(a_{11}+a_{22}+a_{33}), \\ b_2=a_{11}a_{33}+a_{22}a_{33}+a_{11}a_{22}-a_{13}a_{31} \\ -a_{12}a_{21}-a_{23}a_{32}, \\ b_3=a_{13}a_{22}a_{31}+a_{12}a_{21}a_{33}+a_{11}a_{23}a_{32} \\ -a_{11}a_{22}a_{33}-a_{13}a_{21}a_{32}. \end{cases} \tag{25}$$

In terms of (24), we have

$$s^{3\varrho}e^{2s\sigma}+b_1s^{2\varrho}e^{s\sigma}+b_2s^{\varrho}+b_3e^{-s\sigma}=0. \tag{26}$$

Let $s=i\varphi=\varphi(\cos(\pi/2)+i\ \sin(\pi/2))$ be the root of (26); then, one has

$$\begin{cases} \mathscr{G}_1(\varrho)\cos\ 2\ \varphi\sigma+\mathscr{G}_2(\varrho)\sin\ 2\ \varphi\sigma+\mathscr{G}_3(\varrho)\cos\ \varphi\sigma+\mathscr{G}_4(\varrho)\sin\ \varphi\sigma=0, \\ \mathscr{S}_1(\varrho)\cos\ 2\ \varphi\sigma+\mathscr{S}_2(\varrho)\sin\ 2\ \varphi\sigma+\mathscr{S}_3(\varrho)\cos\ \varphi\sigma+\mathscr{S}_4(\varrho)\sin\ \varphi\sigma=0, \end{cases} \tag{27}$$

where

$$\begin{cases} \mathscr{G}_1(\varrho)=\varphi^{3\varrho}\cos\dfrac{3\varrho\pi}{2}+b_2\varphi^{\varrho}\cos\dfrac{\varrho\pi}{2}, \\ \mathscr{G}_2(\varrho)=b_2\varphi^{\varrho}\sin\dfrac{\varrho\pi}{2}-\varphi^{3\varrho}\sin\dfrac{3\varrho\pi}{2}, \\ \mathscr{G}_3(\varrho)=b_1\varphi^{2\varrho}\cos\varrho\pi+b_3, \\ \mathscr{G}_4(\varrho)=-b_1\varphi^{2\varrho}\sin\varrho\pi, \\ \mathscr{S}_1(\varrho)=\varphi^{3\varrho}\sin\dfrac{3\varrho\pi}{2}+b_2\varphi^{\varrho}\sin\dfrac{\varrho\pi}{2}, \\ \mathscr{S}_2(\varrho)=\varphi^{3\varrho}\cos\dfrac{3\varrho\pi}{2}-b_2\varphi^{\varrho}\cos\dfrac{\varrho\pi}{2}, \\ \mathscr{S}_3(\varrho)=b_1\varphi^{2\varrho}\sin\varrho\pi, \\ \mathscr{S}_4(\varrho)=b_1\varphi^{2\varrho}\cos\varrho\pi-b_3. \end{cases} \tag{28}$$

In (28), let

$$\begin{cases} c_1=\cos\dfrac{3\varrho\pi}{2}, \\ c_2=b_2\cos\dfrac{\varrho\pi}{2}, \\ c_3=b_2\sin\dfrac{\varrho\pi}{2}, \\ c_4=-\sin\dfrac{3\varrho\pi}{2}, \\ c_5=b_1\cos\varrho\pi, \\ c_6=b_3, \\ c_7=-b_1\sin\varrho\pi, \\ c_8=\sin\dfrac{3\varrho\pi}{2}, \\ c_9=b_2\sin\dfrac{\varrho\pi}{2}, \\ c_{10}=\cos\dfrac{3\varrho\pi}{2}, \\ c_{11}=-b_2\cos\dfrac{\varrho\pi}{2}, \\ c_{12}=b_1\sin\varrho\pi, \\ c_{13}=b_1\cos\varrho\pi, \\ c_{14}=-b_3, \end{cases} \tag{29}$$

and then, (28) takes the form:

$$\begin{cases} \mathscr{G}_1(\varrho)=c_1\varphi^{3\varrho}+c_2\varphi^{\varrho}, \\ \mathscr{G}_2(\varrho)=c_3\varphi^{\varrho}+c_4\varphi^{3\varrho}, \\ \mathscr{G}_3(\varrho)=c_5\varphi^{2\varrho}+c_6, \\ \mathscr{G}_4(\varrho)=c_7\varphi^{2\varrho}, \\ \mathscr{S}_1(\varrho)=c_8\varphi^{3\varrho}+c_9\varphi^{\varrho}, \\ \mathscr{S}_2(\varrho)=c_{10}\varphi^{3\varrho}+c_{11}\varphi^{\varrho}, \\ \mathscr{S}_3(\varrho)=c_{12}\varphi^{2\varrho}, \\ \mathscr{S}_4(\varrho)=c_{13}\varphi^{2\varrho}+c_{14}. \end{cases} \tag{30}$$

For (27), we consider two cases.

Case 1. If $\sin\ \varphi\sigma=\sqrt{1-\ \cos^2\ \varphi\sigma}$, then the first equation of (27) becomes

$$\mathscr{G}_1(\varrho)\left(2\cos^2\varphi\sigma-1\right)+2\mathscr{G}_2(\varrho)\cos\varphi\sigma\sqrt{1-\cos^2\varphi\sigma}+\mathscr{G}_3(\varrho)\cos\varphi\sigma+\mathscr{G}_4(\varrho)\sqrt{1-\cos^2\varphi\sigma}=0. \tag{31}$$

Hence,

$$\left[2\mathscr{G}_2(\varrho)\cos\varphi\sigma\sqrt{1-\cos^2\varphi\sigma}+\mathscr{G}_4(\varrho)\sqrt{1-\cos^2\varphi\sigma}\right]^2=\left[\mathscr{G}_1(\varrho)\left(2\cos^2\varphi\sigma-1\right)+\mathscr{G}_3(\varrho)\cos\varphi\sigma\right]^2, \tag{32}$$

which leads to

$$\vartheta_1\cos^4\varphi\sigma+\vartheta_2\cos^3\varphi\sigma+\vartheta_3\cos^2\varphi\sigma+\vartheta_4\cos\varphi\sigma+\vartheta_5=0, \tag{33}$$

where

$$\begin{cases}\vartheta_1=4\mathscr{G}_1^2(\varrho)+4\mathscr{G}_2^2(\varrho),\\ \vartheta_2=4\mathscr{G}_1(\varrho)\mathscr{G}_3(\varrho)+4\mathscr{G}_2(\varrho)\mathscr{G}_4(\varrho),\\ \vartheta_3=\mathscr{G}_3^2(\varrho)+\mathscr{G}_4^2(\varrho)-4\mathscr{G}_1^2(\varrho)-4\mathscr{G}_2^2(\varrho),\\ \vartheta_4=-\left[2\mathscr{G}_1(\varrho)\mathscr{G}_3(\varrho)+4\mathscr{G}_2(\varrho)\mathscr{G}_4(\varrho)\right],\\ \vartheta_5=\mathscr{G}_1^2(\varrho)-\mathscr{G}_4^2(\varrho).\end{cases} \tag{34}$$

Set $\cos\varphi\sigma=r$, and let

$$z(r)=r^4+\frac{\vartheta_2}{\vartheta_1}r^3+\frac{\vartheta_3}{\vartheta_1}r^2+\frac{\vartheta_4}{\vartheta_1}r+\frac{\vartheta_5}{\vartheta_1}. \tag{35}$$

Hence,

$$\frac{\mathrm{d}z(r)}{\mathrm{d}r}=4r^3+\frac{3\vartheta_2}{\vartheta_1}r^2+\frac{2\vartheta_3}{\vartheta_1}r+\frac{\vartheta_4}{\vartheta_1}. \tag{36}$$

Denote

$$r^3+\frac{3\vartheta_2}{\vartheta_1}r^2+\frac{2\vartheta_3}{\vartheta_1}r+\frac{\vartheta_4}{\vartheta_1}=0. \tag{37}$$

Set $p=r+(\vartheta_2/4\vartheta_1)$, and then, (37) takes the form

$$p^3+f_1p+f_2=0, \tag{38}$$

where

$$f_1=\frac{\vartheta_3}{2\vartheta_1}-\frac{3\vartheta_2^2}{16\vartheta_1^2},\qquad f_2=\frac{\vartheta_2^3}{32\vartheta_1^3}-\frac{\vartheta_2\vartheta_3}{8\vartheta_1^2}+\frac{\vartheta_4}{4\vartheta_1}. \tag{39}$$

Let

$$q_1=\left(\frac{f_2}{2}\right)^2+\left(\frac{f_1}{3}\right)^3,\qquad q_2=\frac{-1+i\sqrt{3}}{2}. \tag{40}$$

It follows from (38) that

$$\begin{cases}p_1=\sqrt[3]{-\frac{f_2}{2}+\sqrt{q_1}}+\sqrt[3]{-\frac{f_2}{2}-\sqrt{q_1}},\\ p_2=\sqrt[3]{-\frac{f_2}{2}+\sqrt{q_1}\,q_2}+\sqrt[3]{-\frac{f_2}{2}-\sqrt{q_1}\,q_2^2},\\ p_3=\sqrt[3]{-\frac{f_2}{2}+\sqrt{q_1}\,q_2^2}+\sqrt[3]{-\frac{f_2}{2}-\sqrt{q_1}\,q_2}.\end{cases} \tag{41}$$

According to the discussion above, one easily obtains the expression of $\cos\varphi\sigma$. Then, one easily gets the expression of $\sin\varphi\sigma$. Here, we suppose that

$$\cos\varphi\sigma=g_1(\varphi),\qquad \sin\varphi\sigma=g_2(\varphi). \tag{42}$$

Then,

$$g_1^2(\varphi)+g_2^2(\varphi)=1. \tag{43}$$

With the aid of Matlab 7.0, one can get the root (say φ) of equation (43). Then, one obtains

$$\sigma^{1k}=\frac{1}{\varphi}\left[\arccos g_1(\varphi)+2k\pi\right],\quad k=0,1,2,\ldots \tag{44}$$

Case 2. If $\sin\varphi\sigma=-\sqrt{1-\cos^2\varphi\sigma}$, applying the same way to this case, we can obtain

$$\cos\varphi\sigma=h_1(\varphi),\qquad \sin\varphi\sigma=h_2(\varphi). \tag{45}$$

Then,

$$h_1^2(\varphi)+h_2^2(\varphi)=1. \tag{46}$$

By Matlab 7.0, one can obtain the root (say φ) of equation (46). So,

$$\sigma^{2k}=\frac{1}{\varphi}\left[\arccos h_1(\varphi)+2k\pi\right],\quad k=0,1,2,\ldots \tag{47}$$

Set

$$\sigma_0=\min\left\{\sigma^{1k},\sigma^{2k}\right\},\quad k=0,1,2,\ldots, \tag{48}$$

In the sequel, we check the transversality condition of the appearance of Hopf bifurcation. We give the hypothesis as follows: $(\mathscr{M}_2)\mathscr{Z}_{11}\mathscr{Z}_{21}+\mathscr{Z}_{12}\mathscr{Z}_{22}>0$, where

$$
\begin{cases}
\mathscr{Z}_{11} = 3\varrho\varphi_0^{3\varrho-1}\left[\cos\dfrac{(3\varrho-1)\pi}{2}\cos\ 2\varphi_0\sigma_0 - \sin\dfrac{(3\varrho-1)\pi}{2}\sin\ 2\varphi_0\sigma_0\right] \\
+ 2\varphi_0^{3\varrho}\sigma_0\left[\cos\ \dfrac{3\varrho\pi}{2}\cos\ 2\varphi_0\sigma_0 - \sin\ \dfrac{3\varrho\pi}{2}\sin\ 2\varphi_0\sigma_0\right] \\
+ 2b_1\varrho\varphi_0^{2\varrho-1}\left[\cos\dfrac{(2\varrho-1)\pi}{2}\cos\ \varphi_0\sigma_0 - \sin\dfrac{(2\varrho-1)\pi}{2}\sin\ \varphi_0\sigma_0\right] \\
+ b_1\sigma_0\varphi_0^{2\varrho}\left[\cos\varrho\pi\ \cos\ \varphi_0\sigma_0 - \sin\varrho\pi\ \sin\ \varphi_0\sigma_0\right] \\
+ b_2\varrho\varphi_0^{\varrho-1}\cos\dfrac{(\varrho-1)\pi}{2} - b_3\sigma_0\cos\ \varphi_0\sigma_0, \\
\mathscr{Z}_{12} = 3\varrho\varphi_0^{3\varrho-1}\left[\cos\dfrac{(3\varrho-1)\pi}{2}\sin\ 2\varphi_0\sigma_0 + \sin\dfrac{(3\varrho-1)\pi}{2}\cos\ 2\varphi_0\sigma_0\right] \\
+ 2\varphi_0^{3\varrho}\sigma_0\left[\cos\ \dfrac{3\varrho\pi}{2}\sin\ 2\varphi_0\sigma_0 + \sin\ \dfrac{3\varrho\pi}{2}\cos\ 2\varphi_0\sigma_0\right] \\
+ 2b_1\varrho\varphi_0^{2\varrho-1}\left[\cos\dfrac{(2\varrho-1)\pi}{2}\sin\ \varphi_0\sigma_0 + \sin\dfrac{(2\varrho-1)\pi}{2}\cos\ \varphi_0\sigma_0\right] \\
+ b_1\sigma_0\varphi_0^{2\varrho}\left[\cos\varrho\pi\ \sin\ \varphi_0\sigma_0 + \sin\varrho\pi\ \cos\ \varphi_0\sigma_0\right] \\
+ b_2\varrho\varphi_0^{\varrho-1}\sin\dfrac{(\varrho-1)\pi}{2} + b_3\sigma_0\sin\ \varphi_0\sigma_0, \\
\mathscr{Z}_{21} = b_3\varphi_0\sin\ \varphi_0\sigma_0 - 2\varphi_0^{3\varrho+1}\left[\cos\dfrac{(3\varrho+1)\pi}{2}\cos\ 2\varphi_0\sigma_0 - \sin\dfrac{(3\varrho+1)\pi}{2}\sin\ 2\varphi_0\sigma_0\right] \\
- 2\left(b_2\varrho_0^{2\sigma}\sin\ \sigma\pi + b_1\varrho_0^{\sigma}\sin\dfrac{\sigma\pi}{2}\right)\varrho_0\cos\ 2\varrho_0\eta_0, \\
- b_1\varphi_0^{2\varrho+1}\left[\cos\dfrac{(2\varrho+1)\pi}{2}\cos\ 2\varphi_0\sigma_0 - \sin\dfrac{(2\varrho+1)\pi}{2}\sin\ 2\varphi_0\sigma_0\right], \\
\mathscr{Z}_{22} = b_3\varphi_0\cos\ \varphi_0\sigma_0 - 2\varphi_0^{3\varrho+1}\left[\cos\dfrac{(3\varrho+1)\pi}{2}\sin\ 2\varphi_0\sigma_0 + \sin\dfrac{(3\varrho+1)\pi}{2}\cos\ 2\varphi_0\sigma_0\right] \\
- b_1\varphi_0^{2\varrho+1}\left[\cos\dfrac{(2\varrho+1)\pi}{2}\sin\ 2\varphi_0\sigma_0 + \sin\dfrac{(2\varrho+1)\pi}{2}\cos\ 2\varphi_0\sigma_0\right].
\end{cases}
\tag{49}
$$

Lemma 5. *Suppose that $s(\sigma) = \xi(\sigma) + i\eta(\sigma)$ is a root of equation (26) near $\sigma = \sigma_0$ such that $\xi(\sigma_0) = 0, \eta(\sigma_0) = \varphi_0$; then, one has* $\mathrm{Re}[ds/d\sigma]|_{\sigma=\sigma_0,\varphi=\varphi_0} > 0$.

Proof. In terms of equation (26), one knows that

$$\begin{aligned} &3\varrho s^{3\varrho-1}e^{2s\sigma}\frac{ds}{d\sigma} + 2s^{3\varrho}e^{2s\sigma}\left(\frac{ds}{d\sigma}\sigma + s\right) \\ &+ 2b_1\varrho s^{2\varrho-1}e^{s\sigma}\frac{ds}{d\sigma} + b_1e^{s\sigma}s^{2\varrho}\left(\frac{ds}{d\sigma}\sigma + s\right) + b_2\varrho s^{\varrho-1}\frac{ds}{d\sigma} - b_3e^{-s\sigma}\left(\frac{ds}{d\sigma}\sigma + s\right) = 0, \end{aligned} \tag{50}$$

which leads to

$$\begin{aligned} &\left[3\varrho s^{3\varrho-1}e^{2s\sigma} + 2s^{3\varrho}e^{2s\sigma}\sigma + 2b_1\varrho s^{2\varrho-1}e^{s\sigma}\right. \\ &\left. + b_1e^{s\sigma}s^{2\varrho}\sigma + b_2\varrho s^{\varrho-1} - b_3e^{-s\sigma}\sigma\right]\frac{ds}{d\sigma} \\ &= b_3se^{-s\sigma} - 2s^{3\varrho+1}e^{2s\sigma} - b_1s^{2\varrho+1}e^{s\sigma}. \end{aligned} \tag{51}$$

Then,

$$\left[\frac{ds}{d\sigma}\right]^{-1} = \frac{\mathscr{Z}_1(s)}{\mathscr{Z}_2(s)} - \frac{\sigma}{s}, \tag{52}$$

where

$$\begin{cases} \mathscr{Z}_1(s) = 3\varrho s^{3\varrho-1}e^{2s\sigma} + 2s^{3\varrho}e^{2s\sigma}\sigma + 2b_1\varrho s^{2\varrho-1}e^{s\sigma} \\ + b_1e^{s\sigma}s^{2\varrho}\sigma + b_2\varrho s^{\varrho-1} - b_3e^{-s\sigma}\sigma, \\ \mathscr{Z}_2(s) = b_3se^{-s\sigma} - 2s^{3\varrho+1}e^{2s\sigma} - b_1s^{2\varrho+1}e^{s\sigma}. \end{cases} \tag{53}$$

So,

$$\mathrm{Re}\left\{\frac{ds}{d\sigma}\right\}|_{\sigma=\sigma_0,\varphi=\varphi_0} = \mathrm{Re}\left\{\frac{Z_1(s)}{Z_2(s)}\right\}|_{\sigma=\sigma_0,\varphi=\varphi_0} = \frac{\mathscr{Z}_{11}\mathscr{Z}_{21} + \mathscr{Z}_{12}\mathscr{Z}_{22}}{\mathscr{Z}_{21}^2 + \mathscr{Z}_{22}^2}. \tag{54}$$

By $(\mathscr{M}_2)$, one obtains

$$\mathrm{Re}\left\{\left[\frac{ds}{d\sigma}\right]^{-1}\right\}|_{\sigma=\sigma_0,\varphi=\varphi_0} > 0. \tag{55}$$

This finishes the proof of Lemma 5.

Suppose that

$$\begin{aligned} &(\mathscr{M}_3) b_1 > 0, \\ &b_1b_2 > b_3, \\ &b_3 > 0. \end{aligned} \tag{56}$$

□

Lemma 6. *Provided that $\sigma = 0$ and $(\mathscr{M}_3)$ is fulfilled, then system (3) is locally asymptotically stable.*

Proof. If $\sigma = 0$, then (24) takes the form

$$\lambda^3 + b_1\lambda^2 + b_2\lambda + b_3 = 0. \tag{57}$$

By $(\mathscr{M}_3)$, one knows that all roots λ_i of (57) satisfy $|\arg(\lambda_i)| > ((\varrho\pi)/2)\,(i = 1, 2, 3, 4)$. Thus, one knows that Lemma 6 is right. The proof finishes.

Based on the investigation above, we have the following conclusion. □

Theorem 3. *Provided that $(\mathscr{M}_1)$–$(\mathscr{M}_3)$ hold true, then $U_0(u_{1*}, u_{1*}, u_{3*})$ of system (3) is locally asymptotically stable if $\sigma \in [0, \sigma_0)$, and a Hopf bifurcation exists near $U_0(u_{1*}, u_{1*}, u_{3*})$ if $\sigma = \sigma_0$.*

4. Computer Simulations

In this paper, we apply implicit Euler's scheme which is introduced in [52] to carry our numerical simulations. Given the following fractional-order predator-prey model

$$\begin{cases} \dfrac{d^\varrho u_1(t)}{dt^\varrho} = u_1(t)\left[8 - 3u_1(t-\sigma) - 2u_2(t-\sigma) + 0.3u_3(t-\sigma)\right], \\ \dfrac{d^\varrho u_2(t)}{dt^\varrho} = u_2(t)\left[7 - 2u_1(t-\sigma) - 2u_2(t-\sigma) + 0.3u_3(t-\sigma)\right], \\ \dfrac{d^\varrho u_3(t)}{dt^\varrho} = u_3(t)\left[6 + 0.2u_1(t-\sigma) + 0.2u_2(t-\sigma) - 3u_3(t-\sigma)\right], \end{cases} \tag{58}$$

we can easily know that model (58) possesses the equilibrium point $U_0(1.0000, 2.8384, 2.2559)$. Let $\varrho = 0.79$. Then, $r_1 = 8, \gamma_2 = 7, \gamma_3 = 6, \alpha_{11} = 3, \alpha_{12} = 2, \alpha_{13} = 0.3, \alpha_{21} = 2, \alpha_{22} = 2, \alpha_{23} = 0.3, \alpha_{31} = 0.2, \alpha_{32} = 0.2$, and $\alpha_{33} = 3$. Hence, $a_{11} = -3, a_{12} = -2, a_{13} = 0.3, a_{21} = -5.6788, a_{22} = -5.6788,, a_{23} = 0.6768, a_{31} = 0.4512, a_{32} = 0.4512, a_{33} = -6.7677, \varphi_0 = 0.3127$, and $\sigma_0 = 0.192$. Then, $b_1 = 15.4465, b_2 = 113.7636, b_3 = 151.8836, \mathscr{Z}_{11} = 0.3742, \mathscr{Z}_{12} = 0.6425, \mathscr{Z}_{21} = 0.5004$, and $\mathscr{Z}_{22} = 0.7157$. Thus, the hypothesis $(\mathscr{M}_1)$–$(\mathscr{M}_3)$ of

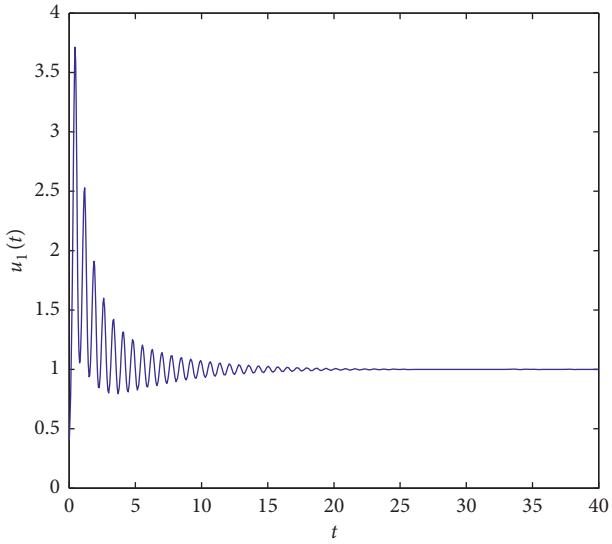

Figure 1: State variable $u_1(t)$ versus time t of system (58) when $\sigma = 0.18 < \sigma_0 = 0.192$.

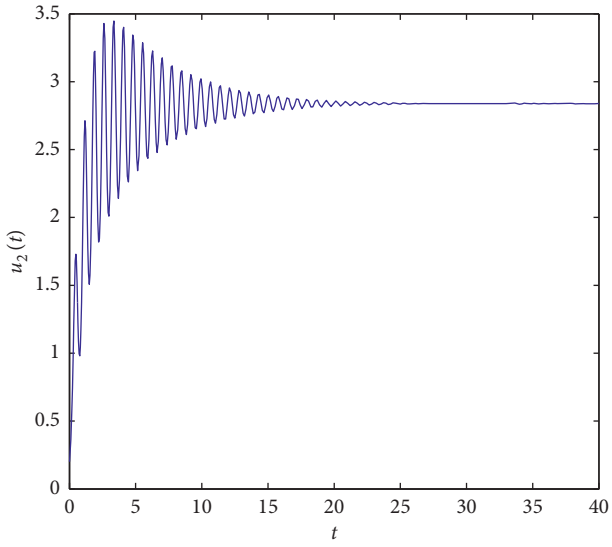

Figure 2: . State variable $u_2(t)$ versus time t of system (58) when $\sigma = 0.18 < \sigma_0 = 0.192$.

Theorem 3 hold true. If $\sigma \in [0, 0.192)$, the positive equilibrium point $U_0(1.0000, 2.8384, 2.2559)$ of system (58) is locally asymptotically stable. For this case, we choose $\sigma = 0.18 < \sigma_0 = 0.192$. The simulation plots are displayed in Figures 1–3. Figures 1–3 reveal that if σ is less than $\sigma_0 = 0.192$, then the densities of competing species u_1 and u_2 of system (58) will be tardily close to 1.0000, 2.8384, respectively, and the density of cooperating species u_3 of system (58) will be tardily close to 2.2559. When $\sigma \in [0.192, +\infty)$, then system (58) loses its stability and Hopf bifurcation behavior emerges. For this case, we choose $\sigma = 0.33$. The numerical simulation diagrams are presented in Figures 4–6. Figures 4–6 confirm that when σ is greater than $\sigma_0 = 0.192$, then the densities of competing species u_1 and u_2 and the density of cooperating species u_3 will remain

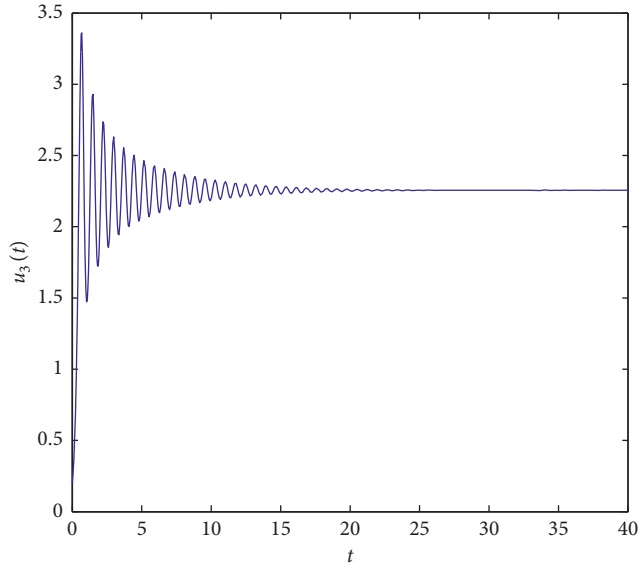

Figure 3: State variable $u_3(t)$ versus time t of system (58) when $\sigma = 0.18 < \sigma_0 = 0.192$.

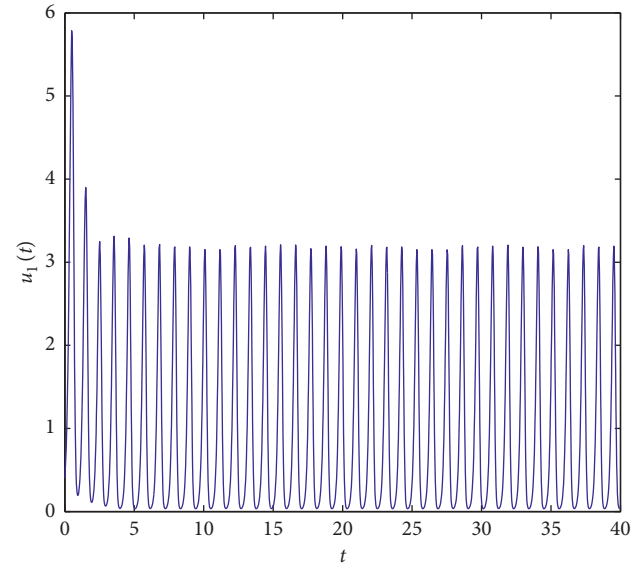

Figure 4: State variable $u_1(t)$ versus time t when $\sigma = 0.33 > \sigma_0 = 0.192$.

periodic motion around the positive equilibrium point $U_0(1.0000, 2.8384, 2.2559)$, namely, Hopf bifurcation phenomenon takes place around $U_0(1.0000, 2.8384, 2.2559)$. In order to illustrate the bifurcation phenomenon intuitively, we plot the bifurcation diagrams (see Figures 7–9). From Figures 7–9, we can easily see that the bifurcation value is 0.192. In addition, we give the relationship table between φ_0 and σ_0 in Table 1.

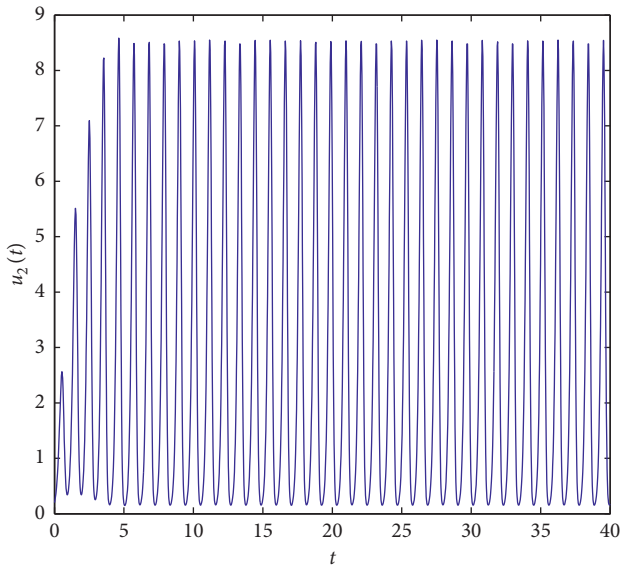

Figure 5: State variable $u_2(t)$ versus time t when $\sigma = 0.33 > \sigma_0 = 0.192$.

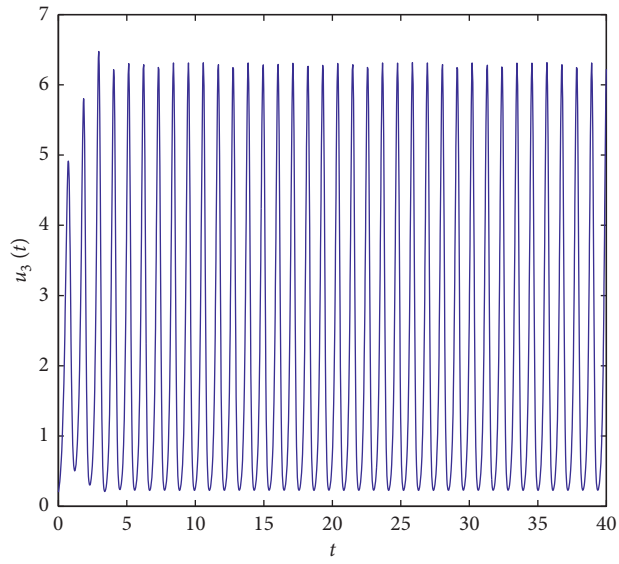

Figure 6: State variable $u_3(t)$ versus time t when $\sigma = 0.33 > \sigma_0 = 0.192$.

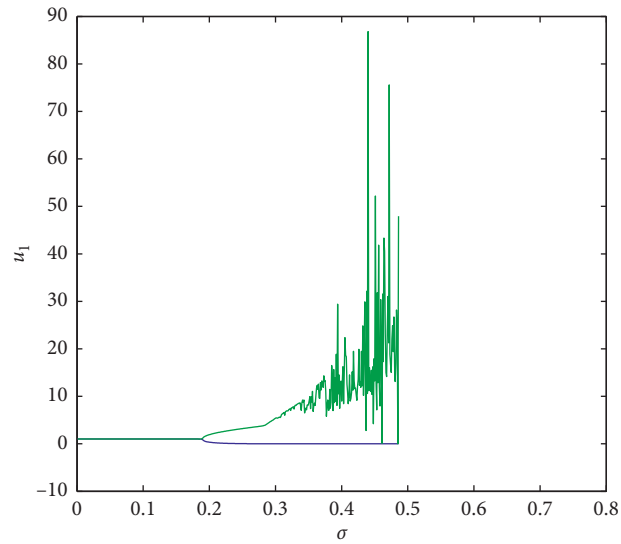

Figure 7: Bifurcation diagram for system (58): σ versus u_1.

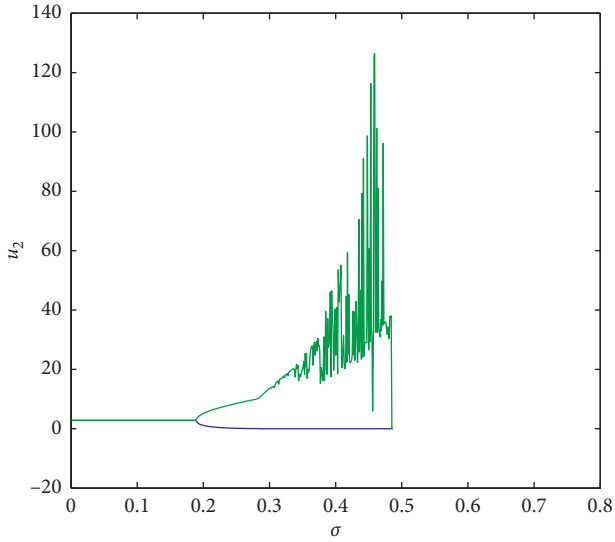

Figure 8: Bifurcation diagram for system (58): σ versus u_2.

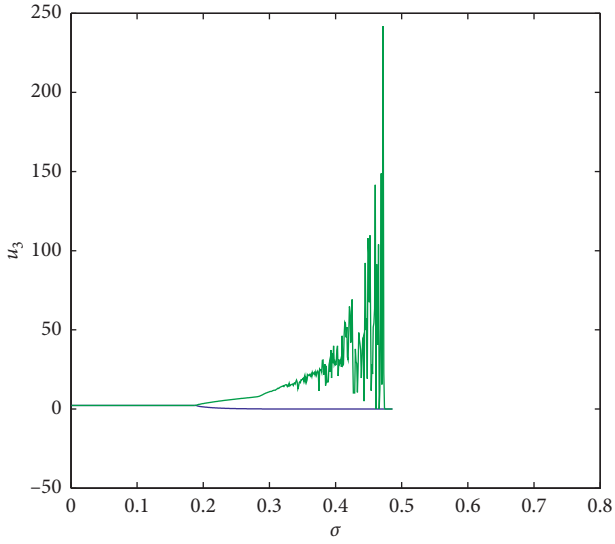

Figure 9: Bifurcation diagram for system (58): σ versus u_3.

Table 1: The magnitude relation of φ_0 and σ_0 for system (58).

φ_0	σ_0
0.3127	0.1920
0.3499	0.2173
0.4957	0.3218
0.5200	0.3400
0.6880	0.4732
0.7832	0.5543
1.0108	0.7651
1.0483	0.8022
1.1556	0.9123

5. Conclusions

Based on the previous works on predator-prey models and noticing the effect of feedback delay between the predators and preys, we have established a new fractional-order competitor-competitor-mutualist Lotka–Volterra model. We have found the conditions to ensure the existence, uniqueness, and nonnegativity of the involved fractional-order prey-predator model. Applying the Laplace transform, stability theorem, and Hopf bifurcation theory of fractional-order dynamical systems, we set up a novel sufficient criterion to guarantee the local stability and the emergence of Hopf bifurcation of the involved fractional-order predator-prey system. The study shows that the time delay has a vital effect on controlling the stability. To check the rationality of theoretical predictions, we design the program to implement simulation experiments. The established analytical conclusions have crucial guiding significance in preserving the coexistence of biological populations. In this paper, we assume that the feedback time delay of different species is same. Of course, we can also deal with the different delay cases. We will focus on this topic in near future.

Data Availability

No data were used to support this study.

Conflicts of Interest

The author declares that they have no competing interest.

References

[1] M. Das, A. Maiti, and G. P. Samanta, "Stability analysis of a prey-predator fractional order model incorporating prey refuge," *Ecological Genetics and Genomics*, vol. 7-8, pp. 33–46, 2018.

[2] Z. Wang, Y. Xie, J. Lu, and Y. Li, "Stability and bifurcation of a delayed generalized fractional-order prey-predator model with interspecific competition," *Applied Mathematics and Computation*, vol. 347, pp. 360–369, 2019.

[3] J. Alidousti and E. Ghafari, "Dynamic behavior of a fractional order prey-predator model with group defense, Chaos," *Solitons and Fractals*, vol. 134, Article ID 109688, 2020.

[4] S. K. Sasmal and Y. Takeuchi, "Dynamics of a predator-prey system with fear and group defense," *Journal of Mathematical Analysis and Applications*, vol. 481, no. 11, Article ID 123471, 2020.

[5] K. Ryu and W. Ko, "Asymptotic behavior of positive solutions to a predator-prey elliptic system with strong hunting cooperation in predators," *Physica A: Statistical Mechanics and Its Applications*, vol. 531, Article ID 121726, 2019.

[6] J. S. Guo, K. I. Nakamura, T. Ogiwara, and C. C. Wu, "Traveling wave solutions for a predator-prey system with two predators and one prey," *Nonlinear Analysis: Real World Applications*, vol. 54, Article ID 103111, 2020.

[7] H. Zhang, Y. Cai, S. Fu, and W. Wang, "Impact of the fear effect in a prey-predator model incorporating a prey refuge," *Applied Mathematics and Computation*, vol. 356, pp. 328–337, 2019.

[8] T. F. Weng, H. J. Yang, C. G. Gu, J. Zhang, and M. Small, "Predator-prey games on complex networks," *Communications in Nonlinear Science and Numerical Simulation*, vol. 79, Article ID 104911, 2019.

[9] A. M. C. Sauve, R. A. Taylor, and F. Barraquand, "The effect of seasonal strength and abruptness on predatorCprey dynamics," *Journal of Theoretical Biology*, vol. 491, Article ID 110175, 2020.

[10] V. Tiwari, J. P. Tripathi, S. Mishra, and R. K. Upadhyay, "Modeling the fear effect and stability of non-equilibrium patterns in mutually interfering predator-prey systems," *Applied Mathematics and Computation*, vol. 371, Article ID 124948, 2020.

[11] D. Pal, T. K. Kar, A. Yamauchi, and B. Ghosh, "Balancing maximum sustainable yield and ecological resilience in an exploited two-predator one-prey system," *Biosystems*, vol. 187, Article ID 104064, 2020.

[12] J. Li, X. Zhu, X. Lin, and J. Li, "Impact of cannibalism on dynamics of a structured predator-prey system," *Applied Mathematical Modelling*, vol. 78, pp. 1–19, 2020.

[13] M. Chen, R. Wu, B. Liu, and L. Chen, "Spatiotemporal dynamics in a ratio-dependent predator-prey model with time delay near the Turing-Hopf bifurcation point," *Communications in Nonlinear Science and Numerical Simulation*, vol. 77, pp. 141–167, 2019.

[14] P. Yang, "Hopf bifurcation of an age-structured prey-predator model with Holling type II functional response incorporating a prey refuge," *Nonlinear Analysis: Real World Applications*, vol. 49, pp. 368–385, 2019.

[15] F. Y. Wei and Q. Y. Fu, "Hopf bifurcation and stability for predator-prey systems with Beddington-DeAngelis type functional response and stage structure for prey incorporating refuge," *Applied Mathematical Modelling*, vol. 40, no. 11, pp. 126–134, 2016.

[16] Y. Song and S. Yuan, "Bifurcation analysis in a predator-prey system with time delay," *Nonlinear Analysis: Real World Applications*, vol. 7, no. 2, pp. 265–284, 2006.

[17] Y. Song and X. Zou, "Spatiotemporal dynamics in a diffusive ratio-dependent predator-prey model near a Hopf-Turing bifurcation point," *Computers and Mathematics with Applications*, vol. 67, no. 10, pp. 1978–1997, 2014.

[18] Y. Song, S. Wu, and H. Wang, "Spatiotemporal dynamics in the single population model with memory-based diffusion and nonlocal effect," *Journal of Differential Equations*, vol. 267, no. 11, pp. 6316–6351, 2019.

[19] D. Duan, B. Niu, and J. Wei, "Hopf-Hopf bifurcation and chaotic attractors in a delayed diffusive predator-prey model with fear effect," *Chaos, Solitons and Fractals*, vol. 123, pp. 206–216, 2019.

[20] J. Wang, J. Wei, and J. Shi, "Global bifurcation analysis and pattern formation in homogeneous diffusive predator-prey systems," *Journal of Differential Equations*, vol. 260, no. 4, pp. 3495–3523, 2016.

[21] S. Guo, "Bifurcation and spatio-temporal patterns in a diffusive predator-prey system," *Nonlinear Analysis: Real World Applications*, vol. 42, pp. 448–477, 2018.

[22] S. J. Guo and S. L. Yan, "Hopf bifurcation in a diffusive Lotka-Volterra type system with nonlocal delay effect," *Journal of Differential Equations*, vol. 260, no. 15, pp. 781–817, 2016.

[23] M. Das and G. P. Samanta, "A delayed fractional order food chain model with fear effect and prey refuge," *Mathematics and Computers in Simulation*, vol. 178, pp. 218–245, 2020.

[24] M. Das and G. P. Samanta, "A fractional order COVID-19 epidemic transmission model: stability analysis and optimal control," June 5, 2020. Available at SSRN: https://ssrn.com/abstract=36359383.

[25] M. Das and G. P. Samanta, "A prey-predator fractional order model with fear effect and group defense," *International Journal of Dynamics and Control*, vol. 9, pp. 334–349, 2020.

[26] C. J. Xu, "Delay-induced oscillations in a competitor-competitor-mutualist Lotka-Volterra model," *Complexity*, vol. 2017, p. 12, Article ID 2578043, 2017.

[27] X. Lv, P. Yan, and S. Lu, "Existence and global attractivity of positive periodic solutions of competitor-competitor-mutualist Lotka-Volterra systems with deviating arguments," *Mathematical and Computer Modelling*, vol. 51, no. 5-6, pp. 823–832, 2010.

[28] I. Oztuk and F. Ozkose, "Stability analysis of fractional order mathematical model of tumor-immune system interaction, Chaos," *Solitons and Fractals*, vol. 133, Article ID 109614, 2020.

[29] W. Zhou, C. Huang, M. Xiao, and J. Cao, "Hybrid tactics for bifurcation control in a fractional-order delayed predator-prey model," *Physica A: Statistical Mechanics and Its Applications*, vol. 515, pp. 183–191, 2019.

[30] C. Huang, H. Li, and J. Cao, "A novel strategy of bifurcation control for a delayed fractional predator-prey model," *Applied Mathematics and Computation*, vol. 347, pp. 808–838, 2019.

[31] M. Javidi and N. Nyamoradi, "Dynamic analysis of a fractional order prey-predator interaction with harvesting," *Applied Mathematical Modelling*, vol. 37, no. 20-21, pp. 8946–8956, 2013.

[32] S. Mondal, M. Biswas, and N. Bairagi, "Local and global dynamics of a fractional-order predator-prey system with habitat complexity and the corresponding discretized fractional-order system," *Journal of Applied Mathematics and Computing*, in press, 2020.

[33] H. A. A. El-Saka, S. Lee, and B. Jang, "Dynamic analysis of fractional-order predator-prey biological economic system with Holling type II functional response," *Nonlinear Dynamics*, vol. 96, no. 1, pp. 407–416, 2019.

[34] H. L. Li, L. Zhang, C. Hu, Y. L. Jiang, and Z. D. Teng, "Dynamical analysis of a fractional-order predator-prey model incorporating a prey refuge," *Journal of Applied Mathematics and Computing*, vol. 54, no. 1-2, pp. 435–449, 2017.

[35] A. A. Elsadany and A. E. Matouk, "Dynamical behaviors of fractional-order Lotka-Volterra predator-prey model and its discretization," *Journal of Applied Mathematics and Computing*, vol. 49, no. 1-2, pp. 269–283, 2015.

[36] F. A. Rihan, S. Lakshmanan, A. H. Hashish, R. Rakkiyappan, and E. Ahmed, "Fractional-order delayed predator-prey systems with Holling type-II functional response," *Nonlinear Dynamics*, vol. 80, no. 1-2, pp. 777–789, 2015.

[37] Y. K. Xie, Z. Wang, B. Meng, and X. Huang, "Dynamical analysis for a fractional-order prey-predator model with Holling III type functional response and discontinuous harvest," *Applied Mathematics Letters*, vol. 106, Article ID 106342, 2020.

[38] J. Alidousti, "Stability and bifurcation analysis for a fractional prey-predator scavenger model," *Applied Mathematical Modelling*, vol. 81, pp. 342–355, 2020.

[39] C. Xu, M. Liao, P. Li, Y. Guo, Q. Xiao, and S. Yuan, "Influence of multiple time delays on bifurcation of fractional-order neural networks," *Applied Mathematics and Computation*, vol. 361, pp. 565–582, 2019.

[40] M. Xiao, W. X. Zheng, J. Lin, G. Jiang, L. Zhao, and J. Cao, "Fractional-order PD control at Hopf bifurcations in delayed fractional-order small-world networks," *Journal of the Franklin Institute*, vol. 354, no. 17, pp. 7643–7667, 2017.

[41] A. K. O. Tiba and A. F. R. Araujo, "Control strategies for Hopf bifurcation in a chaotic associative memory," *Neurocomputing*, vol. 323, pp. 157–174, 2019.

[42] B. Tao, M. Xiao, Q. Sun, and J. Cao, "Hopf bifurcation analysis of a delayed fractional-order genetic regulatory network model," *Neurocomputing*, vol. 275, pp. 677–686, 2018.

[43] H. Li, C. D. Huang, and T. X. Li, "Dynamic complexity of a fractional-order predator-prey system with double delays," *Physica A: Statistical Mechanics and Its Applications*, vol. 526, Article ID 120852, 2019.

[44] F. A. Rihan and G. Velmurugan, "Dynamics of fractional-order delay differential model for tumor-immune system, Chaos," *Solitons & Fractals*, vol. 132, Article ID 109592, 2020.

[45] I. Podlubny, *Fractional Differential Equations*, Academic Press, New York, NY, USA, 1999.

[46] B. Bandyopadhyay and S. Kamal, *Stabliization and Control of Fractional Order Systems: A Sliding Mode Approach*, Vol. 317, Springer, Heidelberg, Germany, 2015.

[47] Y. Li, Y. Q. Chen, and I. Podlubny, "Stability of fractional-order nonlinear dynamic systems: Lyapunov direct method and generalized Mittag-Leffler stability," *Computers and Mathematics with Applications*, vol. 59, no. 5, pp. 1810–1821, 2009.

[48] Z. M. Odibat and N. T. Shawagfeh, "Generalized Taylor's formula," *Applied Mathematics and Computation*, vol. 186, no. 1, pp. 286–293, 2007.

[49] D. Matignon, "Stability results for fractional differential equations with applications to control processing," *Computational Engineering in Systems Applications*, vol. 2, pp. 963–968, 1996.

[50] X. Wang, Z. Wang, and J. Xia, "Stability and bifurcation control of a delayed fractional-order eco-epidemiological model with incommensurate orders," *Journal of the Franklin Institute*, vol. 356, no. 15, pp. 8278–8295, 2019.

[51] W. Deng, C. Li, and J. Lü, "Stability analysis of linear fractional differential system with multiple time delays," *Nonlinear Dynamics*, vol. 48, no. 4, pp. 409–416, 2007.

[52] F. A. Rihan, S. Lakshmanan, A. H. Hashish, R. Rakkiyappan, and E. Ahmed, "Fractional-order delayed predator-prey systems with Holling type-II functional response," *Nonlinear Dynamics*, vol. 80, no. 1-2, pp. 777–789, 2015.

Hindawi
Complexity
Volume 2021, Article ID 6634156, 5 pages
https://doi.org/10.1155/2021/6634156

Research Article

Deep ChaosNet for Action Recognition in Videos

Huafeng Chen,[1] **Maosheng Zhang**,[2] **Zhengming Gao**,[1] **and Yunhong Zhao**[1]

[1]*School of Computer Engineering, Jingchu University of Technology, Jingmen, China*
[2]*School of Mathematics and Statistics, Yulin Normal University, Yulin, China*

Correspondence should be addressed to Huafeng Chen; chenhuafeng@jcut.edu.cn

Received 2 October 2020; Revised 30 January 2021; Accepted 2 February 2021; Published 13 February 2021

Academic Editor: Zhouchao Wei

Current methods of chaos-based action recognition in videos are limited to the artificial feature causing the low recognition accuracy. In this paper, we improve ChaosNet to the deep neural network and apply it to action recognition. First, we extend ChaosNet to deep ChaosNet for extracting action features. Then, we send the features to the low-level LSTM encoder and high-level LSTM encoder for obtaining low-level coding output and high-level coding results, respectively. The agent is a behavior recognizer for producing recognition results. The manager is a hidden layer, responsible for giving behavioral segmentation targets at the high level. Our experiments are executed on two standard action datasets: UCF101 and HMDB51. The experimental results show that the proposed algorithm outperforms the state of the art.

1. Introduction

Human action recognition in videos is an important area in computer vision, receiving sustained attention from the researchers due to its potential applications such as video supervision, entertainment, user interface, sports, video understanding, and patient monitoring. Current action recognition methods can be classified into three categories by action feature: chaos-based feature [1], manual feature [2], and deep learned feature. Inspired by the chaos-based feature and deep learned feature, we propose deep ChaosNet for action recognition to autonomously learn the nonlinear dynamical feature in video action.

2. Related Works

In this section, we briefly review the literature of action recognition from the chaos-based feature, manual feature, and deep learned feature.

2.1. Chaos-Based Feature. Ali et al. [3] introduced a human action recognition architecture by using the theory of chaotic systems to model and analyze nonlinear dynamics of human actions. Trajectories of reference joints are used as the representation of the nonlinear dynamical system that is generating the action. Xia et al. [4] proposed a human behavior recognition method based on chaotic invariant features and relevance vector machine (RVM). The trajectory generated by the motion of the human joint points is extracted to represent the nonlinear system of human action behavior, and the time delay is estimated by the C-C method. The chaotic invariants representing human behavior are extracted, and the RVM algorithm is used to identify human behavior. Venkataraman and Turaga [1] proposed to use the descriptor of the shape of the dynamical attractor as the feature representation of the nature of dynamics to solve the drawbacks of traditional approaches.

2.2. Manual Feature. Since human behavior is composed of body movements, general human behavior characteristics are based on the underlying visual movement characteristics. The underlying visual features are easy to extract and represent, and the underlying visual motion features of the same action have a certain degree of robustness under different cameras, so they are widely used in early human behavior recognition. There are two categories on human behavior characteristics: local feature representation and global feature representation. Existing global feature descriptions represent the formation of global

spatiotemporal cues through single-frame global features and video frame sequences from aspects of human body contours, posture joint points, and saliency segmentation such as the motion history image algorithm (motion history image, MHI) proposed by Bobick and Davis [5], the adaptation of the shape context algorithm (adaptation of the shape context) proposed by Zhang et al. [6], and the kinematic feature proposed by Ali and Shah [7]. Local feature description of underlying action features is still a hotspot in human behavior recognition research in recent years. Researchers considered the changes in the motion field between frames and proposed various local spatiotemporal feature descriptions, such as STIP [8], MoSIFT [9, 10], and dense trajectories [2, 11].

2.3. Deep Learned Feature. It includes two aspects of deep learning: action convolution features and action timing features. The former uses convolutional neural networks (CNNs) to learn the local depth features of human behavior from different modal data such as RGB image frames and optical flow of behavior videos [12]. On the basis of behavioral convolutional features, it uses methods such as recurrent neural network (RNN), time-series segment network, or linear coding to learn time-series features in multiple stages of behavior development [13]. Due to limited memory capacity of the GPU/CPU and different lengths of behavior duration (shown as different video frames), it is difficult to send all behavior video frames into the deep learning framework for feature learning. Therefore, it is necessary to perform key frame sampling on the behavior video in the behavior recognition process. Most of the existing behavior recognition algorithms use equal sampling [13] or sequential sampling [14–16], ignoring the differences in the development process of human behavior, and the key frames obtained are less representative.

3. Deep ChaosNet Framework

Inspired by Wang et al. and Balakrishnan et al. [15, 17], we propose deep ChaosNet framework for action recognition. The framework is illustrated in Figure 1. Deep ChaosNet features are extracted from video frames. And then, the features are sent to the low-level LSTM encoder and high-level LSTM encoder for obtaining low-level coding output and high-level coding results, respectively. The agent is a behavior recognizer for producing recognition results. The agent, based on hierarchical reinforcement learning, is mainly composed of manager and worker. Manager is a hidden layer, responsible for giving behavioral segmentation targets at the high level. Worker determines the spatiotemporal area of the video subsegment that best characterizes the segmentation target according to the segmentation target and outputs the segmentation recognition result.

3.1. Structure of the Network. The network system structure is shown in Figure 2. The manager LSTM unit obtains environmental status information $[h_t^M]$ according to the input $[c_{t-1}^M, h_{t-1}^W]$ and derives meaningful behavioral stage goals, which are used as the worker LSTM input to guide the worker to select the spatiotemporal region of the next behavioral video subsegment; the formula is as follows:

$$\begin{aligned} h_t^M &= S^M\left(h_{t-1}^M, \left[c_t^M, h_{t-1}^W\right]\right), \\ g_t &= u_M\left(h_t^M\right). \end{aligned} \tag{1}$$

S^M is the manager LSTM nonlinear function, and u_M is responsible for mapping the environmental state information h_t^M to the behavioral stage target g_t. The worker LSTM unit obtains context information h_t^W according to the input $[c_{t-1}^W, g_t]$. Based on h_t^W, we predict the next key frame position d_t, sampling area l_t, and behavior category p_t.

For manager and worker, this project uses a visual attention mechanism to explore areas of salient behavior. The manager attention model mainly explores the significant segment information of the behavior, and the worker attention model assists in searching the behavior key frames and significant areas within the frame. The parameters C_t^M and C_t^W are calculated as follows:

$$\begin{aligned} C_t^M &= \sum \alpha_{t,i}^M h_i^{E_m}, \\ \alpha_{t,i}^M &= \frac{\exp\left(e_{t,i}^M\right)}{\sum_{k=1}^n \exp\left(e_{t,k}^M\right)}, \\ e_{t,i}^M &= m^T \tanh\left(W_a^M h_i^{E_m} + U_a^M h_{t-1}^M + b_a^M\right), \\ C_t^W &= \sum \alpha_{t,i}^W h_i^{E_w}, \\ \alpha_{t,i}^W &= \frac{\exp\left(e_{t,i}^W\right)}{\sum_{k=1}^n \exp\left(e_{t,k}^W\right)}, \\ e_{t,i}^W &= w^T \tanh\left(W_a^W h_i^{E_m} + U_a^W h_{t-1}^W + b_a^W\right). \end{aligned} \tag{2}$$

3.2. Deep Learning Process. The worker strategy learning process is a standard reinforcement learning process. At each step t of the worker, the worker will give a classification prediction result P_t, and then the environment will give a reward R_t, so the goal of worker strategy learning is to minimize the negative value of the reward function. The loss function is

$$L\left(\theta_w\right) = -E_{p_t \sim \pi_{\theta_w}}\left[R\left(p_t\right)\right]. \tag{3}$$

Manager does not directly interact with the environment, and its strategy learning process cannot copy the worker. Compared with manager's time t, the worker strategy $\pi_{\theta_w}(p_t; g_t)$ is relatively stable, and this strategy directly affects the worker's behavior classification output results $p_{t,c}$ at time c. At this point, although the manager is a hidden layer, its strategic goal should be to minimize the negative value of the current reward. The loss function is

$$L\left(\theta_M\right) = -E_{g_t}\left[R\left(g_t\right)\pi\left(p_{t,c}; g_t\right)\right]. \tag{4}$$

4. Experiments and Results

We verify the proposed deep ChaosNet on two standard action datasets: UCF101 [18] and HMDB51 [19]. UCF101 is

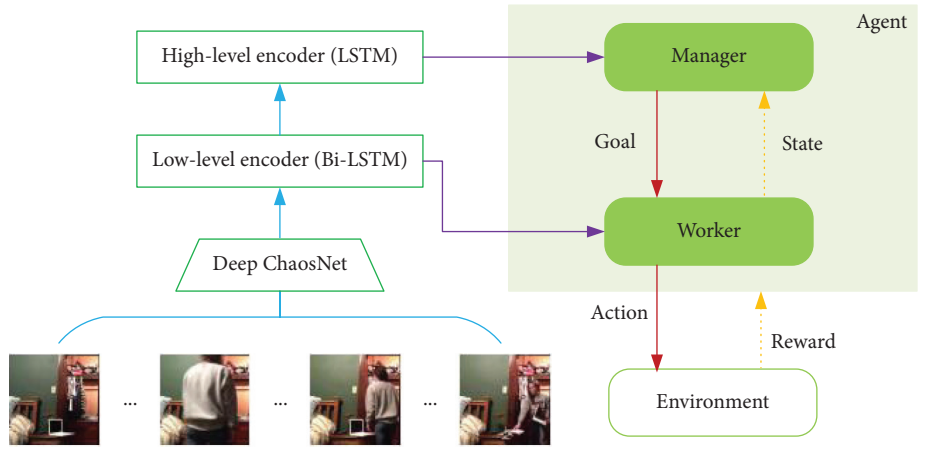

Figure 1: Illustration of the pipeline of the proposed deep ChaosNet feature extraction.

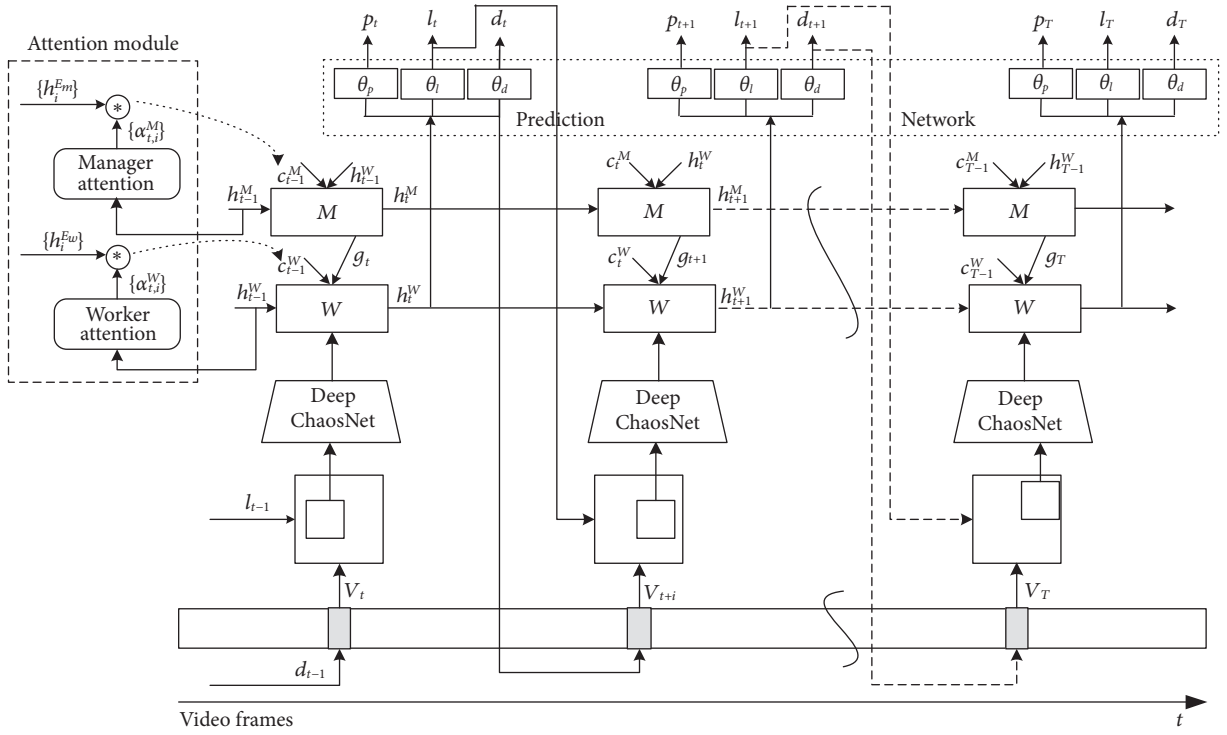

Figure 2: Illustration of the multilayer feature fusing.

an action recognition dataset of realistic action videos with 101 action categories collected from YouTube. Videos of the 101 action categories are divided into 25 groups, and each group can contain 4~7 action videos. Videos from the same group may share some common features, such as similar backgrounds and similar viewpoints. HMDB51 contains 51 types of actions, a total of 6849 videos which are collected from YouTube, Google Video, etc. Each action contains at least 51 videos with a resolution of $320 * 240$.

In the experiments, we construct 7-layer deep ChaosNet for both action datasets. The outputs of the deep ChaosNet are 2048-dim frame features, which are then projected to 512-dim. We use Bi-LSTM with hidden size 512 as the low-level encoder and LSTM with hidden size 256 as the high-level encoder [20]. The worker network consisted of worker LSTM with hidden size 1024. The manager network was composed of manager LSTM with hidden size 256, an attention module, and a linear layer that projected the output of the LSTM into the latent goal space. The environment internal critic was also an RNN, which contained a GRU, a built-in word embedding, a linear layer, and a sigmoid function.

We compare deep ChaosNet with the state-of-the-art deep learning methods [2, 12–16]. The comparison results are listed in Table 1. As shown in the table, the proposed deep ChaosNet exceeds the manual features [2] by 7.3% on UCF101 and by 5.8% on HMDB51. Our method is beyond the action convolution features [12] by 0.2% on UCF101 and

Table 1: Comparison of the proposed method with the state-of-the-art approaches.

Method	UCF101 (%)	HMDB51 (%)
Wang et al. [2]	86.0	60.1
Wu et al. [13]	88.0	59.4
Wang et al. [15]	89.1	65.2
Donahue et al. [14]	90.3	63.2
Chen et al. [16]	92.4	62.0
Sun et al. [12]	93.1	63.3
Deep ChaosNet	93.3	65.9

by 2.6% on HMDB51. The proposed method also outperforms the action timing features [13–16] by 1.1% on UCF101 and 0.7% on HMDB51 at least. Overall, our deep ChaosNet method surpasses all the state-of-the-art methods and becomes the new state of the art.

5. Conclusions

We extend ChaosNet to the deep neural network and apply it to action recognition. We deepen the hidden layers of ChaosNet, and then we separately input still frames and motions among frames into the deep network to extract spatial and temporal action features. The features act as the input for the attention-based action recognition framework. We verify our method on two standard action datasets: UCF101 and HMDB51, and the experimental results indicate that the proposed algorithm is competitive compared with the state of the art.

Data Availability

The data used to support the findings of this study are available from UCF101 (https://www.crcv.ucf.edu/research/data-sets/ucf101/), K. Soomro, A. R. Zamir, and M. Shah, UCF101: a dataset of 101 human action classes from videos in the Wild, CRCV-TR-12-01, November 2012, and HMDB51 (https://serre-lab.clps.brown.edu/resource/hmdb-a-large-human-motion-database/), H. Kuehne, H. Jhuang, E. Garrote, T. Poggio, and T. Serre, HMDB: a large video database for human motion recognition, ICCV, 2011.

Conflicts of Interest

The authors declare that they have no conflicts of interest.

Acknowledgments

This work was supported by the Natural Science Foundation of Hubei Province (Grant no. 2019CFC850), the Outstanding Youth Science and Technology Innovation Team Project of Colleges and Universities in Hubei Province (Grant no. T201923), the National Natural Science Foundation of China (Grant no. 61761044), and the Cultivation Project of Jingchu University of Technology (Grant no. PY201904).

References

[1] V. Venkataraman and P. Turaga, "Shape distributions of nonlinear dynamical systems for video-based inference," *Institute of Electrical and Electronics Engineers Transactions on Pattern Analysis and Machine Intelligence*, vol. 38, no. 12, pp. 2531–2543, 2016.

[2] H. Wang, A. Kläser, C. Schmid, and C.-L. Liu, "Dense trajectories and motion boundary descriptors for action recognition," *International Journal of Computer Vision*, vol. 103, no. 1, pp. 60–79, 2013.

[3] S. Ali, A. Basharat, and M. Shah, "Chaotic invariants for human action recognition," in *Proceedings of the 2007 IEEE 11th International Conference on Computer Vision*, pp. 1–8, IEEE, Rio De Janeiro, Brazi, October 2007.

[4] L.-m. Xia, J.-x. Huang, and L.-z. Tan, "Human action recognition based on chaotic invariants," *Journal of Central South University*, vol. 20, no. 11, pp. 3171–3179, 2013.

[5] A. F. Bobick and J. W. Davis, "The recognition of human movement using temporal templates," *Institute of Electrical and Electronics Engineers Transactions on Pattern Analysis and Machine Intelligence*, vol. 23, no. 3, pp. 257–267, 2001.

[6] Z. Zhang, Y. Hu, S. Chan, and L.-T. Chia, "Motion context: a new representation for human action recognition," in *European Conference on Computer Vision*, pp. 817–829, Springer, Berlin, Germany, 2008.

[7] S. Ali and M. Shah, "Human action recognition in videos using kinematic features and multiple instance learning," *Institute of Electrical and Electronics Engineers Transactions on Pattern Analysis and Machine Intelligence*, vol. 32, pp. 288–303, 2008.

[8] I. Laptev, M. Marszalek, C. Schmid, and B. Rozenfeld, "Learning realistic human actions from movies," in *Proceedings of the 2008 IEEE Conference on Computer Vision and Pattern Recognition*, pp. 1–8, IEEE, Anchorage, AK, USA, June 2008.

[9] M.-y. Chen and A. Hauptmann, *Mosift: Recognizing Human Actions in Surveillance Videos*, Springer, Berlin, Germany, 2009.

[10] H. Chen, J. Chen, H. Li, Z. Xu, and R. Hu, "Compressed-domain based camera motion estimation for realtime action recognition," in *Proceedings of the Pacific Rim Conference on Multimedia*, pp. 85–94, Springer, Hangzhou, China, November 2006.

[11] H. Wang, A. Kläser, C. Schmid, and C.-L. Liu, "Action recognition by dense trajectories," in *Proceedings of the CVPR 2011*, pp. 3169–3176, IEEE, Colorado Springs, CO, USA, June 2011.

[12] S. Sun, Z. Kuang, L. Sheng, W. Ouyang, and W. Zhang, "Optical flow guided feature: a fast and robust motion representation for video action recognition," in *Proceedings of the IEEE Conference on Computer Vision and Pattern Recognition*, pp. 1390–1399, Seattle, WA, USA, June 1994.

[13] Z. Wu, X. Wang, Y.-G. Jiang, H. Ye, and X. Xue, "Modeling spatial-temporal clues in a hybrid deep learning framework for video classification," in *Proceedings of the 23rd ACM*

International Conference on Multimedia, pp. 461–470, Brisbane, Australia, July 2017.

[14] J. Donahue, L. Anne Hendricks, S. Guadarrama et al., "Long-term recurrent convolutional networks for visual recognition and description," in *Proceedings of the IEEE Conference on Computer Vision and Pattern Recognition*, pp. 2625–2634, Seattle, WA, USA, June 1994.

[15] L. Wang, Y. Qiao, X. Tang, and L. Van Gool, "Actionness estimation using hybrid fully convolutional networks," in *Proceedings of the IEEE Conference on Computer Vision and Pattern Recognition*, pp. 2708–2717, Seattle, WA, USA, June 1994.

[16] H. Chen, J. Chen, R. Hu, C. Chen, and Z. Wang, "Action recognition with temporal scale-invariant deep learning framework," *China Communications*, vol. 14, no. 2, pp. 163–172, 2017.

[17] H. N. Balakrishnan, A. Kathpalia, S. Saha, and N. Nagaraj, "ChaosNet: a chaos based artificial neural network architecture for classification," *Chaos: An Interdisciplinary Journal of Nonlinear Science*, vol. 29, no. 11, p. 113125, 2019.

[18] K. Soomro, A. R. Zamir, and M. Shah, "Ucf101: a dataset of 101 human actions classes from videos in the wild," 2012, https://arxiv.org/abs/1212.0402.

[19] H. Kuehne, H. Jhuang, E. Garrote, T. Poggio, and T. Serre, "Hmdb: a large video database for human motion recognition," in *Proceedings of the 2011 International Conference on Computer Vision*, pp. 2556–2563, IEEE, Barcelona, Spain, November 2011.

[20] X. Wang, W. Chen, J. Wu, Y. F. Wang, and W. Y. Wang, "Video captioning via hierarchical reinforcement learning," in *Proceedings of the IEEE Conference on Computer Vision and Pattern Recognition*, Las Vegas, NV, USA, June 2016.

Hindawi
Complexity
Volume 2021, Article ID 8861465, 7 pages
https://doi.org/10.1155/2021/8861465

Research Article

Control of Chaotic Calcium Oscillations in Biological Cells

Quanbao Ji[1] and Min Ye[2]

[1]*School of Mathematics and Physics, Guangxi University for Nationalities, Nanning 530006, Guangxi, China*
[2]*School of Education Science, Guangxi University for Nationalities, Nanning 530006, Guangxi, China*

Correspondence should be addressed to Min Ye; 44225749@qq.com

Received 29 September 2020; Revised 29 October 2020; Accepted 21 January 2021; Published 4 February 2021

Academic Editor: Zhouchao Wei

The contribution of this present paper is to propose a method that combines a chemical Brusselator reaction-diffusion system with a biological cell system via gap junction for controlling and visualizing the frequency and magnitude of chaotic intracellular calcium oscillations in two cell types, including nonexcitable cells and the glial cells. This produces a wide variety of oscillatory behaviors similar to those reported in numerous biological experiments. We particularly show that in the majority of chaos cases, the reactor to cell coupling can induce the generation of regular calcium oscillations as the coupling strength is varied. Together with the proposed method of coupled models, the regularity of these chaotic oscillations enables us to gain better understanding and extensive insights into the overall coupling dynamics.

1. Introduction

Cell is characterized by basic structural and functional unit, as seen under the electron microscope in tissues of organisms. As the most important chemical signals in the cytosol of living cells, calcium ion (Ca^{2+}) is indispensable for biological signaling pathway in various physiological activities of human body and participates in many physiological functions, such as heart beat discrimination, muscle contraction, and gene expression [1–4]. Different types of Ca^{2+} oscillations, which are encoded into complex and diverse biological signals through the variation of calcium flux, induce brain plasticity in two ways simultaneously, amplitude modulation and frequency modulation [5–10].

In contrast with nonexcitable cell, glia, which are approximately 10 times more in number than nonexcitable cell, are unable to generate similar response by an electrical signal. It is well-known that glia has no electrically excitable effects on the plasma membrane [11]. Trying to explain the dynamical mechanism of chaotic Ca^{2+} oscillation in nonexcitable cell and glia, a lot of mathematical models were established in the field of calcium signaling with purpose of investigating various types of Ca^{2+} oscillations in the experiment (for review, see [12]). In recent years, many chaos control methods, such as adaptive control, feedback control, fuzzy control, and sliding mode control are proposed.

Here, we focus on a new approach that can help to control intracellular chaotic Ca^{2+} oscillation amplitude and frequency from a mathematical point of view in two types of cell systems. On this neurophysiological basis of their finds, mathematical models of control associated with membrane ion channels were discussed for describing different types of Ca^{2+} oscillations [13–23]. The question remains whether the dynamical mechanism correlated by systme parameter is efficient for controlling the intracellular oscillations in glia. Therefore, it is becoming increasingly clear that assent to creation of precise chaotic Ca^{2+} regulation is interesting, since the process can reveal the dynamical mechanism of regular and chaotic attractors controlled by the system parameter.

2. Mathematical Models

The aim of the present paper is to investigate reversible control of the amplitude and the frequency of chaotic Ca^{2+} oscillation in two different kinds of mathematical models proposed by Borghans et al., Lavrentovich and Hemkin, and Zhao et al. as examples that regulate the intracellular chaotic

calcium oscillations [24–26]. The evolution of Borghans model is governed by the following equations:

$$\begin{cases} \dfrac{dX}{dt} = J_{in} + J_{leak} - J_{pump} + J_{er} - J_{out}, \\ \dfrac{dY}{dt} = J_{pump} - J_{leak} - J_{er}, \\ \dfrac{dZ}{dt} = J_A - J_D - J_C, \end{cases} \tag{1}$$

where

$$\begin{aligned} J_{in} &= k_{in} r + k_{in2}, \\ J_{leak} &= r k_{leak} \frac{Z^4}{Z^4 + K_a^4} \times \frac{Y^2}{Y^2 + K_y^2} \times \frac{X^4}{X^4 + K_z^4}, \\ J_C &= eZ, \\ J_{er} &= k_f Y, \\ J_{pump} &= k_{kump} \frac{X^2}{X^2 + K_2^2}, \\ J_{out} &= k_{out} X, \\ J_A &= r k_p, \\ J_D &= k_d \frac{X^4}{X^4 + K_d^4} \times \frac{Y^2}{Y^2 + K_p^2}. \end{aligned} \tag{2}$$

There are three variables that represent the dynamics of nonexcitable cell model proposed by Borghans et al.: the free Ca^{2+} concentrations in the cytosol (X), the free Ca^{2+} concentrations in ER (Y), and inositol trisphosphate (IP_3) concentration in the cytosol (Z). Between cytosol and ER, most of Ca^{2+} fluxes were considered: leak Ca^{2+} from ER into cytosol (J_{leak}), Ca^{2+} uptake from cytosol into ER (J_{pump}), and Ca^{2+} from ER into cytosol (J_{er}). The parameter *r* denotes the stimuli level from outer space through the membrane of nonexcitable cell and into the cytosol, and hence we choose this parameter to be the control parameter to regulate the calcium oscillatory behaviors. Most of other parameter values used here are taken from our previous literatures in Ref. [18, 21, 22].

A mathematical one-pool model proposed by Lavrentovich et al. is also considered as another example of manipulating chaotic Ca^{2+} oscillation in glia cell type. Three differential equations in the Lavrentovich model form the relationship between the same variables appearing in the Borghans model.

$$\begin{cases} \dfrac{dCa_{cyt}}{dt} = v_{in} - k_{out} Ca_{cyt} + v_{CICR} - v_{serca} + k_f \left(Ca_{er} - Ca_{cyt} \right), \\ \dfrac{dCa_{er}}{dt} = v_{serca} - v_{CICR} - k_f \left(Ca_{er} - Ca_{cyt} \right), \\ \dfrac{dIP_3}{dt} = v_{PLC} - k_{deg} IP_3, \end{cases} \tag{3}$$

where

$$\begin{aligned} v_{serca} &= v_{M2} \left(\frac{Ca_{cyt}^2}{Ca_{cyt}^2 + k_2^2} \right), \\ V_{PLC} &= v_p \left(\frac{Ca_{cyt}^2}{Ca_{cyt}^2 + k_p^2} \right), \\ v_{CICR} &= 4 v_{M3} \left(\frac{k_{CaA}^n Ca_{cyt}^n}{\left(Ca_{cyt}^n + k_{CaA}^n \right) \left(Ca_{cyt}^n + k_{CaI}^n \right)} \right) \\ &\quad \times \left(\frac{IP_3^m}{IP_3^m + k_{ip3}^m} \right) \times \left(Ca_{er} - Ca_{cyt} \right). \end{aligned} \tag{4}$$

This model considers the IP_3 receptor influenced by cytosolic Ca^{2+} which at low Ca^{2+} concentration activates the probability of receptor opening. The parameter v_{in} denotes the Ca^{2+} flow from outside into the glia membrane. By changing value of this parameter, we can mimic spontaneous Ca^{2+} oscillations appearing in biological experiments [23]. We investigated stability dynamics of the Lavrentovich model using similar values of most parameters in our previous studies for derivation [21, 22].

The current paper is aimed at proposing a method to control chaotic Ca^{2+} oscillation by integrating cell model with the reactor via coupling. The Brusselator system is described by the following equations:

$$\begin{cases} \dfrac{dx}{dt} = -(b + 1)x + a x^2 y, \\ \dfrac{dy}{dt} = bx - a x^2 y. \end{cases} \tag{5}$$

This integration seemly occurs via diffusion of Ca^{2+} in cytosolic and ER alternatively, as is illustrated in Figure 1 from our previous study.

Most often biological information is encoded in regulation, variations in magnitude or frequency, and spatial organization of intracellular Ca^{2+}. In this case, Ca^{2+} and IP_3 concentrations act as the co-stimuli to trigger Ca^{2+} releasing from IP_3 receptor, and we add the coupling term (Xk_{c1}-xk_{c2}) to the first equation in (1). In summary, this coupled nonexcitable cell model can be described as follows:

$$\begin{cases} \dfrac{dX}{dt} = J_{in} + J_{leak} - J_{pump} + J_{er} - J_{out} - k_{C1} X + k_{C2} x, \\ \dfrac{dY}{dt} = J_{pump} - J_{leak} - J_{er}, \\ \dfrac{dZ}{dt} = J_A - J_D - J_C, \\ \dfrac{dx}{dt} = 1 - (b + 1)x + a x^2 y + k_{C1} X - k_{C2} x, \\ \dfrac{dy}{dt} = bx - a x^2 y. \end{cases} \tag{6}$$

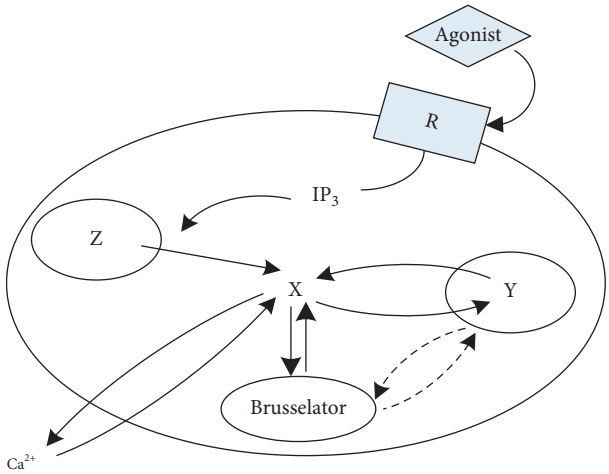

Figure 1: Schematic presentation of integration between the cell model and the Brusselator reactor. This illustration is from [19].

Having presented the artificial mathematical nonexcitable cell model for controlling chaotic Ca^{2+} oscillation, we similarly couple the Brusselator reactor with glia cell system. This integrated coupling system is expressed as follows:

$$\begin{cases} \dfrac{d\mathbf{Ca_{cyt}}}{dt} = \mathbf{v_{in}} - \mathbf{k_{out}}\mathbf{Ca_{cyt}} + \mathbf{v_{CICR}} - \mathbf{v_{serca}} + \mathbf{k_f}\left(\mathbf{Ca_{er}} - \mathbf{Ca_{cyt}}\right) \\ -\mathbf{k_{C1}}\mathbf{Ca_{cyt}} + \mathbf{k_{C2}}\mathbf{x}, \\ \dfrac{d\mathbf{Ca_{er}}}{dt} = \mathbf{v_{serca}} - \mathbf{v_{CICR}} - \mathbf{k_f}\left(\mathbf{Ca_{er}} - \mathbf{Ca_{cyt}}\right), \\ \dfrac{d\mathbf{IP_3}}{dt} = \mathbf{v_{PLC}} - \mathbf{k_{deg}}\mathbf{IP_3}, \\ \dfrac{d\mathbf{x}}{dt} = \mathbf{1} - (\mathbf{b}+\mathbf{1})\mathbf{x} + \mathbf{a}\mathbf{x}^2\mathbf{y} + \mathbf{k_{C1}}\mathbf{Ca_{cyt}} - \mathbf{k_{C2}}\mathbf{x}, \\ \dfrac{d\mathbf{y}}{dt} = \mathbf{b}\mathbf{x} - \mathbf{a}\mathbf{x}^2\mathbf{y}. \end{cases} \tag{7}$$

In our modified models, chaotic Ca^{2+} oscillation can be easily controlled by changing the parameter values of $\mathbf{k_{c1}}$ and $\mathbf{k_{c2}}$, representing the assumed Ca^{2+} flux transport rate both in cytosol and Brusselator reactor, due to the involved variables and coupling of elements.

3. Results

In this section, we investigate possible method for controlling chaotic Ca^{2+} oscillation for understanding the dynamical mechanism. Furthermore, it is not only to control the magnitude and the frequency of chaotic Ca^{2+} oscillation in nonexcitable cell and glia but also to monitor the shape of chaos.

Firstly, we use equation (6) of the nonexcitable cell system to evaluate effectiveness of our method. Chaotic Ca^{2+} oscillations in the coupled system with the parameter $r = 0.95$ are plotted in Figure 2. It is shown that chaotic Ca^{2+} oscillation occurs in this case. As the controlling rate parameters $k_{c1} = 0$, $k_{c2} = 0$, it means that the chemical Brusselator reactor has no effect on the coupled system (6). In Figure 2(a), it shows spiking chaos through complex dynamical activities. The 2D corresponding dimensional phase portrait diagram in (x, y, z)-plane is also plotted in Figure 2(b). One can easily see a basic attractor in the phase portrait.

Secondly, we fix the control parameters k_{c1} and k_{c2} to regulate the chaotic Ca^{2+} oscillations in nonexcitable cell system (6). In Figure 3(a), another spiking chaos can be gained by varying $k_{c1} = 0.002$, $k_{c2} = 0.04$, which is similar to that of Figure 2(a). The main difference is the way how the reduced small-amplitude level can be achieved, which is verified by the corresponding 2D phase diagram in Figure 3(b).

Based on the component-coupled method, an effective manipulation of chaotic Ca^{2+} oscillation is shown in Figure 4 when we choose $k_{c1} = 0.1$ and $k_{c2} = 0.1$. Compared with Figures 2(a) and 3(a), it can be seen that this kind of regulation significantly reduces the amplitude (see Figure 4(a)) and the calcium wave (see Figure 4(b)) in this case. There is a sharp decrease of spiking activity and distinctive shape variation of each chaotic spiking, which is followed by a slower decrease for high control parameter values. Therefore, we use the coupling method as a measure for manipulating the chaotic Ca^{2+} activities of the modified model.

We further examine the control properties of coupled system (6) for different values of controlling parameters k_{c1} and k_{c2} which determine the rate of amplitude and frequency of calcium flux. Figure 5(a) shows the corresponding time series of X for $k_{c1} = 6$ and $k_{c2} = 0.2$, respectively. When the value of k_{c1} and k_{c2} is large enough, the chaotic behavior turns to be a series of regular spiking. The main difference between them is that the phase portrait of spiking oscillation is a stable circle unlike the basic attractor in Figure 5(b). The transition is much different from that of previous time course in Figures 2(a), 3(a), and 4(a).

Finally, we use equation (7) of the glia cell system to test the validity of the coupling method. Time process of chaotic Ca^{2+} oscillations with the parameter $v_{in} = 0.05025$ is shown in Figure 6(a). As $k_{c1} = 0$, $k_{c2} = 0$, it means similar to that in the coupled nonexcitable cell system (6).

The 3D dimensional phase portrait diagram in (Ca_{cyt}, Ca_{er}, IP_3)-plane is also plotted in Figure 6(b), and one can easily see a strange attractor in the middle of portrait diagram.

In contrast with the original chaotic behavior, the shape of chaos in Figure 7(a) is of quite different spiking type as $k_{c1} = 0.0001$, $k_{c2} = 0.0001$, keeping their waveforms changed. The main difference is that this type of firing in Figure 7(a) is called the spiking chaos, while bursting chaos is considered in Figure 6(a). Burst means the system behavior alternates between repetitive firing and steady state, which is caused by the system slow variable. 3D dimensional phase portrait

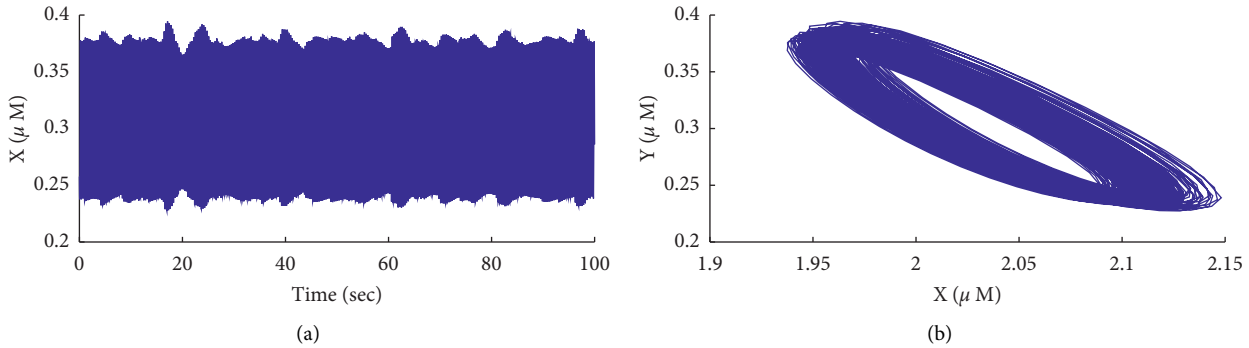

FIGURE 2: Original chaotic Ca^{2+} oscillation in coupled model (6) of nonexcitable cell without control constraints at $r = 0.95$. (a) The respective time course of variable **X** with controlling rate parameters $\mathbf{k_{c1}} = 0$, $\mathbf{k_{c2}} = 0$. (b) 2D projection of the trajectory in **X**, **Y** phase space with controlling rate parameters $\mathbf{k_{c1}} = 0$, $\mathbf{k_{c2}} = 0$.

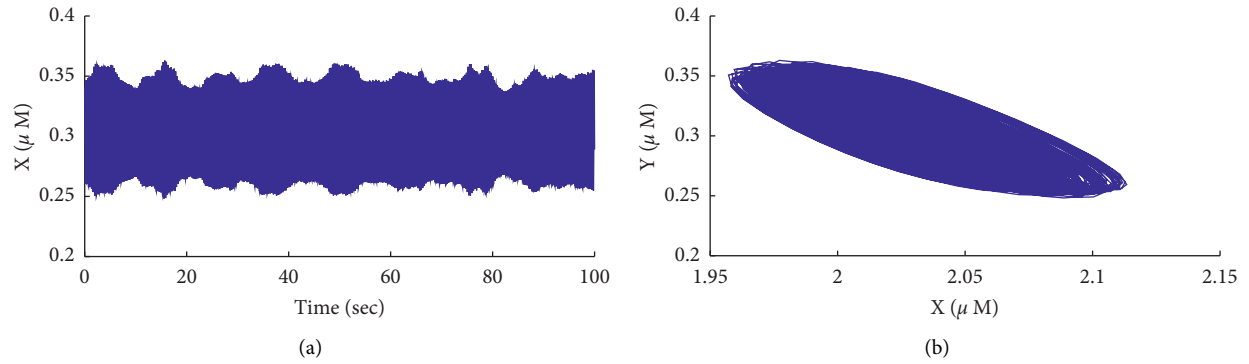

FIGURE 3: Small-amplitude feedback control of chaotic Ca^{2+} oscillation in coupled model (6) of nonexcitable cell at $r = 0.95$. (a) The respective time course of variable X with controlling rate parameters $k_{c1} = 0.002$, $k_{c2} = 0.04$. (b) 2D projection of the trajectory in X, Y phase space with controlling rate parameters $k_{c1} = 0.002$, $k_{c2} = 0.04$.

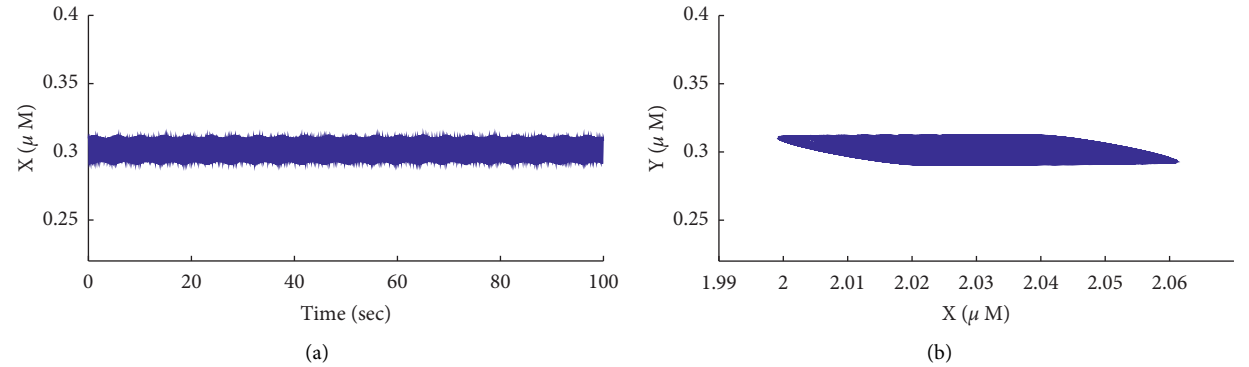

FIGURE 4: Large-amplitude feedback control of chaotic Ca^{2+} oscillation in coupled model (6) of nonexcitable cell at $r = 0.95$. (a) The respective time course of variable X with controlling rate parameters $k_{c1} = 0.1$, $k_{c2} = 0.1$. (b) 2D projection of the trajectory in X, Y phase space with controlling rate parameters $k_{c1} = 0.1$, $k_{c2} = 0.1$.

diagram is drawn in Figure 7(b). More additional portrait circles occur.

When the parameters $k_{c1} = 0.001$, $k_{c2} = 0.01$, the coupled glia cell model begins to burst with quiet different chaotic behavior from the above one with time process shown in Figures 6(a) and 7(a). The results of numerical integration for controlling chaotic calcium flux are shown in Figure 8. Figure 8(a) shows a typical example of burst in a sharp peak, which is followed by several lower frequency oscillatory activities. Figure 8(b) shows the three-dimensional portrait diagram corresponding to Figure 8(a). This type of oscillation is also a regular bursting.

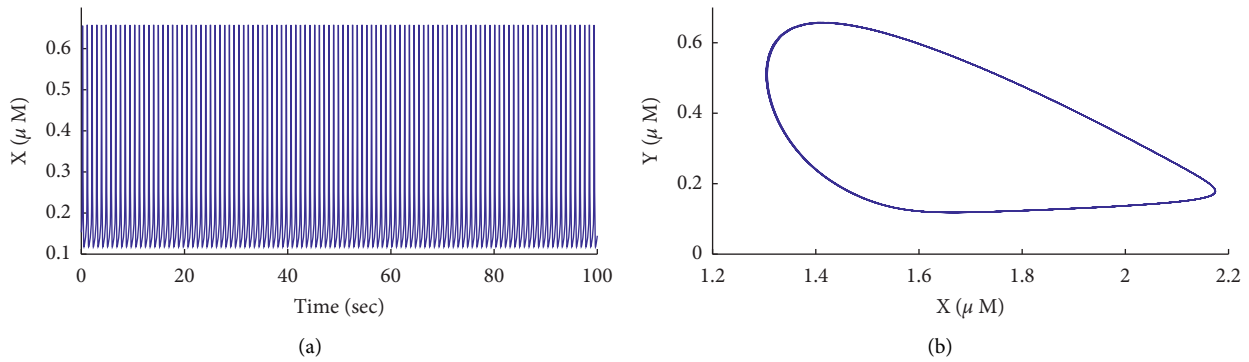

FIGURE 5: Shape, amplitude, and frequency control of chaotic Ca^{2+} oscillation in coupled model (6) of nonexcitable cell at $r = 0.95$. (a) The respective time course of variable X with controlling rate parameters $k_{c1} = 6$, $k_{c2} = 0.2$. (b) 2D projection of the trajectory in X, Y phase space with controlling rate parameters $k_{c1} = 6$, $k_{c2} = 0.2$.

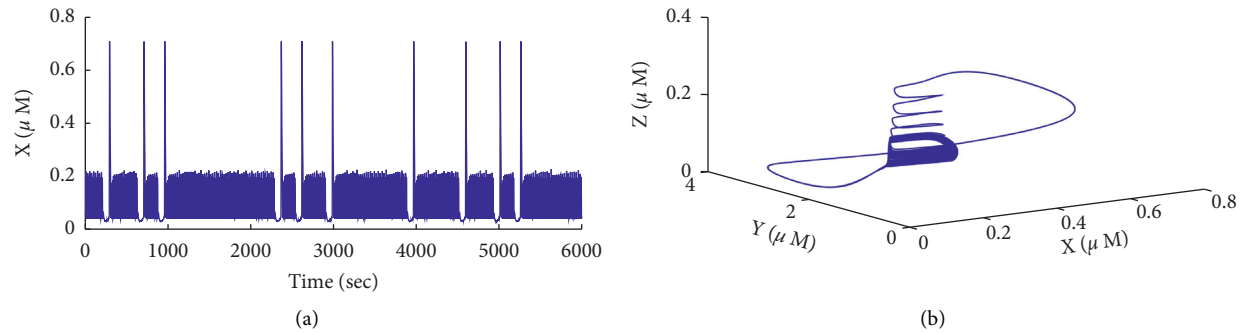

FIGURE 6: Original chaotic Ca^{2+} oscillation in coupled model (7) of the glia cell system without control constraints for the parameter $v_{in} = 0.05025$. (a) The respective time course of variable Ca_{cyt} with controlling rate parameters $k_{c1} = 0$, $k_{c2} = 0$. (b) 3D projection of the trajectory in (Ca_{cyt}, Ca_{cyt}, IP_3) phase space with controlling rate parameters $k_{c1} = 0$, $k_{c2} = 0$.

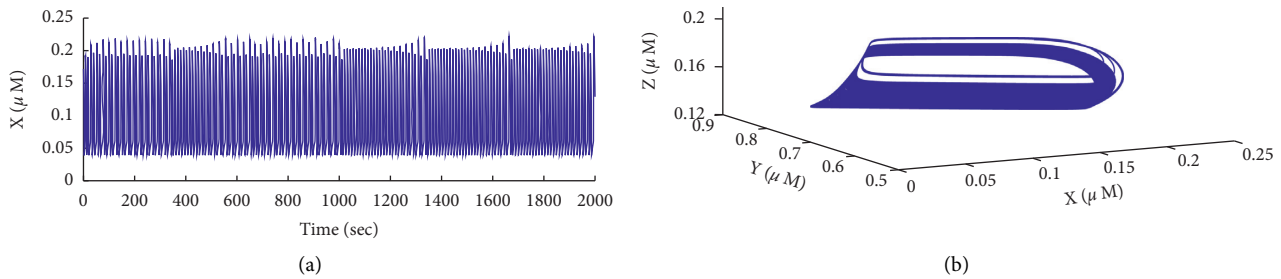

FIGURE 7: Shape and amplitude control of chaotic Ca^{2+} oscillation in coupled model (7) of the glia cell system for the parameter $r_{in} = 0.05025$. (a) The respective time course of variable Ca_{cyt} with controlling rate parameters $k_{c1} = 0.0001$, $k_{c2} = 0.0001$. (b) 3D projection of the trajectory in (Ca_{cyt}, Ca_{cyt}, IP_3) phase space with controlling rate parameters $k_{c1} = 0.0001$, $k_{c2} = 0.0001$.

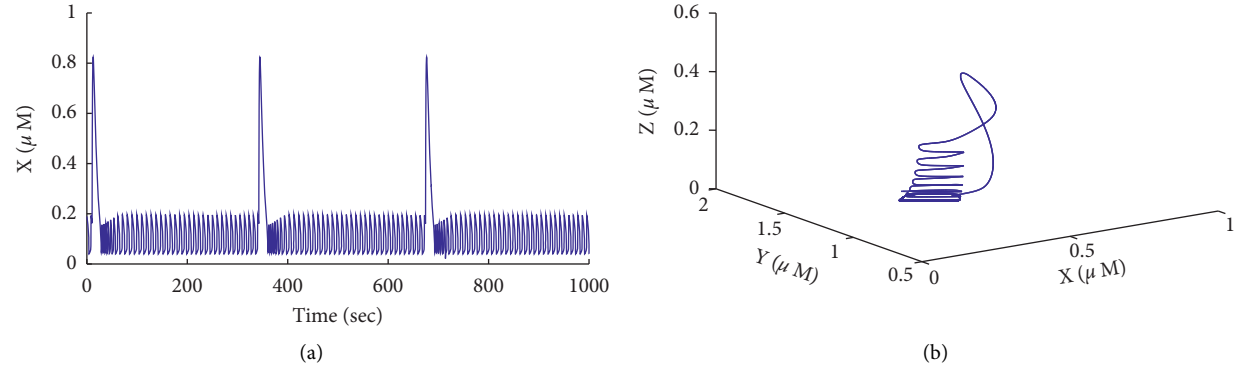

FIGURE 8: Shape, amplitude, and magnitude control of chaotic Ca^{2+} oscillation in coupled model (7) of the glia cell system for the parameter $r_{in} = 0.05025$. (a) The respective time course of variable Ca_{cyt} with controlling rate parameters $k_{c1} = 0.001$, $k_{c2} = 0.01$. (b) 3D projection of the trajectory in (Ca_{cyt}, Ca_{cyt}, IP_3) phase space with controlling rate parameters $k_{c1} = 0.001$, $k_{c2} = 0.01$.

4. Summary

In summary, we have theoretically integrated a chemical Brusselator reactor to the nonexcitable cell and glia models, respectively, based on the coupling method. We aimed at controlling the chaotic Ca^{2+} oscillations. A component-coupled method was introduced by integrating a Brusselator reactor to cell model. This kind of integration not only influences the frequency and magnitude of chaotic calcium flux but also changes the shape of chaotic behavior. The integration method should be regarded as the initial effort for regulating intracellular chaotic Ca^{2+} oscillations in living cells. Validity of this coupling method was verified by changing values of controlling rate, respectively.

Therefore, simulation results in this paper may enhance our understanding of generation and transition mechanism of chaotic Ca^{2+} oscillations in nonexcitable cell and glia cell, which help us better understand the essence of calcium signaling between nonexcitable cell and the glia cell from a mathematical point of view.

Data Availability

The data used to support the findings of this study are included within this article, and the sources from where they were adopted were cited accordingly.

Conflicts of Interest

The authors declare that they have no conflicts of interest.

Authors' Contributions

The authors claim that the research was realized in collaboration with the same responsibility. All authors read and approved the last version of the manuscript.

Acknowledgments

This study was supported by the National Natural Science Foundation of China under grant nos. 12062004 and 11872084 and the Guangxi Natural Science Foundation under grant no. 2020JJA110010.

References

[1] M. V. Sofroniew and H. V. Vinters, "Astrocytes: biology and pathology," *Acta Neuropathologica*, vol. 119, no. 1, pp. 7–35, 2010.

[2] T. R. Chay, "Electrical bursting and luminal calcium oscillation in excitable cell models," *Biological Cybernetics*, vol. 75, no. 5, pp. 419–431, 1996.

[3] J. Sneyd, K. Tsaneva-Atanasova, D. I. Yule, J. L. Thompson, and T. J. Shuttleworth, "Control of calcium oscillations by membrane fluxes," *Proceedings of the National Academy of Sciences*, vol. 101, no. 5, pp. 1392–1396, 2004.

[4] J. F. Aguilar, K. L. Abro, K. Olusola, and Y. Ahmet, "Chaos in a calcium oscillation model via Atangana-Baleanu operator with strong memory," *The European Physical Journal Plus*, vol. 134, p. 140, 2019.

[5] P. Hannanta-anan and B. Y. Chow, "Optogenetic control of calcium oscillation waveform defines NFAT as an integrator of calcium load," *Cell Systems*, vol. 2, no. 4, pp. 283–288, 2016.

[6] M. Marhl, T. Haberichter, M. Brumen, and R. Heinrich, "Complex calcium oscillations and the role of mitochondria and cytosolic proteins," *Biosystems*, vol. 57, no. 2, pp. 75–86, 2000.

[7] T. Haberichter, M. Marhl, and R. Heinrich, "Birhythmicity, trirhythmicity and chaos in bursting calcium oscillations," *Biophysical Chemistry*, vol. 90, no. 1, pp. 17–30, 2001.

[8] E. Smedler and P. Uhlén, "Frequency decoding of calcium oscillations," *Biochimica et Biophysica Acta (BBA)-General Subjects*, vol. 1840, no. 3, pp. 964–969, 2014.

[9] V. V. Matrosov and V. B. Kazantsev, "Bifurcation mechanisms of regular and chaotic network signaling in brain astrocytes," *Chaos: An Interdisciplinary Journal of Nonlinear Science*, vol. 21, no. 2, Article ID 23103, 2011.

[10] M. Marhl, S. Schuster, and M. Brumen, "Mitochondria as an important factor in the maintenance of constant amplitudes of cytosolic calcium oscillations," *Biophysical Chemistry*, vol. 71, no. 2-3, pp. 125–132, 1998.

[11] M. Pekny and M. Nilsson, "Astrocyte activation and reactive gliosis," *Glia*, vol. 50, no. 4, pp. 427–434, 2005.

[12] F. Oschmann, H. Berry, K. Obermayer, and K. Lenk, "From in silico astrocyte cell models to neuron-astrocyte network models: a review," *Brain Research Bulletin*, vol. 136, pp. 76–84, 2018.

[13] T. J. Shuttleworth and O. Mignen, "Calcium entry and the control of calcium oscillations," *Biochemical Society Transactions*, vol. 31, no. 5, pp. 916–919, 2003.

[14] F. Codazzi, M. N. Teruel, and T. Meyer, "Control of astrocyte Ca2+ oscillations and waves by oscillating translocation and activation of protein kinase C," *Current Biology*, vol. 11, no. 14, pp. 1089–1097, 2001.

[15] A. Cornell-Bell, S. Finkbeiner, M. Cooper, and S. Smith, "Glutamate induces calcium waves in cultured astrocytes: long-range glial signaling," *Science*, vol. 247, no. 4941, pp. 470–473, 1990.

[16] D. A. Zacharias, G. S. Baird, and R. Y. Tsien, "Recent advances in technology for measuring and manipulating cell signals," *Current Opinion in Neurobiology*, vol. 10, no. 3, pp. 416–421, 2000.

[17] A. Pietak and M. Levin, "Bioelectrical control of positional information in development and regeneration: a review of conceptual and computational advances," *Progress in Biophysics and Molecular Biology*, vol. 137, pp. 52–68, 2018.

[18] Y. Lu and Q. Ji, "Control of intracellular calcium bursting oscillations using method of self-organization," *Nonlinear Dynamics*, vol. 67, no. 4, pp. 2477–2482, 2012.

[19] Q. Ji, Y. Zhou, Z. Yang, and X. Meng, Evaluation of bifurcationphenomena in a modified Shen-arter model for intracellular Ca2+Ca2+bursting oscillations," *Nonlinear Dynamics*, vol. 84, no. 3, pp. 1281–1288, 2016.

[20] Q. Ji and Y. Lu, "Bifurcations and continuous transitions in a nonlinear model of intracellular calcium oscillations," *International Journal of Bifurcation and Chaos*, vol. 23, no. 2, Article ID 1350033, 2013.

[21] M. Ye and H. K. Zuo, "Stability Analysis of regular and chaotic Ca2+ oscillations in astrocytes," *Discrete Dynamics in Nature and Society*, vol. 2020, Article ID 9279315, 9 pages, 2020.

[22] H. Zuo and M. Ye, "Bifurcation and numerical simulations of Ca2+ oscillatory behavior in astrocytes," *Frontiers in Physics*, vol. 8, 2020.

[23] I. Goto, S. Kinoshita, and K. Natsume, "The model of glutamate-induced intracellular Ca2+ oscillation and intercellular Ca2+ wave in brain astrocytes," *Neurocomputing*, vol. 58–60, pp. 461–467, 2004.

[24] J. M. Borghans, G. Dupont, and A. Goldbeter, "Complex intracellular calcium oscillations A theoretical exploration of possible mechanisms," *Biophysical Chemistry*, vol. 66, no. 1, pp. 25–41, 1997.

[25] M. Lavrentovich and S. Hemkin, "A mathematical model of spontaneous calcium(II) oscillations in astrocytes," *Journal of Theoretical Biology*, vol. 251, no. 4, pp. 553–560, 2008.

[26] Y. Zhao, X. Sun, Y. Liu, and J. Kurths, "Phase synchronization dynamics of coupled neurons with coupling phase in the electromagnetic field," *Nonlinear Dynamics*, vol. 93, no. 3, pp. 1315–1324, 2018.

Hindawi
Complexity
Volume 2021, Article ID 8864981, 7 pages
https://doi.org/10.1155/2021/8864981

Research Article

A Gaussian Process Latent Variable Model for Subspace Clustering

Shangfang Li

School of Mathematics and Statistics, Yulin Normal University, Yulin 537000, Guangxi, China

Correspondence should be addressed to Shangfang Li; monklsf@126.com

Received 27 September 2020; Revised 6 December 2020; Accepted 19 December 2020; Published 13 January 2021

Academic Editor: Zhouchao Wei

Effective feature representation is the key to success of machine learning applications. Recently, many feature learning models have been proposed. Among these models, the Gaussian process latent variable model (GPLVM) for nonlinear feature learning has received much attention because of its superior performance. However, most of the existing GPLVMs are mainly designed for classification and regression tasks, thus cannot be used in data clustering task. To address this issue and extend the application scope, this paper proposes a novel GPLVM for clustering (C-GPLVM). Specifically, by combining GPLVM with the subspace clustering method, our C-GPLVM can obtain more representative latent variable for clustering. Moreover, it can directly predict the new samples by introducing a back constraint in the model, thus being more suitable for big data learning tasks such as analysis of chaotic time series and so on. In the experiment, we compare it with the related GPLVMs and clustering algorithms. The experimental results show that the proposed model not only inherits the feature learning ability of GPLVM but also has superior clustering accuracy.

1. Introduction

In machine learning tasks, data are often distributed in a high-dimensional space and have many redundant features. Training machine learning models in such high-dimensional data may result in not only higher computational and storage complexities but also the model overfitting problem [1]. Existing research studies have shown that high-dimensional data are often embedded in low-dimensional manifold. We therefore can utilize the dimension reduction and feature learning method to learn the low-dimensional manifold and obtain more representative feature for the improvements of machine learning model accuracy and efficiency. Thus, effective feature representation is the key to success of machine learning applications.

In the past decade, many related methods have been proposed, such as dictionary learning [2], autoencoder [3], Gaussian process latent variable model (GPLVM) [4], Isomap [5], and locally linear embedding [6]. Among these models, the GPLVM for nonlinear feature learning has received extensive attention because of its superior feature learning ability and has been used in many applications such as dynamical system [7], modelling and control of nonlinear system [8]. Given a few training samples, it can effectively learn the low-dimensional manifold that is embedded in the high-dimensional space, thus has been widely used in the dimension reduction and data visualization tasks [9, 10].

Although has the abovementioned advantages, the conventional GPLVM is just a fully unsupervised feature learning model, thus cannot meet the demands of real-world applications, when dealing with specific machine leaning tasks such as analysis of chaotic time series, dynamical system [7], and modelling and control of nonlinear system in which we also observe the response values of the inputs. How to modify the GPLVM and improve its performance is the key content of the related research studies. To date, the extensions of this model mainly focus on the supervised and unsupervised learning methods [9, 11, 12]. These methods assume that apart from the input features, we also observe labels of the samples. By their extensions, the GPLVM can effectively utilize the supervised information to improve the classification accuracy of the learned latent variables. However, in the real-world applications, we may also deal with unsupervised clustering tasks in which we cannot

obtain the label information or any other auxiliary information, thus bringing more challenges to application of the GPLVM in clustering tasks.

In order to address the abovementioned issues, this paper proposes a fusion model that combines the GPLVM with the subspace clustering model [13] to simultaneously obtain more representative features and accurate clustering results. Moreover, we also use the back constraint trick [14] in the model, which makes the model predict new samples directly and more suitable for big data learning tasks such as analysis of chaotic time series. In the experiment, we verify the performance of the proposed model on multiple datasets. The experimental results show that our model has much superior clustering performance than the other related models.

2. Related Work

2.1. Gaussian Process Latent Variable Model. The GPLVM is a fully unsupervised and nonlinear latent variable model. In this model, given N observed samples $\mathbf{X} = [\mathbf{x}_1, \ldots, \mathbf{x}_N]^T \in \mathbb{R}^{N \times D}$ (where $\mathbf{x}_n \in \mathbb{R}^D$ denotes the n^{th} training sample), our objective is to learn the corresponding low-dimensional latent variable. In this paper, we use $\mathbf{h}_n \in \mathbb{R}^Q$ ($Q \ll D$) to denotes the latent variable of $\mathbf{x}_n$. Obviously, the GPLVM can realize dimension reduction by learning the latent variables. Specifically, the GPLVM assumes that the generation process of $\mathbf{x}_n$ as follows:

$$x_{nd} = f_d(\mathbf{h}_n) + \epsilon_{nd}, \tag{1}$$

where x_{nd} is the d^{th} feature of the n^{th} training sample, ϵ_{nd} is the noise term that follows a Gaussian distribution $p(\epsilon_{nd}) = N(\epsilon_{nd}|0, \sigma^2)$, and $f_d(\cdot)$ is a function that follows a Gaussian process prior. We use $\mathbf{f}_d$ to denote the N outputs of $f_d(\cdot)$ with inputs $\mathbf{H} = [\mathbf{h}_1, \ldots, \mathbf{h}_N]^T$. Thus, we have $\mathbf{f}_d \sim N(\mathbf{0}, \mathbf{K})$, where $\mathbf{K}$ is the kernel matrix that is computed by using kernel function $k(\cdot, \cdot)$ on the latent variables in $\mathbf{H}$. The i^{th} row and j^{th} column element of $\mathbf{K}$ is computed as $K_{ij} = k(\mathbf{h}_i, \mathbf{h}_j)$. By integrating out the intermediate variable $\mathbf{f}_d$, we can obtainthe following marginal likelihood function:

$$p(\mathbf{X}|\mathbf{H}, \boldsymbol{\theta}) = \prod_{d=1}^{D} p\left(\mathbf{x}_{:,d}|\mathbf{H}, \boldsymbol{\theta}\right) = \prod_{d=1}^{D} \frac{\exp\left(-1/2\mathbf{x}_{:,d}^T\left(\mathbf{K} + \sigma^2\mathbf{I}\right)^{-1}\mathbf{x}_{:,d}\right)}{(2\pi)^{N/2}\left|\mathbf{K} + \sigma^2\mathbf{I}\right|^{1/2}}, \tag{2}$$

where θ denotes the hyperparameters involved in the kernel function and noise distribution. In the model optimization process, the GPLVM learns the latent variable and hyperparameters jointly by maximizing the above likelihood function and obtains the low-dimensional representation finally.

From the abovementioned generation process, as a fully unsupervised dimension reduction model, the GPLVM cannot embed auxiliary information when dealing with specific machine learning tasks, thus cannot meet demands of real-world application. For example, in analysis of chaotic time series, data of similar time will have similar features. If it can utilize this knowledge, the GPLVM will learn more representative features for the task and significantly improve the prediction accuracy. The existing methods for the extension of GPLVM mainly focus on embedding supervised information to improve its classification and regression accuracy, for example, the discriminative GPLVM (D-GPLVM) and supervised GPLVM (S-GPLVM). For the extension to the clustering task, the related works is much fewer. The existing unsupervised GPLVM just focuses on how to preserve the local distance and learn better latent variables or features. For example, local preserving projection GPLVM (LPP-GPLVM) combines the objective of local preserving projection with that of the GPLVM, thus simultaneously learning the low-dimensional representation and preserving the local structures [15]. The GPLVM with back constraints (B-GPLVM) introduces a back-constraint (from observed space to latent space) into the GPLVM. By this way, it can also realize the preservation of local distance.

2.2. Subspace Clustering. The goal of subspace clustering is to segment a set of data samples into different subspaces; thus, similar samples are in the same subspace, while dissimilar samples are in different subspaces. Over the past decade, subspace clustering has been used in various clustering tasks and many well-designed algorithms have been proposed such as Gaussian mixture model- (GMM-) based methods [16, 17], matrix factorization- (MF-) based methods [18, 19], algebra-based methods [20], and spectral clustering methods [13, 21, 22]. Among these models, the subspace clustering method based on spectral clustering has been widely applied because of its concise implementation process and reliable performance. It uses low-rank representation to construct the affinity matrix of the spectral clustering. Its objective is to find the low-rank representation of input data $\mathbf{X}$ by optimizing the following function:

$$\begin{aligned} &\operatorname{argmin}_Z \operatorname{rank}(\mathbf{Z}), \\ &\text{s.t}\,\mathbf{X} = \mathbf{ZX}, \end{aligned} \tag{3}$$

where we assume that each sample can be expressed by the linear combination of other samples. The above low-rank penalty term can be considered as a global constraint on the subspace structure of samples and makes similar samples have similar weights. In general, we can use the following nuclear norm to replace the penalty term:

$$\begin{aligned} &\operatorname{argmin}_Z ||\mathbf{Z}||_*, \\ &\text{s.t. } \mathbf{X} = \mathbf{ZX}, \end{aligned} \tag{4}$$

where we use the nuclear norm $\|\mathbf{Z}\|_*$ to approximate the rank of $\mathbf{Z}$. Considering that the data often contain noise, we use the following formulation to learn the self-representation matrix $\mathbf{Z}$:

$$\operatorname{argmin}_Z \frac{1}{2}\|\mathbf{X}\text{-}\mathbf{ZX}\|_F^2 + \lambda\|\mathbf{Z}\|_*. \tag{5}$$

In low-rank subspace clustering, we can first construct the affinity matrix $\mathbf{W}$ and the Laplace matrix $\mathbf{L}$ and then use spectral clustering to cluster the data. $\mathbf{W}$ and $\mathbf{L}$ can be constructed as follows:

$$\begin{aligned}\mathbf{W} &= |\mathbf{Z}| + |\mathbf{Z}|^T,\\ \mathbf{L} &= \mathbf{D} - \mathbf{W},\end{aligned} \tag{6}$$

where $\mathbf{D}$ denotes a diagonal matrix and $D_{ii} = \sum_{j=1}^{N} W_{ij}$. After obtaining the Laplace matrix, we can optimize the following objective function to obtain the latent variable $\mathbf{H} \in \mathbb{R}^{N\times Q}$:

$$\begin{aligned}&\arg\min_{\mathbf{H}} tr\left(\mathbf{H}^T\mathbf{L}\mathbf{H}\right),\\ &s.t.\ \mathbf{H}^T\mathbf{H} = \mathbf{I}.\end{aligned} \tag{7}$$

Obviously, $\mathbf{H}$ is composed of the eigenvectors corresponding to the Q smallest eigenvalues. At last, we can run the k-means algorithm on the learned $\mathbf{H}$ and obtain the clustering result.

3. Model Construction and Optimization

3.1. Designing of the Gaussian Process Latent Variable Clustering Model. Assuming that there are N observed samples denoted as $\mathbf{X} = [\mathbf{x}_1, \ldots, \mathbf{x}_N]^T$, our goal is to learn the low-dimensional latent variable $\mathbf{H} = [\mathbf{h}_1, \ldots, \mathbf{h}_N]^T$ corresponded to these observed variables and make the latent variable have more superior clustering performance (i.e., make the common clustering algorithms obtain accurate clustering result on the learned $\mathbf{H}$).

In order to achieve the above goal, we assume that the latent variable $\mathbf{H}$ has the following prior distribution:

$$p(\mathbf{H}) = \frac{1}{\mathrm{Z}_0}\exp\left(-\lambda_1 R(\mathbf{H})\right), \tag{8}$$

where p_0 is a constant that makes $\int_H p(\mathbf{H})d\mathbf{H} = 1$ and $R(\mathbf{H})$ has the following form:

$$R(\mathbf{H}) = \sum_{i=1}^{N}\sum_{j=1}^{N}\left\|\mathbf{h}_i - \mathbf{h}_j\right\|_2^2 W_{ij}, \tag{9}$$

where W_{ij} is the i^{th} row and j^{th} column element of the affinity matrix $\mathbf{W}$. Equation (9) often can be written as follows:

$$R(\mathbf{H}) = \mathbf{H}^T\mathbf{L}\mathbf{H}. \tag{10}$$

In this paper, we assume that the generation process observed variables from the latent variable can be constructed by conditional distribution $p(\mathbf{X}|H)$. Thus, from the Bayes formulation, we can obtainthe posterior distribution of latent variable as

$$p(\mathbf{H}|\mathbf{X}) = \frac{p(\mathbf{X}|\mathbf{H})p(\mathbf{H})}{p(\mathbf{X})}. \tag{11}$$

Since $p(\mathbf{X})$ is a constant, we therefore can obtain the optimal latent variable by maximizing the following joint marginal distribution:

$$\arg\max_{\mathbf{H}} p(\mathbf{X}|H\ )p(\mathbf{H}). \tag{12}$$

To introduce the GPLVM into this model, we assume that $\mathbf{X}$ is generated by latent function which follows a Gaussian process prior. Thus, equation (12) can be written as

$$\arg\min_{\mathbf{H},\theta,\sigma} \frac{\mathrm{DN}}{2}\ln\left|\mathbf{K} + \sigma^2\mathbf{I}\right| + \frac{1}{2}tr\left(\mathbf{X}\left(\mathbf{K} + \sigma^2\mathbf{I}\right)^{-1}\mathbf{X}^T\right) + \lambda_1 R(\mathbf{H}), \tag{13}$$

where θ denotes the hyperparameter that is involved in the kernel function and σ^2 denotes the variance of Gaussian noise distribution.

By the above modelling process, the GPLVM can effectively embed the sample similarity information when learning the latent variable, thus improving its latent variable clustering ability. However, how to learn the affinity matrix is still an urgent problem of this paper and other related algorithms such as self-representation learning and subspace clustering. In this paper, we borrow the idea of low-rank self-representation learning and introduce the following low-rank subspace constraints into the model:

$$\mathbf{X} = \mathbf{Z}\mathbf{X}, \quad \mathrm{rank}(\mathbf{Z}) \le c, \mathbf{Z} \ge 0. \tag{14}$$

It is worth noting that, in this paper, we assume that $\mathbf{W} = \mathbf{Z}$, i.e., we directly use matrix $\mathbf{Z}$ as the affinity matrix. This setting is the same as that of [23] and its role is similar to the affinity matrix of the original subspace clustering. This C-GPLVM is very similar to the LPP-GPLVM. However, in the LPP-GPLVM, the Laplace matrix is fixed. Different from LPP-GPLVM, the Laplace matrix in our C-GPLVM can be learned in the training process. Thus, our C-GPLVM has more superior performance than the LPP-GPLVM.

One important limitation of GPLVM and self-representation is that they cannot effectively predict the new samples. To mitigate this problem, we introduce a back constraint on the proposed model. Thus, given a new sample, it can effectively predict the corresponding low-dimensional latent variable using the constraint function. Specifically, given an observed sample $\mathbf{x}_n$, we assume that we can use a function $g(\cdot)$ to obtain latent variable $\mathbf{h}_n$:

$$\mathbf{h}_n = g(\mathbf{x}_n), \tag{15}$$

where $g(\cdot)$ is the neural network function with learnable parameter Φ. At last, we obtain the objective of the proposed model as follows:

$$\begin{aligned}&\arg\min_{\mathbf{\Phi},\theta,\sigma} \frac{\mathrm{DN}}{2}\ln\left|\mathbf{K} + \sigma^2 I\right| + \frac{1}{2}tr\left(\mathbf{X}\left(\mathbf{K} + \sigma^2\mathbf{I}\right)^{-1}\mathbf{X}^T\right) + \lambda_1 R(\mathbf{H}),\\ &\text{s.t. } \mathbf{X} = \mathbf{Z}\mathbf{X}, \quad \mathrm{rank}(\mathbf{Z}) \le c, \mathbf{Z} \ge 0.\end{aligned} \tag{16}$$

The whole model structure is shown in Figure 1.

4. Model Optimization

In order to optimize (16), we transform it into the following optimization problem:

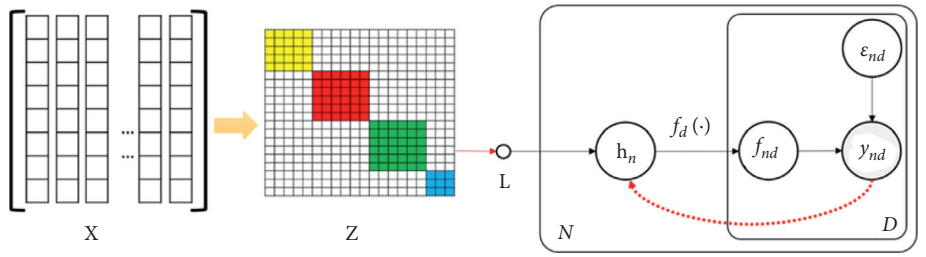

Figure 1: The structure of C-GPLVM.

$$\begin{aligned}\arg\min_{\Phi,\theta,\sigma} \frac{DN}{2}\ln\left|\mathbf{K}+\sigma^2 I\right| + \frac{1}{2}tr\left(\mathbf{X}\left(\mathbf{K}+\sigma^2\mathbf{I}\right)^{-1}\mathbf{X}^T\right) + \lambda_1 R(\mathbf{H}) \\ + \lambda_2\|\mathbf{X}-\mathbf{Z}\mathbf{X}\|_2^2 + \lambda_3\|\mathbf{Z}\|_*, \\ \text{s.t. } \mathbf{Z}\geq 0,\end{aligned} \tag{17}$$

where λ_1, λ_2, and λ_3 are regularization terms. By this formulation, we can use the alternating iterative optimization method to learn all the parameters. First, we fix $\mathbf{Z}$ and write (17) as

$$\begin{aligned}\arg\min_{\Phi,\theta,\sigma} L_p = \arg\min_{\Phi,\theta,\sigma} \frac{DN}{2}\ln\left|\mathbf{K}+\sigma^2\mathbf{I}\right| + \frac{1}{2}tr\left(\mathbf{X}\left(\mathbf{K}+\sigma^2\mathbf{I}\right)^{-1}\mathbf{X}^T\right) \\ + \lambda_1 R(\mathbf{H}).\end{aligned} \tag{18}$$

This problem can be solved effectively by using gradient-based methods, and its gradient with respect to Φ can be computed as

$$\frac{\partial L_p}{\partial \Phi} = \frac{\partial L_p}{\partial \mathbf{K}}\frac{\partial \mathbf{K}}{\partial \Phi} + \lambda_1\frac{\partial R(\mathbf{H})}{\partial \Phi}. \tag{19}$$

The gradients with respect to θ and σ are similar to the above formulation. For the sake of brevity, we have omitted their derivation processes. We then can fix Φ, θ and σ and write (17) as

$$\begin{aligned}\arg\min_{\mathbf{Z}} \lambda_1 R(\mathbf{H}) + \lambda_2\|\mathbf{X}-\mathbf{Z}\mathbf{X}\|_2^2 + \lambda_3\|\mathbf{Z}\|_*, \\ \text{s.t.} \quad \mathbf{Z}\geq 0.\end{aligned} \tag{20}$$

The gradient of the first term with respect to $\mathbf{Z}$ can be computed as

$$\frac{\partial \lambda_1 R(\mathbf{H})}{\partial Z_{n,:}} = \mathbf{e}^T\sum_{j=1}^{N}\left\|\mathbf{h}_n-\mathbf{h}_j\right\|_2^2, \tag{21}$$

where $Z_{n,:}$ denotes the n^{th} row of matrix $\mathbf{Z}$ and $\mathbf{e}\in\mathbb{R}^N$ denotes the vector whose element is 1. The gradient of the second term can be computed as

$$\frac{\partial \lambda_2\|\mathbf{X}-\mathbf{Z}\mathbf{X}\|_2^2}{\partial \mathbf{Z}} = \lambda_2(\mathbf{X}-\mathbf{Z}\mathbf{X})\mathbf{X}^T. \tag{22}$$

The subgradient of the third term is

$$\frac{\partial\|\mathbf{X}\|_*}{\partial \mathbf{X}} = \mathbf{V}\text{sgn}(\mathbf{\Sigma})\mathbf{U}^T. \tag{23}$$

By the above derivations, we can learn the whole model, as descripted in Algorithm 1. The main computation complexity of C-GPLVM is the inversion of the kernel matrix, which has a complexity of $O(N^3)$, where N is the number of training samples. The main storage complexity of this is the storage of kernel matrix, which has a complexity of $O(N^2)$. Thus, both the computation and storage complexities are the same as those of the conventional GPLVM.

5. Experiments and Analysis

5.1. Experimental Setup. To verify the effectiveness of C-GPLVM, we use 8 datasets in the experiments. The detailed information of these datasets is given in Table 1.

The YEAST is a dataset for the prediction of protein localization sites. The USPS is a digits dataset that was gathered at the Center of Excellence in Document Analysis and Recognition at SUNY Buffalo, as part of a project sponsored by the US Postal Service. YALE, JAFFE, and ORL are three face recognition datasets, as shown in Figure 2. TR11, TR41, and TR45 are three textual datasets.

In order to fully verify the advantage of C-GPLVM, we compare it to the related Gaussian process latent variable model (i.e., GPLVM, B-GPLVM, and LPP-GPLVM) and clustering methods, such as spectral clustering method (SC) [24], kernel spectral clustering (KSC) [25], and simplex sparse representation learning (SSR) [21]. All the kernel-based models (GPLVM, LPP-GPLVM, KSC, and C-GPLVM) used Radial Basis Function (RBF) as the kernel function. It is worth noting that some other kernel functions can also be used in the proposed model such as linear kernel, Laplacian kernel, and circular kernel. Furthermore, all the hyperparameters in these kernel functions can also be learned in the same form as descripted in the paper. During the experiment process, the hyperparameters λ_1, λ_2, and λ_3 are chosen from $\{0.01, 0.1, 1, 10, 100\}$. The hyperparameters involved in other models are set to be the same as those of original paper. In the experiment process, we use the Gaussian process toolkit (GPFlow) [1] to implement the GP-based model. Other related models are all implemented with python. All the algorithms are tested on the Windows computer with i7 9700 CPU, 16G RAM.

Input: training set $\mathbf{X}$, dimension Q of latent variable, hyperparameters λ_1, λ_2, λ_3.
Output: parameter Φ and the clustering result.
(1) Pretrain the following model to initialize the latent variable $\mathbf{Z}$

$$\mathbf{Z} = \operatorname{argmin}_{\mathbf{Z}} \quad \lambda_2 \|\mathbf{X} - \mathbf{Z}\mathbf{X}\|_2^2 + \lambda_3 \|\mathbf{Z}\|_* \quad \text{s.t.} \quad \mathbf{Z} \geq 0$$

(2) while ($l_{\text{tol}} \geq 10^{-3}$)
(3) With fixed $\mathbf{Z}$, minimize (18) to obtain Φ, θ, and σ.
(4) With fixed Φ, θ, and σ, minimize (20) to obtain $\mathbf{Z}$.
(5) Calculate the difference l_{tol} of the objective function between the last two iterations
(6) end while
(7) Compute the latent variable $\mathbf{H}$ based on the learned parameter Φ.
(8) Run k-means algorithm on $\mathbf{H}$ to get the final clustering result.

Algorithm 1: The optimization process of C-GPLVM.

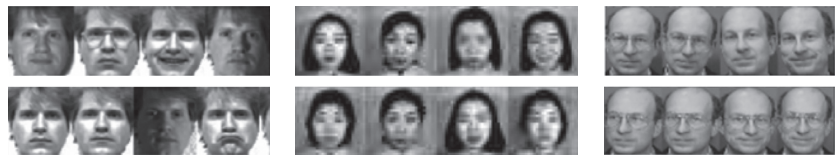

(a) (b) (c)

Figure 2: Samples in YALE, JAFFE, and ORL datasets.

Table 1: The detailed information of the datasets.

Dataset	# of sample	# of feature	# of classes
YALE	165	1024	15
JAFFE	213	676	10
ORL	400	1024	40
YEAST	1484	1470	10
USPS	1854	256	20
TR11	414	6429	9
TR41	878	7454	10
TR45	690	8261	10

Table 2: Accuracy.

	YALE	JAFFE	ORL	YEAST	USPS	TR11	TR41	TR45
GPLVM	29.80 ± 1.01	55.91 ± 2.94	21.58 ± 1.45	19.48 ± 1.49	23.14 ± 2.41	30.01 ± 2.58	42.87 ± 2.94	33.54 ± 2.31
B-GPLVM	32.12 ± 1.58	59.66 ± 2.14	25.17 ± 2.18	23.94 ± 1.54	28.14 ± 1.19	35.47 ± 1.50	48.99 ± 1.37	37.93 ± 2.54
LPP-GPLVM	36.14 ± 1.25	71.49 ± 2.75	38.97 ± 1.94	29.88 ± 1.73	61.71 ± 2.21	51.44 ± 2.20	49.79 ± 1.40	51.83 ± 2.91
SC	50.32 ± 1.23	73.55 ± 2.33	57.96 ± 1.45	**35.91 ± 1.34**	36.45 ± 2.90	52.69 ± 3.32	61.74 ± 1.8	55.91 ± 1.96
KSC	37.21 ± 1.55	72.19 ± 1.98	39.74 ± 2.39	31.18 ± 1.83	63.78 ± 3.87	53.74 ± 1.86	51.12 ± 1.11	53.44 ± 1.99
SSR	53.59 ± 1.09	85.92 ± 2.34	68.22 ± 1.98	27.62 ± 1.92	**64.83 ± 2.39**	41.06 ± 2.33	65.78 ± 2.58	73.45 ± 1.36
C-GPLVM	**55.91 ± 1.38**	**86.14 ± 1.81**	**70.43 ± 1.30**	33.71 ± 1.42	63.16 ± 2.01	**55.89 ± 2.59**	**67.16 ± 2.14**	**75.25 ± 1.90**

Table 3: Purity.

	YALE	JAFFE	ORL	YEAST	USPS	TR11	TR41	TR45
GPLVM	30.48 ± 1.00	53.41 ± 1.84	38.14 ± 1.09	8.47 ± 1.71	21.10 ± 1.66	19.41 ± 1.10	30.11 ± 2.09	34.57 ± 1.49
B-GPLVM	33.19 ± 1.44	56.49 ± 1.58	49.18 ± 1.41	8.56 ± 2.61	25.17 ± 2.17	23.61 ± 1.97	34.17 ± 2.37	38.44 ± 1.56
LPP-GPLVM	41.57 ± 1.11	67.18 ± 2.10	67.18 ± 1.94	12.80 ± 1.54	26.49 ± 1.43	28.15 ± 2.15	53.91 ± 2.34	45.61 ± 2.01
SC	53.24 ± 1.25	82.32 ± 1.02	74.41 ± 1.47	21.47 ± 3.14	28.91 ± 1.84	42.89 ± 1.58	61.84 ± 2.14	48.17 ± 2.17
KSC	45.91 ± 2.17	71.82 ± 1.84	55.91 ± 1.19	11.14 ± 2.14	49.83 ± 1.36	45.77 ± 1.91	44.77 ± 2.91	44.18 ± 2.22
SSR	54.66 ± 2.14	91.10 ± 1.24	83.16 ± 1.84	16.91 ± 2.17	71.99 ± 1.47	28.67 ± 1.43	56.90 ± 2.79	65.10 ± 1.97
C-GPLVM	55.17 ± 2.38	91.84 ± 1.33	82.71 ± 1.94	21.04 ± 2.38	70.61 ± 1.89	47.94 ± 1.95	62.85 ± 2.57	66.73 ± 2.32

Table 4: Normalized mutual information.

	YALE	JAFFE	ORL	YEAST	USPS	TR11	TR41	TR45
GPLVM	30.41 ± 1.40	59.17 ± 1.09	31.90 ± 1.29	19.80 ± 1.41	21.36 ± 1.00	34.82 ± 1.06	39.40 ± 1.61	37.21 ± 1.27
B-GPLVM	32.49 ± 1.66	63.99 ± 1.81	32.81 ± 1.11	28.39 ± 1.58	30.58 ± 1.07	40.59 ± 1.40	49.55 ± 2.06	46.79 ± 1.41
LPP-GPLVM	40.85 ± 1.29	68.46 ± 1.43	40.90 ± 1.09	31.63 ± 1.47	34.83 ± 1.06	48.97 ± 1.38	51.63 ± 2.44	52.88 ± 1.67
SC	50.49 ± 1.84	75.91 ± 2.41	60.49 ± 1.84	**53.71 ± 2.17**	36.49 ± 1.61	57.39 ± 1.20	72.63 ± 2.19	61.98 ± 1.94
KSC	43.50 ± 1.32	77.35 ± 2.01	41.53 ± 1.44	32.59 ± 2.98	61.29 ± 1.65	51.09 ± 1.69	54.81 ± 2.81	55.71 ± 2.11
SSR	57.39 ± 1.09	95.50 ± 1.86	76.41 ± 1.00	43.16 ± 2.73	**73.24 ± 1.10**	83.77 ± 1.43	75.63 ± 2.37	82.69 ± 2.43
C-GPLVM	**58.41 ± 2.17**	**96.01 ± 2.38**	**77.25 ± 1.53**	51.42 ± 1.85	71.11 ± 1.83	**85.64 ± 1.82**	**77.31 ± 2.82**	**83.11 ± 2.28**

5.2. Clustering Results and Analysis. In the experiments, we use clustering accuracy, purity, and normalized mutual information (NMI) as the clustering measurement. At the clustering stage, the latent variables learned by different methods are used as inputs and the k-means algorithm is used to obtain the final clustering methods. The dimension and the number of clusters are set to be the same as the number of classes. At the same time, in order to mitigate the initial value sensitivity problem of k-means method, we randomly initialize and run the k-means method 20 times. Finally, we calculate the mean and standard deviation of these 20 experiments. The experimental results are shown in Tables 2–4, where the best results are given in bold.

From Tables 2–4, we can observe that the GPLVM, as an unsupervised dimension reduction model, usually obtain latent variables that have poor clustering performance. The B-GPLVM and LPP-GPLVM can preserve the local distance of samples during the feature learning process, thus obtaining more representative latent variables. Meanwhile, the LPP-GPLVM obtains much better result than the B-GPLVM which indicates that graph Laplace regularization is more suitable for clustering than back constraints. In general, spectral clustering and subspace clustering methods have better performance than the GPLVM. As we can see, SC, KSC, and SSR outperform GPLVM, B-GPLVM, and LPP-GPLVM. In this paper, the proposed C-GPLVM combines the subspace clustering with GPLVM, thus effectively improving the clustering performance of the GPLVM. As shown in the experimental results, the C-GPLVM has more superior clustering result than other related models in most cases.

6. Conclusion and Future Work

This paper proposes a joint model by combining the low-rank subspace with the back constraint GPLVM to address the poor clustering performance problem of the conventional GPLVM. The proposed C-GPLVM can not only obtain low-dimensional latent variables but also directly predict the new samples, thus effectively extending the application scope of GPLVM on tasks such as analysis of chaotic time series. The experimental results show that the C-GPLVM has much better latent variable learning ability and superior clustering performance. In the future work, we will further extend the C-GPLVM to make it suitable for much bigger dataset and supervise tasks such as classification and regression, improving its efficiency and application scope.

Data Availability

The experimental data used to support the findings of this study have been deposited in the UCI repository (https://archive.ics.uci.edu/ml/index.php).

Conflicts of Interest

The author declares that there are no conflicts of interest regarding the publication of this paper.

Acknowledgments

This work was supported by the Project of Yulin Normal University Research under Grant 2015YJYB03.

References

[1] X. Li and L. Shu, "Kernel based nonlinear dimensionality reduction for microarray gene expression data analysis," *Expert Systems with Applications*, vol. 36, no. 4, pp. 7644–7650, 2009.

[2] K. Kreutz-Delgado, B. D. Murray, K. Engan, T.-W. Lee, and T. J. Sejnowski, "Dictionary learning algorithms for sparse representation," *Neural Computation*, vol. 15, no. 2, pp. 349–396, 2003.

[3] L. Fengfu, Q. Hong, and Z. Bo, "Discriminatively boosted image clustering with fully convolutional auto-encoders," *Pattern Recognition*, vol. 83, pp. 161–173, 2018.

[4] N. D. Lawrence, "Probabilistic non-linear principal component analysis with Gaussian process latent variable models," *Journal of Machine Learning Research*, vol. 6, pp. 1783–1816, 2005.

[5] J. B. Tenenbaum, V. De Silva, J. Langford et al., "A global geometric framework for nonlinear dimensionality reduction," *Science*, vol. 290, no. 5500, pp. 2319–2323, 2000.

[6] S. T. Roweis and L. K. Saul, "Nonlinear dimensionality reduction by locally linear embedding," *Science*, vol. 290, no. 5500, pp. 2323–2326, 2000.

[7] J. M. Wang, A. Hertzmann, D. M. Blei et al., "Gaussian process dynamical models," in *Proceedings of the 18th International Conference on Neural Information Processing Systems*, pp. 1441–1448, Vancouver, Canada, December 2005.

[8] J. Hall, C. E. Rasmussen, J. M. Maciejowski et al., "Modelling and control of nonlinear systems using gaussian processes with partial model information," in *Proceedings of the Conference on Decision and Control*, pp. 5266–5271, Orlando, FL, USA, December 2012.

[9] L. Cai, L. Huang, C. Liu et al., "Age estimation based on improved discriminative Gaussian process latent variable model," *Multimedia Tools and Applications*, vol. 75, no. 19, pp. 11977–11994, 2016.

[10] C. Lu and X. Tang, "Surpassing human-level face verification performance on LFW with gaussianface," in *Proceedings of the Computer Vision and Pattern Recognition*, Columbus, OH, USA, June 2014.
[11] X. Gao, X. Wang, D. Tao et al., "Supervised Gaussian process latent variable model for dimensionality reduction," *Systems Man and Cybernetics*, vol. 41, no. 2, pp. 425–434, 2011.
[12] S. Eleftheriadis, O. Rudovic, M. Pantic et al., "Discriminative shared Gaussian processes for multiview and view-invariant facial expression recognition," *IEEE Transactions on Image Processing*, vol. 24, no. 1, pp. 189–204, 2015.
[13] G. Liu, Z. Lin, Y. Yu et al., "Robust subspace segmentation by low-rank representation," in *Proceedings of the International Conference on Machine Learning*, pp. 663–670, Haifa, Israel, June 2010.
[14] N. D. Lawrence and J. Quinonerocandela, "Local distance preservation in the GP-LVM through back constraints," in *Proceedings of the International Conference on Machine Learning*, pp. 513–520, New York, NY, USA, June 2006.
[15] W. Xiu, "A latent variable model based on local preservation," *Pattern Recognition and Artificial Intelligence*, vol. 23, no. 3, pp. 369–375, 2010.
[16] P. S. Bradley and O. L. Mangasarian, "K-plane clustering," *Journal of Global Optimization*, vol. 16, no. 1, pp. 23–32, 2000.
[17] P. Tseng, "Nearest q-Flat to m Points," *Journal of Optimization Theory and Applications*, vol. 105, no. 1, pp. 249–252, 2000.
[18] J. P. Costeira and T. Kanade, "A multibody factorization method for independently moving objects," *International Journal of Computer Vision*, vol. 29, no. 3, pp. 159–179, 1998.
[19] C. W. Gear, "Multibody grouping from motion images," *International Journal of Computer Vision*, vol. 29, no. 2, pp. 133–150, 1998.
[20] R. Vidal, Y. Yi Ma, and S. Sastry, "Generalized principal component analysis (GPCA)," *IEEE Transactions on Pattern Analysis and Machine Intelligence*, vol. 27, no. 12, pp. 1945–1959, 2005.
[21] J. Huang, F. Nie, H. Huang et al., "A new simplex sparse learning model to measure data similarity for clustering," in *Proceedings of the International conference on Artificial Intelligence*, pp. 3569–3575, New Delhi, India, February 2015.
[22] S. Luo, C. Zhang, W. Zhang et al., "Consistent and specific multi-view subspace clustering," in *Proceedings of the National Conference on Artificial Intelligence*, pp. 3730–3737, Vancouver, Canada, February 2018.
[23] Z. Kang, H. Xu, B. Wang, H. Zhu, and Z. Xu, "Clustering with similarity preserving," *Neurocomputing*, vol. 365, pp. 211–218, 2019.
[24] U. Von Luxburg, "A tutorial on spectral clustering," *Statistics and Computing*, vol. 17, no. 4, pp. 395–416, 2007.
[25] C. Alzate and J. A. K. Suykens, "Multiway spectral clustering with out-of-sample extensions through weighted kernel PCA," *IEEE Transactions on Pattern Analysis & Machine Intelligence*, vol. 32, no. 2, pp. 335–347, 2009.

Hindawi
Complexity
Volume 2021, Article ID 8865522, 11 pages
https://doi.org/10.1155/2021/8865522

Research Article

Dynamic Analysis and Robust Control of a Chaotic System with Hidden Attractor

Huaigu Tian,[1] **Zhen Wang**,[2] **Peijun Zhang**,[1] **Mingshu Chen**,[1] **and Yang Wang**[1]

[1]*Shaanxi Engineering Research Center of Controllable Neutron Source, School of Science, Xijing University, Xi'an 710123, China*
[2]*School of Civil Engineering and Architecture, Xi'an University of Technology, Xi'an 710048, China*

Correspondence should be addressed to Zhen Wang; williamwangz@yeah.net

Received 1 October 2020; Revised 28 November 2020; Accepted 28 December 2020; Published 13 January 2021

Academic Editor: Karthikeyan Rajagopal

In this paper, a 3D jerk chaotic system with hidden attractor was explored, and the dissipativity, equilibrium, and stability of this system were investigated. The attractor types, Lyapunov exponents, and Poincare section of the system under different parameters were analyzed. Additionally, a circuit was carried out, and a good similarity between the circuit experimental results and the theoretical analysis testifies the feasibility and practicality of the original system. Furthermore, a robust feedback controller was designed based on the finite-time stability theory, which guarantees the synchronization of 3D jerk master-slave system in finite time and asymptotically converges to the origin. Finally, we also give verification for the discussion in this paper by numerical simulation.

1. Introduction

As Dr Passival says, "Chaos science is like a river, made up of many tributaries, it comes from all science" [1]. In 1963, Lorenz first constructed a 3D quadratic polynomial ODEs system, and he found the first chaotic attractor in this system [2]. In 1971, Ruelle and Takens first used the chaotic theory in dynamic systems and explained the nature of turbulence and discovered the existence of "strange attractors" [3]. In the following decades, many chaotic attractors were discovered, such as Logistic mapping [4], Rössler attractor [5], Chen's attractor [6], and Lü attractor [7]. For many years, chaotic systems and hyperchaotic systems with self-excited attractors have been the focus of investigation [8], and these systems have unstable equilibria on the boundary of their basins of attraction. In 2011, Leonov pointed out that there are hidden attractors in addition to self-excited attractors in the dynamical systems [9]. The attraction basins of hidden attractors cannot intersect the neighborhood of any equilibria, which is a very important feature for chaotic systems with hidden attractors. The Shilnikov condition cannot verify the chaotic characteristics of the chaotic systems with hidden attractors because of the absence of homologous or heterozygous orbits. Sprott gave some simple chaotic systems with no or one equilibrium by computer numerical search [10–13]. Then, researchers proposed chaotic systems with hidden attractors with only one stable equilibrium [14–18], no equilibria [19–21], any number equilibria [22, 23], and a line equilibrium [24, 25]. Nowadays, chaotic systems with hidden attractors play an important role in nonlinear circuits [26], Van der Pol-Duffing oscillators [27], multilevel DC/DC converters [28], and relay systems with hysteresis [29]. In these dynamical systems, the existence of hidden oscillations can lead to the phenomenon of unstable states in life and industrial production. Hence, it is of great significance to understand the local and global dynamic behaviors of chaotic systems with hidden attractors.

In general, the appearance of hidden attractors is not hoped when a system operates normally. If it happens, this will lead to sudden and large chaotic oscillations and the system may collapse by the perturbation of hidden attractors. Actually, like two sides of a coin, there have been potential application values in the fields of chaos-based secure communication [30], image encryption [31], robust embedded biometric authentication system based on chaos

[32], and so on [33, 34]. It is now well established from a variety of studies that jerk oscillators can display chaos [35]. Kengne studied the finite-time synchronization of the jerk oscillators via theory and experiments [36]. Louodop examined the nonlinearity of Josephson junctions for design chaotic jerk oscillators [37]. Kingni has researched the dynamical behaviors of an autonomous Josephson jerk oscillator with two or no equilibrium points and its application to text encryption [38]. Panahi has studied the collective behavior of chaotic memristive jerk oscillator in dynamical networks [39]. However, in these studies, the dynamical behaviors and related engineering applications of the jerk system are researched, but the control methods of the jerk chaotic systems with hidden attractor are not involved. As regards chaos control, robust methods have always been the focus of research. In order to enhance the robustness of chaotic synchronization, Lenz proposed the robust control method of Lorenz system [40], and Mobayen also presented some robust control technologies [41, 42]. Shen proposed robust synchronization and parameter identification for uncertain chaotic systems with bounded unknown parameters [43]. Ji presented a robust adaptive backstepping synchronization approach for the estimation of uncertain chaotic systems with parameter uncertainties and external disturbances via a fuzzy disturbance observer [44]. Although most of the studies have been given the asymptotical stabilization of the synchronization errors, these studies cannot be synchronized in finite time or guarantee the robustness of the systems. Therefore, it is significant to design a robust finite-time feedback controller with parameter uncertainties for the master-slave synchronization of 3D jerk chaotic system with hidden attractor, which is helpful to solve the problem of sudden chaotic oscillation caused by hidden attractors, thus providing a good reference and inspiration for solving similar engineering oscillation problems. In this paper, we further designed the robust controller and the corresponding chaotic circuit for a 3D jerk system with hidden attractors [45]:

$$\begin{cases} \dot{x}_1 = x_2, \\ \dot{x}_2 = x_3, \\ \dot{x}_3 = -ax_1 - bx_2 - cx_3 + bx_1x_2 + x_2^2, \end{cases} \tag{1}$$

with a, b, and c being real numbers and $a \neq 0$. The organizational structure of this paper is as follows: In Section 2, the chaotic dynamical behavior of 3D jerk system (1) is analyzed by numerical simulation, such as equilibrium stability, time series, bifurcations, Poincare mapping, Lyapunov exponents spectrum (LES), largest Lyapunov exponent (LLE), periodic orbit, and chaotic behavior. In Section 3, the finite-time synchronization problem of chaotic systems with uncertain parameters is discussed, and the finite-time robust feedback control of chaotic system is realized by combining the finite-time stability theorem. In Section 4, the 3D jerk system with hidden attractor circuit is implemented, and the reliability of the robust feedback controller is verified by numerical simulation. Finally, Section 5 gives a conclusive remark.

2. Dynamical Behaviors

2.1. Dissipativity. We can use the dissipativity formula:

$$\mathrm{Div}(V) = \frac{\partial \dot{x}_1(t)}{\partial x_1(t)} + \frac{\partial \dot{x}_2(t)}{\partial x_2(t)} + \frac{\partial \dot{x}_3(t)}{\partial x_3(t)} = -c. \tag{2}$$

So $\dot{V} = -cV$; V here is the volume of the moving space in the phase space motion. It can be easily verified that $\mathrm{Div}(V) = -c < 0$, so if $t = 0$, its volume element is V_0, the volume shrinks to $V_0 e^{-c}$ in time t, and each volume containing the system orbit shrinks to zero as $t \longrightarrow \infty$ at an exponential rate $-c$. Thus, system (1) is dissipative under $c > 0$, and its limit converges and is limited to a point in the form of exponential c, which is the attractor of a chaotic system.

2.2. Equilibria and Stability. Let $\dot{x}_1 = 0, \dot{x}_2 = 0$, and $\dot{x}_3 = 0$, At this time, the 3D jerk system (1) has only one equilibrium $O(0, 0, 0)$. Its Jacobian matrix is

$$J = \begin{pmatrix} 0 & 1 & 0 \\ 0 & 0 & 1 \\ -a & -b & -c \end{pmatrix}. \tag{3}$$

The characteristic polynomial equation is $f(\lambda) = \lambda^3 + c\lambda^2 + b\lambda + a$, according to Routh-Hurwitz criterion: When $c > 0$, $a > 0$, and $bc - a > 0$, there are three negative real parts roots, and the 3D jerk system (1) has a stable node or stable node-foci. When $c > 0$, $a > 0$, and $bc - a < 0$, the 3D jerk system (1) has only one saddle-focus.

2.3. Phase Trajectories and Time Series of the System. The phase orbit of the system with different parameters can directly reflect its states and motion behavior. When the parameters of the 3D jerk system (1) are set as $a = 3.4$, $b = 1$, and $c = 4$ and the initial states $(x_1, x_2, x_3) = (-2, 0, 2.4)$, the 3D jerk system (1) is in chaotic state. The 3D phase space attractor diagram and the projection of attractors of 3D jerk system (1) on three coordinate planes are shown in Figure 1.

As shown in Figure 1, attractors cannot be found by means of equilibria. Therefore, attractors of 3D jerk system (1) are hidden attractors. The time series diagram of x_1, x_2, and x_3 can be obtained by integrating the 3D jerk system (1), as shown in Figure 2.

Figure 2 depicts the aperiodic characteristics of the system, and the oscillation curve is different from completely random noise; and each variable presents aperiodic changes in a continuous bounded range.

2.4. The Effect of Parameters on the System. The nonlinear behavior of the system is mainly influenced by the system parameters. In order to better study the complex dynamic behavior of the 3D jerk system (1), the numerical method is used to analyze the dynamic behavior of the system under different parameters, as shown in Table 1.

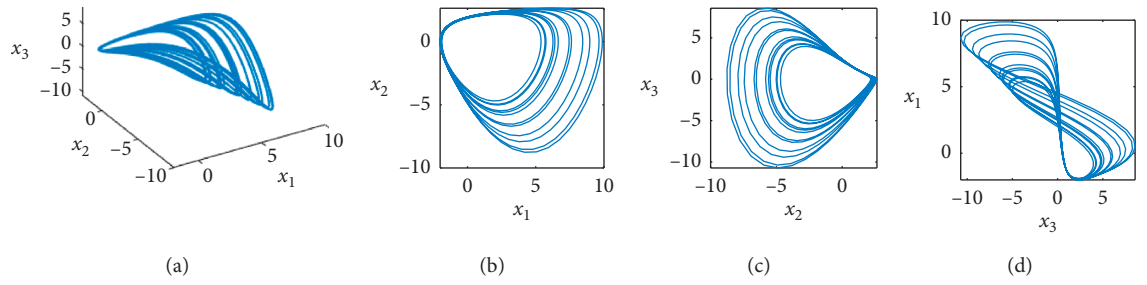

Figure 1: Chaotic attractor of the 3D jerk system (1) and projection in $x_1 - x_2$ plane, $x_2 - x_3$ plane, and $x_3 - x_1$ plane. (a) x_1–x_2–x_3. (b) $x_1 - x_2$. (c) $x_2 - x_3$. (d) $x_3 - x_1$.

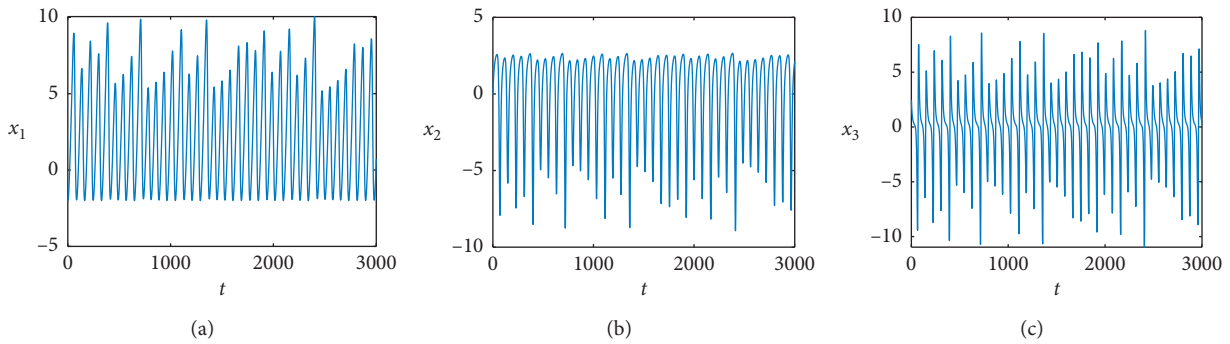

Figure 2: The time series of 3D jerk system (1) in x_1, x_2, and x_3 plane.

Table 1: Various phase portraits of system (1) for some fixed parameters (PVs parameter values, PPs phase portraits, and Ps Poincare section).

PVs	Dynamics	LES	PPs	Ps
$a = 3.31, b = 1, c = 4$	Periodic 1	[0, −0.073, −3.927]	Figure 3(a)	Figure 4(a)
$a = 3.34, b = 1, c = 4$	Periodic 2	[0, −0.056, −3.943]	Figure 3(b)	Figure 4(b)
$a = 3.36, b = 1, c = 4$	Periodic 4	[0, −0.038, −3.964]	Figure 3(c)	Figure 4(c)
$a = 3.40, b = 1, c = 4$	Chaos	[0.072, 0, −4.069]	Figure 1	Figure 4(d)

2.4.1. Phase Space Orbit. The parameters are fixed as $b = 1$ and $c = 4$. When the parameter a is selected as 3.31, 3.34, and 3.36, respectively, the phase diagrams of attractors with periodic 1, periodic 2, and periodic 4 can be obtained, as shown in Figure 3.

2.4.2. Poincare Section. A plane is cut out in the multidimensional phase space, and a pair of conjugate variables x_1 and x_2 are fixed values in this section, which is the Poincare section. Like Section 2.4.1, the parameters are fixed as $b = 1$ and $c = 4$. When the parameter a is selected as 3.31, 3.34, 3.36, and 3.40, respectively, the Poincare section diagram in the state of periodic 1, periodic 2, and periodic 4 periods and chaos can be obtained, as shown in Figure 4.

From Figure 4, when the parameter a is selected as 3.31, 3.34, and 3.36, the Poincare section has only one moving point or a few discrete points, indicating that the behavior of the system is periodic, but when the parameters are selected as $a = 3.40$, the Poincare section is a continuously dense point, and it has the characteristic of fractal structure, which indicates that chaotic behavior will occur.

2.4.3. Lyapunov Exponent. Initial value sensitivity of chaotic systems means that when given a very close initial value, the phase space will diverge with an exponential rate. Lyapunov exponent is to identify whether the system is chaotic or not, according to the characteristics of whether the phase orbit has diffusion [46]. In addition, according to Lyapunov dimension,

$$D_\lambda = j + \frac{1}{\left|\lambda_{j+1}\right|} \sum_{i=1}^{j} \lambda_i. \tag{4}$$

Through Table 1, when $\lambda_1 = 0.072$, $\lambda_2 = 0$, and $\lambda_3 = -4.069$, substituting them into equation (4), the following equation can be obtained:

$$D_\lambda = j + \frac{1}{\left|\lambda_{j+1}\right|} \sum_{i=1}^{j} \lambda_i = 2 + \frac{\lambda_1 + \lambda_2}{\left|\lambda_3\right|} = 2.018. \tag{5}$$

From equation (5), the Lyapunov dimension $D\lambda = 2.018$ for $a = 3.4, b = 1$, and $c = 4$, so the 3D jerk system (1) has fractal Lyapunov dimension, which verifies that system (1) is in a chaotic state when $a = 3.4$. In order to determine

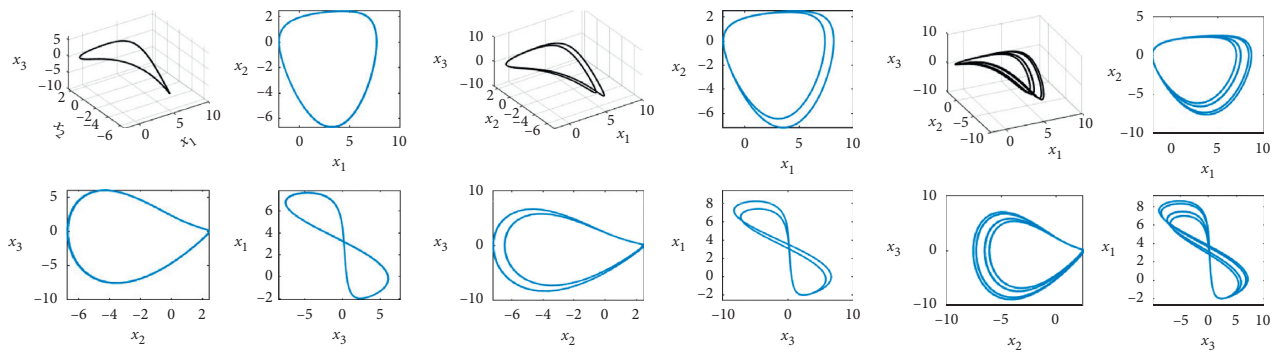

(a) (b) (c)

FIGURE 3: Periodic 1, 2, or 4 orbit of 3D jerk system (1) and projection in $x_1 - x_2$ plane, $x_2 - x_3$ plane, and $x_3 - x_1$ plane. (a) $a = 3:31$, $b = 1$, $c = 4$. (b) $a = 3:34$, $b = 1$, $c = 4$. (c) $a = 3:36$, $b = 1$, $c = 4$.

whether system (1) is chaotic or not, we should calculate the Lyapunov exponents spectrum of system (1) for fixed parameters b, c and let a vary. When a varies in the interval $[3.2, 3.4]$, the Lyapunov exponents spectrum of the 3D jerk system (1) is shown in Figure 5, and the largest Lyapunov exponent of the 3D jerk system (1) is shown in Figure 6.

According to Figure 6, when $a \in [3.36, 3.4]$, the largest Lyapunov exponent $\lambda_1 > 0$ can be observed. This observation is also verified by Table 1.

2.4.4. Bifurcation. The bifurcation diagram of a system can also be used to analyze the state of a system within the parameter range. It can describe the bifurcation state that the state variable changes with the parameter change. Fixed parameters $b = 1$ and $c = 4$. When parameter $a \in [3.3, 3.4]$, the bifurcation diagram of the 3D jerk system (1) is shown in Figure 7.

Through the bifurcation state in Figure 7, when $a \in [3.31, 3.36]$, the 3D jerk system (1) exhibits periodic behaviors, and it presents typical states of periodic 1, periodic 2, and periodic 22; however, when $a = 3.40$, chaotic behavior occurs. Therefore, the 3D jerk system (1) evolves from periodic to chaotic. Then, combined with Lyapunov exponential spectrum in Figure 5, it is clear that the state of system (1) changes when the parameters change, which implies that chaotic behavior can only occur within a certain parameter range.

3. Design of Robust Feedback Controller

3.1. Provision of Robust Controller. Following the 3D jerk system (1), a class of master system with hidden attractors and uncertain parameters is given as

$$\begin{cases} \dot{x}_1 = x_2, \\ \dot{x}_2 = x_3, \\ \dot{x}_3 = -(a + \Delta_1)x_1 - (b + \Delta_2)x_2 - (c + \Delta_3)x_3 + (b + \Delta_2)x_1x_2, \end{cases} \tag{6}$$

where $x = (x_1, x_2, x_3)T$ is the state variable of the master system, and the slave system can be described as follows:

$$\begin{cases} \dot{y}_1 = y_2 + u_1(t), \\ \dot{y}_2 = y_3 + u_2(t), \\ \dot{y}_3 = -(a + \Delta_4)y_1 - (b + \Delta_5)y_2 - (c + \Delta_6)y_3 + y_2^2 + (b + \Delta_5)y_1y_2 + u_3(t), \end{cases} \tag{7}$$

where $y = (y_1, y_2, y_3)T$ is the state variable of the slave system; $u_i(t)$ $(i = 1, 2, 3)$ is the external input control; Δ_i $(i = 1, 2, 3, 4)$ is the parameter uncertain term of master and slave chaotic systems. The synchronization error is defined as $e_i = y_i - x_i$ $(i = 1, 2, 3)$. Therefore, its error system can be expressed as

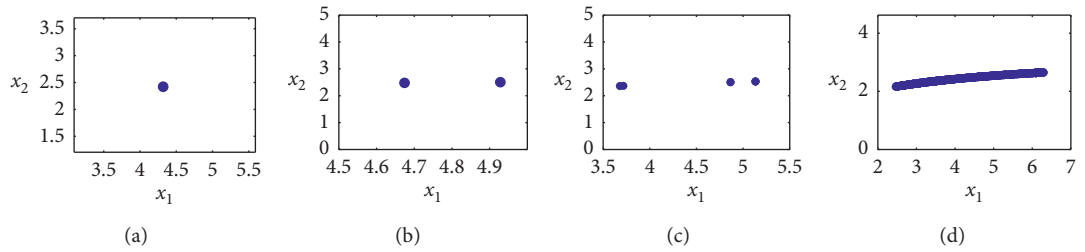

FIGURE 4: Periodic 1, 2, and 4 and chaotic Poincare section of 3D jerk system (1) with different a. (a) $a = 3:31$, $b = 1$, $c = 4$. (b) $a = 3:34$, $b = 1$, $c = 4$. (c) $a = 3:36$, $b = 1$, $c = 4$. (d) $a = 3:40$, $b = 1$, $c = 4$.

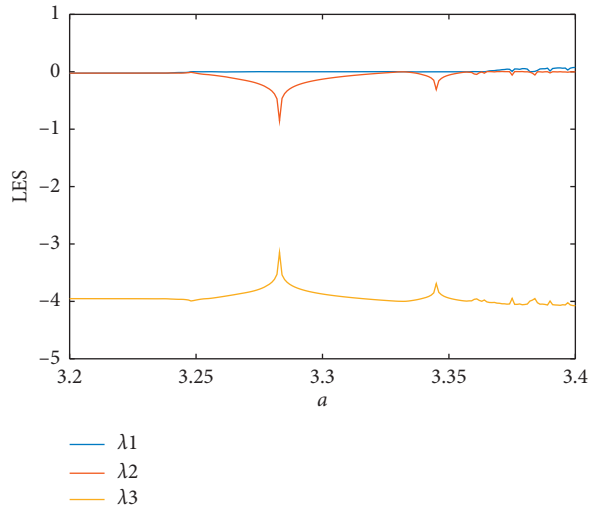

FIGURE 5: Lyapunov exponents spectrum of 3D jerk system (1) for $b = 1$ and $c = 4$.

$$\begin{cases} \dot{e}_1 = e_2 + u_1(t), \\ \dot{e}_2 = e_3 + u_2(t), \\ \dot{e}_3 = -ae_1 - be_2 - ce_3 + y_1y_2(b + \Delta_5) - x_1x_2(b + \Delta_2) + y_2^2 - x_2^2 - \Delta_4y_1 - \Delta_5y_2 - \Delta_6y_3 + v_1x_1 + \Delta_2x_2 + \Delta_3x_3 + u_3(t). \end{cases} \tag{8}$$

Before designing a finite-time robust feedback controller for the synchronization error system (1), the following Lemma 3.1, which plays an important role in the subsequent analysis, is recalled here for convenience.

Lemma 1 (see [47]). *Provided that $V(t)$ is a differentiable and nonnegative scalar function and $V(t)$ satisfies the differential inequality $\dot{V}(t) \le -\varepsilon V^{\alpha}(t)$, where ε and α are positive constants, $\varepsilon > 1$ and $0 < \alpha < 1$, and then we have*

$$V(t) = 0 \quad \text{if } t \ge t_M, \tag{9}$$

where the finite time $t_M \le V^{1-\alpha}(0)/(\varepsilon(1-\alpha))$. $V(0)$ is the initial value and $V(0)$ is bounded.

Based on the above Lemma 3.1, to drive the synchronization error in error system (1) to zero in the finite time, a robust feedback controller is proposed as follows:

$$\begin{cases} u_1(t) = -e_1^{\gamma_1} + ae_3 - e_2, \\ u_2(t) = -e_1^{\gamma_2} + be_3 - e_3, \\ u_3(t) = -e_1^{\gamma_3} + ce_3 - y_1y_2b - \delta_5|y_1y_2|\text{sign}(e_3) + x_1x_2b + \delta_2|x_1x_2|\text{sign}(e_3) \\ -y_2^2 + x_2^2 + \delta_4|y_1|\text{sign}(e_3) + \delta_5|y_2|\text{sign}(e_3) + \delta_6|y_3|\text{sign}(e_3) - \delta_1|x_1|\text{sign}(e_3) - \delta_2|x_2|\text{sign}(e_3) - \delta_3|x_3|\text{sign}(e_3) \end{cases} \tag{10}$$

where $0 < \gamma_i < 1$ $(i = 1, 2, 3)$ and remark $\gamma = \min_{1 \le i \le 3}\{\gamma_i\}$.

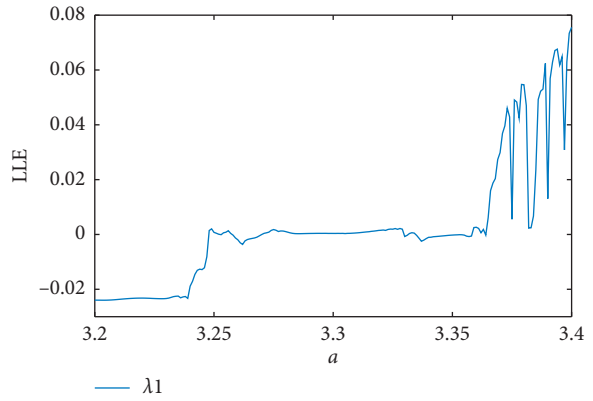

Figure 6: Largest Lyapunov exponent of 3D jerk system (1) for $b = 1$ and $c = 4$.

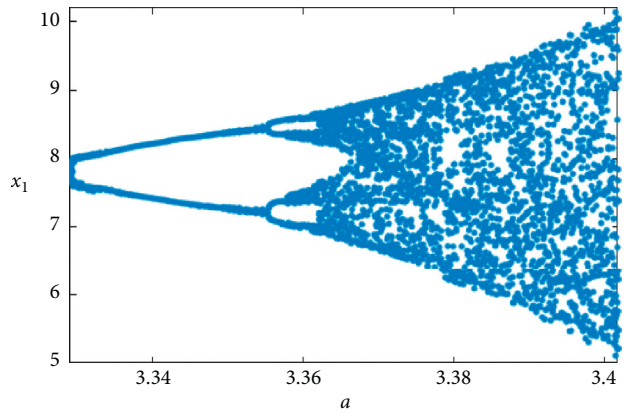

Figure 7: Bifurcation diagram of 3D jerk system (1) with parameters $b = 1$ and $c = 4$.

3.2. Performance Proof of Robust Feedback Controller. To verify the finite-time stability of the error system with the proposed controller (10), the following proof is given.

Assumption 1. Assumes that positive $\delta_i\,(i = 1, 2, 3\ldots)$ makes the parameter uncertainties as $|\Delta_i| \le \delta_i\,(i = 1, 2, 3, \ldots)$.

Theorem 1. *Under the action of robust feedback controller (10), the master system (6) and slave system (7) can achieve synchronization in finite time* $T = 2^{\sigma-1}V^{\sigma}(0)/\sigma$, *where* $\sigma = (1-\gamma)/2$.

Proof. Construct the Lyapunov function $V(t) = 1/2\sum_{i=1}^{3} e_i^2$. Differentiating $V(t)$ gives $\dot{V}(t) = 3\sum_{i=1}^{3} e_i \cdot \dot{e}_i$. Substituting (8) into $\dot{V}(t)$, we can get:

$$\begin{aligned}\dot{V}(t) &= e_1\dot{e}_1 + e_2\dot{e}_2 + e_3\dot{e}_3\\ &= e_1(e_2 + u_1(t)) + e_2(e_3 + u_2(t))\\ &\quad + e_3(-ae_1 - be_2 - ce_3 + y_1y_2(b+\Delta_5) - x_1x_2(b+\Delta_2))\\ &\quad + y_2^2 - x_2^2 - \Delta_4y_1 - \Delta_5y_2 - \Delta_6y_3 + \Delta_1x_1 + \Delta_2x_2 + \Delta_3x_3 + u_3(t).\end{aligned} \tag{11}$$

Then, substituting the controller in (10) into equation (11), we have

$$\begin{aligned}\dot{V}(t) &= e_1(e_2 + ae_3 - e_2 - e_1^{\gamma_1}) + e_2(e_3 + be_3 - e_3 - e_1^{\gamma_2})\\ &\quad + e_3[-ae_1 - be_2\\ &\quad - ce_3 + y_1y_2(b+\Delta_5) - x_1x_2(b+\Delta_2) + y_2^2 - x_2^2\\ &\quad - \Delta_4y_1 - \Delta_5y_2\\ &\quad - \Delta_6y_3 + \Delta_1x_1 + \Delta_2x_2 + \Delta_3x_3 + ce_3 - y_1y_2b\\ &\quad - \delta_5|y_1y_2|\mathrm{sign}(e_3)\\ &\quad + x_1x_2b + \delta_2|x_1x_2|\mathrm{sign}(e_3) - y_2^2 + x_2^2 + \delta_4|y_1|\mathrm{sign}(e_3)\\ &\quad + \delta_5|y_2|\mathrm{sign}(e_3) + \delta_6|y_3|\mathrm{sign}(e_3) - \delta_1|x_1|\mathrm{sign}(e_3)\\ &\quad \left[-\delta_2|x_2|\mathrm{sign}(e_3) - \delta_3|x_3|\mathrm{sign}(e_3) - e_3^{\gamma_3}\right].\end{aligned} \tag{12}$$

Furthermore, simplifying equation (12) can be obtained as follows:

$$\begin{aligned}\dot{V}(t) &= -e_1^{\gamma_1+1} - e_2^{\gamma_2+1} - e_3^{\gamma_3+1} + e_3y_1y_2\Delta_5 - \delta_5|e_3y_1y_2|\\ &\quad - e_3x_1x_2\Delta_2 + \delta_2|e_3x_1x_2|\\ &\quad - e_3y_1\Delta_4 + \delta_4|y_1||e_3| - e_3y_2\Delta_5 + \delta_5|y_2||e_3|\\ &\quad - e_3y_3\Delta_6 + \delta_6|y_3||e_3|\\ &\quad + e_3x_1\Delta_1 - \delta_1|x_1||e_3| + e_3x_2\Delta_2 - \delta_2|x_2||e_3| + e_3x_3\Delta_3\\ &\quad - \delta_3|x_3||e_3|,\end{aligned} \tag{13}$$

where, based on Assumption 1, we can get

$$\dot{V}(t) \le -e_1^{\gamma_1+1} - e_2^{\gamma_2+1} - e_3^{\gamma_3+1}, \tag{14}$$

and then we can know that

$$\begin{aligned}-e_1^{\gamma_1+1} - e_2^{\gamma_2+1} - e_3^{\gamma_3+1} &= -2^{\gamma+1/2}\left[\left(\frac{e_1^2}{2}\right)^{\gamma+1/2} + \left(\frac{e_2^2}{2}\right)^{\gamma+1/2} + \left(\frac{e_3^2}{2}\right)^{\gamma+1/2}\right]\\ &\le -2^{\gamma+1/2}\left(\frac{e_1^2}{2} + \frac{e_2^2}{2} + \frac{e_3^2}{2}\right)^{\gamma+1/2} = -2^{\gamma+1/2}V^{\gamma+1/2}(t).\end{aligned} \tag{15}$$

Thus, we have

$$\dot{V}(t) \leq -2^{\gamma+1/2}V^{\gamma+1/2}(t). \tag{16}$$

According to Lemma 1, we have

$$T = \frac{V^{1-\gamma+1/2}(0)}{2^{\gamma+1/2(1-(\gamma+1/2))}} = \frac{2^{1-\gamma/2}V^{1-\gamma/2}(0)}{1-\gamma}. \tag{17}$$

Let $\sigma = 1 - \gamma/2$; there are $T = 2^{\sigma-1}V^{\sigma}(0)/\sigma$; when $t \geq T$, $e_i \longrightarrow 0\,(i = 1, 2, 3)$. □

4. Circuit Implementation and Numerical Simulation

In this section, in order to verify the correctness of the 3D jerk system (1), the analog circuit is designed, and to illustrate the control effect of the robust feedback controller, the numerical simulation is presented.

4.1. Circuit Implementation. We use LM741 operational amplifiers, AD633 analog multipliers, resistors, and capacitors to design analog circuit, where the gain of multiplier AD633 is 0.1, and the power voltage of operational amplifier LM741 is $E = \pm 15V$, and its output saturated voltages $V_{\text{sat}} \approx \pm 13.5V$. According to the 3D jerk system (1), a chaotic circuit with hidden attractor is designed, as shown in Figure 8.

Due to the limitation of LM741 and AD633 working voltages, the output voltage of the system is reduced to 1/10 of the original. Compress them according to 10 : 1, and carry on time-scale transformation; let $\tau = \tau_0 t$, where $\tau_0 = 100$. Then the 3D jerk system (1) can be expressed as

$$\begin{cases} \dot{x}_1 = -100(-x_2), \\ \dot{x}_2 = -100(-x_3), \\ \dot{x}_3 = -340x_1 - 100x_2 - 400x_3 - 100(-x_1)x_2 - 100(-x_2)x_2. \end{cases} \tag{18}$$

Applying Kirchhoff's law and from Figure 8, the corresponding circuit equations are written as

$$\begin{cases} \dfrac{dx_1}{dt} = -\dfrac{1}{R_1C_1}(-x_2), \\ \dfrac{dx_2}{dt} = -\dfrac{1}{R_4C_2}(-x_3), \\ \dfrac{dx_3}{dt} = -\dfrac{1}{R_7C_3}x_1 - \dfrac{1}{R_8C_3}x_2 - \dfrac{1}{R_{10}C_3}x_3 - \dfrac{1}{10R_9C_3}(-x_1)x_2 - \dfrac{1}{10R_{11}C_3}(-x_2)x_2. \end{cases} \tag{19}$$

where x_1, x_2, and x_3 are related to the voltages on capacitors C_1, C_2, and C_3, respectively. The capacitors $C_1 = C_2 = C_3 = 100\,\text{nF}$. Comparing equation (18) with equation (19) and making the corresponding coefficients be equal, one can obtain the values of resistances as $R1 = R4 = R7 = R9 = R11 = 100\text{k}\Omega$, $R8 = 29.41\text{k}\Omega$, and $R10 = 25\,\text{k}\Omega$. The other resistances are $R2 = R3 = R5 = R6 = R12 = R13 = 10\,\text{k}\Omega$. Under the circuit parameters mentioned above, one can get a phase diagram on the digital oscilloscope as shown in Figure 9.

4.2. Numerical Simulation of Robust Feedback Controller. For the master system (6) and slave system (7), the parameters are set as $a = 3.4$, $b = 1$, and $c = 4$, and when $\Delta_i = 0\,(i = 1, 2, 3, 4, 5, 6)$, the master-slave systems (6) and (7) are in chaotic state. The parameter uncertainties are taken as $\Delta_1 = 0.01\sin(x3)$, $\Delta_2 = 0.02\cos(x_3)$, $\Delta_3 = 0.01\sin(x_3)$, $\Delta_4 = 0.02\sin(y_3)$, $\Delta_5 = 0.01\sin(y_3)$, and $\Delta_6 = 0.01\sin(y_3)$. So $\delta_1 = 0.01, \delta_2 = 0.02$, $\delta_3 = 0.01$, $\delta_4 = 0.02$, $\delta_5 = 0.01$, and $\delta_6 = 0.01$. The control parameters are chosen as $\gamma_1 = 0.6$, $\gamma_2 = 0.8$, and $\gamma_3 = 0.9$. The system initial values are chosen as $x_1 = -2$, $x_2 = 0, x_3 = 2.4$ and $y_1 = 7$, $y_2 = -3$, $y_3 = 7.4$. Under the robust feedback controller (10), the synchronization result is shown in Figure 10.

In Figure 10, the states of master system $x_i\,(i = 1, 2, 3)$ and slave system $y_i\,(i = 1, 2, 3)$ tend to converge, and synchronization is realized in finite time, and the states e_1, e_2, and e_3 of the error system (8) are shown in Figure 11.

From the above simulation results that the error system (8) realizes synchronization in finite time, the phase orbit of the synchronization error system gradually converges to the origin, the reliability of the synchronization method is verified, and the design of the robust feedback controller (10) meets the requirements.

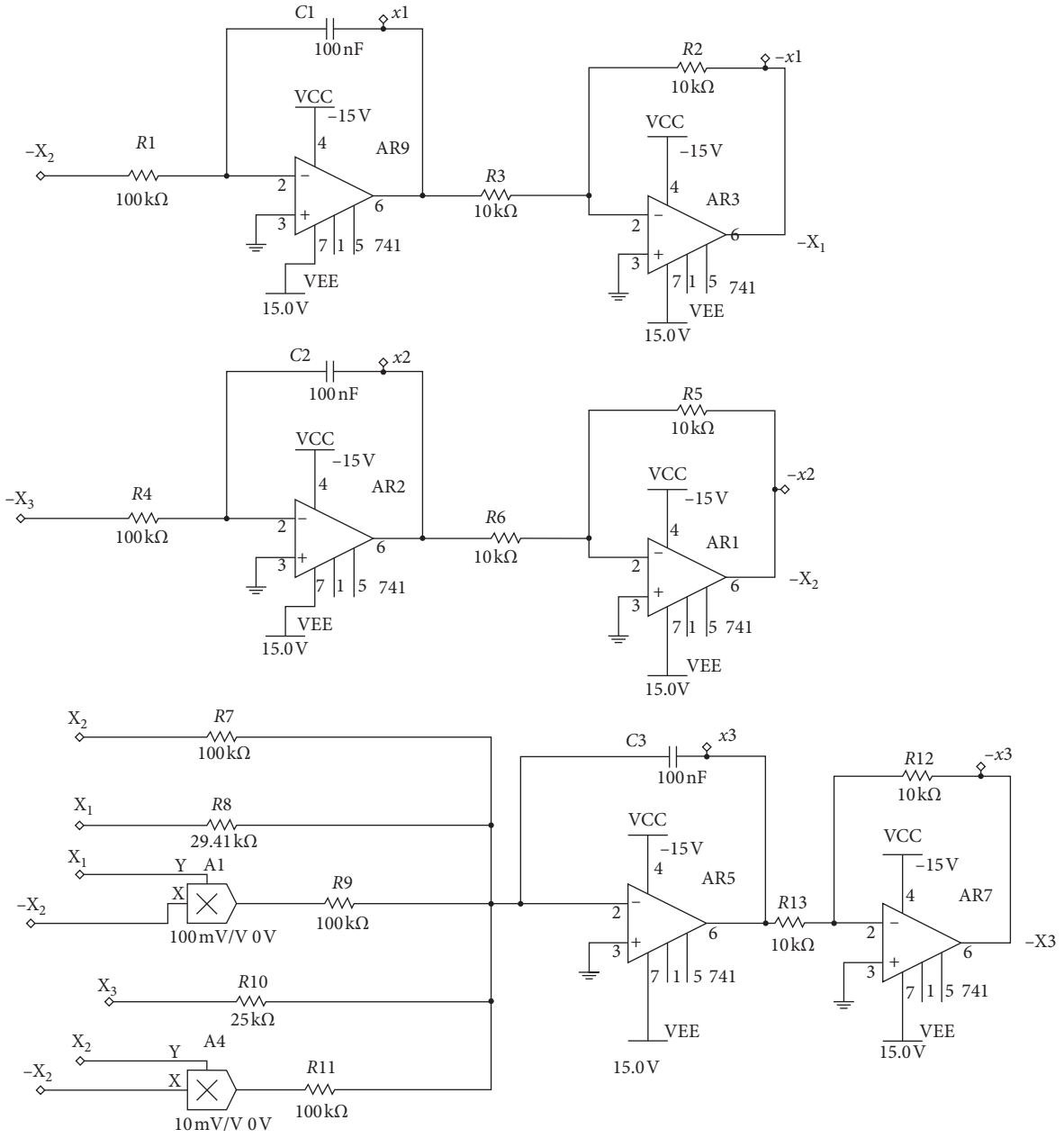

Figure 8: The circuit principle diagram of the 3D jerk system (1).

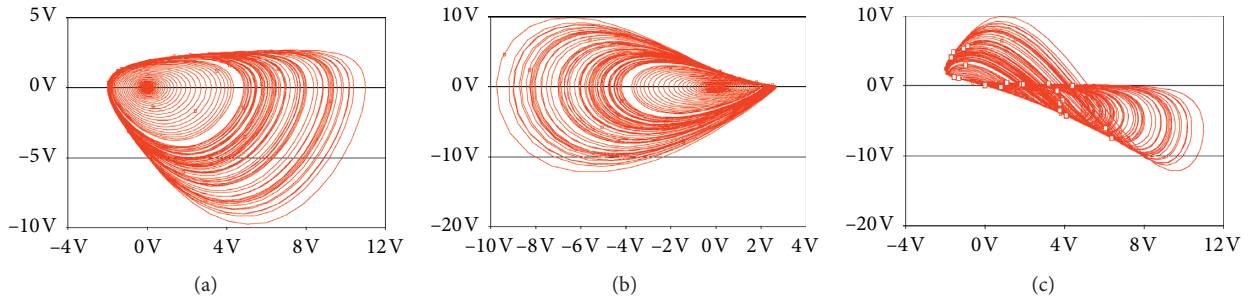

Figure 9: The screenshots of the digital oscilloscope with the 3D jerk system (1) in (a) $x_1 - x_2$ plane, (b) $x_2 - x_3$ plane, and (c) $x_1 - x_3$ plane.

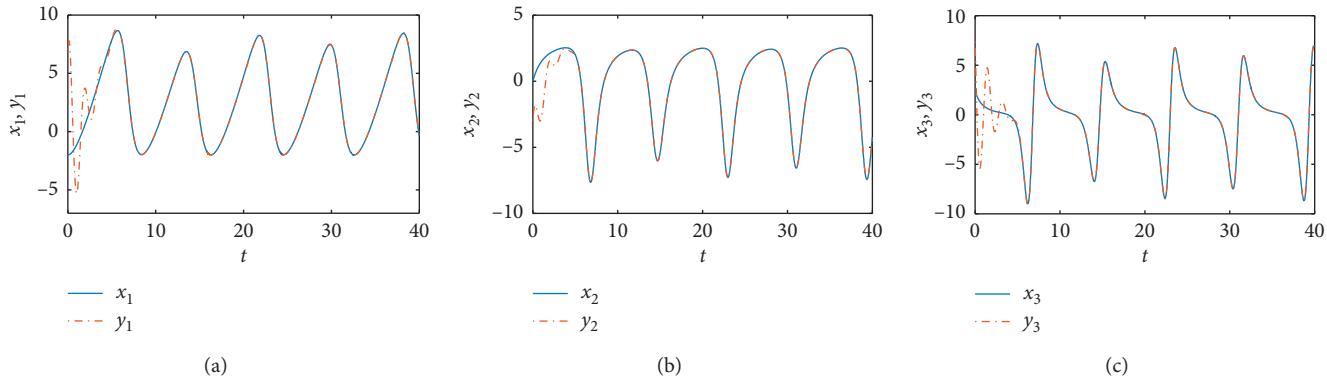

FIGURE 10: 3D jerk master-slave system synchronous orbits. (a) Synchronization of x_1, y_1. (b) Synchronization of x_2, y_2. (c) Synchronization of x_3, y_3.

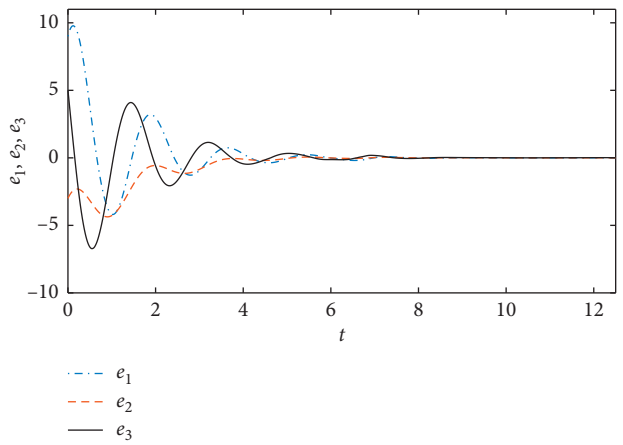

FIGURE 11: Finite-time error e_1, e_2, and e_3 orbit of 3D jerk master-slave system.

5. Conclusion

In this work, the dynamical behaviors of the 3D jerk system with hidden attractor are analyzed by numerical calculation. Furthermore, an analog circuit is designed for implementing and testing our system model. A very good qualitative consistency is shown between the circuit experimental results and the simulations of the theoretical model. Then, for 3D jerk system synchronization and control, a finite-time robust feedback controller was proposed, and the synchronization of 3D jerk chaotic system with hidden attractor was realized in finite time. Finally, mathematical simulation result demonstrated that the performances of the proposed controller are excellent. However, there are still complex dynamics and the topological structure of this system should be exploited, and better synchronization control methods should be found. In addition, the synchronization and control of the master-slave system can be realized through circuit implementation. These will be provided in future works.

Data Availability

The data that support the findings of this study are available within the article.

Conflicts of Interest

The authors declare that they have no conflicts of interest.

Authors' Contributions

All authors contributed equally to this work.

Acknowledgments

This work was supported by the Natural Science Basic Research Plan in Shaanxi Province of China (2020JM-646), the Innovation Capability Support Program of Shaanxi (2018GHJD-21), the Science and Technology Program of Xi'an (2019218414GXRC020CG021-GXYD20.3), and the Fund of Excellent Doctoral Innovation of Xi'an University of Technology, and the Support Plan for Sanqin Scholars Innovation Team in Shaanxi Province of China.

References

[1] J. Gleick and R. C. Hilborn, "Chaos: making a new science," *Physics Today*, vol. 41, no. 11, p. 79, 1988.

[2] E. N. Lorenz, "Deterministic nonperiodic flow," *Journal of the Atmospheric Sciences*, vol. 20, no. 2, pp. 130–141, 1963.

[3] D. Ruelle and F. Takens, "On the nature of turbulence," *Les rencontres physiciens-mathématiciens de Strasbourg-RCP25*, vol. 12, pp. 1–44, 1971.

[4] R. M. May, "Simple mathematical models with very complicated dynamics," *Nature*, vol. 261, no. 5560, pp. 459–467, 1976.

[5] O. Rossler, "An equation for hyperchaos," *Physics Letters A*, vol. 71, no. 2-3, pp. 155–157, 1979.

[6] G. Chen and T. Ueta, "Yet another chaotic attractor," *International Journal of Bifurcation and Chaos*, vol. 9, no. 7, pp. 1465-1466, 1999.

[7] J. Lü and G. Chen, "A new chaotic attractor coined," *International Journal of Bifurcation and Chaos*, vol. 12, no. 3, pp. 659–661, 2002.

[8] N. Yujun, W. Xingyuan, W. Mingjun, and Z. Huaguang, "A new hyperchaotic system and its circuit implementation," *Communications in Nonlinear Science and Numerical Simulation*, vol. 15, no. 11, pp. 3518–3524, 2010.

[9] G. A. Leonov, N. Kuznetsov, O. Kuznetsova, S. Seledzhi, and V. Vagaitsev, "Hidden oscillations in dynamical systems,"

IEEE Transactions on Systems Controller, vol. 6, pp. 54–67, 2011.

[10] J. Sprott, "Simplest dissipative chaotic flow," *Physics Letters A*, vol. 228, no. 4-5, pp. 271–274, 1997.

[11] J. C. Sprott, "Some simple chaotic jerk functions," *American Journal of Physics*, vol. 65, no. 6, pp. 537–543, 1997.

[12] J. C. Sprott, "Some simple chaotic flows," *Physical Review E*, vol. 50, no. 2, p. R647, 1994.

[13] S.-K. Lao, Y. Shekofteh, S. Jafari, and J. C. Sprott, "Cost function based on Gaussian mixture model for parameter estimation of a chaotic circuit with a hidden attractor," *International Journal of Bifurcation and Chaos*, vol. 24, no. 1, Article ID 1450010, 2014.

[14] M. Molaie, S. Jafari, J. C. Sprott, and S. M. R. H. Golpayegani, "Simple chaotic flows with one stable equilibrium," *International Journal of Bifurcation and Chaos*, vol. 23, no. 11, Article ID 1350188, 2013.

[15] V.-T. Pham, S. Jafari, T. Kapitaniak, C. Volos, and S. T. Kingni, "Generating a chaotic system with one stable equilibrium," *International Journal of Bifurcation and Chaos*, vol. 27, no. 4, Article ID 1750053, 2017.

[16] X. Wang and G. Chen, "A chaotic system with only one stable equilibrium," *Communications in Nonlinear Science and Numerical Simulation*, vol. 17, no. 3, pp. 1264–1272, 2012.

[17] Z. Wang, X. Xi, L. Kong, and Z. Wei, "Infinity dynamics and ddf control for a chaotic system with one stable equilibrium," *The European Physical Journal Special Topics*, vol. 229, no. 6-7, pp. 1319–1333, 2020.

[18] Z. Wei and Z. Wang, "Chaotic behavior and modified function projective synchronization of a simple system with one stable equilibrium," *Kybernetika*, vol. 49, no. 2, pp. 359–374, 2013.

[19] S. Jafari, J. C. Sprott, and S. M. R. Hashemi Golpayegani, "Elementary quadratic chaotic flows with no equilibria," *Physics Letters A*, vol. 377, no. 9, pp. 699–702, 2013.

[20] S. Wang, A. Yousefpour, A. Yusuf et al., "Synchronization of a non-equilibrium four-dimensional chaotic system using a disturbance-observer-based adaptive terminal sliding mode control method," *Entropy*, vol. 22, no. 3, p. 271, 2020.

[21] Z. Wei, "Dynamical behaviors of a chaotic system with no equilibria," *Physics Letters A*, vol. 376, no. 2, pp. 102–108, 2011.

[22] X. Wang and G. Chen, "Constructing a chaotic system with any number of equilibria," *Nonlinear Dynamics*, vol. 71, no. 3, pp. 429–436, 2013.

[23] Q. Yang and X. Qiao, "Constructing a new 3d chaotic system with any number of equilibria," *International Journal of Bifurcation and Chaos*, vol. 29, no. 5, Article ID 1950060, 2019.

[24] H. Bao, N. Wang, B. Bao, M. Chen, P. Jin, and G. Wang, "Initial condition-dependent dynamics and transient period in memristor-based hypogenetic jerk system with four line equilibria," *Communications in Nonlinear Science and Numerical Simulation*, vol. 57, pp. 264–275, 2018.

[25] S. Jafari and J. C. Sprott, "Simple chaotic flows with a line equilibrium," *Chaos, Solitons & Fractals*, vol. 57, pp. 79–84, 2013.

[26] G. A. Leonov, N. V. Kuznetsov, and V. I. Vagaitsev, "Hidden attractor in smooth chua systems," *Physica D: Nonlinear Phenomena*, vol. 241, no. 18, pp. 1482–1486, 2012.

[27] S. Brezetskyi, D. Dudkowski, and T. Kapitaniak, "Rare and hidden attractors in van der pol-duffing oscillators," *The European Physical Journal Special Topics*, vol. 224, no. 8, pp. 1459–1467, 2015.

[28] Z. T. Zhusubaliyev and E. Mosekilde, "Multistability and hidden attractors in a multilevel dc/dc converter," *Mathematics and Computers in Simulation*, vol. 109, pp. 32–45, 2015.

[29] Z. T. Zhusubaliyev, E. Mosekilde, V. G. Rubanov, and R. A. Nabokov, "Multistability and hidden attractors in a relay system with hysteresis," *Physica D: Nonlinear Phenomena*, vol. 306, pp. 6–15, 2015.

[30] S. Vaidyanathan, A. Sambas, M. Mamat, and M. Sanjaya, "A new three-dimensional chaotic system with a hidden attractor, circuit design and application in wireless mobile robot," *Archives of Control Sciences*, vol. 27, 2017.

[31] Ü. Çavuşoğlu, S. Panahi, A. Akgül, S. Jafari, and S. Kacar, "A new chaotic system with hidden attractor and its engineering applications: analog circuit realization and image encryption," *Analog Integrated Circuits and Signal Processing*, vol. 98, no. 1, pp. 85–99, 2019.

[32] M. A. Murillo-Escobar, C. Cruz-Hernández, F. Abundiz-Pérez, and R. M. López-Gutiérrez, "A robust embedded biometric authentication system based on fingerprint and chaotic encryption," *Expert Systems with Applications*, vol. 42, no. 21, pp. 8198–8211, 2015.

[33] H. R. Abdolmohammadi, A. J. M. Khalaf, S. Panahi, K. Rajagopal, V. T. Pham, and S. Jafari, "A new 4d chaotic system with hidden attractor and its engineering applications: analog circuit design and field programmable gate array implementation," *Pramana*, vol. 90, no. 6, p. 70, 2018.

[34] A. Akgul, H. Calgan, I. Koyuncu, I. Pehlivan, and A. Istanbullu, "Chaos-based engineering applications with a 3d chaotic system without equilibrium points," *Nonlinear Dynamics*, vol. 84, no. 2, pp. 481–495, 2016.

[35] J. Ma, X. Wu, R. Chu, and L. Zhang, "Selection of multi-scroll attractors in jerk circuits and their verification using pspice," *Nonlinear Dynamics*, vol. 76, no. 4, pp. 1951–1962, 2014.

[36] J. Kengne, Z. Njitacke, and H. Fotsin, "Dynamical analysis of a simple autonomous jerk system with multiple attractors," *Nonlinear Dynamics*, vol. 83, no. 1-2, pp. 751–765, 2016.

[37] P. Louodop, M. Kountchou, H. Fotsin, and S. Bowong, "Practical finite-time synchronization of jerk systems: theory and experiment," *Nonlinear Dynamics*, vol. 78, no. 1, pp. 597–607, 2014.

[38] S. T. Kingni, G. F. Kuiate, V. K. Tamba, V. T. Pham, and D. V. Hoang, "Self-excited and hidden attractors in an autonomous josephson jerk oscillator: analysis and its application to text encryption," *Journal of Computational and Nonlinear Dynamics*, vol. 14, no. 7, 2019.

[39] S. Panahi and S. Jafari, "Synchronization in a network of chaotic memristive jerk oscillators," *The European Physical Journal Special Topics*, vol. 228, no. 10, pp. 2147–2155, 2019.

[40] H. Lenz and D. Obradovic, "Robust control of the chaotic lorenz system," *International Journal of Bifurcation and Chaos*, vol. 7, no. 12, pp. 2847–2854, 1997.

[41] S. Mobayen, "Finite-time stabilization of a class of chaotic systems with matched and unmatched uncertainties: an lmi approach," *Complexity*, vol. 21, no. 5, pp. 14–19, 2016.

[42] S. Mobayen, F. Tchier, and L. Ragoub, "Design of an adaptive tracker forn-link rigid robotic manipulators based on super-twisting global nonlinear sliding mode control," *International Journal of Systems Science*, vol. 48, no. 9, pp. 1990–2002, 2017.

[43] L. Shen and M. Wang, "Robust synchronization and parameter identification on a class of uncertain chaotic systems," *Chaos, Solitons & Fractals*, vol. 38, no. 1, pp. 106–111, 2008.

[44] D. H. Ji, S. C. Jeong, J. H. Park, and S. C. Won, "Robust adaptive backstepping synchronization for a class of uncertain

chaotic systems using fuzzy disturbance observer," *Nonlinear Dynamics*, vol. 69, no. 3, pp. 1125–1136, 2012.

[45] Z. Wang, W. Sun, Z. Wei, and S. Zhang, "Dynamics and delayed feedback control for a 3d jerk system with hidden attractor," *Nonlinear Dynamics*, vol. 82, no. 1-2, pp. 577–588, 2015.

[46] V. M. Millionshchikov, "Theory of characteristic lyapunov indices," *Mathematical Notes of the Academy of Sciences of the USSR*, vol. 7, no. 4, pp. 305–311, 1970.

[47] S. Chen, J. Hu, C. Wang, and J. Lü, "Adaptive synchronization of uncertain Rössler hyperchaotic system based on parameter identification," *Physics Letters A*, vol. 321, no. 1, pp. 50–55, 2004.

Hindawi
Complexity
Volume 2020, Article ID 8844657, 11 pages
https://doi.org/10.1155/2020/8844657

WILEY | Hindawi

Research Article

Multistability in a Fractional-Order Centrifugal Flywheel Governor System and Its Adaptive Control

Bo Yan,[1] **Shaobo He**,[2] **and Shaojie Wang**[1]

[1]*College of Electrical and Information Engineering, Shaoyang University, Shaoyang 422000, China*
[2]*School of Physics and Electronics, Central South University, Changsha 410083, China*

Correspondence should be addressed to Shaobo He; heshaobo_123@163.com

Received 1 October 2020; Revised 16 November 2020; Accepted 24 November 2020; Published 14 December 2020

Academic Editor: Zhouchao Wei

In this paper, a 4D fractional-order centrifugal flywheel governor system is proposed. Dynamics including the multistability of the system with the variation of system parameters and the derivative order are investigated by Lyapunov exponents (LEs), bifurcation diagram, phase portrait, entropy measure, and basins of attraction, numerically. It shows that the minimum order for chaos of the fractional-order centrifugal flywheel governor system is $q = 0.97$, and the system has rich dynamics and produces multiple coexisting attractors. Moreover, the system is controlled by introducing the adaptive controller which is proved by the Lyapunov stability theory. Numerical analysis results verify the effectiveness of the proposed method.

1. Introduction

The centrifugal flywheel governor system is a device for automatically adjusting and controlling the speed of the engine. It has opened the precedent of modern automatic control, marked the birth of modern automatic control technology, and been widely used in modern industry. When the centrifugal flywheel governor system is disturbed, the velocity of the system will change suddenly and the chaotic vibration will be produced [1, 2]. In order to make the centrifugal governor system run stably and play a good role in practical application, it is necessary to study the chaotic dynamics law when the system is disturbed and how to control the chaotic motion to the stable state.

In recent years, the research on chaos and control of the centrifugal flywheel governor system has attracted wide attention of scholars [3–14]. For example, Zhang et al. [3] studied the evolution from Hopf bifurcation to chaos of the centrifugal flywheel governor system subjected to external distance. Gou et al. [4–9] analyzed the chaos forming process of the centrifugal flywheel governor system by the bifurcation diagram, the phase portrait, and Poincare map and controlled the chaotic behavior to the steady orbit by linear and nonlinear feedback control methods. Zhang et al. [10] studied complex dynamical behavior of a class of the centrifugal flywheel governor system and proposed a parametric open-plus-closed-loop approach to control chaos motion to any desired periodic orbit. Rao et al. [11] investigated the global structure of nonlinear response of mechanical centrifugal governor and found a new type of mixed-mode oscillations in the periodic response. Luo et al. [12] addressed chaos suppression of the mechanical centrifugal flywheel governor system with output constraint and fully unknown parameters via adaptive dynamic surface control. Aghababa et al. [13] derived an adaptive robust controller to suppress the chaos of nonautonomous centrifugal flywheel governor systems in a given finite time effectively by using the adaptation laws and Lyapunov control theory. Zhang et al. [14] studied the Hopf bifurcation of the typical autonomous and nonautonomous centrifugal flywheel governor system and discussed the reason of chaotic oscillation of the system.

As far as we know, the fractional-order derivative has been proposed for more than 300 years. It becomes to be a research hotspot in the nonlinear research field. Unlike the integer-order differential operator, the fractional-order differential operator can effectively describe the

physical process with historical memory effect, for instance, Caputo definition and Riemann–Liouville definition [15]. Those fractional calculus have been widely used in theoretical analysis and engineering. Specifically, they have been used in different research fields such as quantum mechanics, electromagnetic oscillation, system control, material mechanics, and other fields [16–19]. Therefore, it is of great theoretical significance to introduce fractional calculus into the study on chaos and control of the centrifugal flywheel governor system. For example, Ge et al. [20] determined the existence of chaos in the fractional-order autonomous and nonautonomous nonlinear centrifugal flywheel governor system by using the bifurcation diagram and phase portrait and realized chaos control of the system by the linear feedback control method. But, the research on chaos and control of the fractional-order system needs to be further expanded, and this study provides a useful reference for the further research of the fractional-order centrifugal flywheel governor system.

In this paper, chaos and its adaptive control of the fractional-order centrifugal flywheel governor system are studied. The outline of this paper is given as follows. In Section 2, the fractional-order centrifugal flywheel governor system is introduced. In Section 3, dynamics of the integer-order centrifugal flywheel governor system are investigated numerically by the bifurcation diagram, LEs, the phase portrait, and the basins of attraction. In Section 4, the adaptive control formula is derived and the chaos control of the system is realized by simulation. In Section 5, the results are summarized.

2. The Fractional-Order Centrifugal Flywheel Governor System

The mechanics model of the centrifugal flywheel governor with external disturbance is depicted in Figure 1, where l, m, r, and ϕ represent the length of the rod, the mass of the fly ball, the distance between the rotational axis and the suspension joint, and the angle between the rotational axis and the rod, respectively. The motor drives the flywheel to rotate with angular velocity ω. The flywheel is joined to the axis through a gear box, so the axis rotates with angular velocity $n\omega$. n is the proportional coefficient, k is the stubborn coefficient of the spring, and g is the gravitational acceleration. Ignoring the mass of the pipe and casing and assuming that the damping coefficient at the joint of the rod head and the ball is c, the motion equation of the system is given by [10, 14]

$$2\left[ml^2\ddot{\phi} - mrl\eta^2\cos\phi - \left(2k + m\eta^2\right)l^2\sin\phi\cos\phi + (2kl + mg)l\sin\phi\right] = -c\dot{\phi}. \tag{1}$$

For the rotational machine, the net torque is the difference between the torque Q produced by the engine and the load torque Q_L, which is available for angular acceleration, which is

$$J\frac{\mathrm{d}\omega}{\mathrm{d}t} = Q - Q_L, \tag{2}$$

where J is the moment of inertia of the machine. As the angle ϕ varies, the position of the control valve which admits the fuel is also varied. Then, equation (2) can be written in the form:

$$J\dot{\omega} = \gamma\cos\phi - \beta, \tag{3}$$

where $\gamma > 0$ is a proportionally constant and β is an equivalent torque of the load. Let

$$\begin{aligned} s &= \frac{\gamma}{J\Omega_n}, \\ F &= \frac{\beta}{J\Omega_n}, \\ d &= \frac{n^2 m}{2\mathrm{kl} + \mathrm{mg}}, \\ b &= \frac{c}{2\mathrm{ml}^2\Omega_n}, \\ e &= \frac{2\mathrm{kl}}{2\mathrm{kl} + \mathrm{mg}}, \\ p &= \frac{n^2\mathrm{ml}}{2\mathrm{kl} + \mathrm{mg}}, \\ \Omega_n &= \sqrt{\frac{2\mathrm{kl} + \mathrm{mg}}{\mathrm{ml}}}, \end{aligned} \tag{4}$$

and change time scale $\tau = \Omega_n t$; let $\varphi = \mathrm{d}\phi/\mathrm{d}\tau$, $x = \phi$, $y = \varphi$, and $z = \omega$, then equation (1) can be written as the standard form of the three-dimensional autonomy system:

$$\begin{cases} \dot{x} = y, \\ \dot{y} = dz^2\cos x + \left(e + pz^2\right)\sin x\cos x - \sin x - by, \\ \dot{z} = s\cos x - F. \end{cases} \tag{5}$$

The above system (4) is proposed with the assumption that the load torque is constant. When the load torque is not constant, it can be represented by a constant term F and a Hamiltonian term $\alpha\sin(\sigma t)$, where F, α, and σ are constants. Then, (4) can be written as

$$\begin{cases} \dot{x} = y, \\ \dot{y} = dz^2\cos x + \left(e + pz^2\right)\sin x\cos x - \sin x - by, \\ \dot{z} = s\cos x - F - \alpha\sin(\sigma t). \end{cases} \tag{6}$$

Let $\sigma t = w$, we can get $\dot{w} = \sigma$ and then equation (6) becomes

$$\begin{cases} \dot{x} = y, \\ \dot{y} = dz^2\cos x + \left(e + pz^2\right)\sin x\cos x - \sin x - by, \\ \dot{z} = s\cos x - F - \alpha\sin(w), \\ \dot{w} = \sigma. \end{cases} \tag{7}$$

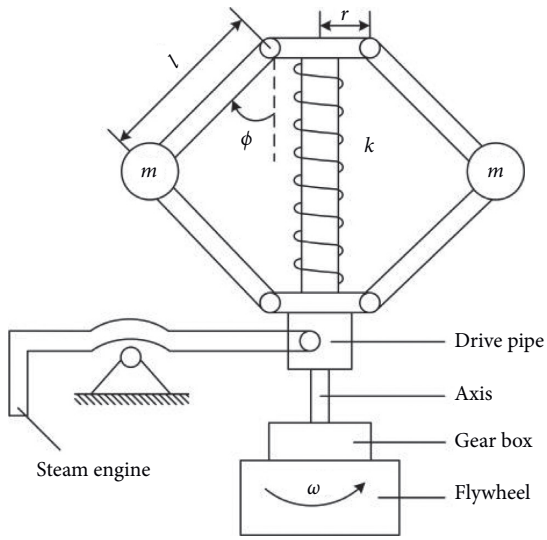

Figure 1: The mechanics model of the centrifugal flywheel governor system.

By introducing the fractional-order derivative to system (7), the fractional-order centrifugal flywheel governor system is obtained, and it is defined by

$$\begin{cases} D_{t_0}^q x = y, \\ D_{t_0}^q y = dz^2 \cos x + \left(e + pz^2\right)\sin x \cos x - \sin x - by, \\ D_{t_0}^q z = s\cos x - F - \alpha \sin(w), \\ D_{t_0}^q w = \sigma, \end{cases} \tag{8}$$

where $D_{t_0}^q$ is the q-order Caputo differential operator [21, 22]. The Caputo fractional-order derivative definition is given by

$$D_{t_0}^q x(t) = \begin{cases} \dfrac{1}{\Gamma(1-q)} \displaystyle\int_{t_0}^{t} \frac{\dot{x}(\tau)}{(t-\tau)} d\tau, & 0 < q < 1, \\ \dot{x}(t), & q = 1, \end{cases} \tag{9}$$

where $q \in R^+$ and $\Gamma(\cdot)$ is the Gamma function.

3. Multistability Analysis

In this section, the bifurcation diagram, LEs, phase portrait, and the basins of attraction are employed to investigate the dynamics of the fractional-order centrifugal flywheel governor system. In the following analyses, we fix the system parameters $d = 0.08$, $p = 0.01$, $e = 0.5$, $b = 0.4$, $F = 1.942$, $\alpha = 0.4$, and $\sigma = 1.0$ and select parameter s as the argument variable. The system is numerically solved by the predictor-corrector algorithm [23–25]. The Matlab source code named "FDE12.m" of the predictor-corrector method can be downloaded online [26]. The method of using "FDE12.m" to solve the fractional-order system is described in detail in reference [27]. The detailed numerical solutions and how to compute LEs of the fractional-order system can be obtained according to reference [28]. The predictor-corrector algorithm is an effective method to solve the fractional-order partial differential equation. For example, Oskouie et al. [24] used the predictor-corrector algorithm to solve the fractional viscoelastic Bernoulli nanobeams differential equation and investigated the effects of fractional derivative order, surface parameters, and others factors on the nonlinear time response. He et al. [25] investigated a fractional-order microscopic chemical system by the predictor-corrector algorithm.

3.1. Bifurcation Analysis. Dynamics of the system with the variation of g and q are analyzed by means of bifurcation diagram, LEs, and phase diagrams. Four cases are investigated.

3.1.1. Case 1. Fix $s = 10$ and vary the derivative order q from 0.94 to 1 with the step size of 3×10^{-4}. Set the initial condition as $[x_0, y_0, z_0, w_0] = [0.005, 0.005, -0.1, 0.1]$ and $[0.5, 0.005, -0.1, 0.1]$. The bifurcation diagram and LEs of the fractional-order centrifugal flywheel governor system are illustrated in Figure 2. In Figure 2(a), blue points represent $x_{\max}$ for the initial values $[x_0, y_0, z_0, w_0] = [0.005, 0.005, -0.1, 0.1]$ and red points for $[x_0, y_0, z_0, w_0] = [0.5, 0.005, -0.1, 0.1]$. But. Figure 2(b) only shows LEs for $[x_0, y_0, z_0, w_0] = [0.005, 0.005, -0.1, 0.1]$. It can be seen from Figure 2 that the system is chaotic when $q > 0.963$, and for other values of q, the system is convergent. Through LE curves in Figure 2(b), we can see that when $q \in [0.963, 0.97]$, the system is not chaotic. But, when $q > 0.97$, the system always has a positive Lyapunov exponent, which shows the system is always in a chaotic state. In addition, the complexity of the system increases with the increase in derivative order q. Therefore, for the fractional-order centrifugal flywheel governor system, the LE curve is more accurate in describing the state of the system than the bifurcation diagram. It can well describe the process of transition from period to chaos. Figure 3(a) shows that when $[x_0, y_0, z_0, w_0] = [0.5, 0.005, -0.1, 0.1]$, the minimum order for chaos of the system is increased but the shape of the bifurcation diagram keeps unchanged which means the initial condition will affect the dynamics of the system. The periodic circles for $q = 0.94$ and 0.968 and chaotic attractors for $q = 0.972$ and 0.99 are shown in Figure 4. It can be seen that the result of phase portrait analysis is consistent with the result of dynamic characteristic analysis, and the chaotic attractors show obvious chaotic characteristic.

3.1.2. Case 2. Fix $q = 0.98$; let the parameter s vary from 2 to 18 with the step size of 0.08, and the initial condition also be $[x_0, y_0, z_0, w_0] = [0.005, 0.005, -0.1, 0.1]$ and $[0.5, 0.005, -0.1, 0.1]$, and then dynamical analysis results are shown in Figure 4. In Figure 4(a), blue points represent $x_{\max}$ for the initial values $[x_0, y_0, z_0, w_0] = [0.005, 0.005, -0.1, 0.1]$ and red points for the initial values $[x_0, y_0, z_0, w_0] = [0.5, 0.005, -0.1, 0.1]$. But, Figure 4(b) only shows LEs for $[x_0, y_0, z_0, w_0] =$

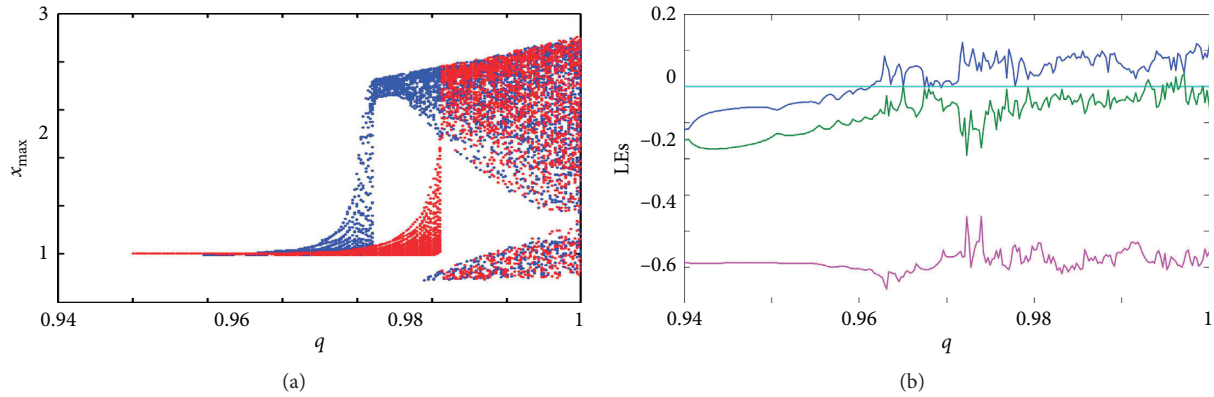

FIGURE 2: The dynamics of the fractional-order centrifugal flywheel governor system vary with derivative order q. (a) Bifurcation diagram. (b) Lyapunov exponent spectrum.

[0.005, 0.005, −0.1, 0.1]. It shows in Figure 4 that the system is chaotic for $s \in [3.5, 13.5]$ and [2.9, 3.1] and is convergent for other values of s. In addition, when $s \in [6, 10]$, the complexity of the system is relatively large. Figure 4(a) shows that when $[x_0, y_0, z_0, w_0] = [0.5, 0.005, -0.1, 0.1]$, the larger complexity interval is reduced, which means that the system will produce the coexistence attractors with different initial conditions.

3.1.3. Case 3. Let the parameter $s \in [3, 15]$ and derivative order $q \in [0.96, 1]$; divide the parameter space into a 150×150 grid. As with above cases, the initial condition is given by $[x_0, y_0, z_0, w_0] = [0.005, 0.005, -0.1, 0.1]$. Then, the maximum Lyapunov exponent-based contour plot in the parameter plane s-q is shown in Figure 5. It can be seen that the chaotic region is mainly observed in the area located in s $\in$ [4.8, 10] and $q \in [0.98, 1]$. In this area, the system has relative larger maximum Lyapunov exponents with lager q. In addition, when s $\in$ [5, 7.8] and $q \in [0.995, 1]$, the value of maximum Lyapunov exponents is bigger. Finally, it also can be found out that the minimum order for chaos is about $q = 0.927$.

3.1.4. Case 4. Fix $q = 0.98$ and $s = 10$, and the initial values are $[x_0, y_0, z_0, w_0] = [x_0, 0.005, -0.1, 0.1]$ and $x_0 \in [0, 2]$. The bifurcation diagram of the fractional-order centrifugal flywheel governor system is shown in Figure 6(a). Similarly, when $[x_0, y_0, z_0, w_0] = [0.005, y_0, -0.1, 0.1]$, $y_0 \in [0, 2]$. The bifurcation diagram of the system is plotted in Figure 6(b). It can be seen that when the initial condition changes, the complexity and state of the system are affected. In addition, different initial value components have different effects on the dynamics of the system. For Figure 6(a), the periodic state can be found at $x_0 = 1$. For Figure 6(b), the complexity is significantly different when $y_0 = 1.21$.

3.2. Basin of Attraction. The coexisting attractor is an important feature of chaotic systems, which has been studied by many scholars. For example, Lai et al. [29–31] used the dynamic evolution with respect to parameters and initial conditions to illustrate the existence coexisting attractors and presented the circuit implementation of the coexisting attractors for some chaotic systems. The basin of attraction is an effective tool to analyze multistability and the phenomenon of the coexistence of attractors [32].

In this paper, the method used is presented. For the proposed system, there are four state variables x, y, z, and w. Thus, four time series are obtained, and they can be defined as $\{x(n); y(n); z(n); w(n);\ n = 1, 2, 3, \ldots, N\}$, where N is the length of the time series. Then, the position of the attractor is defined by

$$P = [\overline{x}, \overline{y}, \overline{z}, \overline{w}], \tag{10}$$

where the mean values of each time series are used. The size of the attractor is given by

$$S = \left[S_x, S_y, S_z, S_w\right], \tag{11}$$

where $S_x = \max(x) - \min(x)$, $S_y = \max(y) - \min(y)$, $S_z = \max(z) - \min(z)$, and $S_w = \max(w) - \min(w)$. Suppose that there are two chaotic attractors, and their time series are defined by $\{x(n); y(n); z(n); w(n);\ n = 1, 2, 3, \ldots, N\}$ and $\{\widetilde{x}(n); \widetilde{y}(n); \widetilde{z}(n); \widetilde{w}(n);\ n = 1, 2, 3, \ldots, N\}$. The error between the positions of the two attractors is given by

$$e_1 = \frac{1}{4}\sqrt{(\overline{x} - \overline{\overline{x}})^2 + (\overline{y} - \overline{\overline{y}})^2} + (\overline{z} - \overline{\overline{z}})^2 + (\overline{w} - \overline{\overline{w}})^2 . \tag{12}$$

while the error regarding the size of the attractors is defined by

$$e_2 = \frac{1}{4}\sqrt{\left(S_x - \widetilde{S}_x\right)^2 + \left(S_y - \widetilde{S}_y\right)^2 + \left(S_z - \widetilde{S}_z\right)^2 + \left(S_w - \widetilde{S}_w\right)^2}. \tag{13}$$

In this paper, we set a parameter *error* to decide whether the obtained attractor is different with existing ones or not. Namely, if both $e_1 >$ error and $e_2 >$ error, the obtained attractor $\{\widetilde{x}(n); \widetilde{y}(n); \widetilde{z}(n); \widetilde{w}(n);\ n = 1, 2, 3, \ldots, N\}$ is a new attractor. Otherwise, it is not a new attractor. In this paper, the value of *error* is set as 50. The flow chart for basins of attraction is shown in Figure 7.

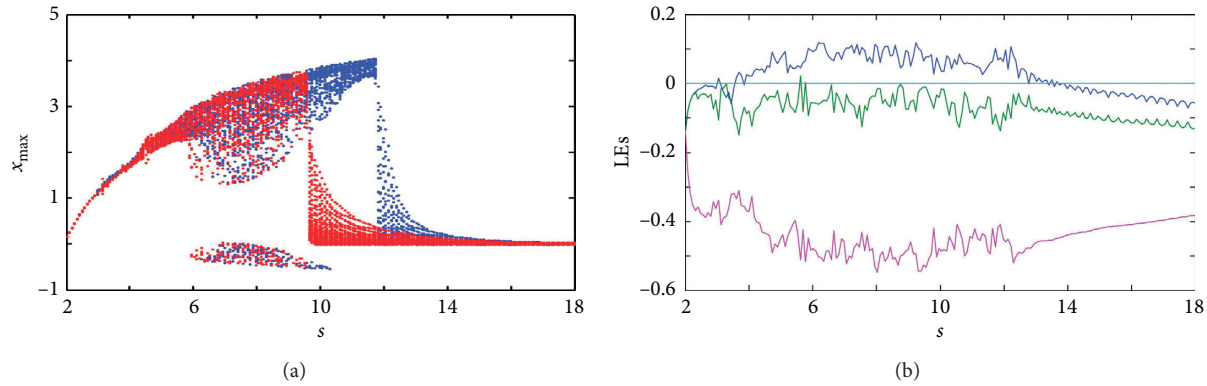

Figure 3: The dynamics of the fractional-order centrifugal flywheel governor system vary with parameter s; (a) Bifurcation diagram. (b) Lyapunov exponent spectrum.

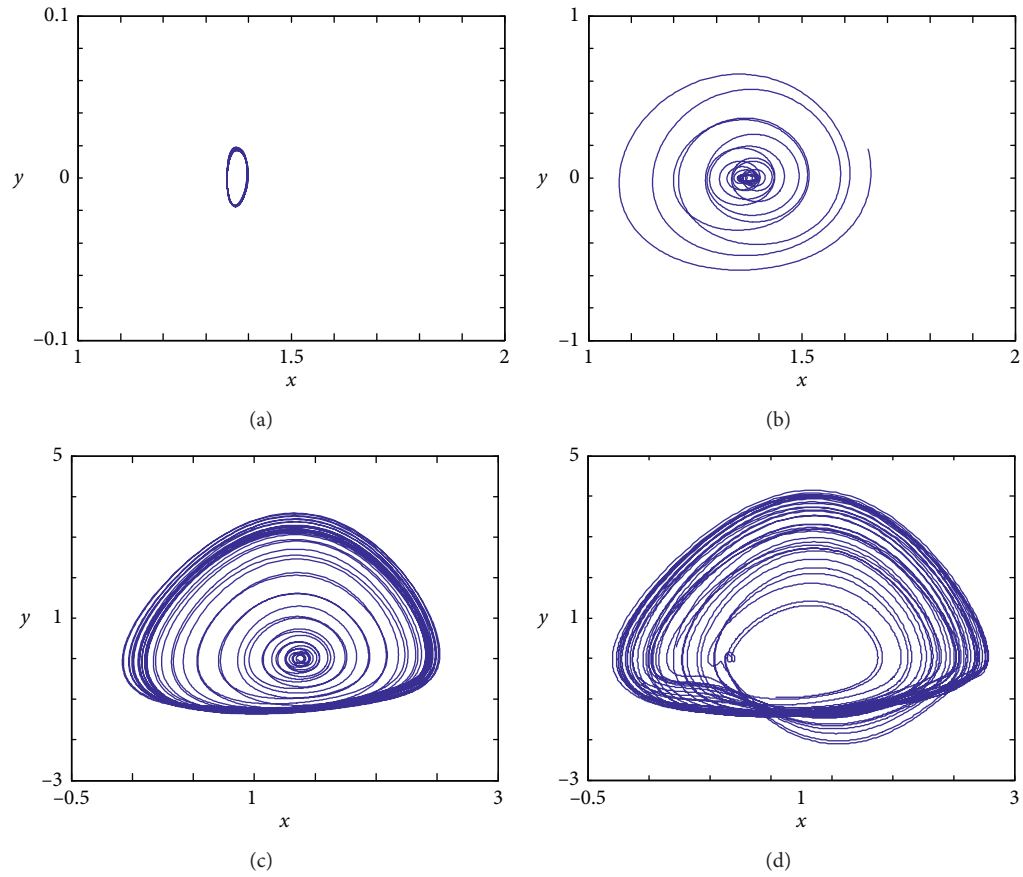

Figure 4: Phase diagrams with different derivative orders: (a) $q = 0.94$; (b) $q = 0.968$; (c) $q = 0.972$; (d) $q = 0.99$.

Fix $s = 10$ and the initial values are set as $[x_0, y_0, z_0, w_0] = [x, y, -0.1; 0.1]$. Variables x and y change from -1 to 1 with the step size of 0.01. Then, the basins of attraction in the x-y plane with different values of q are shown in Figures 8(a)–8(c). Similarly, fix $s = 5$, other conditions remain unchanged, and the responding basins of attraction in the x-y plane with different values of q are shown in Figures 8(d)–8(f). Different colours in Figure 8 represent different attraction fields, so we can see from Figure 8 that when the initial value of the system changes, the fractional-order centrifugal flywheel governor system shows coexisting attractors, and with the increase in derivative order q, the frequency of coexisting attractors increases gradually, but the range and shape of the different attractors remain basically unchanged.

Fix $q = 0.98$, $s = 10$, the initial conditions are given by $[x_0, y_0, z_0, w_0] = [0.005, 0.005, -0.1, 0.1]$, $[0.5, 0.005, -0.1, 0.1]$, and $[0.58, 0.005, -0.1, 0.1]$, and corresponding coexisting attractors are shown in Figures 9(a)–9(c). When $q = 0.99$ and

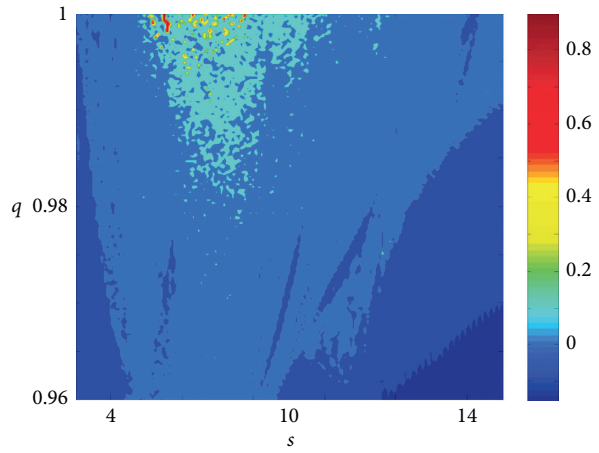

Figure 5: The chaos diagram of the maximum Lyapunov exponent contour plot in the s-q parameter plane.

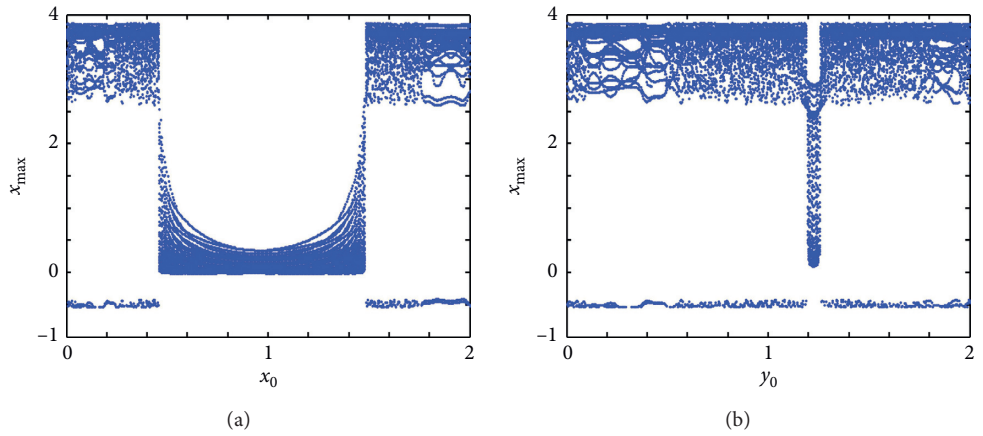

Figure 6: Bifurcation diagram of the fractional-order centrifugal flywheel governor system: (a) x_0 changes and (b) y_0 changes.

$s = 5$, coexisting attractors for the initial conditions $[x_0, y_0, z_0, w_0] = [-0.9, 0.1, -0.1, 0.1]$, $[-0.9, 0.82, -0.1, 0.1]$, and $[-0.9, 0.82, -0.1, 0.1]$ are shown in Figures 9(d)–9(f). Figure 9 shows that when the initial value of the system changes, the attractor of the system shows various states such as chaos, period, quasichaos. In addition, different kinds of chaotic attractors of the same state directly verify the simulation results as shown in (Figure 8).

4. Adaptive Control of Chaos

The process of controlling a chaotic system to a stable state is called chaotic control. At present, the main method of controlling fractional-order chaotic systems is to extend the control method used in integer-order chaotic systems to fractional-order chaotic systems. The main methods of chaos control include: parameter perturbation method [33], feedback control method [34], adaptive control method [35], and neural network method [36]. In this section, the chaos control of the fractional-order centrifugal flywheel governor system is realized by using the adaptive control method. The adaptive chaos control formula is derived, and the numerical simulation of chaos control effect is shown.

4.1. Adaptive Chaos Control Scheme. Consider the controlled chaotic system as follows:

$$\begin{cases} D_{t_0}^q x = y + u_1, \\ D_{t_0}^q y = dz^2 \cos x + \left(e + pz^2\right)\sin x \cos x - \sin x - by + u_2, \\ D_{t_0}^q z = s \cos x - F - \alpha \sin(w) + u_3, \\ D_{t_0}^q w = \sigma + u_4, \end{cases} \tag{14}$$

where x, y, z, and w are state variables and u_1, u_2, u_3, and u_4 are external active control inputs. Then, the adaptive control system can be defined by

$$\begin{cases} u_1 = -y - k_1 x, \\ u_2 = -dz^2 \cos x - \left(e + pz^2\right)\sin x \cos x + \sin x + by - k_2 y, \\ u_3 = -\hat{s}(t)\cos x + F + \alpha \sin(w) - k_3 z, \\ u_4 = -\sigma - k_4 w, \end{cases} \tag{15}$$

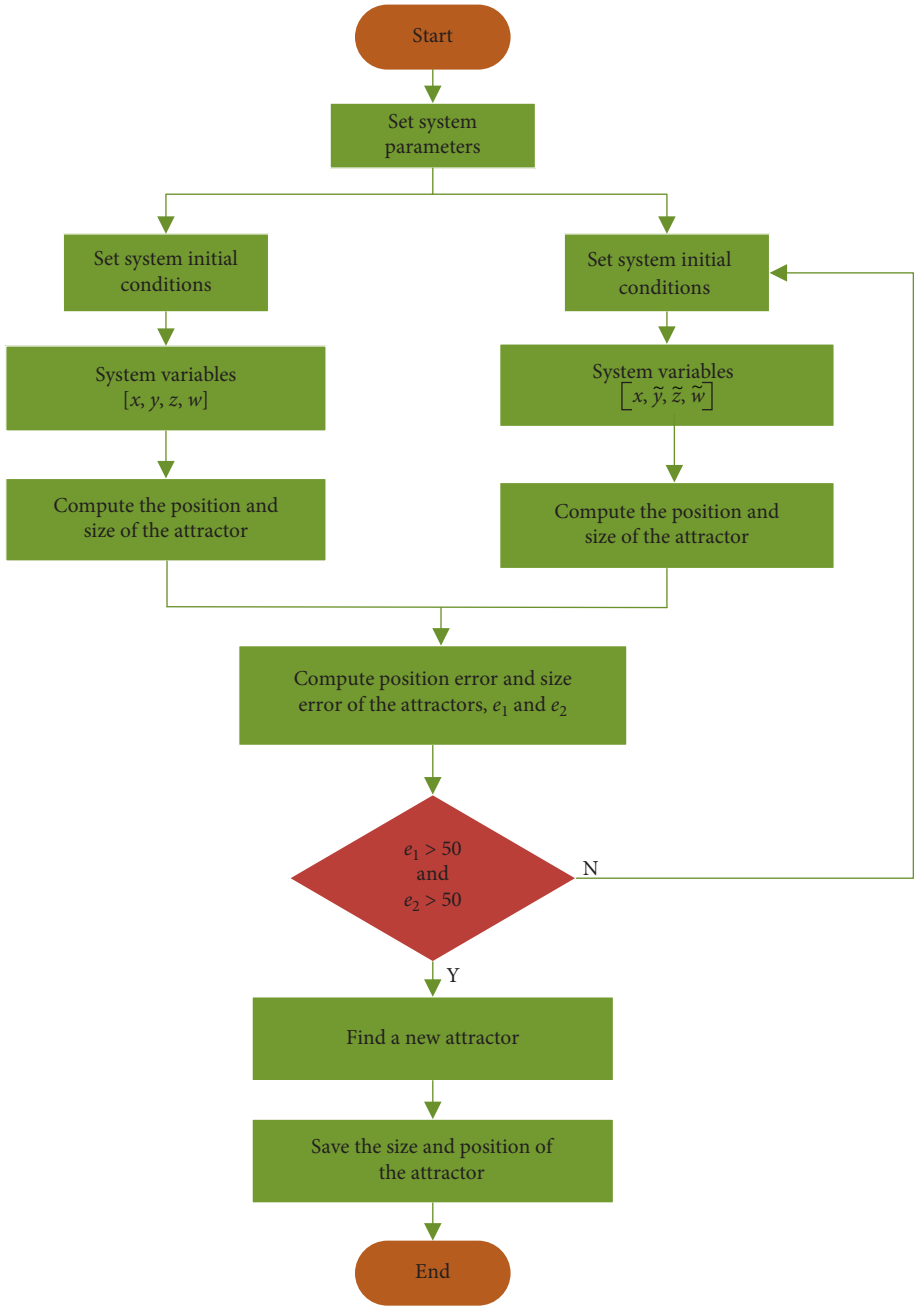

Figure 7: The flow chart for basins of attraction.

where k_1, k_2, k_3, and k_4 are positive gain constants. Substituting (13) into (12), the closed-loop system is obtained as

$$\begin{cases} D_{t_0}^q x = -k_1 x, \\ D_{t_0}^q y = -k_2 y, \\ D_{t_0}^q z = (s - \hat{s}(t))\cos x - k_3 z, \\ D_{t_0}^q w = -k_4 w. \end{cases} \tag{16}$$

Define the parameter s estimation errors as

$$e_s(t) = s - \hat{s}(t). \tag{17}$$

Using (15), we can simplify (14) as

$$\begin{cases} D_{t_0}^q x = -k_1 x, \\ D_{t_0}^q y = -k_2 y, \\ D_{t_0}^q z = e_s(t)\cos x - k_3 z, \\ D_{t_0}^q w = -k_4 w. \end{cases} \tag{18}$$

Differentiating (15) with respect to t, we obtain

$$D_{t_0}^q e_s(t) = -D_{t_0}^q \hat{s}(t). \tag{19}$$

The Lyapunov function is defined by

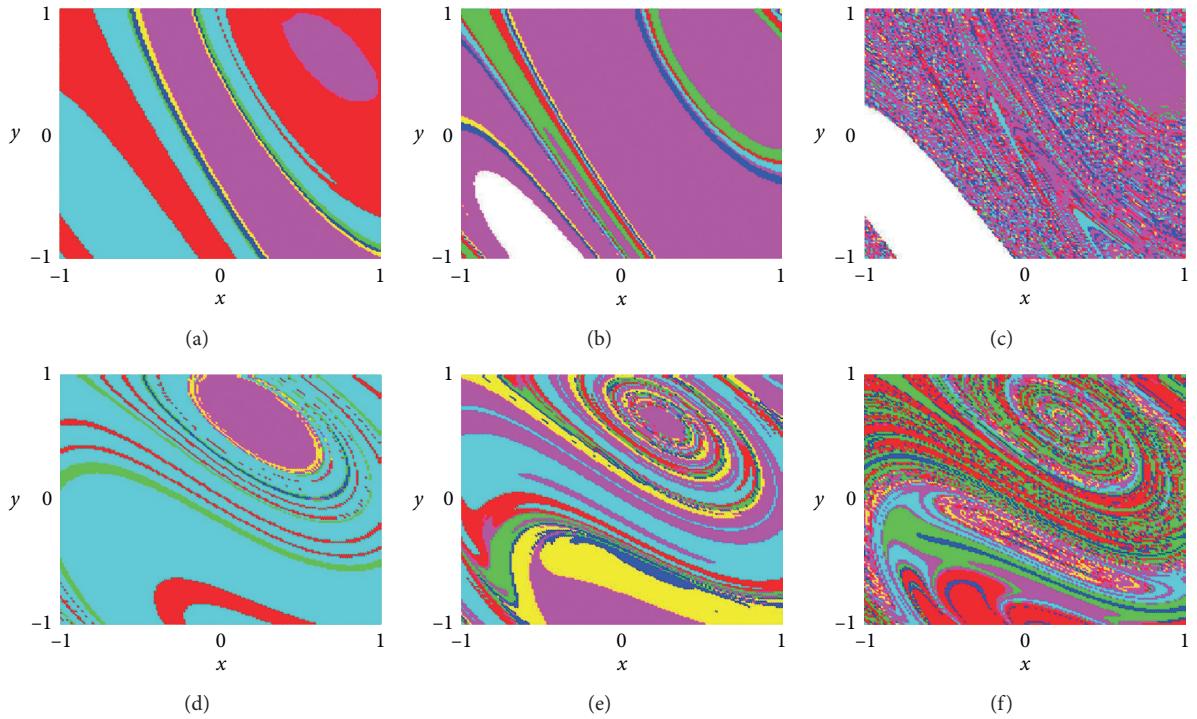

FIGURE 8: The basins of attraction in the x_0-y_0 plane with different parameters: (a) $s = 10$ and $q = 0.97$; (b) $s = 10$ and $q = 0.98$; (c) $s = 10$ and $q = 0.99$; (d) $s = 5$ and $q = 0.97$; (e) $s = 5$ and $q = 0.98$; (f) $s = 5$ and $q = 0.99$.

$$V(x, y, z, w, e_s) = \frac{1}{2}\left(x^2 + y^2 + z^2 + w^2 + \frac{1}{a}e_s^2\right), \tag{20}$$

where a is a positive convergence factor, the controlling convergence rate of parameter estimation error. Differentiating V, we obtain

$$\begin{aligned} V(x, y, z, w, e_s) = &-k_1x^2 - k_2y^2 - k_3z^2 - k_4w^2 \\ &+ e_s\left(z\cos x - \frac{1}{a}D_{t_0}^q\hat{s}\right). \end{aligned} \tag{21}$$

In view of equation (19), we take the parameter update law as

$$D_{t_0}^q\hat{s} = az\cos x. \tag{22}$$

From the formula derivation process above, it can be seen that the controlled chaotic system (12) is globally and exponentially stabilized by the adaptive control law (13) and the parameter update law (20). By substituting the parameter update law (20) into (19), we obtain the time-derivative of V as

$$V(x, y, z, w, e_s) = -k_1x^2 - k_2y^2 - k_3z^2 - k_4w^2. \tag{23}$$

Equation (21) demonstrates that the Lyapunov function V is positive definite on R^8. According to Barbalat's lemma [37], the closed-loop system (19) is globally exponentially stable for all initial conditions $[x_0, y_0, z_0, w_0] \in R^4$. This completes the proof.

4.2. Numerical Analysis. Fix $q = 0.99$, $s = 10$, in order to better demonstrate the effect of chaos control, the initial conditions are set to a large values as $[x_0, y_0, z_0, w_0] = [1, -2, 2, 4]$, and then phase portraits of the fractional-order centrifugal flywheel governor system are shown in Figure 10. We can see that the system is chaotic under these conditions. Let $k_1 = k_2 = k_3 = k_4 = 10$, the convergence factor $a = 20$, the initial value of parameter s is $s_0 = 4$, and the chaos control results of the system are shown in Figure 11. It can be seen that the chaos control of the fractional-order centrifugal flywheel governor system is successfully realized by the adaptive control method. In 1.5 s, each state component of the system is controlled to the stable state, and the estimation error of parameter s approximates the target value.

In order to further analyze the relationship between the convergence factor a and the estimation error e_s, the estimated error curves of the parameter s with different convergence factor a are obtained in Figure 12. It shows that with the increase in the convergence factor a, the estimation error e_s of parameter s converges faster and faster. When a is greater than or equal to 50, the system approaches the target value within 1 s.

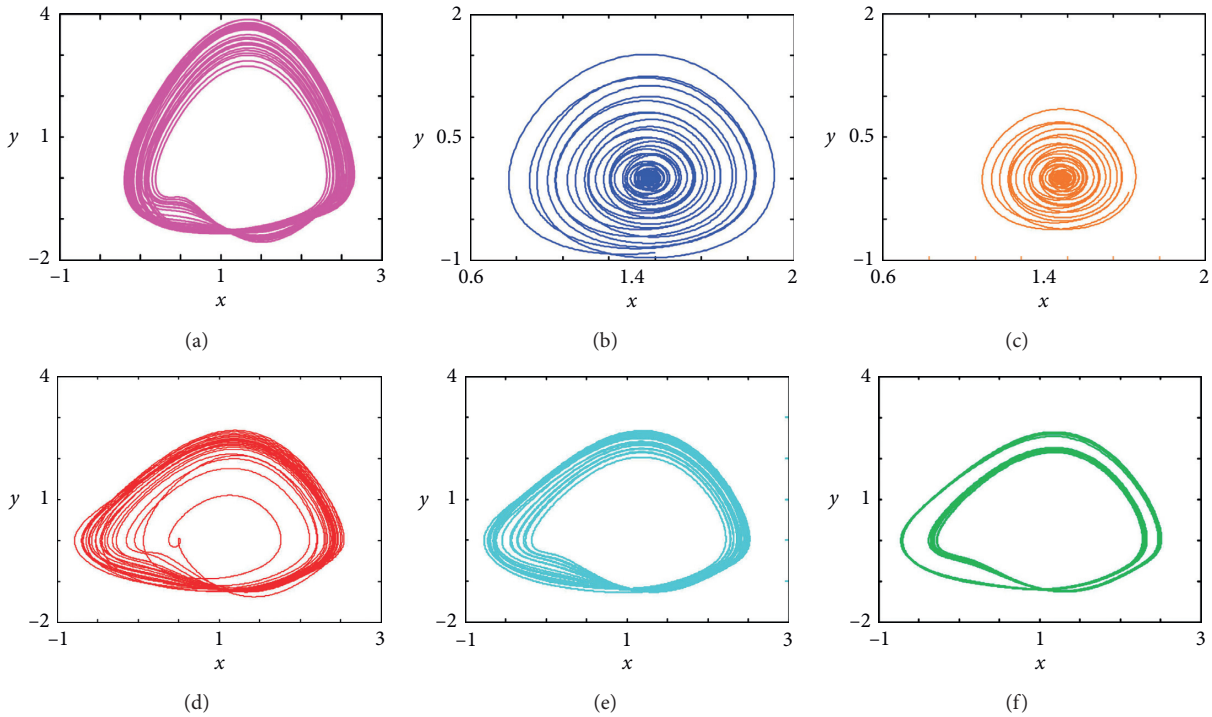

FIGURE 9: Coexisting attractors with different conditions: (a), (b), (c) $q = 0.98$, $s = 10$, and the initial conditions are [0.005, 0.005, −0.1, 0.1], [0.5, 0.005, −0.1, 0.1], and [0.58, 0.005, −0.1, 0.1]; (d), (e), (f) $q = 0.99$, $s = 5$, and the initial conditions are [−0.9, 0.1, −0.1, 0.1], [−0.9, 0.2, −0.1, 0.1], and [−0.9, 0.82, −0.1, 0.1].

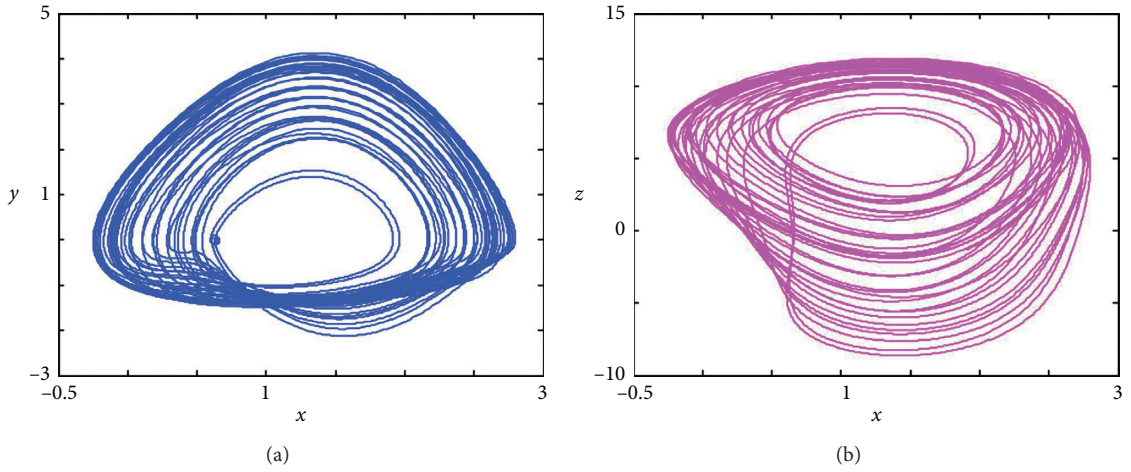

FIGURE 10: Phase diagrams of the fractional-order centrifugal flywheel governor system with initial values [1, −2, 2, 4].

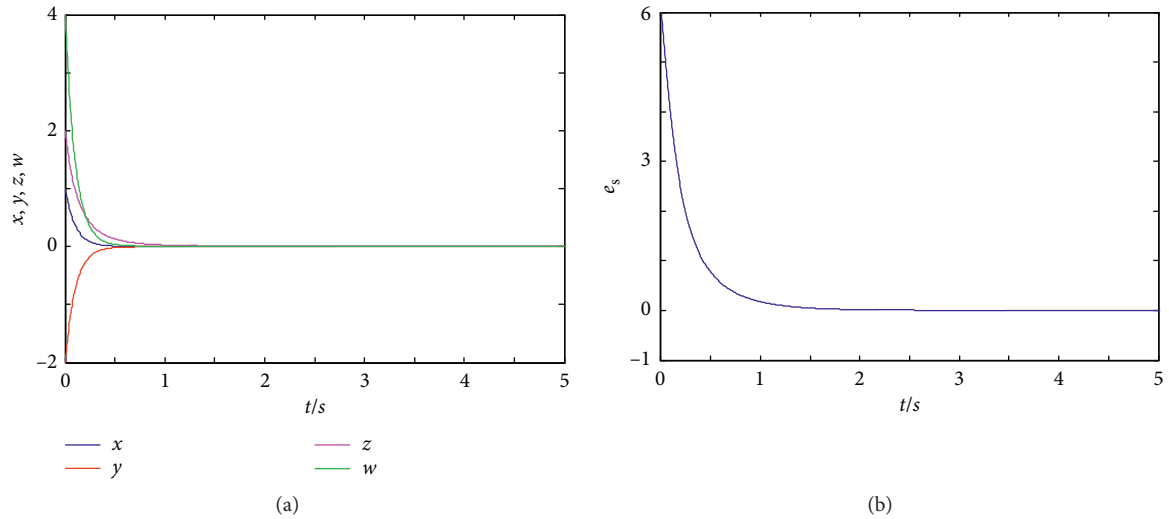

(a) (b)

Figure 11: Control charts of the controlled chaotic system. (a) Time response of state variables. (b) The estimation error of parameter s.

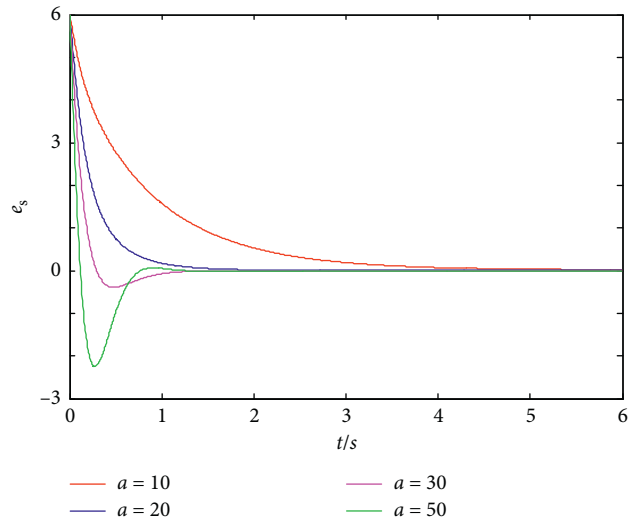

Figure 12: The estimation error of parameter s with different convergence factors.

5. Conclusions

In this paper, dynamics and adaptive control of the fractional-order centrifugal flywheel governor system are investigated. By numerical simulation, the bifurcation diagrams and LEs of the system with different parameters are obtained. The dynamic behavior of the system shown by these two kinds of graphs is in a good agreement, and the LE curve can well describe the process of transition from period to chaos. Coexisting attractors of the system are observed by drawing the basin of attraction, and the attractors with different initial conditions verify the simulation results of the basin of attraction. The adaptive control algorithm designed in this paper effectively realizes the chaos control of the system, and the estimation error e_s of parameter s converges faster and faster with the increase in the convergence factor a.

Data Availability

The data used to support the findings of this study are included within the article.

Conflicts of Interest

The authors declare that they have no conflicts of interest regarding the publication of this paper.

Acknowledgments

This work was supported by the Hunan Provincial Department of Education General Project Fund (no. 18C0743), the National Natural Science Foundation for theoretical physics of China (nos. 61901530 and 11747150), and the Natural Science Foundation of Hunan Province (no. 2020JJ5767).

References

[1] E. J. Beltrami, *Mathematics for Dynamic Modeling*, Academic Press, Cambridge, USA, 1987.

[2] C. Cao, J. Su, and L. Xu, "Chaotic motion of the centrifugal governor," *Journal of Harbin Engineering University*, vol. 18, no. 5, pp. 96–103, 1997.

[3] J. Zhang, Y. Chu, X. Li, and Y. Chang, "Bifurcation and chaos of a type of the centrifugal governor system," *Journal of Mechanical Strength*, vol. 30, no. 3, pp. 362–367, 2008.

[4] X. Gou and G. Luo, "Linear feedback anti-control of chaos for mechanical centrifugal governor system," *Journal of Machine Design*, vol. 22, no. 4, pp. 30–32, 2005.

[5] X. Gou and G. Luo, "Un-feedback chaos controlling problems for mechanical centrifugal governor system," *Journal of Mechanical Strength*, vol. 27, pp. 21–27, 2005.

[6] X. Gou and G. Luo, "Nonlinear feedback anti-control of chaos for mechanical centrifugal flywheel governor systems," *China Mechanical Engineering*, vol. 16, no. 15, pp. 1373–1376, 2005.

[7] J. Wang, H. Wang, and H. Liang, "Chaos and nonlinear feedback control in a flywheel system with a centrifugal

governor," *Mechanical Science and Technology Aerospace Engineering*, vol. 28, no. 2, pp. 238–245, 2009.

[8] J. Wang, H. Wang, and H. Liang, "Chaos and ITS speed feedback control in centrifugal flywheel governor," *Journal of Mechanical Strength*, vol. 32, no. 3, pp. 509–512, 2010.

[9] J. Wang, H. Wang, and H. Liang, "Chaos and control of centrifugal flywheel governor system," *Journal of Machine Design*, vol. 26, no. 9, pp. 34–37, 2009.

[10] J.-G. Zhang, X.-F. Li, Y.-D. Chu, J.-N. Yu, and Y.-X. Chang, "Hopf bifurcations, Lyapunov exponents and control of chaos for a class of centrifugal flywheel governor system Bifurcation and chaos of a type of the centrifugal governor system," *Chaos, Solitons & Fractals*, vol. 39, no. 5, pp. 2150–2168, 2009.

[11] X.-B. Rao, Y.-D. Chu, X. Lu-Xu, Y.-X. Chang, and J.-G. Zhang, "Fractal structures in centrifugal flywheel governor system," *Communications in Nonlinear Science and Numerical Simulation*, vol. 50, pp. 330–339, 2017.

[12] S. Luo, Z. Hou, and T. Zhang, "Performance enhanced design of chaos controller for the mechanical centrifugal flywheel governor system via adaptive dynamic surface control," *AIP Advances*, vol. 6, no. 9, 2016.

[13] M. P. Aghababa and H. P. Aghababa, "Chaos suppression of rotational machine systems via finite-time control method," *Nonlinear Dynamics*, vol. 69, no. 4, pp. 1881–1888, 2012.

[14] R. Zhang, Y. Wang, Z. Zhang, and Q. Bi, "Nonlinear behaviors as well as the bifurcation mechanism in switched dynamical systems," *Nonlinear Dynamics*, vol. 79, no. 1, pp. 465–471, 2015.

[15] R. Gorenflo and F. Mainardi, "Fractional calculus," *Fractals and Fractional Calculus in Continuum Mechanics*, vol. 378, pp. 223–276, 1997.

[16] R. Bhattacharyya, M. Banerjee, M. Heiblum et al., "Melting of interference in the fractional quantum Hall effect: appearance of neutral modes," *Physical Review Letters*, vol. 122, no. 24, Article ID 246801, 2019.

[17] A. C. Escamilla, J. E. Lavín-Delgado, J. F. Gómez-Aguilar, and L. Torres, "Fractional dynamics and synchronization of Kuramoto oscillators with nonlocal, nonsingular and strong memory," *Alexandria Engineering Journal*, vol. 59, no. 4, pp. 1941–1952, 2020.

[18] A. Jajarmi, E. M. Hajipour, and D. Baleanu, "A new approach for the nonlinear fractional optimal control problems with external persistent disturbances," *Journal of the Franklin Institute*, vol. 355, no. 9, pp. 3938–3967, 2018.

[19] P. J. Torvik and R. L. Bagley, "On the appearance of the fractional derivative in the behavior of real materials," *Journal of Applied Mechanics*, vol. 51, no. 2, pp. 725–728, 1984.

[20] Z.-M. Ge and W.-R. Jhuang, "Chaos, control and synchronization of a fractional order rotational mechanical system with a centrifugal governor," *Chaos, Solitons & Fractals*, vol. 33, no. 1, pp. 270–289, 2007.

[21] S. He, K. Sun, and H. Wang, "Solution and dynamics analysis of a fractional-order hyperchaotic system," *Mathematical Methods in the Applied Sciences*, vol. 39, no. 11, pp. 2965–2973, 2016.

[22] Y. Wang, K. Sun, S. He, and H. Wang, "Dynamics of fractional-order sinusoidally forced simplified Lorenz system and its synchronization," *The European Physical Journal Special Topics*, vol. 223, no. 8, pp. 1591–1600, 2014.

[23] D. Kai, N. J. Ford, and A. D. Freed, "A predictor-corrector approach for the numerical solution of fractional differential equations," *Nonlinear Dynamics*, vol. 29, no. 4, pp. 3–22, 2002.

[24] M. F. Oskouie, R. Ansari, and F. Sadeghi, "Nonlinear vibration analysis of fractional viscoelastic Euler-Bernoulli nanobeams based on the surface stress theory," *Acta Mechanica Solida Sinica*, vol. 30, no. 4, pp. 416–424, 2017.

[25] S. He, S. Banerjee, and K. Sun, "Complex dynamics and multiple coexisting attractors in a fractional-order microscopic chemical system," *The European Physical Journal Special Topics*, vol. 228, no. 1, pp. 195–207, 2019.

[26] http://www.sourcecodeonline.com/details/predictorcorrector_pece_method_for_fractional_differential_equations.html.

[27] M.-F. Danca and N. Kuznetsov, "Matlab code for Lyapunov exponents of fractional-order systems," *International Journal of Bifurcation and Chaos*, vol. 28, no. 5, Article ID 1850067, 2018.

[28] B. Yan, S. He, and S. Wang, "Multistability and formation of spiral waves in a fractional-order memristor-based hyperchaotic lu system with No equilibrium points," *Mathematical Problems in Engineering*, vol. 2020, Article ID 2468134, 12 pages, 2020.

[29] Q. Lai, Z. Wan, and P. D. Kamdem Kuate, "Modelling and circuit realisation of a new no-equilibrium chaotic system with hidden attractor and coexisting attractors," *Electronics Letters*, vol. 56, no. 20, p. 1044, 2020.

[30] Q. Lai, Z. Wan, P. D. Kamdem Kuate, and H. Fotsin, "Coexisting attractors, circuit implementation and synchronization control of a new chaotic system evolved from the simplest memristor chaotic circuit," *Communications in Nonlinear Science and Numerical Simulation*, vol. 89, Article ID 105341, 2020.

[31] Q. Lai, B. Norouzi, and F. Liu, "Dynamic analysis, circuit realization, control design and image encryption application of an extended Lü system with coexisting attractors," *Chaos, Solitons & Fractals*, vol. 114, pp. 230–245, 2018.

[32] C. Li and J. C. Sprott, "Multistability in a butterfly flow," *International Journal of Bifurcation and Chaos*, vol. 23, no. 12, Article ID 1350199, 2013.

[33] L. Chen, Y. Chai, and R. Wu, "Linear matrix inequality criteria for robust synchronization of uncertain fractional-order chaotic systems," *Chaos*, vol. 21, no. 4, pp. 251–968, 2011.

[34] J. Chen, C. Li, T. Huang, and X. Yang, "Global stabilization of memristor-based fractional-order neural networks with delay via output-feedback control," *Modern Physics Letters B*, vol. 31, no. 5, p. 1750031, 2017.

[35] C. Lien, S. Vaidyanathan, A. Sambas et al., "A new two-scroll chaotic attractor with three quadratic nonlinearities, its adaptive control and circuit design," *IOP Conference Series: Materials Science and Engineering*, vol. 332, Article ID 012010, 2018.

[36] S. Shao, C. Mou, and J. Wu, "Tracking control for uncertain fractional-order chaotic systems based on disturbance observer and neural network," *Ima Journal of Mathematical Control & Information*, vol. 34, no. 3, pp. 1011–1030, 2017.

[37] F. Wang and Y. Yang, "Correction: fractional order barbalat's lemma and its applications in the stability of fractional order nonlinear systems," *Mathematical Modelling and Analysis*, vol. 22, no. 4, pp. 503–513, 2017.

Hindawi
Complexity
Volume 2020, Article ID 8810901, 9 pages
https://doi.org/10.1155/2020/8810901

Research Article

A Multiscale Chaotic Feature Extraction Method for Speaker Recognition

Jiang Lin,[1] **Yi Yumei**,[1] **Zhang Maosheng**,[2] **Chen Defeng**,[1] **Wang Chao**,[3] **and Wang Tonghan**[4]

[1]*College of Computer and Information Engineering, Institute of Big Data and Internet Innovation, Hunan University of Technology and Business, Changsha 410205, China*
[2]*School of Mathematics and Statistics, Yulin Normal University, Yulin 537000, China*
[3]*National Engineering Research Center for Multimedia Software, Wuhan University, Wuhan 430072, China*
[4]*School of Software, East China University of Technology, Nanchang 330013, China*

Correspondence should be addressed to Jiang Lin; jlcdf@163.com

Received 2 October 2020; Revised 30 October 2020; Accepted 19 November 2020; Published 3 December 2020

Academic Editor: Karthikeyan Rajagopal

In speaker recognition systems, feature extraction is a challenging task under environment noise conditions. To improve the robustness of the feature, we proposed a multiscale chaotic feature for speaker recognition. We use a multiresolution analysis technique to capture more finer information on different speakers in the frequency domain. Then, we extracted the speech chaotic characteristics based on the nonlinear dynamic model, which helps to improve the discrimination of features. Finally, we use a GMM-UBM model to develop a speaker recognition system. Our experimental results verified its good performance. Under clean speech and noise speech conditions, the ERR value of our method is reduced by 13.94% and 26.5% compared with the state-of-the-art method, respectively.

1. Introduction

Speaker recognition is a biometric recognition technique, which can identify speaker identity according to speaker personality information on a speech signal. From the existing biometric recognition, speaker recognition is one of the most convenient and accessible ones due to the abundance of mobile devices, with a microphone, allowing users to be authenticated across multiple environments and devices [1].

Research in speaker recognition has focused increasingly on enhancing robustness in adverse conditions induced by background noise. Many approaches have been proposed to address these challenges; one of the most successful being the *i*-vector technology [2] used jointly with the probabilistic discriminant analysis (PLDA) back-end [3, 4]. In addition to the new utterance level features and back-ends, robust acoustic features are developed to improve the performance of the speaker recognition system.

The cepstrum features (such as MFCC) of speech are the most distinguishing and first used [5] in speaker recognition. However, under the influence of channel distortion and background noise, the cepstral feature distribution of speech will change arbitrarily, which leads to its weak distinguish ability. Therefore, in the early 1990s, a series of feature compensation techniques were proposed to enhance the generalization ability of speech features in recognition [6–8]. The existing feature compensation is mainly including filter compensation, noise model compensation, and empirical compensation.

The main purpose of filter compensation is to reduce noise or relieve the influence of noise on features. This method is based on the fact that channel and environmental distortions are superimposed on the logarithmic spectrum and the cepstrum domain. Furui S. believe that the variation in the channel is the offset of a single coefficient in the cepstrum vector. Therefore, the cepstrum mean subtraction (CMS) method is used to relieve the influence of the channel

[9]. This method also can reduce the channel noise to a certain extent, but this method also impairs the information on the cepstral coefficient. Unlike the CMS method, the relative spectrum feature is proposed to compensate for rapidly changing channel distortions, and it uses moving average filtering to simulate the exponential decay of the mean subtraction [10]. However, this method was later confirmed to have limited improvements in channel mismatch and additive background noise.

The noise model compensation uses the prior knowledge of the noise spectrum to estimate the parameters of the pure speech through the noise model or the influence of noise on the speech. It mainly uses spectral equalization and spectral subtraction to relieve the influence of noise on features. J. Hansen et al. proposed a multidimensional equalization method to reduce the sensitivity of speech features of noise, thereby improving the distinguishing ability of speech features [11]. S.S. Bharti utilized interframe features to estimate the continuous noise spectrum, which can alleviate the problem of noise spectrum changes caused by single-frame estimation in the original spectrum subtraction, and then uses spectrum subtraction to enhance speech features and improve the robustness of speaker features [12]. The noise compensation model method mainly relies on the mathematical model of noise estimation. Because of the uncertainty of noise change, it is difficult to find a mathematical model with good performance.

Empirical compensation is a data-driven method, which is inherently random. Studies have shown that this method is better than the previous two [13]. This method directly uses spectrum comparison based on experience. In the training phase, to estimate the change between the clear speech and the noisy speech, the difference in the feature vector between the two frames is calculated, and the probability distribution is modeled by adding a bias term of this difference. In the evaluation stage, the minimum mean square error prediction method is adopted, and the bias vector is used to convert the noisy test feature vector into the equivalent clear speech feature vector. Afify M et al. proposed a random mapping method [14], which uses the joint distribution of clear speech and noisy speech feature vectors to generate a Gaussian mixture model, and then uses this joint model distribution to predict clear speech. This prediction method has a significant improvement compared with the previous minimum mean square error.

In summary, the method of feature compensation is to improve the distinguishing ability of speech features for reducing the influence of noise on the features. However, as long as noise exists, this improvement is always difficult to avoid the impact on noise on the recognition performance.

In this paper, a novel multiscale chaotic feature is proposed to speaker recognition. The proposed multiscale chaotic feature is evaluated using a nonlinear dynamic model based on wavelet decomposition (multiresolution analysis (MRA)). In our method, an MRA technique is used to capture more finer spectrum information. In speech feature, harmonic feature is an important factor to distinguish different speakers. Because harmonic can represent speaker's tone, tone information is usually distributed over different frequency components. The wavelet decomposition is an adapt method to capture frequency components. Moreover, we also take into account a chaotic characteristic of speech signal. Speech signal is a nonlinear system on long time series. In addition, this nonlinear characteristic should be reflected in speech features to speaker recognition. The chaotic feature based on the nonlinear dynamic model is used widely to the speech application system. The nonlinear dynamic model has been used in various fields of speech processing area, such as speech steganalysis [15], speech synthesis [16], speech recognition [17], and speech encryption [18]. The proposed feature represents the signal chaotic characteristic at different frequency bands.

2. Proposed Speaker Recognition System

To improve the performance of speaker recognition under adverse conditions induced by background noise, we proposed a multiscale chaotic feature extraction method to enhance the robustness of the recognition system. The proposed speaker recognition system is illustrated in Figure 1.

In our proposed system, a time-domain speech signal is treated with short-time frames of N samples by windowing each frame with, e.g., the hamming window. To relieve the influence of noise, we extract a multiscale chaotic feature (MCF) in each frame, which is comprised of multiresolution analysis and chaotic feature. Multiresolution analysis is implanted by wavelet decomposition and chaotic features including the nonlinear dynamic model and acoustics features. More details will be descripted in Section 3. A Gaussian mixture model (GMM) is used to identify each speaker; here, we introduce a universal background model (UBM) for training the distribution of features that are not related to the speaker. The GMM-UBM model is used widely for speaker recognition [19–21] as a classifier; it is a generalization of the GMM model. The GMM-UBM model firstly performs a pretraining for the current speaker by collecting feature data from other speakers, which can solve the problem of recognition performance declining due to the insufficient feature data of the current train speaker. Then, the pretrained model is fine-tuned to the target speaker model by a maximum a posteriori (MAP) adaptive algorithm [22].

3. Multiscale Chaotic Feature

In the speaker recognition systems, the speech feature is vital to recognition performance. The significant discrimination of the feature can distinguish accurate speakers. The acoustic feature (such as MFCC and LPC) has a strong discrimination to speaker recognition of clear speech. However, the performance of classification will decline sharply if the speech signal is disturbed by noise. In order to reduce the disturbance due to environment noise, we introduced a wavelet decomposition and reconstruction technology to enhance the resolution of speech features on the frequency domain. Take account of the speech signal is a nonlinear system, we extract the chaotic feature by the nonlinear dynamic model

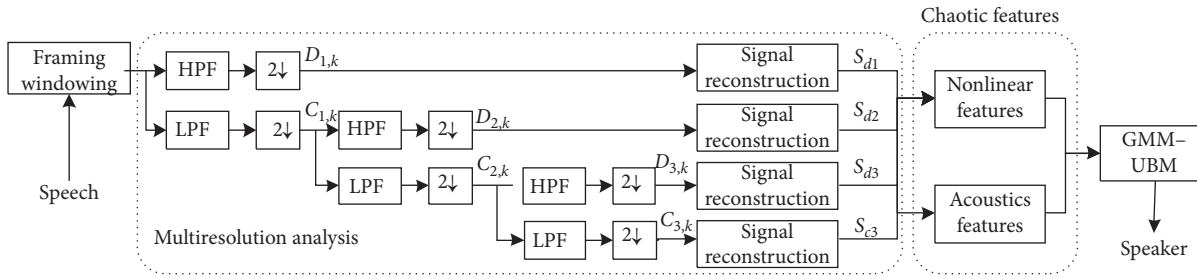

Figure 1: The proposed speaker recognition system using a multiscale chaotic feature.

to improve the recognition rate. In our proposed speaker recognition system, the feature extraction consists of two parts: multiresolution analysis and chaotic feature extraction.

3.1. Multiresolution Analysis. Multiresolution analysis (MRA) is a technique, which forms a set of basis functions through stretch and scale based on wavelets. On large scale, they expanded basis functions to search for significant features, and on smaller scales, they find more details of features. In our system, according to the literature [23] method, the speech signal is decomposed into a number of subband signals by MRA. The MRA is carried out by passing a speech signal $s(n)$ through a series of high pass and low pass filter banks. The speech signal is simultaneously passed through high pass and low pass filters with impulse response $h(n)$ and $g(n)$, respectively. The resulting outputs are the convolution of $s(n)$ with $h(n)$ and $g(n)$, respectively:

$$y_1(n) = s(n) * h(n) = \sum_{k=-\infty}^{\infty} s(k)h(n-k), \tag{1}$$

$$y_2(n) = s(n) * g(n) = \sum_{k=-\infty}^{\infty} s(k)g(n-k). \tag{2}$$

As the literature [23], we selected Daubechies 4 (db4) as the basis function for MRA in this paper. Likewise, we have also tested with other basis functions. We found that the recognition rate achieved with multiscale chaotic features using db4 basis function is higher than those results with other basis functions. Therefore, the db4 basis function is selected for MRA. The filter coefficients h_k and g_k, corresponding to the high pass and low pass filters, respectively, are computed from the following MRA equations [24]:

$$\varphi(n) = \sqrt{2}h_k\varphi(2n-k), \tag{3}$$

$$\psi(n) = \sqrt{2}\sum_k g_k\psi(2n-k), \tag{4}$$

$$s(n) = \sum_k C_{j_o,k}\varphi_{j_o,k}(n) + \sum_{j=1}^{j_o}\sum_k D_{j,k}\psi_{j,k(n)}, \tag{5}$$

where j represents the decomposition scale ($j = 1, 2, \ldots, j_o$) and k denotes the coefficient index of each decomposition scale. At the first level of decomposition ($j = 1$), the detail coefficient $D_{j,k}$ is an output of the high pass filter and the approximation coefficient $C_{j,k}$ is an output of the low pass filter. The detail coefficients and approximation coefficient captured the high frequency and low frequency information, respectively. The approximation band is further decomposed into detail and approximation bands at the next level of decomposition. The repeated decomposition can obtain multiple levels for getting better resolution. In our system, 3-level decomposition is set ($j_o = 3$) as shown in Figure 1. In order to analyse the speech signal to different resolutions, subband signals are reconstructed via each of the approximation and detail coefficients applying inverse discrete wavelet transform (IDWT) [24]. When reconstructing a subband signal, the other subband coefficients are set 0. In this paper, we obtained 4 subbands signals: S_{d1}, S_{d2}, S_{d3}, *and* S_{c3}; these subband signals will be utilized to extract chaotic features.

3.2. Chaotic Feature. In our feature extraction method, acoustic feature and nonlinear feature are extracted. Acoustic feature mainly focuses on speech spectral features (such as MFCC and LPC). Nonlinear feature represents the speech chaotic characteristics using a nonlinear dynamic model.

3.2.1. Acoustic Feature. In acoustic features, we extract Mel frequency cepstrum coefficient (MFCC) and linear prediction coefficient (LPC). MFCC is computed based on the perception characteristics of the human auditory system. In the human auditory system, Mel frequency has a nonlinear relationship to the Hz frequency. We can obtain the Mel spectral feature by the nonlinear relationship as follows:

$$f_{\text{mel}}(f) = 2595 \cdot \log\left(1 + \frac{f}{700Hz}\right), \tag{6}$$

where f denotes the Hz frequency.

LPC represents the frequency envelope of voice; its computation is based on the speech signal digital model. The vocal tract model is a key factor to distinguish different speakers. Therefore, LPC is usually used to represent the vocal tract envelope for various speech recognitions [25, 26]. According to the speech signal digital model, a speech frame signal can be equivalent to a unit pulse sequence to excite the vocal tract. The process is a linear time-invariant system and can be represented as a form of different equations:

$$x(n) = \sum_{i=1}^{p} \alpha_i x(n-i) + e(n), \tag{7}$$

where $x(n)$ is the real signal, the weighting term represents the prediction signal, and $e(n)$ denotes the prediction error. The filter coefficient α_i is calculated according to the minimum mean square error (MSE) criterion of $e(n)$.

3.2.2. Nonlinear Feature. The nonlinear dynamic model is an effective analysis method to study the chaotic characteristics of speech signals. According to this model, the nonlinear characteristics of the speech signal are obtained by processing the speaker signal as an one-dimensional time series. From the Takens embedding theorem, to reconstruct the phase space, one-dimensional speaker signals $(x(1), x(2), \ldots, x(N))$ can be mapped to high-dimensional space by selecting an appropriate minimum delay time τ and embedding dimension m with two parameters. In addition, the high-dimensional spaces after reconstruction are equivalent to the original space [27]. The reconstructed speaker speech signal becomes $X_i = (x(i), x(i+1), \ldots, x(i+(m-1)\tau))$, where $i = 1, 2, \ldots, N-(m-1)\tau$. The key point of chaotic feature extraction includes the analysis of speaker speech signal in a high-dimensional space, the extraction of nonlinear feature parameters under the voice dynamic model.

(1) The minimum delay time: the minimum delay time describes the correlation between the neighboring components of the speaker speech signal $(x(1), x(2), \ldots, x(N))$. In order to reconstruct the phase space of one-dimensional speaker speech signals, we calculate the minimum delay time τ and embedding dimension m by the C-C method [28].

(2) Maximum Lyapunov exponent: the Lyapunov exponent represents the average change rate of the local convergence or divergence of adjacent orbits in the phase space. The maximum Lyapunov exponent λ_1 denotes the speed of orbit convergence or divergence. When $\lambda_1 > 0$, the larger the value of λ_1, the greater the rate of orbital divergence and the greater the degree of chaos. We use the small data size method to compute Lyapunov exponent [28]. The calculation method is as follows:

(1) Calculate the average period P by fast Fourier transform on the time series $(x(1), x(2), \ldots, x(N))$.

(2) Calculate the minimum delay time τ and embedding dimension m by the C-C method.

(3) Reconstruct phase space of series $(x(1), x(2), \ldots, x(N))$ and denote it as $X_i = (x(i), x(i+1), \ldots, x(i+(m-1)\tau))$, $i = 1, 2, \ldots, N-(m-1)\tau$. Then, find the nearest neighbor $X_{i'}$ of each point X_i in the phase space and limit the short separation. Define the distance $d_i(0)$ from the i-th point of the nearest point $X_{i'}$ in its adjacent track:

$$d_i(0) = \left\| X_i - X_{i'} \right\| \quad \left| i - i' \right| > P. \tag{8}$$

(4) Find each point X_i in the phase space and calculate the distance next n unit times of the adjacent point pair:

$$d_i(n) = \left| X_{i+n} - X_{i'+n} \right| \quad n = 1, 2, \ldots, \min(M-i, M-i'). \tag{9}$$

(5) If the orbit, which locates on the nearest point in the neighborhood domain, diverges from an exponential rate of λ_1, then

$$d_i(n) = d_i(0) e^{\lambda_1 n T_s}, \tag{10}$$

where T_s is the sampling period. Taking the logarithm of both sides with the equation, we get

$$\ln d_i(n) = \ln d_i(0) + \lambda_1 n T_s. \tag{11}$$

Take the average of the logarithmic difference in the distance between all adjacent points, which is

$$\text{ave}\lambda(n) = \frac{1}{qT_s} \sum_{i=1}^{q} \left(\ln d_i(n) - \ln d_i(0) \right), \tag{12}$$

where q is the numbers of nonzero $d_j(i)$. Last, we use the least squares method to fit λ_1:

$$\lambda_1 = \frac{\sum_{n=1}^{\min(M-i, M-i')} n\lambda(n)}{\sum_{n=1}^{\min(M-i, M-i')} n^2}. \tag{13}$$

(3) Correlation dimension and Kolmogorov entropy: correlation dimension and Kolmogorov entropy are both nonlinear representation quantities under the nonlinear dynamic model. The correlation dimension describes the self-similar structure of the system. Kolmogorov entropy accurately describes the degree of confusion of the distribution probability of time series. We use the G-P algorithm [29] to calculate the correlation dimension and Kolmogorov entropy at the same time. The algorithm is as follows:

(1) Firstly, we calculate the correlation integral $C(r, m)$ and the $C(r, m) - r$ curve. Reconstruct the m-dimensional phase space. Then, given a critical distance r, search the phase point pair whose distance is less than r, and further calculate the ratio of all phase points. Last, we get the correlation integral function as follows:

$$C(r, m) = \frac{1}{M(M-1)} \sum_{i,j=1, i \neq j}^{N} \theta\left(r - \left\| X_i - X_j \right\| \right), \tag{14}$$

where m is the embedding dimension, M is the total number of phase points, $M = N-(m-1)\tau$, and θ is the Heaviside function, which satisfies $\theta_{(z)} = \begin{cases} 0, & z \leq 0, \\ 1, & z > 0. \end{cases}$

(2) The correlation dimension $D(m)$ is derived by the G-P algorithm as follows:

$$D(m) = \frac{\ln C(r, m)}{\ln r}. \tag{15}$$

Draw the $\ln C(r,m) - \ln r$ curve, and take the slope of the approximate straight line part; the slope is as the correlation dimension D.

(3) The Kolmogorov entropy formula is derived by the G-P algorithm as follows:

$$K = \frac{1}{m\tau} \ln \frac{C(r,m)}{C(r,m+1)}. \quad (16)$$

(4) Hurst exponent: the Hurst exponent (H) may measure the long-term memory of the time series. It can also find the evolution trend of a time series converging on one direction. In addition, the range of H values is 0~1. If $H > 0.5$, it means that the time series has a long-term autocorrelation and means a greater correlation between the context time series. $H < 0.5$ means no autocorrelation in a time series. Extracting the Hurst exponent feature of speaker speech can reflect the level of relevance to the speaker's speech change, so this paper selects the Hurst exponent as one of the nonlinear features. Hurst proposed the H exponent and introduced the rescaled range analysis method [30] to calculate the value. This method is a nonparametric statistical method, which is not affected by the time series distribution.

4. Evaluation and Analysis

4.1. Experiment Setting. In order to evaluate the performance of the proposed speaker recognition system, we carried out 2 experiments under clear speech and noise speech, respectively. To feature selection, we set 3 combinations: (1) acoustic features, (2) nonlinear feature, and (3) chaotic features (acoustic + nonlinear feature). We selected the *i*-vector speaker recognition model in the literature [31] as the baseline system. In the *i*-vector model, MFCC feature is extracted and further obtain the supervector as the speaker feature. Currently, it is the state-of-the-art of speaker feature. The details of the experiment settings are listed in Table 1. In our experiments, the hardware environment is Intel i7 CPU and 8 GB memory. The software environment is Windows 10 OS with 64 bits, the Matlab 2016a, and Voice speech tool package as a develop tool.

4.2. Corpus. TIMIT corpus is used to evaluate our system. The corpus is composed of 630 speakers from different regions, each with 10 sentences. The length of each sentence is 3~5 s, and the sampling frequency is 16 KHz with 16 sampling bits. In the TIMIT database, 630 people are divided into 462 and 168 according to a 3 : 1 ratio, which are used to train the background model and test the recognition system, respectively. Among the voice data of the 168 speakers tested, 9 sentences of each speaker were randomly selected as training data and 1 sentence as test data. The noise library is Noise-92 noise library. White noise and babble noise are selected as experimental objects. Since the two selected noises are associated with daily life scenes, these noises will also be mixed in real life application scenes. Therefore, this noise experiment has certain representative and feasibility.

4.3. Preprocessing. Speech signal is a nonstationary time-varying signal. Preprocessing must be performed first before speech analysis and feature extraction. The preprocessing usually includes endpoint detection, pre-emphasis, windowing, and framing processing. In this paper, endpoint detection adopts a double-threshold method based on zero-crossing rate and energy. The pre-emphasis is carried out by a first-order FIR high pass filter, and the pre-emphasis coefficient is set to 0.97. The frame length is set to 20 ms with 50% overlap.

4.4. Feature Extraction. In the feature extraction phase, we extracted the acoustic features and nonlinear feature for each subband (4 subbands in one frame). Acoustic feature consists of 12-order MFCC coefficients and 4-order LPC coefficients and then calculated statistical features of each coefficient for classifying the statistical features including skewness, kurtosis, mean, variance, and median. Nonlinear feature comprises the minimum delay time, correlation dimension, K entropy, maximum Lyapunov exponent, and Hurst exponent. We also calculate its statistical characteristics, like as maximum value, minimum value, mean, median, and variance. The speaker feature is listed in Table 2.

In order to eliminate the problem of internal dependence of speech features due to different dimensionality, a mean normalization is carried out on features as follows:

$$x = \frac{x - \mu}{\sigma}, \quad (17)$$

where μ and σ denote mean and standard deviation, respectively.

4.5. Results and Analysis. In order to evaluate the discriminability of the proposed feature, we carried out 2 group experiments according to Table 1. Take account of the validity of equal error rate (EER) on speaker recognition evaluation, we selected EER as a metric to evaluate the performance of chaotic features. For EER, more less value, the better performance. In our experiments, the mixture numbers of GMM-UBM are set to 512, and the iteration of the EM train algorithm is 10 times, and the dimension of the T matrix of the *i*-vector model is set to 100. All parameters are obtained by iterative optimization.

4.5.1. Results and Analysis under Clean Speech Condition. The results are listed in Table 2 under clean speech condition. It can be seen from Table 3, if using acoustic feature alone, the ERR is 2.562%, which has a similar performance compared with the *i*-vector model. This shows LPC feature is helpful to identify different speakers because LPC can represent the vocal tract envelope. The EER of nonlinear feature is 2.833%, which is the worst performance compared with other features. However, we find the chaotic feature is the better performance, and the EER value is reduced by 14%

Table 1: The combinations of experiment settings.

Experiment group	Speech type	Noise type	Acoustic feature	Nonlinear feature	Chaotic feature (acoustic + nonlinear)
1	Clean speech	—	√		
				√	
					√
2	Noise speech	White	√		
				√	
					√
		Babble	√		
				√	
					√

Table 2: The speaker chaotic features.

Feature type	Feature ID	Feature parameter	Statistical description
Acoustic feature	1~60	12-order MFCC	Skewness, kurtosis, mean, variance, median
	61~108	4-order LPC	
Nonlinear feature	109~113	Minimum delay time	Maximum, minimum, mean, median, and variance
	114~118	Correlation dimension	
	119~123	K entropy	
	124~128	Maximum Lyapunov exponent	
	129~133	Hurst exponent	

Table 3: The EER value under clean speech condition.

Feature	Acoustic feature	Nonlinear feature	Chaotic feature	*i*-vector model
EER (%)	2.562	2.833	2.149	2.497

Table 4: The EER value under white noise speech condition.

SNR (dB)	Acoustic feature	Nonlinear feature	Chaotic feature	*i*-vector model
30	2.156	2.785	1.59	1.963
25	3.167	3.389	2.531	3.144
20	5.148	5.987	4.121	4.907
15	9.746	10.182	7.115	9.755
10	17.929	18.114	14.152	18.122
5	29.535	30.157	25.144	32.696
0	37.005	39.142	20.504	33.134
Average	14.96	15.68	10.74	14.82

compared with *i*-vector, which shows that the speech chaotic characteristic has a good discrimination.

4.5.2. Results and Analysis under Noise Speech Condition. The purpose of this group experiment is to evaluate the robustness of chaotic features with noise speech. We selected stationary noise (white noise) and nonstationary noise (babble noise) as the disturb signal and set different disturb degrees. The SNR is set to 0 dB, 5 dB, 10 dB, 15 dB, 20 dB, 25 dB, and 30 dB.

Table 4 and Figure 2 show the EER value of speaker recognition under white noise speech condition. From the results, the acoustic feature, nonlinear feature, and *i*-vector model are the similar average EER value. However, the chaotic feature obtained a better performance of recognition compared with other features. The EER values reduced by 27.53% compared with the *i* -vector model. The good performance is attributed to the chaotic characteristic. This also shows that the speech nonlinear features can relieve the disturbance of noise and improve the robustness of speaker recognition.

Table 5 and Figure 3 give the ERR results under nonstationary noise babble condition. Similar with white noise disturb, there is also a good robustness of chaotic feature.

Table 6 shows the average EER values for all experiments. From the results, compared with the *i*-vector model, the EER value reduced by 13.94% and 26.5% under clean speech and noise speech conditions, respectively. Therefore, we believe the following:

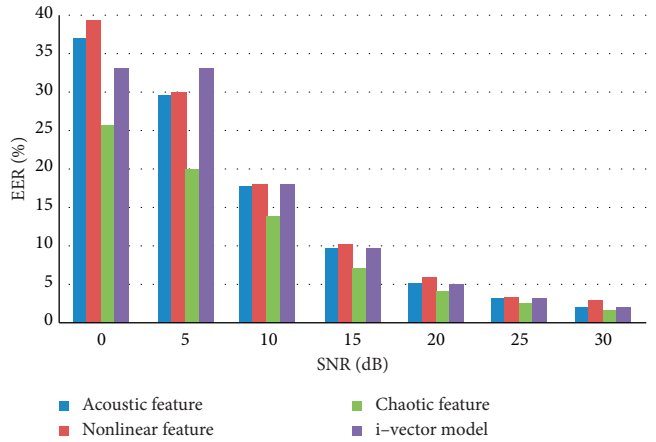

Figure 2: EER results under white noise speech condition.

Table 5: The EER value under babble noise speech condition.

SNR (dB)	Acoustic feature	Nonlinear feature	Chaotic feature	*i*-vector model
0	27.589	30.142	20.092	26.172
5	23.897	25.563	13.095	16.077
10	20.481	21.792	11.607	16.981
15	12.074	13.346	8.103	10.252
20	6.547	5.897	2.918	4.266
25	2.801	2.105	1.691	2.678
30	1.822	2.185	0.901	1.587
Average	13.60	14.43	8.34	11.14

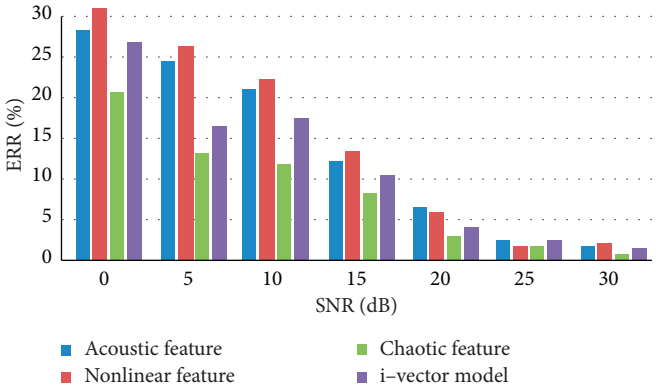

Figure 3: EER results under babble noise speech condition.

Table 6: The average EER value in all experiments.

Feature	Speech type	Acoustic feature	Nonlinear feature	Chaotic feature	*i*-vector model	Compare with *i*-vector
EER (%)	Clean	2.562	2.833	2.149	2.497	↓13.94%
	White	14.96	15.68	10.74	14.82	↓26.5%
	Babble	13.60	14.43	8.34	11.14	

(1) Acoustic feature has a good performance of recognition with clean speech. MFCC and LPC have a perfect discrimination to different speakers. However, the recognition performance will decline if the speech signal is disturbed by environment noise.

(2) Speech chaotic characteristic based on the nonlinear dynamic model has a good compensation for the acoustic feature under environment noise condition. That is, the nonlinear feature can better distinguish different speakers in a noise environment. These benefits of the multiresolution analysis techniques can better capture the frequency information of speakers.

(3) In the proposed method, we only extracted 5 nonlinear parameters, and the feature combination is not optimized. We suggest that feature optimization may improve the robustness of recognition.

5. Conclusion

In this paper, we proposed a novel multiscale chaotic feature for speaker recognition. The MRA technique is used to capture the frequency information of a speaker under environment noise condition. We extracted the nonlinear feature based on speech chaotic characteristics to improve the robustness of recognition. The experiment results show that this method is valid. Therefore, we believe the speech chaotic characteristic is a robust feature to various speech application systems, such as speech recognition and speech emotion recognition. In this paper, the proposed feature is not optimized, and the feature optimization will be the next work.

Data Availability

The data used to support the findings of the study are available from the corresponding author upon request.

Conflicts of Interest

The authors declare that they have no conflicts of interest.

Acknowledgments

This work was supported by the National Natural Science Foundation of China under grants 61762005, 61702472, and 61671335, Hunan Provincial Natural Science Foundation of China under grant 2019JJ40144, Scientific Research Project of the Hunan Province Education Department of China under grants 18A304 and 18B338, and the Key Laboratory of Hunan Province for New Retail Virtual Reality Technology under grant 2017TP1026.

References

[1] V. Vestman, D. Gowda, M. D. Sahidullah, P. Alku, and T. Kinnunen, "Speaker recognition from whispered speech: a tutorial survey and an application of time varying linear prediction," *Speech Communication*, vol. 99, pp. 62–79, 2018.

[2] N. Dehak, P. J. Kenny, R. Dehak, P. Dumouchel, and P. Ouellet, "Front-end factor analysis for speaker verification," *IEEE Transactions on Audio, Speech, and Language Processing*, vol. 19, no. 4, pp. 788–798, 2011.

[3] S. J. Prince and J. H. Elder, "Probabilistic linear discriminant analysis for inferences about identity," in *Proceedings of the 11th IEEE International Conference on Computer Vision*, pp. 1–8, Rio De Janeiro, Brazil, October 2007.

[4] P. Rajan, A. Afanasyev, V. Hautamäki, and T. Kinnunen, "From single to multiple enrollment *i*-vectors: practical PLDA scoring variants for speaker verification," *Digital Signal Processing*, vol. 31, pp. 93–101, 2014.

[5] S. Davis and P. Mermelstein, "Comparison of parametric representations for monosyllabic word recognition in continuously spoken sentences," *IEEE Transactions on Acoustics, Speech, and Signal Processing*, vol. 28, no. 4, pp. 357–366, 1980.

[6] B. A. Acero, "Acoustical and environmental robustness in automatic speech recognition," Ph. D thesis, Carnegie Mellon University, Pittsburgh, PA, USA, 1993.

[7] D. A. Reynolds, "Experimental evaluation of features for robust speaker identification," *IEEE Transactions on Speech and Audio Processing*, vol. 2, no. 4, pp. 639–643, 1994.

[8] R. J. Mammone, X. Xiaoyu Zhang, and R. P. Ramachandran, "Robust speaker recognition: a feature-based approach," *IEEE Signal Processing Magazine*, vol. 13, no. 5, p. 58, 1996.

[9] S. Furui, "Cepstral analysis technique for automatic speaker verification," *IEEE Transactions on Acoustics, Speech, and Signal Processing*, vol. 29, no. 2, pp. 254–272, 1981.

[10] H. Hermansky and N. Morgan, "RASTA processing of speech," *IEEE Transactions on Speech and Audio Processing*, vol. 2, no. 4, pp. 578–589, 1994.

[11] J. H. L. Hansen and M. A. Clements, "Source generator equalization and enhancement of spectral properties for robust speech recognition in noise and stress," *IEEE Transactions on Speech and Audio Processing*, vol. 3, no. 5, pp. 407–415, 1995.

[12] S. S. Bharti, M. Gupta, and S. Agarwal, "A new spectral subtraction method for speech enhancement using adaptive noise estimation," in *Proceedings of the 2016 3rd International Conference on Recent Advances in Information Technology*, Dhanbad, India, March 2016.

[13] A. Acero, "Recursive estimation of nonstationary noise using iterative stochastic approximation for robust speech recognition," *IEEE Transactions on Speech & Audio Processing*, vol. 11, no. 6, pp. 568–580, 2003.

[14] M. Afify, Y. X. Cui, and Y. Gao, "Stereo-based stochastic mapping for robust speech recognition," *IEEE Transactions on Audio, Speech, and Language Processing*, vol. 17, no. 7, pp. 1325–1334, 2009.

[15] O. H. Kocal, E. Yuruklu, and I. Avcibas, "Chaotic-type features for speech steganalysis," *IEEE Transactions on Information Forensics and Security*, vol. 3, no. 4, pp. 651–661, 2008.

[16] H. A. Patil and T. B. Patel, "Chaotic mixed excitation source for speech synthesis," in *Proceedings of the 15th Annual Conference of International Speech Communication Association*, Singapore, Asia, September 2014.

[17] V. Pitsikalis and P. Maragos, "Speech analysis and feature extraction using chaotic models," in *Proceedings of the International Conference on Acoustics, Speech and Signal Processing*, Orlando, FL, USA, May 2002.

[18] K. Gopakumar and F. J. Farsana, "Speech encryption algorithm based on nonorthogonal quantum state with hyperchaotic keystreams," *Advances in Mathematical Physics*, vol. 2020, Article ID 8050934, , 2020.

[19] J. McLaughlin, D. A. Reynolds, and T. P. Gleason, "A study of computation speed-UPS of the GMM-UBM speaker recognition system," in *Proceedings of the European Conference on Speech Communication & Technology*, Budapest, Hungary, September 1999.

[20] Z. Xiong, T. F. Zheng, Z. Song, and W. Wu, "Combining selection tree with observation reordering pruning for efficient speaker identification using GMM-UBM," in *Proceedings of the International Conference on Acoustics Speech & Signal Processing*, Philadelphia, PA, USA, March 2005.

[21] S. Anchal, B. Mukhopadhyay, M. Parvatini, and S. Kar, "GMM-UBM based person verification using footfall signatures for smart home applications," in *Proceedings of the IEEE Global Conference on Signal and Information Processing*, Ottawa, Canada, November 2019.

[22] A. K. Sarkar and S. Umesh, "Investigation of speaker-clustered UBMs based on vocal tract lengths and MLLR matrices for speaker verification," in *Proceedings of the Speaker and Language Recognition Workshop-Odyssey*, Brno, Czech Republic, July 2010.

[23] S. Deb and S. Dandapat, "Multiscale Amplitude feature and significance of enhanced vocal tract information for emotion classification," *IEEE Transactions on Cybernetics*, vol. 49, no. 3, pp. 802–815, 2019.

[24] M. Vetterli and J. Kovacevic, *Wavelets and Subband Coding*, Prentice-Hall, Englewood Cliffs, NJ, USA, 1995.

[25] L. R. Rabiner, M. M. Sondhi, and S. E. Levinson, "A vector quantizer combining energy and LPC parameters and its application to isolated word recognition," *AT & T Bell Laboratories Technical Journal*, vol. 63, no. 5, pp. 721–735, 1984.

[26] J. B. T. Curipe and A. H. Camacho, "Feature extraction using LPC-residual and MelFrequency cepstral coefficients in forensic speaker recognition," *International Journal of Computer and Electrical Engineering*, vol. 5, no. 1, pp. 40–43, 2013.

[27] F. Takens, "Detecting strange attractors in turbulence," in *Lecture Notes in Math*, pp. 366–381, Springer, New York, NY, USA, 1981.

[28] J. Lv, A. Lu, and S. Chen, *Chaotic Time Series Analysis and its Application*, Wuhan University Press, Wuhan, China, 2002, in Chinese.

[29] G. Zhao and Y. Shi, "Computing fractal dimension and the Kolmogorov entropy from chaotic time series," *Chinese Journal of Computational Physics*, vol. 16, no. 3, pp. 310–315, 1999, in Chinese.

[30] H. E. Hurst, "Long-term storage: an experimental study," *Journal of the Royal Statistical Society*, vol. 129, no. 4, pp. 591–593, 1965.

[31] D. G. Da Silva and C. A. Medina, "Evaluation of MSR identity toolbox under conditions reflecting those of a real forensic case (forensic_eval_01)," *Speech Communication*, vol. 94, pp. 42–49, 2017.

Hindawi
Complexity
Volume 2020, Article ID 8884786, 15 pages
https://doi.org/10.1155/2020/8884786

Research Article

Fault Detection of the Power System Based on the Chaotic Neural Network and Wavelet Transform

Zuoxun Wang and Liqiang Xu

School of Electrical Engineering and Automation, Qilu University of Technology (Shandong Academy of Sciences), Jinan 250353, China

Correspondence should be addressed to Zuoxun Wang; wangzuoxun@126.com

Received 4 September 2020; Revised 15 November 2020; Accepted 19 November 2020; Published 1 December 2020

Academic Editor: Karthikeyan Rajagopal

The safety and stability of the power supply system are affected by some faults that often occur in power system. To solve this problem, a criterion algorithm based on the chaotic neural network (CNN) and a fault detection algorithm based on discrete wavelet transform (DWT) are proposed in this paper. MATLAB/Simulink is used to establish the system model to output fault signals and travelling wave signals. Db4 wavelet decomposes the travelling wave signals into detail signals and approximate signals, and these signals are combined with the two-terminal travelling wave location method to achieve fault location. And the wavelet detail coefficients are extracted to input to the proposed chaotic neural network. The results show that the criterion algorithm can effectively determine whether there are faults in the power system, the fault detection algorithm has the capabilities of locating the system faults accurately, and both algorithms are not affected by fault type, fault location, fault initial angle, and transition resistance.

1. Introduction

The rapid development of the power system has led to a gradual increase in voltage levels and increasingly complex transmission lines, and it is more and more difficult to detect power system faults. However, the normal operation of the enterprise and people's production and life are seriously affected by the fault of the power system. Therefore, it is particularly critical to accurately locate the fault point of the power system.

Recently, many scholars in related fields have conducted in-depth and extensive research on power system fault diagnosis. With the further development of artificial intelligence, especially machine learning and data mining, many theories and methods are provided for fault diagnosis. The fault diagnosis methods proposed at present can be summarized as frequency domain feature detection methods and adaptive detection methods. The frequency domain feature detection methods mainly include Fourier transform, wavelet transform, and Hilbert-Huang transform. The adaptive detection methods mainly include neural networks and expert systems. Although these theoretical studies have achieved certain results, there are still some limitations. In [1], single-ended travelling wave fault location method was used to transmission line fault location, but it is difficult to identify the wave head and the positioning accuracy was not high. In [2], integrated empirical mode decomposition (EEMD) was used to optimize empirical mode decomposition (EMD). This method avoided modal aliasing, but introduced false components, resulting in low positioning accuracy. In [3], a fault phase selection method based on high-order multiresolution singular entropy of current fault components is proposed. This method is basically not affected by the fault type, fault location, and transition resistance, but the setting of optimal threshold is complicated.

The wavelet transform is a further improvement and extension on the basis of the Fourier transform. The Fourier transform cannot express the time-frequency localization property of nonstationary signals, and the wavelet transform solves this problem. Wavelet transform not only has good

overall waveform analysis ability but also has outstanding time-frequency localization analysis ability. It can effectively obtain the detailed information of the signal in the time and frequency domains and has the ability to determine the singular point of the signal and analyze the degree of signal distortion [4, 5]. In [6], wavelet transform was applied to fault detection of the fars power distribution system, which improved detection accuracy and achieved good results. Using wavelet transform to analyze signals, the key process is the extraction of approximate features and detailed features. We need to determine the optimal decomposition level, separate the feature components as far as possible, and keep the error apart from the extracted features. The current many methods need either manual setting threshold control or results testing with extracted trend by wavelet transform, which increases the difficulty of extracting feature components and reduces the accuracy of fault detection.

The neural network simulates the neuron network of the human brain, and the values of the neurons in the input layer are mapped to the output layer, so that a certain implicit function relationship is established between the input and the output. At present, the multilayer perceptron neural network theory based on the BP algorithm is most widely used in fault diagnosis. In [7], the MLP neural network was adaptively updated using the BP algorithm to minimize tracking errors, which enhanced the performance of an MLP controller and improved the recognition accuracy. The neural network adopts a knowledge-based nonlinear processing method. Compared with the traditional diagnosis method, it is more flexible in the application of knowledge. At the same time, the neural network has a strong learning ability, and its fault tolerance is better in fault diagnosis, but there are still some defects in the neural network: (1) Neural network needs a large number of samples for training, and it is difficult to obtain sufficient samples in the field of power system fault diagnosis. (2) The neural network was easy to be trapped in local minimum.

To address these problems, a fault detection algorithm based on wavelet transform and the chaotic neural network is proposed in this paper. The chaotic neural network is capable of overcoming the shortcoming of trapping into the local optimum. And it has good performance of fault tolerance and associative memory capabilities. The design parameters of the proposed algorithm are shown in Table 1. The main contributions of this paper are as follows:

(1) A fault phase selection algorithm based on the chaotic neural network is proposed. The fault features extracted by wavelet are input to the chaotic neural network, and the fault type is determined by the corresponding relationship between input and output. And this algorithm is not affected by fault type, fault location, fault initial angle, and transition resistance.

(2) A two-terminal fault detection algorithm based on wavelet transform is proposed. The db4 wavelet is used to detect the travelling wave head to diagnose the fault. This algorithm has high detection accuracy and is not affected by fault type, fault location, fault initial angle, and transition resistance.

Table 1: The design parameters of the proposed algorithm.

Items	Parameter values
The type of mother wavelet	Daubechies 4
Wavelet decomposition layers	4
Wavelet center frequency	0.7143 kHz
Number of neural network input layers	1
Number of neural network hidden layers	1
Number of neural network output layers	1
Input values of the neural network	$W_{u_i}(s,k),\ (i=\alpha,\beta,\gamma,0)$

The remainder of this paper is organized as follows: Section 2 briefly introduces wavelet transform theory and Mallat algorithm. Section 3 discusses the modulus maximum theory, the two-terminal travelling wave location method, and phase-model transformation. Section 4 analyzes the chaotic neural network model. Section 5 summarizes the selection basis of the mother wavelet function. In Section 6, simulation is carried out to illustrate and prove the effectiveness and practicability of the proposed algorithm and compare it with the EMD algorithm. Finally, further discussion and conclusions are in Section 7.

2. Wavelet Transform

2.1. Wavelet Transform Theory. Wavelet transform is the process of convolving the signal with the wavelet basis function, and the signal is decomposed into different frequency bands and time periods [8]. The signal $f(t)$ is expanded under the telescopic-translational signal $\psi_{a,b}(t)$, and the process of decomposing $f(t)$ is called continuous wavelet transform (CWT), and the expression is

$$W_f(a,b) = \langle f, \psi_{a,b} \rangle = |a|^{-(1/2)} \int_{-\infty}^{+\infty} f(t)\overline{\psi}\left(\frac{t-b}{a}\right)\mathrm{d}t. \tag{1}$$

In the above formula, $\psi_{a,b}(t)$ is called the mother wavelet, a is the scaling parameter, and b is the translation parameter. The essence of wavelet transform is to filter the signal with different filters. In the high-frequency region, the high resolution is reflected in time, and in the low-frequency region, the high resolution is reflected in frequency [9, 10].

Since discrete signals are often used in the actual project, $\psi_{a,b}(t)$ is discretized into the following formula:

$$\psi_{j,k}(t) = a_0^{-(j/2)}\psi\left(\frac{t - ka_0^j b_0}{a_0^j}\right) = a_0^{-(j/2)}\psi\left(a_0^{-j}t - kb_0\right). \tag{2}$$

Then, get the discrete wavelet transform (DWT):

$$C_{j,k} = \langle f, \psi_{j,k} \rangle = a_0^{-(j/2)} \int_{-\infty}^{+\infty} f(t)\overline{\psi}\left(a_0^{-j}t - kb_0\right)\mathrm{d}t. \tag{3}$$

Under certain conditions, the signal $f(t)$ can completely be characterized by discrete wavelet coefficient $C_{j,k}$.

2.2. Wavelet Mallat Algorithm

2.2.1. Decomposition Algorithm. The spectrum of $f(t)$ is $f(\omega)$. However, in the actual project, the spectrum is limited. As long as j is selected large enough, $f(t)$ can be expanded with V_{j+1}:

$$f(t) = \sum_n c_{j+1,n}\varphi_{j+1,l}(t). \tag{4}$$

In the above formula, $c_{j+1,n}$ is the scale factor of scale space V_{j+1}, and $c_{j+1,n} = \langle f, \varphi_{j+1,n}\rangle$ and $\varphi_{j+1,k}(t)$ are the scale functions of scale space V_{j+1}.

Because $V_{j+1} = V_j \oplus W_j$, that is, $V_j \perp W_j$, then

$$f(t) = \sum_n c_{j,k}\varphi_{j,k}(t) + \sum_k d_{j,k}\Psi_{j,k}(t). \tag{5}$$

In formula (5), $\sum_n c_{j,k}\varphi_{j,k}(t)$ is the low-frequency component of $f(t)$, which is the approximate part of $f(t)$, and $\sum_k d_{j,k}\Psi_{j,k}(t)$ is the high-frequency component of $f(t)$, which is the detail part of $f(t)$. And the low-frequency coefficient $c_{j,k}$ and the high-frequency coefficient $d_{j,k}$ can be obtained as follows:

$$c_{j,k} = \langle f, \varphi_{j,k}\rangle = \sum_n c_{j+1,n}\overline{h}_{j-2k}, \tag{6}$$

$$d_{j,k} = \langle f, \Psi_{j,k}\rangle = \sum_n c_{j+1,n}\overline{g}_{j-2k}. \tag{7}$$

From the above formula, the coefficient $c_{j,k}$ and the $d_{j,k}$ can be obtained from the coefficient $c_{j+1,k}$ in the space V_{j+1}. The decomposition process is shown in Figure 1.

2.2.2. Reconstruction Algorithm. The essence of the Mallat reconstruction algorithm is the inverse operation of the decomposition algorithm. By substituting equations (6) and (7) into equation (5), we get the following equation:

$$\begin{aligned} f(t) &= \sum_k c_{j,k}\left(\sum_l h_{l-2k}\varphi_{j+1,l}(t)\right) \\ &\quad + \sum_k d_{j,k}\left(\sum_l g_{l-2k}\varphi_{j+1,l}(t)\right) \\ &= \sum_l\left(\sum_k c_{j,k}h_{l-2k} + \sum_k d_{j,k}g_{l-2k}\right)\varphi_{j+1,l}(t). \end{aligned} \tag{8}$$

$l \longrightarrow k$, $k \longrightarrow n$, then, we get

$$c_{j+1,k} = \sum_n c_{j,n}h_{k-2n} + \sum_n d_{j,n}g_{k-2n}. \tag{9}$$

In formula (9), $c_{j+1,k} \in V_{j+1}$, $c_{j,k} \in V_j$, and $d_{j,k} \in W_j$. Reconstruction is the process of calculating $c_{j+1,k}$ from the coefficient $c_{j,k}$ and $d_{j,k}$. The reconstruction process is shown in Figure 2.

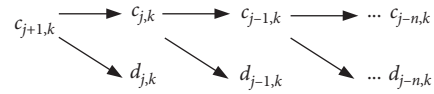

Figure 1: Mallat decomposition process.

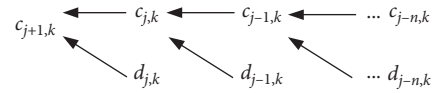

Figure 2: Mallat reconstruction process.

3. Principle of Modulus Maximum Detection

3.1. Modulus Maximum Detection Theory. The original signal discontinuity or its differential discontinuity leads to the singularity of the signal. The essence of singularity detection is to identify the singular point of the signal and analyze the degree of signal distortion. According to the time-frequency localization property of wavelet transform, the signal singularity can be effectively analyzed [11–13].

The wavelet transform with scale s at point u is $W_f(s,u)$, if point u near the point u_0 satisfies $|W_f(s,u)| \le |W_f(s,u_0)|$, then the maximum point at scale s is u_0, and the modulus maximum of the wavelet transform is $|W_f(s,u_0)|$ [14, 15]. Signals at different scales will have different modulus maximum; therefore, the singularity of the signal can be analyzed by extracting the modulus maximum points in the signal. By constructing a smoothing function to smooth the signals of different scales, the first and second order differentials can be extracted to identify the singular points of the signal [16, 17].

The smoothing function $\theta(t)$ satisfies $\int_{-\infty}^{+\infty}\theta(t)\mathrm{d}t = 1$ and $\lim_{t\longrightarrow\pm\infty}\theta(t) = 0$. By constructing the mother wavelet $\psi^{(1)}(t) = (\mathrm{d}\theta/\mathrm{d}t)$ and $\psi^{(2)}(t) = (\mathrm{d}^2\theta/\mathrm{d}t^2)$ and introducing the function $\xi_s(t) = (1/s)\xi(t/s)$, the wavelet transform of $f(t)$ at scale s and point t under is defined as

$$\begin{aligned} W_f^1(s,t) &= f * \psi_s^{(1)}, \\ W_f^2(s,t) &= f * \psi_s^{(2)}. \end{aligned} \tag{10}$$

Expand the above formula as follows:

$$\begin{aligned} W_f^1(s,t) &= <f, \psi_s^{(1)}> = f * \left(s\frac{\mathrm{d}\theta_s}{\mathrm{d}t}\right)(t) = s\frac{\mathrm{d}}{\mathrm{d}t}(f * \theta_s)(t), \\ W_f^2(s,t) &= <f, \psi_s^{(2)}> = f * \left(s^2\frac{\mathrm{d}^2\theta_s}{\mathrm{d}t^2}\right)(t) = s^2\frac{\mathrm{d}^2}{\mathrm{d}t^2}(f * \theta_s)(t). \end{aligned} \tag{11}$$

It can be seen from the above formulas that the wavelet transform $W_f^1(s,t)$ can be obtained by the first order differential and the $W_f^2(s,t)$ can be obtained by the second order differential. The discontinuous point of $f(t)$ corresponds to the modulus maximum point of $W_f^1(s,t)$ and the zero point of $W_f^2(s,t)$ [18, 19]. However, the electrical quantity of the nonfault point will be disturbed during the signal transmission, which will affect the accuracy of the

zero-crossing detection, so the result of the zero-crossing detection is usually not a discontinuity point, but an inflection point of the signal, and the modulus maximum detection is more reliable than zero-crossing detection [20, 21]. After wavelet transform, the discontinuity point of the signal $f(t)$ corresponds to the maximum point of $W_f^1(s,t)$ and the zero point of $W_f^2(s,t)$. According to the definition of wavelet transform $W_f(s,t)$, the maximum point of $|W_f(s,t)|$ reflects the position of the singular point of $f * \theta_s(t)$ [22]. Therefore, the singular point of the signal at different scales can be determined by detecting the maximum point of $|W_f(s,t)|$.

3.2. Two-Terminal Travelling Wave Location Principle. The schematic diagram of the two-terminal travelling wave location method is shown in Figure 3. When a fault occurs at point F, the transient travelling wave propagates to both sides along the transmission line. At the same time, reflection and refraction occur at the point where the wave impedance is discontinuous. Assume that the time when the travelling wave head reaches the detection point M and the detection point N is t_{m1} and t_{n1}, respectively, and after reflection, the time when the wave head reaches the detection point M and N is t_{m2} and t_{n2}, respectively. The total length of the line is L_{MN}, the distance between the fault point F and M is L_{MF}, the distance between F and N is L_{NF}, and the travelling wave propagation speed is v; then,

$$\begin{cases} L_{\mathrm{MF}} = t_{m1} v, \\ L_{\mathrm{NF}} = t_{n1} v, \\ L_{\mathrm{MN}} = L_{\mathrm{MF}} + L_{\mathrm{NF}}. \end{cases} \tag{12}$$

Then, the formula of two-terminal travelling wave location is obtained:

$$L_{\mathrm{MF}} = \frac{L_{\mathrm{MN}} + v\left(t_{m1} - t_{n1}\right)}{2}. \tag{13}$$

The two-terminal travelling wave location method only needs to detect the initial wave head of the fault travelling wave and does not need to consider the reflection and refraction at the discontinuity point of wave impedance [23–25]. Therefore, the location algorithm is more simple. In this paper, the discrete wavelet transform is used to detect the transient travelling wave head, and the time t_{m1} propagated to the detection point M and t_{n1} propagated to the detection point N are used to locate the fault point.

3.3. Phase-Model Transformation. In the three-phase transmission line, the electromagnetic coupling between each phase will affect the precision of fault location. In order to reduce the positioning error caused by electromagnetic coupling, it is necessary to transform the three-phase nonindependent phase components into mutually independent mode components. In this paper, Clarke transformation is used to decouple the signal. The Clarke transformation matrices are as follows:

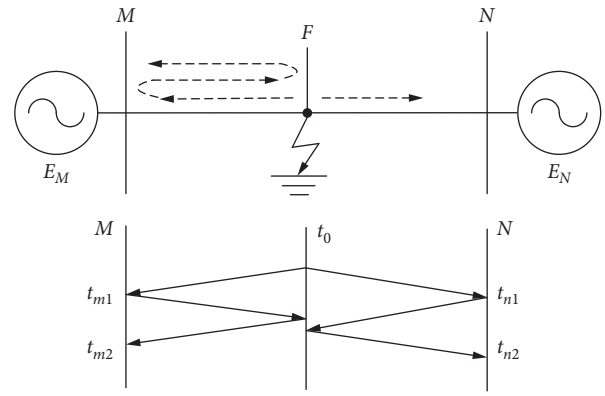

Figure 3: Schematic diagram of fault location.

$$\begin{bmatrix} u_\alpha \\ u_\beta \\ u_0 \end{bmatrix} = \frac{1}{3} \begin{bmatrix} 2 & -1 & -1 \\ 0 & \sqrt{3} & \sqrt{3} \\ 1 & 1 & 1 \end{bmatrix} \begin{bmatrix} u_a \\ u_b \\ u_c \end{bmatrix}, \tag{14}$$

$$\begin{bmatrix} i_\alpha \\ i_\beta \\ i_0 \end{bmatrix} = \frac{1}{3} \begin{bmatrix} 2 & -1 & -1 \\ 0 & \sqrt{3} & \sqrt{3} \\ 1 & 1 & 1 \end{bmatrix} \begin{bmatrix} i_a \\ i_b \\ i_c \end{bmatrix}. \tag{15}$$

In the above formulas, u_a, u_b, and u_c are the phase voltages of the three-phase line.u_α, u_β, and u_0 are the mode components of the phase voltages. i_a, i_b, and i_c are the phase currents of the three-phase line. i_α, i_β, and i_γ are the mode components of the phase currents.

4. Chaotic Neural Network

4.1. Lyapunov Exponent. In the process of dynamic evolution, the phase volume of the dissipative system continuously shrinks the trajectories to a limited range and separates the trajectories from each other. Because of its essential properties, the adjacent trajectories can be repelled and separated. This makes the trajectories converge and separate, separate and converge again, forming a self-similar structure with infinite levels. And this structure is called chaotic attractor. Two phase trajectories will attract or separate at an exponential rate over time. And the Lyapunov exponent is used to measure the degree of attraction or separation. The rate of convergence or divergence of the trajectories is called the Lyapunov exponent, which is often used as an effective parameter to describe the dynamic characteristics of the system. For a dissipative system, one of its Lyapunov exponents must be positive. Therefore, the largest Lyapunov exponent can be used to determine whether the system or signal is chaotic.

For mapping $x_{n+1} = F(x_n)$, in the process of continuous iteration, the two points separate and converge with the change of the value of $\mathrm{d}F/\mathrm{d}x$. Assuming that the discrete exponent caused by each iteration is constant λ. Then, after n times iteration, the two points at the initial distance ε will evolve into the following formula:

$$\varepsilon e^{n\lambda(x_0)} = \left|F^n(x_0+\varepsilon) - F^n(x_0)\right|. \tag{16}$$

Taking the limit $\varepsilon \longrightarrow 0$, $n \longrightarrow \infty$, we get the following formula:

$$\begin{aligned}\lambda(x_0) &= \lim_{n\longrightarrow\infty}\lim_{\varepsilon\longrightarrow 0}\frac{1}{n}\ln\left|\frac{F^n(x_0+\varepsilon) - F^n(x_0)}{\varepsilon}\right| \\ &= \lim_{n\longrightarrow\infty}\frac{1}{n}\ln\left|\frac{\mathrm{d}F^n(x)}{\mathrm{d}x}\right|_{x=x_0}.\end{aligned} \tag{17}$$

It can be obtained from the above formula that

$$\lambda = \lim_{n\longrightarrow\infty}\frac{1}{n}\sum_{i=0}^{n-1}\ln\left|\frac{\mathrm{d}F(x)}{\mathrm{d}x}\right|_{x=x_0}. \tag{18}$$

It can be seen from the above formula that the constant λ is independent of the selection of the initial value, and this constant is the Lyapunov exponent of the system.

The sensitivity of the Lyapunov exponent is related to the contraction and expansion of the phase space motion trajectory. In the direction with negative Lyapunov exponent, the trajectory is contracted and is not sensitive to the initial value. However, in the direction with positive Lyapunov exponent, the motion trajectory is rapidly separated and sensitive to the change of the initial value.

4.2. Chaotic Neural Network Model. The neural network designed in this paper for power system fault phase selection is a three-layer chaotic neural network, composed of an input layer, a hidden layer, and an output layer, as shown in Figure 4. Four nodes are set at the input layer, and four discrete wavelet transform coefficients $W_{u_i}(s,k)$, $(i=\alpha,\beta,\gamma,0)$ are input, respectively. The phase voltages are transformed into the mode components by Clarke phase-mode transformation. The mode components are convolved with discrete wavelet basis function: $\langle u_i, \psi_{s,k}\rangle$, $(i=\alpha,\beta,\gamma,0)$, and the wavelet transform coefficient $W_{u_i}(s,k)$ is obtained, as shown in the following formula:

$$\begin{aligned}W_{u_i}(s,k) &= \langle u_i, \psi_{s,k}\rangle \\ &= a_0^{-(j/2)}\int_{-\infty}^{+\infty} u_i(t)\overline{\psi}\left(a_0^{-j}t - kb_0\right)\mathrm{d}t, \quad (i=\alpha,\beta,\gamma,0).\end{aligned} \tag{19}$$

The number of output layer is 1, and the output result T is "0" or "1." When the output result is "0," it means that the line is operating normally and the starting element does not act; when the output is "1," it means that there are faults in transmission line, the starting element will act, and the protection device will start.

5. Fault Signal Detection Algorithm Based on Daubechie4

5.1. Selection of Wavelet Function. There are certain differences in the transformation characteristics of different wavelet functions. If the selected mother wavelet is different,

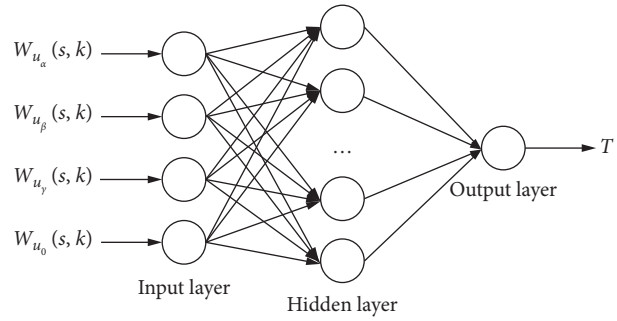

Figure 4: Chaotic neural network model.

the wavelet coefficients are also different; so, before using MATLAB for simulation analysis, we need to select the appropriate mother wavelet function [26]. The selection of wavelet function needs to take into account its vanishing moment, symmetry, and compactly support (support length). The compactly support and vanishing moment determine the influence range of wavelet function at a specific scale, so a compromise must be dealt with when choosing a smaller support length and a higher order vanishing moment [27, 28]. Symmetry describes the smoothness of the signal after wavelet reconstruction. Common wavelet functions and characteristics are shown in Table 2.

In order to further analyze the effect of different wavelets on the detection of discontinuities, we construct a freqbrk signal, which includes a low-frequency sinusoidal signal within $t \in [0, 500]$ and a high-frequency signal within $t \in [500, 1000]$. Three different kinds of wavelet, haar wavelet, sym4 wavelet, and db4 wavelet, are used to 3-layer wavelet decomposition, and the analysis results are shown in Figure 5. The results show that all these three wavelets can detect signal discontinuities, but obviously, the db4 wavelet has a better effect; so, the db4 wavelet is used to detect the singularity of the signal in this paper.

5.2. Algorithm Steps. Combining the characteristics of the fault signal, the criterion algorithm based on the chaotic neural network and the detection algorithm based on wavelet transform are proposed as follows:

(1) Simulink is used to build a power system model and output three-phase voltage signals and three-phase current signals

(2) Travelling wave signal is obtained from three-phase voltage signals and three-phase current signals

(3) The mother wavelet is selected, and the number of decomposition layers is determined

(4) Clarke transformation is used to transform the three-phase voltage signals into mode components

(5) Wavelet transform is performed to the mode components, and the detail coefficients are input to the chaotic neural network

(6) The discrete wavelet transform (DWT) is used to analyze the travelling wave signal f to obtain the

Table 2: Common wavelet functions and characteristics.

Wavelet function	Haar	Daubechies	Biorthogonal	Symlets	Morlet
Representation	Haar	db N	Bior Nr. Nd	sym N	Morl
Support length	1	$2N-1$	$2Nr+1$	$2N-1$	Limited length
Vanishing moment order	1	N	$Nr-1$	N	—
Symmetry	Symmetry	Approximate symmetry	Asymmetry	Approximate symmetry	Symmetry

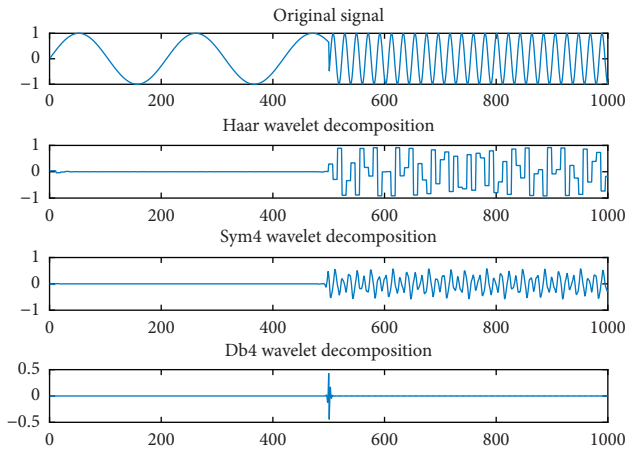

Figure 5: Comparison of different wavelet detection effects.

wavelet coefficients of each layer: $W_1 f(k), W_2 f(k), \ldots, W_j f(k)$

(7) Theoretical analysis and simulation demonstrate the effectiveness of the criterion algorithm and the accuracy of the fault detection algorithm

(8) Simulation results show that both the criterion algorithm and the fault detection algorithm are not affected by fault type, fault location, fault initial angle, and transition resistance

6. Modeling and Simulation

6.1. Build a Power System Model. In this paper, a power system simulation model with a voltage level of 220 kV and power frequency of 50 Hz is built by MATLAB/Simulink, as shown in Figure 6. The system is a dual-power three-phase power supply system, consisting of transmission lines, voltage measuring elements, current measuring elements, oscilloscopes, and fault generators. The three-phase phase angle of the two power sources is 30°, the sampling frequency is 20 kHz, the simulation duration is $T = 0.1$ s, the fault occurrence time is $t_0 = 0.035$ s, and the sampling points are 10000. The system can simulate all kinds of faults that may occur in the power system.

The transmission line parameters are shown in Table 3.

6.2. Signal Extraction

6.2.1. Extract Simulation Signal. By setting the parameters of "three-phase Fault" element, the phase voltages and phase currents of the system can be extracted, as shown in Figures 7 and 8. The effective values of phase voltages and phase currents of the system can be extracted through Scope1 and Scope2, respectively, as shown in Figures 9 and 10. When the fault occurs, the voltage of phase A drops sharply, the voltages of phase B and phase C rise slightly, and the phase currents increase.

6.2.2. Extract Travelling Wave Signal. The phase voltages and phase currents of the three-phase transmission line are obtained through the system model, and the corresponding mode components are obtained with equations (16) and (17). Then, the travelling wave signals detected at the M-side and N-side are obtained, as shown in Figures 11 and 12.

6.3. Simulation Analysis

6.3.1. Simulation of the Chaotic Neural Network Criterion Algorithm. In order to verify the effectiveness of the proposed chaotic neural network criterion algorithm in this paper, the wavelet transform coefficients of four mode components are input. The modulus maximum of wavelet transform coefficients $|W_{u_i}(s,k)|_{\max}$, $(i = \alpha, \beta, \gamma, 0)$ is extracted. And it is analyzed whether this method is accurate and reliable under different operation conditions such as different fault types, fault positions, transition resistances, and fault initial angles. The simulation results are shown in Tables 4–7. Within the allowable error range, it can be seen from $|W_{u_i}(s,k)|_{\max}$, $(i = \alpha, \beta, \gamma, 0)$ that when the power system operates normally, $|W_{u_i}(s,k)|_{\max} = 0$, when phase A is grounded, $|W_{u_\alpha}(s,k)|_{\max} = 2|W_{u_i}(s,k)|_{\max}$, $(i = \beta, \gamma, 0)$, when both phase A and phase B are grounded, $|W_{u_\alpha}(s,k)|_{\max} = |W_{u_\beta}(s,k)|_{\max} = 2|W_{u_i}(s,k)|_{\max}$, $(i = \gamma, 0)$, and when there is a three-phase short circuit fault, $|W_{u_\alpha}(s,k)|_{\max} = |W_{u_\beta}(s,k)|_{\max} = |W_{u_\gamma}(s,k)|_{\max}$. Therefore, it is concluded from Tables 4–7 that when the transmission line operates normally, the output result is 0, and the starting element does not work, and when there is a fault in the line, the output result is 1, and the starting element takes effect. And the proposed criterion algorithm based on the chaotic neural network is not affected by fault types, fault positions, transition resistances, and fault initiation angles.

6.3.2. Simulation of the Wavelet Transform Fault Detection Algorithm. The travelling wave signal is sampled, and 500 sampling points are obtained. Daubechies 4 discrete wavelet transform is used to analyze the travelling wave signal, and the simulation results are shown in Figures 13 and 14. The signal shown in Figure 13 is the detail coefficient of 4-layer wavelet decomposition of the M-side travelling wave. The signal shown in Figure 14 is the detail coefficients of 4-layer

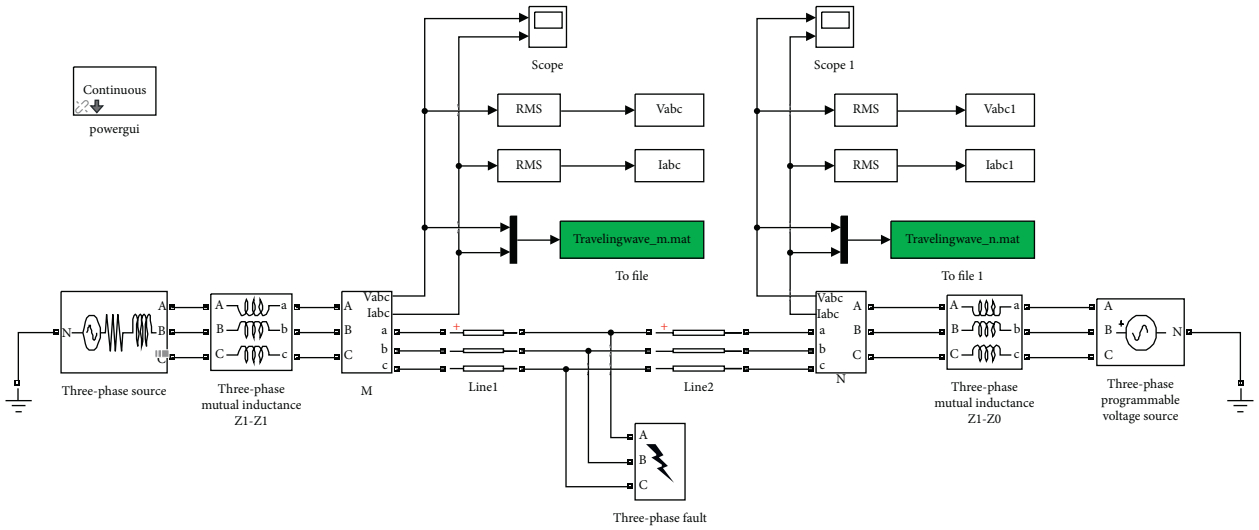

Figure 6: Power system simulation model.

Table 3: The transmission line parameters.

Parameter types	Resistance ($\Omega \cdot km^{-1}$)	Inductance ($H \cdot km^{-1}$)	Capacitance ($F \cdot km^{-1}$)
Positive sequence	0.013	1.33×10^{-3}	9.94×10^{-9}
Zero sequence	0.386	4.126×10^{-3}	7.751×10^{-9}

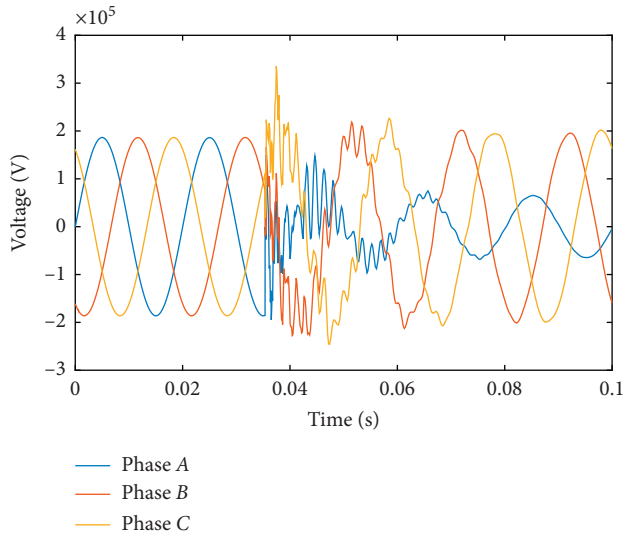

Figure 7: Phase voltages.

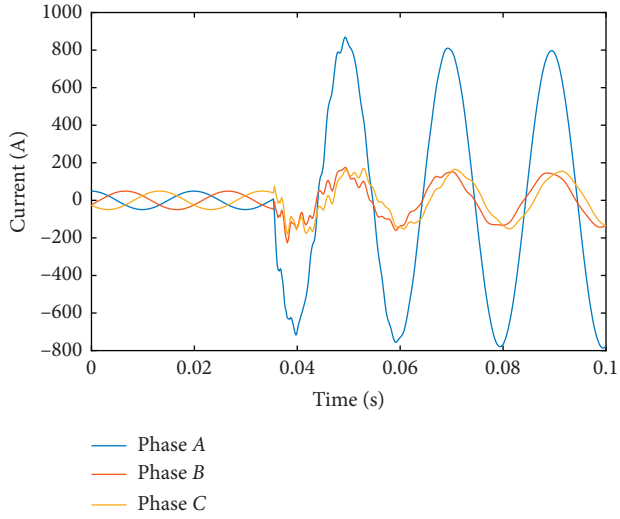

Figure 8: Phase currents.

wavelet decomposition of the N-side travelling wave. It can be seen from Figures 13 and 14 that the amplitude of the detail coefficients (especially the first layer d1 and the second layer d2) change dramatically near the mutation point of the travelling wave signal. This is because the discrete wavelet transform has excellent time-frequency characteristics. The signal is decomposed into multiple layers based on the Mallat algorithm. And the high-frequency components can accurately identify the time when the frequency changed dramatically. Therefore, the wavelet transform is very suitable for the detection of singular points of nonstationary signals.

The first-layer wavelet coefficient d1 can accurately identify the travelling wave heads and the singular points of the travelling wave. The travelling wave heads reflect the time when the fault travelling wave first propagates to the M-side. And the singular points reflect the time when the travelling wave reaches the M-side after being reflected by the fault point and the N-side bus. The proposed algorithm only needs to detect the time when the travelling wave head reaches the two detection points. From d1, $t_{m1} = 35.3$ ms and

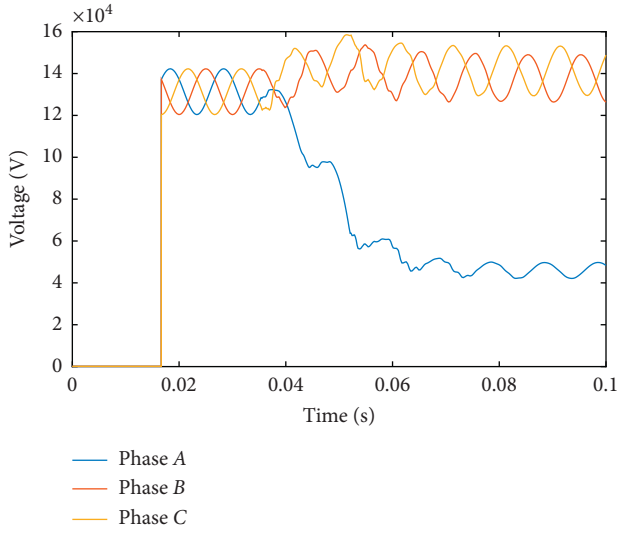

Figure 9: Effective values of phase voltage.

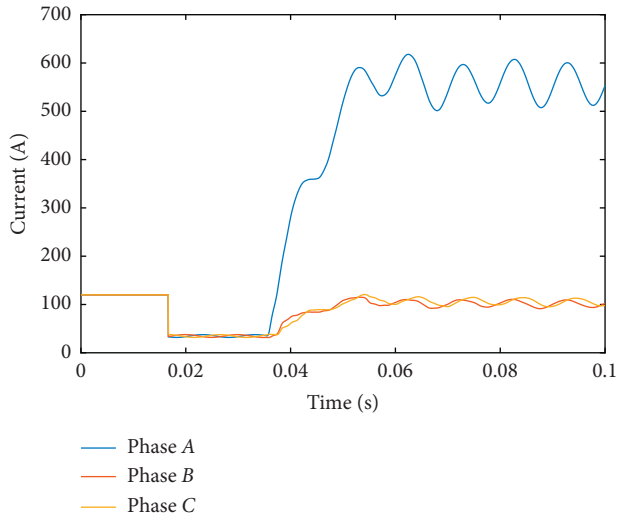

Figure 10: Effective values of phase current.

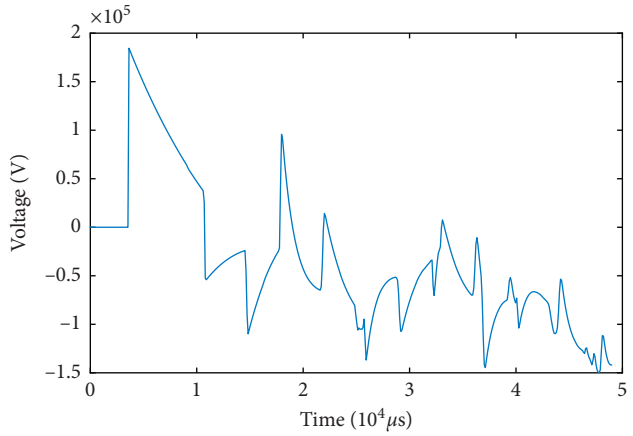

Figure 11: M-terminal travelling wave signal.

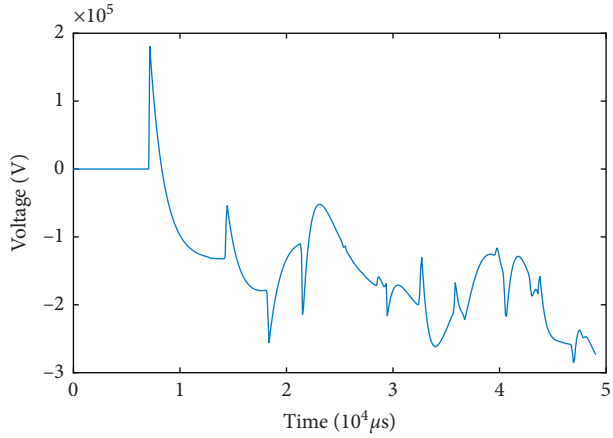

Figure 12: N-terminal travelling wave signal.

Table 4: Simulation results under different fault types.

Operating status	Input layer				Output layer
	$\lvert W_{u_\alpha}(s,k)\rvert_{\max}$	$\lvert W_{u_\beta}(s,k)\rvert_{\max}$	$\lvert W_{u_\gamma}(s,k)\rvert_{\max}$	$\lvert W_{u_0}(s,k)\rvert_{\max}$	
Normal	0	0	0	0	0
AG	3078.21	1529.93	1610.03	1582.61	1
BG	1766.02	3591.40	1690.69	1683.73	1
CG	1404.78	1504.54	2945.62	1498.06	1
AB	3929.07	3894.83	0	0	1
AC	4008.33	0	3968.53	0	1
BC	0	3582.06	3701.39	0	1
ABG	3802.81	4012.10	2070.03	1990.25	1
BCG	1970.89	2909.71	3008.29	2015.88	1
ACG	3202.45	1609.12	3192.81	1513.61	1
ABC	2417.02	2508.16	2588.33	0	1

Table 5: Simulation results under different fault positions.

Fault positions (km)	Operating status	Input layer				Output layer
		$\lvert W_{u_\alpha}(s,k)\rvert_{\max}$	$\lvert W_{u_\beta}(s,k)\rvert_{\max}$	$\lvert W_{u_\gamma}(s,k)\rvert_{\max}$	$\lvert W_{u_0}(s,k)\rvert_{\max}$	
67	Normal	0	0	0	0	0
	AG	3472.44	1736.28	1766.67	1698.22	1
	ABG	2425.53	2567.39	1226.86	1308.91	1
	ABC	2723.74	2781.93	2830.79	0	1
151	Normal	0	0	0	0	0
	AG	4133.33	2078.19	2380.31	2241.77	1
	ABG	3070.92	3256.09	1568.15	1553.21	1
	ABC	2934.37	2843.90	2851.40	0	1
302	Normal	0	0	0	0	0
	AG	3754.87	1867.35	1936.77	2037.56	1
	ABG	3689.83	3551.76	1792.71	1868.42	1
	ABC	1906.88	2038.04	2113.25	0	1

$t_{n1} = 71.6$ ms can be obtained. Then, the distance between the fault point and M terminal is obtained with equation (15): $L_{MF} = 100.082$ km. The fault location error is defined as (|actual fault distance − measuring fault distance|/total length of the transmission line) × 100%; so, the error is 0.027%.

In order to verify the accuracy and good performance of the discrete wavelet transform algorithm proposed in this paper, EMD is performed on the signal as a comparison, as shown in Figures 15 and 16. The signal shown in Figure 15 is the intrinsic mode functions (IMFs) of EMD of the M-side travelling wave. The signal shown in Figure 16 is the IMFs of

Table 6: Simulation results under different transition resistances.

Transition resistance (Ω)	Operating status	Input layer				Output layer
		$\lvert W_{u_\alpha}(s,k)\rvert_{\max}$	$\lvert W_{u_\beta}(s,k)\rvert_{\max}$	$\lvert W_{u_\gamma}(s,k)\rvert_{\max}$	$\lvert W_{u_0}(s,k)\rvert_{\max}$	
0	Normal	0	0	0	0	0
	AG	4365.78	2172.36	2097.10	2206.63	1
	ABG	3054.81	3136.90	1594.07	1662.96	1
	ABC	4015.18	4103.16	3921.64	0	1
50	Normal	0	0	0	0	0
	AG	3907.23	1918.34	1857.20	2032.66	1
	ABG	3267.79	3493.60	1562.87	1608.15	1
	ABC	5109.26	4907.04	5037.21	0	1
200	Normal	0	0	0	0	0
	AG	5172.55	2506.73	2462.11	2463.00	1
	ABG	4931.83	4962.91	2607.12	2732.39	1
	ABC	3088.26	2960.66	2953.33	0	1

Table 7: Simulation results under different fault initial angles.

Fault initial angle (°)	Operating status	Input layer				Output layer
		$\lvert W_{u_\alpha}(s,k)\rvert_{\max}$	$\lvert W_{u_\beta}(s,k)\rvert_{\max}$	$\lvert W_{u_\gamma}(s,k)\rvert_{\max}$	$\lvert W_{u_0}(s,k)\rvert_{\max}$	
30	Normal	0	0	0	0	0
	AG	4561.41	2339.40	2197.10	2179.98	1
	ABG	5637.11	5466.70	2791.33	2832.14	1
	ABC	2593.01	2605.77	2480.19	0	1
60	Normal	0	0	0	0	0
	AG	3168.41	1500.89	1679.20	1592.36	1
	ABG	3612.59	3741.51	1820.42	1825.22	1
	ABC	4026.72	3901.28	4104.57	0	1
180	Normal	0	0	0	0	0
	AG	3152.69	1429.52	1520.77	1501.82	1
	ABG	4010.33	4192.81	2078.19	2165.10	1
	ABC	5123.06	5016.42	4997.11	0	1

the N-side travelling wave. It can be seen from Figures 15 and 16 that only the first-layer component can clearly observe the singular points of the travelling wave. From IMF1, $t_{m1} = 34.6$ ms and $t_{n1} = 70.1$ ms can be obtained, and the distance between the fault point and M terminal is obtained with equation (15): $L_{\mathrm{MF}} = 101.135$ km; so, the error is 0.378%, which is ten times of the algorithm proposed in this paper. It can be seen that the algorithm proposed in this paper is accurate and reliable.

Next, it is analyzed whether this method can locate accurately and reliably under different operation conditions such as different fault types, fault positions, transition resistances, and fault initial angles.

(1) Different Fault Types. The parameters are set as follows: the length of the transmission line is $L_{MN} = 350$ km, the transition resistance is $R_f = 10\ \Omega$, the fault initial angle is $\delta = 30^\circ$, and the fault position is 150 km away from the M-side bus. The simulation results of different fault types are shown in Table 8. The results show that no matter what type of the fault, the measurement error is less than 0.05%.

(2) Different Fault Positions. The parameters are set as follows: the length of the transmission line is $L_{MN} = 350$ km, the transition resistance is $R_f = 10\ \Omega$, the fault initial angle is $\delta = 30^\circ$, and the fault type is A-phase ground fault. The simulation results of different fault positions are shown in Table 9. The results show that the positioning algorithm is not affected by fault positions, and the positioning error is less than 0.03%.

(3) Different Transition Resistances. The parameters are set as follows: the length of the transmission line is $L_{MN} = 350$ km, the fault initial angle is $\delta = 30^\circ$, the fault type is A-phase ground fault, and the fault position is 90 km away from the M-side bus. The simulation results of different transition resistances are shown in Table 10. The results show that the positioning algorithm is not affected by transition resistances, and the positioning error is less than 0.04%.

(4) Different Fault Initial Angles. The parameters are set as follows: the length of the transmission line is $L_{MN} = 350$ km, the transition resistance is $R_f = 10\ \Omega$, the fault type is A-phase ground fault, and the fault position is 132 km away from the M-side bus. The simulation results of different fault initial angles are shown in Table 11. The results show that the positioning algorithm is not affected by fault initial angles, and the positioning error is less than 0.03%.

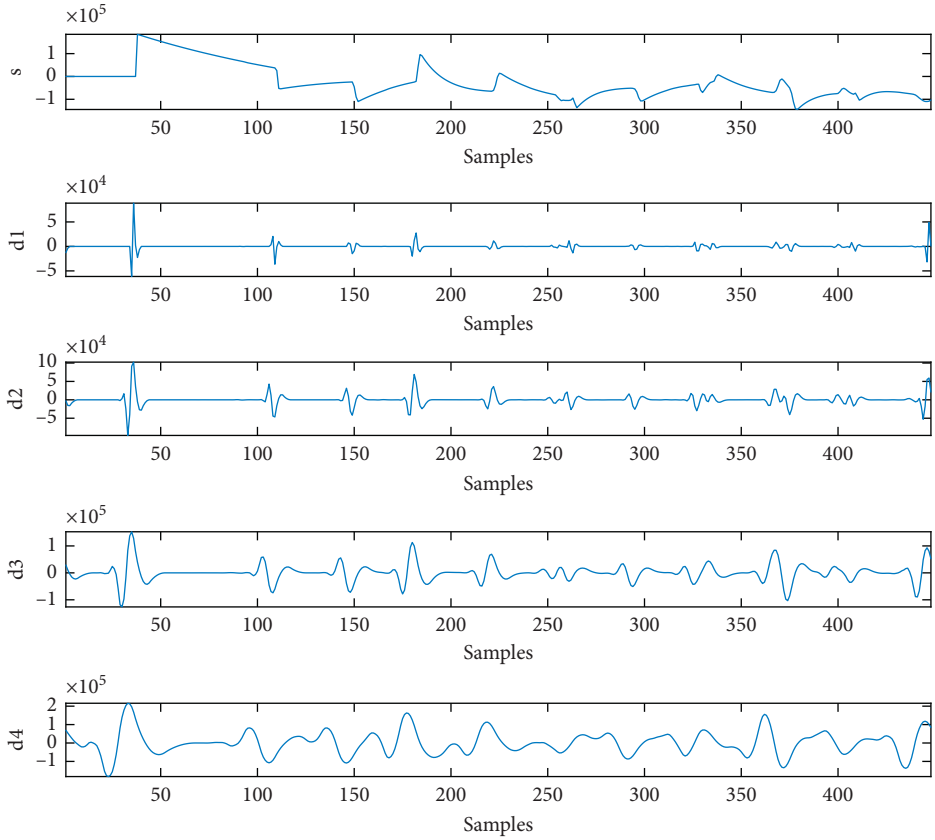

Figure 13: Detail coefficients of the M-terminal travelling wave.

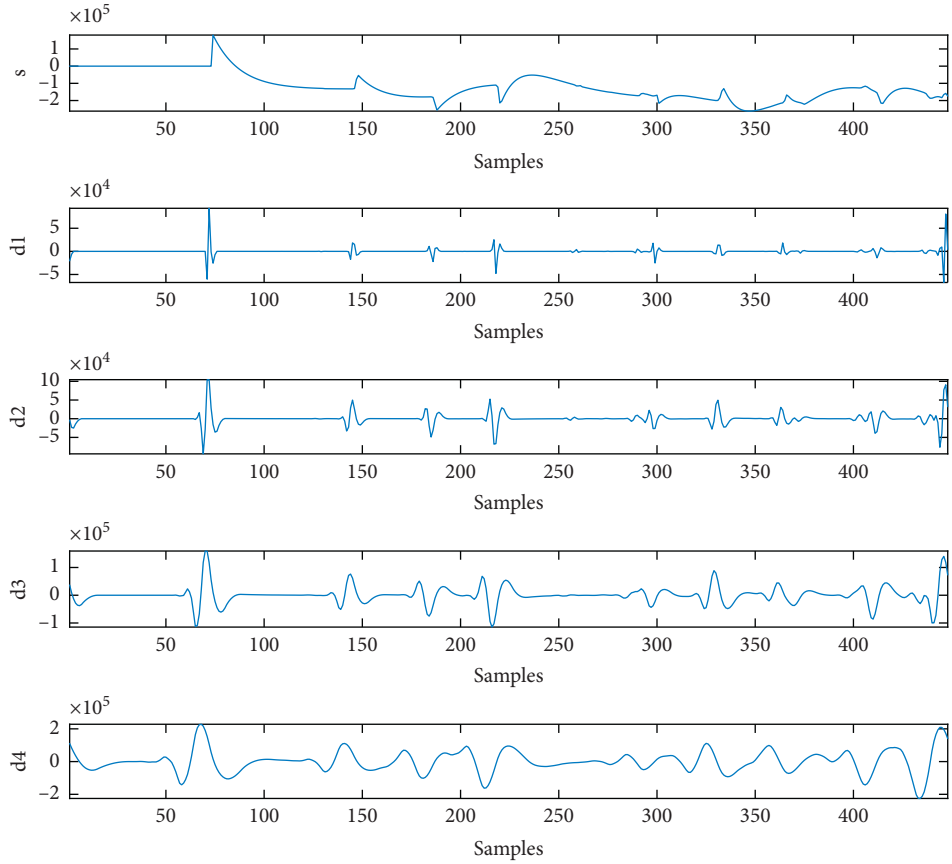

Figure 14: Detail coefficients of the N-terminal travelling wave.

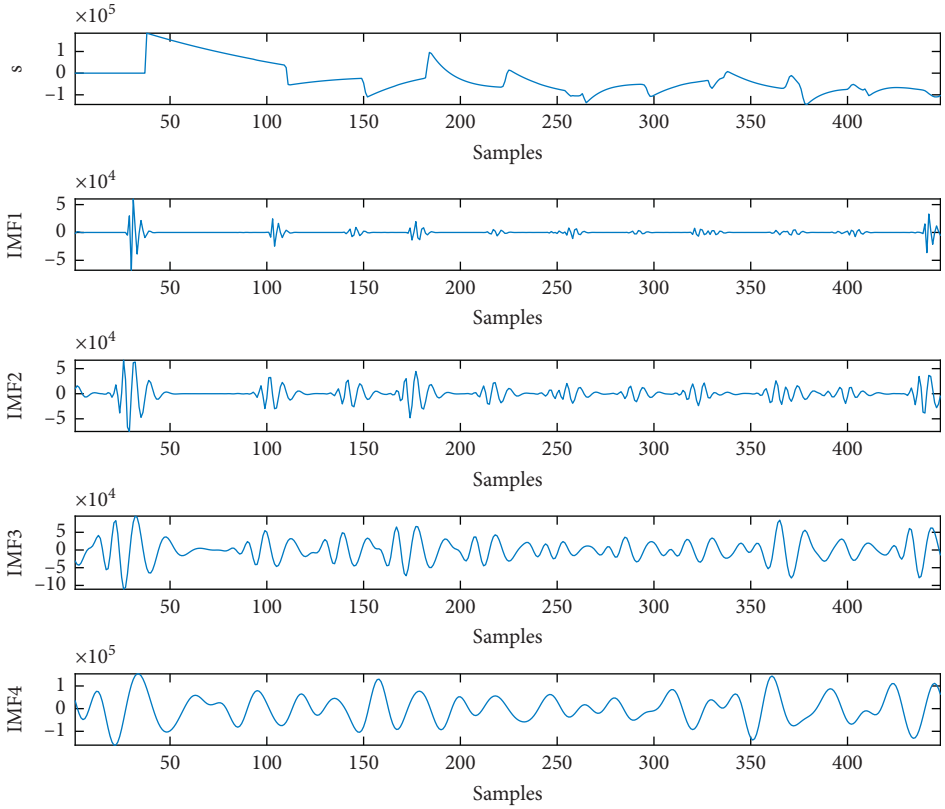

Figure 15: IMFs of the *M*-terminal travelling wave.

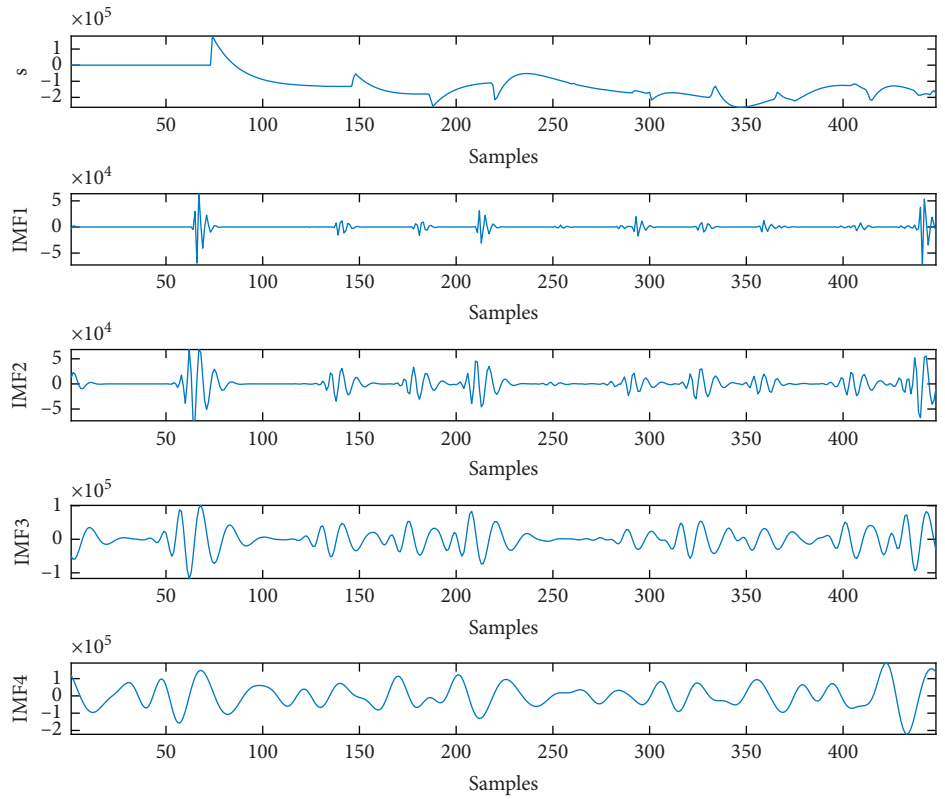

Figure 16: IMFs of the *N*-terminal travelling wave.

Table 8: Simulation results under different fault types.

Fault types	Positioning results (km)	Relative error (%)
AG	150.059	0.017
BG	150.091	0.026
CG	149.942	0.017
AB	149.938	0.018
AC	149.970	0.009
BC	149.892	0.031
ABG	150.078	0.022
ACG	149.839	0.046
BCG	149.901	0.028
ABC	150.103	0.029
ABCG	150.086	0.025

Table 9: Simulation results under different fault positions.

Fault positions/km	Positioning results (km)	Relative error (%)
63	62.937	0.018
98	98.061	0.017
135	135.070	0.020
189	189.077	0.022
210	209.952	0.014
277	277.049	0.014

Table 10: Simulation results under different transition resistances.

Transition resistance (Ω)	Positioning results (km)	Relative error (%)
0	90.092	0.026
10	90.043	0.012
50	89.930	0.020
100	89.927	0.021
150	90.133	0.038
200	89.873	0.036
300	90.071	0.020

Table 11: Simulation results under different fault initial angles.

Fault initial angle (°)	Positioning results (km)	Relative error (%)
0	132.079	0.023
30	132.056	0.016
45	131.967	0.009
60	131.933	0.019
90	132.057	0.016
135	131.908	0.026
165	131.942	0.017

7. Conclusion

When there are faults in the power system, it is very important to implement relay protection quickly and accurately. Travelling wave signals will be generated at the fault point and propagate to both sides of the line. During the transmission of the travelling wave, the forward travelling wave and the travelling wave generated by refraction and reflection superimpose each other, which makes it difficult to determine the wave heads of the travelling wave. Based on the power system model built by MATLAB/Simulink, a criterion algorithm based on the chaotic neural network and a fault detection algorithm based on discrete wavelet transform are proposed in this paper. The criterion algorithm based on the chaotic neural network is capable of overcoming the shortcomings of trapping into the local optimum, and it has good performance of fault tolerance and associative memory capabilities. The fault detection algorithm has the capability of detecting the fault location of transmission lines. The two-terminal travelling wave location method only needs to detect the initial wave head of the fault travelling wave and does not need to consider the

reflection and refraction of the fault travelling wave; so, the location algorithm is more simple. Due to the difference in the transformation characteristics of different wavelet functions, a detection method based on db4 wavelet is determined to obtain more accurate results. After multiresolution wavelet decomposition, we find that the distribution of the energy of the fault signal on each wavelet coefficient is different. The valuable part of the signal is mainly reflected in the specific wavelet coefficients. These detail coefficients are input to the chaotic neural network to verify that the criterion algorithm has the capabilities of determining whether there are faults in transmission lines. And these detail coefficients are used to accurately determine the time when the fault travelling wave head reaches the M-side bus and the N-side bus, and then, the fault position is detected with the two-terminal travelling wave location algorithm. Finally, it is illustrated that both the criterion algorithm and the fault detection algorithm are not affected by fault type, fault positions, transition resistance, and fault initial angle. Therefore, the criterion algorithm based on the chaotic neural network and the fault detection algorithm based on discrete wavelet transform are of great significance, which provide a favorable exploration method for the real-time fault detection of some systems and has a broad and far-reaching application prospect.

Data Availability

No data were used to support this study.

Conflicts of Interest

The authors declare that they have no conflicts of interest.

Acknowledgments

This study was supported by the Postgraduate Tutors' Guidance Ability Improvement Project of Shandong Province (SDYY17076) and the Empirical Research on Innovation of Cultivation Model of Control Graduate Students Based on System Synergy Theory (SDYY18151).

References

[1] Z.-Y. He, K. Liao, X.-P. Li, S. Lin, J.-W. Yang, and R.-K. Mai, "Natural frequency-based line fault location in HVDC lines," *IEEE Transactions on Power Delivery*, vol. 29, no. 2, pp. 851–859, 2014.

[2] A. Soualhi, K. Medjaher, and N. Zerhouni, "Bearing health monitoring based on hilbert-huang transform, support vector machine, and regression," *IEEE Transactions on Instrumentation and Measurement*, vol. 64, no. 1, pp. 52–62, 2015.

[3] J. A. Jiang, P. L. Fan, and C. S. Chen, "A fault detection and faulted phase selection approach for transmission lines with haar wavelet transform," *IEEE PES Transmission and Distribution Conference and Exposition*, vol. 1, no. 1, pp. 285–289, 2003.

[4] S. A. Gafoor, S. K. Yadav, and P. Prashanth, "Transmission line protection scheme using wavelet based alienation coefficients"" in *Proceedings of the IEEE International Conference Power and Energy*, pp. 32–36, Kyiv, Ukraine, 2014.

[5] G. Bayrak, "Wavelet transform-based fault detection method for hydrogen energy-based distributed generators," *International Journal of Hydrogen Energy*, vol. 43, no. 44, pp. 20293–20308, 2018.

[6] M. Kordestani, A. A. Safavi, and A. Sadrzadeh, "A new method to diagnose the type and location of disturbances in fars power distribution system," in *Proceedings of the 24th Iranian Conference on Electrical Engineering ICEE*, pp. 1871–1876, IEEE, Shiraz, Iran, 2016.

[7] M. Kordestani, K. Salahshoor, A. A. Safavi, and M. Saif, "An adaptive passive fault tolerant control system for a steam turbine using a pca based inverse neural network control strategy," in *Proceedings of the World Automation Congress (WAC)*, IEEE, Stevenson, WA, USA, 2018.

[8] M.-F. Guo, N.-C. Yang, and L.-X. You, "Wavelet-transform based early detection method for short-circuit faults in power distribution networks," *International Journal of Electrical Power & Energy Systems*, vol. 99, pp. 706–721, 2018.

[9] J. P. S. Catalão, H. M. I. Pousinho, and V. M. F. Mendes, "Short-term wind power forecasting in Portugal by neural networks and wavelet transform," *Renewable Energy*, vol. 36, no. 4, pp. 1245–1251, 2011.

[10] J. Zhang, H. Sun, Z. Sun, W. Dong, and Y. Dong, "Fault diagnosis of wind turbine power converter considering wavelet transform, feature analysis, judgment and BP neural network," *IEEE Access*, vol. 7, 2019.

[11] N. Ghaffarzadeh, "A new wavelet network based method to estimate the lightning-related risk of failure of power system apparatus," *International Journal of Electrical Power & Energy Systems*, vol. 78, pp. 375–384, 2016.

[12] M. Kordestani, M. Saif, M. E. Orchard, R. Razavi-Far, and K. Khorasani, "Failure prognosis and applications-a survey of recent literature," *IEEE Transactions on Reliability*, vol. 99, pp. 1–21, 2019.

[13] B. Rathore and A. G. Shaik, "Wavelet-alienation based transmission line protection scheme," *IET Generation, Transmission & Distribution*, vol. 11, no. 4, pp. 995–1003, 2017.

[14] P. K. Ray, N. Kishor, and S. R. Mohanty, "Islanding and power quality disturbance detection in grid-connected hybrid power system using wavelet and S-transform," *IEEE Transactions on Smart Grid*, vol. 3, no. 3, pp. 1082–1094, 2012.

[15] H.-C. Seo and S.-B. Rhee, "Novel adaptive reclosing scheme using wavelet transform in distribution system with battery energy storage system," *International Journal of Electrical Power & Energy Systems*, vol. 97, pp. 186–200, 2018.

[16] Y. Shirong, C. Guangju, and X. Yongle, "Wavelet neural network based fault diagnosis in nonlinear analog circuits," *Journal of Systems Engineering and Electronics*, vol. 17, p. 3, 2006.

[17] M. Shafiullah, M. A. Abido, and Z. Al-Hamouz, "Wavelet-based extreme learning machine for distribution grid fault location," *IET Generation, Transmission & Distribution*, vol. 11, no. 17, pp. 4256–4263, 2017.

[18] J. Duan, H. Li, Y. Lei, and L. Tuo, "A novel non-unit transient based boundary protection for HVDC transmission lines using synchrosqueezing wavelet transform," *International Journal of Electrical Power & Energy Systems*, vol. 115, Article ID 105478, 2020.

[19] A. Khaleghi and M. Oukati Sadegh, "Single-phase fault location in four-circuit transmission lines based on wavelet analysis using anfis," *Journal of Electrical Engineering & Technology*, vol. 14, no. 4, pp. 1577–1584, 2019.

[20] L. Sabug, A. Musa, F. Costa, and A. Monti, "Real-time boundary wavelet transform-based DC fault protection system for MTDC grids," *International Journal of Electrical Power & Energy Systems*, vol. 115, Article ID 105475, 2020.

[21] S. Silva, P. Costa, M. Gouvea, A. Lacerda, F. Alves, and D. Leite, "High impedance fault detection in power distribution systems using wavelet transform and evolving neural network," *Electric Power Systems Research*, vol. 154, pp. 474–483, 2018.

[22] F. Xiao, T. Lu, M. Wu, and Q. Ai, "Maximal overlap discrete wavelet transform and deep learning for robust denoising and detection of power quality disturbance," *IET Generation, Transmission & Distribution*, vol. 14, no. 1, pp. 140–147, 2020.

[23] M. Youness, A. Turaj, and S. Alireza, "Fault detection in distribution networks in presence of distributed generations using a data mining-driven wavelet transform," *IET Smart Grid*, vol. 2, no. 2, pp. 163–171, 2019.

[24] C. Beale, C. Niezrecki, and M. Inalpolat, "An adaptive wavelet packet denoising algorithm for enhanced active acoustic damage detection from wind turbine blades," *Mechanical Systems and Signal Processing*, vol. 142, Article ID 106754, 2020.

[25] J. Ding, L. Li, Y. Zheng, C. Zhao, H. Chen, and X. Wang, "Distributed travelling-wave-based fault location without time synchronisation and wave velocity error," *IET Generation, Transmission & Distribution*, vol. 11, no. 8, pp. 2085–2093, 2017.

[26] W. Li, A. Monti, and F. Ponci, "fault detection and classification in medium voltage DC shipboard power systems with wavelets and artificial neural networks," *IEEE Transactions on Instrumentation and Measurement*, vol. 63, p. 11, 2014.

[27] D. Wang, Y. Zhao, C. Yi, K.-L. Tsui, and J. Lin, "Sparsity guided empirical wavelet transform for fault diagnosis of rolling element bearings," *Mechanical Systems and Signal Processing*, vol. 101, pp. 292–308, 2018.

[28] S. Zhang, X. Xiao, and Z. He, "Detection of high-impedance fault in distribution network based on time-frequency entropy of wavelet transform," *IEEJ Transactions on Electrical and Electronic Engineering*, vol. 15, no. 6, pp. 844–853, 2020.

Hindawi
Complexity
Volume 2020, Article ID 8822534, 17 pages
https://doi.org/10.1155/2020/8822534

Research Article

Nonlinear Dynamics of the Quadratic-Damping Helmholtz Oscillator

R. Fangnon,[1] C. Ainamon,[1] A. V. Monwanou,[1] C. H. Miwadinou ,[1,2] and J. B. Chabi Orou[1]

[1]*Laboratoire de Mécanique des Fluides de la Dynamique Nonlinéaire et de la Modélisation des Systèmes Biologiques (LMFDNMSB), Institut de Mathématiques et de Sciences Physiques, Porto-Novo, Benin*
[2]*Département de Physique, ENS-Natitingou, Université Nationale des Sciences Technologies, Ingénierie et Mathématiques (UNSTIM), Abomey, Benin*

Correspondence should be addressed to C. H. Miwadinou; clement.miwadinou@imsp-uac.org

Received 18 August 2020; Revised 14 October 2020; Accepted 23 October 2020; Published 9 November 2020

Academic Editor: Karthikeyan Rajagopal

In this paper, the Helmholtz equation with quadratic damping themes is used for modeling the dynamics of a simple prey-predator system also called a simple Lotka–Volterra system. From the Helmholtz equation with quadratic damping themes obtained after modeling, the equilibrium points have been found, and their stability has been analyzed. Subsequently, the harmonic oscillations have been studied by the harmonic balance method, and the phenomena of resonance and hysteresis are observed. The primary and secondary resonances have been researched by the multiple-scale method, and the conditions of stability of the amplitudes of oscillations are determined. Chaos is detected analytically by the Melnikov method and numerically using the basin of attraction, the bifurcation diagram, the Lyapunov exponent, the phase portrait, and the Poincaré section. The effects of all the parameters of the system are analyzed in detail, and special emphasis is placed on the new parameters. Through this analysis, the complex phenomena such as hysteresis, bistability, amplitude jump, resonances, and chaos have been obtained. The control of the parameters and the necessary conditions to control the aforementioned phenomena have been found.

1. Introduction

Hermann von Helmholtz (1821–1894) is the origin of the very first acoustic resonator that bears his name. In order to extract the harmonics from total sound, he imagined a device made up of receptacles pierced with an orifice depending on their size and a frequency of resonance. To study the complexity of sounds and their perception by the human ear, he used resonators [1]. The dynamics of these resonators are governed by an oscillator equation called the Helmholtz oscillator. This oscillator presents analogies with traditional oscillators, namely, the mass-spring system, the simple pendulum, the circuit (L, C). As fields of application, these resonators are used in certain combustion boilers having concerns of acoustic transmission by the flue pipe in order to dissipate the phenomenon of resonance giving rise to vibrations in some boilers: boiler manufacturers use them to attenuate the noises coming out of the flue pipe. They are also used in cars, aeronautics, musical instruments, room acoustics, bass-reflex speakers, etc. This resonator, taking into account its multiple uses, was a center of interest for a number of researchers who competed with innovations and imaginations in order to solve physical problems on the basis of the functioning of this resonator. Indeed, Doelman et al. studied in [2] the irregularity of tidal oscillations due to the geometry of the basin from the following equation:

$$\ddot{v} + \zeta(v) = \zeta_{\text{ext}} - \gamma(\dot{v}). \tag{1}$$

They have approached in their work a situation which generally has Helmholtz periods ranging from a few minutes to an hour. Balibrea et al. studied in [3] the stability of the structure of the Helmholtz oscillator under changes in the shape of nonlinear periodic disturbances. Komkin and Bykov in [4] had the characteristics of the Helmholtz resonator confirmed from experimental and analytical studies.

In general, dynamic systems and nonlinear sciences constitute a large field of research, given their application in several fields: in mechanics, chemistry, quantum optics, astrophysics, hydrodynamics, electronics, biophysics, and so on [5–25]. Much of the discussion in the physics and engineering literature concerning damped oscillations, linear and nonlinear damping in certain applied systems play an important role since they may be used to suppress large amplitude oscillations or various instabilities, and they can also be used as a control mechanism [26–29]. For example, Soliman and Thompson in [27] and Miwadinou et al. in [28, 29] studied with considerable detail the effects of the damping level on the resonance response of the steady-state solutions and on the basin bifurcation patterns of the escape oscillator. In particular, they analyzed the effect of using different damping levels and how this contributes to the erosion of the safe areas in the phase space. On the contrary, nonlinear damping in vibrations has been investigated in [30–33]. In these different works, the authors studied the effects of nonlinear damping on the dynamics of viscoelastic plates, and interesting conclusions were drawn in relation to these effects on the performance of the viscoelastic plates used.

The Helmholtz oscillator is thus an example of a nonlinear dynamic system which is used to better understand nonlinear phenomena in acoustics, electronics, naval engineering naval, etc. [13–16]. It is in this order of ideas that we find a new model of the Helmholtz oscillator to better analyze the dynamics of a simple Lotka–Volterra system. From various previous works on the Helmholtz oscillator, we note that the new model of Helmholtz can be the seat of many phenomena. We can cite, for example, phenomena such as amplitude jump, hysteresis, nonlinear resonances, chaos, coexistence of attractors, and multistability [13–15]. The search for these phenomena for the new Helmholtz model therefore seems very important. The determination of the states of resonance in a nonlinear dynamic system makes it possible to predict energy exchanges by making the energy proportional to the square of the amplitude of the vibrations [18–21]. For example, in mechanical systems, a sudden increase in the resonance energy can cause damage to the mechanical system, while antiresonance systems can be used to store energy. Furthermore, the interest of nonlinear resonances for the new Helmholtz oscillator is great. Nowadays, most nonlinear vibration techniques focus on the method of modulation of upper harmonics and sidebands, but approaches to detect nonlinear damage based on nonlinear resonances require even more investigation. Thus, the condition giving the relation between the amplitude of vibration and the parameters of the system is crucial for the good choice of the frequency and the amplitude of excitation to trigger a nonlinear resonance effect [34–36]. The most suitable techniques for finding resonances are the harmonic balance and the multiple-scale methods [18, 19, 37]. The object of chaos theory is the study of nonlinear phenomena governed by simple and deterministic laws whose behavior under certain conditions becomes unpredictable. Since its discovery in the 20th century, chaos has been one of the most interesting for dynamic systems in areas such as physics, mathematics, chemistry, biochemistry, economics and finance, epidemiology, and engineering [19–25]. Depending on the field of study, it is sometimes useful or undesirable to the point where many researchers are interested in its prediction and/or control. One of the techniques used for the analytical determination of chaos is the Melnikov method. It is often used to research and predict horseshoe chaos [21, 26, 29].

In this paper, we study resonance, hysteresis, stability, and the chaos of a modified Helmholtz oscillator when it is subjected to an external periodic excitation. To do this, we consider the following system:

$$\ddot{x} + x - x^2 + \mu\dot{x} - \beta\dot{x}^2 + \nu x\dot{x} = F\cos\Omega\tau, \tag{2}$$

where μ, ν, and β, respectively, represent the linear, impure quadratic, and pure quadratic damping coefficients and F and Ω are, respectively, the amplitude and the frequency of external excitation. One of the originalities here is the new model of the Helmholtz equation obtained by reducing the number of variables of the simple Lotka–Volterra system. The new themes are all quadratic damping themes. We determine the fixed points and find their stability and their nature for the autonomous system. We search the effect of the external force on the system by studying the resonances by the methods of the harmonic balance and the multiple scales. Melnikov's method is applied to the system to study its chaotic behavior. These different methods applied to the system allow us to evaluate the influence of various parameters of the system on the state of the system, to predict the variation of the maximum amplitude of the oscillations according to the parameters of the system, and to verify the existence of the phenomenon of jump and hysteresis in the system. The horseshoe chaos and dissipative chaos are also strongly studied and controlled. Analytical results are confirmed by numerical simulations.

The paper is structured as follows: Section 2 gives the mathematical modeling of a quadratic-damping Helmholtz oscillator and analyzes the fixed points and their stability. In Section 3, an in-depth detail of the harmonic oscillations is given. Section 4 deals with primary resonance and secondary resonance, while Section 5 analyzes the horseshoe chaos followed by the Melnikov analysis and the basin of attraction. In Section 6, the numerical analysis of the dissipative chaos is given in detail. Finally, we conclude the paper in Section 7.

2. Model, Fixed Points, and Stability

In this work, we consider the following simple Lotka–Volterra system [12]:

$$\begin{aligned} \dot{\xi} &= K_\xi a\xi - K_\eta\xi\eta, \\ \dot{\eta} &= K_\eta\xi\eta - K_d\eta, \end{aligned} \tag{3}$$

where ξ represents the population of rabbits reproducing in an autocatalytic manner, η is the lynx population, K_d is the lynx mortality rate, K_η provides information on how fast lynxes breed, K_ξ is a speed constant which is the rabbit's

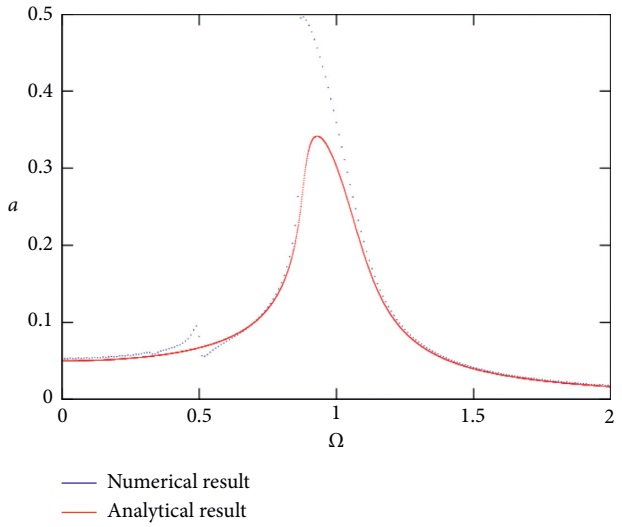

FIGURE 1: Comparison between analytical and numerical frequency-response curve $a(\Omega)$ with the parameters $\beta = 0.05$, $\nu = 1.75$, $\mu = 0.05$, and $F = 0.05$.

reproduction speed, and a is the quantity of grass assumed to be constant. Setting $K_\xi a = \alpha$, $K_\eta = \lambda$, and $K_d = \gamma$, equation (3) becomes

$$\begin{aligned} \dot{\xi} &= \alpha\xi - \lambda\xi\eta, \\ \dot{\eta} &= -\gamma\eta + \lambda\xi\eta. \end{aligned} \tag{4}$$

In order to simplify the calculations, we define $x = \lambda\xi + \lambda\eta$, and we find

$$\begin{aligned} \xi &= \frac{\dot{x} + \gamma x}{\lambda(\gamma + \alpha)}, \\ \eta &= \frac{-\dot{x} + \alpha x}{\lambda(\gamma + \alpha)}. \end{aligned} \tag{5}$$

Replacing equation (5) in equation (4), we obtain

$$\ddot{x} + \omega_0^2 x - \overline{\delta}x^2 + \overline{\mu}\dot{x} - \beta\dot{x}^2 + \overline{\nu}x\dot{x} = 0, \tag{6}$$

with $-\omega_0^2 = \alpha\gamma$, $\overline{\delta} = -\alpha\gamma/(\alpha + \gamma)$, $\beta = 1/(\alpha + \gamma)$, $\overline{\mu} = \gamma - \alpha$, and $\overline{\nu} = (\alpha - \gamma)/\alpha + \gamma$.

When the system is under external periodic excitation, equation (6) becomes

$$\ddot{x} + \omega_0^2 x - \overline{\delta}x^2 + \overline{\mu}\dot{x} - \beta\dot{x}^2 + \overline{\nu}x\dot{x} = F\cos\omega t. \tag{7}$$

Now, setting $\Omega = (\omega/\omega_0)$ and $\tau = \omega_0 t$, one has

$$\ddot{x} + x - \delta x^2 + \mu\dot{x} - \beta\dot{x}^2 + \nu x\dot{x} = F\cos\Omega\tau, \tag{8}$$

with $\delta = (\overline{\delta}/\omega_0^2)$, $\mu = (\overline{\mu}/\omega_0)$, and $\nu = (\overline{\nu}/\omega_0)$.

F and Ω designate, respectively, the amplitude and the frequency of the external periodic excitation; μ, β, and ν are real parameters of the system. Equation (8) represents the equation of a Helmholtz forced oscillator with pure quadratic damping ($\beta\dot{x}^2$) and hybrid damping ($\nu x\dot{x}$). When β and ν are all zero, equation (8) is reduced to the equation of a Helmholtz oscillator [9, 10, 14]. The Helmholtz oscillator is widely used in several areas to study the dynamics of certain systems. Indeed, in naval architects, the Helmholtz oscillator, known as the Helmholtz–Thompson equation, is used to analyze the escape phenomenon. A detailed dynamical analysis of the Helmholtz oscillator is done by Thompson in [9], and Gottwald et al. experimentally studied in [16] the dynamics of this oscillator. Helmholtz–Thompson equation finds direct application in the investigation of the bubble dynamics [17] and is much discussed in the naval architecture literature (see [13]). These concepts continue to find fruitful applications in quantification of capsize resistance [15].

In the remaining of this section, we determine the fixed points of the autonomous Helmholtz oscillator with quadratic damping and study their stability. Indeed, taking $\delta = 1$, the autonomous system is in the following form:

$$\begin{aligned} \dot{x} &= y, \\ \dot{y} &= -x + x^2 - \mu y + \beta y^2 - \nu x y. \end{aligned} \tag{9}$$

Setting $\dot{x} = 0$ and $\dot{y} = 0$, the equilibrium points of (9) are $A_0(0, 0)$ and $A_1(1, 0)$. The eigenvalues λ associated with the fixed point A_0 verify

$$\lambda^2 + \mu\lambda + 1 = 0. \tag{10}$$

As a result,

(i) If $\mu^2 \geq 4$, then $\lambda_1 = -\mu - \sqrt{\mu^2 - 4}/2$ and $\lambda_1 = -\mu + \sqrt{\mu^2 - 4}/2$.

(a) $\mu \leq -2$, the eigenvalues λ_1 and λ_2 are positive. A_0 is an unstable repulsive node.

(b) $\mu \leq 2$, the eigenvalues λ_1 and λ_2 are negative. A_0 is a stable attractive node.

(ii) If $\mu^2 < 4$, then $\lambda_1 = -\mu - i\sqrt{\mu^2 - 4}/2$ and $\lambda_2 = -\mu + i\sqrt{\mu^2 - 4}/2$.

(a) $-2 < \mu < 0$, the eigenvalues λ_1 and λ_2 are complexes whose real parts are positive. A_0 is an unstable repulsive focus.

(b) $0 < \mu < 2$, the eigenvalues λ_1 and λ_2 are complexes whose real parts are negative. A_0 is a stable attractive focus.

Now, the eigenvalues λ associated with the fixed point A_1 are solutions of

$$\lambda^2 + (\mu + \nu)\lambda - 1 = 0. \tag{11}$$

For all values of μ and ν, one has $\lambda_1 = -(\mu + \nu) - \sqrt{(\mu + \nu)^2 + 4}/2$ and $\lambda_2 = -(\mu + \nu) + \sqrt{(\mu + \nu)^2 + 4}/2$. It is easy to note that these eigenvalues are of opposite signs, and therefore, A_1 is a saddle point.

3. Harmonic Oscillations

In this part, we use the harmonic balance method to study harmonic oscillations. For this, we take the solutions of equation (8) in the following form [18, 19, 37]:

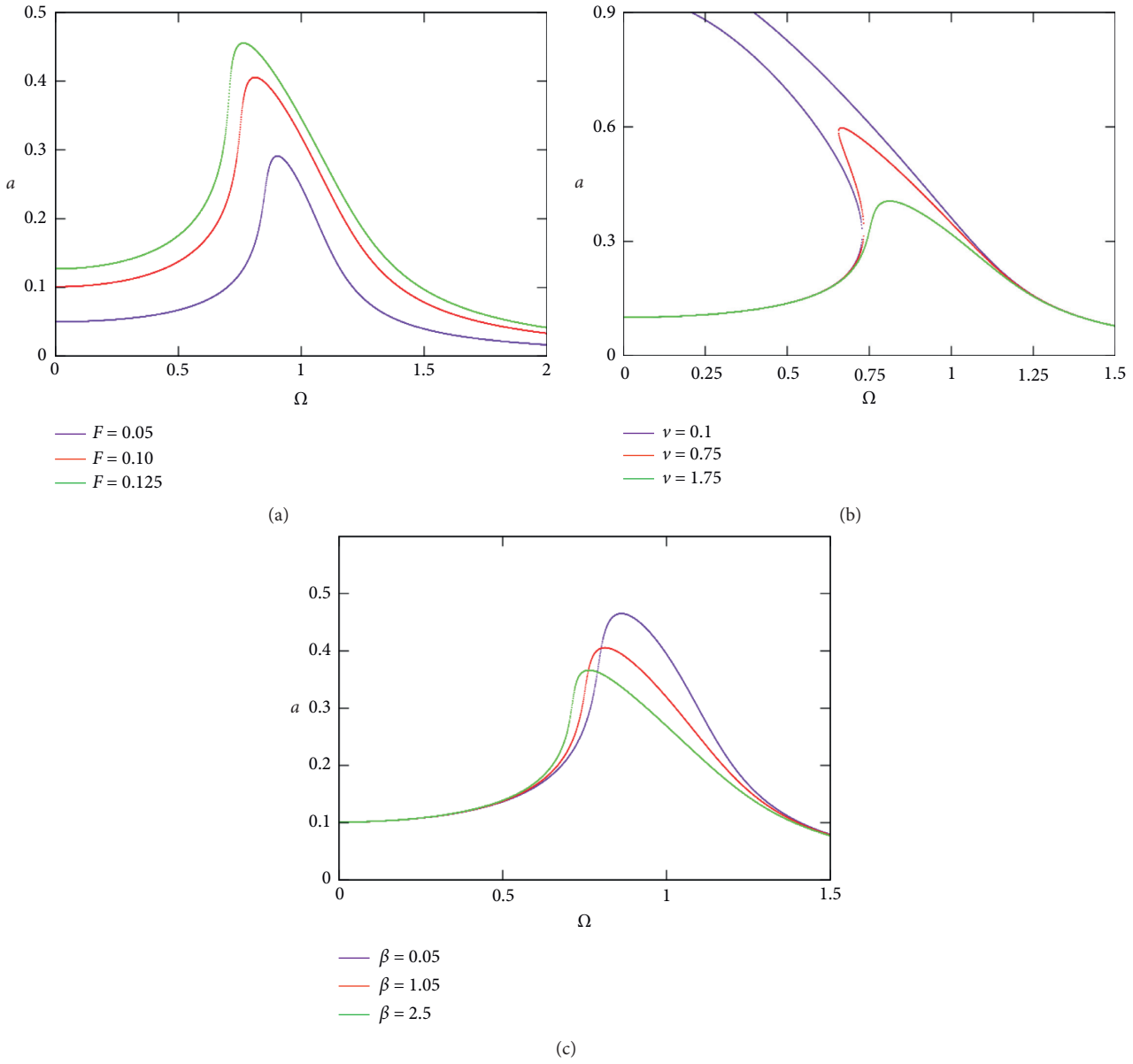

FIGURE 2: Variation curve of the amplitude a as a function of the excitation frequency with $\mu = 0.05$: (a) effect of F, (b) effect of ν, and (c) effect of β.

$$x = a\cos(\Omega\tau + \phi), \tag{12}$$

with $|J| \ll |a|$ and $J^n = 0$ for $(n \geq 2)$. By inserting equation (12) into equation (8), after some mathematical manipulations, we obtain the following expression verified by the amplitude of the harmonic oscillations:

$$\left[\mu a\Omega + \frac{1}{2}\nu\Omega a^3\left(\beta\Omega^2 + 1\right)\right]^2 + \left[-a + a^3\left(\beta\Omega^2 + 1\right) + a\Omega^2\right]^2 = F^2. \tag{13}$$

Before studying the influence of each parameter on the amplitude of the oscillations obtained, we compared the analytical result (equation (13)) to the numerical result by representing in Figure 1 the amplitude a as a function of the external frequency Ω. The basic values of the parameters used here and throughout this work are those used in the literature [9, 14]. We note a coherence between these two results which shows that the system has a nonlinear resonance. Figure 2 shows the effects of the amplitude F of the external force (Figure 2(a)), the coefficient ν of the hybrid quadratic damping term (Figure 2(b)), and the coefficient β of the pure quadratic damping term (Figure 2(c)). Through these figures, we note the presence of stable and unstable amplitudes whose domains of existence are strongly influenced by F, β, and ν. We also note that the amplitude and the frequency of the resonance and the bandwidth lag are strongly influenced by these parameters. Precisely, the amplitude of the response increases with F unlike β and ν. The resonance frequency decreases with the increase of the

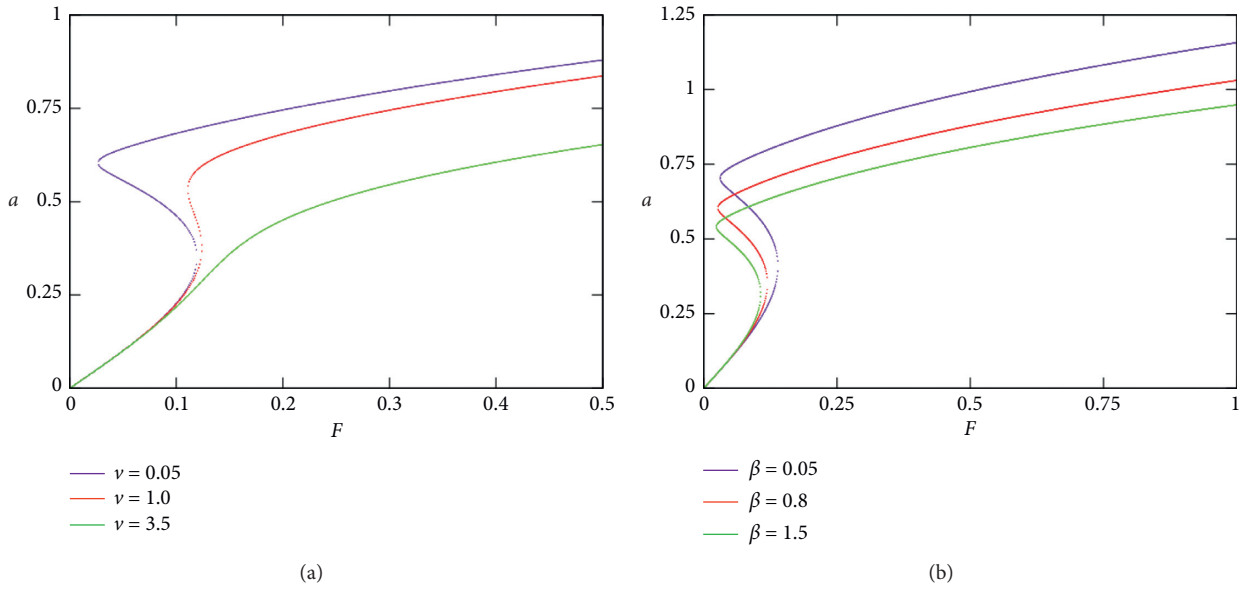

Figure 3: Hysteresis curve giving the variation of a function of F with $\mu = 0.05$ and $\Omega = 0.7$: (a) effect of ν and (b) effect of β.

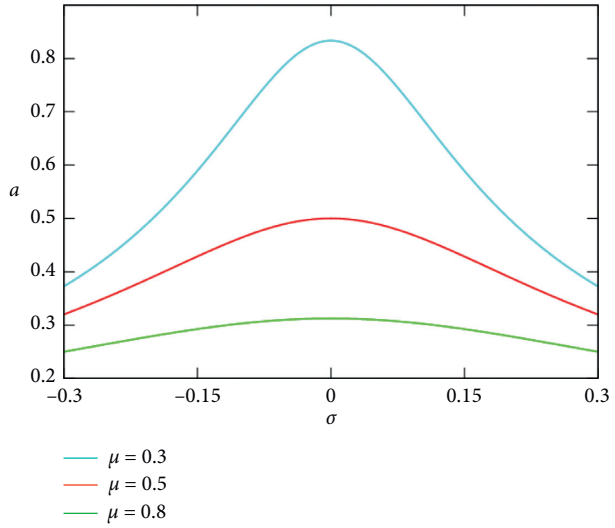

Figure 4: Curve of the variation of a as a function of σ for the primary resonance.

parameters F and β, while it increases with ν. We also notice through Figure 2(b) that the resonance is achieved at infinity if $\nu \leq 0.1$ for fixed values of F and β. On the contrary, a system which undergoes a phenomenon of hysteresis can be considered as a memory system. This application is widely explored in engineering and technology. It is for this reason that the hysteresis and the amplitude jump are studied. Indeed, Figure 3 gives the variation of the amplitude a of the oscillations according to the amplitude F of the external excitation. From this figure, the phenomena of hysteresis and amplitude jump are observed and are influenced by the parameters of the system of which the most important are those of ν and β. During amplitude jump and hysteresis phenomenon processes, for any values of external excitation F, three different amplitudes of oscillations are obtained, among which two are stable and one is unstable (see the curve in red in Figure 3(a), for example). Also, note that the parameter ν can facilitate the appearance as well as the disappearance of each of these two phenomena and therefore will allow them to be controlled. In short, the harmonic oscillations of the system can be accompanied by phenomena of nonlinear resonance, amplitude jump, and hysteresis which are very common and are searched for in memory systems.

4. Primary and Secondary Resonances

In order to analyze the primary and secondary resonances, we use the multiple time-scale method; the solution of equation (8) can be expressed in the following form [18–20]:

$$x(\tau, \varepsilon) = x_0(T_0, T_1) + \varepsilon x_1(T_0, T_1) + \cdots, \quad (14)$$

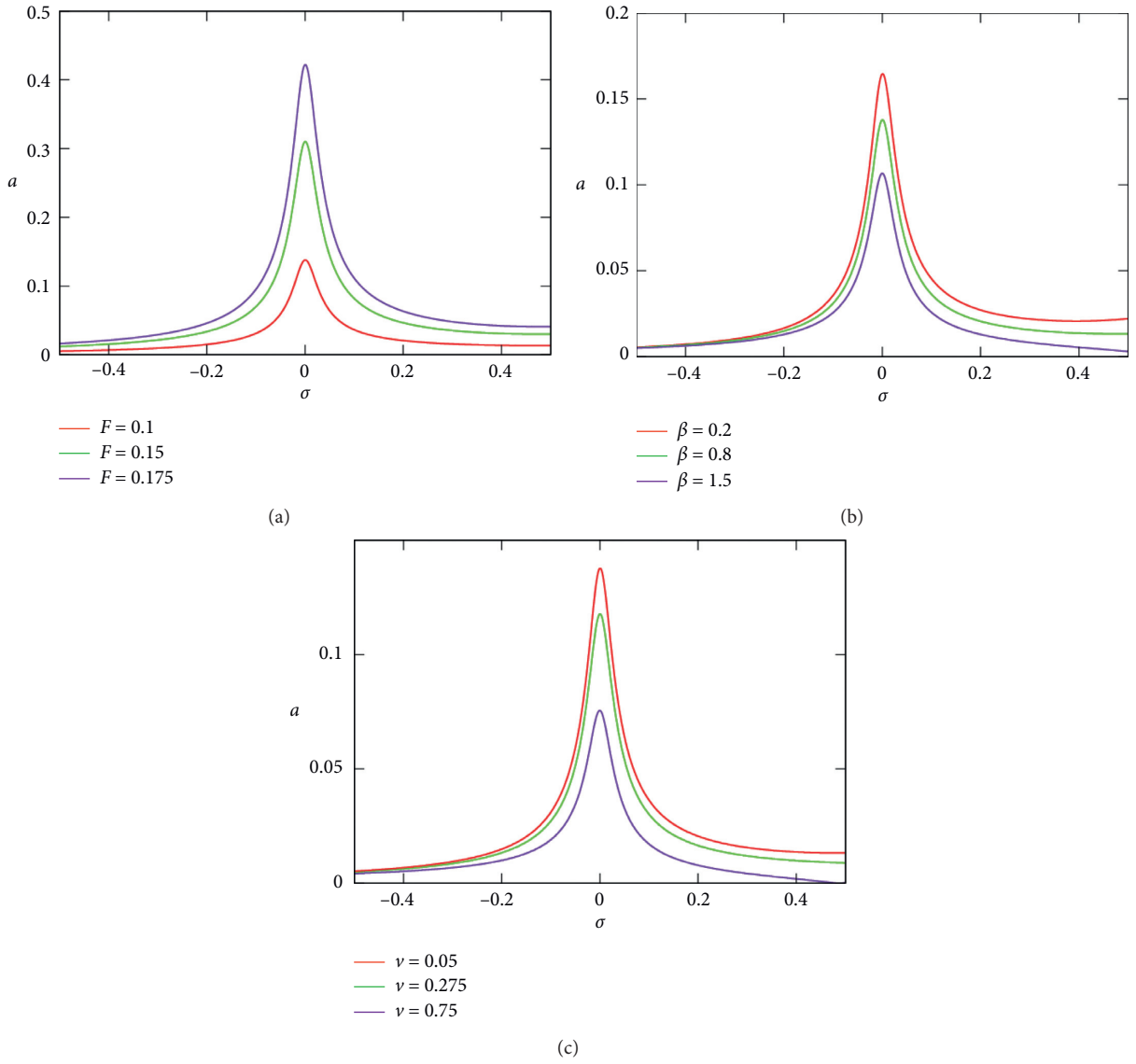

Figure 5: Curve of the variation of a as a function of σ for superharmonic order resonance 2 with $\mu = 0.05$: (a) effect of F, (b) effect of β, and (c) effect of ν.

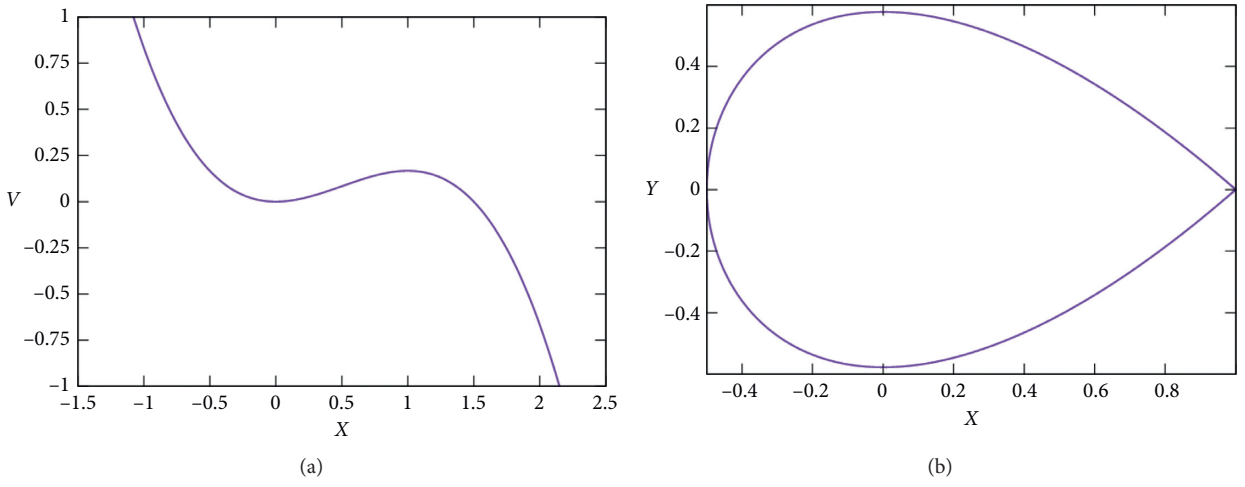

Figure 6: (a) Potential $V(x)$ and (b) homoclinic orbits.

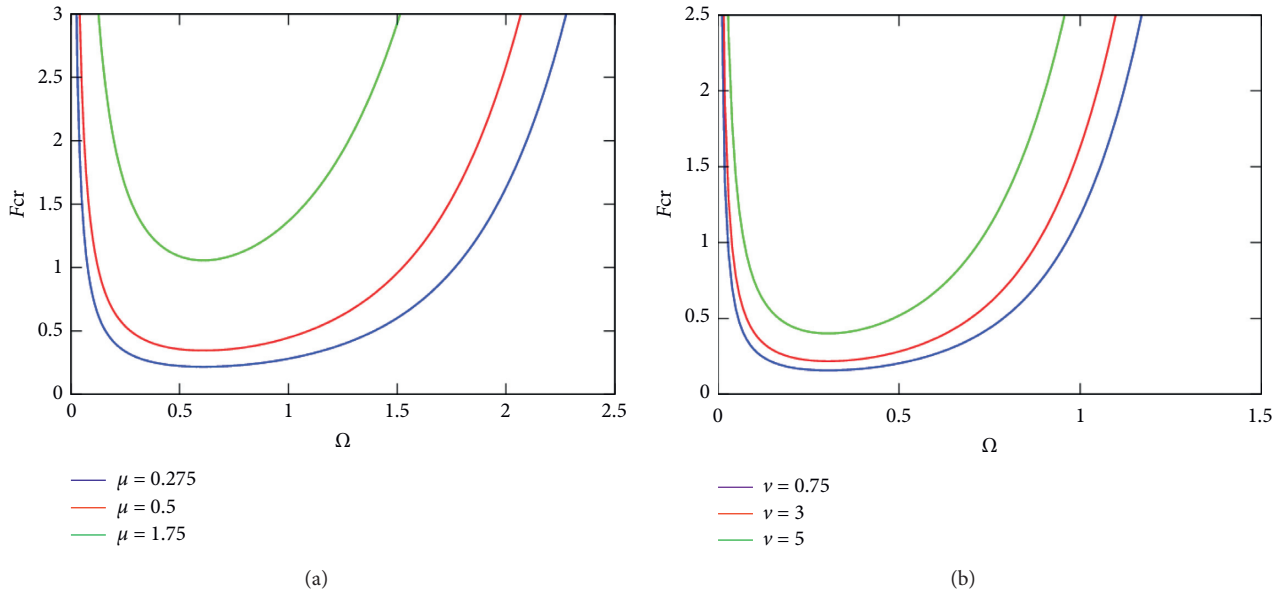

Figure 7: Variation curve of F_{cr} as a function of Ω for the Melnikov chaos: (a) effect of μ and (b) effect of ν.

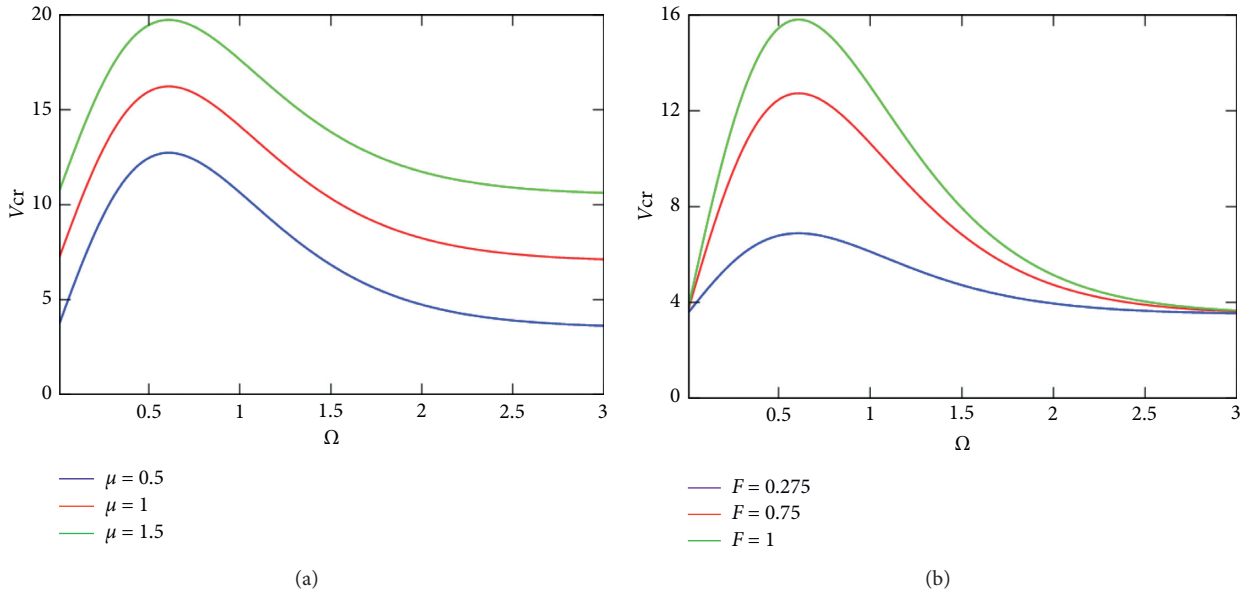

Figure 8: Variation curve of ν_{cr} as a function of Ω for the Melnikov chaos: (a) effect of μ and (b) effect of F.

where $T_0 = \tau$, $T_1 = \varepsilon\tau$, and ε is the small pertubative parameter. The time derivatives transform into

$$\frac{d}{d\tau} = D_0 + \varepsilon D_1 + \cdots, \tag{15}$$

$$\frac{d^2}{d\tau^2} = D_0^2 + 2\varepsilon D_0 D_1 + \cdots, \tag{16}$$

where $D_0 \equiv \partial/\partial T_0$ and $D_1 \equiv \partial/\partial T_1$.

4.1. Primary Resonance. To search for the primary resonance, we disturb all the nonlinear terms and that of the external excitation, and we use formulas (14)–(16). We obtain

$$D_0^2 x_0 + \varepsilon\left(D_0^2 x_1 + 2D_0 D_1 x_0\right) + x_0 + \varepsilon x_1 - \varepsilon x_0^2 + \varepsilon\mu D_0 x_0 - \varepsilon\beta\left(D_0 x_0\right)^2 + \varepsilon\nu x_0 D_0 x_0 = \varepsilon F\cos\Omega\tau. \tag{17}$$

By identification, we get the following.
For ε^0,

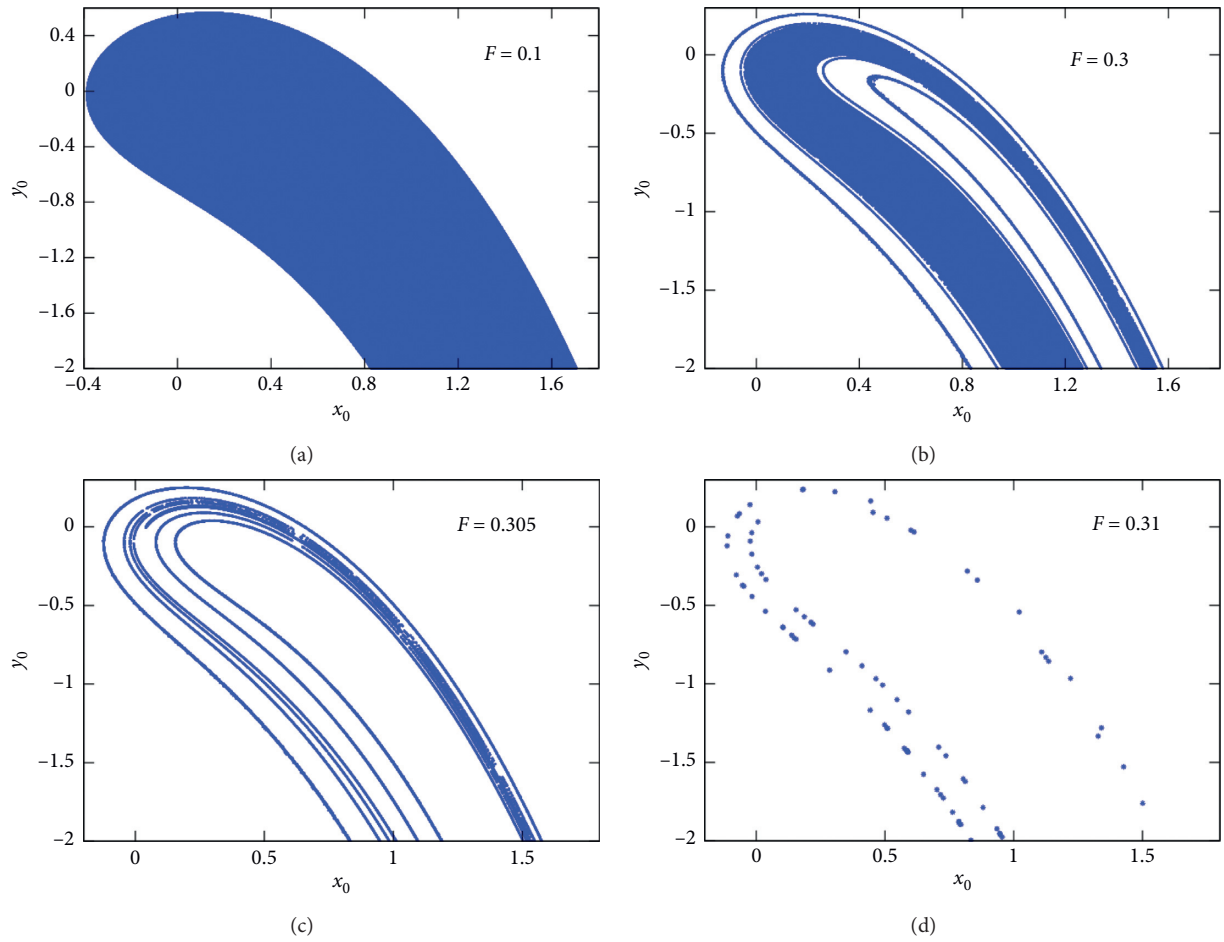

Figure 9: Effect of F on the basin of attraction with $\Omega = 0.297$ and other parameters of Figure 7.

$$D_0^2 x_0 + x_0 = 0. \tag{18}$$

For ε^1,

$$D_0^2 x_1 + x_1 = -2D_0 D_1 x_0 + x_0^2 - \mu D_0 x_0 - \beta (D_0 x_0)^2 - \nu x_0 D_0 x_0 + F\cos\Omega\tau. \tag{19}$$

A solution of equation (18) is

$$x_0 = A(T_1)e^{jT_0} + A^*(T_1)e^{-jT_0}. \tag{20}$$

Inserting equation (20) into equation (19), we obtain

$$(D_0 x_0)^2 = 2AA^* - A^2(T_1)e^{2jT_0} + A^{*2}(T_1)e^{-2jT_0}. \tag{21}$$

The primary resonance appears when $\Omega = 1 + \varepsilon\sigma$, σ is the detuning parameter. So, we have

$$D_0^2 x_1 + x_1 = -2j\frac{dA}{dT_1} - j\mu A - \frac{F}{2}e^{j\sigma T_1} = 0. \tag{22}$$

We take the polar form of A:

$$A = \frac{a}{2}e^{j\theta}, \tag{23}$$

and we put in equation (22). After some mathematical transformations, we obtain

$$a\sigma - ab' = \frac{F}{2}\cos b, \tag{24}$$

$$-a' - \frac{1}{2}\mu a = \frac{F}{2}\sin b, \tag{25}$$

where $b = \sigma T_1 - \theta$. By searching for steady-state solutions, we get

$$(a\sigma)^2 + \left(\frac{1}{2}\mu a\right)^2 = \left(\frac{F}{2}\right)^2. \tag{26}$$

Equation (26) represents the primary resonance equation. Let us now study the stability of the amplitudes of oscillations by posing $a = a_0 + a_1$ and $b = b_0 + b_1$, where (a_0, b_0) is the nontrivial solution and (a_1, b_1) is assumed to be infinite. So,

$$a_1' = -\frac{1}{2}\mu a_1 - \frac{F}{2}b_1\cos b_0,$$
$$b_1' = \frac{F}{2a_0^2}a_1\cos b_0 + \frac{F}{2a_0}b_1\sin b_0. \tag{27}$$

It follows from the calculations that the amplitudes of oscillations are stable if $\mu > 0$ and $\sigma^2 + (\mu^2/4) > 0$. Either the amplitudes of the oscillations are stable for $\mu > 0$ and

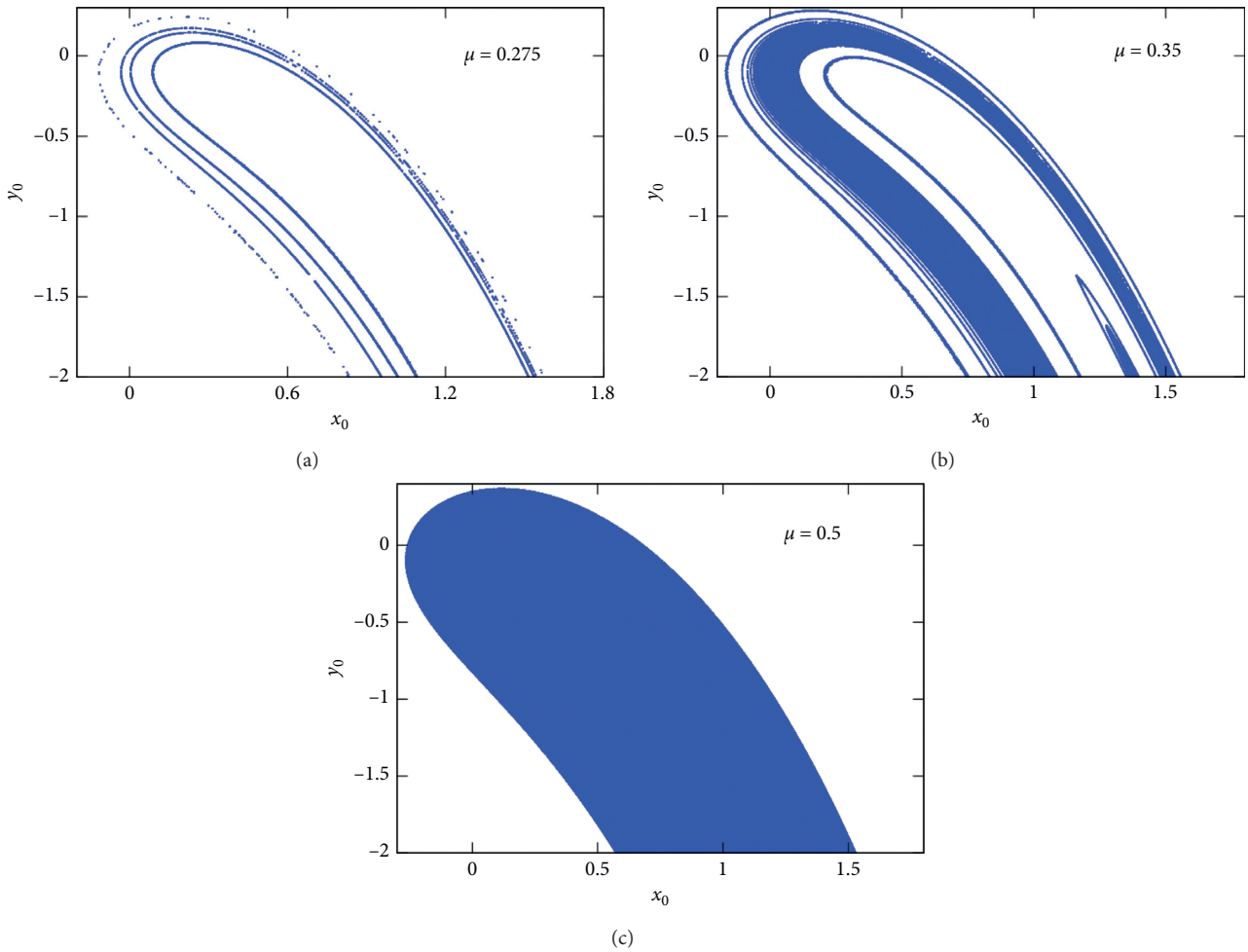

Figure 10: Effect of μ on the basin of attraction with $\Omega = 0.297$, $F = 0.308$, and other parameters of Figure 7.

unstable if $\mu < 0$. Figure 4 shows that when the linear dissipation increases, the amplitude of the response decreases considerably, and the resonance disappears.

4.2. Secondary Resonance. For this case, all the terms of nonlinearity are disturbed apart from the term of external force. So, using formulas (14)–(16), we get the following.

For ε^0,

$$D_0^2 x_0 + x_0 = F\cos\Omega\tau. \tag{28}$$

For ε^1,

$$D_0^2 x_1 + x_1 = -2D_0D_1x_0 + x_0^2 - \mu D_0 x_0 - \beta\left(D_0x_0\right)^2 - \nu x_0 D_0 x_0. \tag{29}$$

A solution of equation (28) is

$$x_0 = A\left(T_1\right)e^{jT_0} + A^*\left(T_1\right)e^{-jT_0} + Be^{j\Omega T_0} + Be^{-j\Omega T_0}, \tag{30}$$

with

$$B = \frac{F}{2\left(1-\Omega^2\right)}. \tag{31}$$

Replacing equation (30) in equation (29), one has

$$2j\frac{dA}{dT_1}e^{jT_0} + j\mu Ae^{jT_0} + \left(-B^2 + \beta B^2\Omega^2 + \nu B^2\Omega\right)e^{2j\Omega T_0} + \left(-2A^*B - \beta\Omega A^*\Omega + \nu A^*\mathrm{B}\right)e^{j(\Omega-1)T_0} + \mathrm{NST} + \mathrm{c.c.} = 0, \tag{32}$$

where NST denotes the nonsecular terms and c.c. denotes the conjugate complexes. By analyzing equation (32), we note that the system has a superharmonic resonance of order 2 and a subharmonic resonance of order 2. After studying, we noted that the superharmonic resonance of order 2 is important and therefore is the only one presented in this work.

Indeed, there is a superharmonic resonance if $2\Omega = 1 + \varepsilon\sigma$. After treatment of equation (32), by considering the secular terms, we obtain

$$2j\frac{dA}{dT_1}e^{jT_0} + j\mu Ae^{jT_0} + \left(-B^2 + \beta B^2\Omega^2 + \nu B^2\Omega\right)e^{j(1+\varepsilon\sigma)T_0}. \tag{33}$$

By inserting the polar form of A,

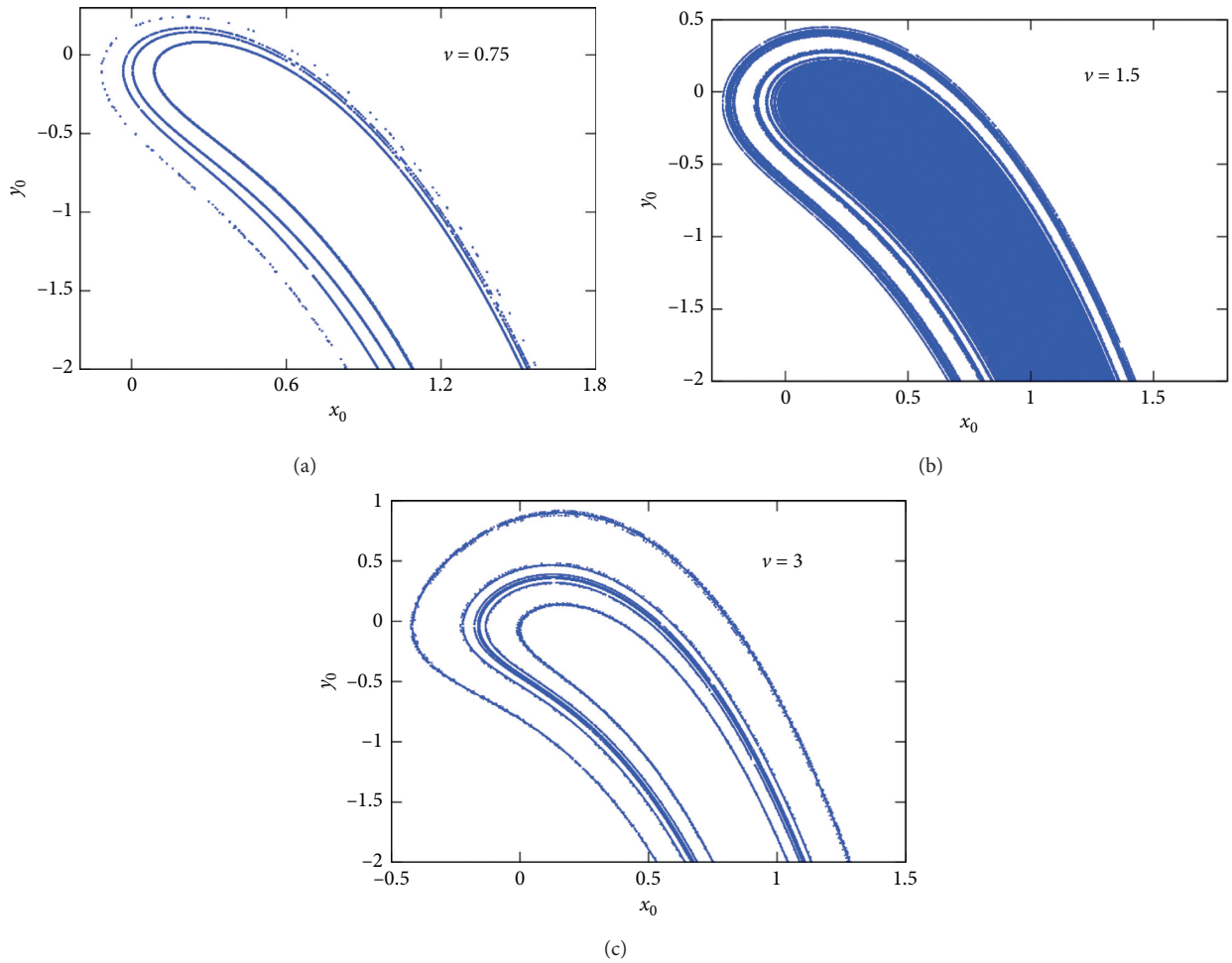

Figure 11: Effect of ν on the basin of attraction with $\Omega = 0.297$, $F = 0.308$, and other parameters of Figure 7.

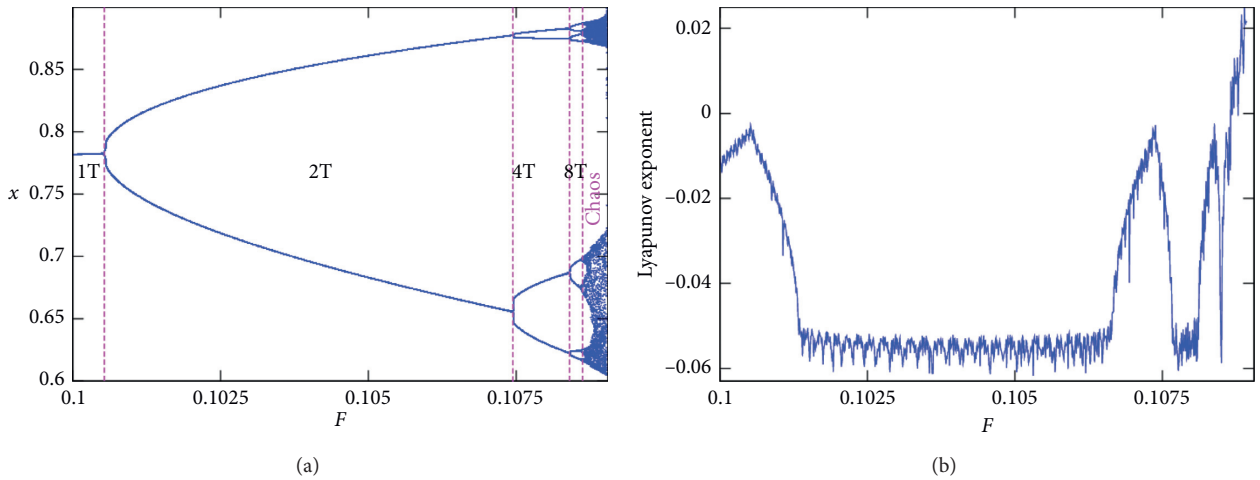

Figure 12: Bifurcation diagram and its corresponding Lyapunov exponent curve of a quadratic-damping Helmholtz oscillator versus F with $\mu = 0.01$, $\Omega = 0.85$, and $\nu = \beta = 0$.

$$A = \frac{a}{2} e^{j\theta(T_1)}, \tag{34}$$

in equation (33) and by canceling the real and imaginary parts, we have

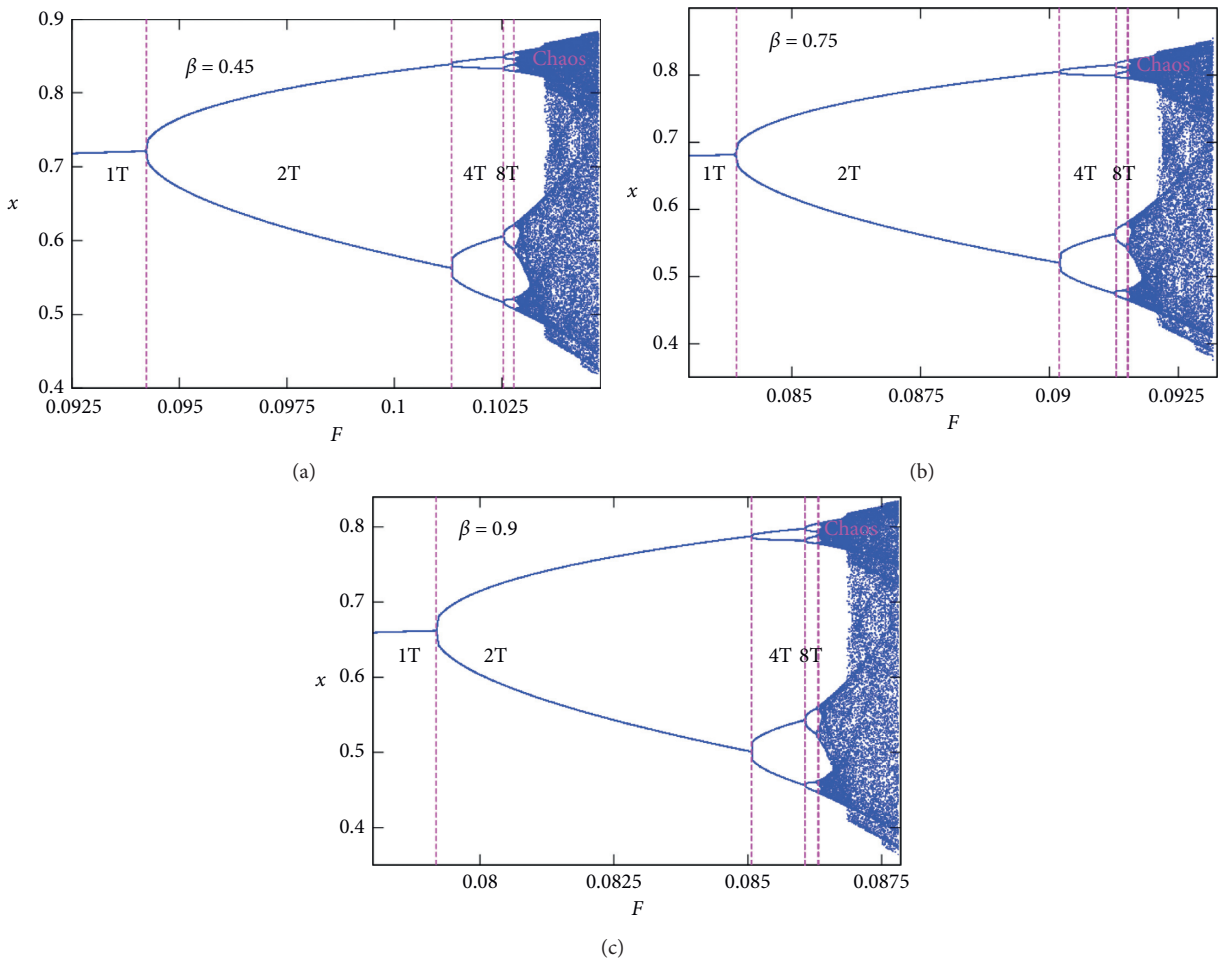

Figure 13: Effect of parameter β on the bifurcation diagram of a quadratic-damping Helmholtz oscillator versus F with $\mu = 0.1$ and $\Omega = 0.85$.

$$\frac{da}{dT_1} + \frac{1}{2}\mu a + \left(-B^2 + \beta B^2\Omega^2 + \nu B^2\Omega\right)\sin\phi = 0,$$
$$a\frac{d\phi}{dT_1} - \sigma a + \left(-B^2 + \beta B^2\Omega^2 + \nu B^2\Omega\right)\cos\phi = 0, \tag{35}$$

where $\phi = \sigma T_1 - \theta$. When looking for solutions of stationary state, the equation of the superharmonic resonance is

$$\left(\frac{1}{2}\mu a\right)^2 + (\sigma a)^2 = \left[\left(-1 + \beta\Omega^2 + \nu\Omega\right)B^2\right]^2. \tag{36}$$

Now, we study the stability of the resonance amplitudes by posing $a = a_0 + a_1$ and $\phi = \phi_0 + \phi_1$, where (a_0, ϕ_0) is the nontrivial solution and (a_1, ϕ_1) is supposed infinite perturbations; we obtain

$$a_1' = -\frac{1}{2}\mu a_1 - P\phi_1\cos\phi_0,$$
$$\phi_1' = \frac{P}{2a_0^2}a_1\cos\phi_0 + \frac{P}{a_0}\phi_1\sin\phi_0, \tag{37}$$

where $P = -B^2 + \beta B^2\Omega^2 + \nu B^2\Omega$.

By taking the characteristic equation of the Jacobian matrix of the previous system and then using the Routh–Hurwitz criterion, we conclude that the amplitudes of oscillations are stable if $\mu > 0$. Figure 5 represents the effects of the parameters F (see Figure 5(a)), β(see Figure 5(b)), and ν (see Figure 5(c)) on the superharmonic resonance obtained for $\mu > 0$.

Whatever the values of these parameters, we effectively note that the amplitudes of the oscillations are stable, and the superharmonic resonance of order 2 is stable because the amplitudes of resonance correspond to the same frequency of resonance. In addition, we notice that the amplitude of resonance increases with the parameters F and δ, while it decreases with the parameters β and ν of quadratic depreciation. Precisely, the superharmonic resonance of order 2 is accentuated when F and δ increase and disappears with β and ν.

5. Horseshoe Chaos

In this section, we analytically determine Smale's horseshoe chaos by Melnikov's method, and then we verify the results numerically by representing the basin of attraction of the

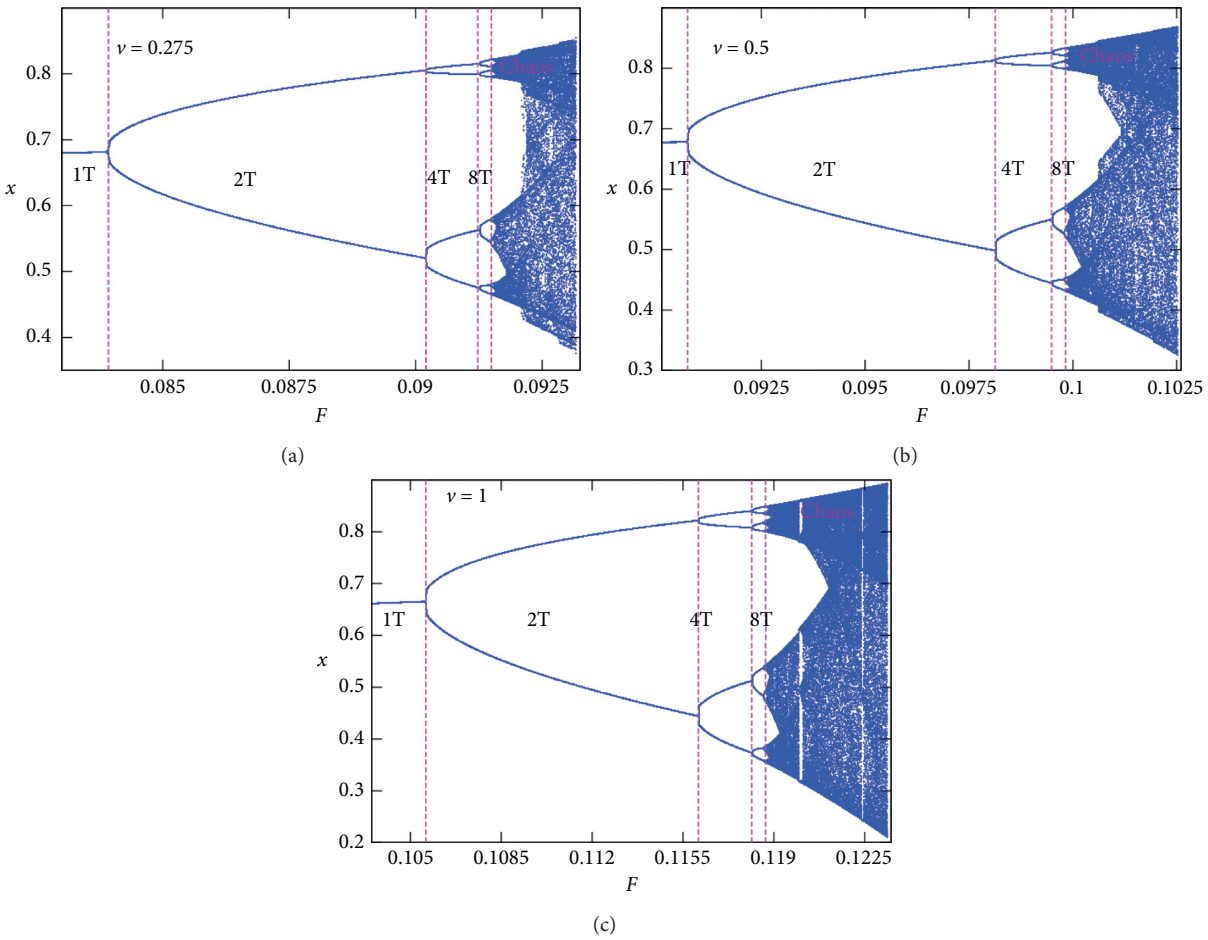

Figure 14: Effect of parameter ν on the bifurcation diagram of a quadratic-damping Helmholtz oscillator versus F with $\mu = 0.1$ and $\Omega = 0.85$.

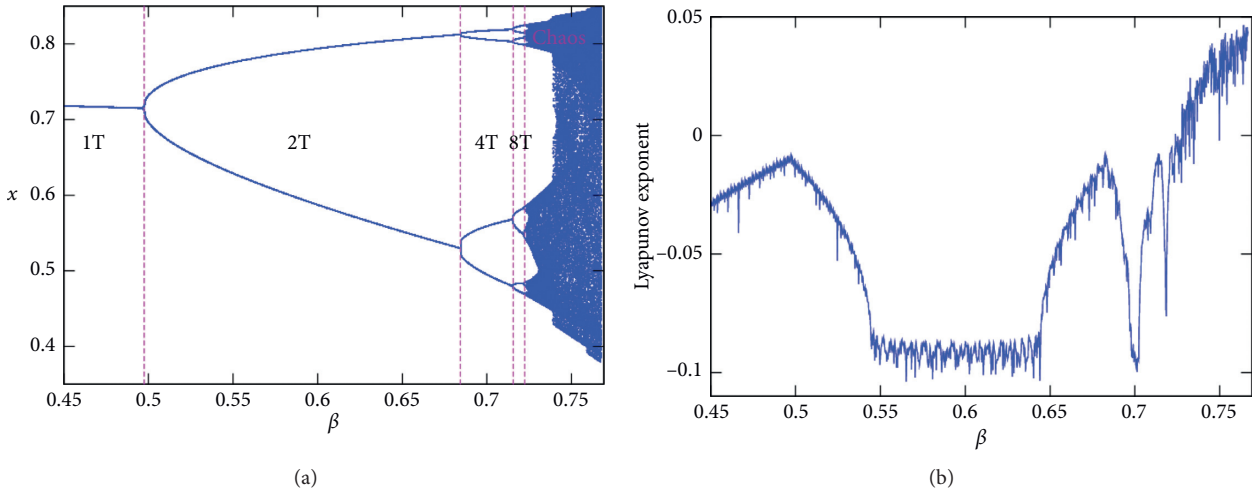

Figure 15: Bifurcation diagram and its corresponding Lyapunov exponent curve of a quadratic-damping Helmholtz oscillator versus β with $\mu = 0.01$, $\Omega = 0.85$, $\nu = 0.275$, and $F = 0.0925$.

system. The unperturbed system of equation (8) can be written as follows:

$$\begin{aligned} \dot{x} &= y, \\ \dot{y} &= x - x^2. \end{aligned} \tag{38}$$

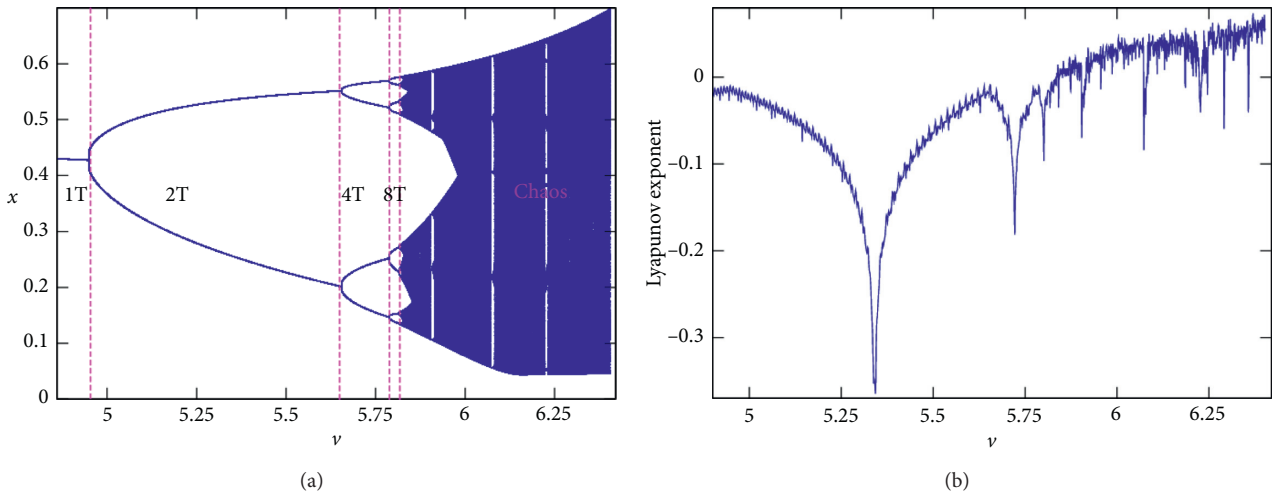

FIGURE 16: Bifurcation diagram and its corresponding Lyapunov exponent curve of a quadratic-damping Helmholtz oscillator versus ν with $\mu = 0.1$, $\Omega = 0.85$, $\beta = 0.75$, and $F = 0.0925$.

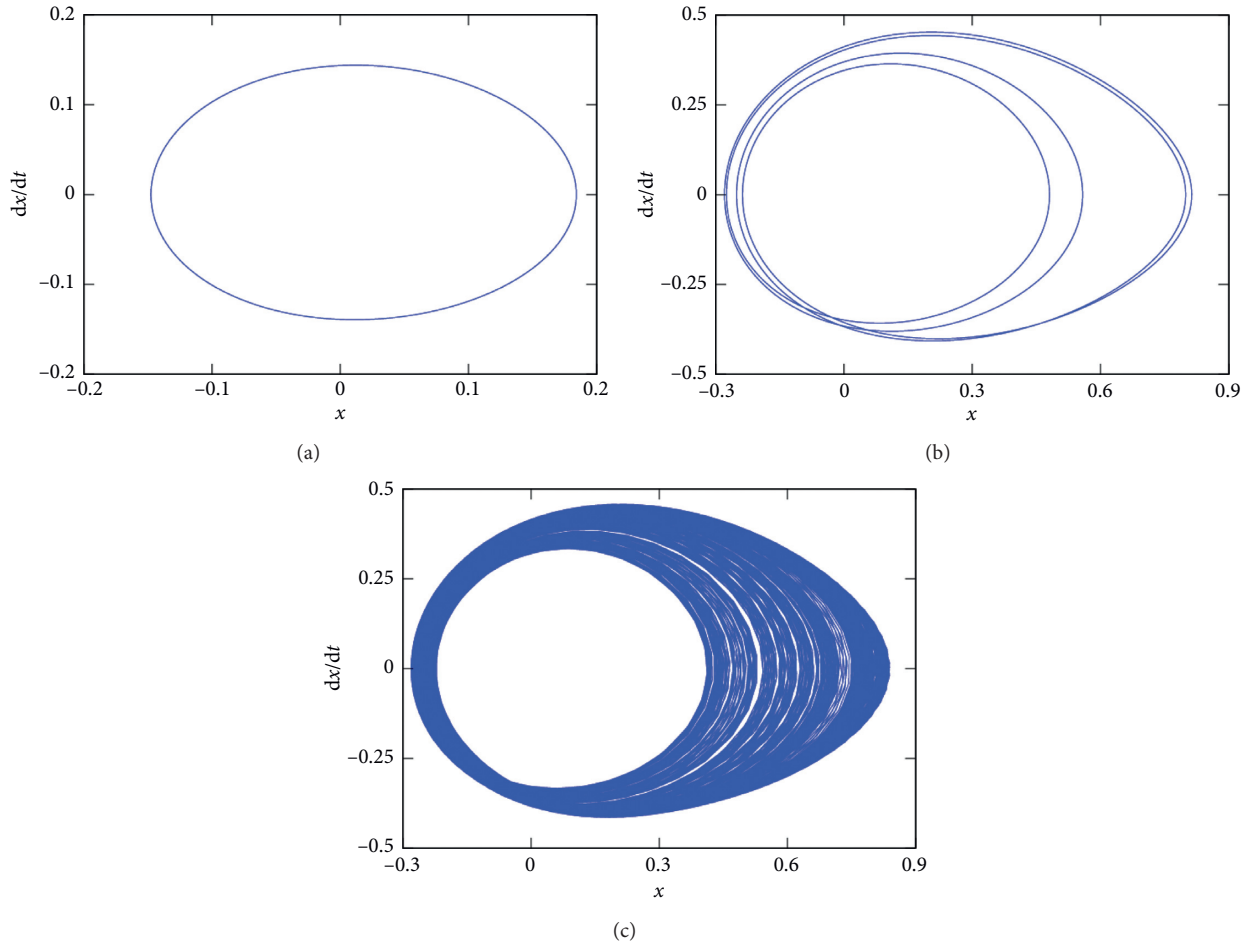

FIGURE 17: Various phase portraits with parameters of Figure 13(b): (a) $F = 0.0425$; (b) $F = 0.091$; (c) $F = 0.0925$.

The potential of the system is defined by

$$V(x) = \frac{1}{2}x^2 - \frac{1}{3}x^3. \tag{39}$$

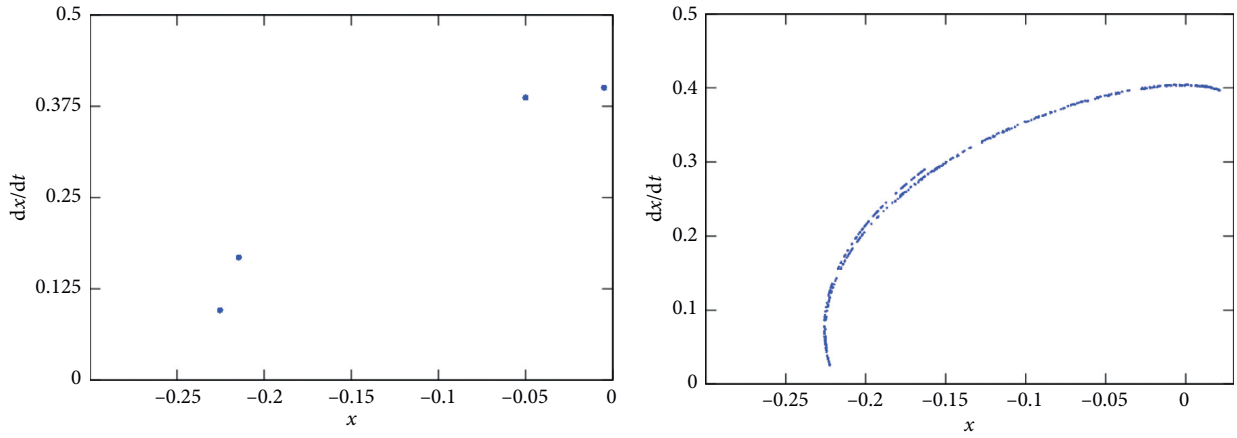

Figure 18: Poincaré section with parameters of Figure 13(b): (a) $F = 0.091$; (b) $F = 0.0925$.

The unperturbed system is Hamiltonian, and associated Hamiltonian is

$$H(x, y) = \frac{1}{2}y^2 + \frac{1}{2}x^2 - \frac{1}{3}x^3. \tag{40}$$

The homoclinical orbits which connect the fixed points of undisturbed system (38) correspond to zero Hamiltonian. By solving the equation $H(x; y) = 0$, we get

$$\begin{aligned} x_h &= 1 - \frac{3}{1 + \cosh\tau}, \\ y_h &= \frac{3\sinh\tau}{[1 + \cosh\tau]^2}. \end{aligned} \tag{41}$$

Figure 6 presents the potential (Figure 6(a)) and homoclinic orbits (Figure 6(b)). It is noted that the potential is a single well and a single hump.

To determine the Melnikov criterion, we put equation (8) in the form

$$\begin{aligned} \dot{x} &= y, \\ \dot{y} &= F\cos\Omega\tau - x + x^2 - \mu y + \beta y^2 - \nu x y. \end{aligned} \tag{42}$$

By definition, the integral of Melnikov is given by [21–25]

$$M(\tau_0) = \int_{-\infty}^{+\infty} f(x_h, y_h) \wedge g(x_h, y_h)\mathrm{d}t, \tag{43}$$

where $f\begin{pmatrix} y \\ -x + x^2 \end{pmatrix}$ and $g\begin{pmatrix} 0 \\ F\cos\Omega\tau - \mu y + \beta y^2 - \nu x y \end{pmatrix}$.

The Melnikov integral becomes

$$M(\tau_0) = \int_{-\infty}^{+\infty} \left(F y_h \cos\Omega\tau - \mu y_h^2 + \beta y_h^3 - \nu x_h y_h^2\right)\mathrm{d}\tau. \tag{44}$$

Replacing equation (41) in equation (44), we compute the integral of Melnikov, and we get

$$M(\tau_0) = -\frac{6\pi\Omega^2 F}{\sinh(\Omega\pi)}\sin(\Omega\tau_0) - \frac{6\mu}{5} - \frac{6\nu}{35}. \tag{45}$$

If $M(\tau_0) = 0$ and $\mathrm{d}M/\mathrm{d}\tau_0 \neq 0$ for some τ_0 and some sets of parameters, then horseshoes exist, and chaos occurs [21–25]. Using this Melnikov criterion for the appearance of the intersection between the perturbed and unperturbed separatrixes, it is found that chaos appears when the following condition is satisfied:

$$F \geq F_{\mathrm{cr}} = \left|\frac{B}{A}\right|, \tag{46}$$

where $A = 6\pi\Omega^2/\sinh(\Omega\pi)$ and $B = -(6\mu/5 + 6\nu/35)$.

The critical value of ν for which Melnikov's chaos appears is

$$\nu_{cr} = \left|-7\mu - \frac{35\pi\Omega^2 F}{\sinh(\Omega\pi)}\right|. \tag{47}$$

Figure 7 represents the variation of the amplitude of the external excitation according to the frequency. In this figure, the domain located below the curve (F_{cr},Ω) indicates the domain where the Helmholtz oscillator with quadratic damping has a regular behavior, and above this curve, the oscillator has a chaotic behavior. From the analysis of Figure 7, it appears that the domain of the existence of chaotic behavior of the oscillator studied decreases with μ and ν. Precisely, the critical value F_{cr} for the appearance of Smale's horseshoe chaos increases with μ and ν. For example, with $\Omega = 0.297$ and Figure 7(a), the chaotic domain corresponds to $F_{\mathrm{cr}} = 0.2$, $F_{\mathrm{cr}} = 0.34$, and $F_{\mathrm{cr}} = 1.04$ for $\mu = 0.275$, $\mu = 0.5$, and $\mu = 1.75$, respectively, and $F_{\mathrm{cr}} = 0.14$, $F_{\mathrm{cr}} = 0.20$, and $F_{\mathrm{cr}} = 0.38$ for $\nu = 0.75$, $\nu = 3$, and $\nu = 5$ (see Figure 7(b)). Then, we represent in Figure 8 the curve (νcr, Ω). We observe through this figure that the domain of the existence of chaotic behavior decreases when each of the parameters μ and F increases. This remark confirms the result of Figure 7(c). In conclusion, the depreciation favors the appearance of the chaos of Melnikov, while the latter is favored by the quadratic force of stiffness. Now, we are going to verify these different results by numerical simulations. Indeed, a better tool to test the validity of the proposed analytical predictions is to investigate numerically the regular

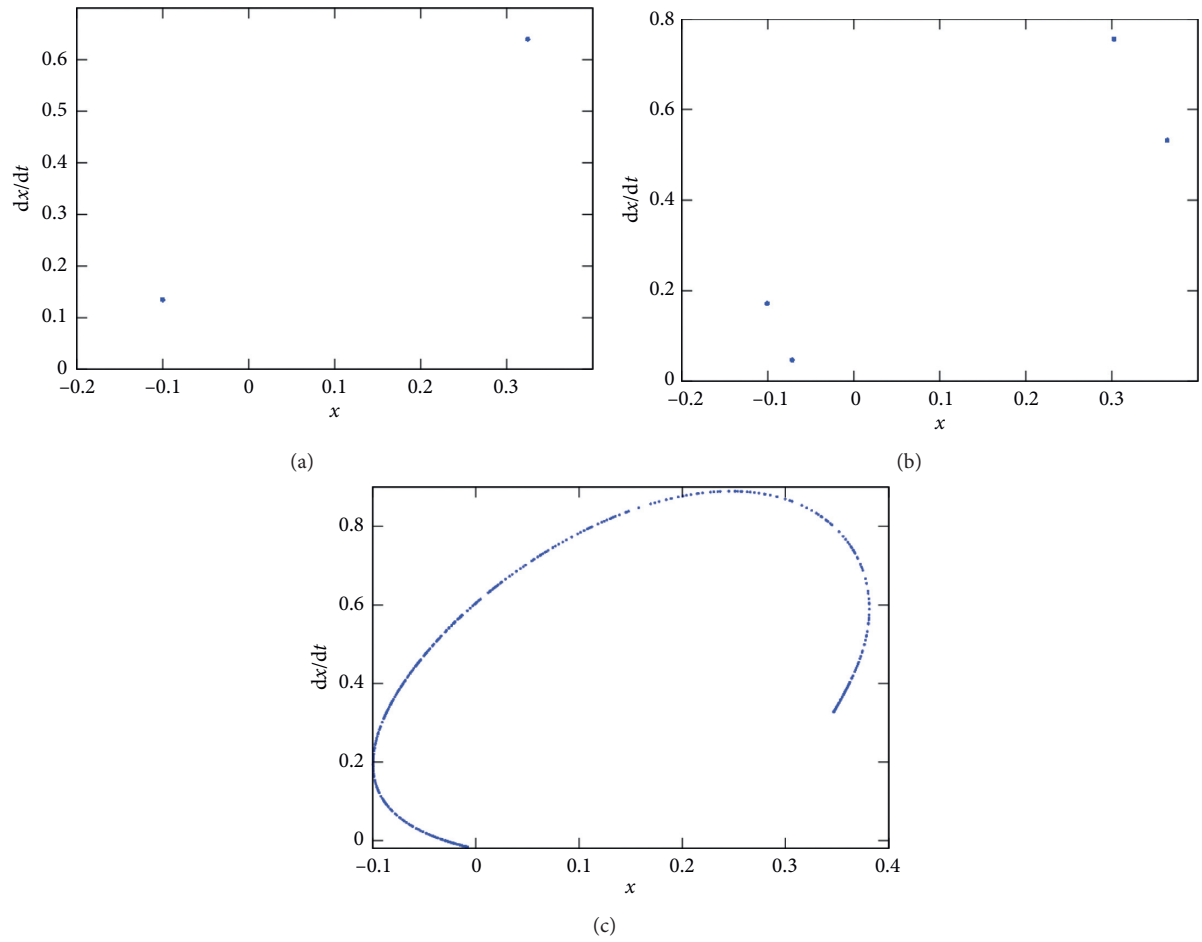

Figure 19: Effect of ν on the Poincaré section with parameters of Figure 16: (a)$\nu = 5.5$; (b)$\nu = 5.75$; (c)$\nu = 6$.

and irregular (fractal) shape of the basins of attraction. The basins are plotted by scanning the initial values x_0 and y_0 of x and y domains, solving numerically differential equation (42) and collecting the initial conditions which attracted the dynamics in the single well of the potential. From the Melnikov critical curve (Figure 7), the results obtained after the numerical simulations are recorded in Figures 9–11 , respectively, which denote the effect of F, μ, and ν. From these different figures, we note that Melnikov's critical value from which Smale's horseshoe chaos appear is confirmed and also that the effects of μ and ν are confirmed. For example, for $F < F_{cr}$, the basin of attraction of the system is smooth thus showing the regular behavior (Figure 9(a)), while for $F > F_{cr}$, the basin becomes eroded (Figures 9(b) and 9(c)) thus proving the presence of Smale's horseshoe chaos. From Figure 10, we observe that the Melnikov critical value increases with μ, and the limits of the basin of attraction become more and more smooth. Finally, we have the same remark for the effect of ν.

6. Bifurcation and Transition to Chaos

In this section, we do numerical simulations to look for transition to dissipative chaos. To do this, the bifurcation diagram, the Lyapunov exponent, the phase portrait, and the Poincaré section are plotted by a direct integration of equation (8) using the fourth-order Runge–Kutta algorithm. Indeed, we analyze the dynamics of the system by taking $\nu = 0$, $\mu = 0$, and $\omega = 0.85$ (these values are the basic values of the parameters used in the literature [9–14]) with the initial condition ($x_0 = 0.2$, $y_0 = 0.2$), and the results obtained are plotted in Figure 12. From this figure, showing a perfect agreement between the bifurcation diagram and its corresponding Lyapunov exponent, we note that the system oscillates when $0 \leq F \leq 0.109$ with rich dynamics. More precisely, if $0 \leq F \leq 0.10085$, the oscillations of the system are periodical, 1T; for $0.10085 < F \leq 0.1075$, there is a doubling of period, and the oscillations become of period −2T. From $0.1075 < F \leq 0.1084$, the dynamics of the system become of period −4T and thereafter pass a behavior period −nT and then become chaotic when $0.10882 \leq F \leq 0.109$. Figures 13 and 14 represent the effects of the pure quadratic parameter β and hybrid quadratic parameter ν of damping, respectively, on the dynamics of the system. Two important observations on the domain of oscillations, in general, and on the domain of chaotic behavior, in particular, are to emerge from the analysis of figures.

Precisely, we observe a phenomenon of successive doubling of period leading to chaos, different domains of which are indicated on the bifurcation diagrams. In other

words, the system passes successively from oscillations of period 1T, 2T, 4T, 8T, and nT to chaotic oscillations. Indeed, increasing the parameter β reduces the oscillation domain of the system but does not have a perceptible effect on the chaotic behavior of the latter (Figure 13).

From Figure 14, we note that the domain of oscillation of the system and that of chaotic behavior increase with the parameter ν. We can therefore note that the parameters β and ν do not act on the system in the same way, and we can therefore use them to control the oscillation domain of the modified Helmholtz oscillator studied and the domain in which the latter possesses chaotic behavior. Finally, Figures 15 and 16 represent the bifurcation diagram and its corresponding Lyapunov exponent with β and ν as control parameters, respectively. These figures show a perfect agreement between the two diagrams and prove that the chaotic behavior is actually favored by the parameter ν. By taking values of F in the appropriate values of each of the behaviors predicted by the bifurcation diagram in Figure 13(b), we obtained the phase portraits and the Poincaré sections of Figures 17 and 18, respectively. We note that the system has a periodic behavior of period −1T for $F = 0.0425$, a multiperiodic behavior of period −4T for $F = 0.091$, and chaotic if $F = 0.0925$. These observations confirm very well the results of Figure 13. Figure 19 represents the Poincaré section of the system for values of ν chosen in different domains of behaviors given by Figure 16. We observe at this level the perfect confirmation of the periodic, multiperiodic, and chaotic behaviors of Figure 16 but also of the effect of the hybrid quadratic damping parameter on the dynamics of the modified Helmholtz oscillator.

7. Conclusions

In this work, we have studied the quadratic-damping Helmholtz oscillator which models the simple Lotka–Volterra system. The determination of the equilibrium points of the oscillator results in the latter having two fixed points, one of which may be a node or a stable focus or unstable, while the second is a saddle point. The harmonic, primary, and secondary second-order resonances are obtained from the results of treatments by the methods of harmonic balance and multiple scales. The phenomena of amplitude jump and hysteresis are also obtained. It appears that the system has two or three amplitudes for the same value of F or which do not have the same stability. This makes the behavior of the oscillator complex and gives it interesting properties and properties that can be used in memory systems. Subsequently, the Melnikov criterion is used to analytically determine Smale's horseshoe chaos. The basins of attraction are used to numerically verify the results obtained, and there is a perfect confirmation of the prediction given by the Melnikov technique. Knowing that the presence of Smale's horseshoe chaos does not exclude the presence of the dissipative chaos, we used bifurcation diagrams, Lyapunov exponents, phase portraits, and the Poincaré section to detect the road to dissipative chaos in the modified Helmholtz oscillator. It appears that the system studied can present very rich and varied behaviors such as periodic, double-periodic, multiperiodic, and chaotic behaviors. Finally, by analyzing numerically the effects of all the parameters of the system, in general, and, in particular, those of the new parameters, we have the domains of these parameters for which the oscillator vibrates and the domains of interesting behaviors. We noted that all the parameters of the system influence the frequencies and amplitudes of oscillation of the latter in the cases of resonance, amplitude jump, and hysteresis. For the road to chaos, we note that F and Ω have significant effects on the dynamics of the system, but the parameter of pure quadratic dissipation β has a less significant effect on the appearance of chaos for the system studied.

Data Availability

No data were used in this study.

Conflicts of Interest

The authors declare that they have no conflicts of interest.

References

[1] F. Bernardot, J. Bruneaux, and J. Matricon, "Un archétype d'oscillateur: le résonateur acoustique de Helmholtz," *Bulletin de l'Union des Physiciens*, vol. 96, pp. 1055–2076, 2002.

[2] A. Doelman, A. Femius Koenderink, and L. R. M. Maas, "Quasi-periodically forced nonlinear Helmholtz oscillators," *Physica D: Nonlinear Phenomena*, vol. 164, no. 1-2, pp. 1–27, 2002.

[3] F. Balibrea, R. Chacón, and M. A. López, "Reshaping-induced order-chaos routes in a damped driven Helmholtz oscillator," *Chaos, Solitons & Fractals*, vol. 24, no. 2, pp. 459–470, 2005.

[4] A. I. Komkin and A. I. Bykov, "Inertial attached neck length of Helmholtz resonators," *Acoustical Physics*, vol. 62, no. 3, pp. 269–279, 2016.

[5] T. Poston and I. N. Stewart, *Catastrophe Theory and its Applications (London: Pitman)*, 1978.

[6] M. E. Goggin and P. W. Milonni, "Driven Morse oscillator: classical chaos, quantum theory, and photodissociation," *Physical Review A*, vol. 37, no. 3, pp. 796–806, 1988.

[7] R. Chacón and J. I. Cirac, "Chaotic and regular behavior of a trapped ion interacting with a laser field," *Physical Review A*, vol. 51, no. 6, pp. 4900–4905, 1995.

[8] J. B. Buchler and H. Einchhorn, "Chaotic Phenomena in Astrophysics," *Annals of the New York Academy of Sciences*, vol. 497, 1987.

[9] J. M. T. Thompson, "Chaotic phenomena triggering the escape from a potential well," *Proceedings of the Royal Society of London*, vol. 421, pp. 195–225, 1989.

[10] J. M. T. Thompson and M. S. Soliman, "Fractal control boundaries of driven oscillators and their relevance to safe engineering design," in *Engineering Applications of Dynamics of Chaos*, W. Szemplinska-Stupnicka and H. Troger, Eds., vol. 319, International Centre for Mechanical Sciences (Courses and Lectures), Springer, Vienna, 1991.

[11] M. S. Soliman, "Basin boundaries with fractal and smooth accumulation properties in systems with single potential well," *Chaos, Solitons & Fractals*, vol. 9, no. 6, 1998.

[12] R. Irving, J. Epstein, and A. Pojman, *An Introduction to Nonlinear Chemical Dynamics: Oscillations, Waves, Patterns*

and Chaos, Oxford University Press, New York, NY, USA, 1998.

[13] J. M. T. Thompson, "Designing against capsize in beam seas: recent advances and new insights," *Applied Mechanics Reviews*, vol. 50, no. 5, pp. 307–325, 1997.

[14] C. Ainamon, S. T. Kingni, V. K. Tamba, J. B. C. Orou, and P. Woafo, "Dynamics, circuitry implementation and control of an autonomous Helmholtz Jerk oscillator," *Journal of Control, Automation and Electrical Systems*, vol. 30, no. 4, pp. 501–511, 2019.

[15] K. J. Spirou, B. Cotton, and G. Cotton, "Analytical expressions of capsize boundary of a ship with roll bias in beam waves," *Journal of Ship Research*, vol. 46, pp. 167–174, 2002.

[16] J. A. Gottwald, L. N. Virgin, and E. H. Dowell, "Routes to escape from an energy well," *Journal of Sound and Vibration*, vol. 187, no. 1, pp. 133–144, 1995.

[17] I. S. Kang and L. G. Leal, "Bubble dynamics in time-periodic straining flows," *Journal of Fluid Mechanics*, vol. 218, pp. 41–69, 1990.

[18] A. H. Nayfey and D. T. Mook, *Nonlinear Oscillations*, Wiley, New York, NY, USA, 1979.

[19] D. L. Olabodé, C. H. Miwadinou, V. A. Monwanou, and J. B. Chabi Orou, "Effects of passive hydrodynamics force on harmonic and chaotic oscillations in nonlinear chemical dynamics," *Physica D: Nonlinear Phenomena*, vol. 386-387, pp. 49–59, 2019.

[20] C. H. Miwadinou, L. A. Hinvi, A. V. Monwanou, and J. B. Chabi Orou, "Nonlinear dynamics of a $$\varvec{\phi^6}-$$ ϕ 6 - modified Duffing oscillator: resonant oscillations and transition to chaos," *Nonlinear Dynamics*, vol. 88, no. 1, pp. 97–113, 2017.

[21] M. S. Siewe, H. Cao, and M. A. F. Sanjuán, "On the occurrence of chaos in a parametrically driven extended Rayleigh oscillator with three-well potential," *Chaos, Solitons & Fractals*, vol. 41, no. 2, pp. 772–782, 2009.

[22] C. H. Miwadinou, A. V. Monwanou, J. Yovogan, L. A. Hinvi, P. R. Nwagoum Tuwa, and J. B. Chabi Orou, "Modeling nonlinear dissipative chemical dynamics by a forced modified Van der Pol-Duffing oscillator with asymmetric potential: chaotic behaviors predictions," *Chinese Journal of Physics*, vol. 56, no. 3, pp. 1089–1104, 2018.

[23] C. H. Miwadinou, A. V. Monwanou, L. A. Hinvi, and J. B. Chabi Orou, "Effect of amplitude modulated signal on chaotic motions in a mixed Rayleigh-Liénard oscillator," *Chaos, Solitons & Fractals*, vol. 113, pp. 89–101, 2018.

[24] C. H. Miwadinou, A. V. Monwanou, A. A. Koukpemedji, Y. J. F. Kpomahou, and J. B. Chabi Orou, "Chaotic motions in forced mixed Rayleigh -Liénard oscillator with external and parametric periodic-excitations," *Journal of Bifurcation and Chaos*, vol. 28, no. 3, Article ID 1830005, 2018.

[25] D. L. Olabod_e, C. H. Miwadinou, V. A. Monwanou, and J. B. Chabi Orou, "Horseshoes chaos and its passive control in dissipative nonlinear chemical dynamics," *Physica Scripta*, vol. 93, 2018.

[26] M. A. F. Sanjuán, "The effect of nonlinear damping on the universal escape oscillator," *International Journal of Bifurcation and Chaos*, vol. 9, no. 4, pp. 735–744, 1999.

[27] M. S. Soliman and J. M. T. Thompson, "The effect of damping on the steady state and basin bifurcation patterns of a nonlinear mechanical oscillator," *International Journal of Bifurcation and Chaos*, vol. 2, no. 1, pp. 81–91, 1992.

[28] C. H. Miwadinou, A. V. Monwanou, and J. B. Chabi Orou, "Effect of nonlinear dissipation on the basin boundaries of a driven two-well modified Rayleigh-duffing oscillator," *International Journal of Bifurcation and Chaos*, vol. 25, no. 2, p. 1550024, 2015.

[29] C. H. Miwadinou, A. V. Monwanou, L. A. Hinvi, A. A. Koukpemedji, C. Ainamon, and J. B. Chabi Orou, "Melnikov chaos in a modified Rayleigh–Duffing oscillator with φ^6 potential," *International Journal of Bifurcation and Chaos*, vol. 26, no. 5, Article ID 1650085, 2016.

[30] M. Amabili, "Derivation of nonlinear damping from viscoelasticity in case of nonlinear vibrations," *Nonlinear Dynamics*, vol. 97, no. 3, pp. 1785–1797, 2019.

[31] M. Amabili, "Nonlinear damping in nonlinear vibrations of rectangular plates: Derivation from viscoelasticity and experimental validation," *Journal of the Mechanics and Physics of Solids*, vol. 118, pp. 275–292, 2018.

[32] P. Balasubramanian, G. Ferrari, and M. Amabili, "Identification of the viscoelastic response and nonlinear damping of a rubber plate in nonlinear vibration regime," *Mechanical Systems and Signal Processing*, vol. 111, pp. 376–398, 2018.

[33] M. Amabili, "Nonlinear damping in large-amplitude vibrations: modelling and experiments," *Nonlinear Dynamics*, vol. 93, pp. 5–18, 2018.

[34] M. I. Evstifeev, A. S. Kovalev, and D. P. Eliseev, "Electromechanical model of RR-Type MEMS gyro with consideration for the platform vibrations," *Gyroscopy and Navigation*, vol. 5, no. 3, pp. 174–180, 2014.

[35] Z. Iskakov and K. Bissembayev, "The nonlinear vibrations of a vertical hard gyroscopic rotor with nonlinear characteristics," *Mechanical Sciences*, vol. 10, no. 2, pp. 529–544, 2019.

[36] R. G. Wang, Y. Chen, and G. W. Cai, "Subharmonic Resonance Analysis of a 2-DOF Controllable Linkage Mechanism System Affected by Self-Excited Inertial Force," *Advanced Materials Research*, vol. 139-141, pp. 2381–2385, 2010.

[37] C. Hayashi, *Nonlinear Oscillations in Physical Systems*, McGraw-Hill, New York, NY, USA, 1964.

Hindawi
Complexity
Volume 2020, Article ID 5179752, 9 pages
https://doi.org/10.1155/2020/5179752

Research Article

Finite-Time Lyapunov Functions and Impulsive Control Design

Huijuan Li and Qingxia Ma

School of Mathematics and Physics, China University of Geosciences, Wuhan 430074, China

Correspondence should be addressed to Huijuan Li; huijuanhongyan@gmail.com

Received 29 July 2020; Revised 28 September 2020; Accepted 6 October 2020; Published 27 October 2020

Academic Editor: Yongjian Liu

In this paper, we introduce finite-time Lyapunov functions for impulsive systems. The relaxed sufficient conditions for asymptotic stability of an equilibrium of an impulsive system are given via finite-time Lyapunov functions. A converse finite-time Lyapunov theorem for controlling the impulsive system is proposed. Three examples are presented to show how to analyze the stability of an equilibrium of the considered impulsive system via finite-time Lyapunov functions. Furthermore, according to the results, we design an impulsive controller for a chaotic system modified from the Lorenz system.

1. Introduction

Impulsive systems have been investigated by researchers, since impulsive systems can describe many practical problems from fields such as engineering, finance, chemistry, and biology (see [1, 2]). In references [1, 3–8], the authors studied the stability of equilibria of impulsive systems. Lyapunov functions are widely used to analyze stability problems of dynamical systems because it is not necessary to compute an analytic solution of the considered system. Many researchers try to relax the conditions imposed on Lyapunov functions. In [1, 2, 9], Lyapunov functions are allowed to be nonincreasing at the impulses. In [10], the conditions imposed on Lyapunov functions are more relaxed. Lyapunov functions could be nonincreasing at some of resetting times. The authors in [6] investigated the stability of hybrid systems by nonmonotonic Lyapunov functions which are not monotonically decreasing along the considered system trajectories. In [11, 12], Lyapunov functions for the considered impulsive system may increase during the continuous part of the trajectory of the state. In [5], Lyapunov functions are monotonically decreasing along the continuous part of the trajectory of the considered system and could increase at the resetting times. Based on the attained results, the authors designed a H_∞ controller for the considered problem. In [13], utilizing results from [2], the author got some sufficient conditions for impulsive control for a class of systems. In [14, 15], the authors studied chaotic communication systems. Then, they designed impulsive control for the considered systems. In [7], stochastic switched systems with impulses and time delay were investigated. Based on vector Lyapunov functions, input-to-state stability of the considered system was discussed. In [16], the authors investigated switched systems with time delay. Lyapunov functions can be nonincreasing at the switching times. According to the results, adaptive control was designed for the considered system. In [17], the authors presented an overview of the research investigations on impulsive control systems. Using Lyapunov functions with relaxed constraints, the authors in [18] discussed sufficient and necessary conditions for asymptotic stability of an equilibrium of a discrete-time homogeneous dynamical system. The results were extended to discrete-time systems in [19, 20]. A converse Lyapunov theorem was proposed for continuous-time systems via Lyapunov functions with relaxed conditions in [21]. In [22], two ways were designed for the computation of Lyapunov functions with relaxed conditions for continuous-time systems. In [23], the authors discussed input-to-state stability for continuous-time systems via input-to-state stable (ISS) Lyapunov functions with relaxed conditions. In [24], the authors proposed relaxed sufficient conditions for asymptotic stability of an equilibrium of time varying

impulsive systems via indefinite Lyapunov functions and designed an impulsive controller for a chaotic system.

In this paper, we will analyze the stability of equilibria of time invariant impulsive systems by Lyapunov functions with relaxed constraints, later named finite-time Lyapunov functions, and then design impulsive control for a chaotic system adapted from the Lorenz system. The ideas of the paper are inspired by the results discussed above. We obtained some novel results. Finite-time Lyapunov functions can increase during some continuous part of the trajectory of the considered system and have positive jumps at some impulses (see Theorem 1, example). It is worthy to point out that a converse finite-time Lyapunov theorem (see Theorem 2) is proposed. Based on Theorem 2, a finite-time Lyapunov function can be constructed for the considered impulsive system. Moreover, we design an impulse controller to get a chaotic system stabilized based on Theorem 1 and Corollary 1.

This paper is organized as follows. In Section 2, we introduce notations and basic definitions. Finite-time Lyapunov functions for impulsive systems are introduced. The main problem studied in this paper is described. In Section 3, the main results are discussed. We first study how to prove the origin of system (1) is asymptotic stable by finite-time Lyapunov functions. Then, a converse finite-time Lyapunov theorem for impulsive systems is obtained, that is, if the origin of system (1) is asymptotically stable and Condition 1 holds, then there exists a finite-time Lyapunov function for system (1). In Section 4, we show the efficiency of our main results via three examples. Especially, Example 3 shows that finite-time Lyapunov functions can increase along some continuous portion of the trajectory of system (31) and increase at some resetting times. Furthermore, according to our main results, we design impulsive control for a chaotic system in Section 5. We present simulation results of the chaotic system with the designed controller. Some concluding remarks are discussed in Section 6.

2. Notations and Preliminaries

The real numbers, the nonnegative real numbers, and the nonnegative integers are denoted by $\mathbb{R}$, $\mathbb{R}_+$, and $\mathbb{Z}_+$, respectively. The Euclidean norm of the real vector $x \in \mathbb{R}^n$ is denoted by $|x|$. For $x = (x_1, \ldots, x_n)^T \in \mathbb{R}^n$, we denote $1-$ norm for x by $|x|_1 = \sum_{i=1,\ldots,n} |x_i|$. The open ball of radius r around z in the norm of $|\cdot|$ is defined by $B(z,r) = \{x \in \mathbb{R}^n || x - z| < r\}$. For a set $\Omega \subset \mathbb{R}^n$, the boundary and the interior of Ω are denoted by $\partial\Omega$ and int Ω, respectively.

It is well known that comparison functions are widely used in stability analysis. Comparison functions are described as follows. If a continuous function $\alpha: \mathbb{R}_+ \longmapsto \mathbb{R}_+$ satisfies $\alpha(0) = 0$ and $\alpha(s) > 0$ for all $s > 0$, then we say it is *positive definite*. A positive definite function is of *class* $\mathcal{K}$ if it is strictly increasing and of *class* $\mathcal{K}_\infty$ if it belongs to the class $\mathcal{K}$ and unbounded. We say a continuous function $\gamma: \mathbb{R}_+ \longmapsto \mathbb{R}_+$ belongs to *class* $\mathcal{L}$ if $\gamma(r)$ is strictly decreasing to 0 as $r \longrightarrow \infty$. A continuous function $\beta: \mathbb{R}_+ \times \mathbb{R}_+ \longmapsto \mathbb{R}_+$ is said to be of *class* $\mathcal{KL}$ if it is of class $\mathcal{K}_\infty$ in the first argument and of class $\mathcal{L}$ in the second argument.

In this paper, we are going to study the stability property of the following system with impulses described by

$$\begin{cases} \dot{x}(t) = f(x(t)), & t \neq t_k,\ k \in \{1, 2, 3, \ldots,\}, \\ x(t_k) = g(x(t_k^-)), & t = t_k,\ k \in \{1, 2, 3, \ldots,\}, \end{cases} \tag{1}$$

where $0 < t_1 < t_2 < \cdots < t_k < \cdots$ are resetting times in $(0, \infty)$ and $\lim_{k \longrightarrow \infty} t_k = \infty$. The functions $f, g: \mathbb{R}^n \longmapsto \mathbb{R}^n$ are locally Lipschitz continuous and satisfy the conditions $f(0) = 0$, $g(0) = 0$. It is evident that the origin is an equilibrium of system (1). Suppose that a sequence of impulse times $\{t_k\}$ is given; the solution of system (1) corresponding to an initial condition $x_0 = x(0)$ is denoted by $x(t, x_0)$. The limits of $x(t)$ from left and right are denoted by $x(t^-)$ and $x(t^+)$, respectively. It is easy to see that the solution $x(t)$ of system (1) is right continuous, that is, it is continuous in $(0, t_1)$, (t_k, t_{k+1}), and the following conditions hold.

$$\begin{aligned} x(t_k^-) &= \lim_{\varepsilon \longrightarrow 0^+} x(t_k - \varepsilon), \\ x(t_k) = x(t_k^+) &= \lim_{\varepsilon \longrightarrow 0^+} x(t_k + \varepsilon). \end{aligned} \tag{2}$$

For a constant $T > 0$ and a sequence of impulse times $\{t_k\}$, we define a positively $T-$ invariant set for system (1).

Definition 1. Given a constant $T > 0$ and a sequence of impulse times $\{t_k\}$, a compact set $\Omega \subset \mathbb{R}^n$ is called a positively $T-$ invariant set for system (1) if for all $x(t, x_0) \in \Omega$, it satisfies $x(t + T, x_0) \in \Omega$ for $t \in \mathbb{R}_+$.

Remark 1. In Definition 1, if $T = 0$ holds, then we call the set Ω a positively invariant set for system (1).

The following definition describes asymptotic stability of system (1) we are interested in.

Definition 2. For system (1), we suppose that a sequence of impulse times $\{t_k\}$ is given. The origin of system (1) is asymptotically stable in a compact set $\Omega \subset \mathbb{R}^n$ if there exists a function $\beta \in \mathcal{KL}$ such that for every initial condition $x_0 \in \Omega$, it holds that

$$|x(t, x_0)| \leq \beta(|x_0|, t), \quad t \geq 0. \tag{3}$$

In the literature, sufficient conditions for asymptotic stability of system (1) were obtained via Lyapunov functions described by the following definition.

Definition 3. Given a sequence of impulse times $\{t_k\}$ for system (1). A continuous function $V: \mathbb{R}^n \longmapsto \mathbb{R}_+$ is said to be a Lyapunov function for system (1) on a compact set $\Omega \subset \mathbb{R}^n$, if there exist functions $\alpha_1, \alpha_2 \in \mathcal{K}_\infty$, a positive definite function $\alpha: \mathbb{R}_+ \longmapsto \mathbb{R}_+$, and a continuous function $\theta: \mathbb{R}_+ \longmapsto [0, 1) \subset \mathbb{R}_+$ such that

(i) (C1)

$$\alpha_1(|x|) \leq V(x) \leq \alpha_2(|x|), \quad \forall x \in \mathbb{R}^n. \tag{4}$$

(ii) (C2)

$$\nabla V(x(t,x_0))f(x(t)) \le -\alpha(V(x(t,x_0))), \quad \text{for}, x_0 \in \Omega t \ne t_k, k \in \{1,2,3,\ldots,\}. \tag{5}$$

(ii) (C3)

$$V(g(x(t,x_0))) \le \theta(V(x(t^-,x_0))), \quad \text{for } x_0 \in \Omega, t = t_k, k \in \{1,2,3,\ldots,\}. \tag{6}$$

We are going to relax the conditions imposed on Lyapunov functions in Definition 3 and then demonstrate how to prove asymptotic stability of system (1) via finite-time Lyapunov functions defined by the following definition.

Definition 4. Consider system (1) with a given impulsive time sequence $\{t_k\}$. A continuous function $V: \mathbb{R}^n \longmapsto \mathbb{R}_+$ is said to be a finite-time Lyapunov function for system (1) on a compact set $\Omega \subset \mathbb{R}^n$, if there exist a positive constant T, functions $\alpha_1, \alpha_2 \in \mathscr{K}_\infty$, and a function $\rho \in \mathscr{K}$ with $\rho < \mathrm{id}$ such that

$$\alpha_1(|x|) \le V(x) \le \alpha_2(|x|), \quad \forall x \in \mathbb{R}^n, \tag{7}$$

$$V(x(T+t,x_0)) \le \rho(V(x(t,x_0))), \quad \text{for } t \ge 0,\ x_0 \in \Omega. \tag{8}$$

Remark 2

(i) From constraint (8), we have that the function V defined in Definition 4 may increase during some continuous portion of the trajectory and at some impulses. It is clear that the conditions imposed on finite-time Lyapunov functions are more relaxed than those on Lyapunov functions defined by Definition 3.

(ii) In order to verify condition (8), we have to construct finite-time Lyapunov functions. However, it is not easy to give a formulation of a finite-time Lyapunov function. Under certain conditions, Theorem 2 will explain how to construct a finite-time Lyapunov function. When we check if the condition (8) holds, it is necessary to calculate the solution $x(T+t,x_0)$. For easy computation, the Euler method will be used to calculate the solution $x(T+t,x_0)$ for examples considered in Section 4.

The following impulsive integral inequality of Gronwall type will be used in deducing inequalities in the proofs of our main results.

Lemma 1. *Let $t_1, t_2, \ldots, t_k, \ldots$, be a strictly increasing sequence of impulse times in $(0,\infty)$ and $\lim_{k\longrightarrow\infty} t_k = \infty$, the function $m: \mathbb{R}_+ \longmapsto \mathbb{R}$ a continuous function for $t \ne t_k$ and right continuous at $t = t_k (k = 1,2,\ldots,)$, and the function $p: \mathbb{R}_+ \longmapsto \mathbb{R}_+$ be a continuous function. Moreover, we assume that*

$$m(t) \le A + \int_0^t p(s)m(s)\mathrm{d}s + \sum_{0<t_k\le t} \lambda_k m(t_k), \quad t \ge 0, k > 0, k \in \mathbb{Z}_+, \tag{9}$$

where $\lambda_k \ge 0$ and A are constants. Then it holds that

$$m(t) \le A \prod_{0<t_k\le t} (1+\lambda_k) e^{\int_0^t p(s)\mathrm{d}s}, \quad t \ge 0. \tag{10}$$

Proof. The proof is similar to the proof of Theorem 16.1 in [25]. □

3. Main Results

In this section, we first demonstrate how to prove asymptotic stability of system (1) via finite-time Lyapunov functions defined by Definition 4. Then, we propose a converse finite-time Lyapunov theorem for system (1).

Theorem 1. *Consider system (1) with a given impulsive time sequence $\{t_k\}$. Let T be a positive constant, and a compact set $\Omega \subset \mathbb{R}^n$ with $0 \in \mathrm{int}\Omega$ be a positively $T-$invariant set for system (1). If there exists a finite-time Lyapunov function $V: \mathbb{R}^n \longmapsto \mathbb{R}$ with T for system (1) on Ω, then the origin of system (1) is asymptotically stable in Ω over the given impulse sequence. Furthermore, an estimate of the domain of attraction of the origin of system (1) is given by $\mathscr{D}_a = \{x \in \Omega | V(x) \le \min_{x\in\partial\Omega} V(x)\}$.*

Proof. According to the conditions, there exist functions $\alpha_1, \alpha_2 \in \mathscr{K}_\infty$ and a function $\rho \in \mathscr{K}$ with $\rho < \mathrm{id}$ such that inequalities (7) and (8) from Definition 4 hold. For any $t > 0$, $t \in \mathbb{R}_+$, there exists a integer $N > 0$ such that $t = \mathrm{NT} + j$, $j \in [0,T)$. Utilizing (8) recursively, we obtain that

$$\begin{aligned} V(x(t,x_0)) &= V(x(NT+j,x_0)) = V(x((N-1)T+T+j,x_0)) \\ &\le \rho(V(x((N-1)T+j,x_0))) \\ &\cdots \\ &\le \rho^N(V(x(j,x_0))) \\ &\le \rho^N(\alpha_2(|x(j,x_0)|)), \end{aligned} \tag{11}$$

where ρ^N represents the $N-$times composition of ρ and α_2 comes from (7). Let $k \in \mathbb{Z}_+$ denote the number of impulsive time $t_i \in [0,j]\,(i \in \mathbb{Z}_+, i > 0)$, and

$$\sigma = \begin{cases} 0, & k = 0, \\ 1, & k \ge 1. \end{cases} \tag{12}$$

The solution $x(t,x_0)$ at time $t = j$ is given by

$$x(j,x_0)=\begin{cases} x_0+\sum_{d=1}^{k} g\left(x\left(t_d^-\right)\right)+\int_0^j f(x(s))\mathrm{d}s, & \text{for } k\geq 1,\\ x_0+\int_0^j f(x(s))\mathrm{d}s, & \text{for } k=0. \end{cases} \tag{13}$$

Using (12), $x(j,x(0))$ is rewritten as

$$x(j,x_0)=x_0+\sigma\sum_{d=1}^{k} g\left(x\left(t_d^-\right)\right)+\int_0^j f(x(s))\mathrm{d}s, \tag{14}$$

for any $j\geq 0$.

Then, we have

$$\begin{aligned}\left|x(j,x_0)-x(0)\right|&\leq\sigma\sum_{d=1}^{k}\left|g\left(x\left(t_d^-\right)\right)-g(x_0)+g(x_0)\right|\\&\quad+\int_0^j\left|f(x(s))-f(x_0)+f(x_0)\right|\mathrm{d}s\\&\leq\sigma\sum_{d=1}^{k}\left|g\left(x\left(t_d^-\right)\right)-g(x_0)\right|+\sigma\sum_{d=1}^{k}\left|g(x_0)\right|\\&\quad+\int_0^j\left|f(x(s))-f(x_0)\right|\mathrm{d}s+\int_0^j\left|f(x_0)\right|\mathrm{d}s.\end{aligned} \tag{15}$$

Using the Lipschitz conditions for f,g, and Lemma 1, we get that

$$\begin{aligned}\left|x(j,x_0)-x_0\right|&\leq\sigma\sum_{d=1}^{k}L_g\left|x\left(t_d^-\right)-x_0\right|+\sigma k\left|g(x_0)\right|\\&\quad+\int_0^j L_f\left|x(s)-x_0\right|\mathrm{d}s+\int_0^j\left|f(x_0)\right|\mathrm{d}s\leq C\left(1+\sigma L_g\right)^k e^{L_f j},\end{aligned} \tag{16}$$

where L_f, L_g are Lipschitz constants for the functions f,g, respectively, and $C=\sigma k\sum_{d=1}^{k}|g(x_0)|+\int_0^j|f(x_0)|\mathrm{d}s$. Therefore, it holds that

$$\begin{aligned}\left|x(j,x_0)\right|&\leq C\left(1+\sigma L_g\right)^k e^{L_f j}+\left|x_0\right|\leq C\left(1+\sigma L_g\right)^k e^{L_f T}+\left|x_0\right|\\&:=H_T\left(\left|x_0\right|\right).\end{aligned} \tag{17}$$

Based on the assumptions on the functions f,g, it is obtained that $H_T(|x(0)|)$ is continuous with respect to $|x_0|$. Moreover, it is clear that $H_T(0)=0$, and $H_T(s)>0$ for $s>0$. Thus, $H_T(|x(0)|)$ is a positive definite function with respect to $|x_0|$. It is easy to see that there exists a function $\gamma\in\mathcal{K}_\infty$ such that $H_T(|x_0|)\leq\gamma(|x_0|)$. Then, it is satisfied that $|x(j,x_0)|\leq\gamma(|x(0)|)$ for all $0\leq j<T$.

The idea of the proof of the existence of the function ρ_1 is inspired by Theorem 2.1 in [21] and Lemma 12 in [22]. Because ρ is positive definite, without loss of generality, we can assume that ρ is invertible, that is, ρ is a one-to-one and onto function. According to Theorem 3.16 in [26] and the above discussion, it holds that ρ^{-1} is continuous and $\rho^{-1}(0)=\rho^{-1}(\rho(0))=0$. Thus, for $t=\mathrm{NT}+j$, we obtain that

$$V\left(x(t,x_0)\right)\leq\rho^{(t/T)}\circ\rho^{-1}\circ\alpha_2\circ\gamma\left(\left|x_0\right|\right). \tag{18}$$

From the above analysis, the function ρ^{-1} is positive definite. Then, there exists a function $\rho_1\in\mathcal{K}_\infty$ satisfying $\rho_1(s)\geq\rho^{-1}(s)$ for $s\geq 0$. Thus, it holds that

$$V\left(x(t,x_0)\right)\leq\rho^{(t/T)}\circ\rho_1\circ\alpha_2\circ\gamma\left(\left|x_0\right|\right). \tag{19}$$

Since the condition $\alpha_1\in\mathcal{K}_\infty$ is satisfied, then the function α_1 is a one-to-one and onto function. Therefore, the function α_1^{-1} exists and $\alpha_1^{-1}\in\mathcal{K}_\infty$ holds. Furthermore, utilizing (7), we have that

$$\left|x(t,x_0)\right|\leq\alpha_1^{-1}\circ\rho^{(t/T)}\circ\rho_1\circ\alpha_2\circ\gamma\left(\left|x_0\right|\right). \tag{20}$$

Let $\beta(|x_0|,t)=\alpha_1^{-1}\circ\rho^{(t/T)}\circ\rho_1\circ\alpha_2\circ\gamma(|x_0|)$. Since $\alpha_1^{-1},\rho_1,\alpha_2,\gamma$ are $\mathcal{K}_\infty$ functions, for fixed t, the function β increases as the argument $|x_0|$ increases. Because $\rho<\mathrm{id}$ holds, for fixed $|x_0|$, the function β decreases as the argument t increases. Therefore, we obtain that $\beta\in\mathcal{KL}$ is a $\mathcal{K}_\infty$ function in the argument $|x_0|$ and a $\mathcal{L}$ function in the argument t. Then, it holds that

$$\left|x(t,x_0)\right|\leq\beta\left(\left|x_0\right|,t\right). \tag{21}$$

Therefore, the origin of system (1) is asymptotically stable in Ω over the given impulse sequence. Moreover, an estimate of the domain of attraction of the origin of system (1) is obtained by $\mathcal{D}_a=\{x\in\Omega|V(x)\leq\min_{x\in\partial\Omega}V(x)\}$. □

Remark 3. To make sure $x(T,x_0)\in\Omega$ for all $x_0\in\Omega$, we have to ensure that the set Ω is a positively $T-$invariant set for system (1).

In the following, a converse finite-time Lyapunov theorem is investigated. To obtain the desired result, it is necessary to require the following condition.

Condition 1. Consider system (1) with a given impulsive time sequence $\{t_k\}$. There exists a $\mathcal{KL}$ function β which satisfies (2) for system (1) and the inequality

$$\beta(s,T)<s, \tag{22}$$

for some $T>0$ and $s>0$.

Theorem 2. *Consider system (1) with a given impulsive time sequence $\{t_k\}$. If the origin of system (1) is asymptotically stable in an invariant set $\Omega\subset\mathbb{R}^n$ over the given impulse sequence and Condition 1 holds, then for any function $\eta\in\mathcal{K}_\infty$, the function $V\colon\mathbb{R}^n\longmapsto\mathbb{R}_+$ with*

$$V(x)=\eta(|x|),\quad \text{for} x\in\mathbb{R}^n \tag{23}$$

satisfies inequalities (7) and (8) with T from Condition 1.

Proof. Because $\eta\in\mathcal{K}_\infty$, it is evident that there exist functions $\alpha_1,\alpha_2\in\mathcal{K}_\infty$ such that inequality (7) holds. Since Condition 1 is satisfied, then there exists a positive constant T such that inequality (22) holds. Thus, we have that

$$V(x(t+T,x_0)) = \eta\left(\left|x(t+T,x_0)\right|\right) = \eta\left(\left|x(T,x(t,x_0))\right|\right) \le \eta\left(\beta\left(\left|x(t,x_0)\right|,T\right)\right) = \eta^{\circ}\beta\left(\eta^{-1}(V(x(t,x_0))),T\right). \tag{24}$$

Let $\rho = \eta^{\circ}\beta(\eta^{-1}(V(x(t,x_0))),T)$. It is obvious that ρ is a positive definite function of the variable $V(x(t,x_0)))$. Based on Condition 1, it is obtained that $\rho(s) < \eta \circ \eta^{-1}(s) = s$ holds. Thus, V satisfies inequality (8) with T from Condition 1. □

Remark 4. Theorem 2 provides a way to construct finite-time Lyapunov functions for systems. However, for the considered system, it is not easy to check if $V(x) = \eta(|x|)$ satisfies inequality (8).

4. Examples

In this section, three examples are presented to illustrate how to analyze stability of impulsive systems with finite-time Lyapunov functions. Based on the definition of finite-time Lyapunov function (see Definition 4), in order to check if a continuous function V: $\mathbb{R}^n \longmapsto \mathbb{R}_+$ is a finite-time Lyapunov function for system (1), it is necessary to calculate $V(x(T,x_0))$ in (8) from Definition 4. For a constant $0 < T < +\infty$, we compute the value of $x(T,x_0)$ of system (1) with respect to an initial condition x_0 by the Euler method with the time step denoted by h_t. In order to simplify the computation, for the following examples, 1-norm $|\cdot|_1$ is utilized.

4.1. Example 1. Consider the following one-dimensional system described by

$$\begin{cases} \dot{x}(t) = -x(t), & t \neq t_k, \\ x(t) = 2x(t_k^-), & t = t_k = \dfrac{3k}{4}, \end{cases} \tag{25}$$

where $x \in \mathbb{R}$, $k > 0, k \in \mathbb{Z}_+$.

Let $V_1(x) = |x|$ be a finite-time Lyapunov function candidate for system (25). To show there exists a constant $T > 0$ such that V_1 satisfies (8) from Definition 4, we calculate $V(x(T,x_0))$ with $T = (3/4), h_t = (1/4)$.

$$\begin{cases} x\left(\dfrac{1}{4},x_0\right) = \dfrac{3}{4x_0}, x\left(\dfrac{1}{2},x_0\right) = \dfrac{9}{16x_0}, \\ x(t_1^-,x_0) = x\left(\left(\dfrac{3}{4}\right)^-,x_0\right) = \dfrac{27}{64x_0}, x\left(\dfrac{3}{4},x_0\right) = \dfrac{27}{32x_0}, \\ x(1,x_0) \le \dfrac{81}{128x_0}, x\left(\dfrac{5}{4},x_0\right) \le \dfrac{243}{512x_0}, \\ x(t_2^-,x_0) = x\left(\left(\dfrac{3}{2}\right)^-,x_0\right) = \dfrac{729}{2048x_0}, x\left(\dfrac{3}{2},x_0\right) = \dfrac{729}{1024x_0}. \end{cases} \tag{26}$$

From the above calculation, the following inequalities hold.

$$V\left(x\left(\frac{3}{4},x_0\right)\right) \le \left(\frac{27}{32}\right)V(x_0), \quad x_0 \in \mathbb{R},$$

$$V\left(x\left(\left(\frac{3}{2}\right)+t,x(t,x_0)\right)\right) \le \left(\frac{27}{32V}\right)(x(t,x_0)), \quad t \in \mathbb{R}_+, x_0 \in \mathbb{R}. \tag{27}$$

Then, it is obvious that V_1 is a finite-time Lyapunov function for system (25) in $\mathbb{R}$. Based on Theorem 1, we have that the origin of system (25) is asymptotically stable in $\mathbb{R}$ over the given impulse sequence (see Figure 1). Figure 1 clearly shows that $V_1(x) = |x|$ is not a Lyapunov function for system (25).

4.2. Example 2. In this section, we consider the following one-dimensional system described by

$$\begin{cases} \dot{x}(t) = x(t), & t \neq t_k, \\ x(t) = \left(\dfrac{1}{2}\right)x(t_k^-), & t = t_k = \dfrac{k}{2}, \end{cases} \tag{28}$$

where $x \in \mathbb{R}$, $k > 0, k \in \mathbb{Z}_+$.

Let $V_2(x) = |x|$ be a finite-time Lyapunov function candidate for system (28). To check if V_2 satisfies condition (8) from Definition 4 with $T = (1/2)$, we have to calculate with $h_t = (1/4)$.

$$\begin{cases} x\left(\left(\dfrac{1}{4}\right),x_0\right) = \left(\dfrac{5}{4x_0}\right), \\ x(t_1^-,x_0) = x\left(\left(\dfrac{1}{2}\right)^-,x_0\right) = \left(\dfrac{25}{16x_0}\right), x\left(\dfrac{1}{2},x_0\right) = \left(\dfrac{25}{32x_0}\right), \\ x\left(\left(\dfrac{3}{4}\right),x_0\right) = \left(\dfrac{125}{128x_0}\right), \\ x(t_2^-,x_0) = x\left((1)^-,x_0\right) = \left(\dfrac{625}{512x_0}\right), x(1,x_0) = \dfrac{625}{1024x_0}. \end{cases} \tag{29}$$

It is evident that the following inequality is satisfied.

$$V_2\left(x\left(\left(\frac{1}{2}\right)+t,x_0\right)\right) \le V_2(x(t,x_0)), \quad t \in \mathbb{R}_+, x_0 \in \mathbb{R}. \tag{30}$$

According to the above analysis, we conclude that V_2 is a finite-time Lyapunov function for system (28) in $\mathbb{R}$. Moreover, utilizing Theorem 1, it is attained that the origin of system (28) is asymptotically stable in $\mathbb{R}$ over the given impulse sequence. Figure 2 demonstrates that V_2 is not a Lyapunov function for system (28).

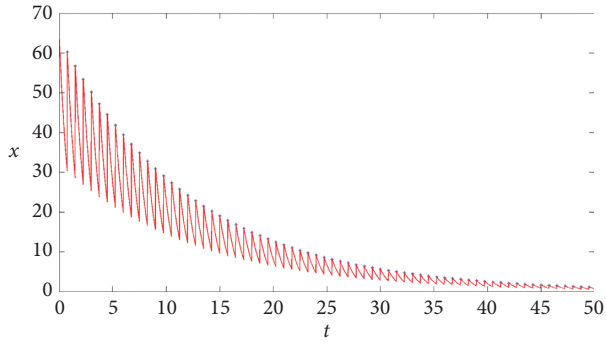

FIGURE 1: The trajectory of the state of system (25) corresponding to the initial condition $x(0) = 64$ and the resetting time $t_k = 0.75k, k = 1, 2, \ldots,$.

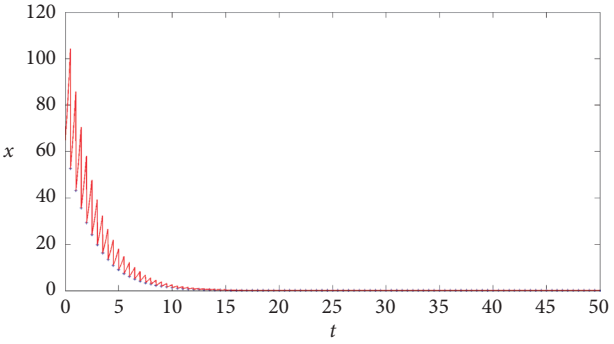

FIGURE 2: The trajectory of the state of system (28) corresponding to the initial condition $x(0) = 64$ and the resetting time $t_k = 0.5k, k = 1, 2, \ldots,$.

4.3. Example 3. We consider the following two-dimensional system described by

$$\begin{cases} \dot{x}_1(t) = -0.2x_2(t), & t \neq t_k, \\ \dot{x}_2(t) = x_1(t) - x_2(t), & t \neq t_k, \\ x_1(t) = x_1(t_k^-) + \left(\frac{1}{8}\right)\sin\left(x_1(t_k^-) + x_2(t_k^-)\right)x_2(t_k^-), & t = t_k = 5k, \\ x_2(t) = x_2(t_k^-) + \left(\frac{1}{8}\right)\cos\left(x_1(t_k^-) + x_2(t_k^-)\right)x_1(t_k^-), & t = t_k = 5k, \end{cases} \tag{31}$$

where $x = (x_1, x_2)^T \in \mathbb{R}^2$, $k > 0$, $k \in \mathbb{Z}_+$.

For system (31), we choose $V_3(x) = |x|_1$ as a finite-time Lyapunov function candidate. Now, we show there exists a constant T such that inequality (8) from Definition 4 is satisfied. The following calculation is done with $T = 5$, $h_t = 1$. For the calculation, we utilize the following notations: $x_{10} = x_1(0), x_{20} = x_2(0), x_{11} = x_1(h_t, x_0), x_{21} = x_2(h_t, x_0), x_{12} = x_1(2h_t, x_0), x_{22} = x_2(2h_t, x_0), \ldots, x_{1k} = x_1(kh_t, x_0), x_{2k} = x_2(kh_t, x_0)$.

$$\begin{cases} x_{11} = x_{10} - 0.2x_{20}, \\ x_{21} = x_{10}, \\ \ldots, \\ x_{14} = 0.44x_{10} - 0.12x_{20}, \\ x_{24} = 0.6x_{10} - 0.16x_{20}, \\ x_1(5^-, x_0) = 0.32x_{10} - 0.088x_{20}, \\ x_2(5^-, x_0) = 0.44x_{10} - 0.12x_{20}, \\ |x_{15}| + |x_{25}| \leq \frac{9}{8} \cdot 0.76|x_0|_1 = 0.855|x_0|_1. \end{cases} \tag{32}$$

Thus, we have that

$$\begin{aligned} &V_3(x(5, x_0)) \leq 0.855V_3(x_0), \\ &V_3(x(5 + t, x_0)) \leq 0.855V_3(x(t, x_0)), \quad t \in \mathbb{R}_+, x_0 \in \mathbb{R}^2. \end{aligned} \tag{33}$$

From the above calculation, it is obvious that V_3 is a finite-time Lyapunov function for system (31) in $\mathbb{R}^2$. Based on Theorem 1, it is obtained that the origin of system (31) is asymptotically stable in $\mathbb{R}^2$ over the given impulse sequence (see Figures 3 and 4). Figure 5 demonstrates that the function V_3 is not a Lyapunov function for system (31).

5. Impulsive Control of a Chaotic System

In this section, based on Theorem 1, impulsive control is designed for a chaotic system described by

$$\dot{x} = Ax + \gamma(x), \tag{34}$$

where $x = (x_1, x_2, x_3)^T \in \mathbb{R}^3$, and

$$A = \begin{pmatrix} -a & a & 0 \\ c & -1 & 0 \\ 0 & 0 & -b \end{pmatrix}, \quad \gamma(x) = \begin{pmatrix} x_2x_3 \\ -x_1x_3 \\ x_1x_2 \end{pmatrix}, \tag{35}$$

in which $a, b, c \in \mathbb{R}$ are positive constants. The constants a and b are called the Prandtl number and Rayleigh number, respectively. In [27], the authors studied system (34) adapted from the Lorenz system.

In order to ensure the origin is an asymptotic stable equilibrium, we design an impulsive controller for system (34) described by

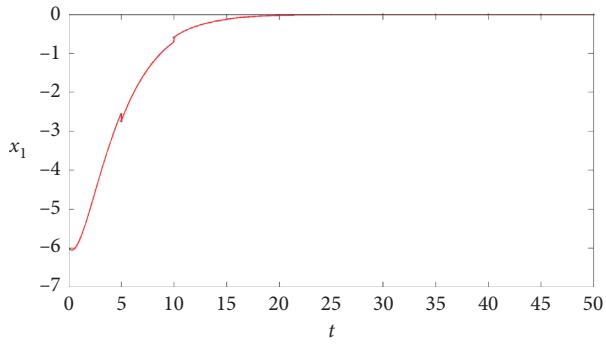

FIGURE 3: The trajectory of the state x_1 of system (31) corresponding to the initial condition $x(0) = (-6,,2)^T$ and the resetting time $t_k = 5k, k = 1, 2, \ldots,$.

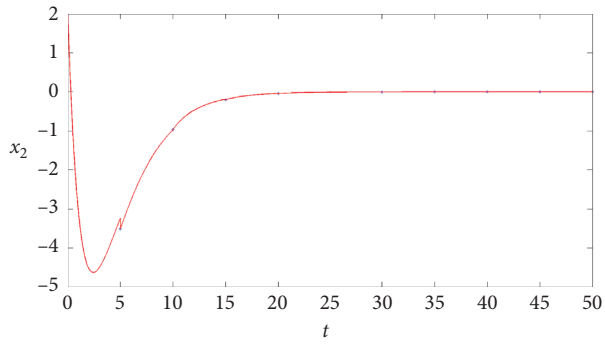

FIGURE 4: The trajectory of the state x_2 of system (31) corresponding to the initial condition $x(0) = (-6,,2)^T$ and the resetting time $t_k = 5k, k = 1, 2, \ldots,$.

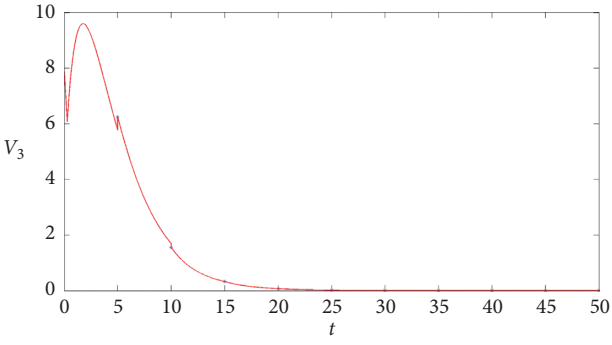

FIGURE 5: The trajectory of the finite-time Lyapunov function V_3 for system (31) with the initial condition $x(0) = (-6, 2)^T$ and the resetting time $t_k = 5k, k = 1, 2, \ldots,$.

$$\begin{cases} \dot{x}(t) = Ax(t) + \gamma(x(t)), & \text{for } t \neq t_k, \\ x(t) = x(t_k^+) = D(x(t_k^-)), & \text{for } t = t_k, \end{cases} \tag{36}$$

where $t_k (k = 1, 2, \ldots,)$, $0 < t_1 < t_2 < \cdots < t_k < t_{k+1} < \cdots$ ($t_k \longrightarrow \infty$ as $k \longrightarrow \infty$) are impulses, $h = t_1 = t_{k+1} - t_k (k = 1, 2, \ldots,)$, and

$$D(x) = \begin{pmatrix} d_{11}(x_1) & d_{12}(x_2) & d_{13}(x_3) \\ d_{21}(x_1) & d_{22}(x_2) & d_{23}(x_3) \\ d_{31}(x_1) & d_{32}(x_2) & d_{33}(x_3) \end{pmatrix}, \tag{37}$$

in which d_{ij}: $\mathbb{R} \longmapsto \mathbb{R}$ are continuous. We assume that there exist constants $\overline{d}_{ij} \in \mathbb{R}_+ (i, j = 1, 2, 3)$ satisfying $|d_{ij}(s)| \leq \overline{d}_{ij}|s|$ for $s \in \mathbb{R}$.

For convenience, the following notations are introduced:

$$\begin{aligned} d_1 &= |\overline{d}_{11}(1 - ah)| + |\overline{d}_{12}ch| + |\overline{d}_{12}hR| + |\overline{d}_{13}hR| \\ &\quad + |\overline{d}_{22}ch| + |\overline{d}_{21}(1 - ah)| + |\overline{d}_{22}hR| + |\overline{d}_{23}hR| \\ &\quad + |\overline{d}_{31}(1 - ah)| + |\overline{d}_{32}ch| + |\overline{d}_{32}hR| + |\overline{d}_{33}hR|, \\ d_2 &= |\overline{d}_{11}ah| + |\overline{d}_{11}hR| + |\overline{d}_{12}(1 - h)| + |\overline{d}_{13}hR| \\ &\quad + |\overline{d}_{22}(1 - h)| + |\overline{d}_{21}hR| + |\overline{d}_{21}ah| + |\overline{d}_{23}hR| \\ &\quad + |\overline{d}_{31}ah| + |\overline{d}_{31}hR| + |\overline{d}_{32}(1 - h)| + |\overline{d}_{33}hR|, \\ d_3 &= |\overline{d}_{11}Rh| + |\overline{d}_{12}hR| + |\overline{d}_{13}(1 - bh)| \\ &\quad + |\overline{d}_{22}Rh| + |\overline{d}_{21}hR| + |\overline{d}_{23}(1 - bh)| \\ &\quad + |\overline{d}_{31}Rh| + |\overline{d}_{32}hR| + |\overline{d}_{33}(1 - bh)|, \end{aligned} \tag{38}$$

where R from Corollary 1 is a positive constant. It is clear that $d_i (i = 1, 2, 3)$ are positive constants.

Corollary 1. *Let $R > 0$ be a constant. Consider system (36) on a bounded set $\mathscr{D} \subset B(0, R) \subset \mathbb{R}^3$. Let $M = \max_{i=1,2,3} c_i$. If $M < 1$ is satisfied, then the function V: $\mathbb{R}^3 \longmapsto \mathbb{R}$ defined by $V(x) = |x|_1$ is a finite-time Lyapunov function for system (36) with $T = h$. Therefore, the origin of system (36) is asymptotically stable in $\mathscr{D}$ over the given impulse sequence.*

Proof. Under the conditions, we prove $V(x) = |x|_1$ is a finite-time Lyapunov function for system (36). It is obvious that there exist functions $\alpha_1, \alpha_2 \in \mathscr{K}_\infty$ such that

$$\alpha_1(|x|) \leq V(x) \leq \alpha_2(|x|). \tag{39}$$

Now, we have to calculate $V(x(h, x_0))$ for system (36) with $x_0 \in \mathscr{D}$ by the Euler method with the step size h. Let $x_0 = (x_{10}, x_{20}, x_{30})^T$.

$$\begin{cases} x_1(h^-, x_0) = x_{10} + [a(x_{20} - x_{10}) + x_{20}x_{30}]h, \\ x_2(h^-, x_0) = x_{20} + [cx_{10} - x_{20} - x_{10}x_{30}]h, \\ x_3(h^-, x_0) = x_{30} + [x_{10}x_{20} - bx_{30}]h, \\ x(h, x_0) = D(x(h^-)). \end{cases} \tag{40}$$

By calculation, it is obtained that $V(x(h, x_0)) \leq M|x_0|_1 = MV(x_0)$. Thus, the function V satisfies inequality (8) from Definition 4. By Theorem 1, we obtain that the origin of system (36) is asymptotically stable in Ω over the given impulse sequence. □

Remark 5. In the proof, we calculate $x(h, x_0)$ by the Euler method with the step size h. The reason for letting the step size being h is that it is easy to estimate the value of $|x(h^-, x_0)|_1$.

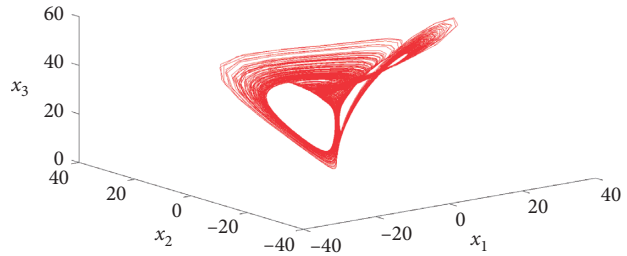

FIGURE 6: The trajectory of the states of system (34) with the coefficients $a = 35$, $b = (8/3)$, and $c = 25$ and the initial condition $x(0) = (3, 4, 5)^T$.

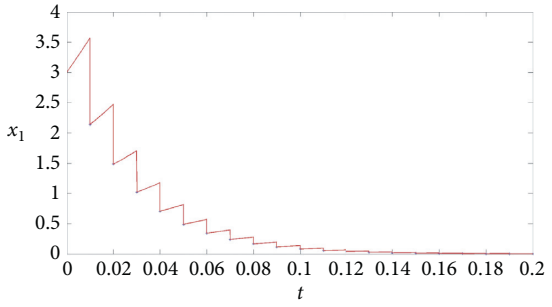

FIGURE 7: The trajectory of the state x_1 of system (36) with the coefficients $a = 35$, $b = (8/3)$, $c = 25$, $t_k = 0.01k(k = 1, 2, \ldots,)$, $d_{ij} = 0(i, j = 1, 2, 3, i \neq j)$, and $d_{ii} = 0.6(i = 1, 2, 3)$ and the initial condition $x(0) = (3, 4, 5)^T$.

5.1. Simulation Results. In this section, system (34) is considered as an example with the coefficients $a = 35$, $b = (8/3)$, $c = 25$, and $x_0 = (3, 4, 5)^T$. Figure 6 shows that a chaotic attractor exists for system (34) with the given conditions and is similar to that for the Lorenz system.

An impulsive controller is designed as follows: $t_k = 0.01k(k = 1, 2, \ldots,)$, $d_{ij} = 0(i, j = 1, 2, 3, i \neq j)$, $d_{ii} = 0.6(i = 1, 2, 3)$. We consider system (36) with the given coefficients on $\mathcal{D} = B(0, 20) \subset \mathbb{R}^3$. The constraints of Corollary 1 are satisfied with $R = 20, h = 0.01$, $M = 0.84$. Then, $V(x) = |x|_1$ is a finite-time Lyapunov function for system (36) with the given coefficients. Hence, the origin of system (36) with the given coefficients is asymptotic stable on $\mathcal{D}$ (see Figures 7–9). Figure 10 clearly shows that V is not a Lyapunov function for system (36).

Remark 6. From Figures 7–9, we obtain that the simulation results are similar to that of [24], since the designed impulsive control is similar to each other. However, from examples of Section 4 and this chaotic system, we can conclude that construction of finite-time Lyapunov functions or design of impulsive control based on Theorem 1 is easier than the method proposed in [24]. The reason for this point is that we do not have to calculate the derivative of Lyapunov function along the continuous part of the trajectory of the considered system.

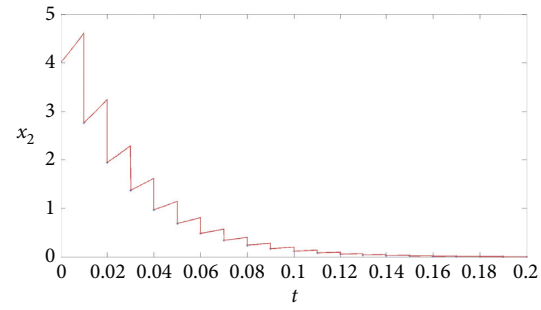

FIGURE 8: The trajectory of the state x_2 of system (36) with the coefficients $a = 35$, $b = (8/3)$, $c = 25$, $t_k = 0.01k(k = 1, 2, \ldots,)$, $d_{ij} = 0(i, j = 1, 2, 3, i \neq j)$, and $d_{ii} = 0.6(i - 1, 2, 3)$ and the initial condition $x(0) = (3, 4, 5)^T$.

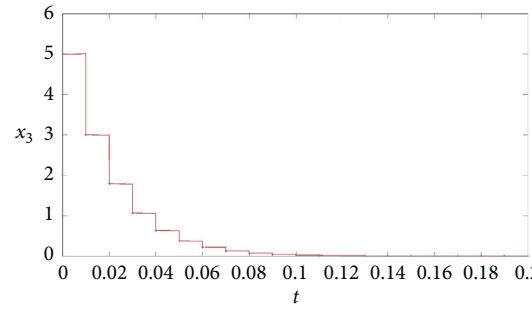

FIGURE 9: The trajectory of the state x_3 of system (36) with the coefficients $a = 35$, $b = (8/3)$, $c = 25$, $t_k = 0.01k(k = 1, 2, \ldots,)$, $d_{ij} = 0(i, j = 1, 2, 3, i \neq j)$, and $d_{ii} = 0.6(i = 1, 2, 3)$ and the initial condition $x(0) = (3, 4, 5)^T$.

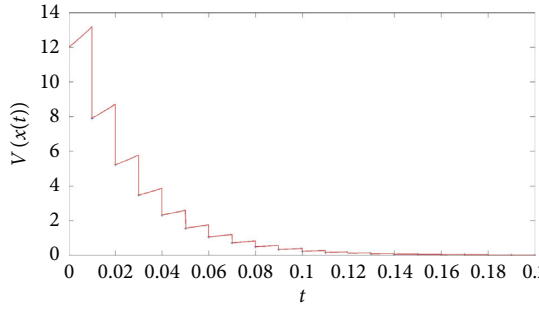

FIGURE 10: The trajectory of the finite-time Lyapunov function V of system (36) with the coefficients $a = 35$, $b = (8/3)$, $c = 25$, $t_k = 0.01k(k = 1, 2, \ldots,)$, $d_{ij} = 0(i, j = 1, 2, 3, i \neq j)$, and $d_{ii} = 0.6$ $(i = 1, 2, 3)$ and the initial condition $x(0) = (3, 4, 5)^T$.

6. Conclusion

In this paper, we introduced the definition of finite-time Lyapunov function for impulsive systems. It was proved that if there exists a finite-time Lyapunov function for system (1), then the origin of system (1) is asymptotically stable (Theorem 1). It is worthy to point out that the conditions imposed on finite-time Lyapunov functions for system (1) are more relaxed

than those on Lyapunov function which decrease along the continuous part of the trajectory or have negative jumps at all impulses. Finite-time Lyapunov functions can increase during some continuous part of the trajectory of the considered system and have positive jumps at some resetting times. This point was demonstrated by example. A converse finite-time Lyapunov theorem (Theorem 2) was proposed. Three examples were presented to illustrate how to analyze stability of the origin of an impulsive system via finite-time Lyapunov functions. According to our main results, impulsive control was designed to ensure the origin of the considered chaotic system is asymptotically stable. Some simulation results of the chaotic system with impulsive control were presented to show how to design an impulsive controller for the chaotic system by finite-time Lyapunov functions.

Data Availability

The data used to support the findings of this study are included within the article. The data used in computation are stated for each example in the article.

Conflicts of Interest

The authors declare that there are no conflicts of interest regarding the publication of this paper.

Acknowledgments

This study was partially supported by the National Natural Science Foundation of China (NSFC11701533) and the Fundamental Research Funds for the Central Universities, China University of Geosciences (Wuhan) (no. CUGGC05).

References

[1] D. D. Bainov and P. S. Simeonov, *System with Impulse Effects: Stability, Theory and Applications*, Academic Press, New York, NY, USA, 1989.

[2] V. Lakshmikantham, D. Bainov, and P. Simeonov, *Theory of Impulsive Differential Equations*, World Scientific, New York, NY, USA, 1989.

[3] M. S. Branicky, "Multiple Lyapunov functions and other analysis tools for switched and hybrid systems," *IEEE Transactions on Automatic Control*, vol. 43, no. 4, pp. 475–482, 1998.

[4] W. M. Haddad, V. S. Chellabonia, and S. Nersesov, *Impulsive and Hybrid Dynamic Systems: Stability, Dissipativity, and Control*, Princeton University Press, Princeton, NY, USA, 2006.

[5] J. Zhao and D. J. Hill, "On stability, L_2-gain and H_∞ control for switched systems," *Automatica*, vol. 44, no. 5, pp. 1220–1232, 2008.

[6] A. Michel and L. Hou, *Stability of Dynamical Systems: On the Role of Monotonic and Non-monotonic Lyapunov Functions*, Birkhäuser Basel, Switzerland, 2015.

[7] W. Ren and J. Xiong, "Vector Lyapunov function based input-to-state stability of stochastic impulsive switched time-delay systems," *IEEE Transactions on Automatic Control*, vol. 64, no. 2, pp. 654–669, 2018.

[8] W. Ren and J. Xiong, "Stability analysis of impulsive switched time-delay systems with state-dependent impulses," *IEEE Transactions on Automatic Control*, vol. 64, no. 9, pp. 3928–3935, 2019.

[9] V. Lakshmikantham and X. Liu, *Stability Analysis in Terms of Two Measures*, World Scientific, New York, NY, USA, 1993.

[10] A. I. Panas, T. Yang, and L. O. Chua, "Experimental results of impulsive synchronization between two Chua's circuits," *International Journal of Bifurcation and Chaos*, vol. 8, no. 3, pp. 639–644, 1998.

[11] V. Lakshmikantham and X. Liu, "Stability criteria for impulsive differential equations in terms of two measures," *Journal of Mathematical Analysis and Applications*, vol. 137, no. 2, pp. 591–604, 1989.

[12] X. Liu, "Stability results for impulsive differential systems with applications to population growth models," *Dynamics and Stability of Systems*, vol. 9, no. 2, pp. 163–174, 1994.

[13] T. Yang, "Impulsive control," *IEEE Transactions on Automatic Control*, vol. 44, no. 5, pp. 1081–1083, 1999.

[14] T. Yang and L. O. Chua, "Impulsive stabilization for control and synchronization of chaotic systems: Theory and application to secure communication," *IEEE Transactions on Circuits and Systems I: Fundamental Theory and Applications*, vol. 44, no. 10, pp. 976–988, 1997.

[15] T. Yang, L.-B. Yang, and C.-M. Yang, "Impulsive control of Lorenz system," *Physica D: Nonlinear Phenomena*, vol. 110, no. 1, pp. 18–24, 1997.

[16] S. Yuan, L. Zhang, and S. Baldi, "Adaptive stabilization of impulsive switched linear time-delay systems: a piecewise dynamic gain approach," *Automatica*, vol. 103, pp. 322–329, 2019.

[17] X. Yang, D. Peng, X. Lv, and X. Li, "Recent progress in impulsive control systems," *Mathematics and Computers in Simulation*, vol. 155, pp. 244–268, 2019.

[18] M. Lazar, A. I. Doban, and N. Athanasopoulos, "On stability analysis of discrete-time homogeneous dynamics," in *Proceedings of the System Theory, Control and Computing (ICSTCC)*, pp. 297–305, Sinaia, Romania, 2013.

[19] R. Geiselhart, *Advances in the stability analysis of large-scale discrete-time systems*, Ph.D. thesis, Universität Würzburg, Würzburg, Germany, 2015.

[20] R. Geiselhart and F. Wirth, "Solving iterative functional equations for a class of piecewise linear $K\infty$-functions," *Journal of Mathematical Analysis and Applications*, vol. 411, no. 2, pp. 652–664, 2014.

[21] A. Doban and M. Lazar, "Computation of Lyapunov functions for nonlinear differential equations via a Yoshizawa—type construction," in *Proceedings of the 10th IFAC Symposium on Nonlinear Control Systems NOLCOS*, pp. 29–34, Monterey, CA, USA, 2016.

[22] H. Li and A. Liu, "Computation of non-monotonic Lyapunov functions for continuous-time systems," *Communications in Nonlinear Science and Numerical Simulation*, vol. 50, pp. 35–50, 2017.

[23] H. Li and J. Wang, "Input-to-state stability of continuous-time systems via finite-time Lyapunov functions," *Discrete & Continuous Dynamical Systems - B*, vol. 25, no. 3, pp. 841–857, 2020.

[24] H. Li and A. Liu, "Asymptotic stability analysis via indefinite Lyapunov functions and design of nonlinear impulsive control systems," *Nonlinear Analysis: Hybrid Systems*, vol. 38, Article ID 100936, 2020.

[25] D. Bainov and P. Simeonov, *Integral Inequalities and Applications*, Kluwer Academic Publishers, Dordrecht, Netherlands, 1992.

[26] A. Browder, *Mathematical Analysis. An Introduction*, Springer, 1996.

[27] G. Qi, G. Chen, S. Du, Z. Chen, and Z. Yuan, "Analysis of a new chaotic system," *Physica A: Statistical Mechanics and its Applications*, vol. 352, no. 2–4, pp. 295–308, 2005.

Hindawi
Complexity
Volume 2020, Article ID 6479087, 5 pages
https://doi.org/10.1155/2020/6479087

WILEY | Hindawi

Research Article

Pontryagin's Maximum Principle for Optimal Control of Stochastic SEIR Models

Ruimin Xu and Rongwei Guo

School of Mathematics and Statistics, Qilu University of Technology (Shandong Academy of Sciences), Jinan 250353, China

Correspondence should be addressed to Rongwei Guo; rongwei_guo@163.com

Received 23 June 2020; Revised 2 August 2020; Accepted 24 September 2020; Published 14 October 2020

Academic Editor: Zhouchao Wei

In this paper, we study the necessary conditions as well as sufficient conditions for optimality of stochastic SEIR model. The most distinguishing feature, compared with the well-studied SEIR model, is that the model system follows stochastic differential equations (SDEs) driven by Brownian motions. Hamiltonian function is introduced to derive the necessary conditions. Using the explicit formulation of adjoint variables, desired necessary conditions for optimal control results are obtained. We also establish a sufficient condition which is called verification theorem for the stochastic SEIR model.

1. Introduction

New corona viruses are very harmful to people. Especially, COVID-19 is currently being spread around the world. It has seriously affected people's lives. Many countries have made good efforts to deal with it and prevent it. At present, the COVID-19 epidemic in China has been basically controlled. It is well known that SEIR models are widely used to model the spreading of infectious diseases in a population. Up to now, many researchers from the world have achieved a variety of both theoretical results and applications, see [1, 2, 7, 9, 15, 16, 18, 20, 21] and the references therein.

However, it is worth pointing that out that SEIR models in the existing literatures are deterministic models. As we know the stochastic events are inevitable in practice, and the stochastic effects that may lead to significant changes, thus, the stochastic SEIR models maybe better to be applied to describe the COVID-19 epidemic. Motivated by the actual situation in reality and the lack of theory, this paper studies the optimal control of stochastic SEIR model. To the best of our knowledge, there were few literatures about the optimal control of epidemic model in the stochastic case. Our main objective is to derive necessary conditions for optimality of the stochastic SEIR model by using the stochastic maximum principle (SMP).

Stochastic optimal control problems have received considerable research attention in recent years due to wide applicability in a number of different fields such as physics, biology, economics, and management science. As it is well known, dynamic programming principle (DPP) and SMP are two main tools to study stochastic control problems. SMP, which provides a necessary condition of an optimal control in stochastic optimal control problems known as the stochastic version of Pontryagin's type [3–6, 8, 11–14, 19], has been the tool predominantly used to study the stochastic optimal control problems and some stochastic differential game problems.

For example, by using SMP, Xu and Shi [17] obtain the feedback form of optimal control for linear-quadratic-Gaussian (LQG) problems to study stochastic large population system with jump diffusion processes. The standard SMP involves solving the adjoint equation and minimizing the Hamiltonian function. We also followed this in our paper. We should point out that the SEIR model studied in [10] is deterministic case, while our SEIR model is stochastic case, that is, the main difference between our model and the model studied in [10].

The organization of this paper is as follows. Section 2 is devoted to the problem formulation and assumptions. Necessary conditions for optimality are introduced in

Section 3. Section 4 aims to prove that the necessary conditions presented in Section 3 are also the sufficient conditions for optimality. Finally, we end our work with some concluding remarks in Section 5.

2. Problem Statement and Assumptions

Throughout this paper, let $T > 0$ be a fixed time horizon and $(\Omega, \mathscr{F}, \mathbb{F}; \mathbb{P})$ be a given complete filtered probability space, on which independent standard one-dimensional Brownian motions $\{W_i(t),\ 1 \le i \le 4\}_{0 \le t \le T}$ are defined. The superscript τ denotes the transpose of vectors or matrices. We suppose that the filtration $\mathscr{F}_t \ge 0$ is generated by the independent standard one-dimensional standard Brownian motions $\{W_i(t),\ 1 \le i \le 4\}_{0 \le t \le T}$.

Let $L^2(0, T; \mathbb{R})$ denote the set of Lebesgue measurable functions $\psi(\cdot)$: $[0, T] \longrightarrow \mathbb{R}$ such that $\int_0^T |\psi(t)|^2 \mathrm{d}t < +\infty$. We write $\varphi(.) \in L^2_{\mathscr{F}}(0, T; \mathbb{R})$ if $\varphi(.)$: $[0, T] \times \Omega \longrightarrow \mathbb{R}$ is an $\mathscr{F}_t$-adapted square-integrable process (i.e., $\mathbb{B}\int_0^T |\varphi(t)|^2 \mathrm{d}t < +\infty$). Let U be nonempty subsets of $\mathbb{R}$. We introduce the admissible control set as

$$\mathscr{U} \coloneqq \left\{ v(\cdot) \mid v(t) \in U, \quad 0 \le t \le T; v(\cdot) \in L^2_{\mathscr{F}}(0, T; \mathbb{R}) \right\}. \tag{1}$$

Now, we introduce our stochastic SEIR model. Let $S(t), E(t), I(t)$, and $R(t)$ represent the number of individuals in the susceptible, exposed, infectious, and recovered compartments at time t, respectively. The total population is denoted by $N(t) = S(t) + E(t) + I(t) + R(t)$. Let $u(t)$ denote the fraction of susceptible individuals being vaccinated per unit of time.

We input the random disturbance proportionally to each variable value in the model and get the following dynamical system:

$$\begin{cases} \mathrm{d}S(t) = (bN(t) - \mu S(t) - \beta S(t) I(t) - u(t) S(t))\mathrm{d}t + \sigma_1 S(t) \mathrm{d}W_1(t), \\ \mathrm{d}E(t) = (\beta S(t) I(t) - (\mu + \epsilon) E(t))\mathrm{d}t + \sigma_2 E(t) \mathrm{d}W_2(t), \\ \mathrm{d}I(t) = (\epsilon E(t) - (\mu + \gamma + a) I(t))\mathrm{d}t + \sigma_3 I(t) \mathrm{d}W_3(t), \\ \mathrm{d}R(t) = (\gamma I(t) - \mu R(t) + u(t) S(t))\mathrm{d}t + \sigma_4 R(t) \mathrm{d}W_4(t), \\ S(0)\& = S\_0, \\ E(0) = E\_0, \\ I(0) = I\_0, \\ R(0) = R\_0. \end{cases} \tag{2}$$

The parameters in the disease transmission model is described as follows: b is the natural birth rate, μ represents the natural death rate, a denotes the death rate due to the disease, and β represents the incidence coefficient of horizontal transmission, and let ϵ be the rate at which the exposed individuals become infectious, and γ is removal rate. Note that the rate of transmission of the disease is $\beta S(t) I(t)$. In the above model, $\sigma = (\sigma_1, \sigma_2, \sigma_3, \sigma_4)$ denotes the random disturbance proportionally to each variable value in the model. The parameters in the model are supposed to be constants for simplicity. For more information about the disease transmission model, we refer the reader to [2, 9, 13] and references within.

The expected cost functional is given by

$$J(u) = \mathbb{E}\left[\int_0^T \left(QI(t) + Gu^2(t) \right) \mathrm{d}t \right], \tag{3}$$

where Q and G are given constants.

The optimal control problem under consideration is as follows.

Problem (P): the objective of the control problem is to find admissible control $u^* \in \mathscr{U}$ such that

$$J(u^*) = \inf_{u \in \mathscr{U}} J(u). \tag{4}$$

A control that solves this problem is called optimal.

3. Necessary Conditions for Optimality

This section focuses on the necessary optimality conditions of Problem (P).

In order to apply the necessary conditions for optimal control in the form of maximum principle, we first introduce some notations. Assume that

$$\begin{aligned} x &\coloneqq \begin{pmatrix} S \\ E \\ I \\ R \end{pmatrix}, \\ A &\coloneqq \begin{pmatrix} b - \mu & b & b & b \\ 0 & -(\mu + \epsilon) & 0 & 0 \\ 0 & \epsilon & -(\mu + \gamma + a) & 0 \\ 0 & 0 & \gamma & -\mu \end{pmatrix}, \\ f_1(x) &\coloneqq \begin{pmatrix} -\beta SI \\ \beta SI \\ 0 \\ 0 \end{pmatrix}, \\ f_2(x) &\coloneqq \begin{pmatrix} -S \\ 0 \\ 0 \\ S \end{pmatrix}, \\ W &\coloneqq \begin{pmatrix} W_1 \\ W_2 \\ W_3 \\ W_4 \end{pmatrix}, \\ \sigma(x) &\coloneqq \mathrm{diag}(\sigma_1 S, \sigma_2 E, \sigma_3 I, \sigma_4 R), \\ L &= (0, 0, Q, 0). \end{aligned} \tag{5}$$

Therefore, stochastic SEIR model (2) can be written as

$$\begin{cases} \mathrm{d}x(t) = \big(Ax(t) + f_1(x(t)) + f_2(x(t))u(t)\big)\mathrm{d}t + \sigma(x(t))\mathrm{d}W(t), \\ x(0) = (S_0, E_0, I_0, R_0)^\tau. \end{cases} \tag{6}$$

The corresponding cost functional is

$$J(u) = \mathbb{E}\left[\int_0^T \big(Lx(t) + Gu^2(t)\big)\mathrm{d}t\right]. \tag{7}$$

Let (x^*, u^*) be the optimal pair of Problem P. The standard Hamiltonian function is given by

$$H(x, p, q, u) = \langle p, Ax + f_1(x) + f_2(x)u\rangle + \sigma(x)q + Lx + Gu^2, \tag{8}$$

where the adjoint variable $(p(.), q(.))$ satisfies

$$\begin{cases} \mathrm{d}p(t) = -H_x[t]\mathrm{d}t + q(t)\mathrm{d}W(t), \\ \mathrm{p}(T) = (0, 0, 0, 0), \end{cases} \tag{9}$$

where $H[t] := H(x^*(t), p(t), q(t), u^*(t))$.

Next, we want to obtain the adjoint variable $(p(.), q(.))$ explicitly. Let $p = (p_S, p_E, p_I, p_R)^\tau$ and $q = (q_S, q_E, q_I, q_R)^\tau$. According to (9), (p, q) are explicitly given by

$$\begin{cases} \mathrm{d}p_S(t) = -\big(b - \mu - \beta I^*(t) - u^*(t)\big)p_S(t)\mathrm{d}t - \beta I^*(t)p_E(t)\mathrm{d}t + \sigma_1 q_S(t)\mathrm{d}W_1(t), \\ \mathrm{d}p_E(t) = -\big(bp_S(t) - (\mu + \epsilon)p_E(t) + \epsilon p_I(t)\big)\mathrm{d}t + \sigma_2 q_E(t)\mathrm{d}W_2(t), \\ \mathrm{d}p_I(t) = -\big(bp_S(t) - \beta S^*(t)p_S(t) + \beta S^*(t)p_E(t) - (\mu + \gamma + a)p_I(t) + \gamma p_R(t) + Q\big)\mathrm{d}t + \sigma_3 q_I(t)\mathrm{d}W_3(t), \\ \mathrm{d}p_R(t) = -\big(bp_S(t) - \mu p_R(t) + u^*(t)p_R(t)\big)\mathrm{d}t + \sigma_4 q_R(t)\mathrm{d}W_4(t). \end{cases} \tag{10}$$

Next, we evaluate the necessary condition for the optimal control. By (8), we have

$$H\_u(x, p, q, u) = -Sp\_S + Sp\_R + 2Gu = 0, \tag{11}$$

which means

$$u^*(t) = \frac{1}{2G}\big(p_S(t) - p_R(t)\big)S^*(t). \tag{12}$$

Now, we summarize the above discussion with the main result of this article.

Theorem 1. *Let (x^*, u^*) be the optimal pair of Problem P with $x^* := (S^*, E^*, I^*, R^*)^\tau$. Then, $u^*(.)$ fulfills (12), where $(p_S(.), p_R(.))$ admits (10).*

4. Sufficient Conditions for Optimality

In this section, we will establish the sufficient maximum principle (also called verification theorem) of Problem P. That is to say, $u^*(.)$ given in (12) is also the sufficient condition of Problem P.

Theorem 2. *Assume that $u^*(.)$ fulfills (12) with state trajectory $x^* := (S^*, E^*, I^*, R^*)^\tau$ which id given such that there exist solutions $(p_S(.), p_R(.))$ to the adjoint equation (10). Then, (x^*, u^*) is the optimal pair of Problem P.*

Proof. For any $u \in \mathcal{U}$, we consider

$$J(u) - J(u^*) = \mathbb{E}\left[\int_0^T \Big(Q\big(I(t) - I^*(t)\big) + G\big(u^2(t) - (u^*(t))^2\big)\Big)\mathrm{d}t\right]. \tag{13}$$

Applying IÔ's formula to $\langle p(.), x(.) - x^*(.)\rangle$, we obtain

$$
\begin{aligned}
&\mathbb{E}\left[\langle p(T), x(T)-x^*(T)\rangle - \langle p(0), x(0)-x^*(0)\rangle\right] \\
&= \mathbb{E}\left[\int_0^T \langle p(t), \mathrm{d}\left(x(t)-x^*(t)\right)\rangle + \int_0^T \langle x(t)-x^*(t), \mathrm{d}p(t)\rangle + \int_0^T q(t)\left(\sigma(x(t))-\sigma\left(x^*(t)\right)\right)\mathrm{d}t\right] \\
&= \mathbb{E}\left[\int_0^T \langle p(t), A\left(x(t)-x^*(t)\right) + f_1(x(t)) - f_1\left(x^*(t)\right) + f_2(x(t))u(t) - f_2\left(x^*(t)\right)u^*(t)\rangle \mathrm{d}t\right] \\
&\quad + \mathbb{E}\left[\int_0^T q(t)\left(\sigma(x(t))-\sigma\left(x^*(t)\right)\right)\right]\mathrm{d}t - \int_0^T \langle x(t)-x^*(t), H_x[t]\rangle \mathrm{d}t \\
&= \mathbb{E}\left[\int_0^T \left(H(x(t), p(t), q(t), u(t)) - Lx(t) - Gu^2(t)\right) - \left(H[t] - Lx^*(t) - G\left(u^*(t)\right)^2\right)\mathrm{d}t\right] \\
&\quad - \mathbb{E}\left[\int_0^T H(x(t), p(t), q(t), u(t)) - H[t] - \langle x(t)-x^*(t), H_x[t]\rangle\right]\mathrm{d}t \\
&= \mathbb{E}\left[\int_0^T H(x(t), p(t), q(t), u(t)) - H[t] - \langle x(t)-x^*(t), H_x[t]\rangle\right]\mathrm{d}t \\
&\quad - \mathbb{E}\left[\int_0^T \left(L\left(x(t)-x^*(t)\right) + G\left(u^2(t) - \left(u^*(t)\right)^2\right)\right)\right]\mathrm{d}t.
\end{aligned} \tag{14}
$$

Combining (6), (9), (13), with (14), one has

$$
0 = \mathbb{E}\left[\int_0^T H(x(t), p(t), q(t), u(t)) - H[t] - \langle x(t)-x^*(t), H_x[t]\rangle \mathrm{d}t\right] - J(u) + J\left(u^*\right) \geq -J(u) + J\left(u^*\right), \tag{15}
$$

where, in the last step, we have used the condition of $u^*(\cdot)$ which fulfills (12).

Therefore, $J(u^*) \leq J(u)$. Hence, we draw the desired conclusion. □

5. Conclusion

Maria do Rosário de et al. [10] considered an optimal control problem with mixed control-state constraint for a SEIR epidemic model of human infectious diseases. Motivated by their pioneering work and the lack of theory, this paper is concerned with the necessary conditions (also, the sufficient conditions) for optimality of the stochastic SEIR model. The model system follows SDEs driven by Brownian motions and with the corresponding cost. It is the first attempt to study this kind of control problem in our technical note, to the authors' knowledge. Using the explicit formulation of adjoint variables, we obtain the desired necessary conditions for optimal control results.

Some interesting topics deserve further investigations. On the one hand, one may determine the optimal control strategies for the stochastic delayed SIR model and compare it with that presented in this work. On the other hand, we shall investigate some more realistic but complex models, such as considering the effects of impulsive perturbations on the system. We leave these investigations in our future work.

Data Availability

The data used to support the findings of the study are available from the corresponding author upon request.

Conflicts of Interest

The authors declare that there are no conflicts of interest regarding the publication of this paper.

Acknowledgments

This research was partially supported by the Project of Shandong Province Higher Educational Science and Technology Program (Grant no. J18KA221), National Natural Science Foundation of China (Grant no. 61973185), Natural Science Foundation of Shandong Province (Grant no. ZR2018MF016), Development Plan of Young Innovation Team in Colleges and Universities of Shandong Province (Grant no.2019KJN011), Shandong Province Key Research and Development Program (Grant no. 2018GGX103054), and Young Doctor Cooperation Foundation of Qilu University of Technology (Shandong Academy of Sciences) (Grant no. 2018BSHZ2008).

References

[1] A. Abdelhadi and L. Hassan, "Optimal control strategy for SEIR with latent period and a saturated incidence rate," *ISRN Applied Mathematics*, vol. 2013, pp. 1–4, 2013.

[2] B. Armbruster and E. Beck, "Elementary proof of convergence to the mean-field model for the SIR process," *Journal of Mathematical Biology*, vol. 75, no. 2, pp. 327–339, 2016.

[3] A. Bensoussan, "Lectures on stochastic control," in *Nonlinear Filtering and Stochastic Control (Cortona, 1981), Lecture Notes in Math. 972*, pp. 1–62, Springer, Berlin, New York, 1982.

[4] J.-M. Bismut, "Conjugate convex functions in optimal stochastic control," *Journal of Mathematical Analysis and Applications*, vol. 44, no. 2, pp. 384–404, 1973.

[5] A. Cadenillas, "A stochastic maximum principle for systems with jumps, with applications to finance," *Systems & Control Letters*, vol. 47, no. 5, pp. 433–444, 2002.

[6] U. G. Haussmann, "General necessary conditions for optimal control of stochastic systems," *Mathematical Programming Studies*, vol. 6, pp. 30–48, 1976.

[7] X. Han, F. Li, and X. Meng, "Dynamics analysis of a nonlinear stochastic SEIR epidemic system with varying population size," *Entropy*, vol. 2018, pp. 1–20, 2018.

[8] H. J. Kushner, "Necessary conditions for continuous parameter stochastic optimization problems," *SIAM Journal on Control*, vol. 10, no. 3, pp. 550–565, 1972.

[9] Q. Liu, D. Jiang, N. Shi, T. Hayat, and B. Ahmad, "Stationary distribution and extinction of a stochastic SEIR epidemic model with standard incidence," *Physica A: Statistical Mechanics and Its Applications*, vol. 476, pp. 58–69, 2017.

[10] P. Maria do Rosário de, I. Kornienko, and H. Maurer, "Optimal control of a SEIR model with mixed constraints and L^1 cost," in *CONTROLO'2014–Proceedings of the 11th Portuguese Conference on Automatic Control*, pp. 135–145, Guimaraes, Portugal, January 2015.

[11] S. Peng, "A general stochastic maximum principle for optimal control problems," *SIAM Journal on Control and Optimization*, vol. 28, no. 4, pp. 966–979, 1990.

[12] S. Peng, "Backward stochastic differential equations and applications to optimal control," *Applied Mathematics & Optimization*, vol. 27, no. 2, pp. 125–144, 1993.

[13] J. Shi and Z. Wu, "Maximum principle for forward-backward stochastic control system with random jumps and applications to finance," *Journal of Systems Science and Complexity*, vol. 23, no. 2, pp. 219–231, 2010.

[14] J. Shi and Z. Wu, "A risk-sensitive stochastic maximum principle for optimal control of jump diffusions and its applications," *Acta Mathematica Scientia*, vol. 31B, no. 2, pp. 419–433, 2011.

[15] N. Sherborne, J. C. Miller, K. B. Blyuss, I. Z. Kiss, and I. Z. Kiss, "Mean-field models for non-Markovian epidemics on networks," *Journal of Mathematical Biology*, vol. 76, no. 3, pp. 755–778, 2018.

[16] X. Wang, H. Peng, and B. Shi, "Optimal vaccination strategy of a constrained time-varying SEIR epidemic model," *Communications in Nonlinear Sciences and Numerical Simulation*, vol. 67, pp. 37–48, 2019.

[17] R. Xu and J. Shi, "-Nash mean-field games for linear-quadratic systems with random jumps and applications," *International Journal of Control*, vol. 114, pp. 1–11, Article ID 108835, 2019.

[18] X. Yi, R. Guo, and Y. Qi, "Stabilization of chaotic systems with both uncertainty and disturbance by the UDE-based control method," *IEEE Access*, vol. 8, no. 1, pp. 62471–62477, 2020.

[19] J. Yong and X. Zhou, *Stochastic Controls: Hamiltonian Systems and HJB Equations, Applied Mathematics*, Vol. 3, Springer-Verlag, New York, NY, USA, 1999.

[20] D. Zhao, T. Zhang, and S. Yuan, "The threshold of a stochastic SIVS epidemic model with nonlinear saturated incidence," *Physica A: Statistical Mechanics and Its Applications*, vol. 443, pp. 372–379, 2016.

[21] X. Zhang and K. Wang, "Stochastic SEIR model with jumps," *Applied Mathematics and Computation*, vol. 239, pp. 133–143, 2014.

Hindawi
Complexity
Volume 2020, Article ID 8821156, 5 pages
https://doi.org/10.1155/2020/8821156

Research Article

A Study on the Complexity of a New Chaotic Financial System

Yi Liao,[1] **Yiran Zhou**,[1] **Fei Xu**,[2] **and Xiao-Bao Shu**[3]

[1]*School of Business Administration, Southwestern University of Finance and Economics, Chengdu, Sichuan 610074, China*
[2]*Department of Mathematics, Wilfrid Laurier University, Waterloo, Ontario, Canada*
[3]*Department of Mathematics, Hunan University, Changsha 410082, China*

Correspondence should be addressed to Fei Xu; fxu.feixu@gmail.com

Received 17 August 2020; Revised 19 September 2020; Accepted 25 September 2020; Published 10 October 2020

Academic Editor: Yongjian Liu

The interaction of elements in a financial system can exhibit complex dynamic behaviours. In this article, we use a system of differential equations to model the evolution of a financial system and study its complexity. Numerical simulations show that the system exhibits a variety of rich dynamic behaviours, including chaos. Bifurcation diagrams show that the system behaves chaotically over a wide range of system parameters.

1. Introduction

Chaotic attractors have attracted the attention of scholars in different fields. Chaos has a wide range of applications in natural science and engineering. The first chaotic system is the Lorenz system [1], which was introduced for weather forecast. Later investigations found that there exist chaotic attractors in the chemical reaction model [2] and electrical circuit [3]. Investigation shows that the generalized Lorenz systems family includes the classical Lorenz system [1], the Chen system [4], and the Lü system [5]. Zhang et al. studied the Lü system and showed that the Lü system is globally bounded using dynamical systems theory [6]. In addition, chaos has a wide range of applications in cryptography and engineering [4, 5, 7]. Investigations have shown that a variety of ecological systems display chaotic behaviours [8, 9]. In recent years, chaotic systems that display multiscroll [10–12] and multiwing [13] chaotic attractors were considered in the literature. Zhang et al. studied the dynamics of a New 5D Hyperchaotic system of Lorenz type and obtained the global exponential attractive set and the ultimate bound set for this system of Lorenz Type [14]. Such chaotic systems display more complex dynamical behaviours and have potential applications in engineering.

A variety of economic and financial systems display complex behaviours. Benhabib et al. studied a series of market models and showed that such systems behave chaotically [15–17]. Grandmont [18] studied the chaos in endogenous competitive business cycles and performed bifurcation analysis. Brock analysed the maximum Lyapunov exponent of quarterly US real GNP data (1947–1985) and confirmed the chaotic behaviours in the data [19].

Research shows that there is chaos in market models, financial systems, and supply chains. For example, Huang and Li used system of differential equations to model a financial system, in which the interactions between interest rate, investment demand, and price index are considered [20]. This model was further investigated by Ma and Chen [21, 22]. The authors performed a complete study on the dynamical properties of the model. Xu, et al. studied the interaction effect among several financial factors in a financial system using mathematical models [23]. Their investigation showed that such model displays rich dynamical behaviours including chaos. Synchronization of the model were considered in their work. Zhang et al. studied a 4D Chaos Financial System [24]. Investigations show that supply chain systems also display a variety of complex dynamical behaviours [25–27].

In this work, we construct a mathematical model to study a financial system using differential equations. The model captures the interaction between a variety of financial factors. The rest of this paper is organized as follows. In

Section 2, we formulate the model. In Section 3, we perform numerical simulations to study the complexity of the model. Conclusions are drawn in Section 4.

2. Model Formulation

In this section, we consider the model formulation of the financial system. Huang and Li proposed a model using differential equations to investigate the behaviour of a financial system containing interest rate, investment demand, and price index [20]. In the following, based on the model presented in [20], we present an alternative model to consider the interplay between the interest rate $x(t)$, the investment demand $y(t)$, and the price index $z(t)$. The model is given by

$$\begin{aligned} \frac{\mathrm{d}x}{\mathrm{d}t} &= gz + (y - a)x, \\ \frac{\mathrm{d}y}{\mathrm{d}t} &= -by^2 - sx^2 + r, \\ \frac{\mathrm{d}z}{\mathrm{d}t} &= -cz - \beta x - py, \end{aligned} \tag{1}$$

where a, b, c, p, r, s, and β are constants. System (1) assumes that the rate of change of interest rate is proportional to the price index. Investment demand significantly influences the interest rate. On one hand, if the investment demand exceeds the saving amount, the bank will increase the interest rate. On the other hand, when the investment demand is low, the saving amount may exceed the investment demand. In this case, the bank has to reduce the interest rate to encourage loan. For the investment demand $y(t)$, it admits a natural growth rate of r. If the interest rate is increased, the investment will be negatively affected. That is to say, the growth rate of the investment demand will decrease. Excessive investment demand will lead to the decrease of the change rate of the investment demand. Therefore, we have $-by^2$ term, where we assume that the rate of change of investment demand is negatively correlated with the square of investment demand. It is assumed that the interest rate has negative correlation on the change rate of the price index with rate β. The change rate of price index will decrease with the increase of investment demand. Compared with the chaotic system proposed in [21], the price index $z(t)$ in the system proposed in this paper is affected by the investment demand $y(t)$. On one hand, an increase in investment demand will inevitably lead to an increase in production, which will lead to a decrease in price. On the other hand, a decrease in investment demand $y(t)$ will lead to a decrease in the amount of products in the market, leading to an increase in the average price.

3. Dynamical Behaviour of the Model

In this section, we investigate the dynamical behaviours of the model (1). System (1) displays chaotic behaviours under the following parameter combinations: $a = 0.3$, $b = 0.02$, $c = 1$, $r = 1$, $s = 0.1$, $p = 0.05$, $g = 1.2$, and $\beta = 1$. With these parameters, the system admits the following equilibrium points:

$$\begin{aligned} E_1 &= (0.04949849664, -7.070201517, 0.3040115792), \\ E_2 &= (0.07616084207, 7.069016737, -0.4296116789), \\ E_3 &= (3.087391472, 1.529728564, -3.163877901), \\ E_4 &= (-3.093050811, 1.471456216, 3.019478000). \end{aligned} \tag{2}$$

Linearizing system (1) at any of its equilibrium $E_* = (x^*, y^*, z^*)$ yields

$$J = \begin{bmatrix} y^* - a & x^* & g \\ -2sx^* & -2by^* & 0 \\ -\beta & -p & -c \end{bmatrix}. \tag{3}$$

By calculating the corresponding eigenvalues of E_1, E_2, E_3, and E_4, we find that these equilibrium points are all unstable.

We then study system (1) numerically to investigate its dynamic behaviours. The phase portrait of model (1) is shown in Figure 1, which shows that the trajectory of the system is a chaotic attractor. Since the model describes the interaction among the three financial factors, the complicated behaviours of the model imply that the interplay between these financial factors causes complex behaviours. It is well known that one of the characteristics of a chaotic system is its pseudo-random behaviour. Next, we examine the time history of the system. As is shown in Figure 2, the time history of system (1) is unpredictable and displays complex and pseudorandom behaviours.

Another characteristic of chaotic systems is their sensitivity to initial conditions. That is to say, for the same system, for the same parameters, different initial values will lead to completely different system behaviours. Here, we use numerical method to show the sensitivity to initial values of the financial system (1). As shown in Figure 3, for system (1), we use initial values (1.2, 1.5, 1.6) to obtain the blue trajectory. Under the same parameters, system (1) with initial values (0.2, 0.5, 0.6) yields red trajectory. From Figure 3, we can see that the trajectories corresponding to different initial conditions are completely different, i.e., chaotic system (1) is sensitive to initial conditions.

Model (1) displays a variety of complicated dynamical behaviours. In the following, we create bifurcation diagrams to illustrate that the system behaves chaotically over a wide range of parameters. In the bifurcation diagram, we show the peak values of state variable y with the variation of r, g, and β.

The bifurcation diagram of system (1) with the variation of r is shown in Figure 4. We find that the system behaves chaotically for $r \in [0.6, 1.8]$. In this model, r is the natural growth rate of the investment demand $y(t)$. The simulation results show that increasing r can effectively reduce the complicate behaviours of the model. Parameter g significantly influences the behaviour of system (1) as well. Bifurcation diagram Figure 5 implies that the system behaves chaotically for $g \in [0.85, 1.5]$. Next, we consider the dynamic

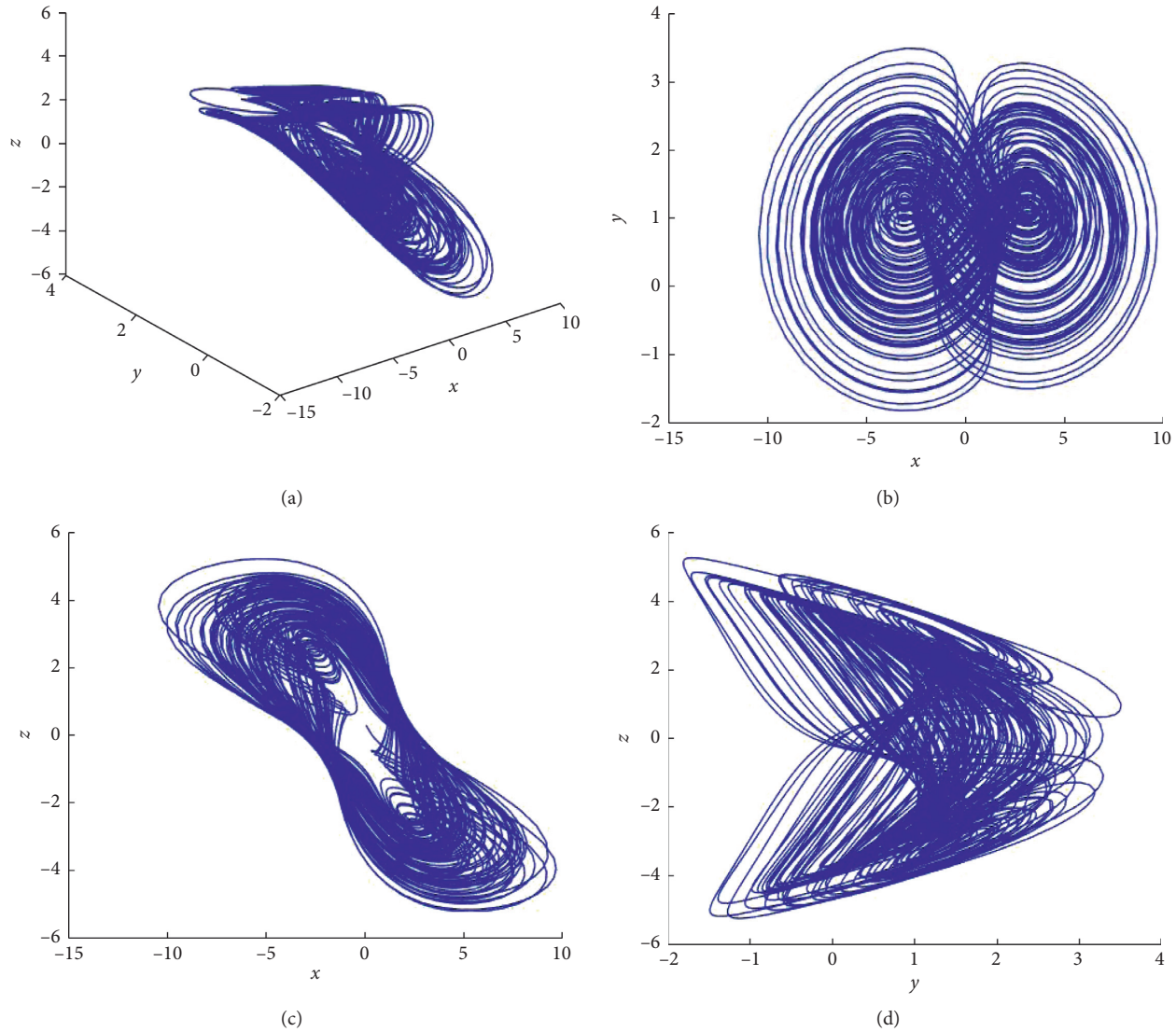

Figure 1: Simulation results of system (1) when $a = 0.3$, $b = 0.02$, $c = 1$, $r = 1$, $s = 0.1$, $p = 0.05$, $g = 1.2$, and $\beta = 1$. (a) In the x-y-z space, (b) projected on the x-y plane, (c) projected on the x-z plane, and (d) projected on the y-z plane.

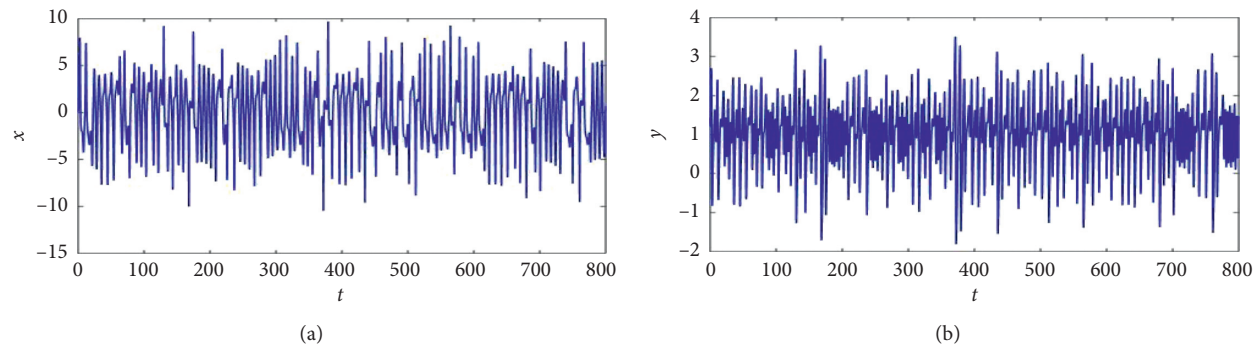

Figure 2: Continued.

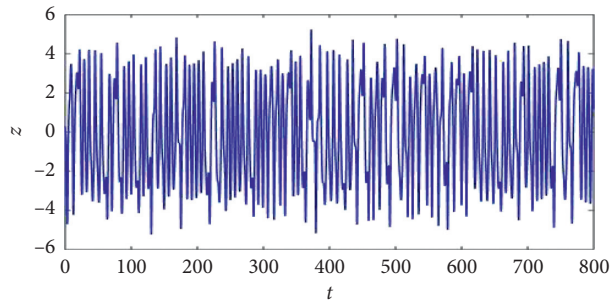

Figure 2: Time history of system (1) for $a = 0.3$, $b = 0.02$, $c = 1$, $r = 1$, $s = 0.1$, $p = 0.05$, $g = 1.2$, and $\beta = 1$. (a) Time history of x, (b) time history of y, and (c) time history of z.

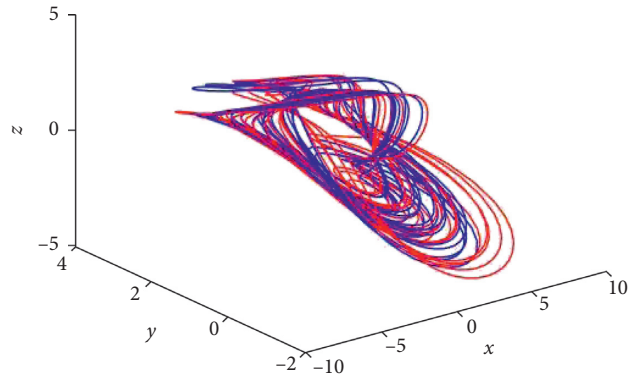

Figure 3: Simulation results of system (1) for $a = 0.3$, $b = 0.02$, $c = 1$, $r = 1$, $s = 0.1$, $p = 0.05$, $g = 1.2$, and $\beta = 1$ in the x-y-z space, where the blue trajectory has the initial condition (1.2, 1.5, 1.6) and the red trajectory has the initial condition (0.2, 0.5, 0.6).

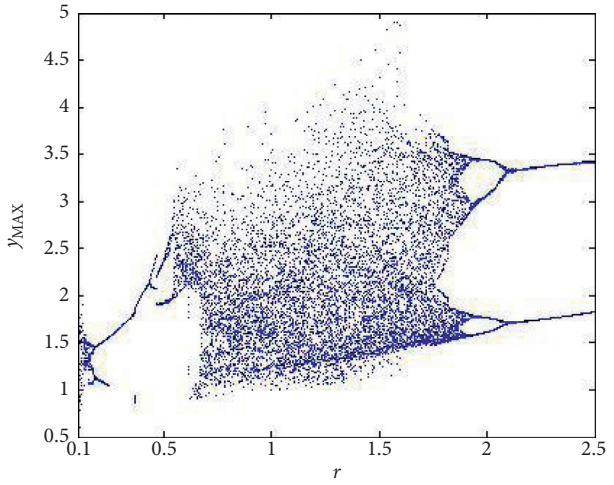

Figure 4: Bifurcation diagram of system (1) as r varies from 0.1 to 2.5. The values of all the other parameters are the same as those in Figure 1.

behaviours of system (1) with the variation of β. As shown in Figure 6, the system displays chaotic attractors for $\beta \in [0.72, 1.26]$.

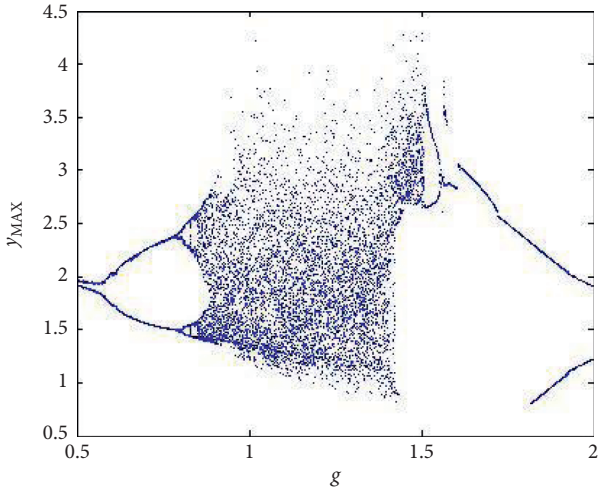

Figure 5: Bifurcation diagram of system (1) as g varies from 0.5 to 2. The values of all the other parameters are the same as those in Figure 1.

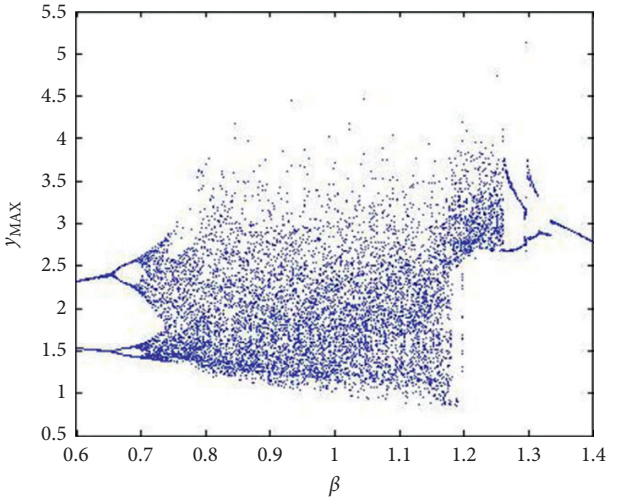

Figure 6: Bifurcation diagram of system (1) as β varies from 0.6 to 1.4. The values of all the other parameters are the same as those in Figure 1.

4. Conclusions

In this paper, we propose a system of differential equations to model the interactions between factors in a financial system. We find that the behaviours of the system are unpredictable and sensitive to the initial conditions, and the time history of the system displays pseudo-random behaviours, which implies the system has chaotic behaviours. The financial system displays a variety of complicated dynamical behaviours including chaos and period-doubling bifurcations. Bifurcation diagrams are created to show that the system behaves chaotically over a wide range of system parameters, which indicates that the interactions among the three factors in the financial model cause complex behaviours.

Data Availability

All the data are included in the article.

Conflicts of Interest

The authors declare that there are no conflicts of interest regarding the publication of this paper.

Acknowledgments

This work was supported by the Innovation Platforms Open Foundation of Hunan Educational Committee (grant no. 541109100002).

References

[1] E. N. Lorenz, "Deterministic nonperiodic flow," *Journal of the Atmospheric Sciences*, vol. 20, no. 2, pp. 130–141, 1963.

[2] O. E. Rössler, "An equation for continuous chaos," *Physics Letters A*, vol. 57, no. 5, pp. 397-398, 1976.

[3] L. Chua, M. Komuro, and T. Matsumoto, "The double scroll family," *IEEE Transactions on Circuits and Systems*, vol. 33, no. 11, pp. 1072–1118, 1986.

[4] G. Chen and T. Ueta, "Yet another chaotic attractor," *International Journal of Bifurcation and Chaos*, vol. 9, no. 7, pp. 1465-1466, 1999.

[5] J. Lü and G. Chen, "A new chaotic attractor coined," *International Journal of Bifurcation and Chaos*, vol. 12, no. 3, pp. 659–661, 2002.

[6] F. Zhang, X. Liao, and G. Zhang, "On the global boundedness of the Lü system," *Applied Mathematics and Computation*, vol. 284, pp. 332–339, 2016.

[7] X. Wang, L. Teng, and X. Qin, "A novel colour image encryption algorithm based on chaos," *Signal Processing*, vol. 92, no. 4, pp. 1101–1108, 2012.

[8] A. Hastings and T. Powell, "Chaos in a three-species food chain," *Ecology*, vol. 72, no. 3, pp. 896–903, 1991.

[9] F. Xu, R. Cressman, R. Cressman, and V. Křivan, "Evolution of mobility in predator-prey systems," *Discrete & Continuous Dynamical Systems - B*, vol. 19, no. 10, pp. 3397–3432, 2014.

[10] F. Xu, P. Yu, and X. Liao, "Global analysis on n-scroll chaotic attractors of modified Chua's circuit," *International Journal of Bifurcation and Chaos*, vol. 19, no. 1, pp. 135–157, 2009.

[11] Y. Ma, Y. Li, G. Zhao, P. Zeng, and Y. Yang, "Research on grid scroll chaotic extended sequence algorithm and its circuit implementation for F-OFDM System," *Complexity*, vol. 2019, Article ID 5904801, 7 pages, 2019.

[12] X. Hu and P. Zhou, "Coexisting three-scroll and four-scroll chaotic attractors in a fractional-order system by a three-scroll integer-order memristive chaotic system and chaos control," *Complexity*, vol. 2020, Article ID 5796529, 7 pages, 2020.

[13] F. Xu, "A class of integer order and fractional order hyperchaotic systems via the Chen system," *International Journal of Bifurcation and Chaos*, vol. 26, no. 6, 2016.

[14] F. C. Zhang, R. Chen, X. Y. Wang, X. S. Chen, C. L. Mu, and X. F. Liao, "Dynamics of a new 5D hyperchaotic system of Lorenz type," *International Journal of Bifurcation and Chaos*, vol. 28, no. 3, 2018.

[15] J. Benhabib and K. Nishimura, "The hopf bifurcation and the existence and stability of closed orbits in multisector models of optimal economic growth," *Journal of Economic Theory*, vol. 21, no. 3, pp. 421–444, 1979.

[16] J. Benhabib and R. H. Day, "Erratic accumulation," *Economics Letters*, vol. 6, no. 2, pp. 113–117, 1980.

[17] J. Benhabib and R. H. Day, "A characterization of erratic dynamics in, the overlapping generations model," *Journal of Economic Dynamics and Control*, vol. 4, pp. 37–55, 1982.

[18] J.-M. Grandmont, "On endogenous competitive business cycles," *Econometrica*, vol. 53, no. 5, pp. 995–1045, 1985.

[19] W. A. Brock, "Distinguishing random and deterministic systems: abridged version," *Journal of Economic Theory*, vol. 40, no. 1, pp. 168–195, 1986.

[20] D. S. Huang and H. Q. Li, *Theory and Method of the Nonlinear Economics*, Sichuan University Press Co., Ltd., Chengdu, China, 1993.

[21] J.-H. Ma and Y.-S. Chen, "Study for the bifurcation topological structure and the global complicated character of a kind of nonlinear finance system (i)," *Applied Mathematics and Mechanics*, vol. 22, no. 11, pp. 1240–1251, 2001.

[22] J.-H. Ma and Y.-S. Chen, "Study for the bifurcation topological structure and the global complicated character of a kind of nonlinear finance system (ii)," *Applied Mathematics and Mechanics*, vol. 22, no. 12, pp. 1375–1382, 2001.

[23] F. Xu, Y. Lai, and X.-B. Shu, "Chaos in integer order and fractional order financial systems and their synchronization," *Chaos, Solitons & Fractals*, vol. 117, pp. 125–136, 2018.

[24] F. Zhang, G. Yang, Y. Zhang, X. Liao, and G. Zhang, "Qualitative study of a 4D chaos financial system," *Complexity*, vol. 2018, Article ID 3789873, 5 pages, 2018.

[25] D. Fu, H.-T. Zhang, A. Dutta, and G. Chen, "A cooperative distributed model predictive control approach to supply chain management," *IEEE Transactions on Systems, Man, and Cybernetics: Systems*, 2019.

[26] L. Yan, F. Xu, J. Liu, K. L. Teo, and M. Lai, "Stability strategies of demand-driven supply networks with transportation delay," *Applied Mathematical Modelling*, vol. 76, pp. 109–121, 2019.

[27] H. Xia, "Improve the resilience of multilayer supply chain networks,," *Complexity*, vol. 2020, Article ID 6596483, 9 pages, 2020.

Hindawi
Complexity
Volume 2020, Article ID 6329404, 7 pages
https://doi.org/10.1155/2020/6329404

Research Article

A Difference Scheme and Its Error Analysis for a Poisson Equation with Nonlocal Boundary Conditions

Chunsheng Feng,[1] **Cunyun Nie**,[2] **Haiyuan Yu**,[1] **and Liping Zhou**[3]

[1]*Hunan Key Laboratory for Computation and Simulation in Science and Engineering, School of Mathematics and Computational Science, Xiangtan University, Xiangtan 411105, China*
[2]*School of Mathematics and Physics, Hunan Institution of Engineering, Xiangtan 411105, China*
[3]*College of Science, Hunan University of Science and Engineering, Yongzhou 425199, China*

Correspondence should be addressed to Chunsheng Feng; spring@xtu.edu.cn and Haiyuan Yu; 2857643924@qq.com

Received 14 July 2020; Revised 12 August 2020; Accepted 17 September 2020; Published 29 September 2020

Academic Editor: Karthikeyan Rajagopal

The elliptic problem with a nonlocal boundary condition is widely applied in the field of science and engineering, such as the chaotic system. Firstly, we construct one high-accuracy difference scheme for a kind of elliptic problem by tactfully introducing an equivalent relation for one nonlocal condition. Then, we obtain the local truncation error equation by the Taylor formula and, initially, prove that the new scheme can reach the asymptotic optimal error estimate $O(h^2|\ln h|)$ in the maximum norm through ingeniously transforming a two-dimensional problem to a one-dimensional one through bringing in the discrete Fourier transformation. Numerical experiments demonstrate the correctness of theoretical results.

1. Introduction

Nonlocal boundary value problems have certainly been one of the fastest growing areas in various application fields, such as chaos, chemistry, biology, and physics [1–7]. Some researchers are interested in numerical methods mainly including finite difference methods, finite element methods, finite volume methods, and other methods [8–16]. Many people have paid close attention to the finite difference method for stationary problems, for instance, the Poisson equation [17–22]. Recently, Zhai et al. put forward some compact four-order and six-order difference schemes for a 2-D Poisson equation but lack theoretical analysis [17]. Some people have studied nonlinear elliptic problems with a nonlocal boundary condition. In 2016, Themistoclakis and Vecchio studied a nonlinear boundary value problem involving a nonlocal operator and proposed a classical numerical algorithm to solve the algebraic system by means of some iterative procedures [18]. Cannon developed a numerical method for a homogeneous, nonlinear, nonlocal, elliptic boundary value problem and proved the existence and uniqueness by a continuous compact mapping and the Brouwer fixed point theorem [19]. Pao and Wang concerned with some numerical methods for a fourth-order semilinear elliptic boundary value problem with nonlocal boundary condition. The fourth-order equation was formulated as a coupled system of two second-order equations which were discretized by the finite difference method [20]. Based on fast discrete Sine transform, Wang et al. designed a fast solver to implement a fourth-order compact finite difference scheme for 1-D, 2-D, and 3-D Poisson equations [21]. Islam et al. developed a collocation method based on the Haar wavelet and a meshless method by analyzing for the solution of a two-dimensional Poisson equation with two different types of nonlocal boundary conditions [22].

Other researchers are interested in parabolic problems [23–27]. Ivanauskas et al. discussed the spectrum of a finite difference operator subject to nonlocal Robin-type boundary conditions and analyzed the spectral properties of finite difference schemes for parabolic equations and also discussed alternating direction methods and constructed some weighted splitting finite difference scheme [23–25]. In 2011,

Ismailov et al. investigated the inverse problem of finding a time-dependent heat source in a parabolic equation with a nonlocal boundary and integral over determination conditions and showed the existence, uniqueness, and continuous dependence upon the data of the solution by using the generalized Fourier method [26, 27]. However, with the scope of the authors' knowledge, there are few literatures that both presented some high-accuracy schemes and showed a theoretical proof for a 2-D elliptic problem with two nonlocal conditions and, furthermore, displayed the corresponding numerical tests. It urges us to go deeply into this problem.

In the present paper, the first novel idea is that we ingeniously construct one high-accuracy difference scheme for a kind of elliptic problem with two nonlocal boundary conditions by introducing an equivalent relations for one nonlocal condition when the solution $u \in C^4(\overline{\Omega})$. The local truncation error equation is obtained by the Taylor formula. The second one is that we initially prove that it is convergent with an asymptotic optimal convergent order of two through tactful transforming a two-dimensional problem to a one-dimensional one by bringing in the discrete Fourier transformation. Numerical tests confirm the correctness of theoretical results.

The remainder of this paper is organized as follows. In section 2, we display the model problem and its discrete scheme. In section 3, we present error estimate by the discrete Fourier transformation. In section 4, we display numerical experiments to support our conclusions. Finally, we draw some conclusions from this paper.

2. The Model Problem and the Difference Scheme

We consider the following second-order elliptic problem with local and nonlocal boundary conditions:

$$\begin{cases} \Delta u = f(x,y), & (x,y) \in \Omega = (0,1)^2, \\ u\,|_{x=0} = \mu_1(y), & 0 < y < 1, \\ u\,|_{x=1} = \mu_2(y), & 0 < y < 1, \\ u\,|_{y=0} - \gamma u\,|_{y=1} = \mu_3(y), & 0 < x < 1, \\ \int_0^1 u \mathrm{d}y = \mu_4(x), & 0 < x < 1, \end{cases} \tag{1}$$

where $f(x,y), \mu_i(y), i = 1,2, \mu_j(x), j = 3,4$ are some given smooth functions and γ is a constant.

To be convenient to discretize the nonlocal boundary, we present an equivalent relation as follows.

Lemma 1. *Assume that the solution $u \in C^2(\overline{\Omega})$ in Problem (1) and that functions $\mu_i(y)$, $i = 1,2, \mu_4(x)$ satisfy consistent properties as follows:*

$$\begin{aligned} \int_0^1 \mu_1(y)\mathrm{d}y &= \mu_4(0), \\ \int_0^1 \mu_2(y)\mathrm{d}y &= \mu_4(1), \end{aligned} \tag{2}$$

and then, the boundary condition $\int_0^1 u\mathrm{d}y = \mu_4(x)$ is equivalent to the following nonlocal boundary condition:

$$u_y\big|_{y=1} - u_y\big|_{y=0} = \int_0^1 f(x,y)\mathrm{d}y - \mu_4''(x). \tag{3}$$

Proof. Integrating two sides of equation (1) about the variable $y$over the interval $[0,1]$ and noticing that condition $\int_0^1 u\mathrm{d}y = \mu_4(x)$, we have

$$\mu_4''(x) + \int_0^1 u_{yy}\mathrm{d}y = \int_0^1 u_{xx}\mathrm{d}y + \int_0^1 u_{yy}\mathrm{d}y = \int_0^1 f(x,y)\mathrm{d}y. \tag{4}$$

That is,

$$u_y\big|_{y=1} - u_y\big|_{y=0} = \int_0^1 f(x,y)\mathrm{d}y - \mu_4''(x). \tag{5}$$

On the other hand, when Condition (3) holds, together with equation (1), we can obtain

$$\int_0^1 u_{xx}\mathrm{d}y = \mu_4''(x). \tag{6}$$

Integrating twice for two sides of the abovementioned expression about the variable x, we have

$$\int_0^1 u\mathrm{d}y = \mu_4(x) + C_1 x + C_2, \tag{7}$$

where C_1 and C_2 are two constants.

From the boundary and consistent conditions $u|_{x=0} = \mu_1(y)$, $\int_0^1 \mu_1(y)\mathrm{d}y = \mu_4(0)$, $u|_{x=1} = \mu_2(y)$, and $\int_0^1 \mu_1(y)dy = \mu_4(1)$, respectively,

$$C_1 = C_2 = 0. \tag{8}$$

Hence,

$$\int_0^1 u\mathrm{d}y = \mu_4(x). \tag{9}$$

This completes the proof of this lemma.

In the following, we will present the finite difference scheme for Problem (1) by utilizing Lemma 1.

We take the following partition for Region Ω along the directions of x and y axes, respectively.

$$\begin{aligned} 0 = x_0 < x_1 < \cdots < x_N = 1, \\ 0 = y_0 < y_1 < \cdots < y_N = 1, \end{aligned} \tag{10}$$

where $x_i = ih$, $y_j = jh$, $h = (1/N)$, and N is the corresponding partition number.

Equation (1) and two local boundary conditions can be discretized as follows:

$$\begin{cases} \dfrac{U_{i-1,j}-2U_{i,j}+U_{i+1,j}}{h^2}+\dfrac{U_{i,j-1}-2U_{i,j}+U_{i,j+1}}{h^2}=f_{i,j}, & i,j=1,2,\ldots,N-1, \\ U_{0,j}=(\mu_1)_j, U_{N,j}=(\mu_2)_j, & j=1,2,\ldots,N-1, \end{cases} \tag{11}$$

where $u_{i,j}$ and $U_{i,j}$ are the exact and approximate solutions of Problem (1) at Point (x_i, y_j), respectively.

From Lemma 1, two nonlocal boundary conditions can be discretized as follows:

$$\begin{cases} U_{i,0}=\gamma U_{i,N}+(\mu_3)_i, \\ \dfrac{1}{h}\left(\dfrac{3}{2}U_{i,N}-2U_{i,N-1}+\dfrac{1}{2}U_{i,N-2}\right)-\dfrac{1}{h}\left(-\dfrac{3}{2}U_{i,0}+2U_{i,1}-\dfrac{1}{2}U_{i,2}\right)=\varphi_i, \\ i=1,2,\ldots,N-1, \end{cases} \tag{12}$$

where $\varphi_i=\int_0^1 f(x_i,y)\mathrm{d}y-\mu_4''(x_i)$. □

3. Error Estimate

To be convenient, we introduce the denotation $A\lesssim B$, which means that there exists some constant $C_1>0$ such that $A\le C_1 B$.

Assume that the solution $u\in C^4(\overline{\Omega})$ in Problem (1), from (11) and (12), and combining with equation (1), we have

$$\begin{cases} \dfrac{e_{i-1,j}-2e_{i,j}+e_{i+1,j}}{h^2}+\dfrac{e_{i,j-1}-2e_{i,j}+e_{i,j+1}}{h^2}=h^2\alpha_{i,j}, & i,j=1,2,\ldots,N-1, \\ e_{0,j}=e_{N,j}=0, & j=1,2,\ldots,N-1, \end{cases} \tag{13}$$

$$\begin{cases} e_{i,0}=\gamma e_{i,N}, \\ \dfrac{1}{h}\left(\dfrac{3}{2}e_{i,N}-2e_{i,N-1}+\dfrac{1}{2}e_{i,N-2}\right)-\dfrac{1}{h}\left(-\dfrac{3}{2}e_{i,0}+2\,e_{i,1}-\dfrac{1}{2}e_{i,2}\right)=h^2\beta_i, \\ i=1,2,\ldots,N-1, \end{cases} \tag{14}$$

where $e_{i,j}=U_{i,j}-u_{i,j}\,(i,j=0,1,\ldots,N)$ is the error of the finite difference solution at Point (x_i, y_j) and $\alpha_{i,j}, \beta_i$ are coefficients of the corresponding local truncation errors, respectively, and they satisfy

$$\begin{aligned} \left|\alpha_{i,j}\right| &\lesssim M_4, \\ \left|\beta_i\right| &\lesssim M, \end{aligned} \tag{15}$$

and $M_k=|u|_{k,\infty}, M=\max\{M_3, M_4\}$.

Firstly, we will introduce the following discrete Fourier transformation:

$$e_{i,j}=\sqrt{2h}\sum_{k=1}^{N-1}\widehat{e}_{k,j}\sin k\pi x_i, \quad i,j=1,2,\ldots,N-1. \tag{16}$$

Similar transformations for $\alpha_{i,j}, \beta_i$, respectively, are as follows:

$$\begin{cases} \alpha_{i,j}=\sqrt{2h}\displaystyle\sum_{k=1}^{N-1}\widehat{\alpha}_{k,j}\sin k\pi x_i, & i,j=1,2,\ldots,N-1, \\ \beta_i=\sqrt{2h}\displaystyle\sum_{k=1}^{N-1}\widehat{\beta}_k\sin k\pi x_i, & i=1,2,\ldots,N-1. \end{cases} \tag{17}$$

Due to the fact that $\sqrt{2h}(\sin k\pi x_i)_{(N-1)\times(N-1)}$ is an orthogonal matrix, the following inverse transformation formulas hold:

$$\begin{cases} \widehat{\alpha}_{k,j} = \sqrt{2h}\sum_{i=1}^{N-1}\alpha_{i,j}\sin i\pi x_k, \quad k, j = 1, 2, \ldots, N-1, \\ \widehat{\beta}_k = \sqrt{2h}\sum_{i=1}^{N-1}\beta_i \sin i\pi x_k, \qquad k = 1, 2, \ldots, N-1. \end{cases} \tag{18}$$

From (15), we have

$$\left|\widehat{\beta}_k\right| \lesssim h^{-(1/2)}, \tag{19}$$

$$\left|\widehat{\alpha}_{k,j}\right| \lesssim h^{-(1/2)}. \tag{20}$$

Taking the discrete Fourier transformation for equations (13) and (14), respectively, for the variable i, we have

$$\begin{cases} \widehat{e}_{k,j-1} - \omega_k \widehat{e}_{k,j} + \widehat{e}_{k,j+1} = h^4 \widehat{\alpha}_{k,j}, \quad j = 1, 2, \ldots, N-1, \\ \widehat{e}_{k,0} = \gamma \widehat{e}_{k,N}, \\ \frac{3}{2}\widehat{e}_{k,N} - 2\widehat{e}_{k,N-1} + \frac{1}{2}\widehat{e}_{k,N-2} + \frac{3}{2}\widehat{e}_{k,0} - 2\widehat{e}_{k,1} + \frac{1}{2}\widehat{e}_{k,2} = h^3 \widehat{\beta}_k, \end{cases} \tag{21}$$

where

$$\begin{aligned} \omega_k &= 2 + 4\sin^2\theta_k, \\ \theta_k &= \frac{k\pi h}{2}. \end{aligned} \tag{22}$$

Let

$$\varepsilon_{k,j} = \widehat{e}_{k,j} + h^4 p_{k,j}, \tag{23}$$

where $p_{k,j}$ satisfies

$$\begin{cases} -p_{k,j-1} + \omega_k p_{k,j} - p_{k,j+1} = \widehat{\alpha}_{k,j}, \quad j = 1, 2, \ldots, N-1, \\ p_{k,0} = p_{k,N} = 0. \end{cases} \tag{24}$$

From (21) and (24), one can see that

$$\begin{cases} \varepsilon_{k,j-1} - \omega_k \varepsilon_{k,j} + \varepsilon_{k,j+1} = 0, \quad j = 1, 2, \ldots, N-1, \\ \varepsilon_{k,0} = \gamma \varepsilon_{k,N}, \\ \frac{3}{2}\varepsilon_{k,N} - 2\varepsilon_{k,N-1} + \frac{1}{2}\varepsilon_{k,N-2} + \frac{3}{2}\varepsilon_{k,0} - 2\varepsilon_{k,1} + \frac{1}{2}\varepsilon_{k,2} = h^3 \widetilde{\beta}_k, \end{cases} \tag{25}$$

where

$$\widetilde{\beta}_k = \widehat{\beta}_k + h\left(\frac{3}{2}p_{k,N} - 2p_{k,N-1} + \frac{1}{2}p_{k,N-2} + \frac{3}{2}p_{k,0} - 2p_{k,1} + \frac{1}{2}p_{k,2}\right). \tag{26}$$

Let

$$\left\|\widehat{\alpha}_k\right\| = \max_{j=1,\ldots,N-1}\left|\widehat{\alpha}_{k,j}\right|. \tag{27}$$

Now, we can obtain the following estimates.

Lemma 2. *Suppose that $p_{k,j}$ satisfies (24). Then, we have*

$$\max_{j=1,\ldots,N-1}\left|p_{k,j}\right| \lesssim \frac{h^{-2}}{k^2}\left\|\widehat{\alpha}_k\right\|. \tag{28}$$

$$\max_{j=0,\ldots,N-1}\left|p_{k,j+1} - p_{k,j}\right| \lesssim h^{-1}\left\|\widehat{\alpha}_k\right\|. \tag{29}$$

Proof. Let $|p_{k,\ell}| = \max_{j=1,\ldots,N-1}|p_{k,j}|$. Then, from (22) and (24), we have

$$\left|\widehat{\alpha}_{k,\ell}\right| = \left|-p_{k,\ell-1} + \omega_k p_{k,\ell} - p_{k,\ell+1}\right| \geq (\omega_k - 2)\left|p_{k,\ell}\right| = 4\sin^2\theta_k\left|p_{k,\ell}\right|. \tag{30}$$

Recalling that $\theta_k = (k\pi h/2)$, $h = (1/N)$ and $1 \leq k \leq N-1$, we get $\theta_k \in (0, (\pi/2))$.

Moreover,

$$\sin\theta_k \geq \frac{2}{\pi}\theta_k = \mathrm{kh}. \tag{31}$$

Therefore, one can easily infer (28).

Let $\delta_{k,i} = \widehat{\alpha}_{k,i} - 4\sin^2\theta_k p_{k,i}$, $i = 1, 2, \ldots, N-1$. From (30), we have

$$\left|\delta_{k,i}\right| \leq 2\left\|\widehat{\alpha}_k\right\|. \tag{32}$$

From (24), we get

$$-p_{k,i-1} + 2p_{k,i} - p_{k,i+1} = \delta_{k,i}. \tag{33}$$

Then, summing the abovementioned equation over$i$ from 1 to j $(1 \leq J \leq N-1)$, we obtain

$$p_{k,j+1} - p_{k,j} = p_{k,1} - p_{k,0} - \sum_{i=1}^{j}\delta_{k,i}. \tag{34}$$

Furthermore, summing (34) over j from 1 to $N-1$ and noticing $p_{k,N} = p_{k,N} = 0$, we get

$$-\left(p_{k,1} - p_{k,0}\right) = (N-1)\left(p_{k,1} - p_{k,0}\right) - \sum_{j=1}^{N-1}\sum_{i=1}^{j}\delta_{k,i}. \tag{35}$$

From (32) and the abovementioned equation, one can obtain

$$\left|p_{k,1} - p_{k,0}\right| \lesssim h^{-1}\left\|\widehat{\alpha}_k\right\|. \tag{36}$$

Therefore, using (32) again together with (34), 29) holds, which completes the proof. □

Theorem 1. *Assume that $u \in C^4(\overline{\Omega})$ and $U_{i,j}$ are the exact and finite difference solutions for Problem (1); then, as $\gamma \neq -1$, for $i, j = 1, 2, \ldots, N-1$, we have*

$$U_{i,j} = u_{i,j} + O\left(h^2|\ln h|\right). \tag{37}$$

Proof. We denote

$$\lambda_k = \left(\sqrt{1 + \sin^2\theta_k} + \sin\theta_k\right)^2, \qquad \theta_k = \frac{k\pi h}{2}, \tag{38}$$

which satisfy

$$\lambda_k + \lambda_k^{-1} = \omega_k, \qquad \sqrt{\lambda_k} - \frac{1}{\sqrt{\lambda_k}} = 2\sin\theta_k. \tag{39}$$

From the former two expressions of (25), we can derive that there exists C_k such that

$$\varepsilon_{k,j} = C_k\left[\left(\lambda_k^j - \lambda_k^{-j}\right) + \gamma\left(\lambda_k^{N-j} - \lambda_k^{-(N-j)}\right)\right]. \tag{40}$$

In fact, we take the value of j as $N, N-1, N-2, 0, 1, 2$ in (40), respectively, and substitute them into the third expression in (25). Then, we obtain

$$C_k = \frac{h^3\widetilde{\beta}_k}{\xi_k(1+\gamma)}, \tag{41}$$

where

$$\xi_k = \frac{3}{2}\left(\lambda_k^N - \lambda_k^{-N}\right) - 2\left(\lambda_k^{N-1} - \lambda_k^{1-N}\right) + \frac{1}{2}\left(\lambda_k^{N-2} - \lambda_k^{2-N}\right) - 2\left(\lambda_k - \lambda_k^{-1}\right) + \frac{1}{2}\left(\lambda_k^2 - \lambda_k^{-2}\right). \tag{42}$$

From (39) and observing that $\theta_k \in (0, (\pi/2))$ and $\lambda_k > 1$, we have

$$\begin{aligned}\xi_k &= \left(\sqrt{\lambda_k} - \frac{1}{\sqrt{\lambda_k}}\right)\left(\lambda_k^{(N/2)} - \lambda_k^{-(N/2)}\right)\left[\frac{3}{2}\left(\lambda_k^{(N-1/2)} - \lambda_k^{(1-N/2)}\right) - \frac{1}{2}\left(\lambda_k^{(N-3/2)} - \lambda_k^{(3-N/2)}\right)\right] \\ &\geq 2\sin\theta_k\left(\lambda_k^{(N/2)} - \lambda_k^{-(N/2)}\right)\left(\lambda_k^{(N-1/2)} - \lambda_k^{(1-N/2)}\right) \\ &\geq 2kh\left(\lambda_k^{(N/2)} - \lambda_k^{-(N/2)}\right)\left(\lambda_k^{(N-1/2)} - \lambda_k^{(1-N/2)}\right).\end{aligned} \tag{43}$$

On the other hand, from (26), (19), (22), and Lemma 2, we have

$$\left|\widetilde{\beta}_k\right| \lesssim h^{-(1/2)}. \tag{44}$$

Synthesizing the estimates on ξ_k and $\widetilde{\beta}_k$: (43) and (44), together with (41), then we have

$$|C_k| \lesssim \frac{h^{(3/2)}}{k}\left(\lambda_k^{(N/2)} - \lambda_k^{-(N/2)}\right)^{-1}\left(\lambda_k^{(N-1/2)} - \lambda_k^{(1-N/2)}\right)^{-1}. \tag{45}$$

Furthermore, from (40),

$$\begin{aligned}\left|\varepsilon_{k,j}\right| &\lesssim |C_k|\left(\lambda_k^{N-1} - \lambda_k^{1-N}\right) \\ &\lesssim \frac{h^{(3/2)}}{k}\,\frac{\lambda_k^{((N-1)/2)} + \lambda_k^{((1-N)/2)}}{\lambda_k^{(N/2)} - \lambda_k^{-(N/2)}} \\ &\lesssim \frac{h^{(3/2)}}{k}\,\frac{\lambda_k^{(N/2)} + \lambda_k^{-(N/2)}}{\lambda_k^{(N/2)} - \lambda_k^{-(N/2)}}.\end{aligned} \tag{46}$$

Due to the fact that

$$\lambda_k^{(N/2)} = \left(\sqrt{1 + \sin^2\theta_k} + \sin\theta_k\right)^N \geq \left(1 + \sin\frac{k\pi}{2N}\right)^N \geq \left(1 + \frac{k}{N}\right)^N \geq \left(1 + \frac{1}{N}\right)^N \geq 2, \tag{47}$$

we have

$$\left|\varepsilon_{k,j}\right| \lesssim \frac{h^{(3/2)}}{k}. \tag{48}$$

From Lemma 2 and (20),

$$\left|\widehat{e}_{k,j}\right| = \left|\varepsilon_{k,j} - h^4 p_{k,j}\right| \leq \left|\varepsilon_{k,j}\right| + h^4\left|p_{k,j}\right| \lesssim \frac{h^{(3/2)}}{k} + \frac{h^2}{k^2}\left|\widehat{\alpha}_k\right| \lesssim \frac{h^{(3/2)}}{k}. \tag{49}$$

Together with the fact that

$$e_{i,j} = U_{i,j} - u_{i,j} = \sqrt{2h}\sum_{k=1}^{N-1}\widehat{e}_{k,j}\sin k\pi x_i, \tag{50}$$

one can obtain (37). This completes the proof of the theorem. □

4. Numerical Experiments

In this section, we carry on some numerical experiments for Problem (1).

Example 1. In Problem (1), we take $\mu_k(y) = 0, k = 1, 2$, $\mu_3(x) = \sin\pi x$ $\mu_4(x) = (e-1)\sin\pi x$, $\gamma = 0$, and the exact solution $u(x, y) = e^y \sin\pi x$. One can easily see that $f(x, y) = (1 - \pi^2)e^y \sin\pi x$.

In this experiment, we take the uniform partition for Region Ω and the step size $h = (1/2^k)$, utilize Scheme (11) and (12), and employ the PCG method to solve the corresponding discrete system. Numerical results are shown as Tables 1 and 2, where the norms $\|v_m\|$ $(m = 2, \infty)$ are defined as $\|v_2\| = (1/N)(\sum_{i=1}^N \sum_{j=1}^N |v_{i,j}|^2)^{(1/2)}$, $|v_\infty| = \max_{1\leq i,j\leq N}|v_{i,j}|$, respectively, and η is the ratio of the errors between the approximate and exact solutions for step sizes h and $(h/2)$. In order to display the pointwise error, we show the corresponding errors for four typical points in Table 2. From the results, one can see that the convergent order is two, which validates the correctness of theoretical results.

Table 1: The errors for finite difference solutions in two norms.

k	$\|u-U\|_2$	η	$\|u-U\|_\infty$	η
4	$4.632E-03$		$1.198E-02$	
5	$1.166E-03$	3.97	$3.004E-03$	3.99
6	$2.924E-04$	3.99	$7.520E-04$	3.99
7	$7.325E-05$	3.99	$1.882E-04$	4.00

Table 2: The errors for finite difference solutions in the pointwise sense.

$(x, y)\, k$	(0.25, 0.25)	η	(0.25, 0.5)	η	(0.5, 0.25)	η	(0.5, 0.5)	η
4	$2.240E-03$		$4.011E-03$		$3.168E-03$		$5.672E-03$	
5	$5.601E-04$	4.00	$1.003E-03$	4.00	$7.921E-04$	4.00	$1.419E-03$	4.00
6	$1.401E-04$	4.00	$2.509E-04$	4.00	$1.981E-04$	4.00	$3.548E-04$	4.00
7	$3.502E-05$	4.00	$6.274E-05$	4.00	$4.953E-05$	4.00	$8.872E-05$	4.00

Table 3: The errors for finite difference solutions in two norms.

k	$\|u-U\|_2$	η	$\|u-U\|_\infty$	η
4	$1.056E-03$		$1.539E-03$	
5	$2.680E-04$	3.94	$3.848E-04$	4.00
6	$6.752E-05$	3.97	$9.623E-05$	4.00
7	$1.695E-05$	3.98	$2.406E-05$	4.00

Table 4: The errors for finite difference solutions in the pointwise sense.

$(x, y)\, k$	(0.25, 0.25)	η	(0.25, 0.5)	η	(0.5, 0.25)	η	(0.5, 0.5)	η
4	$9.571E-04$		$9.827E-04$		$1.536E-05$		$1.474E-03$	
5	$2.394E-04$	4.00	$2.458E-04$	4.00	$3.591E-04$	4.00	$3.685E-04$	4.00
6	$5.984E-05$	4.00	$6.144E-05$	4.00	$8.978E-05$	4.00	$9.214E-05$	4.00
7	$1.496E-05$	4.00	$1.536E-05$	4.00	$2.244E-05$	4.00	$2.304E-05$	4.00

Example 2. In Problem (1), we take $\mu_1(y) = y^2$, $\mu_2(y) = e(1+y)^2$, $\mu_3(x) = -e^x(2x+1)$, $\mu_4(x) = e^x(x^2 + x + (1/3))$, $\gamma = 1$, and the exact solution $u = e^x(x+y)^2$. One can easily obtain $f(x, y) = e^x(x+y)^2 + 4e^x(x+y+1)$.

We take the same methods as in Example 1 and get numerical results shown as Tables 3 and 4. From the results, one can see that the convergent order is two, which also confirms the correctness of theoretical results.

5. Summary and Conclusions

In this paper, firstly, we construct one high-accuracy difference scheme for a kind of elliptic problem with two nonlocal boundary conditions by introducing an equivalent expression for one nonlocal condition. Secondly, we, initially, prove that it is convergent with a saturated order through ingeniously transforming a two-dimensional problem to a one-dimensional one by bringing in the discrete Fourier transformation. Finally, we carry out some numerical tests to verify the correctness of theoretical results.

Data Availability

All data generated or analyzed during this study are included in this article.

Conflicts of Interest

The authors declare that they have no conflicts of interest.

Acknowledgments

This work was partially supported by National Natural Science Foundation of China (Grant no. 11971414), Hunan Province Science and Technology Innovation Plan Project (Grant no. 2018XK2304), and Youth Project of Hunan Provincial Education Department (Grant nos. 18B518 and 18B082).

References

[1] J. Zhou and D. Yang, "Legendre-Galerkin spectral methods for optimal control problems with integral constraint for state

in one dimension," *Computational Optimization and Applications*, vol. 61, no. 1, pp. 135–158, 2015.

[2] H. Niu, D. Yang, and J. Zhou, "Numerical analysis of an optimal control problem governed by the stationary Navier-stokes equations with global velocityconstrained," *Communications in Computational Physics*, vol. 24, no. 5, pp. 1477–1502, 2018.

[3] H. Chen, Y. Liu, C. Feng, A. Liu, and X. Huang, "Dynamics at infinity and existence of singularly degenerate heteroclinic cycles in Maxwell-Bloch system," *Journal of Computational and Nonlinear Dynamics*, vol. 15, no. 10, p. 8, Article ID 101007, 2020.

[4] B. Chen, Y. Liu, Z. Wei, and C. Feng, "New insights into a chaotic system with only a Lyapunov stable equilibrium," *Mathematical Methods in the Applied Sciences*, vol. 43, no. 15, pp. 9262–9279, 2020.

[5] C. Feng, Q. Huang, and Y. Liu, "Jacobi analysis for an unusual 3D autonomous system," *International Journal of Geometric Methods in Modern Physics*, vol. 17, no. 4, p. 20, Article ID 2050062, 2020.

[6] C. Feng, L. Li, Y. Liu, and Z. Wei, "Global dynamics of the chaotic disk dynamo system driven by noise," *Complexity*, vol. 2020, no. 33, 9 pages, Article ID 8375324, 2020.

[7] Y. Liu, Z. Liu, and D. Motreanu, "Existence and approximated results of solutions for a class of nonlocal elliptic variational-hemivariational inequalitie," *Mathematical Methods in the Applied Sciences*, pp. 1–14, 2020.

[8] R. S. Hirsh, "Higher order accurate difference solutions of fluid mechanics problems by a compact differencing technique," *Journal of Computational Physics*, vol. 19, no. 1, pp. 90–109, 1975.

[9] C. V. Pao, "Numerical solutions of reaction-diffusion equations with nonlocal boundary conditions," *Journal of Computational and Applied Mathematics*, vol. 136, no. 1-2, pp. 227–243, 2001.

[10] R. Ma, "A survey on nonlocal boundary value problems," *Applied Mathematics E-Notes*, vol. 7, pp. 257–279, 2007.

[11] G. K. Berikelashvili and N. Khomeriki, "On a numerical solution of one nonlocal boundary-value problem with mixed Dirichlet-Neumann conditions," *Lithuanian Mathematical Journal*, vol. 53, no. 4, pp. 367–380, 2013.

[12] C. Nie and H. Yu, "Some error estimates on the finite element approximation for two-dimensional elliptic problem with nonlocal boundary," *Applied Numerical Mathematics*, vol. 68, pp. 31–38, 2013.

[13] Y. Zhang, "Optimal error estimates of compact finite difference discretizations for the schrödinger-Poisson system," *Communications in Computational Physics*, vol. 13, no. 5, pp. 1357–1388, 2013.

[14] C. Nie, S. Shu, H. Yu, and Q. An, "A high order composite scheme for the second order elliptic problem with nonlocal boundary and its fast algorithm," *Applied Mathematics and Computation*, vol. 227, pp. 212–221, 2014.

[15] T. Wang, "Optimal point-wise error estimate of a compact difference scheme for the coupled Gross-Pitaevskii equations in one dimension," *Journal of Scientific Computing*, vol. 59, no. 1, pp. 158–186, 2014.

[16] J. Zhou, Z. Jiang, H. Xie, and H. Niu, "The error estimates of spectral methods for 1-dimension singularly perturbed problem," *Applied Mathematics Letters*, vol. 100, Article ID 106001, 2020.

[17] S. Zhai, X. Feng, and Y. He, "A new method to deduce high-order compact difference schemes for two-dimensional Poisson equation," *Applied Mathematics and Computation*, vol. 230, pp. 9–26, 2014.

[18] W. Themistoclakis and A. Vecchio, "On the numerical solution of a nonlocal boundary value problem," *Journal of Computational and Applied Mathematics*, vol. 292, pp. 720–731, 2016.

[19] J. R. Cannon and D. J. Galiffa, "On a numerical method for a homogeneous, nonlinear, nonlocal, elliptic boundary value problem," *Nonlinear Analysis: Theory, Methods & Applications*, vol. 74, no. 5, pp. 1702–1713, 2011.

[20] C. V. Pao and Y.-M. Wang, "Numerical methods for fourth-order elliptic equations with nonlocal boundary conditions," *Journal of Computational and Applied Mathematics*, vol. 292, pp. 447–468, 2016.

[21] H. Wang, Y. Zhang, X. Ma, J. Qiu, and Y. Liang, "An efficient implementation of fourth-order compact finite difference scheme for Poisson equation with Dirichlet boundary conditions," *Computers & Mathematics with Applications*, vol. 71, no. 9, pp. 1843–1860, 2016.

[22] S.-U. Islam, A. Imran, and M. Ahmad, "Numerical solution of two-dimensional elliptic PDEs with nonlocal boundary conditions," *Computers and Mathematics with Applications*, vol. 69, no. 3, pp. 180–205, 2015.

[23] F. Ivanauskas, T. Meškauskas, and M. Sapagovas, "Stability of difference schemes for two-dimensional parabolic equations with non-local boundary conditions," *Applied Mathematics and Computation*, vol. 215, no. 7, pp. 2716–2732, 2009.

[24] M. Sapagovas, T. Meškauskas, and F. Ivanauskas, "Numerical spectral analysis of a difference operator with non-local boundary conditions," *Applied Mathematics and Computation*, vol. 218, no. 14, pp. 7515–7527, 2012.

[25] S. Sajavičius, "Stability of the weighted splitting finite-difference scheme for a two-dimensional parabolic equation with two nonlocal integral conditions," *Computers and Mathematics with Applications*, vol. 64, no. 11, pp. 3485–3499, 2012.

[26] M. I. Ismailov, F. Kanca, and D. Lesnic, "Determination of a time-dependent heat source under nonlocal boundary and integral overdetermination conditions," *Applied Mathematics and Computation*, vol. 218, no. 8, pp. 4138–4146, 2011.

[27] A. Hazanee and D. Lesnic, "Determination of a time-dependent coefficient in the bioheat equation," *International Journal of Mechanical Sciences*, vol. 88, pp. 259–266, 2014.

Hindawi
Complexity
Volume 2020, Article ID 1351397, 11 pages
https://doi.org/10.1155/2020/1351397

Research Article

Relaxation Oscillations and Dynamical Properties in Two Time-Delay Slow-Fast Modified Leslie-Gower Models

Yufeng Wang, Youhua Qian, and Bingwen Lin

College of Mathematics and Computer Science, Zhejiang Normal University, Jinhua 321004, China

Correspondence should be addressed to Youhua Qian; qyh2004@zjnu.cn

Received 13 July 2020; Revised 29 August 2020; Accepted 15 September 2020; Published 25 September 2020

Academic Editor: Yongjian Liu

In this paper, we consider two kinds of time-delay slow-fast modified Leslie-Gower models. For the first system, we prove the existence and uniqueness of relaxation oscillation cycle through the geometric singular perturbation theory and entry-exit function. For the second system, we put forward a conjecture that the relaxation oscillation of the system is unique. Numerical simulation also verifies our results for the systems.

1. Introduction

In 2003, Alaoui and Okiye proposed the next modified Leslie–Gower model:

$$\begin{aligned}\frac{\mathrm{d}x}{\mathrm{d}T} &= \left(r_1 - b_1 x - \frac{a_1 y}{x + k_1}\right)x,\\ \frac{\mathrm{d}y}{\mathrm{d}T} &= \left(r_2 - \frac{a_2 y}{x + k_2}\right)y,\end{aligned} \tag{1}$$

where x is the density of a prey, y is the density of a predator, and the parameters $r_1, k_1, a_1, b_1, r_2, k_2$, and a_2 are positive, which play biology roles.

Consider the rescaling,

$$\begin{aligned}x &= \frac{r_1}{b_1}\overline{x},\\ y &= \frac{r_1 r_2}{a_2 b_1}\overline{y},\\ T &= \frac{1}{r_1}t.\end{aligned} \tag{2}$$

Substitute (2) into (1), and we have $\overline{x}$ and $\overline{y}$ in terms of x and y, then we have

$$\begin{aligned}\frac{\mathrm{d}x}{\mathrm{d}t} &= x' = x(1-x) - \frac{axy}{x + e_1},\\ \frac{\mathrm{d}y}{\mathrm{d}t} &= y' = \varepsilon y\left(1 - \frac{y}{x + e_2}\right),\end{aligned} \tag{3}$$

where $a = (a_1 r_2/a_2 r_1), e_1 = (b_1 k_1/r_1), e_2 = (b_1 k_2/r_1)$, and $\varepsilon = (r_2/r_1)$. The parameter ε can be regard as a small parameter in some special models, such as prey hares and predator lynx.

Consider the case where ε is small enough, system (3) could be treat as a slow-fast system which has the fast variable x and the slow one y. Applying the geometric singular perturbation theory, we could study the slow-fast systems [4, 5].

The geometric singular perturbation theory is mathematical rigorous that can analyze dynamics of some slow-fast systems. The study of invariant manifolds in Fenichel's theory [3] is the basis of geometric singular perturbation theory, and the theory guarantees that any compact normally hyperbolic submanifold *So* of the critical manifold *Co* could perturb a locally invariant manifold S_ε $(0 < \varepsilon \ll 1)$, which is *O(ε)*, close to *So*. In recent years, geometric singular perturbation theory contains a fairly broad class of geometric points used to study the slow-fast systems, see, for example, [6–12]. And, for the exchange lemma, see [13, 14].

Recently, Wang and Zhang proved the existence and uniqueness of relaxation oscillation cycle of the slow-fast modified Leslie-Gower model [15]. Valery et al. studied the global dynamics in the Leslie-Gower model with the Allee Effect [16]. Du et al. considered two delays induced Hopf bifurcation and double Hopf bifurcation in a diffusive Leslie-Gower predator-prey system [17]. Karl et al. discussed the bifurcation of critical sets and relaxation oscillations in singular fast-slow systems [18]. Wang and Zhang considered the stability loss delay and smoothness of the return map in slow-fast systems [19]. Ambrosio et al. addressed the canard phenomenon in a slow-fast modified Leslie-Gower model [20]. Xia et al. discussed relaxation oscillations and the mechanism in a periodically excited vector field with pitchfork-Hopf bifurcation [21]. Atabaigi and Barati studied relaxation oscillations and canard explosion in a predator-prey system of Holling and Leslie types [22]. Ai and Sadhu considered the entry-exit theorem and relaxation oscillations in slow-fast planar systems [23].

The rest of the paper is organized as follows: Section 2 introduces the entry-exit function theory. Section 3 studies the first time-delay slow-fast modified Leslie-Gower model. Section 4 investigates another kind of time-delay slow-fast modified Leslie-Gower model.

2. Entry-Exit Function

We are going to consider a slow-fast vector field in the form of

$$\begin{aligned}\frac{\mathrm{d}x}{\mathrm{d}t} &= f(x, y, \varepsilon)x,\\ \frac{\mathrm{d}y}{\mathrm{d}t} &= \varepsilon g(x, y, \varepsilon),\end{aligned} \tag{4}$$

where $(x, y) \in \mathbb{R}^2$ are state-space variables and the parameter ε represents the ratio of time scales. We define the functions f and g satisfying

$$\begin{aligned}&f(0, y, 0) < 0, \quad \text{for } y > 0,\\ &f(0, y, 0) > 0, \quad \text{for } y < 0,\\ &g(0, y, 0) < 0.\end{aligned} \tag{5}$$

For system (4), the y-axis consists of equilibria when $\varepsilon = 0$ and $Y^+ := \{(x, y) \mid x = 0, y > 0\}$ attracting and $Y^- := \{(x, y) \mid x = 0, y < 0\}$ repelling (Figure 1(a)). The Figure 1(b) is the case for $\varepsilon > 0$, since the orbit of system (4) is attracted by the y-axis, the orbit starting at (x_0, y_0) with $y_0 > 0$ and $x_0 > 0$ slightly moves toward the downside at the speed of ε. After the orbit passes positive x-axis, the y-axis begins repelling, then the orbit tends to move away from the negative y-axis at the point $(0, p_0(y_0))$, and then it intersects the line $x = x_0$ at the point whose y-coordinate saying $p_\varepsilon(y_0)$ satisfies $\lim_{\varepsilon \longrightarrow 0} p_\varepsilon(y_0) = p_0(y_0)$, where $p_0(y_0)$ is determined by

$$\int_{y_0}^{p_0(y_0)} \frac{f(0, y, 0)}{g(0, y, 0)} \mathrm{d}y = 0. \tag{6}$$

3. System with Two Positive Time Delays

Consider a system with time delays τ_1 and τ_2, which are sufficiently small constants:

$$\begin{aligned}\frac{\mathrm{d}x}{\mathrm{d}t} &= x' = x(1 - x) - \frac{ay}{x + e_1} x(t - \tau_1),\\ \frac{\mathrm{d}y}{\mathrm{d}t} &= y' = \varepsilon y\left(1 - \frac{y(t - \tau_2)}{x + e_2}\right).\end{aligned} \tag{7}$$

Using the Taylor formula,

$$\begin{aligned}x(t - \tau_1) &\approx x(t) - x'(t)\tau_1,\\ y(t - \tau_2) &\approx y(t) - y'(t)\tau_2.\end{aligned} \tag{8}$$

Substitute (8) into system (7), it yields

$$\begin{aligned}\frac{\mathrm{d}x}{\mathrm{d}t} = x' &= \left(x(1 - x) - \frac{axy}{x + e_1}\right)\frac{x + e_1}{x + e_1 - ay\tau_1}\\ &:= x f(x, y, \varepsilon),\\ \frac{\mathrm{d}y}{\mathrm{d}t} = y' &= \varepsilon y\left(1 - \frac{y}{x + e_2}\right)\frac{x + e_2}{x + e_2 - \varepsilon y\tau_2} := \varepsilon g(x, y, \varepsilon).\end{aligned} \tag{9}$$

3.1. Equilibria

Lemma 1. *For system (9), we have the following result: system (9) and system (3) have the same equilibria. So, that system (9) has equilibria $E_1(0, 0), E_2(0, e_2)$, and $E_3(1, 0)$.*

Moreover, if $ae_2 - e_1 < 0$, system (9) has a unique positive equilibrium $E_*(x_*, y_*)$ with $x_* = ((-(a + e_1 - 1) + \sqrt{(a + e_1 - 1)^2 - 4(ae_2 - e_1)})/2)$, $y_* = x_* + e_2$.

3.2. Hopf Bifurcation. We consider the bifurcation of system (9) at the unique positive equilibrium $E_*(x_*, y_*)$ about parameter τ_1. For convenience, we denote

$$\begin{aligned}F(x, y) &= x\left((1 - x) - \frac{axy}{x + e_1}\right)\frac{x + e_1}{x + e_1 - ay\tau_1},\\ G(x, y) &= \varepsilon y\left(1 - \frac{y}{x + e_2}\right)\frac{x + e_2}{x + e_2 - \varepsilon y\tau_2},\end{aligned} \tag{10}$$

so the linearized system of system (9) at the unique positive equilibrium $E_*(x_*, y_*)$ could be written as

$$\begin{pmatrix} x' \\ y' \end{pmatrix} = \begin{pmatrix} F_x & F_y \\ G_x & G_y \end{pmatrix}\begin{pmatrix} x \\ y \end{pmatrix}, \tag{11}$$

with

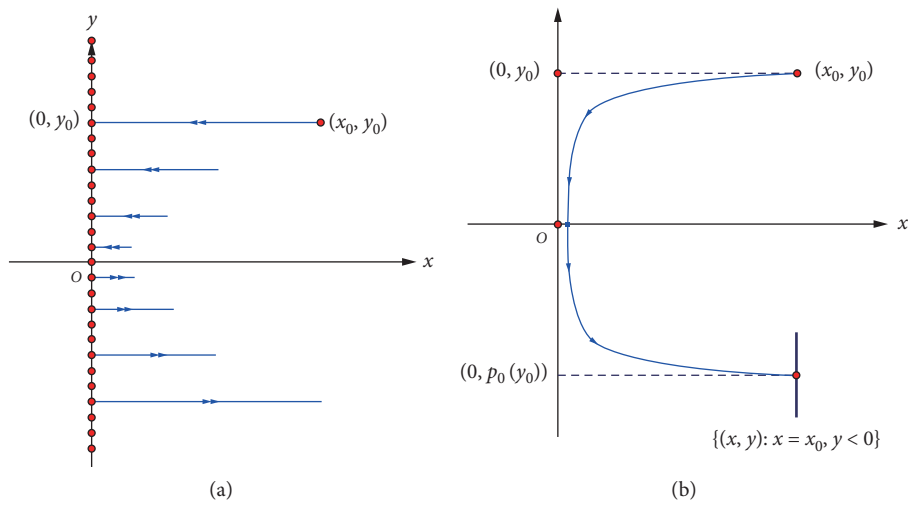

FIGURE 1: (a) For $\varepsilon = 0$, the orbits of system (4) is shown and the y-axis consists of equilibria. (b) For $0<\varepsilon\ll 1$, a symbolic orbit of system (4) starts at (x_0, y_0) and ends at $\{x = x_0, y_0 < 0\}$.

$$F_x = \frac{-2x_*^2 - (e_1 - 1)x_*}{x_* + e_1 - ay_*\tau_1},$$
$$F_y = \frac{-ax_*}{x_* + e_1 - ay_*\tau_1},$$
$$G_x = \frac{\varepsilon(x_* + e_2)}{x_* + e_2 - \varepsilon y_*\tau_2}, \tag{12}$$
$$G_y = \frac{\varepsilon - 2}{1 - \varepsilon\tau_2}.$$

Then, the characteristic equation of system (11) is

$$\lambda^2 - (F_x + G_y)\lambda - G_xF_y = 0. \tag{13}$$

Lemma 2. *For equation (13), we have the following result. If* $\tau_1 = (1 - \varepsilon\tau_2/((2-\varepsilon)ae_2))(1 + (2-\varepsilon/(1-\varepsilon\tau_2))(1-a) - e_1 - 2a)x_* + (e_1/ae_2)$, *then equation (13) has a pair of pure imaginary roots.*

Proof. The condition of equation (13) has a pair of pure imaginary roots:

$$F_x + G_y = 0, \quad G_xF_y < 0. \tag{14}$$

Consider ε, τ_1, and τ_2 are sufficiently small constants. We can easily get $G_x > 0, F_y < 0$, so $G_xF_y < 0$ holds.

According to the equation $F_x + G_y = 0$, we reach

$$\frac{-2x_*^2 - (e_1 - 1)x_*}{x_* + e_1 - ay_*\tau_1} + \frac{\varepsilon - 2}{1 - \varepsilon\tau_2} = 0. \tag{15}$$

Taking $y_* = x_* + e_2$ into equation (15), then we get

$$\frac{2x_*^2 + (e_1 - 1)x_*}{x_* + e_1 - a(x_* + e_2)\tau_1} = \frac{\varepsilon - 2}{1 - \varepsilon\tau_2}, \tag{16}$$

i.e.,

$$\tau_1 = \frac{1 - \varepsilon\tau_2}{(2-\varepsilon)ae_2}\left(1 + \frac{2-\varepsilon}{1-\varepsilon\tau_2}(1-a) - e_1 - 2a\right)x_* + \frac{e_1}{ae_2}. \tag{17}$$

The proof is completed.

Let $\lambda(\tau) = p(\tau) \pm iq(\tau)$ be the pair of pure imaginary roots of equation (13) that are satisfying $p(\tau_1) = 0, q(\tau_1) \neq 0$. Then the following transversality condition holds. □

Lemma 3. *If* $a \neq \sqrt{(a + e_1 - 1)^2 - 4(ae_2 - e_1)}$ *holds, then* $\lambda'(\tau_1) \neq 0$.

Proof. The condition of equation (13) has a pair of pure imaginary roots:

$$\mathrm{Re}\left(\frac{d\lambda}{d\tau_1}\right) = \frac{F_x + G_y}{2a} = \frac{1}{2a}\frac{dF_x}{d\tau_1} = \frac{x_*}{(x_* + e_1 - ay_*\tau_1)^2} \cdot (2x_* + e_1 - 1) = \frac{x_*}{(x_* + e_1 - ay_*\tau_1)^2} \cdot \left(-a + \sqrt{(a + e_1 - 1)^2 - 4(ae_2 - e_1)}\right) \neq 0. \tag{18}$$

The proof is completed.

Denote $\tau_1' = ((1 - \varepsilon\tau_2)/((2-\varepsilon)ae_2))(1 + (2-\varepsilon/(1-\varepsilon\tau_2))(1-a) - e_1 - 2a)x_* + (e_1/ae_2)$. Combining Lemma 2 and Lemma 3, we conclude the following. □

Theorem 1. *For system (9), if* $\tau_1 = \tau_1'$ *and* $a \neq \sqrt{(a + e_1 - 1)^2 - 4(ae_2 - e_1)}$, *then the equilibrium* $E_*(x_*, y_*)$ *is a Hopf bifurcation point and a limit cycle occurs.*

3.3. Dynamics of Limit Systems. Consider the limit systems of system (9). Setting $\varepsilon = 0$ in (9), we reach the fast subsystem:

$$\frac{dx}{dt} = x' = \left(x(1-x) - \frac{axy}{x+e_1}\right)\frac{x+e_1}{x+e_1-ay\tau_1},$$
$$\frac{dy}{dt} = y' = 0. \tag{19}$$

Consider the slow time scale $\tau = \varepsilon t$ and take the singular again, we get the slow subsystem:

$$0 = \left(x(1-x) - \frac{axy}{x+e_1}\right)\frac{x+e_1}{x+e_1-ay\tau_1},$$
$$\frac{dy}{d\tau} = \dot{y} = y\left(1 - \frac{y}{x+e_2}\right)\frac{x+e_2}{x+e_2-\varepsilon y\tau_2}, \tag{20}$$

which is a differential-algebraic equation on the critical set:

$$C_0 = \left\{(x,y) \mid x = 0 \text{ or } y = \frac{(1-x)(x+e_1)}{a} := F(x)\right\}. \tag{21}$$

We restrict the parameters a, e_1, and e_2 to a subset

$$U = \left\{(a,e_1,e_2) \,\middle|\, \sqrt{(a+e_1-1)^2 - 4(ae_2-e_1)} < a < \frac{e_1}{e_2}\right\}. \tag{22}$$

Under this restriction, $E_*(x_*, y_*)$ and $E_2(0, e_2)$ are located in the exclusion part of C_0. Some studies have shown that the branch $\{(x,y) \mid y = F(x), x > 0\ ,\ y > 0\}$ of C_0 has a unique generic fold point $D(x_M, y_M) = ((1-e_1/2), F(1-e_1/2))$. And, the two branches of C_0 cross transversally at the transcritical point $E(x,y) = (0, (e_1/a))$ (Figure 2). Then, the critical set C_0 is divided into four parts by points D and E:

$$C_0^a = \left\{(x,y) \,\middle|\, \frac{(1-e_1)}{2} < x < 1, y = F(x)\right\}, C_0^+$$
$$= \left\{(x,y) \,\middle|\, x = 0, y > \frac{e_1}{a}\right\},$$
$$C_0^r = \left\{(x,y) \,\middle|\, 0 < x < \frac{(1-e_1)}{2}, y = F(x)\right\}, C_0^-$$
$$= \left\{(x,y) \,\middle|\, x = 0, 0 < y < \frac{e_1}{a}\right\}, \tag{23}$$

where C_0^r and C_0^- are normally hyperbolic repelling and C_0^a and C_0^+ are normally hyperbolic attracting.

In fact, when the parameter is limited to U, $E_*(x_*, y_*)$ is on C_0^r and $E_2(0, e_2)$ is on C_0^-.

3.4. Relaxation Oscillation

Lemma 4. *For system (9), there exists a unique* $\overline{y}^*$ $(e_2 < \overline{y}^* < (e_1/a))$ *such that,*

$$\int_{\overline{y}^*}^{y_M} \frac{f(0,y,0)}{g(0,y,0)}\,dy = 0. \tag{24}$$

Proof. Considering the system (9), for $\overline{y} \in (e_2, (e_1/a))$,

$$I(\overline{y}) = \int_{\overline{y}}^{y_M} \frac{f(0,y,0)}{g(0,y,0)}\,dy = \int_{\overline{y}}^{y_M} \frac{1-(ay/e_1)}{y(1-(y/e_2))} \cdot \frac{e_1}{e_1-ay\tau_1}\,dy. \tag{25}$$

So that

$$I(\overline{y}) \longrightarrow -\infty \text{ as } \overline{y} \longrightarrow e_2^+. \tag{26}$$

Furthermore

$$\mathrm{I}\left(\frac{e_1}{a}\right) = \int_{(e_1/a)}^{y_M} \frac{f(0,y,0)}{g(0,y,0)}\,dy$$
$$= \int_{(e_1/a)}^{y_M} \frac{1-(ay/e_1)}{y(1-(y/e_2))} \cdot \frac{e_1}{e_1-ay\tau_1}\,dy > 0. \tag{27}$$

Then, we combine (25) and (27) and conclude that there exist a unique $\overline{y}^*$ $(e_2 < \overline{y}^* < (e_1/a))$ such that,

$$\int_{\overline{y}^*}^{y_M} \frac{f(0,y,0)}{g(0,y,0)}\,dy = 0. \tag{28}$$

The proof is completed.

Let us define x_r to be the x-coordinate of the intersection point of $y = \overline{y}^*$ and C_0^a. Then, define a singular slow-fast cycle γ_0, which contains two slow segments on C_0^a from $(x_r, \overline{y}^*)$ to (x_M, y_M) and on the positive *y-axis* from $(0, y_M)$ to $(0, \overline{y}^*)$ and the two fast connections from (x_M, y_M) to $(0, y_M)$ and $(0, \overline{y}^*)$ to $(x_r, \overline{y}^*)$, respectively. The next theorem explains the existence and uniqueness of the relaxation oscillation. □

Theorem 2. *For system (9), restrict the parameters to subset* U *and let* V *be a tubular neighborhood of* γ_0. *Then, for each fixed* $\varepsilon > 0$ *sufficiently small, system (9) has a unique limit cycle* $\gamma_\varepsilon \subset V$, *which is strongly attracting. Moreover, the cycle* γ_ε *is the unique limit cycle that converges to* γ_0 *in the Hausdorff distance [3] as* $\varepsilon \longrightarrow 0$.

Proof. By Fenichel's theory, the critical submanifold C_0^a perturbs to a nearby slow manifold C_ε^a, which is $O(\varepsilon)$ near C_0^a. By Theorem 2.1 of [9] on the analysis of a jump point, the slow manifold C_ε^a can be continued and passes the fold point $D(x_M, y_M)$, and then it jumps to another attracting branch C_0^+.

Let x_l be a sufficiently small positive number. Define two vertical sections Δ^{in} and Δ^{out} as shown in Figure 2:

$$\Delta^{\text{in}} := \left\{(x_l, y) \in V \,\middle|\, y \in I_{\text{in}}\right\}, \quad \Delta^{\text{out}} := \left\{(x_l, y) \in V \,\middle|\, y \in I_{\text{out}}\right\}, \tag{29}$$

where I_{in} and I_{out} are closed intervals centered at y_M and $y_{\text{out}} = p_0(y_M)$, respectively. Through the flow of system (4), we define the transition map Π: $\Delta^{\text{in}} \longrightarrow \Delta^{\text{in}}$, which is a composition of the next two maps:

$$\Pi_1\text{: } \Delta^{\text{in}} \longrightarrow \Delta^{\text{out}}, \ \Pi_2\text{: } \Delta^{\text{out}} \longrightarrow \Delta^{\text{in}}. \tag{30}$$

Then, Π: $\Delta^{\text{in}} \longrightarrow \Delta^{\text{in}}$ is given by the composition $\Pi: = \Pi_2 \circ \Pi_1$.

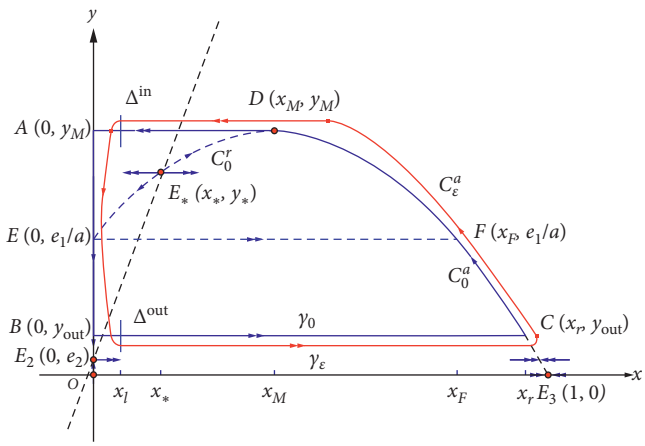

FIGURE 2: Illustration for the relaxation oscillations of system (9). The critical manifold C_0 contains repelling part C_0^r and attracting part C_0^a. The dashed black line is the predator isocline, the red dot is the fold point $D(x_M, y_M)$, the solid blue line is the slow-fast cycle γ_0, the double and single arrows are fast and slow flows, and the solid red is the attracting relaxation oscillation γ_ε.

Now, we analyze the properties of these two maps Π_1 and Π_2.

(a) *Analysis of* Π_1. Use the same proof as Lemma 4, for each $y_0 \in I_{in}$, we can define $p_0(y_0)$, with $e_2 < p_0(y_0) < (e_1/a)$ through the following formula:

$$\int_{p_0(y_0)}^{y_0} \frac{f(0,y,0)}{g(0,y,0)}\,dy = 0. \tag{31}$$

(b) *Analysis of* Π_2. Consider two orbits γ_ε^1 and γ_ε^2 starting on Δ^{out}, from Fenichel's theory, γ_ε^1 and γ_ε^2 will be attracted to C_ε^a at the exponential rate $O(e^{-1/\varepsilon})$. By Theorem 2.1 of [9], γ_ε^1 and γ_ε^2 pass by the generic fold point $D(x_M, y_M)$ contracting exponentially toward each other. Then, they fly to Δ^{in}.

Therefore, according to the results of (a) and (b), we obtain that the transition map Π: $\Delta^{in} \longrightarrow \Delta^{in}$ is a contraction at the exponential rate $O(e^{-1/\varepsilon})$. Then, it follows from the contraction mapping theorem that Π has a unique fixed point in Δ^{in}, which must be stable. This fixed point provides a unique relaxation oscillation cycle $\gamma_\varepsilon \subset V$ of system (9) passing Δ^{in} for each $0 < \varepsilon \ll 1$.

According to Fenichel's theory and Theorem 2.1 of [9], we obtain that the relaxation oscillation cycle γ_ε converges to the slow-fast cycle γ_0 as $\varepsilon \longrightarrow 0$ in the Hausdorff distance.

So, we can get that the relaxation oscillation cycle γ_ε is a unique limit cycle of system (9) located in V for each $0 < \varepsilon \ll 1$.

The theorem is proved. □

3.5. Numerical Simulation. First of all, we provide an example to illustrate Theorem 2.

Select the parameter values $(a, e_1, e_2, \varepsilon, \tau_1, \tau_2) = (1, 0.2, 0.022, 0.01, 0.2, 0.2)$, and it is easy to state that the system (9) has a unique positive equilibrium point $E_*(0.33, 0.36)$. Numerical simulation shows that it has a unique limit cycle. Figure 3 shows the phase portrait and the time series of the relaxation oscillation cycle.

(a) The orbit is shown in red in phase space

(b) Time series with the black dashed curve (prey) and red full curve (predator)

In addition, we compare the phase portrait and time series of system (9) with system (7). Figure 4 presents the phase portrait of system (9) and system (7). We can see that the two curves are very close to each other. Figure 5 shows the time series of system (9) and system (7).

(a) Time series for the relaxation oscillation of the predator with the red dashed curve (system (7)) and the blue full curve (system (9))

(b) Time series for the relaxation oscillation of the prey with the blue dashed curve (system (7)) and the red full curve (system (9)). Time series for the relaxation oscillation of prey with the blue dashed curve (system (4)) and the red full curve (system (6)).

4. System with Two Time Delays

In this section, we consider time delays τ_1 and τ_2 in system (3), then we have

$$\begin{aligned} \frac{dx}{dt} &= x' = x(1-x) - \frac{ax}{x+e_1}\,y(t-\tau_1), \\ \frac{dy}{dt} &= y' = \varepsilon y\left(1 - \frac{y}{x(t-\tau_2)+e_2}\right), \end{aligned} \tag{32}$$

where τ_1 stands for delayed maturation of the predator and τ_2 stands for the time needed to digest the prey.

4.1. Equilibria and Hopf Bifurcation. System (32) has the same equilibria with system (9). So, system (32) has a unique positive equilibrium $E_*(x_*, y_*)$ with $x_* = ((-(a+e_1-1)+\sqrt{(a+e_1-1)^2 - 4(ae_2-e_1)})/2)$, $y_* = x_* + e_2$.

In order to get the conditions for Hopf bifurcation, we reach the linearized system of system (32) at the equilibrium $E_*(x_*, y_*)$:

$$\begin{pmatrix} x' \\ y' \end{pmatrix} = A\begin{pmatrix} x \\ y \end{pmatrix} + B\begin{pmatrix} x(t-\tau_1) \\ y(t-\tau_1) \end{pmatrix} + C\begin{pmatrix} x(t-\tau_2) \\ y(t-\tau_2) \end{pmatrix}, \tag{33}$$

where

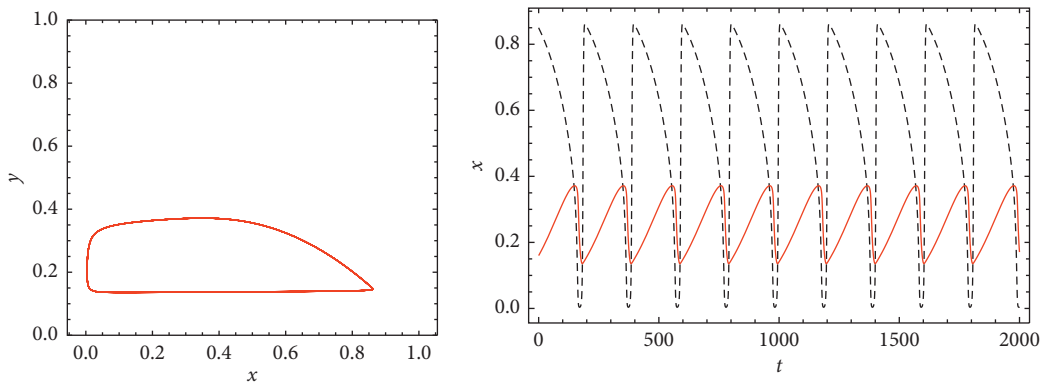

Figure 3: Numerical simulation of system (9).

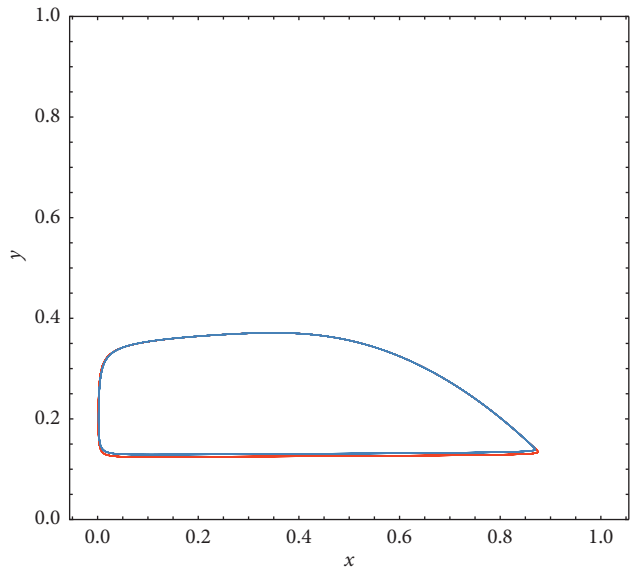

Figure 4: Phase space: the dashed blue curve shows the orbit of system (9) and the red full curve shows the orbit of system (7).

$$A = \begin{pmatrix} 1 - 2x_* - \dfrac{ae_1}{(x+e_1)^2} y(t-\tau_1) & 0 \\ 0 & \varepsilon\left(1 - \dfrac{2y_*}{x(t-\tau_2)+e_2}\right) \end{pmatrix},$$

$$B = \begin{pmatrix} 0 & \dfrac{-ax_*}{x_*+e_1} \\ 0 & 0 \end{pmatrix},$$

$$C = \begin{pmatrix} 0 & 0 \\ \dfrac{\varepsilon y_*^2}{(x(t-\tau_2)+e_2)^2} & 0 \end{pmatrix}. \tag{34}$$

Substituting $y_* = x_* + e_2$ into (34) yields

$$A = \begin{pmatrix} 1 - 2x_* - \dfrac{ae_1}{(x+e_1)^2} y(t-\tau_1) & 0 \\ 0 & \varepsilon\left(1 - \dfrac{2(x_*+e_2)}{x(t-\tau_2)+e_2}\right) \end{pmatrix},$$

$$B = \begin{pmatrix} 0 & \dfrac{-ax_*}{x_*+e_1} \\ 0 & 0 \end{pmatrix},$$

$$C = \begin{pmatrix} 0 & 0 \\ \dfrac{\varepsilon(x_*+e_2)^2}{(x(t-\tau_2)+e_2)^2} & 0 \end{pmatrix}, \tag{35}$$

i.e.,

$$A = \begin{pmatrix} \dfrac{x_*}{x_*+e_1}(2x_*+e_1-1) & 0 \\ 0 & -\varepsilon \end{pmatrix},$$

$$B = \begin{pmatrix} 0 & \dfrac{-ax_*}{x_*+e_1} \\ 0 & 0 \end{pmatrix}, \tag{36}$$

$$C = \begin{pmatrix} 0 & 0 \\ \varepsilon & 0 \end{pmatrix}.$$

Denote $\tau = \tau_1 + \tau_2$, the associated characteristic equation of system (33) can be obtained as follows:

$$\lambda^2 - \left(\frac{x_*}{x_*+e_1}(2x_*+e_1-1) + \varepsilon\right)\lambda + \varepsilon \cdot \left(\frac{ax_*}{x_*+e_1}e^{-\lambda\tau} + \frac{x_*}{x_*+e_1}(2x_*+e_1-1)\right) = 0. \tag{37}$$

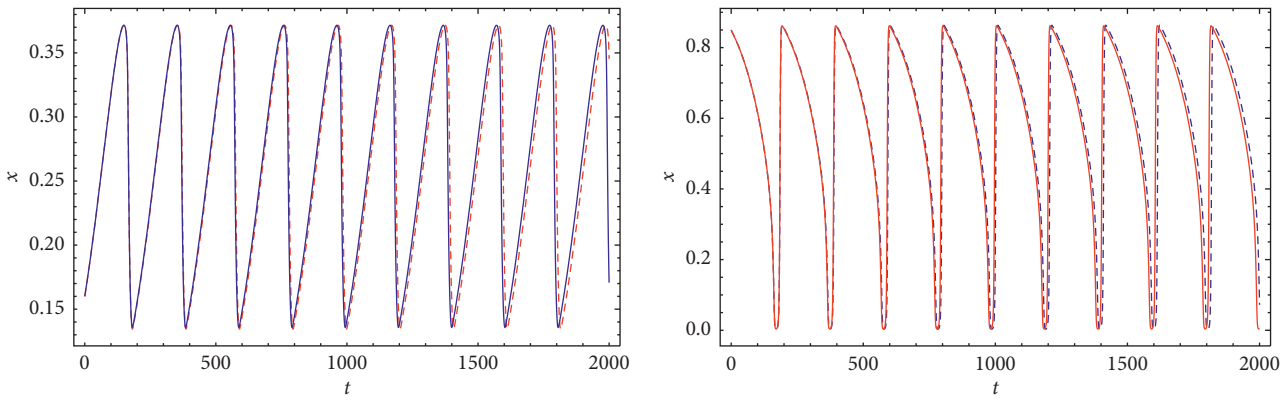

Figure 5: Time series of system (9) and system (7).

Lemma 5. *For equation (37), if* $\sqrt{(a+e_1-1)^2-4(ae_2-e_1)} \geq 2a$, *then equation (37) ha no pairs of pure imaginary roots. If* $\sqrt{(a+e_1-1)^2-4(ae_2-e_1)} < 2a$, *then equation (37) has a pair of pure imaginary roots.*

Proof. Let $\lambda = \pm\omega i$ be the pair of pure imaginary roots of equation (37), then we take $\lambda = \omega i$ into equation (37) with $e^{-\lambda\tau} = e^{-\omega i\tau} = \cos(\omega\tau) - i\sin(\omega\tau)$, it yields

$$-\omega^2 - \left(\frac{x_*}{x_*+e_1}(2x_*+e_1-1)+\varepsilon\right)\omega i,$$

$$+\varepsilon\left(\frac{ax_*}{x_*+e_1}(\cos(\omega\tau)-i\sin(\omega\tau))+\frac{x_*}{x_*+e_1}(2x_*+e_1-1)\right)=0. \tag{38}$$

Separating the real and imaginary parts of equation (38), then we get

$$-\omega^2+\frac{\varepsilon x_*}{x_*+e_1}(2x_*+e_1-1)+\frac{a\varepsilon x_*}{x_*+e_1}\cos(\omega\tau)=0,$$

$$\omega\left(\frac{x_*}{x_*+e_1}(2x_*+e_1-1)+\varepsilon\right)-\frac{a\varepsilon x_*}{x_*+e_1}\sin(\omega\tau)=0. \tag{39}$$

So that

$$\cos(\omega\tau)=\frac{\omega^2-(\varepsilon x_*/x_*+e_1)(2x_*+e_1-1)}{a\varepsilon x_*/(x_*+e_1)}\triangleq Q_0,$$

$$\sin(\omega\tau)=\frac{\omega((x_*/x_*+e_1)(2x_*+e_1-1)+\varepsilon)}{a\varepsilon x_*/(x_*+e_1)}. \tag{40}$$

According to $\sin^2(\omega\tau)+\cos^2(\omega\tau)=1$, we have

$$\omega^4+D\omega^2+E=0, \tag{41}$$

with

$$D=\left(\frac{x_*}{x_*+e_1}(2x_*+e_1-1)+\varepsilon\right)^2-\frac{2\varepsilon x_*}{x_*+e_1}(2x_*+e_1-1)$$

$$=\left(\frac{x_*}{x_*+e_1}(2x_*+e_1-1)\right)^2+\varepsilon^2>0,$$

$$E=\left(\frac{\varepsilon x_*}{x_*+e_1}(2x_*+e_1-1)\right)^2-\left(\frac{a\varepsilon x_*}{x_*+e_1}\right)^2=\left(\frac{\varepsilon x_*}{x_*+e_1}\right)^2$$

$$\cdot\left((2x_*+e_1-1)^2-a^2\right),$$

$$=\left(\frac{\varepsilon x_*}{x_*+e_1}\right)^2(2x_*+e_1-1+a)(2x_*+e_1-1-a). \tag{42}$$

Since

$$2x_*+e_1-1+a=\sqrt{(a+e_1-1)^2-4(ae_2-e_1)}>0,$$

$$2x_*+e_1-1-a=\sqrt{(a+e_1-1)^2-4(ae_2-e_1)}-2a. \tag{43}$$

We can conclude that if $\sqrt{(a+e_1-1)^2-4(ae_2-e_1)} \geq 2a$, that $E \geq 0$, which implies that Equation (41) has no positive roots, so equation (37) has no pairs of pure imaginary roots. Besides, if $\sqrt{(a+e_1-1)^2-4(ae_2-e_1)} < 2a$, then $E<0$ and equation (41) has a positive root:

$$\omega=\sqrt{\frac{-D+\sqrt{D^2-4E}}{2}}, \tag{44}$$

which implies equation (37) has a pair of pure imaginary roots when

$$\tau_{0j}=\frac{\arccos(Q_0)+2j\pi}{\omega},\quad j=0,1,2,\ldots \tag{45}$$

The proof is completed.

Denote $\lambda(\tau) = p(\tau) \pm iq(\tau)$ be the pair of pure imaginary roots of equation (37) that are satisfying $p(\tau_{0j}) = 0$, $q(\tau_{0j}) = \omega$. □

Lemma 6. *(transversality condition) If* $\sqrt{(a+e_1-1)^2 - 4(ae_2 - e_1)} < 2a$ *holds, then* $p'(\tau_{0j}) > 0$, $j = 0, 1, 2, \ldots$.

Proof. Differentiating both sides of equation (37) with respect to τ, we reach

$$2\lambda\frac{d\lambda}{d\tau} + \left(\frac{x_*}{x_* + e_1}(2x_* + e_1 - 1) + \varepsilon\right)\frac{d\lambda}{d\tau} - \lambda\varepsilon\frac{ax_*}{x_* + e_1}e^{-\lambda\tau} = 0, \tag{46}$$

then

$$\left(\frac{d\lambda}{d\tau}\right)^{-1} = \frac{2\lambda + (x_*/x_* + e_1)(2x_* + e_1 - 1) + \varepsilon}{\lambda\varepsilon(ax_*/x_* + e_1)e^{-\lambda\tau}}. \tag{47}$$

So

$$\begin{aligned}\mathrm{Re}\left(\frac{d\lambda}{d\tau}\right)^{-1}_{\tau=\tau_{0j}} &= \mathrm{Re}\left[\frac{2\lambda + (x_*/x_* + e_1)(2x_* + e_1 - 1) + \varepsilon}{\lambda\varepsilon(ax_*/x_* + e_1)e^{-\lambda\tau}}\right]_{\tau=\tau_{0j}} \\ &= \frac{2\omega\cos\omega\tau + [(ax_*/x_* + e_1)(2x_* + e_1 - 1) + \varepsilon]\sin\omega\tau}{(\omega\varepsilon ax_*/x_* + e_1)}, \\ &= \frac{2\omega^2 + D}{(\varepsilon ax_*/x_* + e_1)^2} > 0.\end{aligned} \tag{48}$$

To sum up, we get $p'(\tau_{0j}) > 0$.
The proof is completed. □

Theorem 3. *For system (32), if* $\tau_1 + \tau_2 = \tau_{0j}$, $j = 0, 1, 2, \ldots$, *system (32) undergoes a Hopf bifurcation and* τ_{0j} *are the Hopf bifurcation values.*

Proof. If $\tau_1 + \tau_2 = \tau_{0j}$, $j = 0, 1, 2, \ldots$ then the equation (37) has a pair of purely imaginary roots which satisfy the transversality condition. Thus system (32) undergoes a Hopf bifurcation and τ_{0j} are the Hopf bifurcation values.
The theorem is proved. □

Remark 1. If $0 < \tau_1 + \tau_2 < \tau_{00}$, then $E_*(x_*, y_*)$ is locally asymptotically stable and if $\tau_1 + \tau_2 > \tau_{00}$, then $E_*(x_*, y_*)$ is unstable.

4.2. Analysis of Limit Systems. In order to get rid of the delay τ_1 and τ_2, we denote $x = x_1$, $x(t - \tau_2) = x_2$, $y = y_1$ $y(t - \tau_1) = y_2$. Then, we get

$$\begin{aligned}\frac{dx_1}{dt} &= x_1(1 - x_1) - \frac{ax_1}{x_1 + e_1}y_2, \\ \frac{dx_2}{dt} &= x_2(1 - x_2) - \frac{ax_2}{x_2 + e_1}y(t - \tau_1 - \tau_2), \\ \frac{dy_1}{dt} &= \varepsilon y_1\left(1 - \frac{y_1}{x_2 + e_2}\right), \\ \frac{dy_2}{dt} &= \varepsilon y_2\left(1 - \frac{y_2}{x(t - \tau_1 - \tau_2) + e_2}\right),\end{aligned} \tag{49}$$

i.e.,

$$\begin{aligned}\frac{dx_1}{dt} &= x_1(1 - x_1) - \frac{ax_1}{x_1 + e_1}y_2, \\ \frac{dx_2}{dt} &= x_2(1 - x_2) - \frac{ax_2}{x_2 + e_1}y_1(t - \tau), \\ \frac{dy_1}{dt} &= \varepsilon y_1\left(1 - \frac{y_1}{x_2 + e_2}\right), \\ \frac{dy_2}{dt} &= \varepsilon y_2\left(1 - \frac{y_2}{x_1(t - \tau) + e_2}\right).\end{aligned} \tag{50}$$

When $\tau = 0$, system (50) goes to

$$\begin{aligned}\frac{dx_1}{dt} &= x_1(1 - x_1) - \frac{ax_1}{x_1 + e_1}y_2, \\ \frac{dx_2}{dt} &= x_2(1 - x_2) - \frac{ax_2}{x_2 + e_1}y_1, \\ \frac{dy_1}{dt} &= \varepsilon y_1\left(1 - \frac{y_1}{x_2 + e_2}\right), \\ \frac{dy_2}{dt} &= \varepsilon y_2\left(1 - \frac{y_2}{x_1 + e_2}\right).\end{aligned} \tag{51}$$

Consider the case where ε is small enough, system (51) could be viewed as a slow-fast system which has the fast variable $X = \begin{pmatrix} x_1 \\ x_2 \end{pmatrix}$ and the slow variable $Y = \begin{pmatrix} y_1 \\ y_2 \end{pmatrix}$. We have

$$\begin{aligned}f(X, Y, \varepsilon) &= (f_1, f_2) \\ &= \left(x_1(1 - x_1) - \frac{ax_1}{x_1 + e_1}y_2, x_2(1 - x_2) - \frac{ax_2}{x_2 + e_1}y_1\right).\end{aligned} \tag{52}$$

Then, we arrive at the critical set:

$$C_0 = \left\{(x, y) \in \mathbb{R}^2 \times \mathbb{R}^2 \mid f(X, Y, 0) = 0\right\} = C_0^1 \cup C_0^2 \cup C_0^3 \cup C_0^4. \tag{53}$$

with

$$C_0^1 = \{x_1 = 0\ ,\ x_2 = 0\},$$
$$C_0^2 = \left\{x_1 = 0\ ,\ y_1 = \frac{1}{a}(1 - x_2)(x_2 + e_1)\right\},$$
$$C_0^3 = \left\{y_2 = \frac{1}{a}(1 - x_1)(x_1 + e_1), x_2 = 0\right\},$$
$$C_0^4 = \left\{y_2 = \frac{1}{a}(1 - x_1)(x_1 + e_1), y_1 = \frac{1}{a}(1 - x_2)(x_2 + e_1)\right\}. \tag{54}$$

Since

$$D_X f = \begin{pmatrix} 1 - 2x_1 - \dfrac{ae_1y_2}{(x_1 + e_1)^2} & 0 \\ 0 & 1 - 2x_2 - \dfrac{ae_1y_1}{(x_2 + e_1)^2} \end{pmatrix}, \tag{55}$$

Then, the eigenvalues of matrix (55) are

$$\mu_1 = 1 - 2x_1 - \frac{ae_1y_2}{(x_1 + e_1)^2},$$
$$\mu_2 = 1 - 2x_2 - \frac{ae_1y_1}{(x_2 + e_1)^2}. \tag{56}$$

Thus, we reach the attractive part and the repulsive part of C_0^1 are, respectively,

$$C_0^{1a} = \left\{x_1 = 0, x_2 = 0, y_1 > \frac{e_1}{a}, y_2 > \frac{e_1}{a}\right\},$$
$$C_0^{1r} = \left\{x_1 = 0, x_2 = 0, y_1 < \frac{e_1}{a}, y_2 < \frac{e_1}{a}\right\}. \tag{57}$$

The attractive part and the repulsive part of C_0^2 are, respectively,

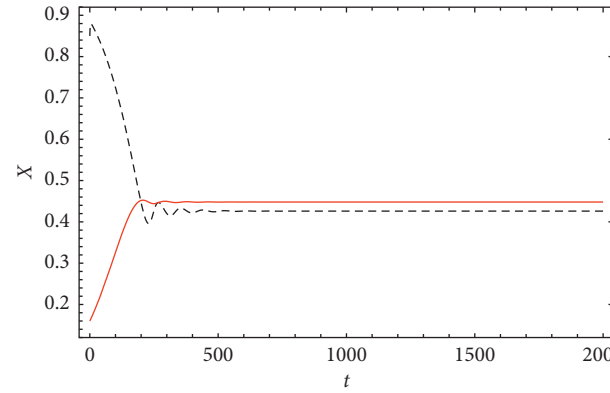

FIGURE 6: Choose $(\tau_1, \tau_2) = (3, 1)$ satisfying $\tau_1 + \tau_2 = 4 < \tau_{00}$, then the equilibrium $E_*(x_*, y_*)$ of system (32) is asymptotically stable. Time series with the black dashed curve (prey) and red full curve (predator).

$$C_0^{2a} = \left\{x_1 = 0, x_2 > \frac{1 - e_1}{2}, y_1 = \frac{1}{a}(1 - x_2)(x_2 + e_1), y_2 > \frac{e_1}{a}\right\},$$
$$C_0^{2r} = \left\{x_1 = 0, 0 < x_2 < \frac{1 - e_1}{2}, y_1 = \frac{1}{a}(1 - x_2)(x_2 + e_1), y_2 < \frac{e_1}{a}\right\} \tag{58}$$

The attractive part and the repulsive part of C_0^3 are, respectively,

$$C_0^{3a} = \left\{x_1 > \frac{1 - e_1}{2}, x_2 = 0, y_1 > \frac{e_1}{a}, y_2 = \frac{1}{a}(1 - x_1)(x_1 + e_1)\right\},$$
$$C_0^{3r} = \left\{0 < x_1 < \frac{1 - e_1}{2}, x_2 = 0, y_1 < \frac{e_1}{a}, y_2 = \frac{1}{a}(1 - x_1)(x_1 + e_1)\right\}. \tag{59}$$

and the attractive part and the repulsive part of C_0^4 are, respectively,

$$C_0^{4a} = \left\{x_1 > \frac{1 - e_1}{2}, x_2 > \frac{1 - e_1}{2}, y_1 = \frac{1}{a}(1 - x_2)(x_2 + e_1), y_2 = \frac{1}{a}(1 - x_1)(x_1 + e_1)\right\},$$
$$C_0^{4r} = \left\{0 < x_1 < \frac{1 - e_1}{2}, 0 < x_2 < \frac{1 - e_1}{2}, y_1 = \frac{1}{a}(1 - x_2)(x_2 + e_1), y_2 = \frac{1}{a}(1 - x_1)(x_1 + e_1)\right\}. \tag{60}$$

4.3. Conjecture of the System. In this section, we combine the result of Subsection 4.1 and Subsection 4.2 and propose a conjecture.

Conjecture 1. *If* $x_* > (1 - e_1/2)$ *and* $(x_*/x_* + e_1)(2x_* + e_1 - 1) + \varepsilon = 0$, *then the equilibrium* $E_*(x_*, y_*)$ *is a Hopf bifurcation point of system (51) and a periodic solution is bifurcated from* $E_*(x_*, y_*)$. *Moreover, the relaxation oscillation cycle of the system (51) is unique.*

4.4. Numerical Simulation. We show some numerical simulations in this part to verify our theoretical results.

For system (32), we choose the parameter values $(a, e_1, e_2, \varepsilon) = (0.805, 0.2, 0.022, 0.01)$, then we get $(x_*, y_*) = (0.422, 0.444)$. A series of calculations gives us that $\tau_{00} \approx 11.50$. Thus, we choose $(\tau_1, \tau_2) = (3, 1)$, and then the equilibrium $E_*(x_*, y_*)$ of system (32) is asymptotically stable (Figure 6). Besides, we choose $(\tau_1, \tau_2) = (3, 13)$ and get the periodic solutions of system (32) (Figure 7).

For system (51), we choose the parameter values $(a, e_1, e_2, \varepsilon) = (1, 0.2, 0.022, 0.01)$. Figure 8 shows the phase portrait and the time series of the relaxation oscillation cycle.

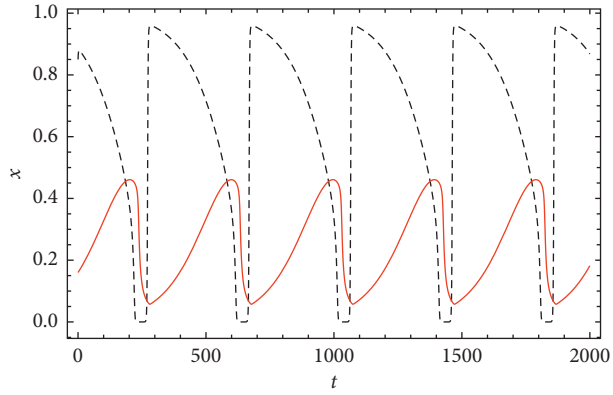

FIGURE 7: Choose $(\tau_1, \tau_2) = (3, 13)$ satisfying $\tau_1 + \tau_2 = 16 > \tau_{00}$, and then reach the periodic solutions of system (32) (time series with the black dashed curve (prey) and red full curve (predator)).

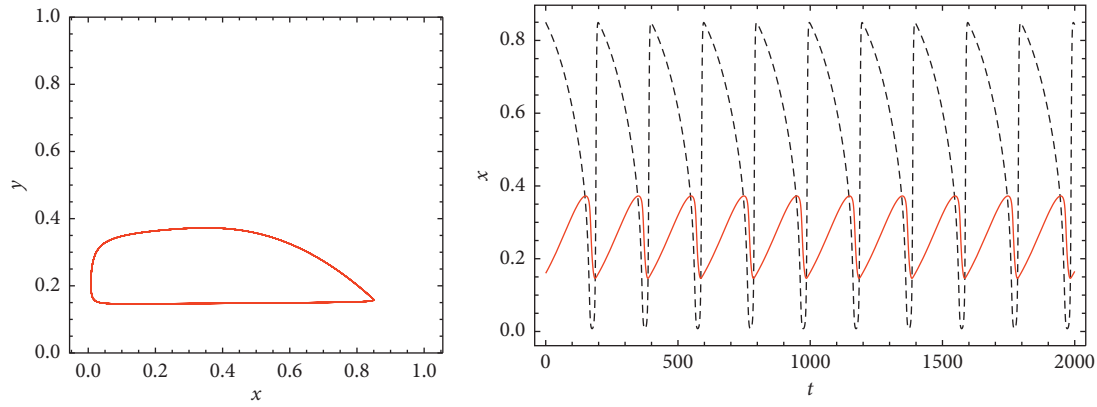

FIGURE 8: Numerical simulation of system (51). (a) The orbit is shown in red in the phase space. (b) Time series with the black dashed curve (prey) and red full curve (predator).

5. Conclusion

In this paper, we mainly study two kinds of time-delay slow-fast modified Leslie-Gower models. For the first system, through the geometric singular perturbation theory and entry-exit function, we prove the existence and uniqueness of relaxation oscillation cycle. For another system, when $\tau = \tau_1 + \tau_2$ crosses some critical values τ_{0j}, the Hopf bifurcation occurs. Meanwhile, we put forward a conjecture that the relaxation oscillation cycle of the system is unique when $\tau = 0$. Numerical simulation verified our theoretical results and indicated that our method is effective. Our results show that delay affects the stability of the positive equilibrium and produces more complex dynamics than the model without delay.[1, 2]

Data Availability

All data, models, and code generated or used during the study are included within the article.

Conflicts of Interest

The authors declare that they have no conflicts of interest.

Acknowledgments

The authors gratefully acknowledge the support of the National Natural Science Foundation of China (NNSFC) through grant no.11572288 and the Natural Science Foundation of Zhejiang through grant no.LY20A020003.

References

[1] M. A. Aziz-Alaoui and M. Daher Okiye, "Boundedness and global stability for a predator-prey model with modified Leslie-Gower and Holling-type II schemes," *Applied Mathematics Letters*, vol. 16, no. 7, pp. 1069–1075, 2003.

[2] Y. Zhu and K. Wang, "Existence and global attractivity of positive periodic solutions for a predator-prey model with modified Leslie-Gower Holling-type II schemes," *Journal of Mathematical Analysis and Applications*, vol. 384, no. 2, pp. 400–408, 2011.

[3] N. Fenichel, "Geometric singular perturbation theory for ordinary differential equations," *Journal of Differential Equations*, vol. 31, no. 1, pp. 53–98, 1979.

[4] C. Kuehn, *Multiple Time Scale Dynamics Applied Mathematical Sciences*, Springer, Berlin, Germany, 2015.

[5] G. Hek, "Geometric singular perturbation theory in biological practice," *Journal of Mathematical Biology*, vol. 60, no. 3, pp. 347–386, 2010.
[6] C. K. R. T. Jones, "Geometric singular perturbation theory," *Dynamical Systems*, vol. 1609, pp. 44–118, 1995.
[7] W. Liu, "Exchange lemmas for singular perturbation problems with certain turning points," *Journal of Differential Equations*, vol. 167, no. 1, pp. 134–180, 2000.
[8] W. Liu, "Geometric singular perturbations for multiple turning points: invariant manifolds and exchange lemmas," *Journal of Dynamics and Differential Equations*, vol. 18, no. 3, pp. 667–691, 2006.
[9] M. Krupa and P. Szmolyan, "Extending geometric singular perturbation theory to nonhyperbolic points---fold and canard points in two dimensions," *SIAM Journal on Mathematical Analysis*, vol. 33, no. 2, pp. 286–314, 2001.
[10] M. Krupa and P. Szmolyan, "Relaxation oscillation and canard explosion," *Journal of Differential Equations*, vol. 174, no. 2, pp. 312–368, 2001.
[11] M. Krupa and M. Wechselberger, "Local analysis near a folded saddle-node singularity," *Journal of Differential Equations*, vol. 248, no. 12, pp. 2841–2888, 2010.
[12] R. Arditi and L. R. Ginzburg, "How species interact: altering the standard view on trophic ecology," *Environmental Health Perspectives*, vol. 114, no. 11, pp. 142-143, 2012.
[13] S. Schecter and I. Deng's lemma, "Exchange lemmas 1: deng's lemma," *Journal of Differential Equations*, vol. 245, no. 2, pp. 392–410, 2008.
[14] S. Schecter, "Exchange lemmas 2: general exchange lemma," *Journal of Differential Equations*, vol. 245, no. 2, pp. 411–441, 2008.
[15] C. Wang and X. Zhang, "Relaxation oscillations in a slow-fast modified Leslie-Gower model," *Applied Mathematics Letters*, vol. 87, pp. 147–153, 2019.
[16] V. A. Gaiko and C. Vuik, "Global dynamics in the leslie-gower model with the allee Effect," *International Journal of Bifurcation and Chaos*, vol. 28, no. 12, Article ID 1850151, 2018.
[17] Y. F. Du, B. Niu, and J. J. Wei, "Two delays induce Hopf bifurcation and double Hopf bifurcation in a diffusive Leslie-Gower predator-prey system," *Chaos*, vol. 29, Article ID 013101, 2019.
[18] H. M. N. Karl, A. Peter, and D. D. Peter, "Bifurcation of critical sets and relaxation oscillations in singular fast-slow systems," *Nonlinearity*, vol. 33, pp. 2853–2904, 2020.
[19] C. Wang and X. Zhang, "Stability loss delay and smoothness of the return map in slow-fast systems," *SIAM Journal on Applied Dynamical Systems*, vol. 17, no. 1, pp. 788–822, 2018.
[20] B. Ambrosio, M. A. Aziz-Alaoui, and R. Yafia, "Canard phenomenon in a slow-fast modified Leslie-Gower model," *Mathematical Biosciences*, vol. 295, pp. 48–54, 2018.
[21] Y. Xia, Z. Zhang, and Q. Bi, "Relaxation oscillations and the mechanism in a periodically excited vector field with pitchfork-Hopf bifurcation," *Nonlinear Dynamics*, vol. 101, no. 1, pp. 37–51, 2020.
[22] A. Atabaigi and A. Barati, "Relaxation oscillations and canard explosion in a predator-prey system of Holling and Leslie types," *Nonlinear Analysis: Real World Applications*, vol. 36, pp. 139–153, 2017.
[23] S. Ai and S. Sadhu, "The entry-exit theorem and relaxation oscillations in slow-fast planar systems," *Journal of Differential Equations*, vol. 268, no. 11, pp. 7220–7249, 2020.

Hindawi
Complexity
Volume 2020, Article ID 7672303, 10 pages
https://doi.org/10.1155/2020/7672303

Research Article

Route to Chaos and Bistability Analysis of Quasi-Periodically Excited Three-Leg Supporter with Shape Memory Alloy

Manisekaran Varadharajan,[1] Prakash Duraisamy ,[2] and Anitha Karthikeyan[3]

[1]*Department of Metallurgical and Materials Engineering, Defence University, Bishoftu, Ethiopia*
[2]*Department of Mechanical and Industrial Engineering, EiTM, Mekelle University, Mek'ele, Ethiopia*
[3]*Nonlinear Systems and Applications, Faculty of Electrical and Electronics Engineering, Ton Duc Thang University, Ho Chi Minh City, Vietnam*

Correspondence should be addressed to Prakash Duraisamy; duraiprakash83@gmail.com

Received 27 June 2020; Revised 2 August 2020; Accepted 8 September 2020; Published 19 September 2020

Academic Editor: Yongjian Liu

In this paper, the effect of quasi-periodic excitation on a three-leg supporter configured with shape memory alloy is investigated. We derived the equation of motion for the system using the supporter configuration and polynomial constitutive model of the shape memory alloys (SMAs) based on Falk model. Two sets of parameters and symmetric initial conditions are used to analyze the system. The system responded with a chaotic attractor and a strange nonchaotic attractor. Coexistence of these attractors is studied and discussed with corresponding phase portrait, bifurcation plot, and cross section of basin of attraction. We confirm the quasi-periodic excitation results with generation of strange nonchaotic attractors as discussed in the literature. The special properties like symmetricity and bistability are revealed and the parameter ranges of existence of such behaviors are discussed. The system is analyzed for different phases and the existence of bistability in martensite phase and transition phase is explained. While the system enters into austenite phase, the bistability behavior vanishes. The results provide insight knowledge into dynamical response of a quasi-periodically excited SMA leg support system and will be useful for design improvements and controller design.

1. Introduction

For the last two decades, shape memory alloys (SMAs) gained attention of the researchers because of their salient behavior and their versatile application in a wide range of fields [1–10]. SMAs are metallic alloys that hold the ability to regain their original shape from plastic deformation through thermal processing. SMAs holding hysteretic loop with super elasticity means the ability to recover from large elastic strains (up to 8%) also permits the material to resist large cyclic deformations, without residual strains [4, 5]. The mechanism behind SMAs behavior is related to martensitic phase transformation that the alloy undergoes when subjected to stress and/or temperature changes. Essentially, there are two basic crystalline states in SMAs: austenite and martensite. Martensitic transformation is a nondiffusive process, which happens due to differences between involved constituents [2]. Hence, while we design a mechanical system using SMAs, it is mandatory to investigate the behavior of the system in both martensitic phase and austenitic phase, as well as in transition phase [6, 7, 9].

The three-leg supporter is a mechanical system that is widely used in aircraft industries and machining industries. It can provide adequate inclinations with required motion for precise movement of platform. While SMAs are introduced in three-leg platform, precise movement and maintaining the position can be easily achieved but the challenges are enormous.

Major challenge can be identified as constitutive model for representing the deformation behavior of SMAs. In order to explore all potentialities of SMAs, there is an increasing interest in the development of mathematical models capable of describing the main behaviors of these alloys. SMA thermomechanical behavior can be modeled by either

microscopic or macroscopic points of view. Using Devonshire's theory, the unique properties of SMAs were modeled by Falk [8] and a simplified, refined one-dimensional model is formulated and discussed in [9]. This model is analyzed based on polynomial-free energy potential [10].

In 1984, Grebogi [11] found strange attractors that are not chaotic and named them Strange Nonchaotic Attractors (SNAs). The dynamics of SNAs that are neither regular nor chaotic indicate that the shape is neither a finite set of points nor piecewise differentiable manifold. The interesting phenomenon is that while the system undergoes quasi-periodically excited forces, these SNAs are generated. Many researches were carried out on such SNAs [12–21]. In [22], quasi-periodically excited nonautonomous system is investigated and various shapes of SNAs are discussed. In [23], the authors developed some no-autonomous systems with quasi-periodic coefficients and revealed more complicated dynamics of unusual types.

The three-leg supporter system does not need to be subjected to periodic excitation; hence, investigation for quasi-periodic excitation provides exact scenario of real-time situations. Coexistence of two or more attractors is not good for a mechanical system; it intricates the design and control of the system. Observing how many coexisting attractors are present in the system and investigating the parameter range and corresponding initial conditions are very important. Many literatures showed the coexistence of attractors in mechanical systems and studied their behaviors [24–27].

Motivated by the aforementioned discussion, in this paper, we analyzed the three-leg supporter with shape memory alloy for quasiperiodic forcing. The quasi-periodic excitation is achieved by taking golden ratio of irrational number. The rest of this paper is organized as follows. Section 2 provides the mathematical modeling of three-leg supporter with shape memory alloy. Section 3 deals with stability analysis. Section 4 reports the symmetricity property and the bistability property and its ranges. Finally, Section 5 summarizes the conclusion.

2. System Modeling

In this paper, we analyze a three-leg supporter as shown in Figure 1. The setup under consideration consists of two disks (top and base) with radii B_1 and B_2, respectively. The top disk is supported by three SMA rods having length L and cross-sectional area A. These three legs are located 120° with each other on the base disk.

The masses of SMA rods are considerably less, so we assume that the mass of the structure is fully concentrated at the rigid mass disk. Applying force P on the center of the rigid disk, and because of the symmetricity of the structure, we considered the vertical motion only. Based on the force

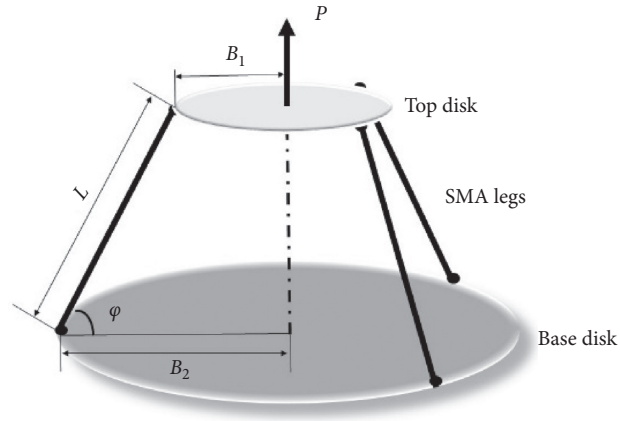

Figure 1: Three-leg supporter with shape memory alloys (SMAs).

analysis, the vertical forces can be calculated as follows: Vertical forces = $P - 3$(internal force in each bar) $\sin\varphi$.

The equation of motion is derived [28] as follows:

$$-3F\sin\varphi + P = m\ddot{X} + c\dot{X}, \tag{1}$$

where m is mass and P is applied force on the center of the rigid disk. F is internal force in each bar, X is vertical displacement, φ is angle between the leg and the base disk, and c is viscous damping coefficient.

Geometrical relations are considered in the following way:

$$\begin{aligned} B &= B_2 - B_1, \\ L &= \sqrt{B^2 + X^2}. \end{aligned} \tag{2}$$

The legs are made up of shape memory alloys (SMAs). There have been a horde of literatures that proved that SMAs possess nonlinear behavior because of their hysteretic nature while subjected to temperature changes. In order to consider such phenomenon, various constitutive models were developed. There are different ways to describe the thermomechanical behavior of SMAs. Here, we considered the polynomial constitutive model proposed by Falk [8]. He formulated the below-mentioned fifth-degree polynomial constitutive relation for analyzing the nonlinear behavior of SMAs:

$$\sigma = a_1(T - T_M)\varepsilon - a_2\varepsilon^3 + a_3\varepsilon^5, \tag{3}$$

where ε = axial strain $= L/(L_0 - 1) = \cos\varphi_0/(\cos\varphi - 1)$, T_M is the temperature below which the martensitic phase is stable, T is temperature, a_1, a_2, a_3 are material constants, and T_A is the temperature above which austenite is stable $= T_M + 1/(4(a_2^2/a_1a_3))$.

By substituting geometrical relations equation (2) and fifth-degree polynomial constitutive relation (3) in equation

(1), we can get the equation of motion of the three-leg supporter with shape memory alloy as follows:

$$m\ddot{X} + c\dot{X} + \frac{3AX}{L_0}\left\{\begin{array}{c} [a_1(T-T_M) - 3a_2 + 5a_3] \\ +[-a_1(T-T_M) + a_2 - a_3]\dfrac{L_0}{\sqrt{X^2+B^2}} + [3a_2 - 10a_3]\dfrac{\sqrt{X^2+B^2}}{L_0} \\ +[-a_2 + 10a_3]\dfrac{X^2+B^2}{L_0^2} - 5a^3\dfrac{\sqrt[3]{X^2+B^2}}{L_0^3} + a_3\dfrac{\left(X^2+B^2\right)^2}{L_0^4} \end{array}\right\} = P(t). \tag{4}$$

$P(t)$ is the force applied to the three-leg supporter. Most of the literatures discussed the response of the system for periodic excitation but quasi-excitation is the one that will give more real situations for analyzing the nonlinear behaviors keeping this in mind. In this paper, we consider quasi-periodic excitation in the following form:

$$P(t) = P_0[\sin(\Omega_1 t) + \sin(\Omega_2 t)]. \tag{5}$$

The necessary condition to get quasi-excitation, (Ω_1/Ω_2) should be irrational number [20, 29]. For our analysis, we take the golden ratio of irrational number $\Omega_1 = 0.5$, $\Omega_2 = ((\sqrt{5}-1)/2)$.

The dimensionless equation is derived from the equation of motion:

$$\begin{aligned} \dot{x} &= y, \\ \dot{y} &= \gamma[\sin(\Omega_1\tau) + \sin(\Omega_2\tau)] - \eta y + x\left\{\begin{array}{c} -[(\theta-1) - 3\alpha_2 - 5\alpha_3] + \dfrac{[(\theta-1) - \alpha_2 + \alpha_3]}{\sqrt{\left(x^2+b^2\right)}} \\ -[3\alpha_2 - 10\alpha_3]\sqrt{\left(x^2+b^2\right)} + [\alpha_2 - 10\alpha_3]\left(x^2+b^2\right) \\ +5\alpha_3\sqrt[3]{\left(x^2+b^2\right)} - \alpha_3\left(x^2+b^2\right)^2 \end{array}\right\}, \end{aligned} \tag{6}$$

where $\omega_0^2 = (3Aa_1T_M/mL_0)$, $\gamma = (P_0/mL_0\omega_0^2)$, $\eta = (c/m\omega_0)$, $\alpha_2 = (a_2/a_1T_M)$, $\alpha_3 = (a_3/a_1T_M)$, $\Omega_1 = (\omega_1/\omega_0)$, $\Omega_2 = (\omega_2/\omega_0)$, $b = (B/L_0)$, $\theta_A = (T_A/T_M)$, $x = (X/L_0)$, $\theta = (T/T_M)$, and $\tau = \omega_0 t$.

3. Stability Analysis

In order to find the equilibrium point, we considered an unforced system from equation (6). We discarded the forcing term $\gamma[\sin(\Omega_1\tau) + \sin(\Omega_2\tau)]$. Then the equations are equated to zero. The equations become as follows:

$$\begin{aligned} 0 &= y, \\ 0 &= -\eta y + x\left\{\begin{array}{c} -[(\theta-1) - 3\alpha_2 - 5\alpha_3] + \dfrac{[(\theta-1) - \alpha_2 + \alpha_3]}{\sqrt{\left(x^2+b^2\right)}} \\ -[3\alpha_2 - 10\alpha_3]\sqrt{\left(x^2+b^2\right)} + [\alpha_2 - 10\alpha_3]\left(x^2+b^2\right) \\ +5\alpha_3\sqrt[3]{\left(x^2+b^2\right)} - \alpha_3\left(x^2+b^2\right)^2 \end{array}\right\}. \end{aligned} \tag{7}$$

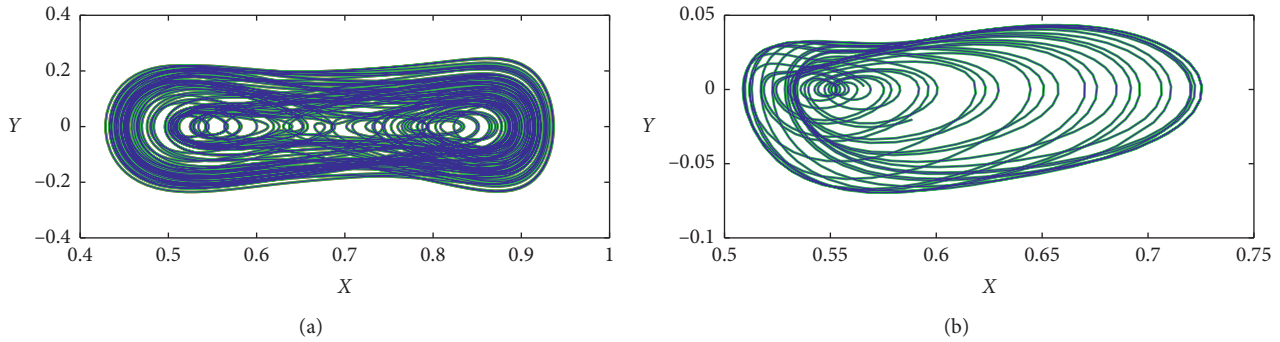

Figure 2: Phase portrait of system (7): for (a) $\eta = 0.1$ and initial condition [0.6, 0] chaotic attractor and for (b) $\eta = 1.5$ and initial condition [0.5, 2] attracting tori.

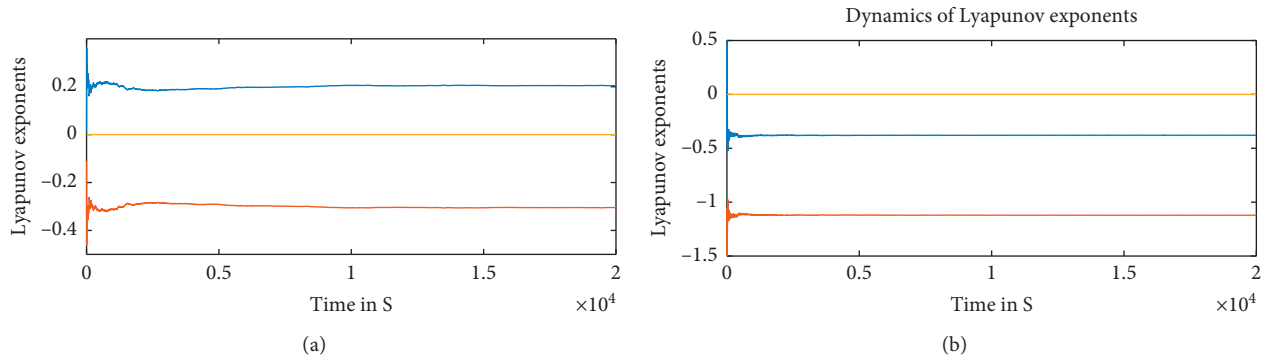

Figure 3: Lyapunov exponents. (a) For $\eta = 0.1$ and initial condition of [0.6, 0]; (b) for $\eta = 1.5$ and initial condition of [0.5, 2].

For the parameter values,

$$\alpha_2 = 124; \alpha_3 = 14505; \gamma = 0.045; b = 0.7071; \theta = 0.69; \eta = 0.1, \tag{8}$$

and equilibrium point {−0.00113, 0} is found.

We derived the Jacobian matrix for equation (7) given as

$$J = \begin{bmatrix} 0 & 1 \\ A_1 & -\eta \end{bmatrix}, \tag{9}$$

where

$$A_1 = \begin{cases} 3a_2 - 5a_3 - \theta - \dfrac{a_2 - a_3 - \theta + 1}{\sqrt{b^2 + x^2}} - a_3\left(b^2 + x^2\right)^2 + 5a_3\sqrt[3]{b^2 + x^2} - (3a_2 - 10a_3)\sqrt{b^2 + x^2} \\ +(a_2 - 10a_3)\left(b^2 + x^2\right) + \dfrac{x(2x(a_2 - 10a_3)) - (x(3a_2 - 10a_3))}{\sqrt{b^2 + x^2}} - 4a_3x\left(b^2 + x^2\right) \\ +\dfrac{x(a_2 - a_3 - \theta + 1)}{\sqrt[3]{b^2 + x^2}} + 15a_3x\sqrt{b^2 + x^2} + 1. \end{cases} \tag{10}$$

The characteristic equation is formulated for the Jacobian matrix on the equilibrium point:

$$\lambda^2 + 0.1\lambda - 39.6866 = 0. \tag{11}$$

Corresponding eigenvalues are found as

$$\lambda_1 = 6.2499; \lambda_2 = -6.3499, \tag{12}$$

and we have eigenvalues with one positive and negative value; hence, the equilibrium point can be a saddle node.

4. Dynamic Analysis

In this paper, we analyzed system (6) for different θ values to study the behavior during martensitic phase ($\theta = 0.69$), transition phase ($\theta = 1.04$), and austenitic phase ($\theta = 1.30$).

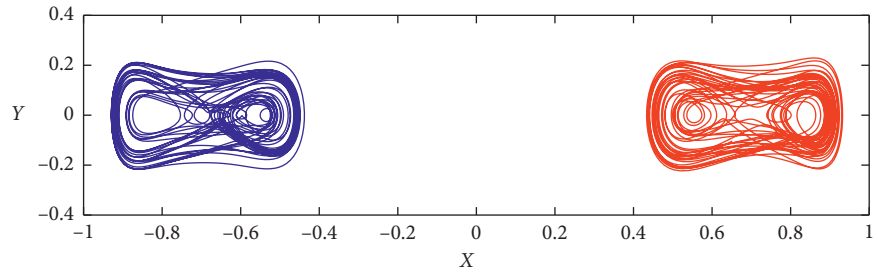

Figure 4: Chaotic attractors for initial conditions of [0.6, 0] and [−0.5, 0].

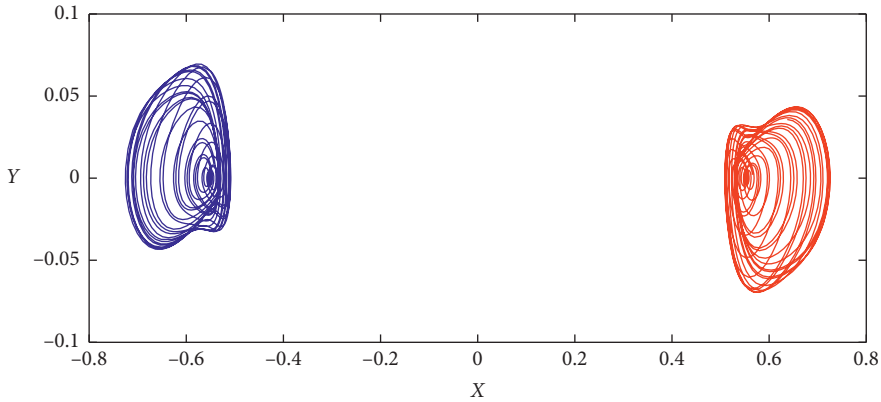

Figure 5: Tori attractors for initial conditions of [0.5, 2] and [−0.5, −2].

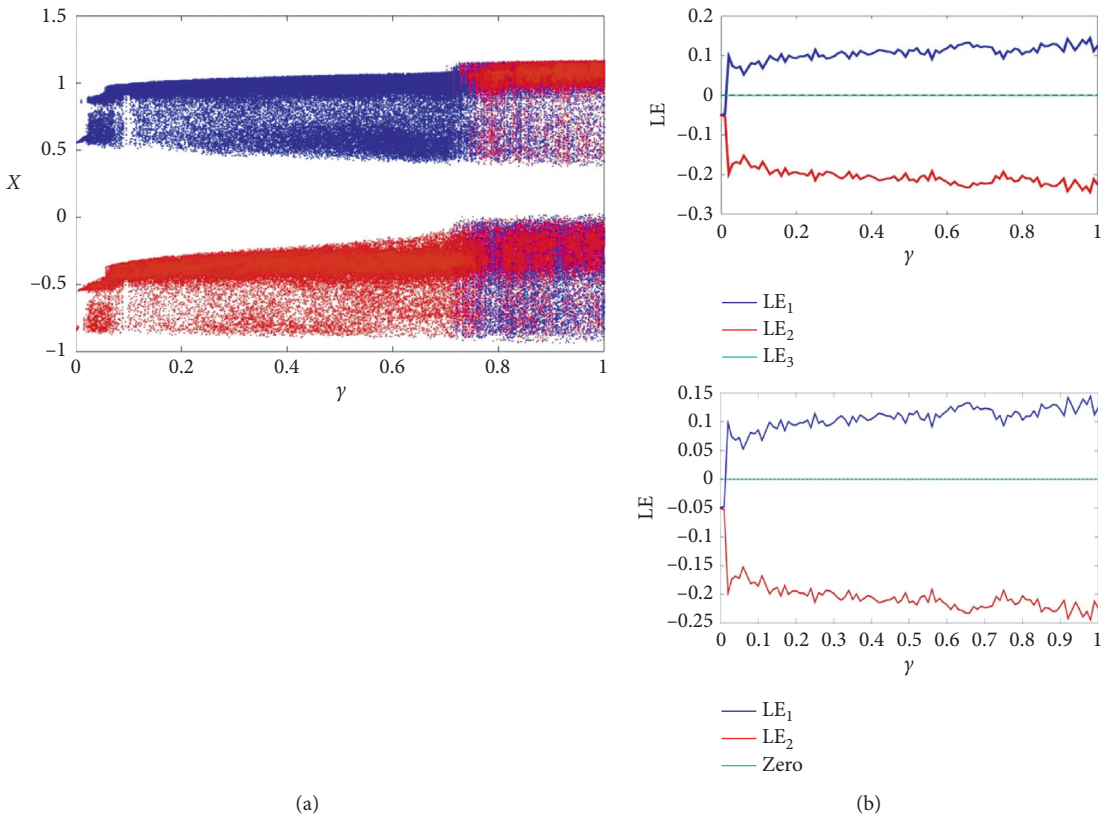

Figure 6: (a) Bistability of system (7) with the blue plots showing the forward continuation (increase parameter γ from 0 to 1) and the red plots showing backward continuation (decrease parameter γ from 1 to 0) with reinitialization of the initial conditions. (b) Corresponding Lyapunov exponents.

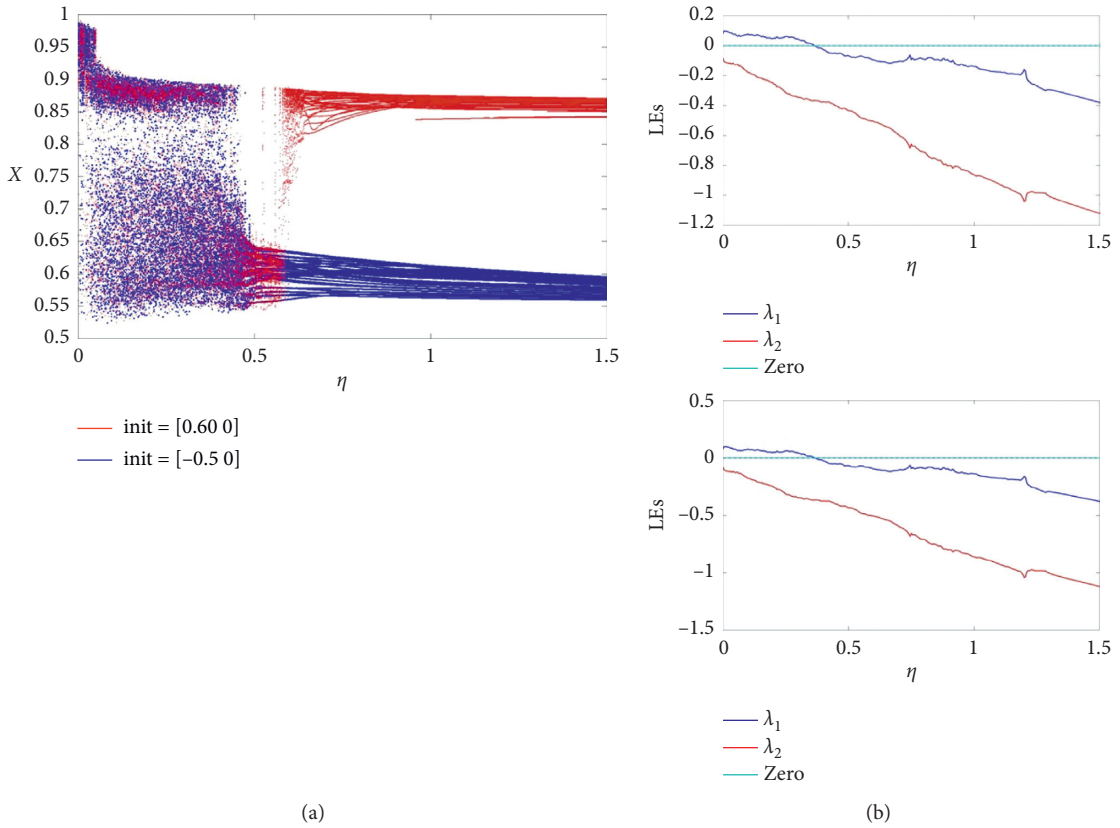

Figure 7: (a) Bistability of system (8) with the blue plots showing the forward continuation (increase parameter η from 0 to 1.5) and the red plots showing backward continuation (Decrease parameter from 1 to 0) with reinitialization of the initial conditions. (b) Corresponding Lyapunov exponents.

4.1. Case (A) during Martensitic Phase. In this case, we considered low temperature ($\theta = 0.69$), and dynamical behavior of the system during martensitic phase is analyzed. In the model, we supplied $a_2 = 124$, $a_3 = 14505$, $b = 0.7071$, $\gamma = 0.045$, $\Omega_1 = 0.5$, and $\Omega_2 = ((\sqrt{5} - 1)/2)$. Meanwhile, $\eta = 0.1$ and, for the initial condition [0.6, 0], chaotic attractor is observed. Also, we have $\eta = 1.5$ and, for the initial condition [0.5, 2], attracting tori is found. We present the phase portraits of chaotic attractor and tori in Figures 2(a) and 2(b) correspondingly.

The Lyapunov exponents are estimated using Wolf's algorithm [30], for the runtime of 20,000 s. Figure 3(a) shows a positive Lyapunov exponent with value of 0.204674, and the positive Lyapunov exponent confirms that it is a chaotic attractor. In Figure 3(b), both Lyapunov exponents have negative value; hence, they are concluded as attracting tori.

We extend our investigation for special properties; in Figure 4, we show that the system holds symmetric chaotic attractor for initial conditions of [0.6, 0] and [−0.5, 0], which clearly explains the sensitiveness of the system with initial conditions. Similarly, in Figure 5, we show symmetricity of the attracting tori.

System (7) is analyzed for the property of bistability. In this section, we perform the bifurcation analysis for system (7). Bistability is dangerous in mechanical systems and makes the controllability complex. Hence, it is mandatory

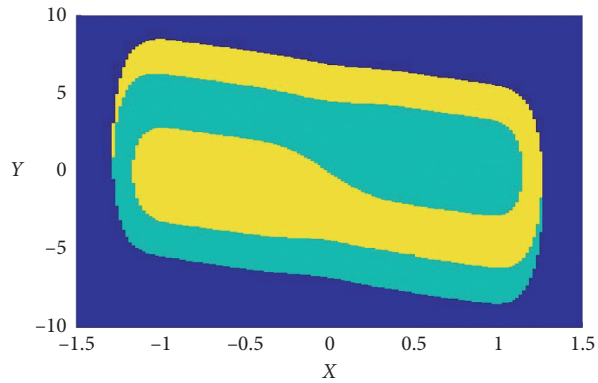

Figure 8: Cross section of the basins of attraction of the two coexisting attractors in the x-y-plane.

to analyze the existence of bistability in mechanical systems and explicate the region of such coexistence of attractors. We considered γ as bifurcation parameter and keep all the other parameters fixed. By plotting local maxima of the coordinate x in terms of the increasing (or decreasing) parameter with step size of 0.0003, this approach is known as forward and backward continuation, representing a simple way to localize the window in which the system possesses multistability. The existence of

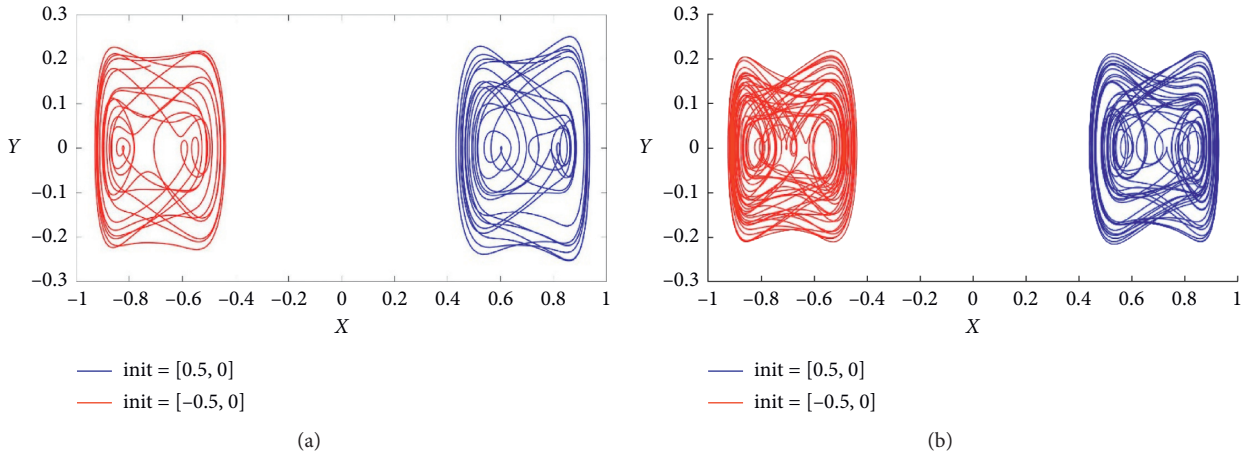

Figure 9: Phase portrait of system (7) for $\theta = 1.04$ and $\gamma = 0.045$. (a) $\eta = 0.01$; (b) $\eta = 0.1$. Remaining parameters are kept as in (9).

bistability can be confirmed by comparing the forward (Figure 6, blue) and backward (Figure 6, red) bifurcation diagrams. The corresponding Lyapunov exponents are plotted in Figure 6(b).

The bifurcation plot in Figure 7(a) portrays the existence of bistability when varying the η parameter. The maximum Lyapunov exponents for forward continuation are plotted with blue color and backward continuation is plotted with red color. Corresponding Lyapunov exponents are plotted in Figure 7(b).

A necessary tool for analyzing the bistability (coexistence of attractors) is the basin of attraction. All attractors, whether they are periodic oscillation, attracting tori, or strange attractors, are surrounded by a basin of attraction representing the set of initial conditions in the state space whose orbits approach and map out the attractor as time approaches infinity. Figure 8 depicts the cross section of the basin of attraction of two coexisting attractors in the x-y-plane. The plott is obtained for the parameter values as it is in (9). Initial conditions in the blue region lead to unbounded orbits, those in the yellow region lead to the chaotic attractor, and those in the cyan region lead to the attracting tori.

4.2. Case (B) during Transition Phase. The intermediate temperature ($\theta = 1.04$) where both austenite and martensite are stable is now considered. Unlike the previous case, the parameter η does not have a big influence in this case. We plotted the phase portraits of the system for $\eta = 0.01$ (Figure 9) and $\eta = 0.1$ (Figure 10), both showing similar chaotic attractor. But we could observe symmetric properties from Figures 9(a) and 9(b).

However, variation in parameter γ still holds bistability. Figure 10 shows the existence of different oscillation in the system dynamics. We showed the bifurcation diagram for the range $0 \le \gamma \le 0.05$; we can clearly identify the bistability portions 0 to 0.005 from Figure 11. In Figure 12, we present the basin of attraction in order to show the different attractors.

4.3. Case (C) during Austenitic Phase. In this case, the response of the system in higher temperature ($\theta = 1.30$) is

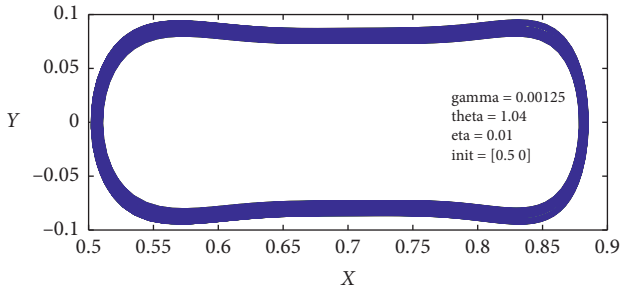

Figure 10: Phase portrait of system (7) for $\theta = 1.04$, $\eta = 0.01$, and $\gamma = 0.00125$. Remaining parameters are kept as in (9).

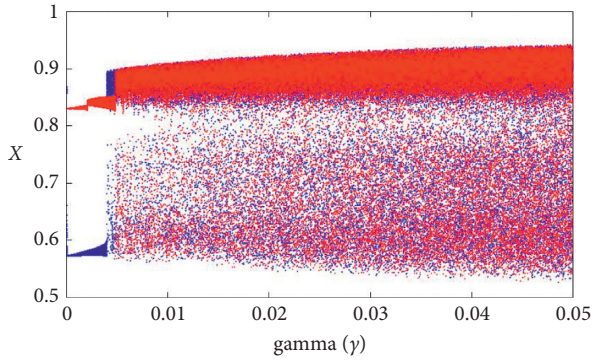

Figure 11: Bifurcation diagram for $\theta = 1.04$ and $\eta = 0.01$ with the blue plots showing the forward continuation (increase the parameter $0 \le \gamma \le 0.05$) and the red plots showing backward continuation.

investigated, where the austenitic phase is stable. During this phase, the system shows sustainable chaotic oscillations for different η values as shown in Figure 12. Influence of parameter γ is analyzed using the bifurcation diagrams as shown in Figures 13 and 14. In Figure 13, we could see that γ varied from 0 to 1 and η is taken as 0.01. Chaotic oscillation is observed and does not show bistability behavior. Similarly,

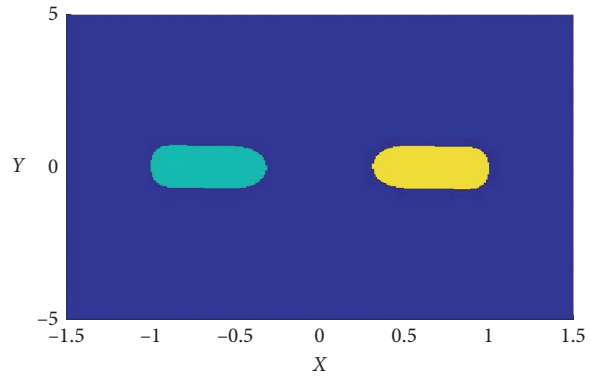

Figure 12: Cross section of the basins of attraction of the two coexisting attractors in the x-y-plane (Case B).

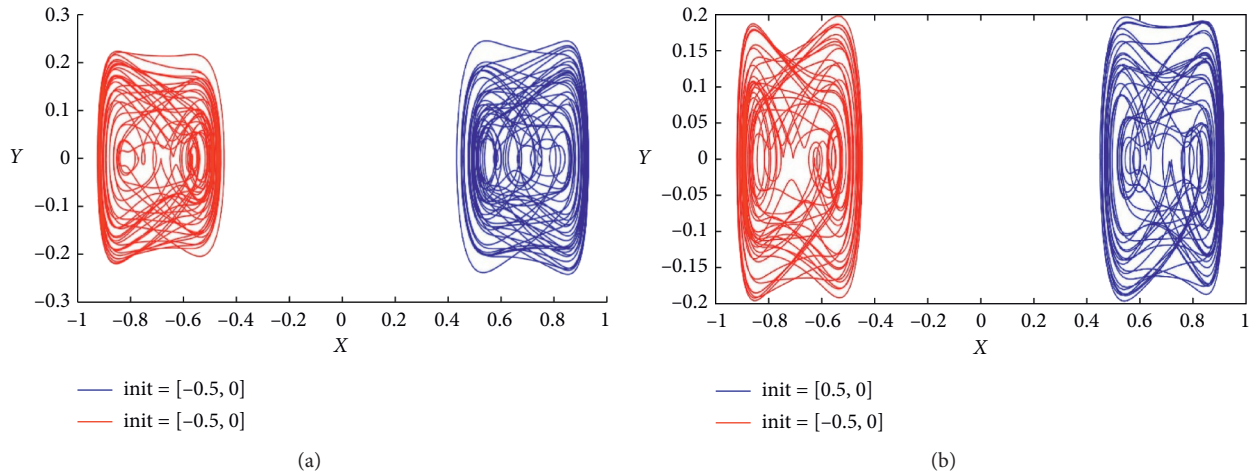

Figure 13: Phase portrait of system (7) for $\theta = 1.30$ and $\gamma = 0.045$. (a) $\eta = 0.01$; (b) $\eta = 0.1$. Remaining parameters are kept as in (9).

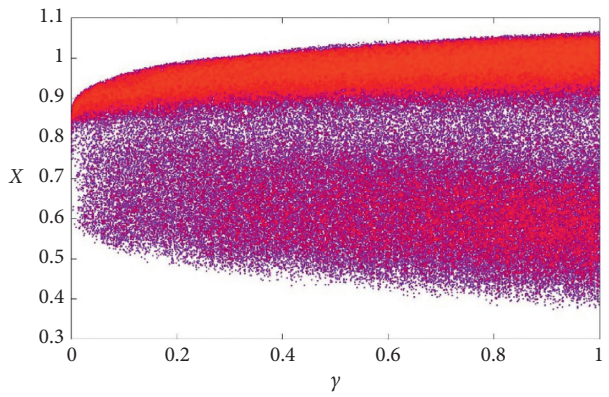

Figure 14: Bifurcation diagram of system (7) for $\theta = 1.30$ and $\eta = 0.01$ with the blue plots showing the forward continuation (increase the parameter $0 \le \gamma \le 1$) and the red plots showing backward continuation.

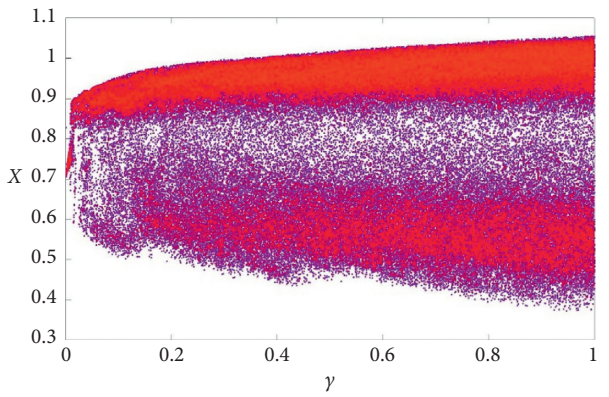

Figure 15: Bifurcation diagram of system (7) for $\theta = 1.30$ and $\eta = 0.1$ with the blue plots showing the forward continuation (increase the parameter $0 \le \gamma \le 1$) and the red plots showing backward continuation.

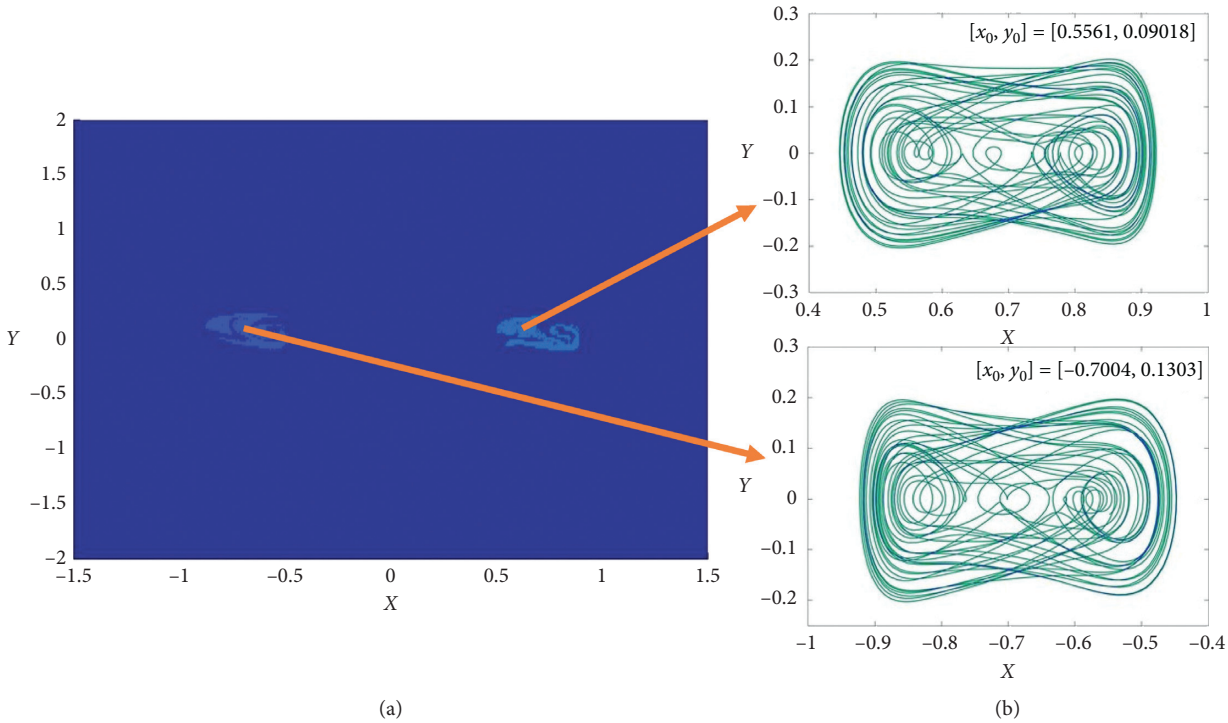

Figure 16: Cross section of the basins of attraction of the two coexisting attractors in the x-y-plane (Case C).

while we increase the η value to 0.1, the system does not show any bistability. Basin of attraction is also provided in Figure 15. It is worth noting that the three-leg supporter system suffers from bistability during martensitic (Figure 16) and transition phases but does not suffer from it if it operates in austenitic phase (higher temperature).

5. Conclusion

In this paper, a quasi-periodically excited three-leg supporter with shape memory alloy is investigated for bistability behavior. The existence of chaotic strange attractor and an attracting tori has been evolved and depicted in phase portraits; hence, it is clear that considering quasi-periodic excitation holds the property of bistability. Chaotic strange attractor is confirmed by showing positive Lyapunov exponents. The presence of symmetric behavior is revealed and shown for the corresponding initial conditions; this kind of behavior is interesting for controlling the system. Bifurcation plots presented in Section 4 show the behavioral changes of γ and η; hence, we can easily understand the bistability nature of the system for particular range of values. Cross section of basin of attraction is plotted for showing the pool of initial conditions, where we can get the chaotic attractor and the attracting tori. More importantly, in our study, we showed that the bistability behavior is present only during martensitic and transition phases and not in austenitic phase. We firmly believe that the analysis will be very helpful during designing and developing control algorithm of three-leg platform with shape memory alloys.

Data Availability

The data used to support the findings of this paper are included within the manuscript.

Conflicts of Interest

The authors declare that there are no conflicts of interest regarding the publication of this paper.

References

[1] A. S. Marcelo, "Nonlinear dynamics and chaos in shape memory alloy systems," *International Journal of Non-linear Mechanics*, vol. 70, pp. 2–19, 2015.

[2] R. J. Wasilevski, "On the nature of the martensitic transformation," *Metallurgical Transactions A*, vol. 6, pp. 1405–1418, 1975.

[3] K. Otsuka and X. Ren, "Recent developments in the research of shape memory alloys," in *Institute of Materials Science*, University of Tsukuba, Tsukuba, Japan, 1999.

[4] C. E. Borroni-Bird, "Smarter vehicles. smart structures and materials 1997: industrial and commercial applications of smart structures technologies," in *Proceedings of the SPIE-the International Society for Optical Engineering*, San Diego, CA, USA, March 1997.

[5] T. Borden, "Shape memory alloys: forming a tight fit," *Mechanical Engineering*, vol. 113, no. 10, pp. 66–72, 1991.

[6] M. A. Savi and A. M. B. Braga, "Chaotic vibrations of na oscillator with shape memory," *Journal of the Brazilian Society of Mechanical Sciences and Engineering*, vol. 15, no. 1, pp. 1–20, 1993.

[7] M. A. Savi and A. M. B. Braga, "Chaotic response of a shape memory oscillator with internal constraints," in *Proceedings of*

the XII the Brazilian Congress of Mechanical Engineering (COBEM 93–ABCM), pp. 33–36, Brasilia, Brazil, December 1993.

[8] F. Falk, "Model free-energy, mechanics and thermodynamics of shape memory alloys," *ACTA-Metallurgica*, vol. 28, no. 12, pp. 1773–1780, 1980.

[9] F. Falk and P. Konopka, "Three-dimensional Landau theory describing the martensitic transformation of shape memory alloys," *Journal De Physique*, vol. 2, pp. 61–77, 1990.

[10] P. Alberto and A. savi Marcelo, "An overview of constitutive models for shape memory alloys," *Mathematical Problems in Engineering*, vol. 2006, no. 43, Article ID 056876, 2006.

[11] C. Grebogi, E. Ott, S. Pelikan, and J. A. Yorke, "Strange attractors that are not chaotic," *Physica D: Nonlinear Phenomena*, vol. 13, no. 1-2, pp. 261–268, 1984.

[12] Z. I. Bezhaeva and V. I. Oseledets, "An example of a strange nonchaotic attractor," *Functional Analysis and Its Applications*, vol. 30, no. 4, pp. 223–229, 1996.

[13] M. Ding, C. Grebogi, and E. Ott, "Evolution of attractors in quasiperiodically forced systems: from quasiperiodic to strange nonchaotic to chaotic," *Physical Review A*, vol. 39, no. 5, pp. 2593–2598, 1989.

[14] U. Feudel, J. Kurths, and A. S. Pikovsky, "Strange non-chaotic attractor in a quasiperiodically forced circle map," *Physica D: Nonlinear Phenomena*, vol. 88, no. 3-4, pp. 176–186, 1995.

[15] J. F. Heagy and S. M. Hammel, "The birth of strange nonchaotic attractors," *Physica D: Nonlinear Phenomena*, vol. 70, no. 1-2, pp. 140–153, 1994.

[16] À. Jorba, J. C. Tatjer, C. Núñez, and R. Obaya, "Old and new results on strange nonchaotic attractors," *International Journal of Bifurcation and Chaos*, vol. 17, no. 11, pp. 3895–3928, 2007.

[17] G. Keller, "A note on strange nonchaotic attractors," *Fundamenta Mathematicae*, vol. 151, no. 2, pp. 139–148, 1996.

[18] S. P. Kuznetsov, A. S. Pikovsky, and U. Feudel, "Birth of a strange nonchaotic attractor: a renormalization group analysis," *Physical Review E*, vol. 51, pp. 1629–1632, 1995.

[19] F. J. Romeiras, A. Bondeson, E. Ott, T. M. Antonsen, and C. Grebogi, "Quasiperiodically forced dynamical systems with strange nonchaotic attractors," *Physica D: Nonlinear Phenomena*, vol. 26, no. 1-3, pp. 277–294, 1987.

[20] F. J. Romeiras, A. Bondeson, E. Ott, T. M. Antonsen, and C. Grebogi, "Quasiperiodic forcing and the observability of strange nonchaotic attractors," *Physica Scripta*, vol. 40, no. 3, pp. 442–444, 1989.

[21] K. V. Avramov and O. V. Gendelman, "Quasiperiodic forced vibrations of a beam interacting with a nonlinear spring," *Acta Mechanica*, vol. 19, no. 2, pp. 17–35, 2007.

[22] Xu Zhang, "Dynamics of nonautonomous ordinary differential equations with quasi-periodic coefficients," *International Journal of Bifurcation and Chaos*, vol. 27, no. 6, 2017.

[23] X. Zhang and G. Chen, "Chaotic and non-chaotic strange attractors of a class of non-autonomous systems," *Chaos: An Interdisciplinary Journal of Nonlinear Science*, vol. 28, no. 2, Article ID 023102, 2018.

[24] U. Feudel, C. Grebogi, L. Poon, and J. A. Yorke, "Dynamical properties of a simple mechanical system with a large number of coexisting periodic attractors," *Chaos, Solitons & Fractals*, vol. 9, no. 1-2, pp. 171–180, 1998.

[25] K. Rajagopal, A. Karthikeyan, and P. Duraisamy, "Bifurcation analysis and chaos control of a fractional order portal frame with nonideal loading using adaptive sliding mode control," *Shock and Vibration*, vol. 2017, Article ID 2321060, 2017.

[26] K. Rajagopal, D. Prakash, R. Weldegiorgis, and A. Karthikeyan, "Multistability in horizontal platform system with and without time delays," *Shock and Vibration*, vol. 2018, Article ID 1092812, 2018.

[27] P. Prakash, K. Rajagopal, J. P. Singh, and B. K. Roy, "Megastability in a quasi-periodically forced system exhibiting multistability, quasi-periodic behaviour, and its analogue circuit simulation," *AEU-International Journal of Electronics and Communications*, vol. 92, pp. 111–115, 2018.

[28] Z. Huang, C. Du, and Y. Li, "Bifurcation and chaos of a shape memory alloy supporter," in *Proceedings of the 2008 7th World Congress on Intelligent Control and Automation*, Chongqing, China, June 2008.

[29] M. Agrawal, A. Prasad, and R. Ramaswamy, "Quasiperiodic forcing of coupled chaotic systems," *Physical Review E*, vol. 81, Article ID 026202, 2010.

[30] A. Wolf, J. B. Swift, H. L. Swinney, and J. A. Vastano, "Determining Lyapunov exponents from a time series," *Physica D: Nonlinear Phenomena*, vol. 16, no. 3, pp. 285–317, 1985.

Hindawi
Complexity
Volume 2020, Article ID 8864585, 11 pages
https://doi.org/10.1155/2020/8864585

Research Article

Fractal Dimension for the Nonautonomous Stochastic Fifth-Order Swift–Hohenberg Equation

Yanfeng Guo,[1,2] **Chunxiao Guo**,[3] **and Yongping Xi**[3]

[1]*School of Mathematics and Physics, China University of Geosciences, Wuhan 430074, Hubei, China*
[2]*School of Science, Guangxi University of Science and Technology, Liuzhou 545006, Guangxi, China*
[3]*School of Science, China University of Mining and Technology, Beijing 100083, China*

Correspondence should be addressed to Chunxiao Guo; guochunxiao1983@sina.com

Received 13 August 2020; Revised 27 August 2020; Accepted 5 September 2020; Published 16 September 2020

Academic Editor: Karthikeyan Rajagopal

Some dynamics behaviors for the nonautonomous stochastic fifth-order Swift–Hohenberg equation with additive white noise are considered. The existence of pullback random attractors for the nonautonomous stochastic fifth-order Swift–Hohenberg equation with some properties is mainly investigated on the bounded domain and unbounded domain, through the Ornstein–Uhlenbeck transformation and tail-term estimates. Furthermore, on the basis of some conditions, the finiteness of fractal dimension of random attractor is proved.

1. Introduction

Swift and Hohenberg proposed the Swift–Hohenberg (S-H) equation as a model for the convective instability in the Rayleigh–Bénard convection in 1997 [1]. There have been some results for the classical S-H equation [2–6]. Peletier and his collaborators have studied the S-H equation from different aspects, such as the stability of stationary solutions and pattern selections of solutions [7–9]. Recently, some results about pullback attractor [10, 11] and uniform attractor [12] of S-H equation are investigated. As we know, more and more authors investigated the random attractors and have obtained many important results. Meanwhile, there has been tremendous interest in developing the fractal dimension estimate of random attractors in recent years (see [13–19] and the references there in).

We consider the stochastic fifth-order S-H equation driven by additive white noise:

$$\begin{aligned} &du + \left(\Delta^2 u + 2\Delta u + au + u^5 - g(x,t)\right)dt \\ &\quad = \phi(x)dW(t), \quad ((x,t) \in D \times (\kappa, +\infty), \kappa \in \mathbb{R}, \end{aligned} \tag{1}$$

with boundary condition

$$u(t,x) = 0, \quad x \in \partial D, \tag{2}$$

and the initial condition

$$u(x,\kappa) = u_\kappa(x), \quad x \in D, \tag{3}$$

where $a > 0$ and $D \subset \mathbb{R}^2$ is a bounded smooth domain.

There are some results about dynamics behaviors for the classical autonomous stochastic S-H equation [20, 21]. Except for the study of the existence of the random attractor [22–24], Zhou et al. have established an efficient theory about the finite fractal dimensions of random attractor [25, 26]. To our knowledge, the fractal dimension estimate has been barely studied for the random attractors of the stochastic fifth-order S-H equation yet. According to the ideas in [21, 25–28], stochastic dynamics behaviors of the random attractor are considered for stochastic equations (1)–(3) in two cases.

Firstly, we mainly give the existence of random attractor for the fifth-order S-H equation corresponding to (1)–(3). A few results about the dynamics behaviors of the fifth-order S-H equation with additive noise have been given when the nonlinear term is five ordered. Due to the increasing order, more difficult terms can be produced to derive uniform estimates for the solution of equations

(1)–(3). In order to overcome these difficulties aroused by the fifth-order term, we mainly use the method of integration by parts after Ornstein–Uhlenbeck transformation. Notice that the uniform estimates are independent of bounded region D, and we can obtain the existence of random attractor by proving that the random dynamical system is asymptotically compact through tail-term estimates on unbounded domain $\mathbb{R}^2$.

Secondly, we are devoted to the finiteness of fractal dimension for the random attractor of (1)–(3). Because of the complexity of proving the boundedness of fractal dimension on unbounded domain, we pay attention to studying the fifth-order S-H equation on bounded domain D. Furthermore, we will discuss the case of unbounded domain. Here, in order to obtain the boundedness of the fractal dimension, some sufficient conditions are proposed [16–18].

2. Preliminaries

We give the theorem related to random attractors. Since these conclusions are classic, we will not discuss them in detail, and readers can check the relevant literature [22–24, 29, 30].

In this paper, we will use $\|\cdot\|$ to denote the norm and $(\cdot,\cdot)$ to denote the inner product in $L^2(\mathbb{R}^2)$ or $L^2(D)$, where D is a bounded smooth domain. In the case of bounded domain, for simplicity, we use the notation H to present the space $L^2(D)$. We will write the norm of $L^p(\mathbb{R}^2)(L^p(D))$ as $\|\cdot\|_{L^p}$ and use $\|\cdot\|_X$ to denote the norm of Banach space X and $\|\cdot\|_s$ to denote the norm in $H^s(D)$ or $H^s(\mathbb{R}^2)$.

The continuous random dynamical system will be showed for the stochastic fifth-order S-H equation on $L^2(\mathbb{R}^2)$ (or $L^2(D)$):

$$\mathrm{d}u + \left(\Delta^2 u + 2\Delta u + au + u^5 - g(x,t)\right)\mathrm{d}t = \sum_{i=1}^{m} \phi_i(x)\mathrm{d}W_i(t), \tag{4}$$

with boundary condition

$$u(t,x) = 0, \quad x \in \partial D, \tag{5}$$

and with the initial condition

$$u(x,\kappa) = u_\kappa(x), x \in D, \tag{6}$$

where $\phi_i(x) \in H^4(\mathbb{R}^2)(i = 1,\ldots,m)$ is the smooth enough function. W is a two-sided real-value Wiener process on a probability space and $g(x,\cdot) \in C_b(\mathbb{R}, H)$ is given.

Let $\tilde{z}(\omega) = -a\int_{-\infty}^{0} e^{a\kappa}\omega(\kappa)\mathrm{d}\kappa, \omega \in \Omega$, which is a unique stationary solution of the equation [29]:

$$\mathrm{d}\tilde{z} + a\tilde{z}\mathrm{d}t = \mathrm{d}W. \tag{7}$$

In addition, for each fixed $\omega \in \Omega$, $\tilde{z}(\theta_t\omega)$ is pathwise continuous. And there is a tempered function $r(\omega) > 0$:

$$\left|\tilde{z}(\theta_t\omega)\right|^2 + \left|\tilde{z}(\theta_t\omega)\right|^p \le e^{a-6/2|t|} r(\omega), \quad t \in \mathbb{R}, \mathrm{P-a.e.}\omega \in \Omega. \tag{8}$$

Given a translation $v(t,\kappa,\omega,v_\kappa) = u(t,\kappa,\omega,u_\kappa) - z(\theta_t\omega)$, one yields $v_\kappa = u_\kappa - z(\omega)$, where $z(\theta_t\omega) = \phi(x)\tilde{z}(\theta_t\omega)$. Then, we obtain

$$\begin{aligned}\frac{\mathrm{d}v}{\mathrm{d}t} &+ \Delta^2 v + 2\Delta v + 2\Delta z(\theta_t\omega) + av + \Delta^2 z(\theta_t\omega) + v^5 \\ &+ z^5(\theta_t\omega) + 5v^4 z(\theta_t\omega) + 10v^3 z^2(\theta_t\omega) + 10v^2 z^3(\theta_t\omega) \\ &+ 5vz^4(\theta_t\omega) = g(x,t),\end{aligned} \tag{9}$$

$$v(t,x) = 0, \quad x \in \partial D, \tag{10}$$

$$v(\kappa,\kappa,\omega,x) = v_\kappa(\omega) = u_\kappa(x) - z(\omega). \tag{11}$$

By the Galerkin method, for all $v_\kappa \in H$, as proved in [31], one can show that systems (9)–(11) are well-posed for every $\omega \in \Omega$ in H. A continuous cocycle Φ: $\mathbb{R}^+ \times \mathbb{R} \times \Omega \times H \longrightarrow H$ is defined by

$$\Phi(t,\kappa,\omega,u_\kappa) = \Phi(t,\kappa,\omega)u_\kappa = u(t+\kappa,\kappa,\theta_{-\kappa}\omega,u_\kappa), \tag{12}$$

and a cocycle Ψ: $\mathbb{R}^+ \times \mathbb{R} \times \Omega \times H \longrightarrow H$ by

$$\Psi(t,\kappa,\omega,v_\kappa) = \Psi(t,\kappa,\omega)v_\kappa = v(t+\kappa,\kappa,\theta_{-\kappa}\omega,v_\kappa), \tag{13}$$

where $v_\kappa = u_\kappa - z(\omega)$. Notice that the continuous dynamical systems Φ and Ψ are equivalent. Similarly, Φ: $\mathbb{R}^+ \times \mathbb{R} \times \Omega \times L^2(\mathbb{R}^2) \longrightarrow L^2(\mathbb{R}^2)$ is a continuous cocycle.

Let $B = \{B(\kappa,\omega): \kappa \in \mathbb{R}, \omega \in \Omega\}$, which are a family of bound nonempty subsets of H (or $L^2(\mathbb{R}^2)$) and

$$\lim_{t\longrightarrow+\infty} e^{-ct}\left\|B(\kappa+t,\theta_t\omega)\right\|^2 = 0, \quad \forall c > 0, \kappa \in \mathbb{R}, \omega \in \Omega, \tag{14}$$

where $\|B\| = \sup_{u\in B}\|u\|$. Here, we always assume that $\mathscr{D}$ is the collection of all tempered families of nonempty subsets of H. Furthermore, we prove that there exist $\mathscr{D}$-pullback attractors for cocycle Φ. In the whole paper, we assume $g(x,\cdot) \in C_b(\mathbb{R}, H)$ with

$$\|g\|^2 = \sup_{t\in\mathbb{R}}\|g(\cdot,t)\|^2 < +\infty. \tag{15}$$

3. Some Uniform Estimates

The uniform estimates are derived for solutions of systems (9)–(11) on bounded domain D and $\mathbb{R}^2$, respectively.

Lemma 1. *Suppose $a > 6$ and (8) holds. Then, for every $\kappa \in \mathbb{R}, \omega \in \Omega$, and $B = \{B(\kappa,\omega): \kappa \in \mathbb{R}, \omega \in \Omega\} \in \mathscr{D}$, there is a $T_0(\kappa,\omega,B) \ge 1$ satisfying*

$$\begin{aligned}\left\|v(\kappa,\kappa-t,\theta_{-\kappa}\omega,v_{\kappa-t})\right\|^2 &\le r_0(\kappa,\omega), \\ \left\|u(\kappa,\kappa-t,\theta_{-\kappa}\omega,u_{\kappa-t})\right\|^2 &\le r_1(\kappa,\omega),\end{aligned} \tag{16}$$

for $\forall t \ge T_0(\kappa,\omega,B)$, where v is the solution of systems (9)–(11), $v_{\kappa-t} + z(\theta_{-t}\omega) \in B(\kappa-t,\theta_{-t}\omega)$, and $r_0(\kappa,\omega)$ and $r_1(\kappa,\omega)$ are two tempered random variables.

Proof. From (9), we deduce

$$\begin{aligned}\frac{1}{2}\frac{\mathrm{d}}{\mathrm{d}t}\|v\|^2+\|\Delta v\|^2 &= -a\|v\|^2-\|v\|_{L^6}^6\\ &\quad-\left(2\Delta v+2\Delta z(\theta_t\omega)+\Delta^2 z(\theta_t\omega),v\right)\\ &\quad-\left(z^5(\theta_t\omega)+5v^4 z(\theta_t\omega)+10v^3z^2(\theta_t\omega),v\right)\\ &\quad-5\left(2v^2z^3(\theta_t\omega)+vz^4(\theta_t\omega),v\right)+(g(t),v).\end{aligned} \tag{17}$$

Since

$$\begin{aligned}\left(10v^3z^2(\theta_t\omega),v\right)&=10\int_D v^4z^2(\theta_t\omega)\mathrm{d}x\ge 0,\left(5vz^4(\theta_t\omega),v\right)\\ &=5\int_D v^2z^4(\theta_t\omega)\mathrm{d}x\ge 0,\end{aligned} \tag{18}$$

applying the Hölder inequality and the ε–Young inequality, one gets

$$\begin{aligned}\frac{\mathrm{d}}{\mathrm{d}t}\|v\|^2+\|v\|_{L^6}^6+(a-6)\|v\|^2+\|\Delta v\|^2 &\le C\left(\left|\widetilde{z}(\theta_t\omega)\right|^{10}\right.\\ &\quad\left.+\left|\widetilde{z}(\theta_t\omega)\right|^6+\left|\widetilde{z}(\theta_t\omega)\right|^2\right)\\ &\quad+\frac{1}{a}\|g(t)\|^2\doteq F(\theta_t\omega)\\ &\quad+\frac{1}{a}\|g(t)\|^2,\end{aligned} \tag{19}$$

when $r\ge\kappa-t$, by the Gronwall inequality on $[\kappa-t,r]$ and substituting $\theta_{-\kappa}\omega$ for ω, one has

$$\begin{aligned}\left\|v(r,\kappa-t,\theta_{-\kappa}\omega,v_{\kappa-t})\right\|^2 &\le e^{-(a-6)(r+t-\kappa)}\left\|v_{\kappa-t}\right\|^2\\ &\quad+\int_{\kappa-t}^{r}\left(e^{(6-a)(r-s)}F(\theta_{s-\kappa}\omega)+\frac{e^{(6-a)(r-s)}}{a}\|g(s)\|^2\right)\mathrm{d}s\\ &\le e^{-(a-6)t}\left\|v_{\kappa-t}\right\|^2+\int_{-\infty}^{0}\left(e^{-(6-a)s}F(\theta_s\omega)\right.\\ &\quad\left.+\frac{e^{-(6-a)s}}{a}(g(s+\kappa)]^2\right)\mathrm{d}s.\end{aligned} \tag{20}$$

From (20), since $v_{\kappa-t}+z(\theta_{-t}\omega)\in B(\kappa-t,\theta_{-t}\omega)$, and $B=\{B(\kappa,\omega)\colon \kappa\in\mathbb{R},\omega\in\Omega\}$ is tempered, and there is $T_0=T_0(\kappa,\omega,B)>1$ satisfying

$$e^{-(a-6)t}\left\|v_{\kappa-t}\right\|^2\le 1,\ \forall t\ge T_0. \tag{21}$$

From (20), we can deduce

$$\begin{aligned}&\left\|v(\kappa,\kappa-t,\theta_{-\kappa}\omega,v_{\kappa-t}\right\|^2\\ &\le 1+C\int_{-\infty}^{0}e^{\frac{(a-6)s}{2}}r(\omega)\mathrm{d}s+\frac{1}{a}\int_{-\infty}^{0}\|(s+\kappa)\|^2e^{(a-6)s}\mathrm{d}s\\ &\le e^{-(a-6)t}\left\|v_{\kappa-t}\right\|^2+\frac{2C}{a-6}r(\omega)+\frac{1}{a}\int_{-\infty}^{0}e^{(a-6)s}\|g(s+\kappa)\|^2\mathrm{d}s\\ &\doteq r_0(\kappa,\omega),\ \forall t\\ &\ge T_0(\kappa,\omega,B).\end{aligned} \tag{22}$$

For all $v_{\kappa-t}+z(\theta_{-t}\omega)\in B(\kappa-t,\theta_{-t}\omega)$, we have

$$\begin{aligned}\left\|u(\kappa,\kappa-t,\theta_{-\kappa}\omega,u_{\kappa-t})\right\|^2 &\le 2\|z(\omega)\|^2+2\\ &\quad+C\left(\int_{-\infty}^{0}e^{(a-6)s/2}r(\omega)\mathrm{d}s\right.\\ &\quad\left.+\int_{-\infty}^{0}\|g(s+\kappa)\|^2e^{(a-6)s}\mathrm{d}s\right)\\ &\doteq r_1(\kappa,\omega),\ \forall\kappa\in\mathbb{R},\omega\in\Omega.\end{aligned} \tag{23}$$

Denote

$$K(\kappa,\omega)=\left\{u\in H\colon \|u\|^2\le r_1(\kappa,\omega),\omega\in\Omega\kappa\in\mathbb{R}\right\}\in\mathscr{D}. \tag{24}$$

Then, $K(\kappa,\omega)$ is an absorbing set for Φ in $\mathscr{D}$ □

Remark 1. Using the Gronwall lemma, we can obtain the following results. For every $\kappa\in\mathbb{R},\omega\in\Omega$, and $B=\{B(\kappa,\omega)\colon \kappa\in\mathbb{R},\omega\in\Omega\}\in\mathscr{D}$, there is a $T_1(\kappa,\omega,B)\ge T_0\ge 1$ satisfying

$$\begin{aligned}&\int_{\kappa-1}^{\kappa}\left\|v(s,\kappa-t,\theta_{-\kappa}\omega,v_{\kappa-t})\right\|^2\mathrm{d}s\le r_2(\kappa,w),\forall t\ge T_1(\kappa,\omega,B),\\ &\int_{-t}^{0}e^{(a-6)s}\left\|\Delta v(s+\kappa,\kappa-t,\theta_{-\kappa}\omega,v_{\kappa-t})\right\|^2\mathrm{d}s\\ &\quad+\int_{-t}^{0}e^{(a-6)s}\left\|v(s+\kappa,\kappa-t,\theta_{-\kappa}\omega,v_{\kappa-t})\right\|_{L^6}^6\mathrm{d}s\\ &\quad\le r_3(\kappa,\omega),\forall t\ge T_1(\kappa,\omega,B),\end{aligned} \tag{25}$$

where v is the solution of systems (9)–(11), $v_{\kappa-t}+z(\theta_{-t}\omega)\in B(\kappa-t,\theta_{-t}\omega)$, and $r_2(\kappa,w)$ and $r_2(\kappa,w)$ are tempered random variables.

Lemma 2. *Suppose $a>6$ and (15) holds. Then, for every $\kappa\in\mathbb{R},\omega\in\Omega$, and $B=\{B(\kappa,\omega)\colon \kappa\in\mathbb{R},\omega\in\Omega\}\in\mathscr{D}$, there is a $T_1(\kappa,\omega,B)\ge T_0\ge 1$ satisfying*

$$\left\|\Delta v(\kappa,\kappa-t,\theta_{-\kappa}\omega,v_{\kappa-t})\right\|^2\le r_4(\kappa,\omega),\forall t\ge T_1(\kappa,\omega,B), \tag{26}$$

where v is the solution of systems (9)–(11), $v_{\kappa-t}+z(\theta_{-t}\omega)\in B(\kappa-t,\theta_{-t}\omega)$, and $r_4(\kappa,w)$ and $r_5(\kappa,w)$ are tempered random variables.

Proof. By (9), one obtains

$$\begin{aligned}&\frac{1}{2}\frac{\mathrm{d}}{\mathrm{d}t}\|\Delta v\|^2+\left(2\Delta v,\Delta^2v\right)+\left(2\Delta z(\theta_t\omega)+\Delta^2z(\theta_t\omega),\Delta^2v\right)\\ &+a\|\Delta v\|^2+\|\Delta v\|^2+\left(v^5,\Delta^2v\right)+\left(z^5(\theta_t\omega),\Delta^2v\right)\\ &+\left(\left(v^4z(\theta_t\omega),\Delta^2v\right)+\left(10v^3z^2(\theta_t\omega),\Delta^2v\right)\right.\\ &+\left(10v^2z^3(\theta_t\omega),\Delta^2v\right)+\left(5vz^4(\theta_t\omega)\Delta^2v\right)=\left(g(x,t),\Delta^2v\right).\end{aligned} \tag{27}$$

It is easy to get

$$\left|2\left(\Delta v, \Delta^2 v\right)\right| \le \frac{1}{4}\left\|\Delta^2 v\right\|^2 + 4\|\Delta v\|^2. \tag{28}$$

It can easily be shown that

$$\begin{aligned}\left|\left(2\Delta z\left(\theta_t\omega\right), \Delta^2 v\right)\right| &\le \frac{1}{12}\left\|\Delta^2 v\right\|^2 + C\left\|\Delta z\left(\theta_t\omega\right)\right\|^2,\\ \left|\left(g\left(x,t\right), \Delta^2 v\right)\right| &\le \frac{1}{12}\left\|\Delta^2 v\right\|^2 + 3\|g\left(t\right)\|^2.\end{aligned} \tag{29}$$

It is evident that

$$\left|\left(\Delta^2 z\left(\theta_t\omega\right), \Delta^2 v\right)\right| \le \frac{1}{12}\left\|\Delta^2 v\right\|^2 + C\left\|z\left(\theta_t\omega\right)\right\|^2. \tag{30}$$

Since

$$\begin{aligned}\|v\|_{L^8} &\le C\left\|\Delta^2 v\right\|^{3/16}\|v\|^{13/16},\\ \|v\|_{L^4} &\le C\left\|\Delta^2 v\right\|^{1/8}\|v\|^{7/8},\end{aligned} \tag{31}$$

we deduce that

$$\begin{aligned}\left|\left(5v^4 z\left(\theta_t\omega\right), \Delta^2 v\right)\right| &\le 5\|v\|_{L^8}^4\left\|\Delta^2 v\right\|\left\|z\left(\theta_t\omega\right)\right\|_{L^\infty} C\\ &\left\|\Delta^2 v\right\|^{7/4}\|v\|^{13/4}\left\|z\left(\theta_t\omega\right)\right\|_{L^\infty} \le \frac{1}{12}\left\|\Delta^2 v\right\|^2\\ &+ C\left\|z\left(\theta_t\omega\right)\right\|_{L^\infty}^8,\\ \left|\left(5vz^4\left(\theta_t\omega\right), \Delta^2 v\right)\right| &\le 5\|v\|_{L^4}\left\|\Delta^2 v\right\|\left\|z\left(\theta_t\omega\right)\right\|_{L^{16}}^4\\ &\le C\left\|\Delta^2 v\right\|^{9/8}\left\|z\left(\theta_t\omega\right)\right\|_{L^{16}}^4 \le \frac{1}{12}\left\|\Delta^2 v\right\|^2\\ &+ C\left\|z\left(\theta_t\omega\right)\right\|_{L^{16}}^{64/7},\end{aligned} \tag{32}$$

where we have used the boundedness of $\|v\|$. It shows that

$$\left|\left(z^5\left(\theta_t\omega\right), \Delta^2 v\right)\right| \le \frac{1}{12}\left\|\Delta^2 v\right\|^2 + C\left\|z\left(\theta_t\omega\right)\right\|_{L^{10}}^{10}. \tag{33}$$

Similarly, we can get

$$\begin{aligned}&\left|\left(10v^3 z^2\left(\theta_t\omega\right), \Delta^2 v\right)\right|\\ &\le 10\|v\|_{L^{12}}^3\left\|\Delta^2 v\right\|\left\|z\left(\theta_t\omega\right)\right\|_{L^8}^2\\ &\le C\left\|\Delta^2 v\right\|^{13/8}\left\|z\left(\theta_t\omega\right)\right\|_{L^8}^2\|v\|^{19/8} \le C\left\|\Delta^2 v\right\|^{13/8}\left\|z\left(\theta_t\omega\right)\right\|_{L^8}^2\\ &\le \frac{1}{12}\left\|\Delta^2 v\right\|^2 + C\left\|z\left(\theta_t\omega\right)\right\|_{L^8}^{32/3},\\ &\left|\left(10v^2 z^3\left(\theta_t\omega\right), \Delta^2 v\right)\right|\\ &\le 10\|v\|_{L^8}^2\left\|\Delta^2 v\right\|\left\|z\left(\theta_t\omega\right)\right\|_{L^{12}}^3\\ &\le C\left\|\Delta^2 v\right\|^{3/8}\|v\|^{13/8}\left\|\Delta^2 v\right\|\left\|z\left(\theta_t\omega\right)\right\|_{L^{12}}^3\\ &\le C\left\|\Delta^2 v\right\|^{11/8}\left\|z\left(\theta_t\omega\right)\right\|_{L^{12}}^3 \le \frac{1}{12}\left\|\Delta^2 v\right\|^2 + C\left\|z\left(\theta_t\omega\right)\right\|_{L^{12}}^{48/5}.\end{aligned} \tag{34}$$

Similarly, we have the following estimates:

$$\begin{aligned}&\int_D (\nabla v)^2 v^3\left(\nabla^2 v\right)\mathrm{d}x\\ &\le \|\nabla v\|_{L^\infty}^2\left\|\nabla^2 v\right\|\|v\|_{L^6}^3\\ &\le C\|v\|\left\|\Delta^2 v\right\|\|\Delta v\|\|v\|_{L^6}^3 \le C\left\|\Delta^2 v\right\|\|\Delta v\|\|v\|_{L^6}^3\\ &\le \frac{1}{240}\left\|\Delta^2 v\right\|^2 + C\|\Delta v\|^2\|v\|_{L^6}^6,\\ \left(v^5, \Delta^2 v\right) &= -5\int_D v^4\nabla v\left(\nabla^3 v\right)\mathrm{d}x = 5\int_D \nabla\left(\nabla v v^4\right)\left(\nabla^2 v\right)\mathrm{d}x\\ &= 5\int_D\left(\nabla^2 v v^4 + 4\left(\nabla v\right)^2 v^3\right)\left(\nabla^2 v\right)dx\\ &= 5\int_D\left(\nabla^2 v\right)^2 v^4 dx + 20\int_D (\nabla v)^2 v^3\left(\nabla^2 v\right)\mathrm{d}x,\end{aligned} \tag{35}$$

where $\int_D (\nabla^2 v)^2 v^4 \mathrm{d}x \ge 0$.

Finally, we obtain

$$\frac{\mathrm{d}}{\mathrm{d}t}\|\Delta v\|^2 + (2a-8)\|\Delta v\|^2 \le C\|v\|_{L^6}^6\|\Delta v\|^2 + H\left(\theta_t\omega\right) + 3\|g\left(t\right)\|^2, \tag{36}$$

where

$$\begin{aligned}H\left(\theta_t\omega\right) = C\Big(&\left|\tilde{z}\left(\theta_t\omega\right)\right|^2 + \left|\tilde{z}\left(\theta_t\omega\right)\right|^{10} + \left|\tilde{z}\left(\theta_t\omega\right)\right|^{32/3}\Big)\\ &+ \left|\tilde{z}\left(\theta_t\omega\right)\right|^8 + \left|\tilde{z}\left(\theta_t\omega\right)\right|^{64/7} + \left|\tilde{z}\left(\theta_t\omega\right)\right|^{48/5}.\end{aligned} \tag{37}$$

Therefore,

$$\frac{\mathrm{d}}{\mathrm{d}t}\|\Delta v\|^2 \le C\|v\|_{L^6}^6\|\Delta v\|^2 + H\left(\theta_t\omega\right) + 3\|g\left(t\right)\|^2. \tag{38}$$

For $s \in [\kappa-1, \kappa]$, choosing $t \ge T_1\left(\kappa, \omega, B\right) \ge 1$, by the Gronwall inequality on the interval $[s, \kappa]$, we obtain

$$\begin{aligned}&\left\|\Delta v\left(\kappa, \kappa-t, \theta_{-\kappa}\omega, v_{\kappa-t}\right)\right\|^2\\ &\le e^{\int_{\kappa-1}^{\kappa} C\|v\|_{L^6}^6 d\sigma}\Big(\left\|\Delta v\left(s, \kappa-t, \theta_{-\kappa}\omega, v_{\kappa-t}\right)\right\|^2\\ &+ \int_{\kappa-1}^{\kappa} H\left(\theta_{r-\kappa}\omega\right)\mathrm{d}r\\ &+ 3\int_{\kappa-1}^{\kappa}\|g\left(r\right)\|^2\mathrm{d}r\Big).\end{aligned} \tag{39}$$

By Remark 1, one can obtain

$$\int_{\kappa-1}^{\kappa}\left\|v\left(s, \kappa-t, \theta_{-\kappa}\omega, v_{\kappa-t}\right)\right\|_{L^6}^6\mathrm{d}s \le Cr_3\left(\kappa, \omega\right). \tag{40}$$

Now, one can integrate (39) with respect to s. Then,

$$\left\|\Delta v\left(\kappa,\kappa-t,\theta_{-\kappa}\omega,v_{\kappa-t}\right)\right\|^2 \le e^{\int_{\kappa-1}^{\kappa} C\|v\|_{L^6}^6 \mathrm{d}\sigma}\left(\int_{\kappa-1}^{\kappa}\left\|\Delta v\left(s,\kappa-t,\theta_{-\kappa}\omega,v_{\kappa-t}\right)\right\|^2\mathrm{d}s+\int_{-1}^{0}\left(H\left(\theta_r\omega\right)+3\|g(r+\kappa)\|^2\right)\mathrm{d}r\right)\le e^{Cr_3(\kappa,\omega)}\left(r_2(\kappa,\omega)+\frac{2C}{a-6}r(\omega)+3\int_{-1}^{0}\|g(r+\kappa)\|^2\mathrm{d}r\right). \tag{41}$$

By Remark 1, (39)–(41), we can obtain

$$\left\|\Delta v\left(\kappa,\kappa-t,\theta_{-\kappa}\omega,v_{\kappa-t}\right)\right\|^2 \le r_4(\kappa,\omega). \tag{42}$$

Furthermore,

$$\left\|\Delta u\left(\kappa,\kappa-t,\theta_{-\kappa}\omega,u_{\kappa-t}\right)\right\|^2 \le r_5(\kappa,\omega). \tag{43}$$

□

Theorem 1. *Suppose $a>6$ and (15) holds. There exists a unique $\mathscr{D}$-pullback random attractor $\mathscr{A}=\{\mathscr{A}(\kappa,\omega):\kappa\in\mathbb{R},\omega\in\Omega\}\in\mathscr{D}$ in $H=L^2(D)$ for continuous cocycle Φ of systems (1) and (2).*

In the proof of the above lemmas, we find that all the estimates of solution do not depend on bounded domains D, so these estimates are also valid for unbounded domain.

Lemma 3. *Suppose $a>6$ and (15) holds. Then, for every $\kappa\in\mathbb{R},\omega\in\Omega$, and $B=\{B(\kappa,\omega):\kappa\in\mathbb{R},\omega\in\Omega\}\in\mathscr{D}$, there are $T_2(\kappa,\omega,B,\epsilon)\ge T_1\ge 1$ and $k_3(\kappa,\omega,\epsilon)\ge 1$ satisfying*

$$\int_{|x|\ge k}\left|v\left(\kappa,\kappa-t,\theta_{-\kappa}\omega,v_{\kappa-t}\right)\right|^2\mathrm{d}x\le\epsilon,\ \forall t\ge T_2(\kappa,\omega,B,\epsilon),k\ge k_3, \tag{44}$$

where v is the solution of systems (9)–(11) and $v_{\kappa-t}+z(\theta_{-t}\omega)\in B(\kappa-t,\theta_{-t}\omega)$.

Proof. Let $0\le\theta(s)\le 1\,(s\in\mathbb{R}^+)$ be a smooth function. When $0\le s\le 1$, $\theta(s)=0$. When $s\ge 2$, $\theta(s)=1$. Then, $|\theta'(s)|+|\theta''(s)|<C$. Multiplying (21) with $\theta(|x|^2/k^2)v$, we have

$$\begin{aligned}&\frac{1}{2}\frac{\mathrm{d}}{\mathrm{d}t}\int_{\mathbb{R}^2}\theta\left(\frac{|x|^2}{k^2}\right)|v|^2\mathrm{d}x+\int_{\mathbb{R}^2}\theta\left(\frac{|x|^2}{k^2}\right)v\left(\Delta^2v+2\Delta v\right)\mathrm{d}x\\&+\int_{\mathbb{R}^2}\theta\left(\frac{|x|^2}{k^2}\right)v\left(2\Delta z(\theta_t\omega)+av+v^5+\Delta^2z(\theta_t\omega)\right)\mathrm{d}x\\&+5\int_{\mathbb{R}^2}\theta\left(\frac{|x|^2}{k^2}\right)vz\left(v^4+2v^3z+2v^2z^2+vz^3+\frac{1}{5}z^4\right)\mathrm{d}x\\&=\int_{\mathbb{R}^2}\theta\left(\frac{|x|^2}{k^2}\right)vg(x,t)\mathrm{d}x.\end{aligned} \tag{45}$$

For the estimate of $\int_{\mathbb{R}^2}\theta(|x|^2/k^2)v\Delta^2v\mathrm{d}x$, similar to [21], it follows that

$$\begin{aligned}\int_{\mathbb{R}^2}\theta\left(\frac{|x|^2}{k^2}\right)v\Delta^2v\mathrm{d}x\ge&-\frac{C}{k}\left(\|v\|^2+\|\nabla v\|^2+\|\Delta v\|^2\right)\\&+\int_{\mathbb{R}^2}\theta\left(\frac{|x|^2}{k^2}\right)|\Delta v|^2\mathrm{d}x.\end{aligned} \tag{46}$$

In addition, there are

$$\begin{aligned}&\left|\int_{\mathbb{R}^2}\theta\left(\frac{|x|^2}{k^2}\right)v\Delta v\mathrm{d}x\right|\le\frac{1}{2}\int_{\mathbb{R}^2}\theta\left(\frac{|x|^2}{k^2}\right)|\Delta v|^2\mathrm{d}x+\frac{1}{2}\int_{\mathbb{R}^2}\theta\left(\frac{|x|^2}{k^2}\right)|v|^2\mathrm{d}x,\\&\left|\int_{\mathbb{R}^2}\theta\left(\frac{|x|^2}{k^2}\right)v\Delta^2z(\theta_t\omega)\mathrm{d}x\right|\le\frac{a}{2}\int_{\mathbb{R}^2}\theta\left(\frac{|x|^2}{k^2}\right)|v|^2\mathrm{d}x+C\int_{\mathbb{R}^2}\theta\left(\frac{|x|^2}{k^2}\right)\left|\Delta^2z(\theta_t\omega)\right|^2\mathrm{d}x,\\&\cdot\int_{\mathbb{R}^2}\theta\left(\frac{|x|^2}{k^2}\right)vg(x,t)\mathrm{d}x\le\frac{1}{2}\int_{\mathbb{R}^2}\theta\left(\frac{|x|^2}{k^2}\right)|v|^2\mathrm{d}x+C\int_{\mathbb{R}^2}\theta\left(\frac{|x|^2}{k^2}\right)|g(t)|^2\mathrm{d}x.\end{aligned} \tag{47}$$

Similarly, we get

$$\begin{aligned}\left|\int_{\mathbb{R}^2}\theta\left(\frac{|x|^2}{k^2}\right)v\Delta z(\theta_t\omega)\mathrm{d}x\right|\le&\frac{1}{2}\int_{\mathbb{R}^2}\theta\left(\frac{|x|^2}{k^2}\right)|v|^2\mathrm{d}x\\&+C\int_{\mathbb{R}^2}\theta\left(\frac{|x|^2}{k^2}\right)\left|\Delta z(\theta_t\omega)\right|^2\mathrm{d}x,\end{aligned} \tag{48}$$

where we have used the boundedness of function θ.

It is easy to obtain the following estimates:

$$\left|\int_{\mathbb{R}^2}\theta\left(\frac{|x|^2}{k^2}\right)v^5 z(\theta_t\omega)\mathrm{d}x\right| \le \frac{1}{10}\int_{\mathbb{R}^2}\theta\left(\frac{|x|^2}{k^2}\right)|v|^6\mathrm{d}x + C\int_{\mathbb{R}^2}\theta\left(\frac{|x|^2}{k^2}\right)|z(\theta_t\omega)|^6\mathrm{d}x,$$
$$\left|\int_{\mathbb{R}^2}\theta\left(\frac{|x|^2}{k^2}\right)vz^5(\theta_t\omega)\mathrm{d}x\right| \le \frac{1}{2}\int_{\mathbb{R}^2}\theta\left(\frac{|x|^2}{k^2}\right)|v|^2\mathrm{d}x + C\int_{\mathbb{R}^2}\theta\left(\frac{|x|^2}{k^2}\right)|z(\theta_t\omega)|^{10}\mathrm{d}x, \tag{49}$$

$$\left|\int_{\mathbb{R}^2}\theta\left(\frac{|x|^2}{k^2}\right)v^3z^3(\theta_t\omega)\mathrm{d}x\right| \le \frac{1}{20}\int_{\mathbb{R}^2}\theta\left(\frac{|x|^2}{k^2}\right)|v|^6\mathrm{d}x + C\int_{\mathbb{R}^2}\theta\left(\frac{|x|^2}{k^2}\right)|z(\theta_t\omega)|^6\mathrm{d}x. \tag{50}$$

Because $\int_{\mathbb{R}^2}\theta(|x|^2/k^2)v^4z^2(\theta_t\omega)\mathrm{d}x \ge 0$ and $\int_{\mathbb{R}^2}\theta(|x|^2/k^2)v^2z^4(\theta_t\omega)\mathrm{d}x \ge 0$, one yields

$$\frac{\mathrm{d}}{\mathrm{d}t}\int_{\mathbb{R}^2}\theta\left(\frac{|x|^2}{k^2}\right)|v|^2\mathrm{d}x + (a-6)\int_{\mathbb{R}^2}\theta\left(\frac{|x|^2}{k^2}\right)|v|^2\mathrm{d}x \le \frac{C}{k}\left(\|v\|^2 + \|\nabla v\|^2 + \|\Delta v\|^2\right) + C\int_{\mathbb{R}^2}\theta\left(\frac{|x|^2}{k^2}\right)\left(|\Delta z|^2 + |z|^6 + |\Delta^2 z|^2 + |z|^{10}\right)\mathrm{d}x + C\int_{\mathbb{R}^2}\theta\left(\frac{|x|^2}{k^2}\right)|g(t)|^2\mathrm{d}x. \tag{51}$$

Applying the Gronwall lemma on $[\kappa - t, \kappa]$, one gets

$$\begin{aligned}\int_{\mathbb{R}^2}\theta\left(\frac{|x|^2}{k^2}\right)|v(\kappa,\kappa-t,\theta_{-\kappa}\omega,v_{\kappa-t})|^2\mathrm{d}x &\le e^{-(a-6)t}\|v_{\kappa-t}\|^2 + \frac{C}{k}\int_{-t}^{0}e^{(a-6)s}\Big(\|v(s+\kappa,\kappa-t,\theta_{-\kappa}\omega,v_{\kappa-t})\|^2\\ &\quad + \|\nabla v(s+\kappa,\kappa-t,\theta_{-\kappa}\omega,v_{\kappa-t})\|^2 + \|\Delta v(s+\kappa,\kappa-t,\theta_{-\kappa}\omega,v_{\kappa-t})\|^2\Big)\mathrm{d}s\\ &\quad + C\int_{-\infty}^{0}e^{(a-6)s}\int_{\mathbb{R}^2}\theta\left(\frac{|x|^2}{k^2}\right)\left(|\Delta z(\theta_s\omega)|^2 + |\Delta^2 z(\theta_s\omega)|^2 + |z(\theta_s\omega)|^6 + |z(\theta_s\omega)|^{10}\right)\mathrm{d}x\mathrm{d}s\\ &\quad + C\int_{-\infty}^{0}e^{(a-6)s}\int_{\mathbb{R}^2}\theta\left(\frac{|x|^2}{k^2}\right)|g(s+\kappa)|^2\mathrm{d}x\mathrm{d}s.\end{aligned} \tag{52}$$

Noticing $v_{\kappa-t} + z(\theta_{-t}\omega) \in B(\kappa - t, \theta_{-t}\omega)$ and $B \in \mathscr{D}$, there is a $T_2 \ge T_1(t,\omega,B,\epsilon)$. When $t \ge T_2$, we have

$$e^{-(a-6)t}\|v_{\kappa-t}\|^2 \le \frac{\epsilon}{4}. \tag{53}$$

From (51), combining with Remark 1, if $\epsilon > 0$, there is a $k_1(\kappa,\epsilon) \ge 1$ satisfying

$$\frac{C}{k}\int_{-t}^{0}e^{(a-6)s}\left(\|v\|^2 + \|\Delta v\|^2\right)\mathrm{d}s \le \frac{\epsilon}{4}, \forall k \ge k_1(\kappa,\epsilon). \tag{54}$$

And there is a $k_2 = k_2(\epsilon) \ge k_1(\kappa,\epsilon)$ such that

$$C\int_{-\infty}^{0}e^{(a-6)s}\int_{\mathbb{R}^2}\theta\left(\frac{|x|^2}{k^2}\right)\left(|\Delta z(\theta_s\omega)|^2 + |\Delta^2 z(\theta_s\omega)|^2 + |z(\theta_s\omega)|^6 + |z(\theta_s\omega)|^{10}\right)\mathrm{d}x\mathrm{d}s \le C\epsilon\int_{-\infty}^{0}e^{(a-6)s}\left(|\tilde{z}(\theta_s\omega)|^2 + |\tilde{z}(\theta_s\omega)|^6 + |\tilde{z}(\theta_s\omega)|^{10}\right)\mathrm{d}s \le \frac{\epsilon}{4}, k \ge k_2. \tag{55}$$

Meanwhile, there is a $k_3(\kappa,\epsilon) \ge k_2$ satisfying

$$C\int_{-\infty}^{0} e^{(a-6)s}\int_{\mathbb{R}^2}\theta\left(\frac{|x|^2}{k^2}\right)|g(s+\kappa)|^2\mathrm{d}x\mathrm{d}s\le\frac{\epsilon}{4},\ k\ge k_3(\kappa,\epsilon). \tag{56}$$

By (51)–(56), we deduce

$$\int_{|x|\ge k}\left|v\left(\kappa,\kappa-t,\theta_{-\kappa}\omega,v_{\kappa-t}\right)\right|^2\mathrm{d}x\le\epsilon,\quad \forall k\ge k_3(\kappa,\epsilon). \tag{57}$$

□

Lemma 4. *Suppose $a>6$ and (15) holds. Then, given $\epsilon>0$ and $B=\{B(,\omega):\kappa\in\mathbb{R},\ \omega\in\Omega\}\in\mathscr{D}$, $\exists T_2=T_2(\kappa,\omega,B,\epsilon)\ge T_1\ge 1$, and $k_4=k_4(\omega,\epsilon)>0$, the solution $u(\kappa,\kappa-t,\theta_\kappa\omega,u_{\kappa-t})=v(\kappa,\kappa-t,\theta_\kappa\omega,v_{\kappa-t})+z(\theta_t\omega)$ satisfies the following inequality:*

$$\int_{|x|\ge k'}\left|u\left(\kappa,\kappa-t,\theta_{-\kappa}\omega,u_{\kappa-t}\right)\right|^2\mathrm{d}x\le\epsilon,\quad \forall t\ge T_2,k'\ge k_4, \tag{58}$$

where $v_{\kappa-t}+z(\theta_{-t}\omega)\in B(\kappa-t,\theta_{-t}\omega)$.

Proof. Since $z(\theta_t\omega)\in H^4(\mathbb{R}^2)$, then there exists a $k_1'>0$ such that

$$\int_{|x|\ge k_1'}\left|z\left(\theta_t\omega\right)\right|^2\mathrm{d}x\le\epsilon\left|\widetilde{z}\left(\theta_t\omega\right)\right|^2. \tag{59}$$

By Lemma 3, $\exists k_2'>k_3>0$, then

$$\int_{|x|\ge k_2'}\left|v\left(\kappa,\kappa-t,\theta_{-\kappa}\omega,v_{\kappa-t}\right)\right|^2\mathrm{d}x\le\frac{\epsilon}{4},\quad \forall t\ge T_2(\kappa,\omega,B,\epsilon). \tag{60}$$

By (55) and (56), $\forall t\ge T_2$ and $k'\ge k_4=\max\{k_1',k_2'\}$, one gets

$$\int_{|x|\ge k'}\left|u\left(\kappa,\kappa-t,\theta_{-\kappa}\omega,u_{\kappa-t}\right)\right|^2\mathrm{d}x\le\epsilon. \tag{61}$$

□

4. Finiteness of Fractal Dimension

Now, we are devoted to the existence of random attractor on $\mathbb{R}^2$ for the random dynamical system Φ.

Lemma 5. *Suppose $a>6$ and (15) holds. Then, $\mathscr{D}$-pullback asymptotically compact holds in $L^2(\mathbb{R}^2)$ for continuous cocycle Φ of (1) and (2).*

Similar to the method in [30], we only give the sketch of the proof for Lemma 5.

Firstly, the weak convergence

$$\Phi\left(t_n,\kappa-t_n,\theta_{-t_n}\omega,u_{0,n}\right)\rightarrow\xi \tag{62}$$

can be given in $L^2(\mathbb{R}^2)$.

Secondly, by Lemma 4, there exist enough large t and M satisfying

$$\int_{|x|\ge M}\left|\Phi\left(t,\kappa-t,\theta_{-t}\omega,u_0\right)\right|^{2\mathrm{d}x\le\epsilon}. \tag{63}$$

Denote the set $Q_M=\{x\in\mathbb{R}^2:|x|\le M\}$. By the estimates of Lemma 2, the embedding $H^2(Q_M)\mapsto L^2(Q_M)$ is compact. It follows that the strong convergence

$$\Phi\left(t_n,\kappa-t_n,\theta_{-t_n}\omega,u_{0,n}\right)\longrightarrow\xi \tag{64}$$

holds in $L^2(\mathbb{R}^2)$.

According to [30], the following theorem is easily obtained. The proof is omitted.

Theorem 2. *Suppose $a>6$ and (15) holds. Then, the continuous cocycle Φ corresponding to problems (1) and (2) has a unique $\mathscr{D}$-pullback attractor $\mathscr{A}=\{\mathscr{A}(\kappa,\omega):\kappa\in\mathbb{R},\omega\in\Omega\}\in\mathscr{D}$ in $L^2(\mathbb{R}^2)$.*

By Theorem 1, similar to the continuous cocycle Φ defined in (12), the random dynamical system Ψ defined in (13) has a unique $\mathscr{D}$-pullback attractor, denoted by $\widetilde{\mathscr{A}}=\left\{\widetilde{\mathscr{A}}(\kappa,\omega):\kappa\in\mathbb{R},\omega\in\Omega\right\}$ in $H=L^2(D)\in\mathscr{D}$. The boundedness of fractal dimension is proved for the random dynamical system Ψ. Because of complexity of proof on unbounded domain, we pay attention to studying the case of bounded domain D. Especially, the space $L^2(D)$ is denoted by H.

Assume that $\{\chi(\kappa,\omega)\}_{\kappa\in\mathbb{R},\omega\in\Omega}$ of X are a family of bounded closed random subsets, which satisfy the below conditions. For $\forall\omega\in\Omega,\kappa\in\mathbb{R}$, the following holds:

$H1$: there is tempered random variable R_ω, which is not dependent on κ and satisfies the diameter $\|\chi(\kappa,\omega)\|_X$ of $\chi(\kappa,\omega)$ controlled by R_ω, and $R_{\theta_t\omega}(\forall t\in\mathbb{R})$ is continuous.

$H2$: for $\forall t>0$, $\chi(t+\kappa,\theta_t\omega)=\Psi(t,\kappa,\omega)\chi(\kappa,\omega)$.

$H3$: there are random variables $C_0(\omega)\ge 0$, positive numbers λ,δ,t_0, and projector P_m: $X\longrightarrow P_mX$ satisfying

$$\left\|P_m\Psi(t_0,\kappa,\omega)v-P_m\Psi(t_0,\kappa,\omega)u\right\|_X\le e^{\int_0^{t_0}C_0(\theta_s\omega)\mathrm{d}s}\|v-u\|_X, \tag{65}$$

$$\left\|(I-P_m)\Psi(t_0,\kappa,\omega)v-(I-P_m)\Psi(t_0,\kappa,\omega)u\right\|_X\le\left(e^{-\lambda t_0}+\delta e^{\int_0^{t_0}C_0(\theta_s\omega)\mathrm{d}s}\right)\|v-u\|_X, \tag{66}$$

for any $u,v\in\chi(\kappa,\omega)$, $\kappa\in\mathbb{R}$, and $\omega\in\Omega$, where λ,δ,t_0,m do not depend on κ,ω.

$H4$: $\lambda,\delta,t_0,C_0(\omega)$ satisfy the following conditions:

$$\begin{cases} 0 \le E[C_0(\omega)] < \infty, \\ \lambda \ge 32E[C_0(\omega)], \\ 0 < \delta \le \dfrac{1}{32}, \\ 4\ln 2 \le \lambda t_0 \le 8\ln 2, \end{cases} \tag{67}$$

where "E" denotes the expectation of random variables.

Once these conditions $(H1)$–$(H4)$ are satisfied, the finiteness of fractal dimension can be obtained by further calculation [18, 25]. We know that conditions $(H1)$ and $(H2)$ hold.

Lemma 6. *Let $\omega \in \Omega, \kappa \in \mathbb{R}, t \ge 0$. We have*

$$\begin{aligned} &\left\|\varphi_1(t+\kappa, \kappa, \theta_{-\kappa}\omega, \varphi_{1\kappa}(\theta_{-\kappa}\omega)) - \varphi_2(t+\kappa, \kappa, \theta_{-\kappa}\omega, \varphi_{2\kappa}(\theta_{-\kappa}\omega))\right\| \\ &\le e^{\int_0^t (1-a)\mathrm{d}s}\left\|\varphi_{1\kappa} - \varphi_{2\kappa}\right\|, \varphi_{1\kappa}, \varphi_{2\kappa} \in \widetilde{\mathscr{A}}. \end{aligned} \tag{68}$$

Proof. Let $\varphi_j(r) = \varphi_j(r, \kappa, \omega, \varphi_{j\kappa}(\omega))$, $y(r) = \varphi_1(r) - \varphi_2(r)$, $j = 1, 2$, when $r \ge \kappa$. By equation (9), we have

$$\begin{cases} \dfrac{\mathrm{d}y}{\mathrm{d}t} + \Delta^2 y + 2\Delta y + ay + f(\varphi_1) - f(\varphi_2) = 0, \ r \ge \kappa, \\ y(r, \omega, x) = 0, \ x \in \partial D, \\ y(\kappa, \omega, x) = y_\kappa(\omega, x), \ \kappa \in \mathbb{R}, x \in D, \end{cases} \tag{69}$$

where $f(\zeta) = (\zeta + z)^5$. Multiplying equation (69) with $y(r)$, noticing that

$$\int_D y(f(\varphi_1) - f(\varphi_2))\mathrm{d}x \ge 0, \tag{70}$$

we have

$$\frac{\mathrm{d}}{\mathrm{d}r}\|y(r)\|^2 \le 2(1-a)\|y(r)\|^2, \ \forall r \ge \kappa. \tag{71}$$

By the Gronwall inequality, we obtain the estimate (68).

Let $\{e_j\}_{j\in\mathbb{N}}$ be the eigenvectors of operator $-\Delta$ corresponding to the eigenvalues $\{\lambda_j\}_{j\in\mathbb{N}}$ with $-\Delta e_j = \lambda_j e_j$ for $j \in \mathbb{N}$. Let H_n be the space spanned by $\{e_j\}_{j=1}^n$ and $P_n: H \longrightarrow H_n$ be the orthonormal projector. Let $Q_n: H \longrightarrow H_n^\perp$ be the defined by $P_n v = v_n$ for $v \in H$, with $v = v_n + v_n^\perp$, where $v_n \in H_n, v_n^\perp \in H_n^\perp$. Then,

$$\lambda_{n+1}\|Q_n v\|^2 \le \|v\|_1^2. \tag{72}$$

□

Lemma 7. *For $\varphi_{1\kappa}, \varphi_{2\kappa} \in \widetilde{\mathscr{A}}(\kappa, \omega)$, there are a random variable $C_0(\omega) \ge 0$ and a projector $P_n: H \longrightarrow H_n$ satisfying*

$$\begin{aligned} &\left\|(I - P_n)\Psi(t, \kappa, \theta_{-\kappa}\omega)\varphi_{1\kappa}(\theta_{-\kappa}\omega) - (I - P_n)\right. \\ &\quad \left.\Psi(t, \kappa, \theta_{-\kappa}\omega)\varphi_{2\kappa}(\theta_{-\kappa}\omega)\right\|, \\ &\le \left(e^{(4-a-1/4\lambda_{n+1}^2)t} + \delta_n e^{\int_0^t C_0(\theta_s\omega)\mathrm{d}s}\right)\left\|\varphi_{1\kappa} - \varphi_{2\kappa}\right\|, \end{aligned} \tag{73}$$

and

$$\begin{aligned} &\left\|P_n\Psi(t, \kappa, \theta_{-\kappa}\omega)\varphi_{1\kappa}(\theta_{-\kappa}\omega) - P_n\Psi(t, \kappa, \theta_{-\kappa}\omega)\varphi_{2\kappa}(\theta_{-\kappa}\omega)\right\| \\ &\le e^{\int_0^t C_0(\theta_s\omega)\mathrm{d}s}\left\|\varphi_{1\kappa} - \varphi_{2\kappa}\right\|, \quad \forall \kappa \in \mathbb{R}, \omega \in \Omega, t \ge 0, \end{aligned} \tag{74}$$

where

$$\delta_n = \frac{1}{\sqrt{\lambda_{n+1}}}. \tag{75}$$

Proof. Multiplying equation (69) with $y_n = Q_n y$ in H, it follows that

$$\begin{aligned} &\left|(2\Delta y, y_n)\right| \le \frac{1}{4}\|\Delta y\|^2 + 4\left\|y_n\right\|^2, \\ &\|\nabla v\|^2 \le C\|\Delta v\|\|v\| \le r_1(\omega) + Cr_8(\omega) = M_0^2(\theta_r\omega). \end{aligned} \tag{76}$$

Then, there exists a ϑ between $\varphi_1(r)$ and $\varphi_2(r)$ such that

$$\begin{aligned} (f(\varphi_1) - f(\varphi_2), y_n) &\le 5\left(\int_D (\vartheta + z(\theta_r\omega))^{12}\mathrm{d}x\right)^{1/3} \\ &\quad \cdot \left(\int_D y^2\mathrm{d}x\right)^{1/2}\left(\int_D y_n^6\mathrm{d}x\right)^{1/6} \\ &\le C\left(\|\vartheta\|_{H_0^1}^4 + \left\|z(\theta_r\omega)\right\|_{L^{12}}^4\right)\|y\|\left\|y_n\right\|_{L^6} \\ &\le C\left(M_0^4(\theta_r\omega) + \left\|z(\theta_r\omega)\right\|_{L^{12}}^4\right)^2\|y\|^2 \\ &\quad + \frac{1}{2}\left\|\Delta y_n\right\|^2 \end{aligned} \tag{77}$$

and

$$\frac{\mathrm{d}}{\mathrm{d}t}\left\|y_n\right\|^2 + \left(\frac{1}{2}\lambda_{n+1}^2 + 2a - 8\right)\left\|y_n\right\|^2 \le C\left(M_0^4(\theta_r\omega) + \left\|z(\theta_r\omega)\right\|_{L^{12}}^4\right)^2\|y\|^2. \tag{78}$$

Applying Gronwall lemma to (78) and combining (68), one gets

$$\begin{aligned}\left\|y_n(\kappa+t,\kappa,\theta_{-\kappa}\omega,y_\kappa(\theta_{-\kappa}\omega))\right\|^2 &\le \left\|y_n(\kappa)\right\|^2 e^{\int_\kappa^{\kappa+t}\left(8-2a-1/2\lambda_{n+1}^2\right)\mathrm{d}s}+\int_\kappa^{\kappa+t}C\left(M_0^4(\theta_{r-\kappa}\omega)+\left\|z(\theta_{r-\kappa}\omega)\right\|_{L^{12}}^4\right)^2\left\|\varphi_1(r)-\varphi_2(r)\right\|^2\\ &e^{\int_r^{\kappa+t}\left(8-2a-1/2\lambda_{n+1}^2\right)\mathrm{d}s}\mathrm{d}r\le\left\|y_n(\kappa)\right\|^2 e^{\int_0^t\left(8-2a-1/2\lambda_{n+1}^2\right)\mathrm{d}s}\\ &+\left\|\varphi_{1\kappa}-\varphi_{2\kappa}\right\|^2\int_\kappa^{\kappa+t}C\left(M_0^4(\theta_{r-\kappa}\omega)+\left\|z(\theta_{r-\kappa}\omega)\right\|_{L^{12}}^4\right)^2 e^{\int_\kappa^r 2(1-a)ds}e^{\int_r^{\kappa+t}\left(8-2a-1/2\lambda_{n+1}^2\right)\mathrm{d}s}\mathrm{d}r\le\left\|y_n(\kappa)\right\|^2\\ &e^{\int_0^t\left(8-2a-1/2\lambda_{n+1}^2\right)\mathrm{d}s}+\left\|\varphi_{1\kappa}-\varphi_{2\kappa}\right\|^2 e^{\int_0^t(8-2a)\mathrm{d}s}\int_0^t C\left(M_0^4(\theta_{r-\kappa}\omega)+\left\|z(\theta_{r-\kappa}\omega)\right\|_{L^{12}}^4\right)^2 e^{-1/2\lambda_{n+1}^2(t-r)}\mathrm{d}r.\end{aligned}\tag{79}$$

Noticing $\sqrt{x}<e^x\,(x\ge 0)$, we have

$$\begin{aligned}&\int_0^t C\left(M_0^4(\theta_r\omega)+\|z(\theta_r\omega)\|_{L^{12}}^4\right)^2\cdot e^{-1/2\lambda_{n+1}^2(t-r)}\mathrm{d}r\le\left(\int_0^t C^2\cdot\left(M_0^4(\theta_r\omega)+\|z(\theta_r\omega)\|_{L^{12}}^4\right)^4\mathrm{d}r\right)^{\frac{1}{2}}\\ &\left(\int_0^t e^{-\lambda_{n+1}^2(t-r)}\mathrm{d}r\right)^{1/2}\le\frac{1}{\lambda_{n+1}}e^{\int_0^t C^2\left(M_0^4(\theta_r\omega)+\|z(\theta_r\omega)\|_{L^{12}}^4\right)^4\mathrm{d}r}.\end{aligned}\tag{80}$$

By (79),

$$\left\|y_n(\kappa+t,\kappa,\theta_{-\kappa}\omega,y_\kappa(\theta_{-\kappa}\omega))\right\|^2\le\left(e^{\int_0^t\left(8-2a-1/2\lambda_{n+1}^2\right)\mathrm{d}s}+\frac{1}{\lambda_{n+1}}e^{\int_0^t\left(8-2a+C^2\left(M_0^4(\theta_s\omega)+\|z(\theta_s\omega)\|_{L^{12}}^4\right)^4\right)\mathrm{d}s}\right)\left\|\varphi_{1\kappa}-\varphi_{2\kappa}\right\|^2/\tag{81}$$

Thus,

$$\left\|y_n(\kappa+t,\kappa,\theta_{-\kappa}\omega,y_\kappa(\theta_{-\kappa}\omega))\right\|\le\left(e^{\int_0^t\left(4-a-1/4\lambda_{n+1}^2\right)\mathrm{d}s}+\frac{1}{\sqrt{\lambda_{n+1}}}e^{\int_0^t\left(4-a+C^2/2\left(M_0^4(\theta_s\omega)+\|z(\theta_s\omega)\|_{L^{12}}^4\right)^4\right)\mathrm{d}s}\right)\left\|\varphi_{1\kappa}-\varphi_{2\kappa}\right\|,\tag{82}$$

where $C_0(\omega)=4-a+C^2/2\,(M_0^4(\omega)+\|z(\omega)\|_{L^{12}}^4)^4$. Then, (73) holds. From (68), it follows that (74) holds. □

Lemma 8. *The expectations of $C_0(\omega), C_0^2(\omega)$ are finite, that is,*

$$0\le E\left[C_0(\omega)\right],E\left[C_0^2(\omega)\right]<\infty.\tag{83}$$

Proof. Notice that $\widetilde{z}(\theta_t\omega)$ satisfies $E[|\widetilde{z}(\theta_t\omega)|^r]=\Gamma(1+r/2)/\sqrt{\pi}$, for all $r>0, t\in\mathbb{R}$, and Γ satisfies the equality [25]:

$$\begin{aligned}&\Gamma\left(\frac{1+2k}{2}\right)=\frac{(2k-1)(2k-3)\cdots 3\cdot 1}{2^k}\\ &\sqrt{\pi},\Gamma\left(\frac{1+(2k+1)}{2}\right)=k!,\ \forall k\in\mathbb{N}.\end{aligned}\tag{84}$$

By $M_0^2(\omega)=r_1(\omega)+C\cdot r_8(\omega)$,

$$\begin{aligned}C_0(\omega)&=\overline{C}\left(1+r_1^8(\omega)+r_8^8(\omega)+\left\|z(\theta_t\omega)\right\|_{L^{12}}^{16}\right),\\ C_0^2(\omega)&=C_1+C_2r_1^{16}(\omega)+C_3r_8^{16}(\omega)+C_4\left\|z(\theta_t\omega)\right\|_{L^{12}}^{32},\end{aligned}\tag{85}$$

where $\overline{C},C_1,C_2,C_3,C_4$ are positive constants.

Since $r_1(\omega),r_8(\omega)$ are tempered, we obtain $E[r_1^8(\omega)]<\infty$, $E[r_8^8(\omega)]<\infty$ and $E[r_1^{16}(\omega)]<\infty$, $E[r_8^{16}(\omega)]<\infty$. By the properties of $\widetilde{z}(\theta_t\omega)$, we get

$$\begin{aligned}E\left[\left\|z(\theta_t\omega)\right\|_{L^{12}}^{16}\right]&=\|\phi(x)\|_{L^{12}}^{16}\cdot E\left[\left|\widetilde{z}(\theta_t\omega)\right|^{16}\right]\\ &=\|\phi(x)\|_{L^{12}}^{16}\frac{15\cdot 13\cdot 11\cdots 3\cdot 1}{2^8}<\infty,\\ E\left[\left\|z(\theta_t\omega)\right\|_{L^{12}}^{32}\right]&=\|\phi(x)\|_{L^{12}}^{32}\cdot E\left[\left|\widetilde{z}(\theta_t\omega)\right|^{32}\right]\\ &=\|\phi(x)\|_{L^{12}}^{32}\frac{31\cdot 29\cdot 27\cdots 3\cdot 1}{2^{16}}<\infty.\end{aligned}\tag{86}$$

Then,

$$E[C_0(\omega)] = \overline{C}\left(1 + E\left[r_1^8(\omega)\right] + E\left[r_8^8(\omega)\right] + E\left[\left\|z(\theta_t\omega)\right\|_{L^{12}}^{16}\right]\right) < \infty,$$
$$E\left[C_0^2(\omega)\right] = C_1 + C_2E\left[r_1^{16}(\omega)\right] + C_3E\left[r_8^{16}(\omega)\right] + C_4E\left[\left\|z(\theta_t\omega)\right\|_{L^{12}}^{32}\right] < \infty. \tag{87}$$

Now, based on the conclusions of Lemmas 7 and 8, the main result is presented. □

Theorem 3. *The finiteness of fractal dimension for $\widetilde{\mathscr{A}}(\kappa,\omega)$ holds, that is,*

$$\dim_f \widetilde{\mathscr{A}}(\kappa,\omega) \le \frac{8n_0\ln\left(\sqrt{n_0}\,\lambda_{n_0+1}^{1/2}+1\right)}{\ln 2} < \infty, \kappa \in \mathbb{R}, \omega \in \Omega, \tag{88}$$

where $n_0 = \min\{n\colon \lambda_{n+1} \ge \max\{(128E[C_0(\omega)] + 16 - 4a)^{1/2}, 1024\}\} < \infty$.

Proof. Comparing (66) and (73), we see that

$$\lambda = \frac{1}{4}\lambda_{n+1}^2 + a - 4 \longrightarrow \infty, \delta = \frac{1}{\sqrt{\lambda_{n+1}}} \longrightarrow 0, as\, n \longrightarrow \infty. \tag{89}$$

By (67) and Lemma 8, $\exists n_0 \in \mathbb{N}$, we deduce

$$\frac{1}{4}\lambda_{n+1}^2 + a - 4 \ge 32E[C_0(\omega)], 0 < \frac{1}{\sqrt{\lambda_{n+1}}} < \frac{1}{32}. \tag{90}$$

Take $t = t_0 > 0$ in (73) and (74) such that the following inequality is satisfied:

$$0 < \frac{16\ln 2}{\lambda_{n+1}^2 + 4a - 16} \le t_0 \le \frac{32\ln 2}{\lambda_{n+1}^2 + 4a - 16} < \infty. \tag{91}$$

If $(H1)$–$(H4)$ holds, the following estimate is similar to [25]; here, we omit the details. Then,

$$\dim_f \widetilde{\mathscr{A}}(\kappa,\omega) \le \frac{8n_0\ln\left(\sqrt{n_0}/\delta+1\right)}{\ln 2} = \frac{8n_0\ln\left(\sqrt{n_0}\,\lambda_{n_0+1}^{1/2}+1\right)}{\ln 2} < \infty, \forall \kappa \in \mathbb{R}, \omega \in \Omega. \tag{92}$$

□

Data Availability

The raw data supporting the conclusions of this article will be made available by the authors, without undue reservation, to any qualified researcher.

Conflicts of Interest

The authors declare that there are no conflicts of interest regarding the publication of this paper.

Acknowledgments

The paper was supported by the National Natural Science Foundation of China (nos. 11771444 and 11861013), Guangxi Natural Science Foundation (no. 2017GXNSFAA198221), Promotion of the Basic Capacity of Middle and Young Teachers in Guangxi Universities (no. 2017KY0340), and Fundamental Research Funds for the Central Universities, China University of Geosciences (Wuhan) (no. 2018061).

References

[1] J. Swift and P. C. Hohenberg, "Hydrodynamic fluctuations at the convective instability," *Physical Review A*, vol. 15, no. 1, pp. 319–328, 1977.

[2] D. Blömker, M. Hairer, and G. A. Pavliotis, "Stochastic Swift-Hohenberg equation near a change of stability,"vol. 11, pp. 27–37, in *Proceedings of the International Conference on Differential Equations*, vol. 11, Comenius University, Bratislava, Slovakia, July 2005.

[3] M. F. Hilali, S. Métens, P. Borckmans, and G. Dewel, "Pattern selection in the generalized Swift-Hohenberg model," *Physical Review E*, vol. 51, no. 3, pp. 2046–2052, 1995.

[4] G. Lin, H. Gao, J. Duan, and V. J. Ervin, "Asymptotic dynamical difference between the nonlocal and local Swift-Hohenberg models," *Journal of Mathematical Physics*, vol. 41, no. 4, pp. 2077–2089, 2000.

[5] J. Lega, J. V. Moloney, and A. C. Newell, "Swift-Hohenberg equation for lasers," *Physical Review Letters*, vol. 73, no. 22, pp. 2978–2981, 1994.

[6] L. Song, Y. Zhang, and T. Ma, "Global attractor of a modified Swift-Hohenberg equation in spaces," *Nonlinear Analysis: Theory, Methods & Applications*, vol. 72, no. 1, pp. 183–191, 2010.

[7] L. A. Peletier and V. Rottschäfer, "Pattern selection of solutions of the Swift-Hohenberg equation," *Physica D: Nonlinear Phenomena*, vol. 194, no. 1-2, pp. 95–126, 2004.

[8] L. A. Peletier and V. Rottschäfer, "Large time behaviour of solutions of the Swift-Hohenberg equation," *Comptes Rendus Mathematique*, vol. 336, no. 3, pp. 225–230, 2003.

[9] L. A. Peletier and J. F. Williams, "Some canonical bifurcations in the Swift-Hohenberg equation," *SIAM Journal on Applied Dynamical Systems*, vol. 6, no. 1, pp. 208–235, 2007.

[10] S. H. Park and J. Y. Park, "Pullback attractor for a non-autonomous modified swift-hohenberg equation," *Computers & Mathematics with Applications*, vol. 67, no. 3, pp. 542–548, 2014.

[11] Z. Wang and X. Du, "Pullback attractors for modified Swift-Hohenberg equation on unbounded domains with non-autonomous deterministic and stochastic forcing terms," *Journal of Applied Analysis and Computation*, vol. 7, pp. 207–223, 2017.

[12] L. Xu and Q. Ma, "Existence of the uniform attractors for a non-autonomous modified Swift-Hohenberg equation," *Advances in Differential Equations*, vol. 2015, pp. 1–11, 2015.

[13] J. C. Robinson, *Infinite-Dimensional Dynamical Systems*, Cambridge University Press, Cambridge, UK, 2001.

[14] R. Temam, *Infinite-Dimensional Dynamical Systems in Mechanics and Physics*, Springer-Verlag, New York, NY, USA, 2nd edition, 1997.

[15] C. Foias and E. J. Olson, "Finite fractal dimension and Hölder-Lipschitz parameterization," *Indiana University Journal*, vol. 45, pp. 603–616, 1996.
[16] J. A. Langa and J. C. Robinson, "Fractal dimension of a random invariant set," *Journal de Mathématiques Pures et Appliquées*, vol. 85, no. 2, pp. 269–294, 2006.
[17] G. Wang and Y. Tang, "Fractal dimension of a random invariant set and applications," *Journal of Applied Mathematics*, vol. 2013, Article ID 415764, , 2013.
[18] A. Debussche, "On the finite dimensionality of random attractors," *Stochastic Analysis and Applications*, vol. 15, no. 4, pp. 473–491, 1997.
[19] J. A. Langa, "Finite-dimensional limiting dynamics of random dynamical systems," *Dynamical Systems*, vol. 18, no. 1, pp. 57–68, 2003.
[20] Y. Guo, "Dynamics and invariant manifolds for a nonlocal stochastic Swift-Hohenberg equation," *Journal of Inequalities and Applications*, vol. 2015, no. 366, 2015.
[21] C. Guo, Y. Chen, and Y. Guo, "Random attractors of stochastic local Swift-Hohenberg equation with additive noise," *Journal of Inequalities and Applications*, vol. 2016, no. 228, 2016.
[22] P. W. Bates, K. Lu, and B. Wang, "Random attractors for stochastic reaction-diffusion equations on unbounded domains," *Journal of Differential Equations*, vol. 246, no. 2, pp. 845–869, 2009.
[23] H. Crauel, A. Debussche, and F. Flandoli, "Random attractors," *Journal of Dynamics and Differential Equations*, vol. 9, no. 2, pp. 307–341, 1997.
[24] H. Crauel and F. Flandoli, "Attractors for random dynamical systems," *Probability Theory and Related Fields*, vol. 100, no. 3, pp. 365–393, 1994.
[25] S. Zhou, Y. Tian, and Z. Wang, "Fractal dimension of random attractors for stochastic non-autonomous reaction-diffusion equations," *Applied Mathematics and Computation*, vol. 276, pp. 80–95, 2016.
[26] S. Zhou and Z. Wang, "Finite fractal dimensions of random attractors for stochastic FitzHugh-Nagumo system with multiplicative white noise," *Journal of Mathematical Analysis and Applications*, vol. 441, no. 2, pp. 648–667, 2016.
[27] M. Polat, "Global attractor for a modified Swift-Hohenberg equation," *Computers & Mathematics with Applications*, vol. 57, no. 1, pp. 62–66, 2009.
[28] B. Wang, "Asymptotic behavior of non-autonomous fractional stochastic reaction-diffusion equations," *Nonlinear Analysis*, vol. 158, pp. 60–82, 2017.
[29] L. Arnold, *Random Dynamical Systems*, Springer-Verlag, New York, NY, USA, 1998.
[30] B. Wang, "Random attractors for the stochastic FitzHugh-Nagumo system on unbounded domains," *Nonlinear Analysis*, vol. 71, no. 7-8, pp. 2811–2828, 2009.
[31] M. Marion, "Finite-dimensional attractors associated with partly dissipative reaction-diffusion systems," *SIAM Journal on Mathematical Analysis*, vol. 20, no. 4, pp. 816–844, 1989.

Hindawi
Complexity
Volume 2020, Article ID 9840860, 26 pages
https://doi.org/10.1155/2020/9840860

Research Article

Nonlinear Resonant Responses, Mode Interactions, and Multitime Periodic and Chaotic Oscillations of a Cantilevered Pipe Conveying Pulsating Fluid under External Harmonic Force

Y. F. Zhang,[1] T. Liu ,[2] and W. Zhang [2]

[1]*School of Aerospace Engineering, Shenyang Aerospace University, Shenyang, Liaoning 110136, China*
[2]*Beijing Key Laboratory of Nonlinear Vibrations and Strength of Mechanical Structures, College of Mechanical Engineering, Beijing University of Technology, Beijing 100124, China*

Correspondence should be addressed to T. Liu; liu_tao@yahoo.com and W. Zhang; sandyzhang0@yahoo.com

Received 2 June 2020; Accepted 22 July 2020; Published 28 August 2020

Guest Editor: Yongjian Liu

The nonlinear resonant responses, mode interactions, and multitime periodic and chaotic oscillations of the cantilevered pipe conveying pulsating fluid are studied under the harmonic external force in this research. According to the nonlinear dynamic model of the cantilevered beam derived using Hamilton's principle under the uniformly distributed external harmonic excitation, we combine Galerkin technique and the method of multiple scales together to obtain the average equation of the cantilevered pipe conveying pulsating fluid under 1 : 3 internal resonance and principal parametric resonance. Based on the average equation in the polar form, several amplitude-frequency response curves are obtained corresponding to the certain parameters. It is found that there exist the hardening-spring type behaviors and jumping phenomena in the cantilevered pipe conveying pulsating fluid. The nonlinear oscillations of the cantilevered pipe conveying pulsating fluid can be excited more easily with the increase of the flow velocity, external excitation, and coupling degree of two order modes. Numerical simulations are performed to study the chaos of the cantilevered pipe conveying pulsating fluid with the external harmonic excitation. The simulation results exhibit the existence of the period, multiperiod, and chaotic responses with the variations of the fluid velocity or excitation. It is found that, in the cantilevered pipe conveying pulsating fluid, there are the multitime nonlinear vibrations around the left-mode and the right-mode positions, respectively. We also observe that there exist alternately the periodic and chaotic vibrations of the cantilevered pipe conveying pulsating fluid in the certain range.

1. Introduction

Pipes conveying fluid are widely utilized in many engineering fields, such as aeronautic, astronautic, and mechanical engineering systems. It is extremely important for us to ensure the efficient utilization and safe operation of the pipe conveying fluid system, and its stable and safe operations are closely related to all aspects of the personal life and industrial production. However, the applications of the pipes conveying pulsating fluid are particularly challenging because they undergo the large deformations and significant stresses. The large deformations often lead to the nonlinear vibrations of the pipes conveying pulsating fluid. One of the main reasons for the nonlinear vibrations of the pipes conveying pulsating fluid is the time-varying flow speed and external harmonic excitation. Pulsating flow due to the pump operation can cause a parametric excitation loading in the pipes conveying fluid. The nonlinear oscillations of the pipes conveying pulsating fluid will lead to the structure damages. As we all know, there are three typical types of nonlinear oscillations in the structures and systems, namely, the periodic, quasi-periodic, and chaotic oscillations. In fact, the chaotic oscillations of the pipes conveying pulsating fluid are dangerous because the amplitudes of the chaotic oscillations are larger than those of the periodic oscillations, which have been the object of increasing attention in engineering applications. However, there is less research on the nonlinear oscillations of the cantilevered pipe conveying

pulsating fluid with 1 : 3 internal resonance when the fluid is transported at a critical speed through the pipe. Therefore, it is of great significance for us to study the nonlinear oscillations of the cantilevered pipe conveying pulsating fluid under the case of 1 : 3 internal resonance.

The pipe conveying fluid mainly consists of three important elements: pipeline, fluid, and external environment. It is necessary to establish a mathematical model for obtaining a reasonable description of the pipes conveying fluid. The beam model is usually used for analysis of the vibration when the pipe diameter is much smaller than the length. The nonlinear dynamic study of the pipe conveying fluid system began in 1980s. Researches for the pipes conveying pulsating fluid have become a hot field of engineering and science [1–4]. Holmes and Marsden [5, 6] established the first dynamic model of motion for the pipe conveying fluid through considering the nonlinear factors. They studied the bifurcation phenomena caused by the velocity and the axial force and summed up the bifurcation motion characteristics of the pipe conveying fluid system. According to Hamilton's principle and Euler-Bernoulli beam theory, Huo and Wang [7] derived the differential governing equation of motion for a vertical cantilevered pipe conveying fluid when the pipe exhibits the deploying or retracting motions and discussed the influence of the deploying or retracting speed, mass ratio, and fluid velocity on the dynamic responses and stability. Based on the modified strain gradient theory in conjunction with Euler-Bernoulli beam model, Hosseini and Bahaadini [8] studied the size-dependent stability of the cantilever micropipes conveying fluid and examined the influences of the geometric parameters on the natural frequencies and the flutter critical speeds. Askarian et al. [9] researched the dynamic stability of a vertical clamped-free pipe conveying pulsatile flow by using Euler-Bernoulli beam theory.

In addition, some scholars also provided several different mathematical models to investigate the vibrations of the pipes conveying fluid. According to the nonlinear Novozhilov shell theory for the isotropic materials, Tubaldi et al. [10] established a fully coupled fluid-structure interaction model and studied the nonlinear vibrations of the circular cylindrical shells conveying pulsatile flow with the flexible boundary conditions subjected to the pulsatile pressure. Bai et al. [11] simulated the varying density fluid of the vertical cantilevered pipe conveying fluid by a new mathematical model.

After the establishment of the rational mathematical model, the further researches on the vibrations of the pipes conveying fluid are mainly focused on three significant aspects. Firstly, the vibration characteristics and instability conditions of the pipes conveying fluid are studied, which have different boundary conditions, material properties, and functions. Secondly, the problems of the nonlinear dynamics are studied to understand the nonlinear vibration characteristics of the pipes conveying fluid because the pipes can be regarded as the complex nonlinear dynamical systems. Thirdly, the transfer mechanism of the energy between two modes and the internal resonance are studied to avoid the chaotic vibrations of the pipes conveying fluid.

More and more researches about model and analysis have been published with the continuous development of modern computing and analytical techniques. Bajaj et al. [12] researched the nonlinear vibration responses of the pipes conveying fluid and analyzed the influences of flow rate, mass ratio, and pressure on the nonlinear vibrations and found that Hopf bifurcation occurs under the certain conditions. Sri Namchchivaya and Tien [13, 14] examined the nonlinear vibrations of the supported pipes conveying pulsating fluid and found that the trivial solution of the averaged equation loses its stability through the simple or double zero bifurcations in the vicinity of the subharmonic resonance. Based on a semianalytical approach, Sarkar and Paidoussis [15] obtained the proper orthogonal modes to describe the nonlinear oscillations of a cantilevered pipe conveying fluid and to explore the nonlinear dynamics of the pipe by means of the low-dimensional model. McDonald and Sri Namachchivaya [16] studied the local bifurcation behaviors of parametrically excited simply supported pipes conveying fluid and the stability of solution where the energy transfer may happen from the high-frequency to low-frequency vibration modes.

Yoshizawa et al. [17] established the dynamic model of the pipes conveying fluid under the fixed-hinge boundary conditions and studied the vibration responses under the effect of pulse flow. For the pipe conveying fluid system, Hou and Zeng [18] obtained numerical solutions of the transverse vibration equation through using the finite element method. Setoodeh and Afrahim [19] investigated the nonlinear vibrations of the functionally graded materials micropipes conveying fluid. An explicit expression of the nonlinear fundamental frequency was given by using the homotopy analysis method. Kheiri and Païdoussis [20] derived the equation of motion for a typical flexible pipe conveying fluid by using the generalized Hamilton's principle. Gan et al. [21] simplified the equation of motion to the random variable and researched the vibration characteristics of the pipes conveying fluid clamped at both ends. Zhang et al. [22] established three-dimensional nonlinear equations of motion for the pipes conveying fluid under the general boundary conditions. The natural frequencies of the pipes under different boundary conditions were calculated and the nonlinear dynamic characteristics were analyzed. Wang and Liu [23] studied the transverse vibration and stability of the functionally graded material pipe conveying fluid by utilizing the symplectic method.

Based on the fluid-structure interaction, Liang et al. [24] studied the free vibration of the pipes conveying fluid through using the linear and nonlinear complex mode approach. Liang et al. [25] gave the analysis of the nonlinear free vibration for the spinning viscoelastic pipes conveying fluid. Liang et al. [26] studied the transverse free vibration of the spinning pipes conveying fluid and found that the qualitative stability of the pipes mainly relies on the fluid-structure interaction and mass ratio. Liang et al. [27] established a dynamic model of simply supported spinning pipes conveying fluid with the axial deployment and studied the transverse free vibration involving the time-dependent parameters. Liang et al. [28] researched the coupled

flexural-torsional vibrations of the pipes conveying fluid spinning on an eccentric axis. Recently, Liang et al. [29] investigated the parametric vibrations of the pipes conveying fluid by the nonlinear normal modes and numerical iterative approach.

Several papers researched the nonlinear dynamic characteristics of the pipes conveying fluid. Li and Paidoussis [30] studied the nonlinear oscillations of a standing cantilevered pipe conveying fluid and showed that the chaotic oscillations of the cantilevered pipe exist when the gravity parameter was sufficiently perturbed off the doubly degenerate point. Based on the theoretical and experimental methods, Semler and Paidoussis [31, 32] analyzed the nonlinear oscillations of the cantilevered pipe conveying fluid with a sinusoidally perturbed flow velocity and studied the nonlinear dynamic responses of the cantilevered pipe conveying fluid with a small mass attached at the free end. They found that there exist the jumping phenomena and quasi-periodic and chaotic oscillations. Jin and Zou [33] studied the stability and nonlinear dynamics of the cantilevered pipe conveying fluid with the motion limiting constraints and a linear spring support and analyzed the local behaviors in the neighborhood of a double degenerate point. Ghayesh et al. [34] researched the nonlinear dynamic characteristics of the pipes conveying fluid through considering the lateral and longitudinal displacements and found that the cantilevered pipe will generate the flutter through Hopf bifurcation at the critical velocity. Wang et al. [35] studied the nonlinear oscillations of the pipes conveying fluid under the loose constraint boundary conditions. Askarian et al. [36] investigated the nonlinear oscillations of an extensible cantilevered pipe conveying pulsating flow with a nozzle attached to the end of the pipe.

For high-dimensional nonlinear dynamical systems, due to the existence of the modal interactions, there exist the relationships among several types of internal resonances, which can lead to different nonlinear oscillations [37–40]. Panda and Kar [41] established the nonlinear dynamic model of the pipes conveying fluid under the hinged boundaries at both ends and studied the nonlinear dynamic characteristics of the pipes. Ni et al. [42] simplified the pipes conveying fluid to the constant coefficients gyroscopic system and studied the nonlinear oscillations of the pipes on the nonlinear elastic foundation under $3:1$ internal resonance. Zhang and Chen [43] used the multiple-scale method to determine the steady-state solutions of a pipe conveying fluid under $2:1$ internal resonance. Mao et al. [44] investigated the forced oscillations of the pipe conveying fluid with $3:1$ internal resonance around the bending configuration. Zhang et al. [45] established the nonlinear dynamic model of the cantilevered pipe conveying pulsating fluid under the external harmonic excitation and analyzed the multipulse orbits and chaotic oscillations with $1:2$ internal resonance through utilizing the energy phase method. Recently, Ding et al. [46] investigated the nonlinear vibration isolation of the pipes conveying fluid through using the quasi-zero stiffness characteristics.

To avoid the damage of the pipes conveying pulsating fluid caused by chaotic oscillations, we study the nonlinear oscillations of the pipes conveying pulsating fluid under $1:3$ internal resonance. Based on the nonlinear dynamic model of the cantilevered beam, the nonlinear dynamic equations of motion for the cantilevered pipe conveying pulsating fluid under the uniformly distributed harmonic excitation and average equations are obtained through using the combination of the multiple-scale method and Galerkin technique under $1:3$ internal resonance and principal parametric resonance. We analyze the nonlinear resonant responses and the mode interactions of the cantilevered pipe conveying pulsating fluid. Moreover, numerical simulations are performed to study the multitime periodic and chaotic oscillations of the cantilevered pipe conveying pulsating fluid under the external harmonic excitation. It is found that, in the cantilevered pipe conveying pulsating fluid, there are the multitime nonlinear and chaotic oscillations around the left-mode and the right-mode positions, respectively.

2. Equation of Motion and Perturbing Analysis

We consider a cantilevered pipe conveying pulsating fluid, where A is the internal cross-sectional area, L is the length of a tubular cantilevered beam, m is the mass per unit length of the pipe, EI is the flexural rigidity, M is the conveying fluid mass per unit length with an axial velocity U which may vary with respect to time, and f is an external harmonic force, as shown in Figure 1. It is assumed that initially vertical position along the X-axis is located in the direction of gravity and the nonlinear vibrations occur in the (X, Y) plane for the cantilevered pipe conveying pulsating fluid.

The basic assumptions of the cantilevered pipe and the fluid are made as follows:

(i) The fluid is incompressible.

(ii) The diameter of the pipe is small compared to its length. Therefore, the pipe behaves like an Euler-Bernoulli beam.

(iii) The vibration of the pipe is planar, and the deflections of the pipe are large.

(iv) The rotatory inertia and shear deformation are neglected.

(v) The pipe centerline has inextensible property in the case of a cantilevered pipe.

Based on researches given by Semler et al. [3], Païdoussis [4], and Zhang et al. [45], the nonlinear partial differential governing equation of motion for the cantilevered pipe conveying pulsating fluid is derived through utilizing Hamilton's principle under the external harmonic excitation:

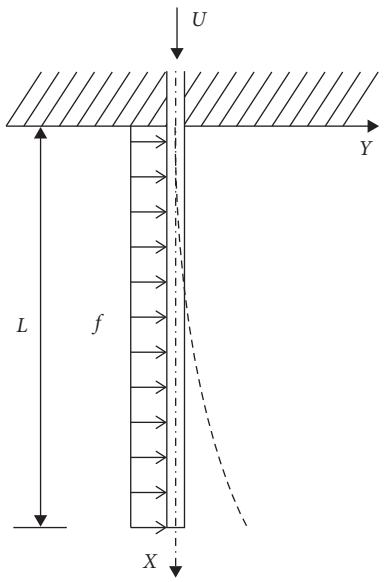

Figure 1: The dynamic model of a cantilevered pipe conveying pulsating fluid is given.

$$
\begin{aligned}
&(m+M)\ddot{y} + 2MU\dot{y}'\left(1+y'^2\right) + (m+M)gy'\left(1+\frac{1}{2}y'^2\right) \\
&+ y''\left[MU^2\left(1+y'^2\right) + (M\dot{U} - (m+M)g)(L-s)\right. \\
&\left.\cdot\left(1+\frac{1}{2}y'^2\right)\right] + EI\left(y'''' + 4y'y''y''' + y''^3 + y''''y'^2\right) \\
&- y''\left[\int_s^L\int_0^s (m+M)\left(\dot{y}'^2 + y'\ddot{y}'\right)\mathrm{d}s\mathrm{d}s\right. \\
&\left.+ \int_s^L\left(\frac{1}{2}M\dot{U}y'^2 + 2MUy'\dot{y}' + MU^2y'y''\right)\mathrm{d}s\right] \\
&+ y'\int_0^s (m+M)\left(\dot{y}'^2 + y'\ddot{y}'\right)\mathrm{d}s + f = 0.
\end{aligned}
\tag{1}
$$

In this paper, we assume that the cantilevered pipe conveying pulsating fluid is made of Kelvin-Voigt type viscoelastic material. Therefore, we have

$$
\begin{aligned}
\sigma &= E\varepsilon + E\dot{\varepsilon}, \\
E &= E\left(1 + a\frac{\partial}{\partial t}\right).
\end{aligned}
\tag{2}
$$

In order to obtain the dimensionless governing equation of motion for the cantilevered pipe conveying pulsating fluid, the transformations of the variables and the parameters are introduced as

$$
\begin{aligned}
\xi &= \frac{s}{L}, \\
\eta &= \frac{y}{L}, \\
\tau &= \left(\frac{EI}{m+M}\right)^{1/2}\frac{t}{L^2}, \\
\alpha &= \left(\frac{EI}{m+M}\right)^{1/2}\frac{a}{L^2}, \\
U^* &= \left(\frac{M}{EI}\right)^{1/2}UL, \\
\gamma &= \frac{m+M}{EI}L^3g, \\
\beta &= \frac{m}{m+M}, \\
f^* &= \frac{L^3}{EI}f.
\end{aligned}
\tag{3}
$$

For simplicity, the notation * is omitted in the following analysis. We obtain the dimensionless partial differential governing equation of motion for the cantilevered pipe conveying pulsating fluid:

$$
\begin{aligned}
&\alpha\dot{\eta}'''' + \eta'''' + \ddot{\eta} + 2U\sqrt{\beta}\dot{\eta}'\left(1+\eta'^2\right) + \eta''\left[U^2\left(1+\eta'^2\right)\right. \\
&\left.+ (\dot{U}\sqrt{\beta} - \gamma)(1-\xi)\left(1+\frac{3}{2}\eta'^2\right)\right] \\
&+ \gamma\eta'\left(1+\frac{1}{2}\eta'^2\right) + \left(1+\alpha\frac{\partial}{\partial\tau}\right)\left(\eta''''\eta'^2 + 4\eta'\eta''\eta''' + \eta''^3\right) \\
&- \eta''\left[\int_\xi^1\int_0^\xi\left(\eta'^2 + \eta'\ddot{\eta}'\right)\mathrm{d}\xi\mathrm{d}\xi + \int_\xi^1\left(\frac{1}{2}\dot{U}\sqrt{\beta}\eta'^2\right.\right. \\
&\left.\left.+ 2U\sqrt{\beta}\eta'\dot{\eta}'^2 + U^2\eta'\eta''\right)\mathrm{d}\xi\right] \\
&+ \eta'\int_0^\xi\left(\dot{\eta}'^2 + \eta'\ddot{\eta}'\right)d\xi + f = 0.
\end{aligned}
\tag{4}
$$

It is assumed that the flow velocity U is represented as a periodic perturbation $U = U_0 + U_1\cos\Omega_1 t$. In the meantime, the external excitation f is described as a periodic perturbation $f = F + f_1\cos\Omega_2 t$.

We find that there exist the gyroscopic terms in equation (4), which means that the damping of the cantilevered pipe conveying pulsating fluid is too large to ignore. The traditional methods dealing with the nonlinear oscillations are first discretized by Galerkin method and then are analyzed by the perturbation method. However, these methods usually cancel the coefficients related to the gyroscopic terms and lose a lot of important information. In order to retain the gyroscopic terms as much as possible, we use a combining method of both the multiple-scale method and Galerkin method to obtain the average equation of the cantilevered pipe conveying pulsating fluid.

For the perturbation analysis, equation (4) is simplified and the following expression is given for the cantilevered pipe conveying pulsating fluid:

$$\begin{aligned} M\ddot{\eta} + G\dot{\eta} + K\eta = {} & \varepsilon F(\eta) - \varepsilon N(\eta) \\ & - 2\varepsilon U_1\sqrt{\beta}\dot{\eta}'\cos\Omega_1 t - 2\varepsilon\eta'' U_0 U_1\cos\Omega_1 t \\ & - \varepsilon\eta''\Omega_1 U_1\sqrt{\beta}(1-\xi)\sin\Omega_1 t, \end{aligned} \tag{5}$$

where ε represents the small-scale transformation and other parameters are given as follows:

$$\begin{aligned} M &= I, \\ G &= 2U_0\sqrt{\beta}\,\frac{\partial}{\partial x} + \alpha\frac{\partial}{\partial x^4}, \\ K &= \left[U_0^2 - \gamma(1-\xi)\right]\frac{\partial}{\partial x^2} + \gamma\frac{\partial}{\partial x} + \frac{\partial}{\partial x^4}, \end{aligned} \tag{6a}$$

$$F(\eta) = -F - f_1\cos\Omega_2 t, \tag{6b}$$

$$\begin{aligned} N(\eta) = {} & 2U_0\sqrt{\beta}\dot{\eta}'\eta'^2 + \eta''\eta'^2\left[U_0^2 - \frac{3}{2}\gamma(1-\xi)\right] + \frac{1}{2}\gamma\eta'^3 \\ & + \left(1 + a\frac{\partial}{\partial\tau}\right)\left(\eta''''\eta'^2 + 4\eta'\eta''\eta''' + \eta''^3\right) \\ & - \eta''\int_\xi^1\int_0^\xi\left(\eta'^2 + \eta'\ddot{\eta}'\right)\mathrm{d}\xi\mathrm{d}\xi \\ & - \eta''\int_\xi^1\left(2U_0\sqrt{\beta}\,\eta'\dot{\eta}'^2 + U_0^2\eta'\eta''\right)\mathrm{d}\xi \\ & + \eta'\int_0^\xi\left(\dot{\eta}'^2 + \eta'\ddot{\eta}'\right)\mathrm{d}\xi. \end{aligned} \tag{6c}$$

The method of multiple scales [47] is applied to the partial differential equation (5) to obtain the uniform solutions in the following form:

$$\eta(t,\varepsilon) = \eta_0(T_0,T_1) + \varepsilon\eta_1(T_0,T_1), \tag{7}$$

where $T_0 = t$ and $T_1 = \varepsilon t$.

Then, the derivatives with respect to t become

$$\begin{aligned} \frac{\mathrm{d}}{\mathrm{d}t} &= \frac{\partial}{\partial T_0}\frac{\partial T_0}{\partial t} + \frac{\partial}{\partial T_1}\frac{\partial T_1}{\partial t} + \cdots = \frac{\partial}{\partial T_0} + \varepsilon\frac{\partial}{\partial T_1} + \cdots \\ &= D_0 + \varepsilon D_1 + \cdots, \end{aligned} \tag{8a}$$

$$\frac{\mathrm{d}^2}{\mathrm{d}t^2} = \left(D_0 + \varepsilon D_1 + \cdots\right)^2 = D_0^2 + 2\varepsilon D_0 D_1 + \varepsilon^2 D_1^2 + \cdots, \tag{8b}$$

where $D_0 = (\partial/\partial T_0)$ and $D_1 = (\partial/\partial T_1)$.

Substituting equations (7), (8a), and (8b) into equations (6a)–(6c) and eliminating the secular terms, we obtain the following:

ε^0:

$$MD_0^2\eta_0 + G(D_0\eta_0) + K\eta_0 = 0. \tag{9}$$

ε^1:

$$\begin{aligned} MD_0^2\eta_1 + GD_0\eta_1 + K\eta_1 = {} & -F - f_1\cos\Omega_2 t \\ & - 2U_0\sqrt{\beta}\,\frac{\partial^2\eta_0}{\partial T_0\partial X}\left(\frac{\partial\eta_0}{\partial X}\right)^2 + \frac{\partial^2\eta_0}{\partial X^2}\left(\frac{\partial\eta_0}{\partial X}\right)^2\left(U_0^2 - \frac{3}{2}\gamma(1-\xi)\right) - \frac{1}{2}\gamma\left(\frac{\partial\eta_0}{\partial X}\right)^3 \\ & - \left(1 + \alpha\frac{\partial}{\partial T_0}\right)\left[\frac{\partial^4\eta_0}{\partial X^4}\left(\frac{\partial\eta_0}{\partial X}\right)^2 + 4\frac{\partial\eta_0}{\partial X}\frac{\partial^2\eta_0}{\partial X^2}\frac{\partial^3\eta_0}{\partial X^3} + \left(\frac{\partial^2\eta_0}{\partial X^2}\right)^3\right] \\ & + \frac{\partial^2\eta_0}{\partial X^2}\left[\int_\xi^1\int_0^\xi\left(\left(\frac{\partial\eta_0}{\partial X}\right)^2 + \frac{\partial\eta_0}{\partial X}\frac{\partial^3\eta_0}{\partial T_0^2\partial X}\right)\mathrm{d}\xi\mathrm{d}\xi + \int_0^\xi\left(2U_0\sqrt{\beta}\,\frac{\partial\eta_0}{\partial X}\frac{\partial^2\eta_0}{\partial T_0\partial X} + U_0^2\frac{\partial\eta_0}{\partial X}\frac{\partial^2\eta_0}{\partial X^2}\right)\mathrm{d}\xi\right] \\ & - \frac{\partial\eta_0}{\partial X}\int_0^\xi\left(\frac{\partial^2\eta_0}{\partial T_0\partial X} + \frac{\partial\eta_0}{\partial X}\frac{\partial^3\eta_0}{\partial T_0^2\partial X}\right)\mathrm{d}\xi - 2U_1\sqrt{\beta}\,\frac{\partial^2\eta_0}{\partial T_0\partial X}\cos\Omega_1 t \\ & - \frac{\partial^2\eta_0}{\partial X^2}\left[2U_0U_1\cos\Omega_1 t - \Omega_1 U_1\sqrt{\beta}\,(1-\xi)\sin\Omega_1 t\right] - 2MD_0D_1\eta_0 - GD_1\eta_0. \end{aligned} \tag{10}$$

The boundary conditions are given as

$$y(0) = y'(0) = 0,$$
$$y''(L) = y'''(L) = 0. \tag{11}$$

In order to simplify the cantilevered pipe conveying pulsating fluid to the finite dimension by using Galerkin discretization, the modal function is selected as a beam function:

$$\varphi_j(\xi) = \cos h\left(\beta_j x\right) - \cos\left(\beta_j x\right) - \lambda_j\left[\sin h\left(\beta_j x\right) - \sin\left(\beta_j x\right)\right]. \tag{12}$$

The general solution of equation (9) is expressed as follows:

$$\eta\left(T_0, T_1, \xi\right) = \sum_{j=0}^{N} \varphi_j(\xi) A_j\left(T_1\right) e^{i\omega_j T_0} + cc, \tag{13}$$

where we take the nonlinear oscillations of the cantilevered pipe conveying pulsating fluid into account in the first two oscillation modes:

$$\eta\left(T_0, T_1, x\right) = \varphi_1(x) A_1\left(T_1\right) e^{i\omega_1 T_0} + \varphi_3(x) A_2\left(T_1\right) e^{i\omega_3 T_0} + cc. \tag{14}$$

Substituting equation (14) into equation (5) and after a series of calculations and simplification, the approximate frequency relationships are obtained as follows:

$$\omega_1^2 = \left(\alpha_{12} - \frac{\alpha_{11}\widetilde{L}}{2}\right)\gamma + \alpha_{11} U\left(U + \frac{\widetilde{L}\sqrt{\beta}}{2}\right), \tag{15a}$$

$$\omega_3^2 = \left(\alpha_{22} - \frac{\alpha_{21}\widetilde{L}}{2}\right)\gamma + \alpha_{21} U\left(U + \frac{\widetilde{L}\sqrt{\beta}}{2}\right), \tag{15b}$$

where $\widetilde{L}$, β, and U, respectively, represent the length, mass ratio, and flow velocity, and α_{11}, α_{12}, α_{21}, α_{22}, and γ are the system parameters and dimensionless parameters.

According to the geometries and the material properties of the cantilevered pipe conveying pulsating fluid, the parameters are chosen as $\beta = 0.9$, $U = 3$, $\alpha_{11} = -1.9$, $\alpha_{12} = 11$, $\alpha_{21} = -4.8$, $\alpha_{22} = 30$, and $\gamma = 2$. The length $\widetilde{L}$ is selected as the variable. The first-order and third-order natural frequencies are solved, as shown in the Campbell diagram in Figure 2. We find that the natural frequencies of the first-order and third-order oscillation modes for the cantilevered pipe conveying fluid decrease as the length increases. It is observed that 1 : 3 internal resonance happens in the cantilevered pipe conveying pulsating fluid.

We only consider the case of 1 : 3 internal resonance, principle parameter resonance, and 1/2 subharmonic resonance for equation (5). In this resonant case, there exist the following relations:

$$\omega_1 = \frac{1}{2}\Omega_1 + \varepsilon\sigma_1,$$
$$\omega_3 = \frac{3}{2}\Omega_1 + \varepsilon\sigma_2, \tag{16}$$
$$\Omega_1 = \frac{1}{2}\Omega_2,$$

where σ_1 and σ_2 are two detuning parameters.

Substituting equations (12), (14), and (16) into equation (10) yields

$$\begin{aligned} MD_0^2\eta_1 + GD_0\eta_1 + K\eta_1 = {} & \Gamma_1 e^{iT_0\left((1/2)\Omega_1 + \varepsilon\sigma_1\right)} + \Gamma_2 e^{iT_0\left((3/2)\Omega_1 + \varepsilon\sigma_2\right)} - q_1 e^{(1/2)iT_0\Omega_1} \\ & + \Gamma_3 e^{iT_0\left((1/2)\Omega_1 - \varepsilon\sigma_1\right)} + \Gamma_4 e^{iT_0\left((1/2)\Omega_1 + \varepsilon\sigma_2\right)} + \Gamma_5 e^{iT_0\left((3/2)\Omega_1 + \varepsilon\sigma_1\right)} + cc + \mathrm{NST}, \end{aligned} \tag{17}$$

where

$$\begin{aligned} \Gamma_1 = {} & i\Omega A_{11}^2 A_{12}\left(U_0\sqrt{\beta}\, m_1 + \frac{3}{2}\alpha m_2\right) + i\Omega A_{11} A_{21} A_{22}\left(2U_0\sqrt{\beta}\, m_3 + \frac{3}{2}\alpha m_4\right) \\ & + A_{11}^2 A_{12}\left(3U_0^2 m_5 - \gamma m_6 - 3m_7 + \frac{3}{4}\Omega^2 m_8\right) \\ & + A_{11} A_{21} A_{22}\left(U_0^2 m_9 - \gamma m_{10} + m_4 + \Omega^2 m_{11}\right) - i\Omega_1 \dot{A}_{11} M\varphi_1 - \dot{A}_{11} G\varphi_1, \end{aligned} \tag{18a}$$

$$\begin{aligned} \Gamma_2 = {} & i\Omega A_{21}^2 A_{22}\left(3U_0\sqrt{\beta}\, n_1 + \alpha n_2\right) + i\Omega A_{11} A_{12} A_{21}\left(6U_0\sqrt{\beta}\, n_3 + \alpha n_4\right) \\ & + A_{21}^2 A_{22}\left(3U_0^2 n_5 - \gamma n_6 + n_7 + \Omega^2 n_8\right) \\ & + A_{11} A_{12} A_{21}\left(U_0^2 n_9 - \gamma n_{10} + n_4 + \Omega^2 n_{11}\right) - 3i\Omega_1 \dot{A}_{21} M\varphi_2 - \dot{A}_{21} G\varphi_2, \end{aligned} \tag{18b}$$

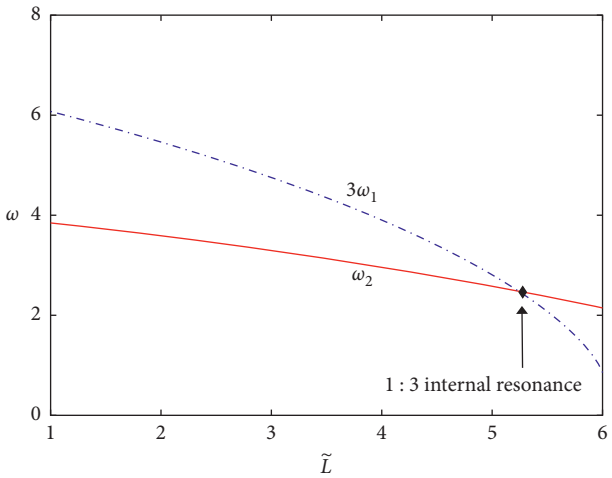

FIGURE 2: The Campbell diagram of the cantilevered pipe conveying pulsating fluid is obtained in the case of 1 : 3 internal resonance.

$$\Gamma_3 = A_{11}A_{12}^2\left(-\frac{1}{2}\Omega_1^2 m_{12} - i\Omega_1 U_0\sqrt{\beta}\, m_{13} + U_0^2 m_{14}\right) + i\Omega A_{11}A_{12}A_{21}\left(6U_0\sqrt{\beta}\, n_3 + \alpha n_4\right) + A_{11}A_{21}A_{22}\left(-\Omega_1^2 m_{15} - i\Omega_1 U_0\sqrt{\beta}\, m_{16} + U_0^2 m_{17}\right) + \frac{1}{2}iU_1\sqrt{\beta}A_{12}\Omega_1 m_{18} - U_0U_1A_{12}m_{19}, \tag{18c}$$

$$\Gamma_4 = \frac{1}{2}iA_{21}\Omega_1 U_1\sqrt{\beta}m_{20} - A_{21}U_0U_1 m_{21}, \tag{18d}$$

$$\Gamma_5 = \frac{1}{2}iA_{11}\Omega_1 U_1\sqrt{\beta}n_{12} - A_{11}U_0U_1 n_{13}. \tag{18e}$$

The solution exists when the nonhomogeneous equation corresponding to equation (17) satisfies that the right side of the equation is orthogonal to the solution of its homogeneous accompanying equation. Thus, we have

$$\int_0^1\left(\Gamma_1 - f_1 e^{-i\sigma_1 T_1} + \Gamma_3 e^{-2i\sigma_1 T_1} + \Gamma_4 e^{-iT_1(\sigma_1-\sigma_2)}\right)\overline{\varphi}_1 \mathrm{d}x = 0, \tag{19a}$$

$$\int_0^1\left(\Gamma_2 + \Gamma_5 e^{-iT_1(\sigma_2-\sigma_1)}\right)\overline{\varphi}_2 \mathrm{d}x = 0. \tag{19b}$$

Let A_1 and A_2 be of the following forms:

$$A_1(T_1) = \frac{1}{2}\left(a_1 e^{i\varphi_1}\right)\cdot e^{-i(\sigma_1 T_1 - 2m\pi)},$$
$$A_2(T_1) = \frac{1}{2}\left(a_2 e^{i\varphi_2}\right)\cdot e^{-i(\sigma_2 T_1 - 2n\pi)}. \tag{20}$$

Substituting equation (20) into equations (19a) and (19b) and separating the real and imaginary parts, the averaged equations in the polar form are obtained as follows:

$$\dot{a}_1 = \frac{1}{8}(\beta_{14} + \beta_{111} - \beta_{10}\cos 2\varphi_1 + \beta_{16}\sin 2\varphi_1)a_1a_2^2 + \frac{1}{2}(\beta_{17}\sin 2\varphi_1 - \beta_{18}\cos 2\varphi_1)a_1 + \frac{1}{8}(\beta_{13} + \beta_{110})a_1^3 + \frac{1}{2}[\beta_{19}\sin(\varphi_1 - \varphi_2) - \beta_{20}\cos(\varphi_1 - \varphi_2)]a_2 - F\sin\varphi_1 - \mu a_1, \tag{21a}$$

$$a_1\dot{\varphi}_1 = \frac{1}{8}(\beta_{12} + \beta_{10}\sin 2\varphi_1 + \beta_{16}\cos 2\varphi_1)a_1a_2^2 + \frac{1}{2}(\beta_{17}\cos 2\varphi_1 + \beta_{18}\sin 2\varphi_1)a_1 + \frac{1}{8}(\beta_{11} - \beta_{15})a_1^3 + \frac{1}{2}[\beta_{19}\cos(\varphi_1 - \varphi_2) + \beta_{20}\sin(\varphi_1 - \varphi_2)]a_2 - F\cos\varphi_1 - \sigma_1 a_1, \tag{21b}$$

$$\dot{a}_2 = \frac{1}{8}\beta_{23}a_2^3 + \frac{1}{8}\beta_{24}a_2a_1^2 + \frac{1}{2}[\beta_{25}\sin(\varphi_1 - \varphi_2) + \beta_{26}\cos(\varphi_1 - \varphi_2)]a_1 - \mu a_2, \tag{21c}$$

$$a_2\dot{\varphi}_2 = \frac{1}{8}\beta_{21}a_2^3 + \frac{1}{8}\beta_{22}a_2a_1^2 + \frac{1}{2}[\beta_{25}\cos(\varphi_1 - \varphi_2) + \beta_{26}\sin(\varphi_1 - \varphi_2)]a_1 - \sigma_2 a_2. \tag{21d}$$

In order to obtain the averaged equations in the Cartesian form, we express A_1 and A_2 in the following forms:

$$\begin{aligned} A_1(T_1) &= [x_1(T_1) - ix_2(T_1)]e^{-i(o_1T_1 - 2m\pi)}, \\ A_2(T_1) &= [x_3(T_1) - ix_4(T_1)]e^{-i(o_2T_1 - 2n\pi)}. \end{aligned} \tag{22}$$

Based on the same way as the aforementioned analysis, the averaged equations in the Cartesian form are obtained for the cantilevered pipe conveying pulsating fluid:

$$\begin{aligned} \dot{x}_1 = {} & (\beta_{17} - \mu)x_1 - (\beta_{18} + \sigma_1)x_1 + \beta_{19}x_3 + \beta_{20}x_4 + (\beta_{11} - \beta_{15})x_1\left(x_1^2 + x_2^2\right) + (\beta_{12} - \beta_{16})x_1\left(x_3^2 + x_4^2\right) \\ & - (\beta_{13} + \beta_{110} - p_{15})x_2\left(x_1^2 + x_2^2\right) - (\beta_{14} + \beta_{111} - 2p_{17})x_2\left(x_3^2 + x_4^2\right), \end{aligned} \tag{23a}$$

$$\begin{aligned} \dot{x}_2 = {} & (\beta_{17} - \mu)x_2 - (\beta_{18} - \sigma_1)x_1 - \beta_{19}x_4 + \beta_{20}x_3 + (\beta_{11} + \beta_{15})x_2\left(x_1^2 + x_2^2\right) + (\beta_{12} + \beta_{16})x_2\left(x_3^2 + x_4^2\right) \\ & - (\beta_{13} - \beta_{110} - p_{15})x_1\left(x_1^2 + x_2^2\right) - (\beta_{14} - \beta_{111} - 2p_{17})x_1\left(x_3^2 + x_4^2\right) - Fp_0, \end{aligned} \tag{23b}$$

$$\begin{aligned} \dot{x}_3 = {} & -\mu x_3 - \sigma_2 x_4 + \beta_{25}x_1 + \beta_{26}x_2 + \beta_{21}x_3\left(x_3^2 + x_4^2\right) + \beta_{22}x_3\left(x_1^2 + x_2^2\right) \\ & - \beta_{23}x_4\left(x_3^2 + x_4^2\right) - \beta_{24}x_4\left(x_1^2 + x_2^2\right), \end{aligned} \tag{23c}$$

$$\begin{aligned} \dot{x}_4 = {} & -\mu x_4 + \sigma_2 x_3 - \beta_{25}x_2 + \beta_{26}x_1 + \beta_{21}x_4\left(x_3^2 + x_4^2\right) + \beta_{22}x_4\left(x_1^2 + x_2^2\right) \\ & + \beta_{23}x_3\left(x_3^2 + x_4^2\right) + \beta_{24}x_3\left(x_1^2 + x_2^2\right), \end{aligned} \tag{23d}$$

where the coefficients are given, respectively, as

$$\begin{aligned} \beta_{10} &= \Omega_1 U_0 \sqrt{\beta} p_{16}, \\ \beta_{11} &= U_0 \sqrt{\beta} p_1 + \frac{3}{2}\alpha p_2, \\ \beta_{12} &= 2U_0 \sqrt{\beta} p_3 + \frac{3}{2}\alpha p_4, \\ \beta_{13} &= 3U_0^2 p_5 - \gamma p_6 + 3p_7 + \frac{3}{4}\Omega^2 p_8, \\ \beta_{14} &= U_0^2 p_9 - \gamma p_{10} + p_4 + \Omega^2 p_{11}, \\ \beta_{15} &= \Omega_1 U_0 \sqrt{\beta} p_{13}, \\ \beta_{16} &= U_0^2 p_{17} - \Omega^2 p_{15}, \\ \beta_{17} &= \frac{1}{2}U_1 \Omega_1 \sqrt{\beta} p_{18}, \\ \beta_{18} &= U_0 U_1 p_{19}, \\ \beta_{19} &= \frac{1}{2}\Omega_1 U_1 \sqrt{\beta} p_{20}, \\ \beta_{110} &= U_0^2 p_4 - \frac{1}{2}\Omega^2 p_{12}, \\ \beta_{111} &= U_0^2 p_{17} - \Omega^2 p_{15}, \\ \beta_{20} &= U_0 U_1 p_{21}, \\ \beta_{21} &= \Omega\left(3U_0 \sqrt{\beta} q_1 + \alpha q_2\right), \\ \beta_{22} &= \Omega\left(6U_0 \sqrt{\beta} q_3 + \alpha q_4\right), \\ \beta_{23} &= 3U_0^2 q_5 - \gamma q_6 + q_7 + \Omega^2 q_8, \\ \beta_{24} &= U_0^2 q_9 - \gamma q_{10} + q_4 + \Omega^2 q_{11}, \\ \beta_{25} &= \frac{1}{2}\Omega_1 U_1 \sqrt{\beta} q_{12}, \\ \beta_{26} &= U_0 U_1 q_{13}. \end{aligned} \tag{24}$$

Equations (21a)–(21d) and (23a)–(23d) describe the nonlinear oscillations of the cantilevered pipe conveying pulsating fluid under the external harmonic excitation. It is known that the constant solutions of the averaged equation correspond to the periodic solutions of the original system, the periodic solutions of the averaged equation correspond to the quasi-periodic solutions of the original system, and the chaotic solutions of the averaged equation correspond to the chaotic solutions of the original system.

3. Analysis of Resonant Responses

The resonant response curves are the important basis for judging and studying the nonlinear oscillations. They include many complex nonlinear dynamic phenomena. The practical problems can be solved better by analyzing these phenomena. Based on the averaged equations (21a)–(21d) in the polar form, we analyze the amplitude-frequency response curves to reveal the nonlinear oscillations of the cantilevered pipe conveying pulsating fluid. Since φ_1 and φ_2 are all constant, we make $\varphi_1 = \varphi_2 = 0.25\pi$. Therefore, we

obtain the amplitude-frequency response functions of the cantilevered pipe conveying pulsating fluid:

$$\left[\frac{1}{8}(\beta_{13}+\beta_{110})a_1^3+\frac{1}{8}(\beta_{14}+\beta_{111})a_1a_2^2-\frac{1}{2}\beta_{20}a_2-\frac{\sqrt{2}}{2}F-\mu a_1\right]^2 + \left[\frac{1}{8}(\beta_{11}+\beta_{15})a_1^3+\frac{1}{8}\beta_{12}a_1a_2^2+\frac{1}{2}(\beta_{19}-\beta_{20})a_2-\frac{\sqrt{2}}{2}F-\sigma_1 a_1\right]^2 = \left(\frac{1}{8}\beta_{110}a_1a_2^2-\frac{1}{2}\beta_{18}a_1\right)^2+\left(\frac{1}{8}\beta_{16}a_1a_2^2+\frac{1}{2}\beta_{17}a_1\right)^2, \tag{25a}$$

$$\left(\frac{1}{8}\beta_{24}a_2a_1^2+\frac{1}{8}\beta_{23}a_2^3\right)^2+\left(\frac{1}{8}\beta_{22}a_2a_1^2+\frac{1}{8}\beta_{21}a_2^3\right)^2 = \left(\frac{1}{2}\beta_{26}a_1+\mu a_2\right)^2+\left(\frac{1}{2}\beta_{25}a_1+\sigma_2 a_2\right)^2. \tag{25b}$$

Two cases of the amplitude-frequency response curves [48, 49] are considered for the cantilevered pipe conveying pulsating fluid:

(1) There is no coupling effect between the first-order and third-order oscillation modes. We only consider the decoupled case and set $a_2 = 0$ in equation (25a) and $a_1 = 0$ in equation (25b).

(2) We let an amplitude change when another is fixed because the amplitude is much smaller than that in the case of weak coupling; namely, set $a_2 = 1$ in equation (25a) and $a_1 = 1$ in equation (25b).

We obtain the amplitude-frequency response curves in the decoupled and coupled cases based on equations (25a) and (25b). Based on the geometries and the material properties of the cantilevered pipe conveying pulsating fluid, the basic parameters are chosen as

$$\begin{aligned}
U_0 &= 1.5,\\ F &= 2.5,\\ \beta &= 0.9,\\ \gamma &= 2,\\ \mu &= 4,\\ U_1 &= 3.5,\\ \Omega &= 1.2,\\ \Omega_1 &= 10,\\ p_1 &= 2\times 10^3,\\ p_2 &= 4,\\ p_3 &= 2,\\ p_4 &= 8,\\ p_5 &= 10,\\ p_6 &= 2,\\ p_7 &= -20,\\ p_8 &= 1,\\ p_9 &= 100,\\ p_{10} &= -1,\\ p_{11} &= -3,\\ p_{12} &= -14,\\ p_{13} &= -6,\\ p_{14} &= -10,\\ p_{15} &= 14,\\ p_{16} &= 10,\\ p_{17} &= 4,\\ p_{18} &= -1,\\ p_{19} &= 20,\\ p_{20} &= 30,\\ p_{21} &= 12,\\ p_{22} &= 1,\\ p_{23} &= 1,\\ p_{24} &= 6,\\ q_1 &= 15,\\ q_2 &= 16,\\ q_3 &= -4.7,\\ q_4 &= 18,\\ q_5 &= 18,\\ q_6 &= 7,\\ q_7 &= 4,\\ q_8 &= 14,\\ q_9 &= 11,\\ q_{10} &= 11,\\ q_{11} &= 260,\\ q_{12} &= 3,\\ q_{13} &= 0.25.
\end{aligned} \tag{26}$$

For both the decoupled and coupled cases, when the velocity parametric excitation is $U_0 = 1.5$ and external excitation is $F = 2.5$, it is found that the cantilevered pipe conveying pulsating fluid has the hardening spring characteristics because the amplitude-frequency response curves bend to right, as shown in Figures 3(a) and 3(b). The blue line represents the coupled case and the red line gives the decoupled case. The bending of the amplitude-frequency response curves also leads to the multiple amplitudes and bifurcations. The multiple amplitudes mean that there are several possible responses in the cantilevered pipe conveying pulsating fluid. The actual response among several possible responses depends on the initial conditions. Hence, the typical jumping phenomena of the nonlinear oscillations can be observed for the cantilevered pipe conveying pulsating fluid. Comparing the amplitude-frequency response curves between two cases given in Figure 3(a), we find that the amplitude of the coupled case is larger and the resonant response interval is wider than the decoupled case. The coupling effect of two oscillation modes will not change the

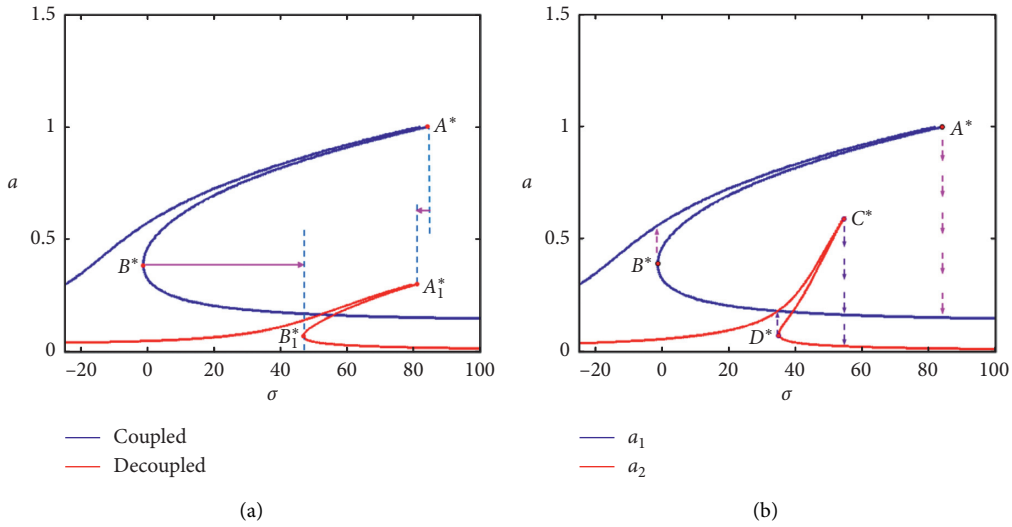

Figure 3: The amplitude-frequency response curves of the cantilevered pipe conveying pulsating fluid are obtained when flow velocity is $U_0 = 1.5$ and external force is $F = 2.5$. (a) Coupling influence on amplitude-frequency response curves; (b) amplitude-frequency response curves of the first-order and third-order modes.

system's stiffness but will cause a stronger nonlinear resonant response. Furthermore, it can be also observed that the amplitude of the first-order mode is larger than that of the third-order mode in the coupled case, as shown in Figure 3(b). In the coupled case, there exists the mode interaction between two oscillation modes. Therefore, the amplitude-frequency response curves of the coupled case are considered for the cantilevered pipe conveying pulsating fluid in the following analysis.

In the weak coupling cases, the influences of the flow velocity U_0, external excitation F, and mass parameter β on the amplitude-frequency response curves are analyzed in Figures 4(a)–4(c), where the mass parameter β denotes the ratio of the pipe mass and total mass. Figure 4(a) illustrates the amplitude-frequency response curves of the cantilevered pipe conveying pulsating fluid when the flow velocities are $U_0 = 1.5$ and $U_0 = 2.0$, respectively. With the increases of the flow velocity U_0, it is obviously found that the amplitude is larger and the resonant response interval is wider for the cantilevered pipe conveying pulsating fluid, as shown in Figure 4(a). The increase of flow velocity will not change the system's stiffness but will cause a stronger nonlinear resonant response. These characteristics indicate that the cantilevered pipe conveying pulsating fluid obtains the more external energy. Figure 4(b) gives the amplitude-frequency response curves of the cantilevered pipe conveying pulsating fluid when the external excitations are $F = 2.5$ and $F = 7.0$, respectively. In Figure 4(b), we find that the increase of the external excitation F mainly results in the larger amplitude, which has little effect on the resonant response interval. Figure 4(c) shows the amplitude-frequency response curves of the cantilevered pipe conveying pulsating fluid when the mass parameters are $\beta = 0.9$ and $\beta = 0.7$, respectively. In Figure 4(c), as the mass parameter β decreases, which means that the pipe mass is lighter, we find that the nonlinear stiffness of the cantilevered pipe conveying pulsating fluid does not change. However, it is observed that the resonance of the cantilevered pipe conveying pulsating fluid is more easily excited and the amplitudes of the nonlinear oscillations are greater when mass parameters are smaller.

The effects of the flow velocity and external excitation on the amplitude-frequency response curves are investigated for the cantilevered pipe conveying pulsating fluid in Figures 5(a) and 5(b) under the coupling cases. We set $\sigma = 10$ and other parameters are the same as the parameters given in Figures 3 and 4. The amplitude-frequency response curves of the flow velocity are given in Figure 5(a). It can be shown that the amplitudes of the cantilevered pipe conveying pulsating fluid increase with the increase of the flow velocity. Thus, the energy of the fluid motion is transferred into the energy of the cantilevered pipe. The fluid-structure interaction occurs in the cantilevered pipe conveying pulsating fluid. There are two jumping phenomena on the amplitude-frequency response curves with the increase of the flow velocity: one is jumping up and one is jumping down. The oscillations of the cantilevered pipe conveying pulsating fluid are stable at a lower amplitude. The increase and decrease of the amplitudes alternatively change with the increase of the flow velocity. It is indicated that the flow velocity will affect the nonlinear oscillation behaviors of the cantilevered pipe conveying pulsating fluid in a certain range. The amplitude-frequency response curves of the external excitation are given in Figure 5(b). The amplitudes of the cantilevered pipe conveying pulsating fluid become larger with the gradual increase of the external excitation. The sudden increase in the amplitude of the cantilevered pipe conveying pulsating fluid appears when a jumping phenomenon occurs. It is illustrated that the cantilevered pipe conveying pulsating fluid will obtain more energy to create the larger amplitude with the increase of the external excitation.

We explore the influences of different parameters on the amplitude-frequency and force-amplitude response curves in the cantilevered pipe conveying pulsating fluid, respectively. In

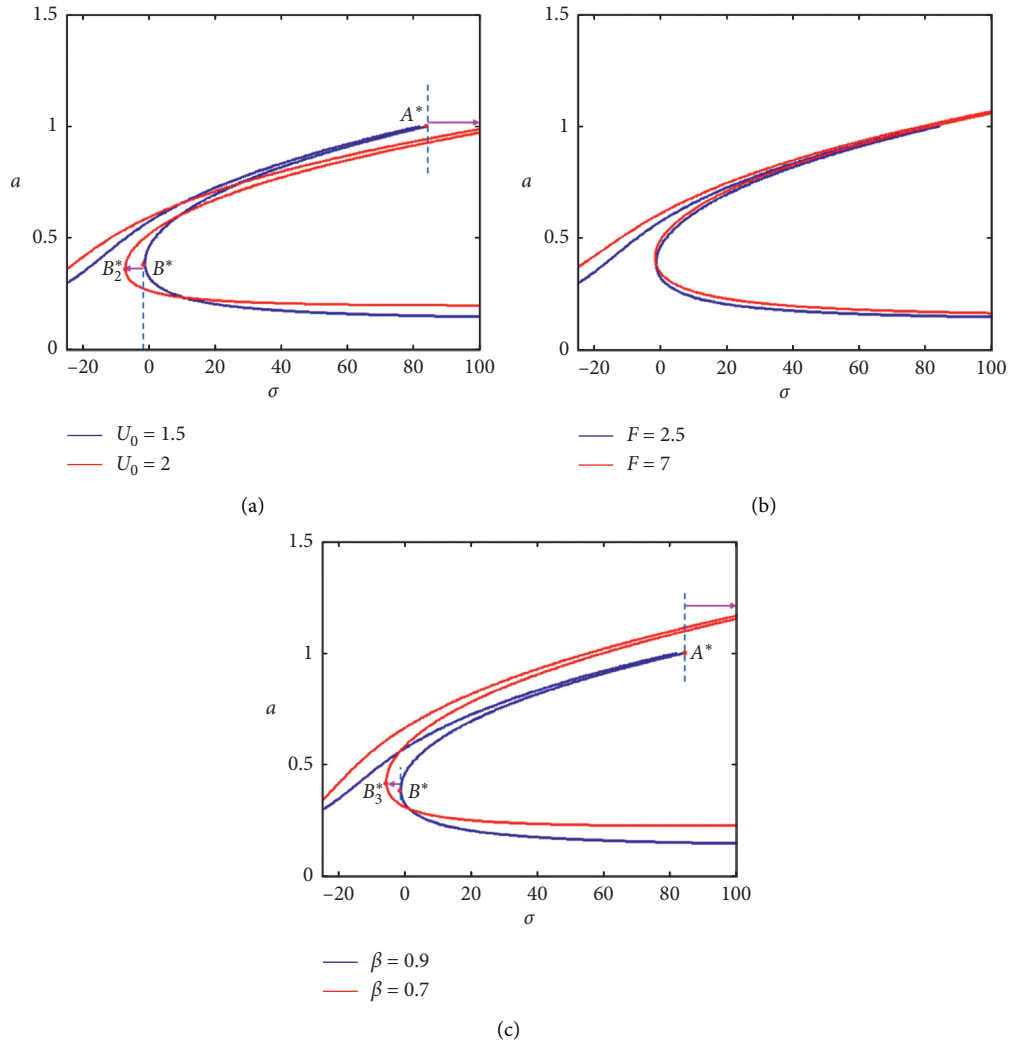

FIGURE 4: The amplitude-frequency response curves of the cantilevered pipe conveying pulsating fluid are obtained in the coupling case with different parameters. (a) Amplitude-frequency response curves when flow velocities $U_0 = 1.5$ and $U_0 = 2.0$, (b) amplitude-frequency response curves when external forces $F = 2.5$ and $F = 7.0$, and (c) amplitude-frequency response curves when mass parameters $\beta = 0.9$ and $\beta = 0.7$.

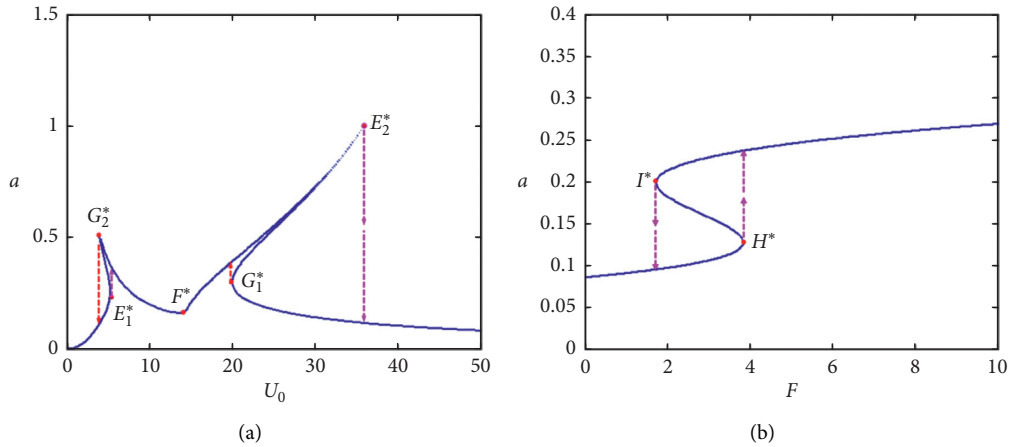

FIGURE 5: The amplitude-frequency response curves of the cantilevered pipe conveying pulsating fluid are obtained. (a) Amplitude-response curves on flow velocity; (b) amplitude-response curves on external excitation.

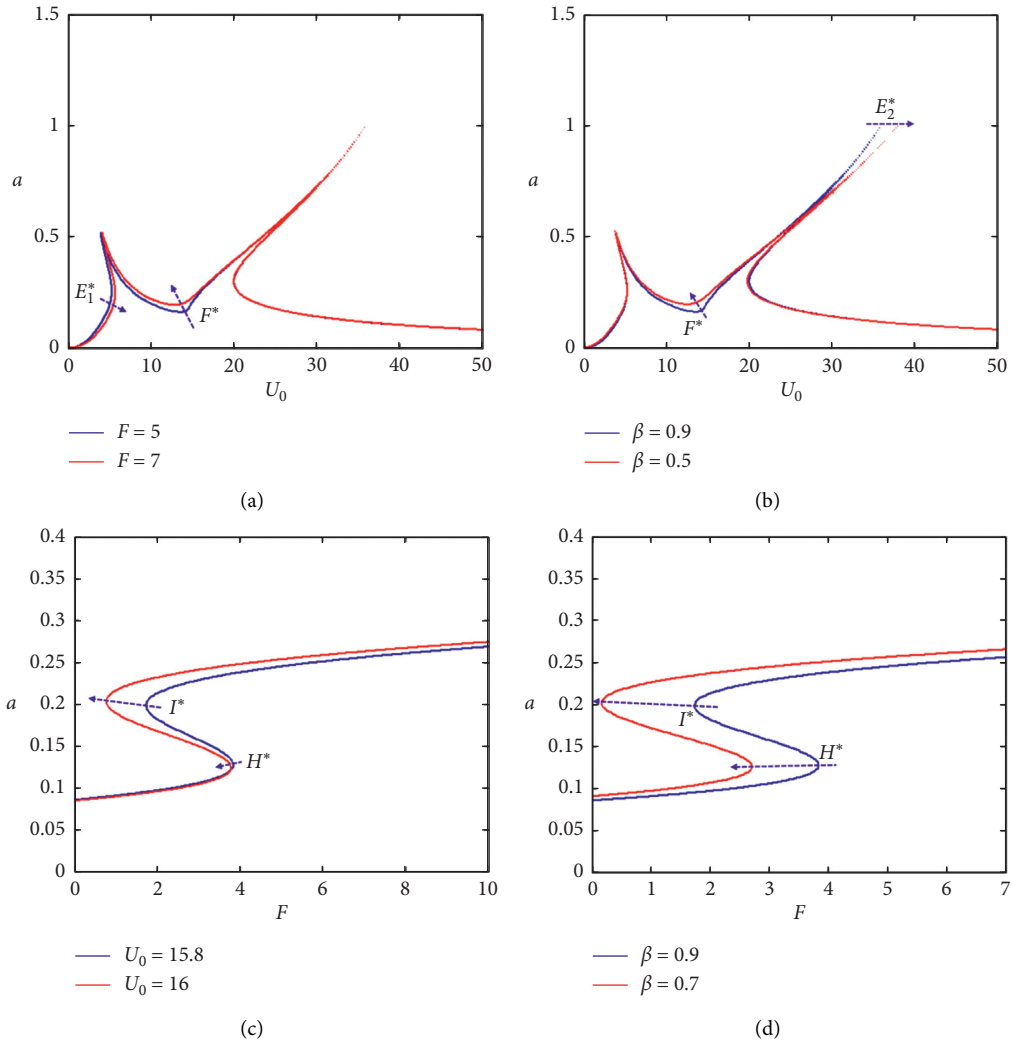

FIGURE 6: The influences of different parameters on the amplitude-frequency response curves and force-amplitude response curves are given for the cantilevered pipe conveying pulsating fluid. (a) Amplitude-frequency response curves on flow velocity when $F = 5$ and $F = 7$, (b) amplitude-frequency response curves on flow velocity when mass parameters $\beta = 0.9$ and $\beta = 0.5$, (c) force-amplitude response curves on external force when flow velocities $U_0 = 15.8$ and $U_0 = 16$, and (d) force-amplitude response curves on external force when mass parameters $\beta = 0.9$ and $\beta = 0.7$.

Figures 6(a)–6(d), the changes of the amplitude-frequency and force-frequency response curves in each figure are caused by changing one parameter while other parameters remain unchanged. The influences of different parameters, such as the parametric excitation and mass parameter, on the amplitude-frequency response curves are studied, as shown in Figures 6(a) and 6(b). Figure 6(a) gives the relations between the amplitudes and flow velocity U_0 for the cantilevered pipe conveying pulsating fluid when the parametric excitations induced to the flow velocity are $F = 5.0$ and $F = 7.0$, respectively. Figure 6(b) indicates the relations on the amplitudes versus the flow velocity U_0 in the cantilevered pipe conveying pulsating fluid when the mass parameters are $\beta = 0.9$ and $\beta = 0.7$, respectively. We find that the amplitudes of the nonlinear oscillations for the cantilevered pipe conveying pulsating fluid become larger as the parametric excitation increases and the mass parameter decreases. This indicates that when the pipe mass is lighter, the amplitudes of the nonlinear oscillations are greater. In Figures 6(c) and 6(d), we study the influences of the external excitations on the force-amplitude response curves. Figure 6(c) demonstrates the relations between the amplitudes versus the external excitations F in the cantilevered pipe conveying pulsating fluid when the flow velocities are $U_0 = 15.8$ and $U_0 = 16.0$, respectively. We find that the amplitudes of the nonlinear oscillations for the cantilevered pipe conveying pulsating fluid become larger when the flow velocity is larger. Figure 6(d) shows the relations on the amplitudes versus the external excitations F in the cantilevered pipe conveying pulsating fluid when the mass parameters are $\beta = 0.9$ and $\beta = 0.7$, respectively. It is found that the nonlinear oscillations of the cantilevered pipe conveying pulsating fluid more easily happen with the decrease of the mass parameter β.

Based on the analyses of the amplitude-frequency response curves, it can be found that the hardening-spring type behaviors and jumping phenomena are exhibited for the cantilevered pipe conveying pulsating fluid. The jumping phenomena also occur in the force-amplitude response curves versus the flow velocity and external excitation. Moreover, it is known that the flow

velocity, external excitation, and coupling degree of two oscillation modes can affect the nonlinear oscillations of the cantilevered pipe conveying pulsating fluid under the external harmonic force. The nonlinearity bends the amplitude-frequency response curves to the right when the cantilevered pipe conveying pulsating fluid has the hardening-spring type behaviors. The bending of the amplitude-frequency response curves leads to the occurrence of the jumping phenomena. The hardening-spring type behavior and jumping phenomena mean that the oscillation amplitudes of the cantilevered pipe conveying pulsating fluid increase firstly and change abruptly. The energy of the fluid motion is transferred into the energy of the cantilevered pipe when the flow velocity increases. Thus, the fluid-structure interaction happens for the cantilevered pipe conveying pulsating fluid. The nonlinear resonance of the large amplitude for the cantilevered pipe conveying pulsating fluid can be stimulated with the increase of these factors.

4. Numerical Simulations of Periodic and Chaotic Oscillations

In order to study the nonlinear dynamic properties of the cantilevered pipe conveying pulsating fluid, the influences of the velocity parametric excitation and external excitation on the nonlinear oscillations of the pipe are investigated. In this section, the average equations (23a)–(23d) in the Cartesian coordinate system are numerically simulated to find the multitime periodic and the chaotic oscillations of the cantilevered pipe conveying pulsating fluid under the external harmonic excitation based on the fourth-order Runge-Kutta algorithm [50–52]. We choose the velocity parametric and external excitations as the controlling parameters to study the complicated nonlinear dynamics of the cantilevered pipe conveying pulsating fluid, respectively. The initial conditions are chosen as $x_1 = 0$, $x_2 = 0.1$, $x_3 = 0$, and $x_4 = 0.1$. Other parameters are chosen as

$$\begin{aligned}
\beta &= 0.9,\\
\gamma &= 7,\\
\mu &= 15,\\
\sigma &= 7.7,\\
\Omega &= 15,\\
\Omega_1 &= 8.6,\\
\alpha &= 0.7,\\
p_0 &= -3,\\
p_1 &= 0.5,\\
p_2 &= -11,\\
p_3 &= 2,\\
p_4 &= 8,\\
p_5 &= -10,\\
p_6 &= -13,\\
p_7 &= 16,\\
p_8 &= -10,\\
p_9 &= -1,\\
p_{10} &= -10,\\
p_{11} &= -3,\\
p_{12} &= -14,\\
p_{13} &= -6,\\
p_{14} &= -1,\\
p_{15} &= 14,\\
p_{16} &= 10,\\
p_{17} &= 4,\\
p_{18} &= -9,\\
p_{19} &= 2,\\
p_{20} &= 1,\\
p_{21} &= 4,\\
p_{22} &= 1,\\
p_{23} &= 1,\\
p_{24} &= 6,\\
q_1 &= -5,\\
q_2 &= -6,\\
q_3 &= -4.7,\\
q_4 &= 18,\\
q_5 &= 18,\\
q_6 &= 7,\\
q_7 &= 4,\\
q_8 &= 14,\\
q_9 &= -1,\\
q_{10} &= -11,\\
q_{11} &= 9,\\
q_{12} &= -10,\\
q_{13} &= 3.
\end{aligned} \tag{27}$$

To reveal the nonlinear dynamic behaviors of the cantilevered pipe conveying pulsating fluid, the bifurcation diagrams, maximum Lyapunov exponents, phase portraits, waveforms, and Poincare map are depicted. Figures 7 and 8 present the bifurcation diagrams and maximum Lyapunov exponents to demonstrate the multitime nonlinear oscillation of the cantilevered pipe conveying pulsating fluid by varying the velocity parametric excitation and external excitation, respectively.

In order to study the influences of the flow velocities on the multitime nonlinear oscillations of the cantilevered pipe conveying pulsating fluid, we set the external excitation while other parameters remain unchanged. The bifurcation diagrams and maximum Lyapunov exponents of the

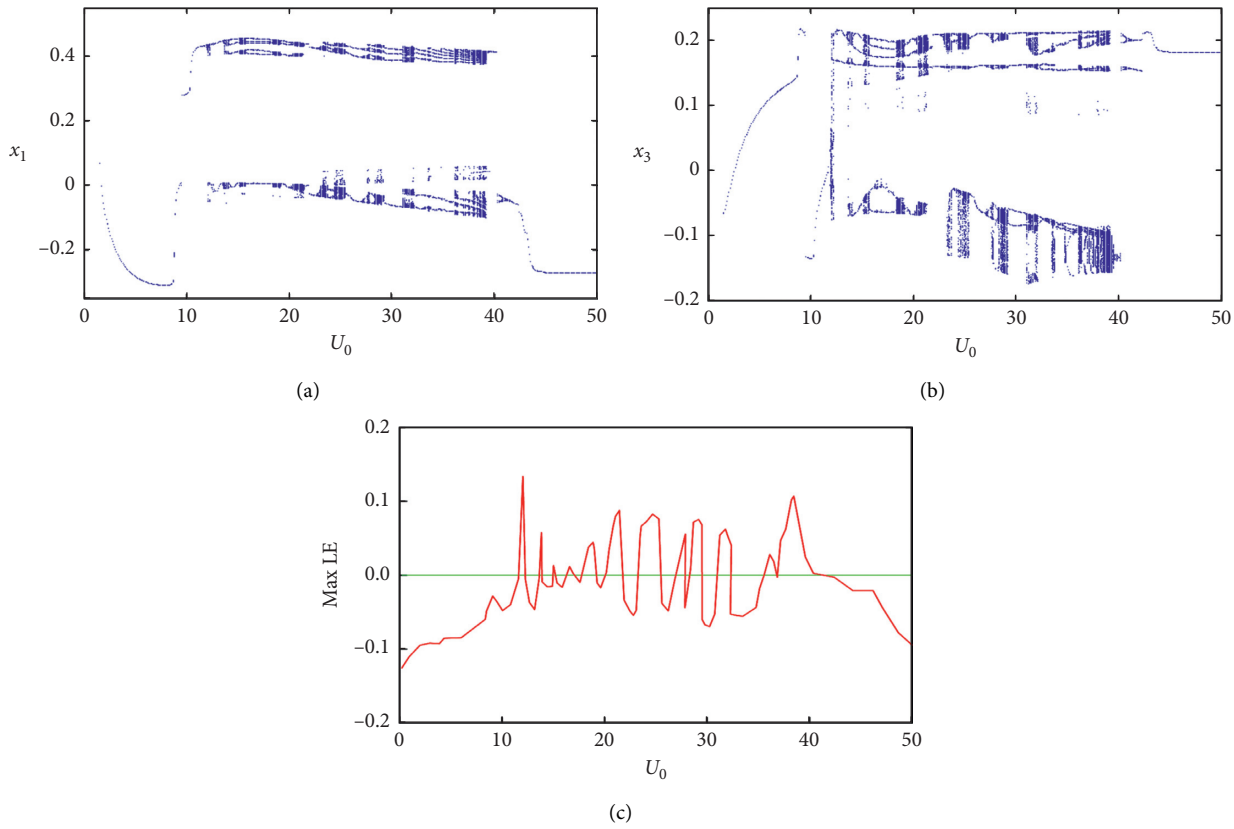

FIGURE 7: The bifurcation diagrams and maximum Lyapunov exponents of the cantilevered pipe conveying pulsating fluid are given for the parametric excitations of the flow velocities when the external excitation is $F = 7$. (a) x_1 versus flow velocity, (b) x_3 versus flow velocity, and (c) maximum Lyapunov exponents versus flow velocity.

cantilevered pipe conveying pulsating fluid with the change of the flow velocity are shown in Figure 7 when the external excitation $F = 7$. According to changing characteristics of the bifurcation diagram, with the increase of the flow velocities, the period oscillations of the cantilevered pipe conveying pulsating fluid appear at the beginning, the multitime quasi-period oscillations appear, and the multitime chaotic oscillations happen. With the increase of the flow rate, the multiple periodic windows appear for the cantilevered pipe conveying pulsating fluid. This illustrates the alternating change of the periodic and chaotic oscillations. When the flow rate increases to a particular value, the motion of the cantilevered pipe conveying pulsating fluid evolves to a stable period-1 oscillation. The maximum Lyapunov exponents given in Figure 7(c) describe the intervals of the flow velocity for the chaotic vibrations.

Based on numerical simulations corresponding to the aforementioned analyses, we further investigate the effects of the external excitations on the nonlinear dynamics of the cantilevered pipe conveying pulsating fluid when the flow velocity is $U_0 = 12$ and other parameters remain unchanged, as shown in Figure 8. It is found that the changing characteristics of the oscillations with the increase of the external excitations are similar to those with the increase of the flow velocities for the cantilevered pipe conveying pulsating fluid. The periodic oscillation appears at the beginning, and then the multitime periodic oscillation appears, and, finally, the multitime chaotic oscillations occur for the cantilevered pipe conveying pulsating fluid under the external harmonic excitation. With the further increase of the external excitation, several periodic oscillation windows appear for the cantilevered pipe conveying pulsating fluid. When the external excitation increases to a particular value, the motions of the cantilevered pipe conveying pulsating fluid eventually become the chaotic oscillations from the intermittent chaos. The intermittent chaos is verified in Figure 8(c) by whether the maximum Lyapunov exponent is positive.

We present a variety of figures to confirm the vibrations of the cantilevered pipe conveying pulsating fluid corresponding to different flow rates and different external excitations. In Figures 9–17, Figures(a) and (c) represent the phase portraits on the planes (x_1, x_2) and (x_3, x_4), Figures (b) and (d) depict the waveforms on the planes (t, x_1) and (t, x_3), Figure(e) denotes three-dimensional phase portrait in the space (x_1, x_2, x_3), and Figure(g) depicts Poincare map on the plane (x_1, x_2), respectively. The aforementioned

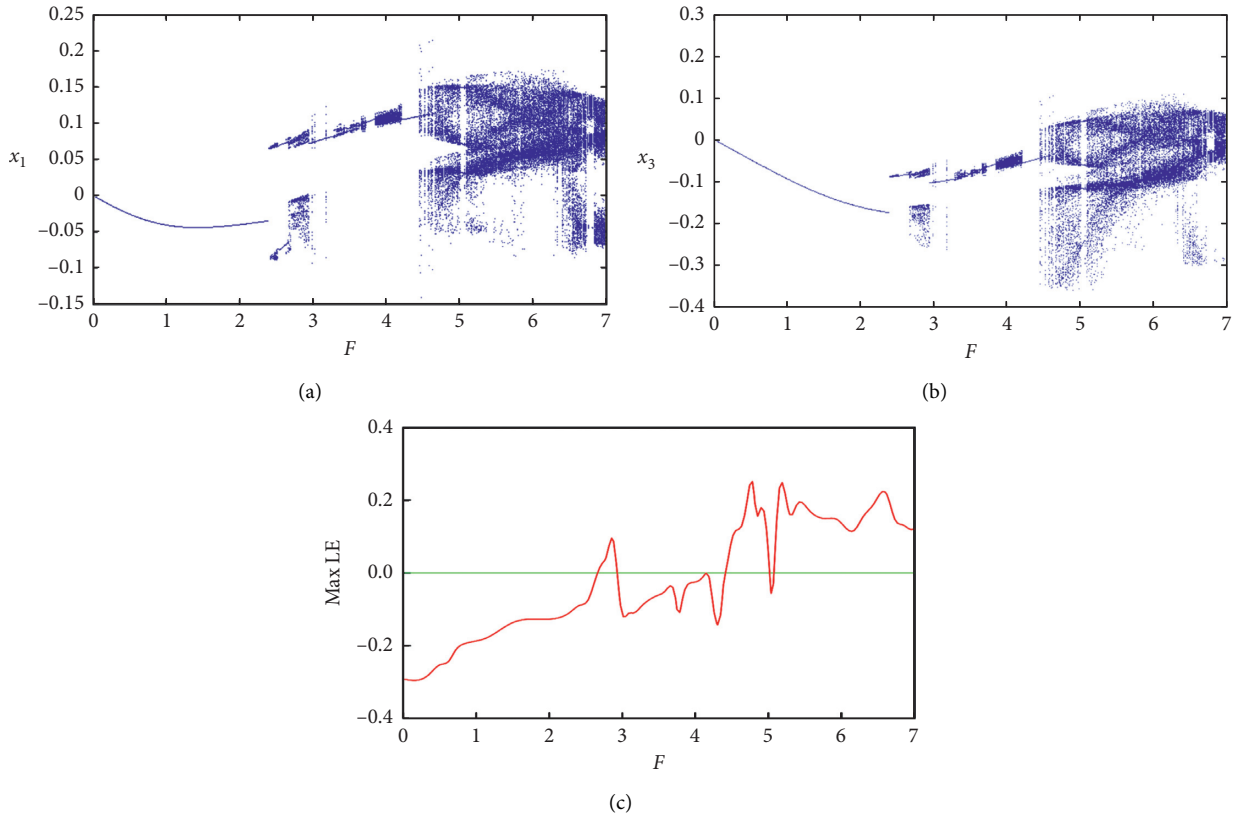

FIGURE 8: The bifurcation diagrams and maximum Lyapunov exponents of the cantilevered pipe conveying pulsating fluid are obtained for the external excitations when the flow velocity is $U_0 = 12$. (a) x_1 versus external excitation, (b) x_3 versus external excitation, and (c) maximum Lyapunov exponents versus flow velocity.

figures are the effective tools to judge the chaotic oscillations of the cantilevered pipe conveying pulsating fluid. Whether the waveforms are regular or irregular, these indicate that the motions of the cantilevered pipe conveying pulsating fluid are the periodic or chaotic oscillations. The phase diagram is the projection curve of the solution in the phase plane and phase space. The closed curve represents the periodic oscillation, and the phase portraits of the chaotic oscillations are the repeating unclosed curve confined within a bounded region. According to Poincare mapping, the periodic and quasi-periodic oscillations are the isolated points and curves on Poincare cross section. The nonlinear oscillations of the cantilevered pipe conveying pulsating fluid are the multitime chaotic oscillations when the discrete point sets appear with the infinite self-similar structures on Poincare cross section.

According to the characteristics of each figure for different motions, there exist the periodic, multitime quasi-periodic, and multitime chaotic oscillations of the cantilevered pipe conveying pulsating fluid under different velocity parametric excitations, as shown in Figures 9–13. Figure 9 gives the periodic oscillation of the cantilevered pipe conveying pulsating fluid when the velocity parametric excitation is $U_0 = 11.0$. Figure 10 indicates that there exists the period-2 oscillation of the cantilevered pipe conveying pulsating fluid when the velocity parametric excitation is $U_0 = 19.5$. Based on the definition of the coordinate system, we know that the right is positive and the left is negative for the cantilevered pipe conveying pulsating fluid. It is found that, in the cantilevered pipe conveying pulsating fluid, there are the nonlinear oscillations around the left-mode and right-mode positions, respectively. The first-order and third-order oscillation modes of the cantilevered pipe conveying pulsating fluid vibrate twice times around the right-mode position and then vibrate twice times around the left-mode position, as shown in Figures 10(b) and 10(d). Between the left-mode and right-mode nonlinear oscillations, there exists one-time oscillation around the vertical equilibrium position in the cantilevered pipe conveying pulsating fluid. This is a typical nonlinear dynamic phenomenon.

Figure 11 illustrates that the multiperiodic oscillation happens when the velocity parametric excitation is $U_0 = 23.2$. From Figure 11(b), it is demonstrated that, in the first-order mode of the nonlinear oscillations, there exists one-time oscillation around the right-mode position and then there exists twice-time oscillation around the left-mode position. For the third-order mode, there exists twice-time

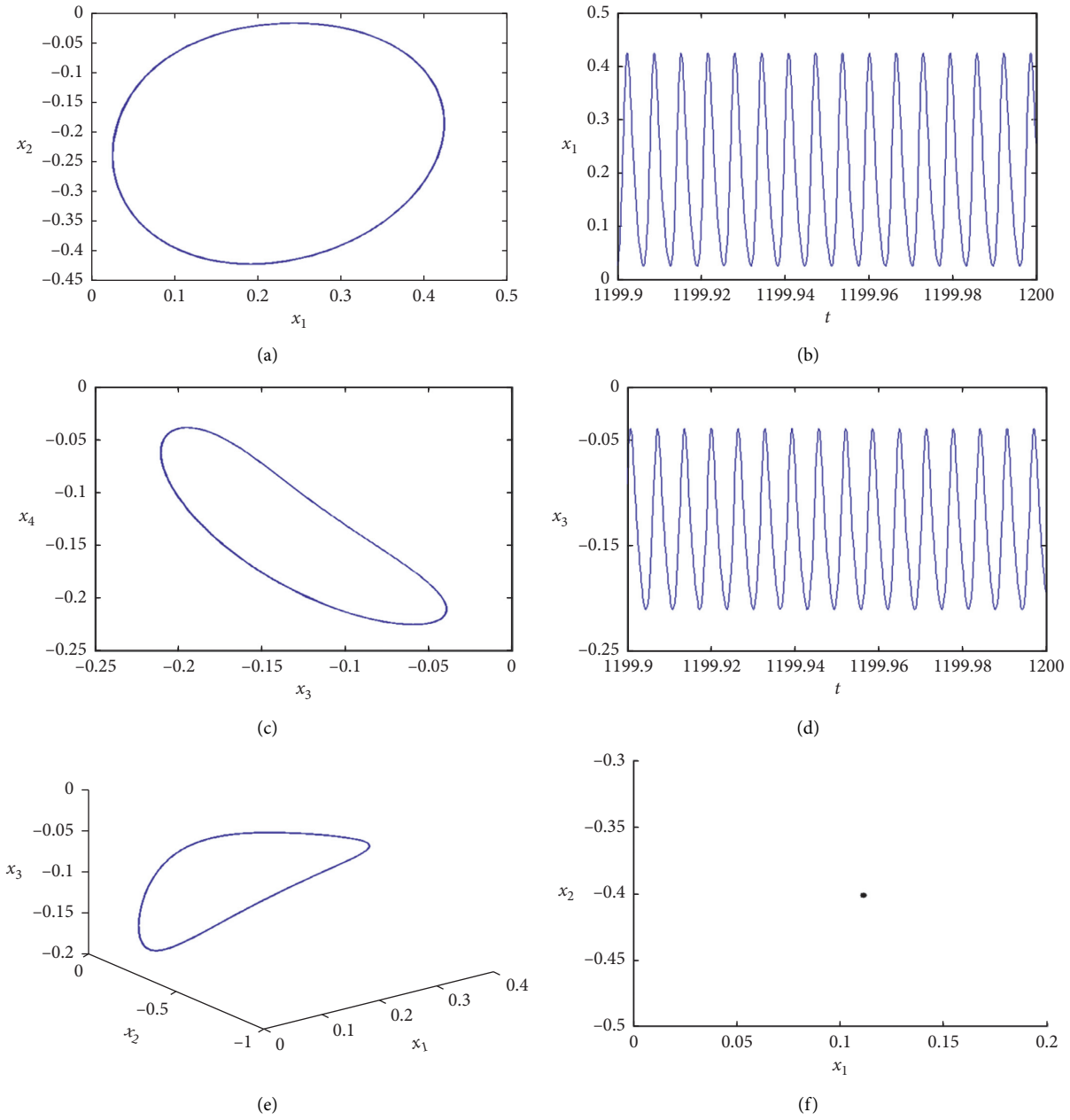

Figure 9: The periodic oscillation of the cantilevered pipe conveying pulsating fluid is obtained when the parametric excitation of the flow velocity is $U_0 = 11.0$. (a) Phase portrait on plane (x_1, x_2), (b) waveform on plane (t, x_1), (c) phase portrait on plane (x_3, x_4), (d) waveform on plane (t, x_3), (e) three-dimensional phase portrait in space (x_1, x_2, x_3), and (g) Poincare map on plane (x_1, x_2).

oscillation around the right-mode position and then there exists one-time oscillation around the left-mode position in the cantilevered pipe conveying pulsating fluid, as shown in Figure 11(d).

Figure 12 indicates that there exist the multitime chaotic oscillations when the velocity parametric excitation is $U_0 = 31.5$. Around the left-mode and right-mode positions, the chaotic oscillations of the cantilevered pipe conveying pulsating fluid are the irregular motions. Figure 13 indicates that the motion of the cantilevered pipe conveying pulsating fluid again returns to the period-1 oscillation when the velocity parametric excitation is $U_0 = 42.5$. In this case, it is found from Figure 13(b) that the first-order mode of the cantilevered pipe conveying pulsating fluid is the oscillation around the left-mode position. However, the third-order vibration mode of the cantilevered pipe conveying pulsating

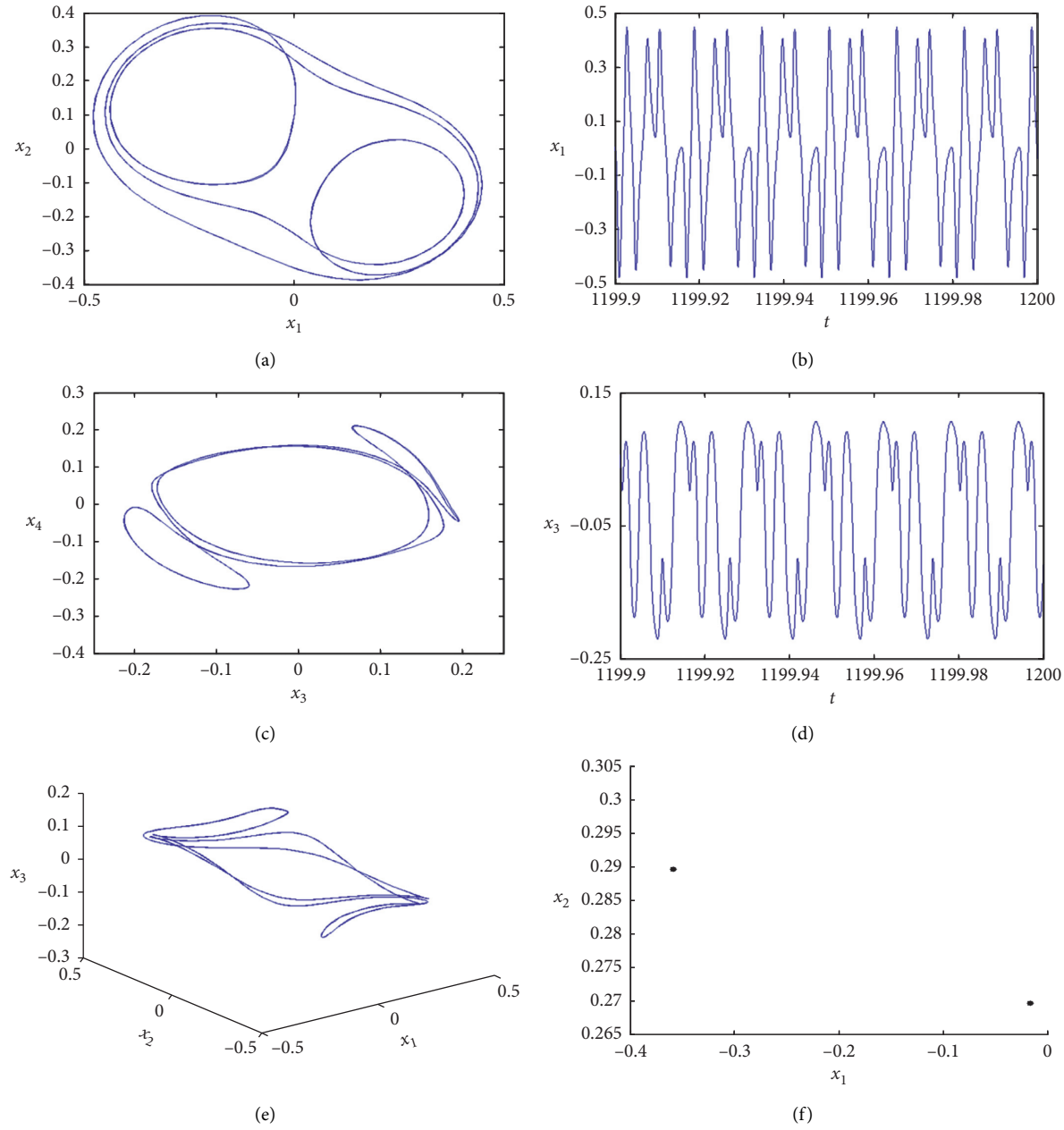

FIGURE 10: The period-2 oscillation of the cantilevered pipe conveying pulsating fluid is obtained when the parametric excitation of the flow velocity is $U_0 = 19.5$. (a) phase portrait on plane (x_1, x_2), (b) waveform on plane (t, x_1), (c) phase portrait on plane (x_3, x_4), (d) waveform on plane (t, x_3), (e) three-dimensional phase portrait in space (x_1, x_2, x_3), and (g) Poincare map on plane (x_1, x_2).

fluid is a motion around the right-mode position, as shown in Figure 13(d).

We also find the periodic, multitime periodic, and multitime chaotic oscillations of the cantilevered pipe conveying pulsating fluid under different external excitations, as shown in Figures 14–17. Figure 14 gives the multiperiodic oscillation of the cantilevered pipe conveying pulsating fluid when the external excitation is $F = 2.9$. It is observed from Figure 14(b) that, for the first-order mode, the motions of the cantilevered pipe conveying pulsating fluid vibrate three times around the right-mode position and twice times around the left-mode position. For the third-order mode, the vibrations of the cantilevered pipe conveying pulsating fluid move twice times around the right-mode position and three times around the left-mode position, as shown in Figure 14(d). In addition, it is observed

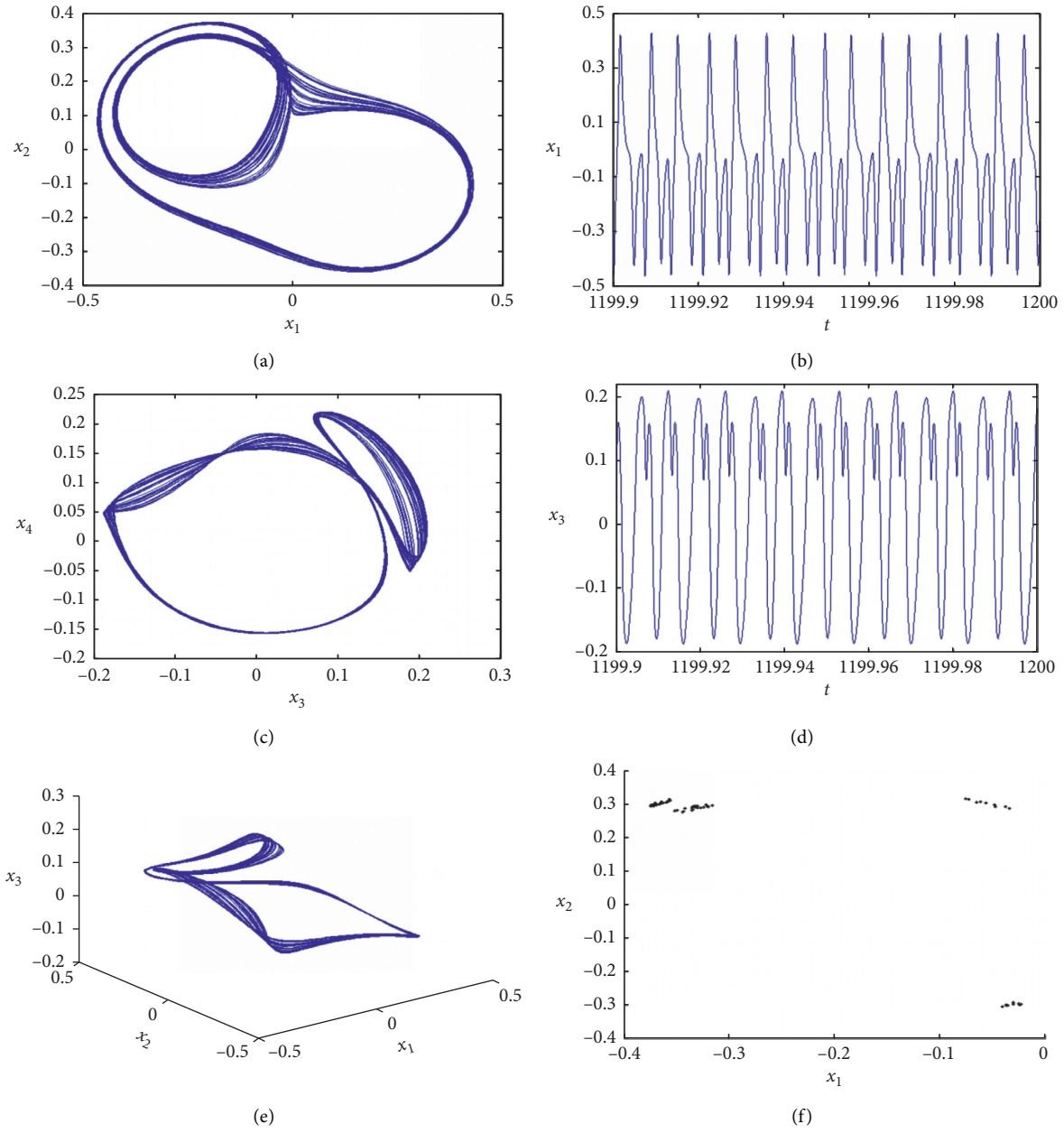

FIGURE 11: The multiperiodic oscillation of the cantilevered pipe conveying pulsating fluid is obtained when the parametric excitation of the flow velocity is $U_0 = 23.2$. (a) Phase portrait on plane (x_1, x_2), (b) waveform on plane (t, x_1), (c) phase portrait on plane (x_3, x_4), (d) waveform on plane (t, x_3), (e) three-dimensional phase portrait in space (x_1, x_2, x_3), and (g) Poincare map on plane (x_1, x_2).

from Figure 14 that the nonlinear oscillations of the cantilevered pipe conveying pulsating fluid also have the motions around the vertical equilibrium position.

Figure 15 indicates that the multitime periodic oscillation happens for the cantilevered pipe conveying pulsating fluid when the external excitation is $F = 4.5$. For the first-order mode, four-time nonlinear oscillations occur around the right-mode position and twice-time nonlinear oscillations occur around the left-mode position in the cantilevered pipe conveying pulsating fluid, as shown in Figure 15(b). It is also found from Figure 15(d) that, for the third-order mode, there are twice-time nonlinear oscillations around the right-mode position and four-time nonlinear oscillations around the left-mode position. Figure 16 represents that the quasi-periodic oscillation occurs when the external excitation is $F = 6.3$. Figure 17 demonstrates that there exist the multi-time chaotic oscillations of the cantilevered pipe conveying pulsating fluid when the external excitation is $F = 6.5$. The

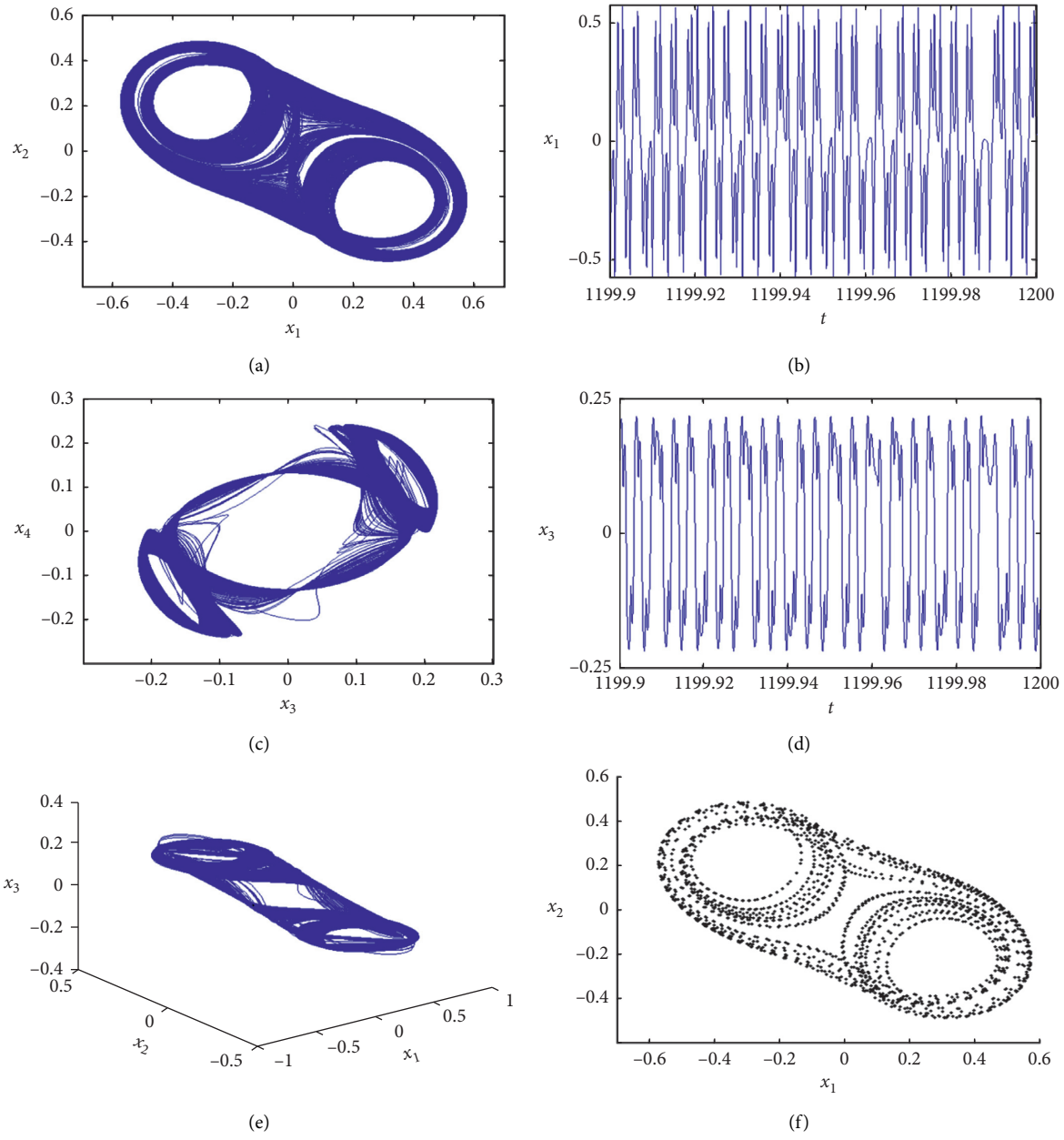

Figure 12: The chaotic oscillations of the cantilevered pipe conveying pulsating fluid are obtained when the parametric excitation of the flow velocity is $U_0 = 31.5$. (a) Phase portrait on plane (x_1, x_2), (b) waveform on plane (t, x_1), (c) phase portrait on plane (x_3, x_4), (d) waveform on plane (t, x_3), (e) three-dimensional phase portrait in space (x_1, x_2, x_3), and (g) Poincare map on plane (x_1, x_2).

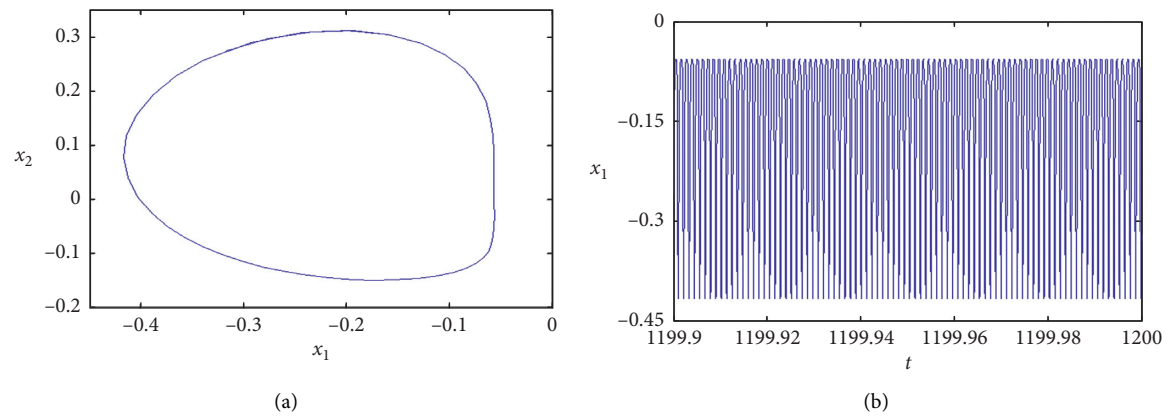

Figure 13: Continued.

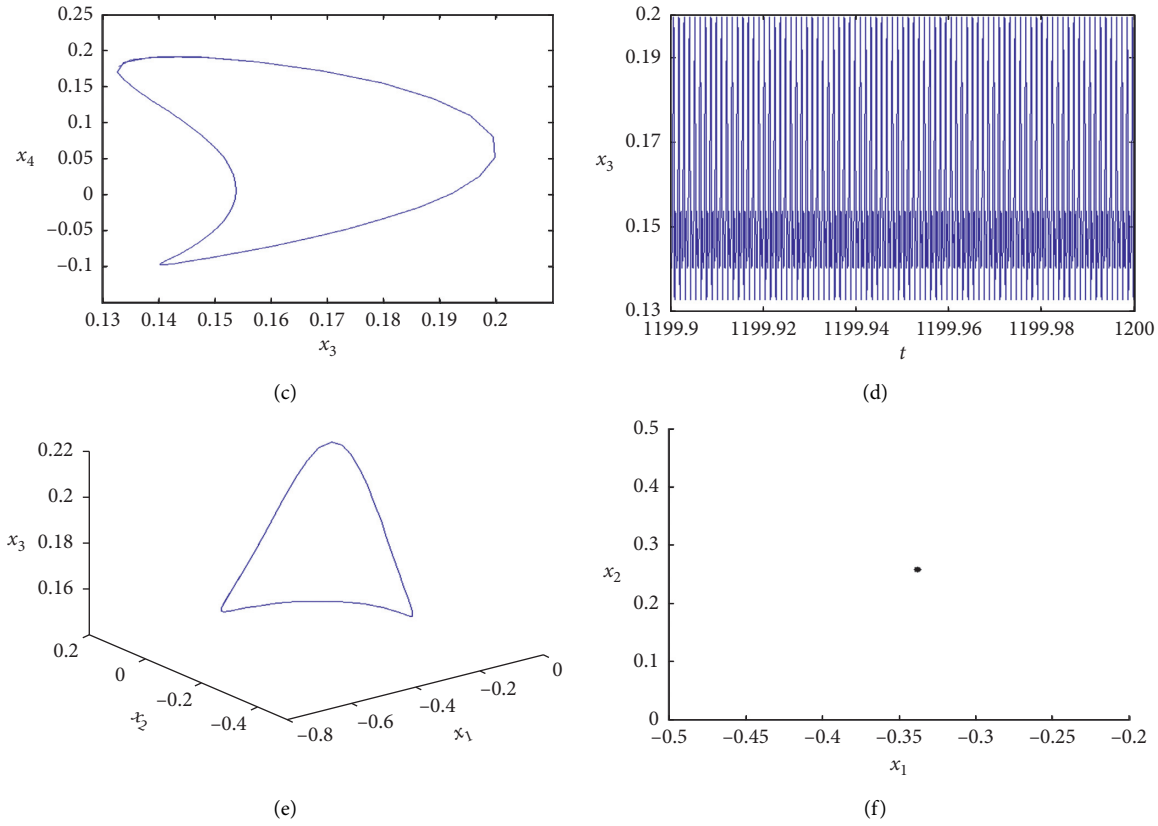

Figure 13: The period-1 oscillation of the cantilevered pipe conveying pulsating fluid is obtained when the parametric excitation of the flow velocity is $U_0 = 42.5$. (a) Phase portrait on plane (x_1, x_2), (b) waveform on plane (t, x_1), (c) phase portrait on plane (x_3, x_4), (d) waveform on plane (t, x_3), (e) three-dimensional phase portrait in space (x_1, x_2, x_3), and (g) Poincare map on plane (x_1, x_2).

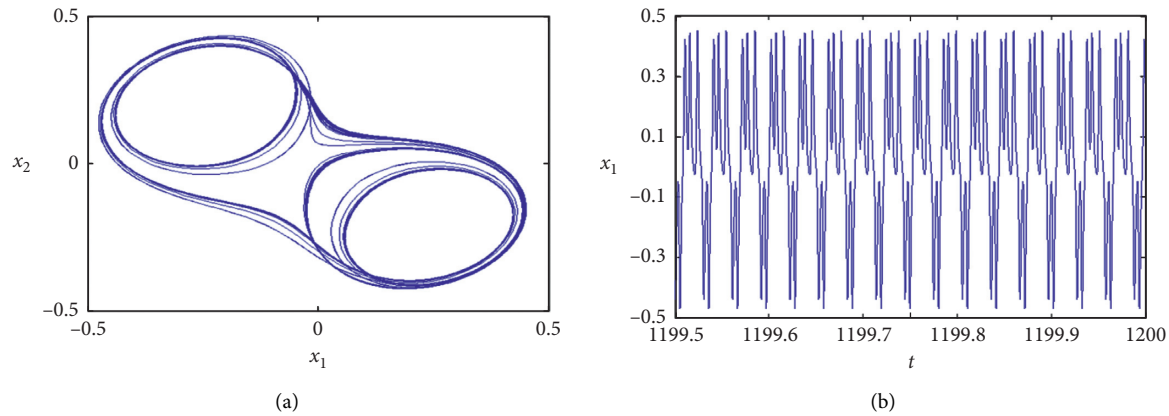

Figure 14: Continued.

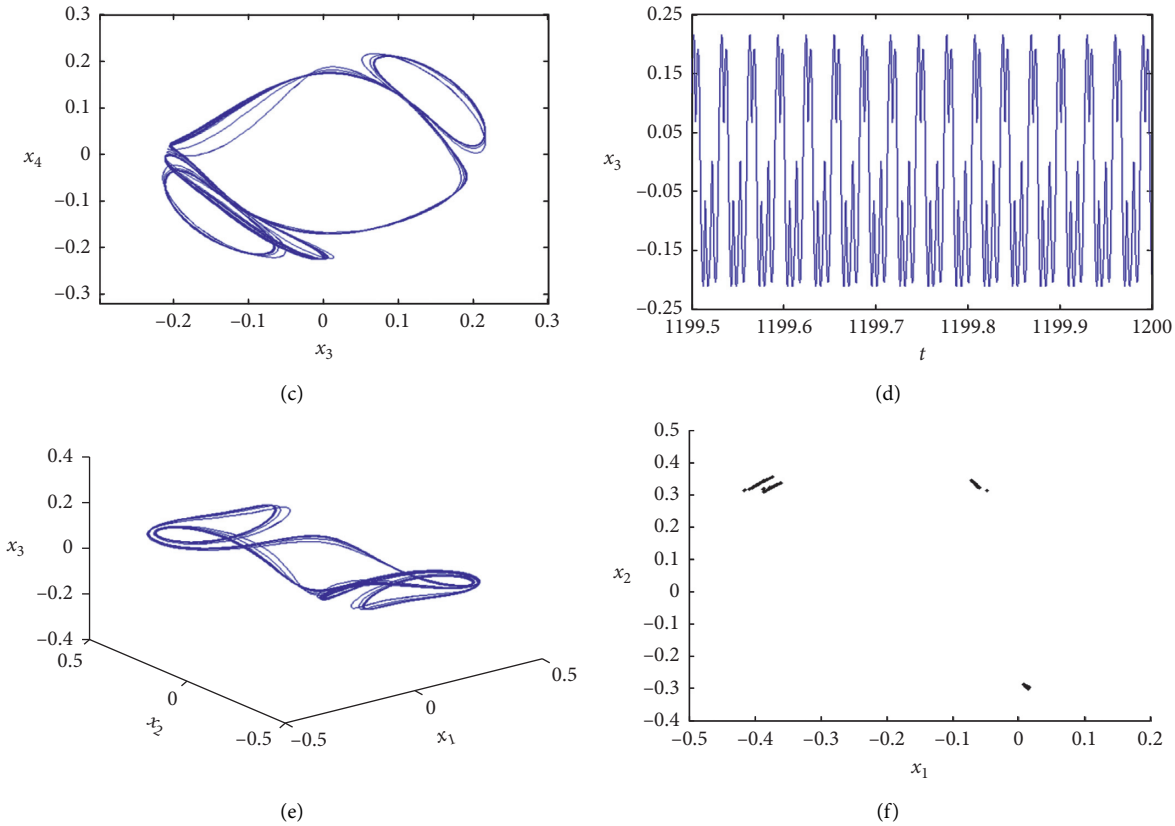

FIGURE 14: The multiperiodic oscillation of the cantilevered pipe conveying pulsating fluid is obtained when the external excitation is $F = 2.9$. (a) Phase portrait on plane (x_1, x_2), (b) waveform on plane (t, x_1), (c) phase portrait on plane (x_3, x_4), (d) waveform on plane (t, x_3), (e) three-dimensional phase portrait in space (x_1, x_2, x_3), and (g) Poincare map on plane (x_1, x_2).

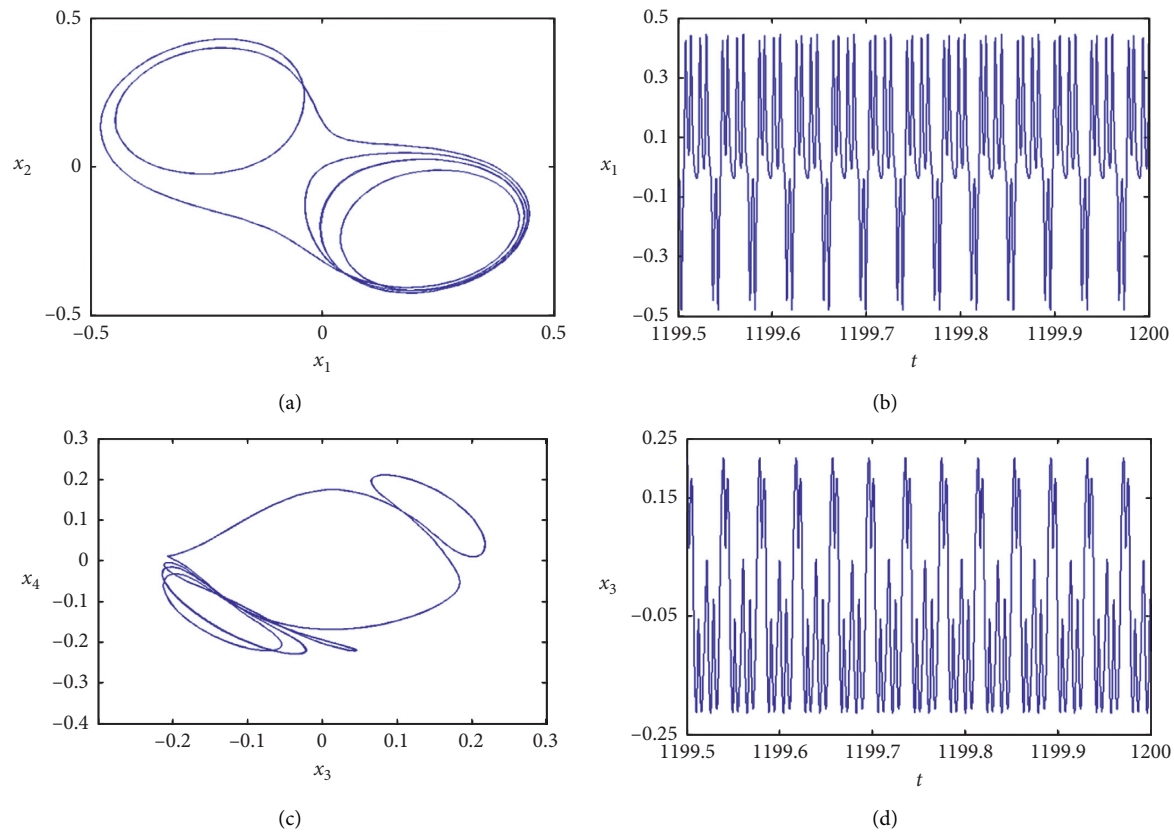

FIGURE 15: Continued.

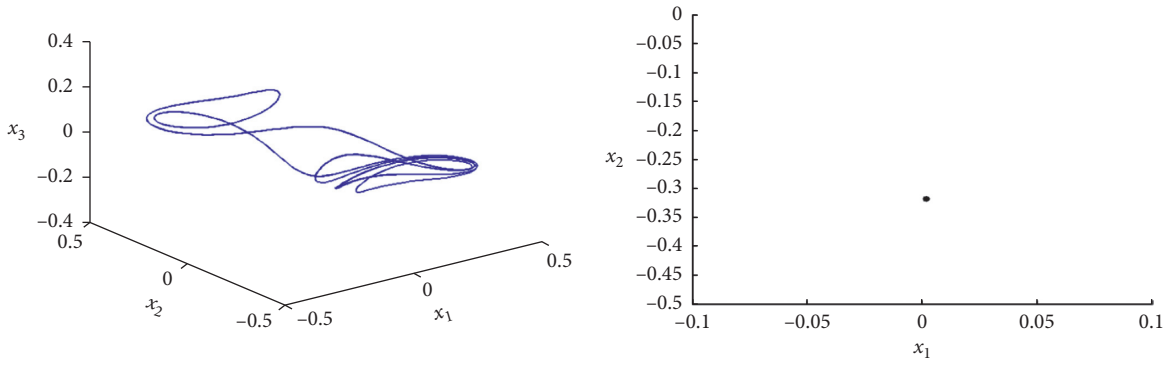

(e) (f)

Figure 15: The multitime periodic oscillation of the cantilevered pipe conveying pulsating fluid is obtained when the external excitation is $F = 4.5$. (a) Phase portrait on plane (x_1, x_2), (b) waveform on plane (t, x_1), (c) phase portrait on plane (x_3, x_4), (d) waveform on plane (t, x_3), (e) three-dimensional phase portrait in space (x_1, x_2, x_3), and (g) Poincare map on plane (x_1, x_2).

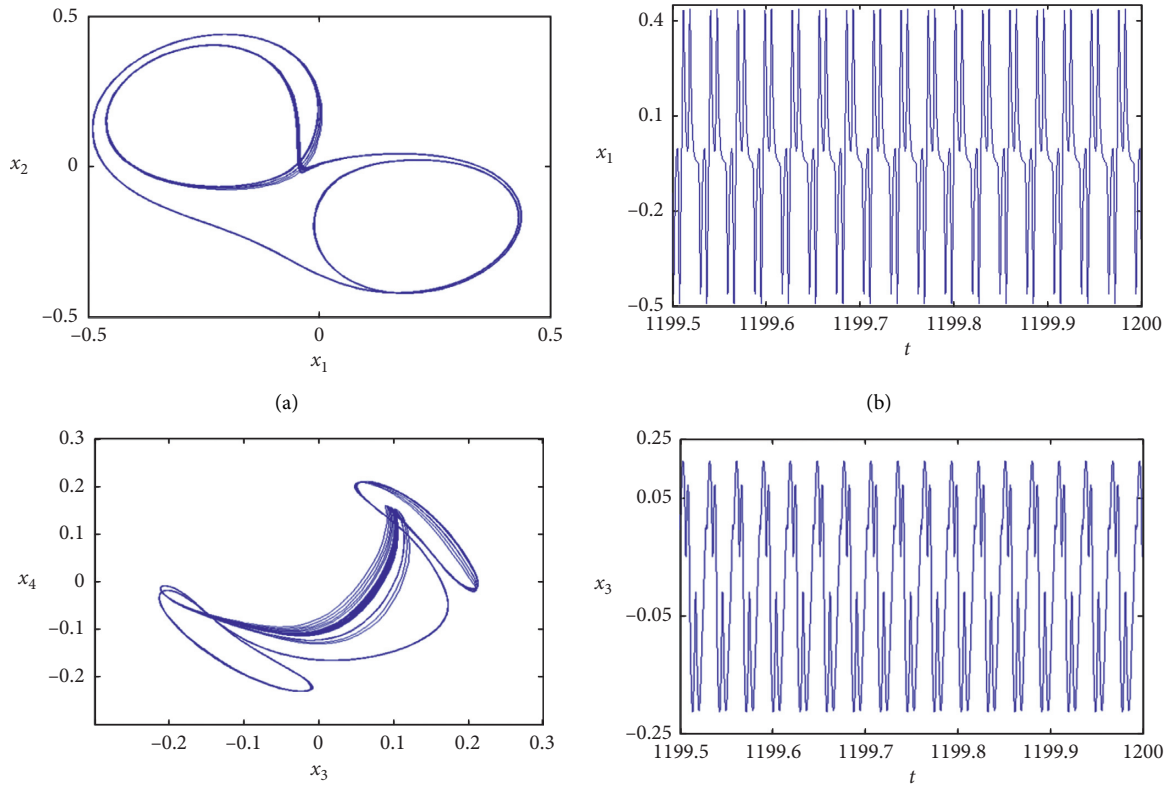

(a) (b)

(c) (d)

Figure 16: Continued.

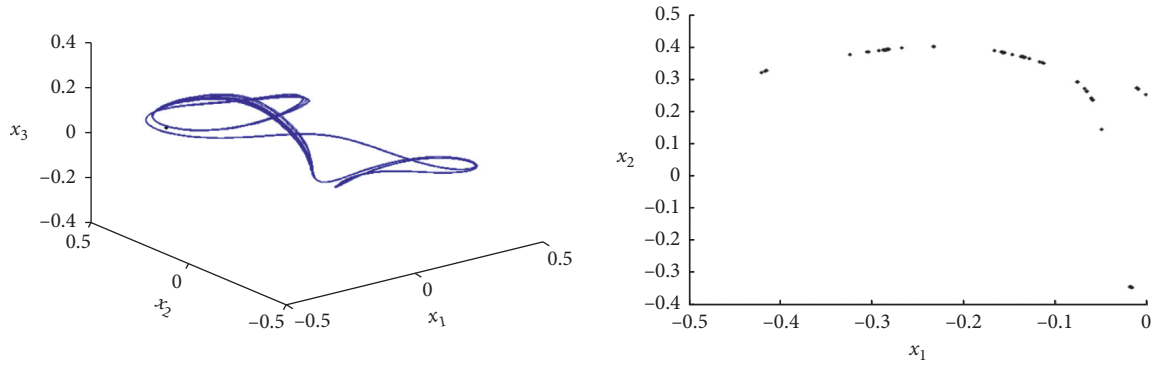

(e) (f)

Figure 16: The quasi-periodic oscillation of the cantilevered pipe conveying pulsating fluid is obtained when the external excitation is $F = 6.3$. (a) Phase portrait on plane (x_1, x_2), (b) waveform on plane (t, x_1), (c) phase portrait on plane (x_3, x_4), (d) waveform on plane (t, x_3), (e) three-dimensional phase portrait in space (x_1, x_2, x_3), and (g) Poincare map on plane (x_1, x_2).

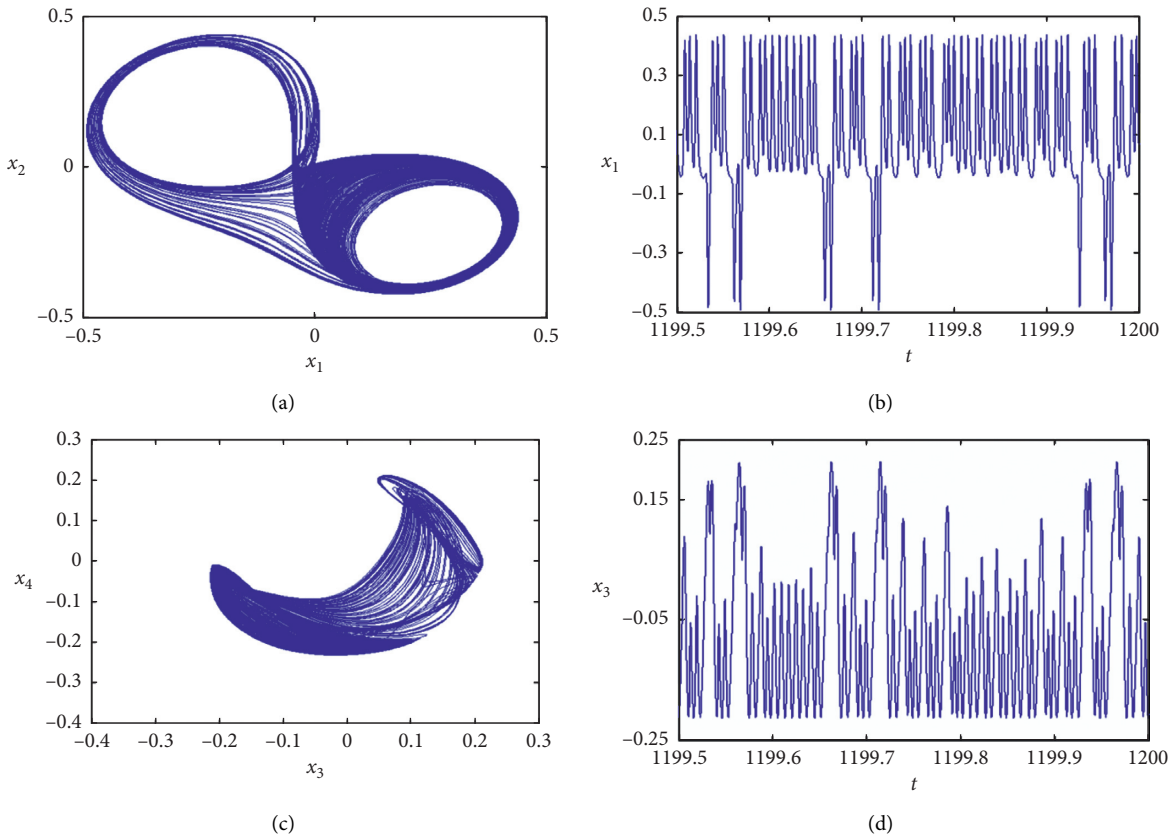

(a) (b)

(c) (d)

Figure 17: Continued.

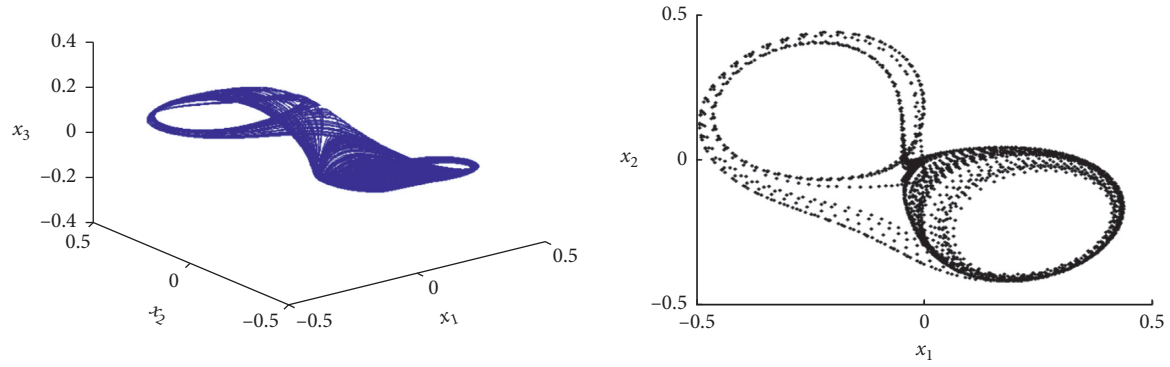

FIGURE 17: The chaotic oscillations of the cantilevered pipe conveying pulsating fluid are obtained when the external excitation is $F = 6.5$. (a) Phase portrait on plane (x_1, x_2), (b) waveform on plane (t, x_1), (c) phase portrait on plane (x_3, x_4), (d) waveform on plane (t, x_3), (e) three-dimensional phase portrait in space (x_1, x_2, x_3), and (g) Poincare map on plane (x_1, x_2).

irregular oscillations around the left-mode and the right-mode positions exist in the cantilevered pipe conveying pulsating fluid under the external harmonic excitation.

Moreover, the oscillations corresponding to different velocity parametric excitations and external excitations are consistent with the bifurcation diagrams of the cantilevered pipe conveying pulsating fluid under the external harmonic force, as shown in Figures 7 and 8. Based on the aforementioned analyses, it can be found that the flow rate and the external excitation can affect the nonlinear oscillations of the cantilevered pipe conveying pulsating fluid under the case of 1 : 3 internal resonance. When the velocity parametric excitation or the external excitation reaches a certain value, the multitime chaotic oscillations will happen in the cantilevered pipe conveying pulsating fluid, and the disorderly motions will lead to the destruction of the cantilevered pipe conveying pulsating fluid under the external harmonic force. Therefore, the velocity parametric excitation and the external excitation causing the multitime chaotic oscillations should be controlled when engineers design and use the infusion tube system.

5. Conclusions

The nonlinear resonant responses and multitime chaotic dynamics of the cantilevered pipe conveying pulsating fluid are investigated under the external harmonic force. Based on the nonlinear partial differential governing equation of motion for the cantilevered pipe conveying pulsating fluid derived by using Hamilton's principle, the 1 : 3 internal resonance and primary parametric resonance-1/2 subharmonic resonance are considered. A combination method of the method of multiple scales and Galerkin technique is utilized to obtain four-dimensional nonlinear averaged equations. Several amplitude-frequency response curves are obtained corresponding to the certain parameters. From the analysis of the amplitude-frequency response curves, it is found that there exist the hardening-spring type behaviors and the jumping phenomena. The jumping phenomena also occur in the amplitude-force response curves versus the flow velocity and external force.

Moreover, we find that the flow velocity, external force, and coupling degree of two order modes can affect the nonlinear vibrations of the cantilevered pipe conveying pulsating fluid under the external harmonic force. The nonlinear vibrations of the cantilevered pipe conveying pulsating fluid can be excited more easily with the increase of the flow velocity, external force, and coupling degree of two order modes. It is known that the nonlinear dynamic behaviors of the cantilevered pipe conveying pulsating fluid under the external harmonic force will be affected due to the flow rate and external excitation under the case of 1 : 3 internal resonance. It is observed that the multitime chaotic vibrations will occur for the cantilevered pipe conveying pulsating fluid when the velocity parametric excitation or external excitation reaches a certain value. From Figures 9–17, it is found that, for the first-order and third-order vibration modes, several-time nonlinear vibrations simultaneously or respectively happen around the right-mode and left-mode positions in the cantilevered pipe conveying pulsating fluid. Therefore, the velocity parametric excitation and external excitation should be controlled when engineers design and use the infusion tube systems.

Data Availability

All data generated or analyzed during this study are included in this published article.

Conflicts of Interest

The authors declare that there are no conflicts of interest regarding the publication of this paper.

Acknowledgments

The authors gratefully acknowledge the support of the National Natural Science Foundation of China (NNSFC) through Grant nos. 11672188, 11832002, and 11427801 and the Funding Project for Academic Human Resources Development in Institutions of Higher Learning under the Jurisdiction of Beijing Municipality (PHRIHLB).

References

[1] D. M. Tang and E. H. Dowell, "Chaotic oscillations of a cantilevered pipe conveying fluid," *Journal of Fluids and Structures*, vol. 2, pp. 263–283, 1988.

[2] M. P. Païdoussis and F. C. Moon, "Nonlinear and chaotic fluid elastic vibrations of a flexible pipe conveying fluid," *Journal of Fluids and Structures*, vol. 2, pp. 567–591, 1988.

[3] C. Semler, G. X. Li, and M. P. Païdoussis, "The non-linear equations of motion of pipes conveying fluid," *Journal of Sound and Vibration*, vol. 5, pp. 577–599, 1994.

[4] M. P. Païdoussis, *Fluid-Structure Interactions: Slender Structures and Axial Flow*, Academic Press, London, UK, 2nd edition, 2014.

[5] P. J. Holmes, "Bifurcations to divergence and flutter in flow-induced oscillations: a finite dimensional analysis," *Journal of Sound and Vibration*, vol. 53, pp. 471–503, 1977.

[6] P. J. Holmes and J. Marsden, "Bifurcation to divergence and flutter in flow-induced oscillations: an infinite dimensional analysis," *Automatica*, vol. 14, pp. 367–384, 1978.

[7] Y. L. Huo and Z. M. Wang, "Dynamic analysis of a vertically deploying retracting cantilevered pipe conveying fluid," *Journal of Sound and Vibration*, vol. 360, pp. 224–238, 2016.

[8] M. Hosseini and R. Bahaadini, "Size dependent stability analysis of cantilever micro-pipes conveying fluid based on modified strain gradient theory," *International Journal of Engineering Science*, vol. 101, pp. 1–13, 2016.

[9] A. R. Askarian, H. Abtahi, R. D. Firouz-Abadi, H. Haddadpour, and E. H. Dowell, "Bending-torsional instability of a viscoelastic cantilevered pipe conveying pulsating fluid with an inclined terminal nozzle," *Journal of Mechanical Science and Technology*, vol. 32, pp. 2999–3008, 2018.

[10] E. Tubaldi, M. Amabili, and M. P. Païdoussis, "Fluid-structure interaction for nonlinear response of shells conveying pulsatile flow," *Journal of Sound and Vibration*, vol. 371, pp. 252–276, 2016.

[11] Y. C. Bai, W. D. Xie, X. F. Gao, and W. H. Xu, "Dynamic analysis of a cantilevered pipe conveying fluid with density variation," *Journal of Fluids and Structures*, vol. 81, pp. 638–655, 2018.

[12] A. K. Bajaj, P. R. Sethna, and T. S. Lundgren, "Hopf bifurcation phenomena in tubes carrying a fluid," *SIAM Journal on Applied Mathematics*, vol. 39, pp. 213–230, 1980.

[13] N. Sri Namchchivaya, "Non-linear dynamics of supported pipe conveying pulsating fluid-I, subharmonic resonance," *International Journal of Non-linear Mechanics*, vol. 24, pp. 185–196, 1989.

[14] N. Sri Namchchivaya and W. M. Tien, "Non-linear dynamics of supported pipe conveying pulsating fluid-II, combination resonance," *International Journal of Non-Linear Mechanics*, vol. 24, pp. 197–208, 1989.

[15] A. Sarkar and M. P. Païdoussis, "A cantilever conveying fluid: coherent modes versus beam modes," *International Journal of Non-Linear Mechanics*, vol. 39, pp. 467–481, 2004.

[16] R. J. McDonald and N. Sri Namachchivaya, "Pipes conveying pulsating fluid near a 0:1 resonance: local bifurcations," *Journal of Fluids and Structures*, vol. 21, pp. 629–664, 2005.

[17] M. Yoshizawa, H. Nao, E. Hasegawa, and Y. Tsujioka, "Lateral vibration of a flexible pipe conveying fluid with pulsating flow," *Transactions of the Japan Society of Mechanical Engineers*, vol. 29, pp. 2243–2250, 2008.

[18] Y. Hou and G. H. Zeng, "Research on nonlinear dynamic characteristics of fluid-conveying pipes system," *Advanced Materials Research*, vol. 228-229, pp. 574–579, 2011.

[19] A. R. Setoodeh and S. Afrahim, "Nonlinear dynamic analysis of FG micro-pipes conveying fluid based on strain gradient theory," *Composite Structures*, vol. 116, pp. 128–135, 2014.

[20] M. Kheiri and M. P. Païdoussis, "On the use of generalized Hamilton's principle for the derivation of the equation of motion of a pipe conveying fluid," *Journal of Fluids and Structures*, vol. 50, pp. 18–24, 2014.

[21] C. B. Gan, S. Q. Guo, H. Lei, and S. X. Yang, "Random uncertainty modeling and vibration analysis of a straight pipe conveying fluid," *Nonlinear Dynamics*, vol. 77, pp. 503–519, 2014.

[22] T. Zhang, H. Ouyang, Y. O. Zhang, and B. L. Lv, "Nonlinear dynamics of straight fluid-conveying pipes with general boundary conditions and additional springs and masses," *Applied Mathematical Modelling*, vol. 40, pp. 7880–7900, 2016.

[23] Z. M. Wang and Y. Z. Liu, "Transverse vibration of pipe conveying fluid made of functionally graded materials using a symplectic method," *Nuclear Engineering and Design*, vol. 298, pp. 149–159, 2016.

[24] F. Liang, X.-D. Yang, Y.-J. Qian, and W. Zhang, "Free vibration analysis of pipes conveying fluid based on linear and nonlinear complex modes approach," *International Journal of Applied Mechanics*, vol. 9, no. 8, Article ID 1750112, 2017.

[25] F. Liang, X.-D. Yang, W. Zhang, and Y.-J. Qian, "Nonlinear free vibration of spinning viscoelastic pipes conveying fluid," *International Journal of Applied Mechanics*, vol. 10, no. 7, Article ID 1850076, 2018.

[26] F. Liang, X. D. Yang, Y. J. Qian, and W. Zhang, "Transverse free vibration and stability analysis of spinning pipes conveying fluid," *International Journal of Mechanical Sciences*, vol. 137, pp. 195–204, 2018.

[27] F. Liang, X. D. Yang, W. Zhang, and Y. J. Qian, "Dynamical modeling and free vibration analysis of spinning pipes conveying fluid with axial deployment," *Journal of Sound Vibration*, vol. 417, pp. 65–79, 2018.

[28] F. Liang, X. D. Yang, W. Zhang, and Y. J. Qian, "Coupled biflexural-torsional vibration of fluid-conveying pipes spinning about an eccentric axis," *International Journal of Structural Stability and Dynamics*, vol. 19, Article ID 1950003, 2019.

[29] F. Liang, X. D. Yang, W. Zhang, Y. J. Qian, and R. V. N. Melnik, "Parametric vibration analysis of pipes conveying fluid by nonlinear normal modes and a numerical iterative approach," *Advances in Applied Mathematics and Mechanics*, vol. 11, pp. 38–52, 2019.

[30] G. X. Li and M. P. Païdoussis, "Stability, double degeneracy and chaos in cantilevered pipes conveying fluid," *International Journal of Non-Linear Mechanics*, vol. 29, pp. 83–107, 1994.

[31] C. Semler and M. P. Païdoussis, "Nonlinear analysis of the parametric resonances of a planar fluid-conveying cantilevered pipe," *Journal of Fluids and Structures*, vol. 10, pp. 787–825, 1996.

[32] M. P. Païdoussis and C. Semler, "Non-linear dynamics of a fluid conveying cantilevered pipe with a small mass attached at the free end," *International Journal of Non-Linear Mechanics*, vol. 33, pp. 15–32, 1998.

[33] J. D. Jin and G. S. Zou, "Bifurcations and chaotic motions in the autonomous system of a restrained pipe conveying fluid," *Journal of Sound and Vibration*, vol. 260, pp. 783–805, 2003.

[34] M. H. Ghayesh, M. P. Païdoussis, and M. Amabili, "Nonlinear dynamics of cantilevered extensible pipes conveying fluid," *Journal of Sound and Vibration*, vol. 332, pp. 6405–6418, 2013.

[35] L. Wang, Z. Y. Liu, A. Abdelkefi, Y. K. Wang, and H. L. Dai, "Nonlinear dynamics of cantilevered pipes conveying fluid: towards a further understanding of the effect of loose constraints," *International Journal of Non-Linear Mechanics*, vol. 95, 2017.

[36] A. R. Askarian, H. Haddadpour, R. D. Firouzabadi, and H. Abtahi, "Nonlinear dynamics of extensible viscoelastic cantilevered pipes conveying pulsatile flow with an end nozzle," *International Journal of Non-linear Mechanics*, vol. 91, pp. 22–35, 2017.

[37] T. Liu, W. Zhang, and J. F. Wang, "Nonlinear dynamics of composite laminated circular cylindrical shell clamped along a generatrix and with membranes at both ends," *Nonlinear Dynamics*, vol. 90, pp. 1393–1417, 2017.

[38] W. Zhang, T. Liu, A. Xi, and Y. N. Wang, "Resonant responses and chaotic dynamics of composite laminated circular cylindrical shell with membranes," *Journal of Sound and Vibration*, vol. 423, pp. 65–99, 2018.

[39] T. Liu, W. Zhang, J. J. Mao, and Y. Zheng, "Nonlinear breathing vibrations of eccentric rotating composite laminated circular cylindrical shell subjected to temperature, rotating speed and external excitations," *Mechanical Systems and Signal Processing*, vol. 127, pp. 463–498, 2019.

[40] W. Zhang, Y. Zheng, T. Liu, and X. Y. Guo, "Multi-pulse jumping double-parameter chaotic dynamics of eccentric rotating ring truss antenna under combined parametric and external excitations," *Nonlinear Dynamics*, vol. 98, pp. 761–800, 2019.

[41] L. N. Panda and R. C. Kar, "Nonlinear dynamics of a pipe conveying pulsating fluid with parametric and internal resonances," *Nonlinear Dynamics*, vol. 49, pp. 9–30, 2007.

[42] Q. Ni, M. Tang, Y. Luo, Y. Wang, and L. Wang, "Internal-external resonance of a curved pipe conveying fluid resting on a nonlinear elastic foundation," *Nonlinear Dynamics*, vol. 76, pp. 867–886, 2014.

[43] Y. L. Zhang and L. Q. Chen, "Steady-state response of pipes conveying pulsating fluid near a 2 : 1 internal resonance in the supercritical regime," *International Journal of Applied Mechanics*, vol. 6, Article ID 1450056, 2014.

[44] X. Y. Mao, H. Ding, and L. Q. Chen, "Steady-state response of a fluid-conveying pipe with 3 : 1 internal resonance in supercritical regime," *Nonlinear Dynamics*, vol. 86, pp. 795–809, 2016.

[45] Y. F. Zhang, M. H. Yao, W. Zhang, and B. C. Wen, "Dynamical modeling and multi-pulse chaotic dynamics of cantilevered pipe conveying pulsating fluid in parametric resonance," *Aerospace Science and Technology*, vol. 68, 2017.

[46] H. Ding, J. C. Ji, and L. Q. Chen, "Nonlinear vibration isolation for fluid-conveying pipes using quasi-zero stiffness characteristics," *Mechanical Systems and Signal Processing*, vol. 121, pp. 675–688, 2019.

[47] A. H. Nayfeh and D. T. Mook, *Nonlinear Oscillations*, Oxford University Press, Oxford, UK, 1979.

[48] J. E. Chen, W. Zhang, X. Y. Guo, and M. Sun, "Theoretical and experimental studies on nonlinear oscillations of symmetric cross-ply composite laminated plates," *Nonlinear Dynamics*, vol. 73, pp. 1697–1714, 2013.

[49] J. E. Chen, W. Zhang, J. Liu, and M. Sun, "Dynamic properties of truss core sandwich plate with tetrahedral core," *Composite Structures*, vol. 134, pp. 869–882, 2015.

[50] Z. Wei, Y. Li, B. Sang, Y. Liu, and W. Zhang, "Complex dynamical behaviors in a 3D simple chaotic flow with 3D stable or 3D unstable manifolds of a single equilibrium," *International Journal of Bifurcation and Chaos*, vol. 29, no. 7, Article ID 1950095, 2019.

[51] Y. J. Liu, F. Nazarimehr, A. J. M. Khalaf, A. Ahmed, and T. Hayat, "Detecting bifurcation points in a memristive neuron model," *The European Physical Journal—Special Topics*, vol. 228, pp. 1943–1950, 2019.

[52] Y. Liu, A. J. M. Khalaf, T. Hayat, A. Alsaedi, V.-T. Pham, and S. Jafari, "A complete investigation of the effect of external force on a 3D megastable oscillator," *International Journal of Bifurcation and Chaos*, vol. 30, no. 1, Article ID 2050012, 2020.

Hindawi
Complexity
Volume 2020, Article ID 3714832, 8 pages
https://doi.org/10.1155/2020/3714832

Research Article

Analytical Solutions for Nonlinear Dispersive Physical Model

Wen-Xiu Ma,[1,2,3,4] **Mohamed R. Ali**,[5] **and R. Sadat**[6]

[1]*Department of Mathematics, Zhejiang Normal University, Jinhua 321004, Zhejiang, China*
[2]*Department of Mathematics, King Abdulaziz University, Jeddah 21589, Saudi Arabia*
[3]*Department of Mathematics and Statistics, University of South Florida, Tampa, FL 33620-5700, USA*
[4]*School of Mathematics, South China University of Technology, Guangzhou 510640, China*
[5]*Department of Basic Science, Faculty of Engineering at Benha, Benha University, 13512, Egypt*
[6]*Department of Mathematics, Zagazig Faculty of Engineering, Zagazig University, Zagazig, Egypt*

Correspondence should be addressed to Wen-Xiu Ma; mawx@cas.usf.edu and Mohamed R. Ali; mohamed.reda@bhit.bu.edu.eg

Received 29 May 2020; Accepted 6 July 2020; Published 28 August 2020

Guest Editor: Zhouchao Wei

Nonlinear evolution equations widely describe phenomena in various fields of science, such as plasma, nuclear physics, chemical reactions, optics, shallow water waves, fluid dynamics, signal processing, and image processing. In the present work, the derivation and analysis of Lie symmetries are presented for the time-fractional Benjamin–Bona–Mahony equation (FBBM) with the Riemann–Liouville derivatives. The time FBBM equation is reduced to a nonlinear fractional ordinary differential equation (NLFODE) using its Lie symmetries. These symmetries are derivations using the prolongation theorem. Applying the subequation method, we then use the integrating factor property to solve the NLFODE to obtain a few travelling wave solutions to the time FBBM.

1. Introduction

Partial differential equations running into the thinking of most of the researchers as it represented the importance in several topics of scientific fields as mechanics, optical fibers, medical sciences (as breast cancer), biological science, turbulent bursts, and oceans waves [1–11].

The differential model has a broad application in many phenomena as in [12–14]. Recently, nonlinear fractional differential equations (NLFDEs) show significantly in engineering and applications of other sciences, for example, electrochemistry, physics, electromagnetics, and signal data processing [15–22].

Getting exact solutions for these forms of equations became an important issue; then, most researchers try to achieve this target. The most effective method for obtaining exact solutions for NLFPDEs is the Lie symmetry reduction method. There are many papers for using Lie's method to obtain explicit solutions for NLFPDEs [23–26].

In our paper, we drive the symmetry vectors for the time FBBM equation and present new closed-form solutions for it. The FBBM equation has many forms [27–30], and we choose to work on the following form:

$$D_t^{\alpha}\psi = -\psi_x - \psi\psi_x + \psi_{xxt}, \tag{1}$$

where ψ_{xxt} is the dissipative term.

The manuscript is prearranged as follows. In Section 2, Lie's group method for FPDEs is exposed. In Section 3, we apply the Lie group reduction method to obtain Lie point symmetry for the time FBBM equation (1). At the end of Section 4, we use these similarity variables to get the reduced equation. In Section 4, we use two methods for solving the resulting ordinary differential equation, the first method is the subequation method and the second method is the integrating factors method to get new solutions that have the properties and form the travelling wave form for the FBBME. In the end, conclusions are written in Section 5.

2. Notations and Introductory

2.1. Fractional Riemann–Liouville Derivative. In this section, we show some definitions for RL fractional derivative [31], which can be considered as follows:

$$D_t^{\alpha} f = \begin{cases} \dfrac{\mathrm{d}^n f(t)}{\mathrm{d}t^n}, & \text{if } n = \alpha, n \in \mathbb{N}, \\ \dfrac{\mathrm{d}^n}{\mathrm{d}t^n} I^{n-\alpha} f(t), & \text{if } 0 \le n-1 < \alpha < n, n \in \mathbb{N}, \end{cases} \tag{2}$$

$$I^{n-\alpha} f(t) = \frac{1}{\Gamma(n-\alpha)} \int_0^t (t-s) f(s) \mathrm{d}s, \quad n > 0, \tag{3}$$

where D_t^{α} is the total differentiation of integer number of orders α, $(\alpha > 0)$, the Gamma function is $\Gamma(n-\alpha)$, and $I^n f(t)$ is the (RL) fractional integral of an order of n.

Definition 1. The partial derivative of order α for Riemann–Liouville definition is presented by

$$\partial_t^{\alpha} = \begin{cases} \dfrac{\partial^n f}{\partial t^n}, & n = \alpha, \\ \dfrac{\partial^n}{\partial t^n} \dfrac{1}{\Gamma(n-\alpha)} \displaystyle\int_0^t (t-s)^{n-\alpha-1} f(s,x) \mathrm{d}s, & 0 \le n-1 < \alpha < n. \end{cases} \tag{4}$$

2.2. Notations for Lie Symmetry Reduction Method for the Time FPDEs. In this section, we show in detail the main notations and definitions that will be used for obtaining the symmetries of NLFPDEs.

Here, we will consider timing NLFPDEs of the form [31–33]

$$\partial_t^{\alpha} \psi = F\left(t, x, \psi, \psi_x, \psi_{xx}\right), \quad (0 < \alpha \le 1). \tag{5}$$

Assume, equation (2) has a Lie vector X in the form

$$X = \xi^1(x,t,u) \frac{\partial}{\partial x} + \xi^2(x,t,u) \frac{\partial}{\partial t} + \eta(x,t,u) \frac{\partial}{\partial u}, \tag{6}$$

where ξ^1, ξ^2, and η can be called as the infinitesimals of the transformations the independent and the dependent variables (x,t,ψ), respectively. Let a one-parameter Lie algebra of infinitesimal transformations be of the following form:

$$\begin{aligned} \overline{t} &= t + \varepsilon \xi^2(t,x,\psi) + O\left(\varepsilon^2\right), \\ \overline{x} &= x + \varepsilon \xi^1(t,x,\psi) + O\left(\varepsilon^2\right), \\ \overline{\psi} &= \psi + \varepsilon \eta(t,x,\psi) + O\left(\varepsilon^2\right), \\ \frac{\partial^{\alpha} \overline{\psi}}{\partial \overline{t}} &= \frac{\partial^{\alpha} \psi}{\partial t^{\alpha}} + \varepsilon \eta_{\alpha}^0(t,x,\psi) + O\left(\varepsilon^2\right), \\ \frac{\partial \overline{\psi}}{\partial \overline{x}} &= \frac{\partial \psi}{\partial x} + \varepsilon \eta^x(t,x,\psi) + O\left(\varepsilon^2\right), \\ \frac{\partial^3 \overline{\psi}}{\partial \overline{x}^2 \partial \overline{t}} &= \frac{\partial^3 \psi}{\partial x^2 \partial t} + \varepsilon \eta^{xxt}(t,x,\psi) + O\left(\varepsilon^2\right), \end{aligned} \tag{7}$$

where $\varepsilon \ll 1$ can be defined as a group parameter, in most cases we take it equal one. The explicit expressions of η^x, η^{xx}, and η^{xxt}, which can be called the prolongation of the infinitesimals and are given by

$$\begin{aligned} \eta^x &= D_x(\eta) - \psi_x D_x\left(\xi^1\right) - \psi_t D_t\left(\xi^2\right), \\ \eta^{xx} &= D_x\left(\eta^x\right) - \psi_{xt} D_x\left(\xi^1\right) - \psi_{xx} D_t\left(\xi^2\right), \\ \eta^{xxt} &= D_x\left(\eta^{xt}\right) - \psi_{xxx} D_x\left(\xi^1\right) - \psi_{xxt} D_x\left(\xi^2\right), \end{aligned} \tag{8}$$

where D_i is the total differentiation operator [34] with respect to the independent variables x^i $(i = 1, 2$, then $x^1 = x, x^2 = t)$:

$$D_i = \frac{\partial}{\partial x^i} + \sum_{\alpha=1}^{q} \psi_i^{\alpha} \frac{\partial}{\partial \psi^{\alpha}} + \sum_{j=1}^{p} \sum_{\alpha=1}^{q} \psi_{ji}^{\alpha} \frac{\partial}{\partial \psi_j^{\alpha}} + \cdots + \sum_{j_1=1}^{p} \cdots \sum_{j_{n-1}=1}^{p} \sum_{\alpha=1}^{q} \psi_{j1,\ldots,jn-1^i}^{\alpha} \frac{\partial}{\partial \psi_{1,\ldots,jn-1^i}^{\alpha}}. \tag{9}$$

Theorem 1. *Equation (1) concedes a one-parameter group of infinitesimal transformations in equation (2) with the Lie Vector X if and just if the accompanying infinitesimal conditions hold:*

$$\mathrm{Pr}^{(\alpha,3)} X(\Delta)|_{\Delta=0} = 0, \tag{10}$$

where $\Delta = D_t^{\alpha} u - F(t,x,u,u_x,u_{xx},\ldots\ldots)$ *and* Pr *is the 3rd prolongation of the infinitesimal generator X.*

Definition 2. Prolonged vector is given by [31]

$$\mathrm{Pr}^{(n)} X = X + \sum_{i=1}^{p} \sum_{\alpha=1}^{q} \xi_i^{\alpha} \frac{\partial}{\partial u_i^{\alpha}} + \cdots + \sum_{j_{1=1}}^{p} \cdots \sum_{j_n=1}^{p} \sum_{\alpha=1}^{q} \xi_{j_1,\ldots,j_n}^{\alpha} \frac{\partial}{\partial u_{j_1,\ldots,j_n}^{\alpha}}, \tag{11}$$

where q is the numbers of dependent variables, p is the numbers of independent variables, $\partial/\partial u_{j_1}^{\alpha} = \partial/\partial u_x^{\alpha}$, and PDE involve derivatives up to order n. Also, the invariance condition [35] gives

$$\xi^2(t,x,u)|_{t=0} = 0. \tag{12}$$

The αthextended infinitesimal, which deals with fractional derivatives, has the following form [36–38]:

$$\eta_\alpha^0 = \frac{\partial^\alpha \eta}{\partial t^\alpha} + \left(\eta_u - \alpha D_t\left(\xi^2\right)\right)\frac{\partial^\alpha u}{\partial t^\alpha} - u\frac{\partial^\alpha \eta_u}{\partial t^\alpha} + \mu - \sum_{n=1}^{\infty}\binom{\alpha}{n} D_t^n\left(\xi^1\right) D_t^{\alpha-n}\left(u_x\right) + \sum_{n=1}^{\infty}\left[\binom{\alpha}{n}\frac{\partial^n \eta_u}{\partial t^n} - \left[\binom{\alpha}{n+1} D_t^{n+1}\left(\xi^2\right)\right] D_t^{\alpha-n}(u)\right], \tag{13}$$

where

$$\mu = \sum_{n=2}^{\infty}\sum_{m=2}^{n}\sum_{k=2}^{m}\sum_{r=2}^{k-1}\binom{\alpha}{n}\binom{n}{m}\binom{k}{r}\frac{1}{k!} \frac{t^{n-\alpha}}{\Gamma(n+1-\alpha)}[-u]^r \frac{\partial^m}{\partial t^m}\left[u^{k-r}\right]\frac{\partial^{n-m+k}}{\partial t^{n-m}\partial u^k}. \tag{14}$$

Remember that

$$\binom{\alpha}{n} = \frac{(-1)^{n-1}\alpha\Gamma(n-\alpha)}{\Gamma(n-\alpha)\Gamma(n+1)}. \tag{15}$$

Due to linearization of the infinitesimal η in u and the presence of $\partial^k \eta/\partial\psi^k$, μ will vanish, where $k \geq 2$ in equation (14).

Lemma 1. *The function $\psi = \theta(x,t)$ can be defined as an invariant solution of (2) if and only if*

(i)$\psi = \theta(x,t)$ is an invariant surface of equation (2)
(ii)$\xi^2(x,t,\theta)\theta_t + \xi^1(x,t,\theta)\theta_x = \eta(x,t,\theta)$

3. Lie Symmetry and Reduction of FBBM Equation

In this partition, the Lie symmetry reduction method was applied to find the similarity variables for a one-dimensional time (FBBM) equation. Suppose that (1) is an invariant under (2); we have that

$$\overline{\psi}_t^\alpha + \overline{\psi}\overline{\psi}_x + \overline{\psi}_x - \overline{\psi}_{xxt} = 0. \tag{16}$$

Thus, $\psi(x,t)$ satisfies equation (1). Applying the third prolongation to (1), we have the accompanying deciding condition, which is given as

$$\eta_\alpha^0 + \psi_x\eta + (\psi+1)\eta^x - \eta^{xxt} = 0. \tag{17}$$

Substituting (7) and (8) into (16) and equaling coefficients in derivatives for x and power of u to zero, the system of equations is obtained:

$$\begin{aligned}
&\binom{\alpha}{n}\partial_t^n \eta_\psi - \binom{\alpha}{n+1} D_t^{n+1}\left(\xi^2\right) = 0, \quad n = 1,2,3\ldots.,\\
&\xi_\psi^2 = \xi_x^2 = \xi_\psi^1 = \xi_t^1 = \eta_{\psi\psi} = 0,\\
&(1-\alpha)\xi_t^2 + 2\xi_x^1 = 0,\\
&\psi\eta_x - \eta_{xxt} + \partial_t^\alpha \eta - \psi\partial_t^\alpha \eta_\psi + \eta_x = 0,\\
&2\xi_{xt}^1 - \eta_{t\psi} = 0.
\end{aligned} \tag{18}$$

By solving the obtained equations in (18), we get the following infinitesimal:

$$\begin{aligned}
\xi^1 &= c_1 + (\alpha-1)c_2 x,\\
\xi^2 &= 2c_2 t,\\
\eta &= -(\alpha+1)c_2(\psi+1),
\end{aligned} \tag{19}$$

where c_1 and c_2 are constants. By the previous infinitesimal, equation (1) has two vector fields in the form

$$X_1 = \frac{\partial}{\partial x}, \tag{20a}$$

$$X_2 = (\alpha-1)x\frac{\partial}{\partial x} + 2t\frac{\partial}{\partial t} - (\alpha+1)(\psi+1)\frac{\partial}{\partial \psi}. \tag{20b}$$

Case 1. For the infinitesimal generator in (20a), we have a characteristic equation in the following form:

$$\frac{dx}{1} = \frac{dt}{0} = \frac{d\psi}{0}. \tag{21}$$

By solving the previous equation, we get the variables t and ψ. Putting $\psi = f(t)$ into (1), we obtain the following fractional ODE:

$$D_t^\alpha f(t) = 0. \tag{22}$$

By solving the above equation, we obtain

$$\psi = a_1 t^{\alpha-1}, \tag{23}$$

where a_1 is constant of integration.

Case 2. For X_2 in equation (20b), the similarity variables for the infinitesimal generator X_2 can be obtained from the equation:

$$\frac{\mathrm{d}x}{(\alpha-1)x} = \frac{\mathrm{d}t}{2t} = -\frac{\mathrm{d}\psi}{(\alpha+1)(\psi+1)}. \tag{24}$$

The previous equation is called the characteristic equation; by solving it, we have the similarity variable as a result in the form:

$$\xi = xt^{-((\alpha-1)/2)}. \tag{25}$$

The group invariant solution

$$\psi(x,t) = t^{-((\alpha+1)/2)} f(\xi) - 1 = g(\xi) - 1, \tag{26}$$

where $f(\xi)$ is a new arbitrary function of ξ and $g(\xi) = t^{-((\alpha+1)/2)} f(\xi)$. By using equation (26), equation (1) is transformed into FODE.

Theorem 3. *The transformation in (25) and (26), which is obtained from the similarity group method, reduces equation (1) to NLFODE as below:*

$$\left(P_{2/\alpha-1}^{(1/2)-(3\alpha/2),\alpha} f\right)(\xi) - \frac{t^{(\alpha+1)/2}}{\Gamma(1-\alpha)} + \left(\frac{-3}{2}\alpha + \frac{1}{2}\right) f_{\xi\xi} - \left(\frac{1}{2}\alpha - \frac{1}{2}\right) f_{\xi\xi\xi} = 0. \tag{27}$$

Using the operator EK fractional differential operator [32, 34],

$$\left(P_{\beta}^{\xi^2,\alpha} f\right)(\xi) = \prod_{j=0}^{n-1}\left(\xi^2 + j - \frac{1}{\beta}\frac{d}{d\xi}\right)\left(K_{\beta}^{\xi^2+\alpha,n-\alpha} f\right)(\xi), \tag{28}$$

$$n = \begin{cases} [\alpha] + 1, & \alpha \neq N, \\ \alpha, & \alpha \in N, \end{cases} \tag{29}$$

where

$$\left(K_{\beta}^{\xi^2,\alpha} f\right)(\xi) = \begin{cases} \frac{1}{\Gamma(\alpha)} \int_1^{\infty} (\psi - 1)^{\alpha-1} \psi^{-(\xi^2+\alpha)} f\left(\xi\psi^{1/\beta}\right) d\psi, & \alpha > 0, \\ f(\xi), & \alpha = 0. \end{cases} \tag{30}$$

Proof. Let $n-1 < \alpha \leq 1$, $n = 1, 2, 3, 4, \ldots$. Depending on the Riemann–Liouville (RL) derivatives, definitions, and similarity variables in (25) and (26), we obtain

$$D_t^{\alpha} g(\xi) = \frac{\partial^n}{\partial t^n}\left[\frac{1}{\Gamma(n-\alpha)} \int_0^t (t-s)^{n-\alpha-1} s^{-((\alpha+1)/2)} f\left(xs^{((1-\alpha)/2)}\right) \mathrm{d}s\right]. \tag{31}$$

Let $v = t/s$ and $\mathrm{d}s = -(t/v^2)\mathrm{d}v$. Thus, (31) becomes

$$D_t^{\alpha} g(\xi) = \frac{\partial^n}{\partial t^n}\left[t^{n-((3\alpha+1)/2)} \frac{1}{\Gamma(n-\alpha)} \int_1^{\infty} (v-1)^{n-\alpha-1} \cdot v^{-(n+((-3\alpha+1)/2))} f\left(\xi v^{(\alpha-1/2)}\right) \mathrm{d}v\right]. \tag{32}$$

Substitute the EK fractional operator in (30) into (32), we have

$$D_t^{\alpha} g(\xi) = \frac{\partial^n}{\partial t^n}\left[t^{n-((3\alpha+1)/2)} \left(K_{(2/\alpha-1)}^{(1-\alpha)/2,n-\alpha} f\right)(\xi)\right]. \tag{33}$$

For simplicity, let $\xi = xt^{-((\alpha-1)/2)}$ and $\phi \in (0, \infty)$; we acquire.

$t\,(\partial/\partial t)\phi(\xi) = tx(-((\alpha-1)/2))t^{-((\alpha-1)/2)-1}\phi\prime(\xi) = -((\alpha-1)/2)\xi(\partial/\partial\xi)\phi(\xi)$. Hence, equation (33) will be rewritten as

$$\begin{aligned} &\frac{\partial^n}{\partial t^n}\left[t^{n-((3\alpha+1)/2)} \left(K_{2/(\alpha-1)}^{(1-\alpha)/2,n-\alpha} f\right)(\xi)\right] \\ &= \frac{\partial^{n-1}}{\partial t^{n-1}}\left[\frac{\partial}{\partial t}\left[t^{n-((3\alpha+1)/2)} \left(K_{2/(\alpha-1)}^{(1-\alpha)/2,n-\alpha} f\right)(\xi)\right]\right] \\ &= \frac{\partial^{n-1}}{\partial t^{n-1}}\left[t^{n-((3\alpha+1)/2)-1}\left(n - \left(\frac{3\alpha+1}{2}\right) - \frac{(\alpha-1)}{2}\xi\frac{\partial}{\partial\xi}\right) \cdot \left(K_{2/(\alpha-1)}^{(1-\alpha)/2,n-\alpha} f\right)(\xi)\right]. \end{aligned} \tag{34}$$

Repeating $n-1$ times, we have

$$\begin{aligned} &\frac{\partial^n}{\partial t^n}\left[t^{n-((3\alpha+1)/2)} \left(K_{2/(\alpha-1)}^{(1-\alpha)/2,n-\alpha} f\right)(\xi)\right] \\ &= \frac{\partial^{n-1}}{\partial t^{n-1}}\left[\frac{\partial}{\partial t}\left[t^{n-((3\alpha+1)/2)} \left(K_{2/(\alpha-1)}^{(1-\alpha)/2,n-\alpha} f\right)(\xi)\right]\right] \\ &= \frac{\partial^{n-1}}{\partial t^{n-1}}\left[t^{n-((3\alpha+1)/2)-1}\left(n - \left(\frac{3\alpha+1}{2}\right) - \frac{(\alpha-1)}{2}\xi\frac{\partial}{\partial\xi}\right) \left(K_{2/(\alpha-1)}^{(1-\alpha)/2,n-\alpha} f\right)(\xi)\right] \\ &\vdots \\ &= t^{-((3\alpha+1)/2)} \prod_{j=0}^{n-1}\left[\left(j - \left(\frac{3\alpha-1}{2}\right) - \frac{(\alpha-1)}{2}\xi\frac{\partial}{\partial\xi}\right) \left(K_{2/(\alpha-1)}^{(1-\alpha)/2,n-\alpha} f\right)(\xi)\right]. \end{aligned} \tag{35}$$

Using the definition of EK fractional differential operator in (28) to rewrite (35), we obtain

$$D_t^{\alpha} g(\xi) = t^{-(3\alpha+1)/2}\left(P_{2/(\alpha-1)}^{(-(3\alpha+1))/2,\alpha} f\right)(\xi). \tag{36}$$

□

Remark 1. The fractional derivative must achieve the linearization property [37, 39]:

$$D_t^{\alpha}(h(t) + k(t)) = D_t^{\alpha}(h(t)) + D_t^{\alpha}(k(t)), \tag{37}$$

$$D_t^{\alpha} t^{\gamma} = \frac{\Gamma(\gamma+1)t^{\gamma-\alpha}}{\Gamma(\gamma-\alpha+1)}, \quad \gamma > \alpha - 1. \tag{38}$$

Using the invariant group solution in (26), (37), and (38), we obtain

$$D_t^{\alpha}\psi(x,t) = D_t^{\alpha} g(\xi) - D_t^{\alpha}(1). \tag{39}$$

Hence,

$$D_t^{\alpha}\psi(x,t) = t^{-(3\alpha+1)/2}\left(P_{(2/\alpha-1)}^{(-(3\alpha+1))/2,\alpha} f\right)(\xi) - \frac{t^{-\alpha}}{\Gamma(1-\alpha)}. \tag{40}$$

Thus, (1) can be reduced to

$$\left(P_{2/(\alpha-1)}^{(1/2)-(3\alpha/2),\alpha} f\right)(\xi) - \frac{t^{(\alpha+1)/2}}{\Gamma(1-\alpha)} + \left(\frac{-3}{2}\alpha + \frac{1}{2}\right) f_{\xi\xi} - \left(\frac{1}{2}\alpha - \frac{1}{2}\right)\xi f_{\xi\xi\xi} = 0, \tag{41}$$

and the theorem is totally proofed.

4. Explicit Solutions for FBBM Equation

4.1. Clarifications for the Subequation Method. The subequation method [39] is presented in this section. Consider the NLFPDE in the form

$$P\left(\psi, \psi_t, \psi_x, D_t^\alpha \psi, D_x^\alpha \psi, \ldots,\right), \quad (0 < \alpha \leq 1), \tag{42}$$

where ψ is a dependent variable, P is a series of ψ and its fractional derivatives, and $D_t^\alpha \psi$ and $D_x^\alpha \psi$ are the Riemann–Liouville (RL) derivatives of ψ w.r.t t and x. Here, we present the principles for the subequation technique. By using the d'Alembert transformation,

$$\psi(x,t) = \psi(\zeta), \quad \zeta = x + ct, \tag{43}$$

where c is constant that will be determined later, and we can rewrite (41) as NLFODE:

$$P\left(\psi, c\psi', \psi'', c^\alpha D_\zeta^\alpha \psi, D_\zeta^\alpha \psi, \ldots,\right), \quad (0 < \alpha \leq 1). \tag{44}$$

According to the subequation procedure, assume that the wave solution will be written in the following form:

$$\psi(\zeta) = a_0 + \sum_{i-1}^{n} a_i \phi(\zeta)^i, \tag{45}$$

where a_i, ($i = 1, \ldots, n$) are constants, which will be determined later, n belongs to integers numbers, which are determined by equaling the highest order derivatives and nonlinear terms in (44) together, and the function $\phi(\zeta)$ achieves the Riccati equation of fractional order

$$D_\zeta^\alpha \phi(\zeta) = \sigma + \phi(\zeta)^2, \tag{46}$$

where σ is a constant. Some trigonometric solutions of the fractional Riccati equation (46) are

$$\phi(\zeta) = \begin{cases} -\sqrt{-\sigma}\, \tan h_\alpha(\sqrt{-\sigma}\,\zeta), & \sigma < 0, \\ -\sqrt{-\sigma}\, \cot h_\alpha(\sqrt{-\sigma}\,\zeta), & \sigma < 0, \\ \sqrt{\sigma} \tan_\alpha(\sqrt{\sigma}\,\zeta), & \sigma > 0, \\ -\sqrt{\sigma} \cot_\alpha(\sqrt{\sigma}\,\zeta), & \sigma > 0, \\ \dfrac{-\Gamma(1+\alpha)}{\zeta^\alpha + w}, & w = \text{constant}, \sigma = 0. \end{cases} \tag{47}$$

By substituting forms (45) into (44) and setting the coefficients of $\phi(\zeta)$ to be zero, we obtain an algebraic system in a_i, ($i = 1, \ldots, n$)and c. By solving the determinate system, we obtain the constants a_i, ($i = 1, \ldots, n$) and c. Substituting these constants and the solutions of (47) into (45), we obtain the closed form solutions of (42).

4.2. Applying the Subequation Method to the Time FBBM Equation. We now implement a subequation method to (1). We will use the transformation

$$\psi(x,t) = \psi(\zeta), \quad \zeta = x + ct, \tag{48}$$

where c is a constant, and this will transform (1) into an NLFODE:

$$c^\alpha D_\zeta^\alpha \psi = -\psi_\zeta - \psi\psi_\zeta + C\psi_{\zeta\zeta\zeta}. \tag{49}$$

We now assume that (49) has the solution in the form

$$\psi(\zeta) = a_0 + \sum_{i-1}^{n} a_i \phi(\zeta)^i, \tag{50}$$

where a_i ($i = 1, ..., n$) are constants, which will be determined, and $\phi(\zeta)$ achieves equation (46).

Balancing the highest order derivative terms with nonlinear terms in equation (49), we obtain $n = 2$. Hence,

$$\psi(\zeta) = a_0 + a_1\phi(\zeta) + a_2\phi(\zeta)^2. \tag{51}$$

We then substitute (51) along with (46) into (49), then collect the coefficients of $\phi(\zeta)$, and set them to equal zero. A set of algebraic equations are obtained in knowns c, a_0, a_1, and a_2. Solving these algebraic equations with the help of the software program (Maple), we get the following values.

Thus, from (47), we obtain five forms of explicit travelling wave solutions of (1), namely,

$$\begin{aligned} c &= \frac{1}{12}\sigma, \\ \sigma &= \sigma, \\ a_0 &= -c^\alpha - 1 + \frac{2}{3}\sigma^2, \\ a_1 &= 0, \\ a_2 &= \sigma. \end{aligned} \tag{52}$$

Thus, from (47), we obtain five forms of explicit travelling wave solutions of (1), namely,

$$\psi_1(x,t) = a_0 + \sigma\left(-\sqrt{-\sigma}\, \tan h_\alpha(\sqrt{-\sigma}\,(x+ct))\right)^2, \quad \sigma < 0, \tag{53}$$

$$\psi_2(x,t) = a_0 + \sigma\left(-\sqrt{-\sigma}\, \cot h_\alpha(\sqrt{-\sigma}\,(x+ct))\right)^2, \quad \sigma < 0, \tag{54}$$

$$\psi_3(x,t) = a_0 + \sigma\left(\sqrt{\sigma} \tan_\alpha(\sqrt{\sigma}\,(x+ct))\right)^2, \quad \sigma > 0, \tag{55}$$

$$\psi_4(x,t) = a_0 + \sigma\left(-\sqrt{\sigma} \cot_\alpha(\sqrt{\sigma}\,(x+ct))\right)^2, \quad \sigma > 0, \tag{56}$$

$$\psi_5(x,t) = a_0 + \sigma\left(\frac{-\Gamma(1+\alpha)}{(x+ct)^\alpha + w}\right)^2, \quad \sigma = 0, \tag{57}$$

where a_0 is arbitrary constant. We plot the result in equation (57) in the three dimensions, contour plot, and density plot, as shown in Figures 1–3, respectively.

4.3. Applying Simple Transformation. We solve the conformable FBBM equation using simple transformation to change the fraction order in partial derivative to nonsolvable ODE. For the reduction of (1) to ODE, we use the following transformation:

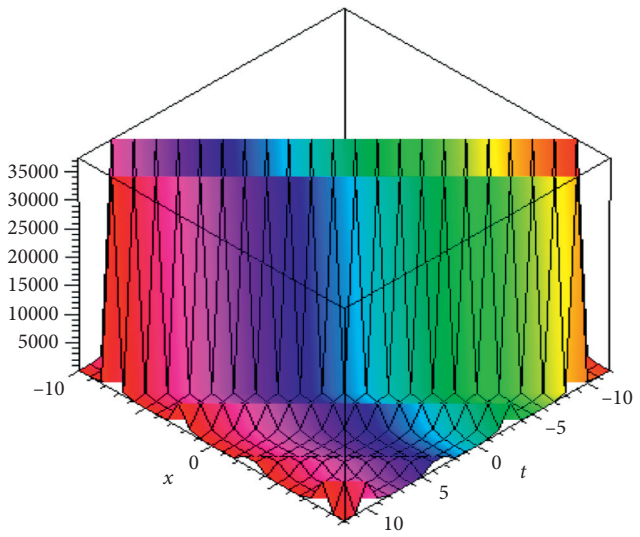

Figure 1: 3D plot for (57) with $\sigma = 10$ and $\alpha = 0.75$.

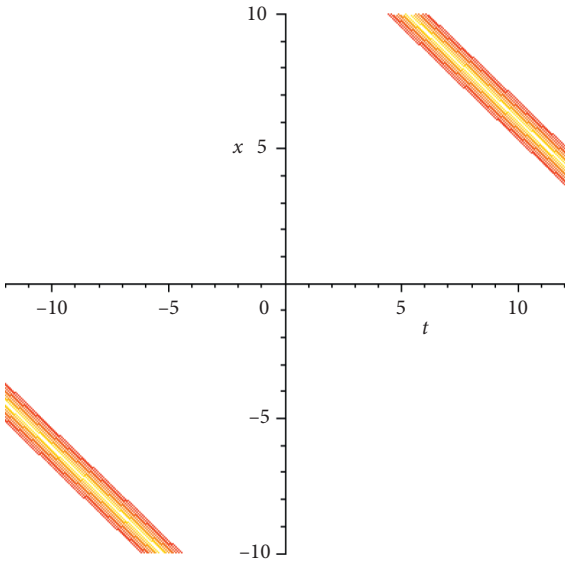

Figure 2: Contour plot of (57) at $\sigma = 10$ and $\alpha = 0.75$.

$$\psi(x,t) = \psi(\zeta), \quad \text{where} \zeta = vx - k\frac{t^{\alpha}}{\alpha}, \tag{58}$$

where v and k are arbitrary constants; we can rewrite (1) as NLODE:

$$kv^2\psi_{\zeta\zeta\zeta} = (k - v)\psi_{\zeta} - v\psi\psi_{\zeta}. \tag{59}$$

This equation has no implicit solution but possesses two integrating factors. We apply the integrating factor technique to obtain an analytical solution for (59).

Equation (59) has two integrating factors (IF) as follows:

$$\begin{aligned} \mu_1 &= \psi(\zeta), \\ \mu_2 &= 1. \end{aligned} \tag{60}$$

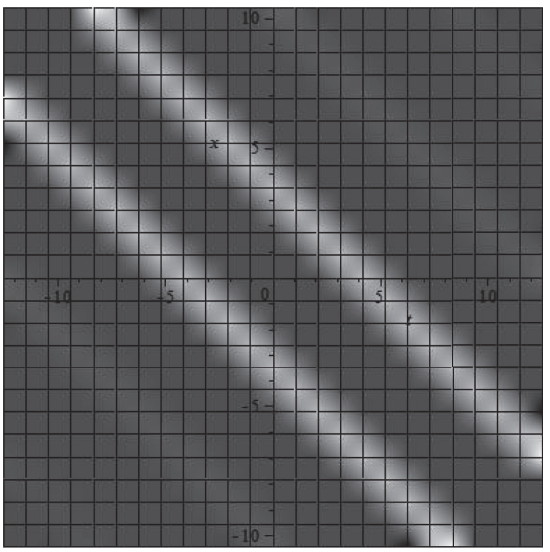

Figure 3: Density plot of (57) at $\sigma = 10$ and $\alpha = 0.75$.

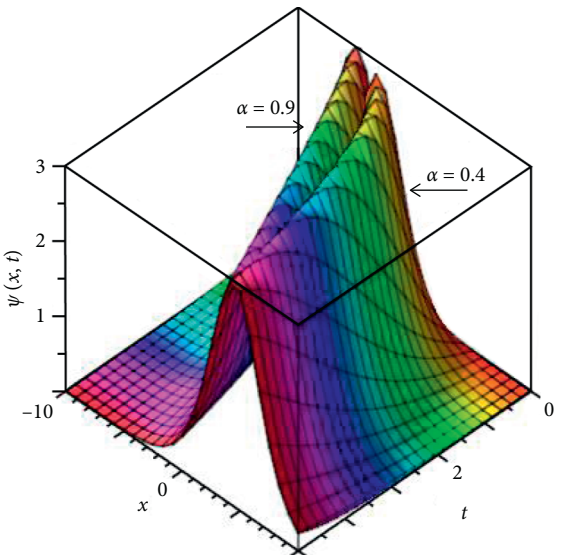

Figure 4: $\psi(x,t)$ at $c = 1, v = -1, k = 1$, and $\alpha = 0.4, 0.9$.

Using these integrating factors by the same steps in [39] and neglecting the constants of integration, equation (59) will be reduced to

$$3kv^2\left(\psi_{\zeta}\right)^2 = 3(k - v)\psi^2 - v\psi^3. \tag{61}$$

By solving this equation, we obtain travelling wave solution for (1):

$$\psi(\zeta) = \frac{1}{v}\left(3\left(-v\tan\left(\frac{1}{2}\frac{\sqrt{-k^2 + kv}\,(-\zeta + c)}{kv}\right)^2 + k - v + k\tan\left(\frac{1}{2}\frac{\sqrt{-k^2 + kv}\,(-\zeta + c)}{kv}\right)^2\right)\right). \tag{62}$$

Replacing $\zeta = \nu x - k(t^{\alpha}/\alpha)$,

$$\psi(x,t) = \frac{1}{\nu}\left(3\left(-\nu\tan\left(\frac{1}{2}\frac{\sqrt{-k^2+k\nu}\,(-\nu x + k(t^{\alpha}/\alpha)+c)}{k\nu}\right)\right)^2 + k - \nu + k\tan\left(\frac{1}{2}\frac{\sqrt{-k^2+k\nu}\,(-\nu x + k(t^{\alpha}/\alpha)+c)}{k\nu}\right)^2\right). \tag{63}$$

In other manner, equation (59) have two Lie vectors. The first one of them reduces it to

$$f_{rr} = \frac{-(f_r)^2}{f} - \frac{-k+\nu+kr}{k\nu^2 f}, \quad \text{where, } f = \psi_{\zeta}, r = \psi. \tag{64}$$

Equation (64) has closed form solution, but, in the back substitution step, we are unable to get $\psi(x,t)$ even if we neglect the values of constants. So, from here, we can say the integrating factor method for reducing and solve ODEs, occasionally, more effectiveness than the Lie reduction method. Result obtained in (63) is plotted in Figure 4 at different values of α. We observe that, by decreasing the value of α, the top of the wave has a parabolic shape.

Comparing our result in (63) with results in [5], specially equation (17), we find that the two solutions are travelling wave solutions, but the amplitude and direction of flow are different.

5. Conclusions

In this paper, we show the importance and the effective of the Lie symmetry reduction method on the FBBM equations. We obtain time FBBM equation's Lie symmetry generators and then reduce the equation to FODE using these symmetry vectors. The projected analysis is extremely effective and dependable for getting similarity solutions for fractional differential equations. New travelling solutions were derived for the FBBM equation using the subequation method.

Data Availability

The data used to support the findings of this study are available from the corresponding author upon request.

Conflicts of Interest

The authors declare that they have no conflicts of interest.

References

[1] N. Savaissou, B. Gambo, H. Rezazadeh, A. Bekir, and S. Y. Doka, "Exact optical solitons to the perturbed nonlinear Schrödinger equation with dual-power law of nonlinearity," *Optical and Quantum Electronics*, vol. 52, no. 6, p. 318, 2020.

[2] W. Gao, H. Rezazadeh, Z. Pinar, H. M. Baskonus, S. Sarwar, and G. Yel, "Novel explicit solutions for the nonlinear Zoomeron equation by using newly extended direct algebraic technique," *Optical and Quantum Electronics*, vol. 52, no. 1, p. 52, 2020.

[3] N. Raza, U. Afzal, A. R. Butt, and H. Rezazadeh, "Optical solitons in nematic liquid crystals with Kerr and parabolic law nonlinearities," *Optical and Quantum Electronics*, vol. 51, no. 4, p. 107, 2019.

[4] H. Rezazadeh, A. Korkmaz, M. Eslami, and S. M. Mirhosseini-Alizamini, "A large family of optical solutions to Kundu–Eckhaus model by a new auxiliary equation method," *Optical and Quantum Electronics*, vol. 51, no. 3, p. 84, 2019.

[5] Korkmaz, A., Exact solutions to some conformable time fractional equations in Benjamin-Bona-Mahony family, 2016.

[6] M. R. Ali and W.-X. Ma, "New exact solutions of Bratu Gelfand model in two dimensions using Lie symmetry analysis," *Chinese Journal of Physics*, vol. 65, pp. 198–206, 2020.

[7] M. R. Ali and W.-X. Ma, "New exact solutions of nonlinear (3 + 1)-dimensional boiti-leon-manna-pempinelli equation," *Advances in Mathematical Physics*, vol. 2019, no. 34, 7 pages, 2019.

[8] M. R. Ali and D. Baleanu, "Haar wavelets scheme for solving the unsteady gas flow in four-dimensional," *Thermal Science*, vol. 24, no. 2 Part B, pp. 1357–1367, 2019.

[9] M. R. Ali, "A truncation method for solving the time-fractional benjamin-ono equation," *Journal of Applied Mathematics*, vol. 2019, no. 18, 7 pages, 2019.

[10] M. R. Ali and A. R. Hadhood, "Hybrid orthonormal bernstein and block-pulse functions wavelet scheme for solving the 2D Bratu problem," *Results in Physics*, vol. 12, pp. 525–530, 2019.

[11] R. Saleh, R. Sadat, and M. Kassem, "Optimal solutions of a (3 + 1)-dimensional B-Kadomtsev-Petviashvii equation," *Mathematical Methods in the Applied Sciences*, vol. 43, no. 4, pp. 1775–1787, 2020.

[12] Z. Sabir, H. A. Wahab, M. Umar, M. G. Sakar, and M. A. Z. Raja, "Novel design of Morlet wavelet neural network for solving second order Lane-Emden equation," *Mathematics and Computers in Simulation*, vol. 172, pp. 1–14, 2020.

[13] Z. Sabir, H. A. Wahab, M. Umar, and F. Erdoğan, "Stochastic numerical approach for solving second order nonlinear singular functional differential equation," *Applied Mathematics and Computation*, vol. 363, Article ID 124605, 2019.

[14] Z. Sabir, F. Amin, D. Pohl, and J. L. G. Guirao, "Intelligence computing approach for solving second order system of Emden-Fowler model," *Journal of Intelligent & Fuzzy Systems*, vol. 38, no. 6, pp. 7391–7406, 2020.

[15] B. Ahmad, S. K. Ntouyas, and A. Alsaedi, "On a coupled system of fractional differential equations with coupled nonlocal and integral boundary conditions," *Chaos, Solitons & Fractals*, vol. 83, pp. 234–241, 2016.

[16] A. I. Aliyu and M. Al-Qurashi, "Invariant subspace and approximate analytic solutions of a fractional model of convective longitudinal fins in thermal conductivity," *The European Physical Journal Plus*, vol. 134, no. 9, p. 417, 2019.

[17] T. F. Nonnenmacher and R. Metzler, "Nonnenmacher and ralf metzler, on the riemann-liouville fractional calculus and some recent applications," *Fractals*, vol. 3, no. 3, pp. 557–566, 1995.

[18] A. I. Aliyu, A. S. Alshomrani, Y. Li, M. Inc, and D. Baleanu, "Existence theory and numerical simulation of HIV-I cure model with new fractional derivative possessing a non-singular kernel," *Advances in Difference Equations*, vol. 2019, no. 1, p. 408, 2019.

[19] B. Lu, "Bäcklund transformation of fractional Riccati equation and its applications to nonlinear fractional partial differential equations," *Physics Letters A*, vol. 376, no. 28-29, pp. 2045–2048, 2012.

[20] A. Isa Aliyu, Y. Li, M. Inc, and D. Baleanu, "Invariant subspaces, exact solutions and classification of conservation laws for a coupled (1 + 1)-dimensional nonlinear Wu-Zhang equation," *Physica Scripta*, vol. 95, no. 3, 2020.

[21] K. Oldham and J. Spanier, *The Fractional Calculus Theory and Applications of Differentiation and Integration to Arbitrary Order*, Elsevier, Amsterdam, Netherlands, 1974.

[22] K. Shah, H. Khalil, and R. A. Khan, "Investigation of positive solution to a coupled system of impulsive boundary value problems for nonlinear fractional order differential equations," *Chaos, Solitons & Fractals*, vol. 77, pp. 240–246, 2015.

[23] D. Baleanu, M. Inc, A. Yusuf et al., "Lie symmetry analysis, exact solutions and conservation laws for the time fractional modified Zakharov-Kuznetsov equation," *Nonlinear Analysis: Modelling and Control*, vol. 22, no. 6, pp. 861–876, 2017.

[24] D. Baleanu, M. Inc, A. Yusuf, and A. I. Aliyu, "Lie symmetry analysis, exact solutions and conservation laws for the time fractional Caudrey-Dodd-Gibbon-Sawada-Kotera equation," *Communications in Nonlinear Science and Numerical Simulation*, vol. 59, pp. 222–234, 2018.

[25] G.-W. Wang, X.-Q. Liu, and Y.-Y. Zhang, "Lie symmetry analysis to the time fractional generalized fifth-order KdV equation," *Communications in Nonlinear Science and Numerical Simulation*, vol. 18, no. 9, pp. 2321–2326, 2013.

[26] M. Inc, A. Yusuf, A. I. Aliyu, and D. Baleanu, "Time-fractional Cahn–Allen and time-fractional Klein–Gordon equations: lie symmetry analysis, explicit solutions and convergence analysis," *Physica A: Statistical Mechanics and Its Applications*, vol. 493, pp. 94–106, 2018.

[27] Q. Feng and F. Meng, "Traveling wave solutions for fractional partial differential equations arising in mathematical physics by an improved fractional Jacobi elliptic equation method," *Mathematical Methods in the Applied Sciences*, vol. 40, no. 10, pp. 3676–3686, 2017.

[28] O. Kolebaje and O. Popoola, "Assessment of the exact solutions of the space and time fractional benjamin-bona-mahony equation via the-expansion method, modified simple equation method, and liu's theorem," *ISRN Mathematical Physics*, vol. 2014, Article ID 217184, 11 pages, 2014.

[29] J. A. Pava, "Stability properties of solitary waves for fractional KdV and BBM equations," *Nonlinearity*, vol. 31, no. 3, pp. 920–956, 2018.

[30] B. Zheng, "A new fractional Jacobi elliptic equation method for solving fractional partial differential equations," *Advances in Difference Equations*, vol. 2014, no. 1, p. 228, 2014.

[31] S. S. Ray and S. Sahoo, "Invariant analysis and conservation laws of $(2+1)$ dimensional time-fractional ZK–BBM equation in gravity water waves," *Computers & Mathematics with Applications*, vol. 75, no. 7, pp. 2271–2279, 2018.

[32] G.-W. Wang and T.-Z. Xu, "Invariant analysis and exact solutions of nonlinear time fractional Sharma-Tasso-Olver equation by Lie group analysis," *Nonlinear Dynamics*, vol. 76, no. 1, pp. 571–580, 2014.

[33] R. Gazizov, A. Kasatkin, and S. Y. Lukashchuk, "Continuous transformation groups of fractional differential equations," *Vestnik Usatu*, vol. 9, no. 3, p. 21, 2007.

[34] P. J. Olver, *Applications of Lie Groups to Differential Equations*, Springer Science & Business Media, Berlin, Germany, 2000.

[35] G. F. Jefferson and J. Carminati, "FracSym: automated symbolic computation of Lie symmetries of fractional differential equations," *Computer Physics Communications*, vol. 185, no. 1, pp. 430–441, 2014.

[36] R. Khalil, M. Al Horani, A. Yousef, and M. Sababheh, "A new definition of fractional derivative," *Journal of Computational and Applied Mathematics*, vol. 264, pp. 65–70, 2014.

[37] V. S. Kiryakova, *Generalized Fractional Calculus and Applications*, CRC Press, Boca Raton, FL, USA, 1993.

[38] M. Eslami and H. Rezazadeh, "The first integral method for Wu-Zhang system with conformable time-fractional derivative," *Calcolo*, vol. 53, no. 3, pp. 475–485, 2016.

[39] S. Zhang and H.-Q. Zhang, "Fractional sub-equation method and its applications to nonlinear fractional PDEs," *Physics Letters A*, vol. 375, no. 7, pp. 1069–1073, 2011.

Hindawi
Complexity
Volume 2020, Article ID 3435018, 5 pages
https://doi.org/10.1155/2020/3435018

WILEY | Hindawi

Research Article

Entropy Schemes for One-Dimensional Convection-Diffusion Equations

Rongsan Chen

School of Mathematics and Physics, China University of Geosciences, Wuhan 430074, China

Correspondence should be addressed to Rongsan Chen; rchen@cug.edu.cn

Received 25 June 2020; Accepted 20 July 2020; Published 31 July 2020

Guest Editor: Karthikeyan Rajagopal

In this paper, we extend the entropy scheme for hyperbolic conservation laws to one-dimensional convection-diffusion equation. The operator splitting method is used to solve the convection-diffusion equation that is divided into conservation and diffusion parts, in which the first-order accurate entropy scheme is applied to solve the conservation part and the second accurate central difference scheme is applied to solve the diffusion part. Numerical tests show that the L^{∞} error achieves about second-order accuracy, but the L^{1} error reaches about forth-order accuracy.

1. Introduction

In this paper, we consider the convection-diffusion equation:

$$u_t + f(u)_x = (A(u))_{xx} + c(x,t), \tag{1}$$

where $A'(u) \geq 0$. Many researchers have developed numerical methods for the convection-diffusion equation and have obtained some superconvergence results [1, 2].

In [3], Li has developed the entropy scheme which contains numerical solution and numerical entropy to compute the linear advection equation. The numerical tests showed that it can achieve very good accuracy and is suitable for long-time computation of smooth solutions. Yanfen and De-Kang investigated the truncation error for the entropy scheme and showed the entropy scheme has superconvergent property in [4]. However, when computing discontinuous solutions, spurious oscillations occurred in the vicinity of the discontinuities. In order to eliminate the spurious oscillations, an entropy-ultra-bee scheme was presented by Li and Mao for computing the linear advection equation. In essence, entropy-ultra-bee scheme is a combination of the entropy scheme and the ultra-bee scheme which can obtain good resolution in smooth regions and sharpen the discontinuity. In [5], Chen and Mao extended the entropy scheme to the nonlinear scalar conservation laws and presented the entropy-TVD scheme. In [6], Cui and Mao extended the entropy scheme to the KdV equation. The scheme is second-order, but the numerical results showed that the scheme has a third-order convergence rate away from extrema. Furthermore, the scheme suits for long-time numerical computing. Chen et al. generalize the entropy-TVD scheme for the one-dimensional shallow water equations in [7]. The entropy scheme was extended to the Euler system in [8, 9].

The significance of the entropy scheme is in methodology. The original Godunov scheme is first-order accurate [10]. Traditional ways to extend it to high-order schemes are to use high-order interpolations in the solution reconstruction in each cell, assuming that the solution is smooth [11–19]. The schemes so developed are no more local as the original Godunov scheme. Different limiting technologies, such as TVD, ENO, and WENO, are then used to eliminate numerical oscillations caused by the presence of discontinuities. Different from the above approach, our scheme numerically computes more physical quantities, which are algebraically related with one another in each cell. The scheme then uses them to reconstruct the solution in the cell by enforcing the algebraic relations among them, with certain TVD limiting to maintain the stability. In doing so, the smooth assumption on the solution is not necessary.

With the solution reconstructed in this way, the numerical errors accumulate in the fashion that the local truncation errors in two successive time steps cancel each other, and this leads to the second-order accuracy of the scheme.

With the entropy scheme designed in this way, it maintains to be local as the original Godunov scheme. Since all the principle and augmented quantities have solid physical meanings and the reconstruction satisfies all the physical algebraic relations among them, the reconstructed solution in each cell physically well simulates the exact solution, even the latter is not smooth in the cell. Important physical properties such as the entropy condition and nonnegativity of mass and pressure are maintained in the scheme. Moreover, the numerical dissipations are quantitatively controlled in that they are used only near discontinuities and extremes of the solution.

In this paper, we mainly introduce the idea, and we choose a kind of convection-diffusion equation in one dimension with the convection part as $f(u)$ for simplicity. We do not consider the other kinds of convection-diffusion equation and high order in this paper. In order to extend to high order, we need to replace the step reconstruction with a higher order polynomial and solve generalized Riemann problems, and the algorithm may be very complicated. We use u^2 as the entropy function in this paper, but the scheme can also be executed in other entropy function, such as $u \log u$.

In this paper, we follow [6] and extend the entropy scheme to a kind of convection-diffusion equation in one dimension. The operator splitting method is used to solve the convection-diffusion equation that is divided into conservation and diffusion parts, in which the first-order accurate entropy scheme is applied to solve the conservation part and the second accurate central difference scheme is applied to solve the diffusion part. Numerical tests show that the L^∞ convergence rate approaches the second order and the L^1 convergence rate approaches the forth order along with the mesh refinement.

The outline of the paper is as follows: in Section 2, we give a description for the scheme in detail; in Section 3, the numerical results that show the convergence rate are provided; and finally, Section 4 is the conclusion.

2. Description of the Scheme

We consider the following initial value problem for the convection-diffusion equation:

$$\begin{cases} u_t + f(u)_x = (A(u))_{xx}, \quad 0 \le x \le 2\pi, \\ u(x,0) = u_0(x), \end{cases} \tag{2}$$

where $A'(u) \ge 0$. Suppose a pair of scalar function $(U(u), F(u))$ such that

$$U'(u) f'(u) = F'(u), \quad U''(u) \ge 0. \tag{3}$$

Multiplied by $U'(u)$ in the two sides of equation (2), equation (2) becomes

$$U(u)_t + F(u)_x = U'(u)(A(u))_{xx}. \tag{4}$$

For simplicity, we use uniform cells with the cell size Δx, and we denote the cells centre by x_j and the cells by $(x_{j-1/2}, x_{j+1/2})$. Δt refers to time increment. We use u^n and U^n to represent a cell-average approximation to the true solution and a cell-average approximation to the entropy of the true solution, respectively. u^n and U^n are defined as

$$\begin{aligned} u_j^n &\simeq \frac{1}{\Delta x} \int_{x_{j-1/2}}^{x_{j+1/2}} u(x, t_n) \mathrm{d}x, \\ U_j^n &\simeq \frac{1}{\Delta x} \int_{x_{j-1/2}}^{x_{j+1/2}} U(x, t_n) \mathrm{d}x. \end{aligned} \tag{5}$$

In this way, the solution to equation (2) and its respective numerical solution are both made up of two entities.

2.1. Operator Splitting. As in [6], we use the operator splitting method to solve equation (2). At first, we divide equation (2) into two parts: the conservation part and the diffusion part. Then, we alternately solve the corresponding conservation part and diffusion part. The conservation and diffusion parts of equation (2) are defined, respectively, as

$$\begin{cases} u_t + f(u)_x = 0, \\ U(u)_t + F(u)_x = 0, \\ u(x,0) = u_0(x), U(u(x,0)) = U(u_0(x)), \end{cases} \tag{6}$$

$$\begin{cases} u_t = (A(u))_{xx}, \\ U(u)_t = U'(u)(A(u))_{xx}, \\ u(x,0) = u_0(x), U(u(x,0)) = U(u_0(x)). \end{cases} \tag{7}$$

2.2. Numerical Scheme for Equation (6). The entropy scheme with the half-step reconstruction is used to solve equation (6) (for details, refer to [5, 8]). The entropy scheme proceeds three steps as follows.

2.2.1. Step Reconstruction. A piecewise constant function with a half step is used to reconstruct the solution in each cell:

$$R(x; u^n, U^n) = u_j^n + \begin{cases} -d_j^n, & x_{j-1/2} < x \le x_j, \\ +d_j^n, & x_j < x \le x_{j+1/2}, \end{cases} \tag{8}$$

with d_j^n the half step (HS) of the reconstruction. The reconstruction (8) satisfies

$$\frac{1}{h} \int_{x_{j-1/2}}^{x_{j+1/2}} R(x; u^n, U^n) \mathrm{d}x = u_j^n. \tag{9}$$

In order to compute the HS d_j^n, we require

$$\frac{1}{h} \int_{x_{j-1/2}}^{x_{j+1/2}} U(R(x; u^n, U^n)) \mathrm{d}x = U_j^n, \tag{10}$$

i.e., the entropy cell-average of the reconstructed solution is equal to the numerical entropy in each cell. We can compute d_j^n from equation (10).

2.2.2. Evolution. Solve the initial value problem (IVP) as follows:

$$\begin{cases} v_t + f(v)_x = 0, & t_n < t \le t_{n+1}, \\ v(x, t_n) = R(x; u^n, U^n). \end{cases} \tag{11}$$

For the linear equation, the exact solution to the problem is $R(x-t; u^n, U^n)$. For the nonlinear equation, the approximate solution to the problem can be reconstructed [18]. We denote the solution of (11) as $v(x,t)$.

2.2.3. Cell Averaging. Compute u_j^{n+1} and U_j^{n+1} as in the following:

$$\begin{aligned} u_j^{n+1} &= \frac{1}{h}\int_{x_{j-1/2}}^{x_{j+1/2}} v(x, t_{n+1})\mathrm{d}x, \\ U_j^{n+1} &= \frac{1}{h}\int_{x_{j-1/2}}^{x_{j+1/2}} U(v(x, t_{n+1}))\mathrm{d}x. \end{aligned} \tag{12}$$

In practice, we compute u_j^{n+1} and U_j^{n+1} in the following flux forms:

$$u_j^{n+1} = u_j^n - \lambda\left(\widehat{f}_{j+1/2}^n - \widehat{f}_{j-1/2}^n\right), \tag{13}$$

$$U_j^{n+1} = \frac{1}{h}\int_{x_{j-1/2}}^{x_{j+1/2}} U(R(x; u^n, U^n))\mathrm{d}x - \lambda\left(\widehat{F}_{j+1/2}^n - \widehat{F}_{j-1/2}^n\right), \tag{14}$$

where the numerical flux $\widehat{f}_{j+1/2}^n = f(v(x_{j+1/2}, t))$ and $\widehat{F}_{j+1/2}^n = F(v(x_{j+1/2}, t))$.

2.3. Numerical Scheme for Equation (7). We use central difference to approximate the second derivatives and use the Euler forward time discretization for equation (7). The final scheme has the following form:

$$u_j^{n+1} = u_j^n + \frac{\Delta t}{\Delta x^2}\left(A\left(u_{j+1}^n\right) - 2A\left(u_j^n\right) + A\left(u_{j-1}^n\right)\right), \tag{15}$$

$$U_j^{n+1} = U_j^n + \frac{\Delta t}{\Delta x^2}U'\left(u_j^n\right)\left(A\left(u_{j+1}^n\right) - 2A\left(u_j^n\right) + A\left(u_{j-1}^n\right)\right). \tag{16}$$

We use the operator splitting method so that the initial problem (2) with initial data u^n and U^n is split into two subproblems. One proceeds as follows:

(a) Solve the conservation part of equation (2) with u^n and U^n to obtain a provisional solution u^* and U^* for the next time level.

(b) Solve the diffusion part of equation (2) by using u^* and U^* as initial condition.

This gives the final solution u^{n+1} and U^{n+1} for the new time level $n+1$. From (13), (14), (15), and (16), we can obtain the final scheme in the following:

$$\begin{aligned} u_j^{n+1} &= u_j^n - \lambda\left(\widehat{f}_{j+1/2}^n - \widehat{f}_{j-1/2}^n\right) + \frac{\Delta t}{\Delta x^2}\left(A\left(u_{j+1}^n\right)\right. \\ &\quad \left. - 2A\left(u_j^n\right) + A\left(u_{j-1}^n\right)\right), \\ U_j^{n+1} &= \frac{1}{h}\int_{x_{j-1/2}}^{x_{j+1/2}} U(R(x; u^n, U^n))\mathrm{d}x - \lambda\left(\widehat{F}_{j+1/2}^n - \widehat{F}_{j-1/2}^n\right) \\ &\quad + \frac{\Delta t}{\Delta x^2}U'\left(u_j^n\right)\left(A\left(u_{j+1}^n\right) - 2A\left(u_j^n\right) + A\left(u_{j-1}^n\right)\right). \end{aligned} \tag{17}$$

Remark 1. The entropy scheme described in Section 2.2 for equation (6) is first-order accurate away from extrema [8], and the difference scheme in Section 2.3 for equation (7) is second-order away from extrema.

3. Numerical Experiments

In this section, we use the entropy scheme to compute one-dimensional convection-diffusion equation. In the following, two examples come from [1] and the CFL number is taken to be 0.2.

Example 1. Consider the following initial value problem:

$$\begin{cases} u_t + u_x = \varepsilon u_{xx}, \\ \left(u^2\right)_t + \left(u^2\right)_x = 2uu_{xx}, \\ u(x, 0) = \sin(x), \\ u(0, t) = u(2\pi, t). \end{cases} \tag{18}$$

The exact solution to this problem is

$$u(x,t) = e^{-\varepsilon t}\sin(x - t). \tag{19}$$

We take ε as 1 and 0.01, respectively. We conduct the computation with 20, 40, 80, 160, 320, and 640 cells, respectively; the computational time is $t = 1.0$; and we present the L^1 and L^∞ errors and orders of convergence of $\varepsilon = 1$ in Table 1. We observe that the L^∞ orders of convergence approach the second order and the L^1 orders of convergence approach the forth order along with the mesh refinement. We present the L^1 and L^∞ errors and orders of convergence of $\varepsilon = 0.01$ in Table 2. We can see from Table 2 that the orders of convergence of L^∞ error are greater than 2, and the orders of convergence of L^1 error are greater than 4.

Example 2. Consider the following initial value problem.

$$\begin{cases} u_t + \left(u^2\right)_x = u_{xx} + c(x,t), \\ \left(u^2\right)_t + \left(\frac{4}{3}u^3\right)_x = 2uu_{xx} + 2uc(x,t), \\ u(x, 0) = \sin(x), \\ u(0, t) = u(2\pi, t), \end{cases} \tag{20}$$

Table 1: Example 1, $\varepsilon = 1$, numerical errors and orders of convergence at $t = 1$.

Cells	L^∞ error	Order	L^1 error	Order
10	$1.611E-002$	—	$8.543E-004$	—
20	$6.794E-003$	1.245	$1.244E-004$	2.779
40	$2.249E-003$	1.594	$1.250E-005$	3.315
80	$5.346E-004$	2.072	$7.563E-007$	4.047
160	$1.388E-004$	1.945	$5.398E-008$	3.808
320	$4.017E-005$	1.788	$4.052E-009$	3.735
640	$9.336E-006$	2.105	$2.113E-010$	4.261

Table 2: Example 1, $\varepsilon = 0.01$, numerical errors and orders of convergence at $t = 1$.

Cells	L^∞ error	Order	L^1 error	Order
10	$6.221E-002$	—	$6.749E-003$	—
20	$2.727E-002$	1.189	$1.237E-003$	2.447
40	$1.081E-002$	1.334	$1.563E-004$	2.984
80	$6.226E-003$	0.796	$1.602E-005$	3.286
160	$1.509E-003$	2.044	$7.360E-007$	4.444
320	$2.582E-004$	2.547	$2.784E-008$	4.724
640	$3.933E-005$	2.714	$1.332E-009$	4.385

Table 3: Example 2, numerical errors and orders of convergence at $t = 1$.

Cells	L^∞ error	Order	L^1 error	Order
10	$3.168E-002$	—	$1.629E-003$	—
20	$7.198E-003$	2.137	$1.045E-004$	3.962
40	$2.302E-003$	1.644	$8.759E-006$	3.577
80	$5.877E-004$	1.970	$5.960E-007$	3.877
160	$1.561E-004$	1.912	$3.916E-008$	3.927
320	$4.321E-005$	1.853	$2.640E-009$	3.890
640	$1.222E-005$	1.822	$2.046E-010$	3.689

where $c(x,t) = -e^{-2t}\cos(x-t)(e^t - 2 \quad \sin(x-t))$. The exact solution to this problem is

$$u(x,t) = e^{-t}\sin(x-t). \tag{21}$$

Equation (20) is a convection-diffusion equation with a nonlinear convective term. We conduct the computation with 20, 40, 80, 160, 320, and 640 cells, respectively; the computational time is $t = 1.0$; and we present the L^1 and L^∞ errors and orders of convergence in Table 3. We can see from Table 3 that the L^∞ orders of convergence approach the second order and the L^1 orders of convergence approach the forth order along with the mesh refinement.

4. Conclusions

In this paper, the entropy scheme is extended to one-dimensional of convection-diffusion equation. We divide the convection-diffusion equation into two parts and use the operator splitting method to solve it. The first-order accurate entropy scheme is applied to solve the conservation part, and the second accurate central difference scheme is applied to solve the diffusion part. We have presented two numerical examples, and the numerical results show that the L^∞ orders of convergence approach the second order and the L^1 orders of convergence approach the forth order along with the mesh refinement. As for other kinds of convection-diffusion equation, only minor modifications need to be made to the algorithm. The extension to two dimensions is our future work.

Data Availability

The data used to support the findings of this study are available from the corresponding author upon request.

Conflicts of Interest

The author declares that there are no conflicts of interest.

Acknowledgments

The research was supported by the National Natural Science Foundation of China (no. 11201436) and Fundamental Research Funds for the Central Universities, China University of Geosciences (Wuhan).

References

[1] Y. Cheng and C.-W. Shu, "Superconvergence of local discontinuous galerkin methods for one-dimensional convection-diffusion equations," *Computers & Structures*, vol. 87, no. 11-12, pp. 630–641, 2009.

[2] X. Zhang, Y. Liu, and C.-W. Shu, "Maximum-principle-satisfying high order finite volume weighted essentially nonoscillatory schemes for convection-diffusion equations," *SIAM Journal on Scientific Computing*, vol. 34, no. 2, pp. A627–A658, 2012.

[3] H. Li, "Second-order entropy dissipation scheme for scalar conservation laws in one space dimension," Master's thesis, Shanghai University, Shanghai, China, 2002.

[4] C. Yanfen and M. De-Kang, "Error self-canceling of a difference scheme maintaining two conservation laws for linear advection equation," *Mathematics of Computation*, vol. 81, no. 278, pp. 715–741, 2011.

[5] R. Chen and D.-K. Mao, "Entropy-TVD scheme for nonlinear scalar conservation laws," *Journal of Scientific Computing*, vol. 47, no. 2, pp. 150–169, 2011.

[6] Y. Cui and D.-K. Mao, "Numerical method satisfying the first two conservation laws for the Korteweg-de Vries equation," *Journal of Computational Physics*, vol. 227, no. 1, pp. 376–399, 2007.

[7] R. Chen, M. Zou, and L. Xiao, "Entropy-TVD scheme for the shallow water equations in one dimension," *Journal of Scientific Computing*, vol. 71, no. 2, pp. 822–838, 2017.

[8] H. Li, Z. Wang, and D.-K. Mao, "Numerically neither dissipative nor compressive scheme for linear advection equation and its application to the Euler system," *Journal of Scientific Computing*, vol. 36, no. 3, pp. 285–331, 2008.

[9] R. Chen and D. Mao, "Improved entropy-ultra-bee scheme for the Euler system of gas dynamics," *Journal of Computational Mathematics*, vol. 35, no. 2, pp. 213–243, 2017.

[10] S. K. Godunov, "A finite difference method for computation of discontinuous solutions of the equations of fluid dynamics," *Matematicheskii Sbornik*, vol. 47, pp. 357–393, 1959.

[11] P. Colella, "A direct Eulerian MUSCL scheme for gas dynamics," *SIAM Journal on Scientific and Statistical Computing*, vol. 6, no. 1, pp. 104–117, 1985.

[12] P. Colella and P. Woodward, "The numerical simulation of two-dimensional fluid flow with strong shocks," *Journal of Computational Physics*, vol. 54, no. 1, pp. 115–173, 1984.
[13] P. Colella and P. R. Woodward, "The piecewise parabolic method (PPM) for gas-dynamical simulations," *Journal of Computational Physics*, vol. 54, no. 1, pp. 174–201, 1984.
[14] A. Harten, S. Osher, B. Engquist, and S. R. Chakravarthy, "Some results on uniformly high-order accurate essentially nonoscillatory schemes," *Applied Numerical Mathematics*, vol. 2, no. 3–5, pp. 347–377, 1986.
[15] A. Harten, B. Engquist, S. Osher, and S. R. Chakravarthy, "Uniformly high order accurate essentially non-oscillatory schemes, III," *Journal of Computational Physics*, vol. 71, no. 2, pp. 231–303, 1987.
[16] A. Harten and S. Osher, "Uniformly high-order accurate nonoscillatory schemes. I," *SIAM Journal on Numerical Analysis*, vol. 24, no. 2, pp. 279–309, 1987.
[17] G.-S. Jiang and C.-W. Shu, "Efficient implementation of weighted ENO schemes," *Journal of Computational Physics*, vol. 126, no. 1, pp. 202–228, 1996.
[18] R. J. LeVeque, *Finite Volume Methods for Hyperbolic Problems*, Cambridge University Press, Cambridge, UK, 2002.
[19] C.-W. Shu and S. Osher, "Efficient implementation of essentially non-oscillatory shock-capturing schemes, II," *Journal of Computational Physics*, vol. 83, no. 1, pp. 32–78, 1989.

Hindawi
Complexity
Volume 2020, Article ID 6246808, 12 pages
https://doi.org/10.1155/2020/6246808

Research Article

A One-Sided Competition Mathematical Model for the Sterile Insect Technique

Anis Ben Dhahbi,[1,2] Yassine Chargui,[1,2] Salah Mahmoud Boulaaras,[3,4] and Sana Ben Khalifa[1,5]

[1]*Department of Physics, College of Science and Arts at Ar Rass, Qassim University, P.O. Box 53, Ar Rass 51921, Saudi Arabia*
[2]*Tunis El Manar University, Faculty of Sciences of Tunis, 2092 Tunis, Tunisia*
[3]*Department of Mathematics, College of Science and Arts at Ar Rass, Qassim University, P.O. Box 53, Ar Rass 51921, Saudi Arabia*
[4]*Laboratory of Fundamental and Applied Mathematics of Oran (LMFAO) University of Oran Ahmed Benbella, Oran, Algeria*
[5]*Laboratory of Energy and Materials (LabEM), ESSTHS, University of Sousse, 4011 H. Sousse, Tunisia*

Correspondence should be addressed to Sana Ben Khalifa; sana.benkhalifa19@gmail.com

Received 6 June 2020; Accepted 8 July 2020; Published 30 July 2020

Guest Editor: Karthikeyan Rajagopal

We study a simple mathematical model describing the dynamics of a wild-type pest insects population experiencing competition from sterile insects (one-sided competition). This model can be used for conceiving control strategies based on the Sterile Insect Technique (SIT) or the Incompatible Insect Technique (IIT), aiming to reduce or eradicate Red Palm Weevil (RPW) populations in some target regions. We show that suppression may occur for continuous and periodic release strategies for various intraspecific and interspecific submodels except in the case of a single release strategy where a strong Allee effect is required.

1. Introduction

Over the past few decades, there has been an increasing interest in the effectiveness of the biological methods for the control of insect pests. The aim is to replace the existing insecticide-based control strategies. The SIT is a tool that has proven to be effective in the field for the areawide control of some insects. This method, suggested initially by Knipling [1, 2] and collaborators, relies on the release of a large number of sterilized males, without affecting their ability to mate. These released insects compete for mates with the wild-type males, and any wild-type female inseminated by a sterile male has no progeny. Then, if sufficient sterile males are released for a long enough period, most of the wild-type females in the field mate with the released sterile males and thus produce no viable offspring. The average fertility of the target population could be reduced leading to the control or even in certain situations to the eradication of the pest insects from large areas. The first successful areawide SIT programs have been operated against the screwworm population in Florida in the early 1950s. Since then, the technique has been applied to combat various agricultural pests and disease vectors, such as the Mediterranean fruit fly (medfly), the RPW in coconut and date palm gardens, and the tsetse fly in Africa (see Ref. [3] for a general review of the SIT and its applications). Given the experienced efficiency of the SIT, it is now believed by population ecologists that this tool should be included as a component of large programs of pest insects management.

Furthermore, other biocontrol methods, with similar acting principles as the classical SIT, are being developed. Particularly, we mention the IIT and Population replacement (PR). These two techniques utilize the Cytoplasmic Incompatibility (CI) property of the *Wolbachia* bacterium. This bacteria is known to infect various Arthropods, among them the RPW. Then, since *Wolbachia*-infected males (W-males) are not able to fertilize uninfected eggs, due to CI, the massive releases of W-males act like the classical SIT. On the

other hand, the CI-property increases the progeny of W-females considerably. Thus, as *Wolbachia* is maternally inherited, releasing a large number of W-females into a target population may lead to a high abundance of *Wolbachia*-infected insects (population replacement), as was observed, for instance, with the Californian *Culex pipiens* [4]. This will eventually result in the elimination or the reduction of the pest population [5].

In view of the above considerations, many works have been oriented particularly to theoretical studies, especially of the SIT and the IIT, using mathematical modelling (see, for example, [5–12] and references therein). The main objectives are the understanding and the analysis of suppression mechanisms as well as the knowledge of explicit mathematical conditions for the total extinction of the target pests population. This may be very crucial to a SIT/IIT programme, since it permits to estimate its cost as it highlights the features to be considered when taking decision about strategies to adopt. Thus, various classes of models have been applied to these techniques, including deterministic, stochastic, continuous-time, discrete-time, and hybrid approaches (see Ref. [13] for a discussion of the relative merits of different models). The virtues of analytic models are their generality and the precision with which the actions of different parameters of the strategy can be predicted. On the other hand, their major shortcoming is the simplification which must be allowed to make the models mathematically tractable.

In this paper, we consider a simplified, but fairly reasonable, mathematical model for the extermination process using the SIT/IIT. As will be argued later, we assume the sterile-fertile interaction to be a one-sided competition that solely affects the fertile population negatively. This scenario is mathematically implemented by modifying the interspecific competition term in a recent predator-predator model for SIT [14]. Then, using an approximate averaging procedure, we derive analytically the mathematical conditions necessary to achieve the eradication of the wild population in finite time. In particular, relations between the extinction time, the size of the released sterile males, and model's parameters are explicitly obtained. Next, we compare our analytical findings with exact numerical results in order to assess the accuracy of the used approximations.

This paper is organized as follows. In Section 2, we present and argue our general mathematical model for the interactive dynamics between wild and sterile insects. In Sections 3 and 4, this model is used to approximate the conditions analytically to achieve the total extinction of the target population for different release strategies of sterile individuals. The obtained results are then discussed after being confronted with predictions of exact numerical calculations. In Section 5, we discuss the limitations and weaknesses of the considered model. In the last section, we give our conclusion.

2. Model Formulation

2.1. Assumptions and Equation Dynamics. The model considered in this work assumes continuous-time, deterministic and density-dependent growth of pest insects [15]. We also adopt most of the general assumptions, which apply to biological situations, originally discussed in [15]. Moreover, we assume that released sterile individuals are male-only and that all sorts of external factors, such as migration, environmental factors, mutation, and selection play no role. In addition, to keep the model simple, we do not include any stage distinction (one-stage model). Furthermore, it is agreed that, for many insects, most of the density dependence occurs in larval survivorship as a result of competition for natural resources [16]. Hence, we argue that sterile-fertile competition is a one-sided competition. Indeed it is widely admitted that SIT emphasis the competition for mates rather than for natural resources. Such competition obviously affects only the fertile population. Conversely, the sterile population is not affected by the presence of fertile individuals neither through the competition for mates (sterile individuals) nor through the competition for natural resources (no larval survivorship in the field). It is why we think that predator-predator and cannibalism models are not convenient for SIT modelling. Thus, we shall assume henceforth a one-sided competition affecting wild-type insects solely.

Mathematically, the model for these two species is described by a one-stage nonlinear dynamic system whose properties appear to depend essentially on the form of the growth rate of a native wild-type population $N(t)$, and their interaction with the sterile individuals of density $M(t)$. Consider the following density-dependent evolution equations subject to one-sided competition:

$$\frac{\mathrm{d}M}{\mathrm{d}t} = -\frac{1}{\tau_s}M + m_R, \quad t \geq 0, \tag{1}$$

$$\frac{\mathrm{d}N}{\mathrm{d}t} = rNF(N) - \delta MH(N), \quad t \geq 0, \tag{2}$$

where m_R is a function of time characterizing the release strategy of sterile males whose average life-time is τ_s. The term $rF(N)$ is the per-capita growth rate of wild-type population. The parameter r allows us to scale, if needed, the continuous function $F(N)$ so that $\max_N F(N) = 1$. In that case, r is the maximum per-capita growth rate without any interference from other individuals in the population. The density dependence of adult pest insects growth rate can be seen as a remanent feature of natural resource limitation at the larval stage. The interaction term $\delta MH(N)$ describes the sterile-fertile one-sided competition where $H(N)$ is the functional response and the parameter δ is the interaction rate between the two species. Note that the death rate of the wild-type population has been ignored in equation (2).

2.2. Intraspecific and Interspecific Competitions. The choice of the intraspecific competition model appears to condition the population dynamics. While early studies tended to assume the population growth rate to be logistic, more recently, much attention has been paid to the impact of the Allee effect, as the latter was shown to affect virtually all aspects of species interactions in space and time [17, 18].

This negative competition effect refers to a decrease in the per-capita growth rate at low population densities, which may increase the extinction risk of low-density populations [19, 20]. This effect arises from a number of sources such as difficulties in finding mates, social dysfunction, and inbreeding depression [21] and may have potential importance in the dynamics of small populations [22, 23], as well as in population diffusion processes [24–27].

Let us assume that the wild-type population has a stable steady state $F(N_s^h) = 0$: that is, the carrying capacity of the niche in the absence of sterile males. When the Allee effect is sufficiently strong, there is also an unstable steady density N_u^l of wild-type insects, such that $0 < N_u^l < N_s^h$, and for which $F(N_u^l) = 0$. These states are given in Table 1, for the two types of function $F(N)$ that we are going to consider in this work.

For F_2 the submodel, the condition $0 < \alpha < \beta$ ensures a strong Allee effect [24]. Thus, the parameter α can be defined as "Allee effect constant"; the bigger α is, the stronger the Allee effect will be.

On the other hand, for interspecific submodels, describing the one-sided competition between sterile and fertile populations, we shall consider functional responses of Holling type in addition to a flat mating rate response. The latter are shown in Table 2. For Holling type-II and type-III responses, the parameter s measures the "satiation" effect: the mating with fertile wild-type females by a unit number of a sterile male cannot continue to grow linearly with the number of wild-type females available but must "saturate" at the value $1/s$ (see for instance [28, 29]). If the number of available male matings equals or exceeds the number of available female matings, then all available matings with fertile females occur. Besides, as long as mating is random, the proportion of fertile female matings to fertile and sterile males will not be altered by the presence of females that were fecundated. It is obvious that this submodels are not equivalent and some criteria based on field experiments and state-of-the-art for SIT should be considered when drawing conclusions regarding their applicability.

Table 1: Intraspecific growth submodels of wild-type insect growth rate.

$F(N)$	N_s^h	N_u^l
$F_1(N) = 1 - (N/\beta)$	β	0
$F_2(N) = k_2(1 - (N/\beta))(N/(\gamma + N))$, $\gamma > 0$	β	0
$F_3(N) = k_3(\alpha - N)(N - \beta)$, $0 < \alpha < \beta$	β	α

N_s^h and N_u^l stand, respectively, for the highest stable steady state and the lowest unstable one. To meet $\max_N F = 1$ condition, the normalization constants should be set at $k_2 = \beta/(2\gamma + \beta - 2\sqrt{\gamma(\gamma+\beta)})$ and $k_3 = 4/(\alpha - \beta)^2$.

Table 2: Interspecific models of sterile-fertile competition.

$H(N)$	Submodel
$H_I(N) = N$	Holling type-I
$H_{II}(N) = N/(1 + sN)$	Holling type-II
$H_{III}(N) = N^2/(1 + sN^2)$	Holling type-III
$H_{IV}(N) = 1/s$	Flat mating rate

The parameter s is a positive real number.

3. Extinction Condition

Regarding the cost and the duration of SIT, it is crucial to have information on the underlying factors of the Threshold Amount of Sterile Males (TASM) to be released in order to achieve total extinction. Our procedure will provide a good estimation of TASM for various competition submodels and release strategies, by relating the condition for total extinction to the initial number, M_{init}, of sterile individuals released in the niche.

Firstly, it is assumed that insect population density is initially in a stable steady state. Then, to take into account the eventual Allee effect, we merely have to reduce the pest population density from β to α_{sup} in order to achieve extinction. In practical terms, this requires that interspecific competition should be stronger than the intraspecific competition as N goes from β to α_{sup} in the typical time scale τ_e of a given release strategy. Furthermore, by integrating equation (2) between 0 and τ_e we get the following:

$$N(\tau_e) = \beta + \int_0^{\tau_e} [rNF(N) - \delta MH(N)]\,\mathrm{d}t. \tag{3}$$

The extinction condition, $N(\tau_e) \le \alpha_{\text{sup}}$, leads then to the following equation:

$$r\langle NF(N)\rangle - \delta\langle MH(N)\rangle \le -\frac{(\beta - \alpha_{\text{sup}})}{\tau_e}, \tag{4}$$

where the symbol $\langle\cdot\rangle$ denotes the time average over the interval $(0, \tau_e)$. Then, equation (4) can be rewritten as follows:

$$\langle MH\rangle \ge \frac{1}{\delta}\left[r\langle NF\rangle + \frac{(\beta - \alpha_{\text{sup}})}{\tau_e}\right]. \tag{5}$$

Since $H(N(t))$ and $M(t)$ are measurable functions over $(0, \tau_e)$, then it is possible to use Hölder's inequality, according to which we have the following equation:

$$\langle MH\rangle \le \langle M^p\rangle^{1/p}\langle H^q\rangle^{1/q}, \tag{6}$$

where $p, q \in\ ]1, +\infty[$ and $1/p + 1/q = 1$. This yields a more stringent extinction condition, given by the following equation:

$$\langle M^p\rangle^{1/p} \ge \frac{1}{\delta\langle H^q\rangle^{1/q}}\left[r\langle NF\rangle + \frac{(\beta - \alpha_{\text{sup}})}{\tau_e}\right]. \tag{7}$$

The last formula summarizes the effects of each term in equation (2) on the minimum size of the sterile males to be released. Moreover, a key component of our approach is to replace the time-averaged functionals of $N(t)$ in equation (7), $\langle H^q\rangle$ and $\langle NF\rangle$, by their values on $\langle N\rangle$, and to adopt a linear approximation for $\langle N\rangle$, that is,

$$\langle N\rangle \approx \frac{\alpha_{\text{sup}} + \beta}{2}. \tag{8}$$

These approximations should naturally result in some errors, and we shall rely on numerical simulations to check

their validity. On the other hand, the adopted approximation of the averaged functionals of $N(t)$ removes the dependence of equation (7) on the parameter q, and leaves us a free choice of parameter p. Later, the value of p will be chosen so as to get the best fit for numerical results. Tables 3 and 4 give $\langle NF(N)\rangle$ and $\langle H(N)\rangle$ for various models of growth rate and sterile-fertile interaction.

4. Mass Release Strategies

A given control strategy may succeed or fail depending largely not only on various ecological characteristics of the target species but also on the choice of the mass release strategy of sterile males. In order to investigate the parameters that govern the effectiveness of SIT control strategies, in what follows, we apply the above results for three different strategies for the release of sterile males, which are the single release, the constant release, and the periodic release.

4.1. Single Mass Release. Although a single release strategy may be seen as an unusual practice, its investigation could highlight relevant parameters to be considered for other release strategies. For single mass release, the sterile population density follows the law:

$$\frac{dM}{dt} = -\frac{1}{\tau_s} M. \tag{9}$$

so that $M(t) = M_{\text{init}} e^{-t/\tau_s}$ where τ_s is the sterile insects average life-time and M_{init} is the initially released number. For this strategy, the sterile males are gone after the release generation and have no more effect. Therefore, the wild-type population is expected to decrease under the SIT effect within a time scale τ_e of the order of τ_s. An interesting result is that for a single release strategy, extinction does not occur for F_1 and F_2, for all Holling type submodels considered in this work. Indeed, for a weak Allee effect, the condition (4) requiring an effective negative growth rate that could not be satisfied as $\Delta t \longrightarrow +\infty$. Because of the exponentially decreasing effect of sterile insects, there exits a time t_0 after which the wild population recovers persistent positive growth rate until it reaches its highest stable steady state again. This result is well proved by numerical calculations as illustrated in Figure 1, which displays the behavior of the wild-type population $N(t)$ corresponding to F_1 and F_2 for interspecific submodels H_{I}, H_{II}, and H_{III}.

Then, only a strong Allee effect allows for effective extinction when the single release strategy is chosen. In this case, we have the following:

$$\langle M^p(t)\rangle^{1/p} = \left[\frac{\tau_s}{p\tau_e}\left(1 - e^{-p\tau_e/\tau_s}\right)\right]^{1/p}. \tag{10}$$

Table 3: Average factors for various intraspecific models of wild-type insect growth rate.

$F(N)$	$\langle NF\rangle$
$F_1(N)$	$\beta/4$
$F_2(N)$	$\beta^3/4(2\gamma+\beta)(2\gamma+\beta-2\sqrt{\gamma(\gamma+\beta)})$
$F_3(N)$	$(\beta+\alpha)/2$

Table 4: Average factors for various interspecific models of sterile-fertile competition.

$H(N)$	$\langle H\rangle$
$H_{\text{I}}(N)$	$(\beta+\alpha_{\text{sup}})/2$
$H_{\text{II}}(N)$	$(\beta+\alpha_{\text{sup}})/2 + s(\beta+\alpha_{\text{sup}})$
$H_{\text{III}}(N)$	$(\beta+\alpha_{\text{sup}})^2/4 + s(\beta+\alpha_{\text{sup}})^2$
$H_{\text{IV}}(N)$	$1/s$

Hence, according to equation (7), for the F_3 submodel, the TASM to achieve effective extinction in population size with a single release, within a period of time τ_e, is given by the following equation:

$$M_{\text{TASM}} = \left(\frac{p\tau_e e^{p\tau_e/\tau_s}}{\tau_s(e^{p\tau_e/\tau_s} - 1)}\right)^{1/p} \frac{1}{\delta\langle H\rangle}\left[\frac{r}{2}(\beta+\alpha) + \frac{\beta-\alpha}{\tau_e}\right]. \tag{11}$$

Before proceeding further, we would like to make some comments on Flores's work [14]. Flores used a model with H_{I} and a nonnormalized F_3, $(k_3 = 1)$, with $r = 1$ and assuming $\tau_e = \tau_s$ which should yield the following equation:

$$M_{\text{TASM}} = \left(\frac{pe^p}{e^p - 1}\right)^{1/p} \frac{(\beta-\alpha)}{\delta(\beta+\alpha)}\left[\frac{2}{\tau_s} + \frac{\left(\beta^2-\alpha^2\right)}{4}\right]. \tag{12}$$

It is worth emphasizing here that Flores's result, quoted in [14], does not show any dependence on τ_s. Numerical simulations agree with the above result for a large range of parameters as shown in Figure 2. In particular, we find that numerical M_{TASM} exhibit an explicit dependence on the life-time of sterile insects corroborating our claim that results in [14] were incomplete.

For an empirical investigation of this result, let us consider the case where, $\beta \gg \alpha$., we get for the same assumptions:

$$M_{\text{TASM}} = \frac{1}{\delta}\left(\frac{pe^p}{e^p - 1}\right)^{1/p}\left[\frac{1}{\tau_s} + \frac{1}{8}\beta^2\right]. \tag{13}$$

It is interesting to notice that for this choice, the minimum sterile insect amount to release goes like β^2. This is counter-intuitive if we learn that for entomologists its is widely assumed that M_{TASM} should go like β: *constant ratio behavior*. This shortcoming is due in part to the fact that F_3 is

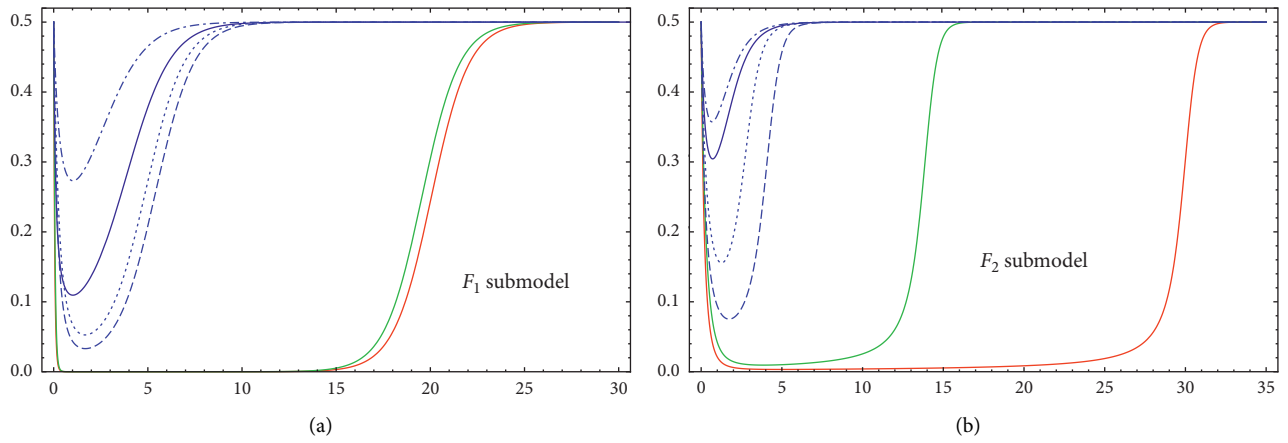

FIGURE 1: Plots of $N(t)$ for single release strategy in cases of F_1 and F_2 for interspecific models H_{I}, H_{II}, and H_{III}. Solid (broken) lines correspond to $M_{\mathrm{init}} = 20$ ($M_{\mathrm{init}} = 5$) in the case of F_1 and to $M_{\mathrm{init}} = 6$ ($M_{\mathrm{init}} = 4$) in the case of F_2.

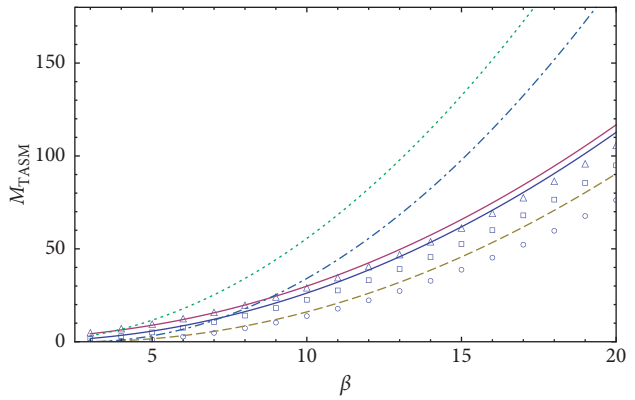

FIGURE 2: Theoretical and simulated M_{TASM} as a function of β. Our (Flores) theoretical result is represented by thick (dotted) line (for $\tau_s = 5$ and $\alpha = 0.8$), thin (dotted) line (for $\tau_s = 0.5$ and $\alpha = 0.8$), and dashed (dot-dashed) line (for $\tau_s = 5$ and $\alpha = 2.8$). Rectangles, triangles, and circles correspond to simulated results for the same choices of parameters τ_s and α, respectively. The remaining parameters values are $\delta = 1$ and $p = 13$.

not normalized. On the other hand, it is quite interesting to see that for a normalized growth rate, the *constant ratio behavior* of the TASM can only be obtained through the submodel of interspecific competition. This requires $H(N)$ to be a slowly varying function which is achieved for H_{II}, H_{III}, and H_{IV}. The work on our assumptions leads here to the following:

$$M_{\mathrm{TASM}} = \frac{1}{\delta\langle\widehat{H}\rangle}\left(\frac{pe^p}{e^p - 1}\right)^{1/p}\left[r + \frac{2}{\tau_s}\frac{(\beta-\alpha)}{(\beta+\alpha)}\right]. \tag{14}$$

On the other hand, for $\beta \gg \alpha$, we have $\langle\widehat{H}_{\mathrm{II-III-IV}}\rangle \simeq \beta/2$. Therefore we get the following equation:

$$M_{\mathrm{TASM}} = \frac{r\beta}{\delta}\left(\frac{pe^p}{e^p - 1}\right)^{1/p}\left[\frac{1}{r\tau_s} + \frac{1}{2}\right], \tag{15}$$

proving that our assumptions allow us to obtain the empirically justified behavior. In the Flores model, symmetric competition between fertile and sterile insects seems to be related to the availability of resources. Although in finite niche, natural resources are limited, for adult insects, it is not a limiting factor. Limited resources are much more critical at juvenile stages (larval) when there is no fertile-sterile competition [30]. Therefore, fertile-sterile competition on resource need not affect a population's growth rate. Competition is strictly related to mating.

Note that more realistic models would be compliant with the empirical "sterile-to-fertile ratio" consideration that is the sterile-to-fertile males ratio is one of the most relevant parameters in SIT programmes [31].

To test the theoretical predictions presented above, evolution equation (2) was solved numerically using *Mathematica 9*. The initial wild-type population was supposed to be at its highest stable steady state. The numerical computations for the three submodels closely agree with the analytical result, as shown in Figure 3.

4.2. Continuous Mass Release. Multiple releases are usually necessary to eradicate target populations. A continuous release strategy is an idealization of what is done in practice. Here, we assume that the release of sterile males is performed uniformly in time with a rate m. Under this assumption, the population dynamics is governed by the following system:

$$\frac{\mathrm{d}M}{\mathrm{d}t} = -\frac{1}{\tau_s}M + m. \tag{16}$$

Ignoring the transitory exponential decaying solution we have the following:

$$M(t) = \tau_s m, \tag{17}$$

yielding

$$m_{\mathrm{TASM}} = \frac{1}{\tau_s\delta\langle\widehat{H}\rangle}\left[r\langle F\rangle + \frac{2}{\tau_e}\frac{\left(\beta - \alpha_{\mathrm{sup}}\right)}{\left(\beta + \alpha_{\mathrm{sup}}\right)}\right]. \tag{18}$$

In addition, as the continuous release strategy is based on a long-time scale: $\tau_e \gg 1$, the extinction condition becomes as follows:

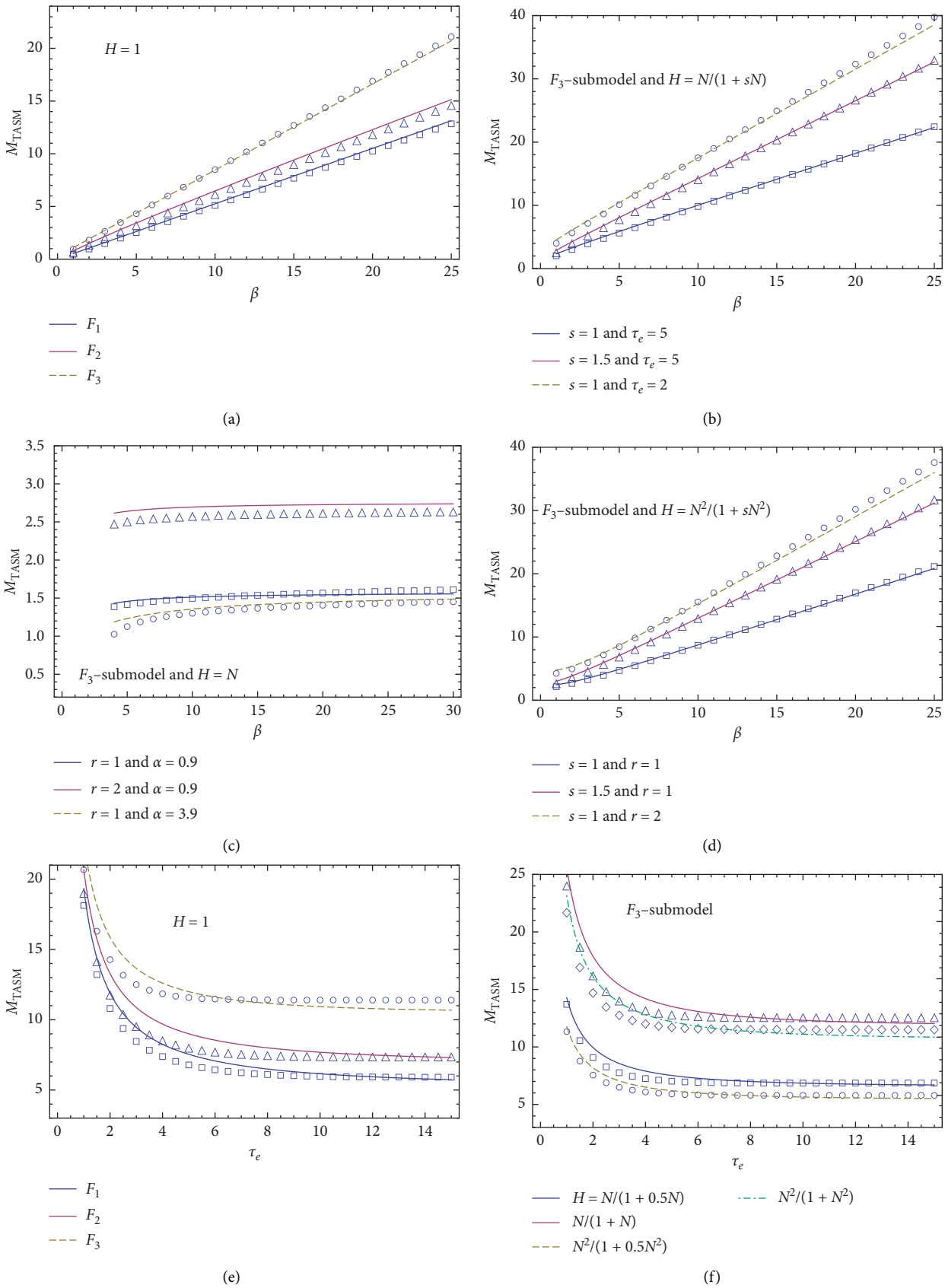

FIGURE 3: Theoretical and simulated M_{TASM}, in the case of single mass release strategy, as a function of β and as a function of τ_e. The remaining parameters values are $\delta = 1$, $\gamma = 0.5$, and $p = 13$. (a) Parameters values are as follows: $r = 1$, $\tau_s = 8$, $\tau_e = 5$, and $\alpha = 0.8$, (b) parameters values are as follows: $r = 1$, $\tau_s = 8$, and $\alpha = 0.8$, (c) parameters values are as follows: $\tau_s = 8$ and $\tau_e = 6$, (d) parameters values are: $\tau_e = 5$, $\tau_s = 8$, and $\alpha = 0.8$, (e) parameters values are as follows: $r = 1$, $\tau_s = 15$, $\beta = 15$, and $\alpha = 0.8$, (f) parameters values are as follows: $r = 1$, $\tau_s = 15$, $\beta = 15$, and $\alpha = 0.8$.

$$m_{\mathrm{TASM}} = \frac{r}{\tau_s \delta} \frac{\langle F \rangle}{\langle \widehat{H} \rangle}. \tag{19}$$

In particular, for all intraspecific and interspecific submodels, and for $\beta \gg \alpha$ we expect the following:

$$m_{\mathrm{TASM}} = \frac{r\beta}{2\tau_s \delta}. \tag{20}$$

This result is of utmost interest as it clearly shows the relevant factors that should be considered for SIT. Numerical results summarized in Figure 4 show that all submodels closely agree with the theory.

4.3. Periodic Mass Release. A periodic release strategy is the most effective in what is done in practice. The sterile insect population dynamics goes as follows:

$$\frac{\mathrm{d}M}{\mathrm{d}t} = -\frac{1}{\tau_s} M + m(1 + \varepsilon \cos(\omega t + \varphi)), \tag{21}$$

where ε, ω, and φ are independent constants with $|\varepsilon| \leq 1$. Ignoring the exponentially decaying transitory solution we get the following:

$$M(t) = \tau_s m \left(1 + \frac{\varepsilon}{1 + \tau_s^2 \omega^2} \cos(\omega t + \varphi) + \frac{\varepsilon \tau_s \omega}{1 + \tau_s^2 \omega^2} \sin(\omega t + \varphi) \right). \tag{22}$$

The extinction dynamics depend on the relative time scales described by $\omega\tau_s$ and $\omega\tau_e$. Notice that in practice, the period of mass-releases is usually chosen to be close to the average life-time of sterile males, and the relative time scale $\omega\tau_s$ is so of the order of some units. Furthermore, the nature of this strategy implies that the extinction time τ_e is well above the average life-time τ_s.

Next, for this strategy, we shall use the result (7) with $p = 2$ (when Hölder's inequality reduces to Cauchy–Schwartz inequality). This yields the following extinction condition:

$$m_{\mathrm{TASM}} = \left(1 + \frac{\varepsilon^2}{2(1 + \tau_s^2 \omega^2)} \right)^{-1/2} \frac{1}{\tau_s \delta \langle \widehat{H} \rangle} \left[r\langle F \rangle + \frac{2}{\tau_e} \frac{(\beta - \alpha_{\mathrm{sup}})}{(\beta + \alpha_{\mathrm{sup}})} \right], \tag{23}$$

where we have neglected terms in $1/\omega\tau_e$ in the calculation of $\langle M^p \rangle^{1/p}$. We can see that for $\omega\tau_s \gg 1$ we recover the continuous release strategy result. Cases where $\omega\tau_s \ll 1$ yield the following:

$$m_{\mathrm{TASM}} = \frac{1}{\tau_s \delta \sqrt{1 + (\varepsilon^2/2)} \langle \widehat{H} \rangle} \left[r\langle F \rangle + \frac{2}{\tau_e} \frac{(\beta - \alpha_{\mathrm{sup}})}{(\beta + \alpha_{\mathrm{sup}})} \right], \tag{24}$$

with respect to the first two cases, for this release strategy, several parameters should be taken into account, namely ε, ω, and φ. This result is of utmost interest as it clearly shows the relevant factors that should be considered for SIT. Numerical results summarized in Figure 5 show that all submodels closely agree with the theory.

5. Limitations of the Model

In this section, we summarise the main weaknesses of this study. First, we are aware that the assumptions introduced in our model suffer from possible violations. Some of the more obvious are as follows:

(i) The hypothesis that the carrying capacity of a given environment is constant does not describe the real situation when the latter and thus the density-dependent death rate may vary between good and poor patches. Hence, the effect of time-varying carrying capacity should be investigated.

(ii) We have assumed a simple constant dispersal weevils rates, but unlikely, sterile males do not disperse uniformly, although releases in SIT programmes must be very heterogeneous over the treatment area. Weevils require food, mates, oviposition sites, and refugia as essential resources [32], foraging for these resources is a dynamic process. For instance, it has been observed that the RPW adjusts its activity in response to the change of weather factors and climatic conditions [33, 34]. Furthermore, human managements, like the application of pesticides or the presence of pheromone traps, also have an effect on the distribution of weevils.

(iii) Pests dispersal has been ignored; however, a more realistic model should take it into account. Host availability, susceptibility and its location in space are one of the major determinants of spatial distribution.

In addition, we have some objections to raise against the model, of which we will mention the two most important ones. First, the model does not account for time lags in the working of density on growth rate. In the RPW, for example, it may take several weeks or months before larvae develop into mature individuals [35, 36]. The logistic model may be adequate in this respect for organisms with a simple life cycle but has to be modified for organisms with more complex life cycles. This has led to so-called time lag models (see, among others, [37, 38]). These models show that such lags may lead to considerable fluctuations in the density of populations instead of stable equilibrium densities.

Second, remating in wild RPW females is common in nature; the probability that a wild female will remake after mating with a sterile male is highly relevant to the effectiveness of the SIT. The model considers the competition as related to mating but does not take into account the remating behavior. Sterile males are less able than wild males to suppress remating in wild females. This effect is increased in males that have been colonized for a longer time. Many factors are involved in the interaction between wild and sterile, sexual maturity synchronization, compatibility, etc., but further field data and investigations are needed to consider all these parameters and to incorporate them in the model.

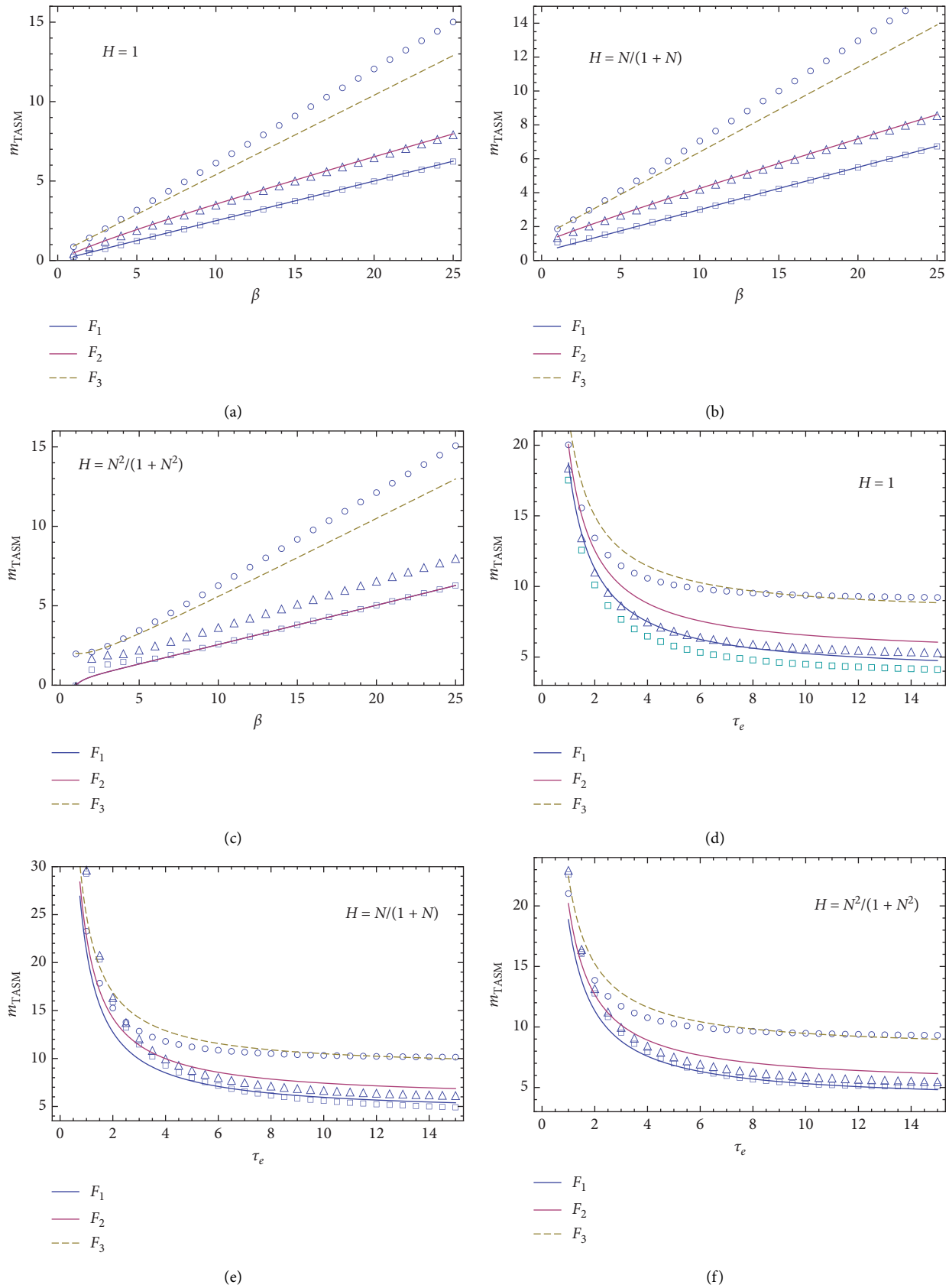

FIGURE 4: Theoretical and simulated m_{TASM}, in the case of continuous mass release strategy, as a function of β and as a function of τ_e. Parameters values are $r = 1$, $\delta = 1$, $\tau_s = 1$, $\alpha = 0.8$, and $\gamma = 0.5$. (a) Parameters values are $\tau_e = 500$, (b) parameters values are $\tau_e = 500$, (c) parameters values are $\tau_e = 100$, (d) parameters values are $\beta = 15$ (e) parameters values are $\beta = 15$, and (f) parameters values are $\beta = 15$.

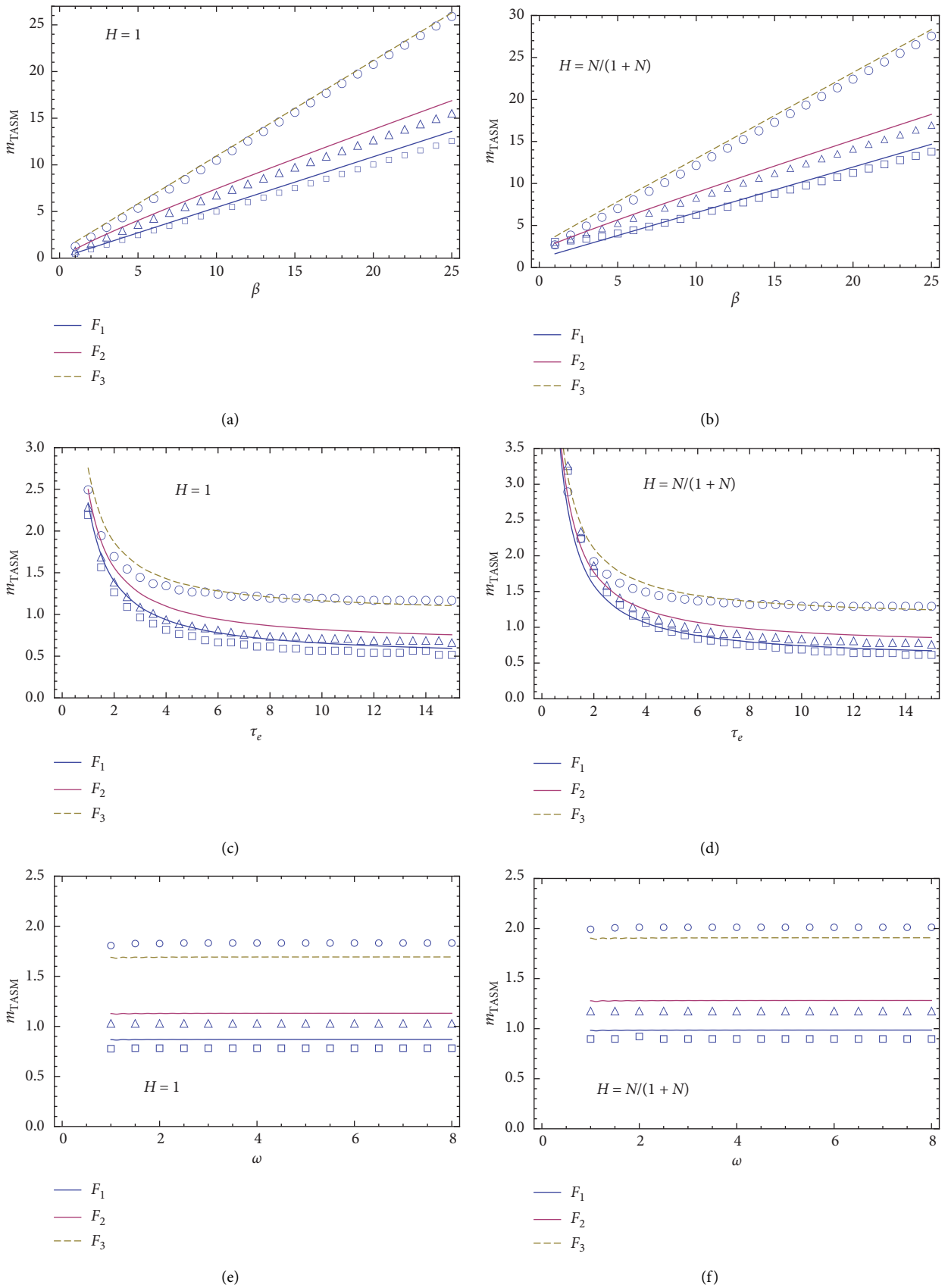

FIGURE 5: Theoretical and simulated m_{TASM}, in the case of periodic mass release strategy, as a function of β, as a function of τ_e, and as a function of ω. Parameters values are $r = 1$, $\varepsilon = 0.5$, $\varphi = 0$, $\alpha = 0.8$, $\gamma = 0.5$, and $(\eta = 0.18)$. (a) Parameters values are $\gamma = 1$, $\tau_s = 0.5$, $\tau_e = 30$, and $\omega = 1$, (b) parameters values are $\gamma = 1$, $\tau_s = 0.5$, $\tau_e = 30$, and $\omega = 1$, (c) parameters values are $\gamma = 2$, $\tau_s = 4$, $\omega = 5$, and $\beta = 15$, (d) parameters values are $\gamma = 2$, $\tau_s = 4$, $\omega = 5$, and $\beta = 15$, (e) parameters values are $\gamma = 1$, $\tau_s = 5$, $\tau_e = 25$, and $\beta = 15$, and (f) parameters values are $\gamma = 1$, $\tau_s = 5$, $\tau_e = 25$, and $\beta = 15$.

6. Discussion and Conclusion

Let us begin our discussion with a comparison between the three release strategies. To do so, two criteria have to be retained, namely: the *total number* of released sterile males, M_{SM}, and the time required to obtain effective extinction, τ_e. These criteria are the most relevant when dealing with the cost of a SIT program. It is worth noting that M_{SM} and τ_e are closely correlated. However, the way of this correlation depends particularly on the release strategy. Indeed, the total numbers $M_{\mathrm{SM}}^{(S)}, M_{\mathrm{SM}}^{(C)}$ and $M_{\mathrm{SM}}^{(P)}$ released within the three strategies, single, continuous, and periodic, respectively, are given by the following equation:

$$M_{\mathrm{SM}}^{(S)} = M_{\mathrm{TASM}}^{(S)},$$

$$M_{\mathrm{SM}}^{(C)} = \tau_{e,c} m_{\mathrm{TASM}}^{(C)},$$

$$M_{\mathrm{SM}}^{(P)} = \tau_{e,p}\left(1 + \frac{\varepsilon}{\omega\tau_{e,p}}\left[\sin\left(\omega\tau_{e,p} + \varphi\right) - \sin\varphi\right]\right) m_{\mathrm{TASM}}^{(P)} \approx \tau_{e,p} m_{\mathrm{TASM}}^{(P)}, \tag{25}$$

where subscripts s, c and p in τ_e are used to distinguish between effective extinction times relative to the three release strategies. Using theoretical results obtained above for extinction conditions, we can firstly deduce that, for a given couple of intraspecific and interspecific submodels, total numbers of sterile males consumed in continuous and periodic release strategies are almost-equal, for the same extinction time: $\tau_{e,c} = \tau_{e,p}$. Figure 6 illustrates the behaviors of the three total numbers, $M_{\mathrm{SM}}^{(S)}, M_{\mathrm{SM}}^{(C)}$, and $M_{\mathrm{SM}}^{(P)}$ with the extinction time, for the same initial number of the wild population. Particularly, we remark that the total number of sterile males consumed in a single release strategy roughly decays exponentially with the extinction time. However, within a continuous or a periodic release strategy, the total numbers of sterile males used increases linearly with the duration of the extinction process. We should note that results for $M_{\mathrm{SM}}^{(C)}$ and $M_{\mathrm{SM}}^{(P)}$ are valid only for $\tau_{e,c/p}$ well above τ_s since in deriving equations (18) and (23), we have ignored the exponentially decaying parts in the expressions of the wild population numbers $M(t)$, and obviously, such an approximation is valid only for long times in comparison with τ_s.

In summary, the paper develops an approach that extends the SIT continuous model for various density-dependent growth rates and interspecific competition functionals. This yields a flexible general model that allows for a substantial simplification of the SIT dynamics and can bias the results in comparison with reality. The model is mathematically interesting because it can produce such a wide range of dynamical behaviors including logistic, strong, and weak Allee effects as well as various response functions for interspecific competition.

Within this general model, analytical and numerical results indicate that eradication of the insect pest is conditional upon the size of the sterile mass release exceeding a critical value. This critical quantity has been determined for various submodels and for three release strategies; single, continuous, and periodic. In all cases,

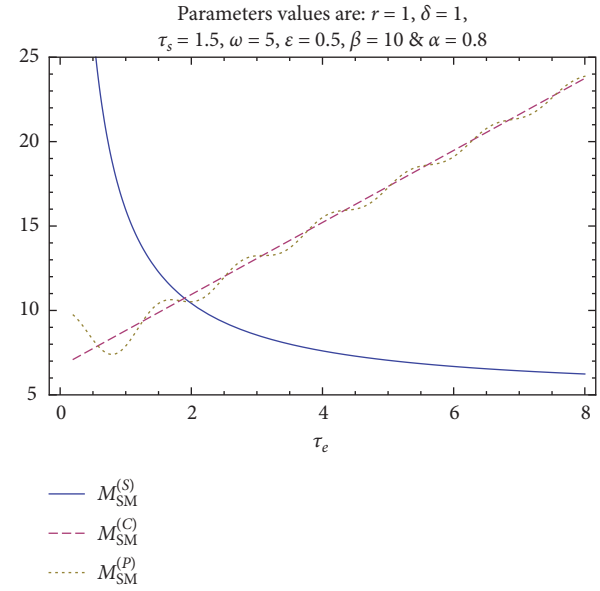

Figure 6: The total number of sterile males, relative to single, continuous, and periodic release strategies, is plotted as functions of the extinction time τ_e for the intraspecific and interspecific submodels F_3 and H_{II}

numerical computations closely agree with the analytical analysis. The study allowed us to identify the most important parameters which control the choice of release strategies. It also shows that for various release strategies, the sterile weevils life-time is a key parameter in the determination of the TASM. However, the presented model should be seen as a first approximation allowing comparing between idealized sterile male releases in order to get an insight of how these strategies will perform in the field. Indeed, real field mass release programs suffer from many complications that arise from the interaction of several biotic and abiotic factors: weather conditions, host availability, migration of insects, poor timing of release, lack of competitiveness of released weevils, and a multitude of other factors that are crucial to lead a successful release. While it is not possible to include all of these factors in modelling SIT, a great improvement of our model can be gained by introducing controls into the population's dynamics. This can be done a priori in the same manner as with the well-known Lotka–Volterra model, using already existing techniques, such as the speed gradient method and Emel'yanov method. This extension of the model would be the subject of a forthcoming study.

Finally, let us note that the sterile insect technique has a pest density-dependent suppressive action. It has the attribute of increasing efficiency with decreasing target population density. A given chemical or biological insecticide achieves about the same degree of control, whether the pests are abundant or scarce [31]. Therefore, these genetic control methods can be effectively integrated with other density independent and density dependant methods especially when the objective is to manage total populations on an areawide basis.

Data Availability

No data were used to support this study.

Conflicts of Interest

The authors declare that they have no conflicts of interest.

Acknowledgments

The third author would like to thank his Professors/Scientists Pr. Mohamed Haiour, Pr. Ahmed-Salah Chibi, and Pr. Azzedine Benchettah at Annaba University in Algeria for the important content of masters and PhD courses in pure and applied mathematics which he received during his studies. Moreover, he thanks them for the additional help they provided to him during office hours in their office about the few concepts/difficulties he had encountered, and he appreciates their talent and dedication for their postgraduate students currently and previously. In addition, the authors gratefully acknowledge Qassim University, represented by the Deanship of Scientific Research, on the material support for this research under the number 6766-alrasscac-bs-2019-2-2-I during the academic year 1441 AH/2019 AD.

References

[1] E. F. Knipling, "Possibilities of insect control or eradication through the use of sexually sterile males 1," *Journal of Economic Entomology*, vol. 48, no. 4, pp. 459–462, 1955.

[2] E. F. Knipling, *Screwworm Eradication: Concepts and Research Leading to the Sterile Male Method*, pp. 409–418, Smithsonian Institution Publication, Washington, DC, USA, 1959.

[3] V. A. Dyck, J. Hendrichs, and A. S. Robinson, *The Sterile Insect Technique, Principles and Practice in Area-wide Integrated Pest Management*, Springer, Dordrecht, Netherlands, 2006.

[4] J. L. Rasgon and T. W. Scott, "Wolbachia and cytoplasmic incompatibility in the California culex pipiens mosquito species complex: parameter estimates and infection dynamics in natural populations," *Genetics*, vol. 165, no. 4, pp. 2029–2038, 2003.

[5] P.-A. Bliman, D. Cardona-Salgado, Y. Dumont, and O. Vasilieva, "Implementation of control strategies for sterile insect techniques," *Mathematical Biosciences*, vol. 314, pp. 43–60, 2019.

[6] C. Dufourd and Y. Dumont, "Modeling and simulations of mosquito dispersal. The case of *Aedes albopictus*," *Biomath*, vol. 1, no. 2, p. 17, 2012.

[7] C. Dufourd and Y. Dumont, "Impact of environmental factors on mosquito dispersal in the prospect of sterile insect technique control," *Computers & Mathematics with Applications*, vol. 66, no. 9, pp. 1695–1715, 2013.

[8] Y. Dumont and J. M. Tchuenche, "Mathematical studies on the sterile insect technique for the chikungunya disease and *Aedes albopictus*," *Journal of Mathematical Biology*, vol. 65, no. 5, pp. 809–855, 2012.

[9] J. Li and Z. Yuan, "Modelling releases of sterile mosquitoes with different strategies," *Journal of Biological Dynamics*, vol. 9, no. 1, pp. 1–14, 2015.

[10] J. Li, L. Cai, and Y. Li, "Stage-structured wild and sterile mosquito population models and their dynamics," *Journal of Biological Dynamics*, vol. 11, no. sup1, pp. 79–101, 2016.

[11] M. Huang, X. Song, and J. Li, "Modelling and analysis of impulsive releases of sterile mosquitoes," *Journal of Biological Dynamics*, vol. 11, no. 1, pp. 147–171, 2017.

[12] J. Li, "New revised simple models for interactive wild and sterile mosquito populations and their dynamics," *Journal of Biological Dynamics*, vol. 11, no. sup2, pp. 316–333, 2017.

[13] W. G. Costello and H. M. Taylor, "Mathematical models of the sterile male technique of insect control," in *Mathematical Analysis of Decision Problems in Ecolog (Lect. Notes Biomath., 51*, A. Charnes and W. R. Lynn, Eds., Springer-Verlag, Berlin, Germany, pp. 318–359, 1975.

[14] J. C. Flores and R. Beltran, "Gause's exclusion principle revisited: artificial modified species and competition," *Journal of Physics A: Mathematical and General*, vol. 33, no. 27, pp. 4877–4882, 2000.

[15] H. Barclay and M. Mackauer, "The sterile insect release method for pest control: a density-dependent model," *Environmental Entomology*, vol. 9, no. 6, pp. 810–817, 1980.

[16] D. R. Miller and D. E. Weidhaas, "Equilibrium populations during a sterile-male release Program1," *Environmental Entomology*, vol. 3, no. 2, pp. 211–216, 1974.

[17] M. Gyllenberg, J. Hemminki, and T. Tammaru, "Allee effects can both conserve and create spatial heterogeneity in population densities," *Theoretical Population Biology*, vol. 56, no. 3, pp. 231–242, 1999.

[18] F. Courchamp, L. Berec, and J. Gascoigne, *Allee Effects in Ecology and Conservation*, Oxford University Press, Oxford, UK, 2008.

[19] J. M. Cushing and J. T. Hudson, "Evolutionary dynamics and strong Allee effects," *Journal of Biological Dynamics*, vol. 6, no. 2, pp. 941–958, 2012.

[20] G. Livadiotis and S. Elaydi, "General Allee effect in two-species population biology," *Journal of Biological Dynamics*, vol. 6, no. 2, pp. 959–973, 2016.

[21] M. A. McCarthy, "The Allee effect, finding mates and theoretical models," *Ecological Modelling*, vol. 103, no. 1, pp. 99–102, 1997.

[22] R. Lande, S. Engen, and B.-E. Saether, "Optimal harvesting, economic discounting and extinction risk in fluctuating populations," *Nature*, vol. 372, no. 6501, pp. 88–90, 1994.

[23] T. Stephan and C. Wissel, "Stochastic extinction models discrete in time," *Ecological Modelling*, vol. 75-76, no. 76, pp. 183–192, 1994.

[24] M. A. Lewis and P. Kareiva, "Allee dynamics and the spread of invading organisms," *Theoretical Population Biology*, vol. 43, no. 2, pp. 141–158, 1993.

[25] R. R. Veit and M. A. Lewis, "Dispersal, population growth, and the Allee effect: dynamics of the house finch invasion of eastern North America," *The American Naturalist*, vol. 148, no. 2, pp. 255–274, 1996.

[26] V. Rapisarda, C. Loreto, E. Vitale et al., "Incidence of sharp and needle-stick injuries and mucocutaneous blood exposure among healthcare workers," *Future Microbiology*, vol. 14, no. 9s, pp. 27–31, 2019.

[27] R. Ragusa, G. Giorgianni, L. Lupo et al., "Healthcare-associated *Clostridium difficile* infection: role of correct hand hygiene in cross-infection control," *Journal of Preventive Medicine and Hygiene*, vol. 59, no. 2, pp. E145–E151, 2018.

[28] H. I. Freedman, *Deterministic Mathematical Models in Population Ecology*, Dekker, NewYork, NY, USA, 1980.

[29] R. May, *Stability and Complexity in Model Ecosystems*, Princeton University Press, Princeton, NJ, USA, 1974.

[30] J. Hendrichs, A. S. Robinson, J. P. Cayol, and W. Enkerlin, "Medfly areawide sterile insect technique programmes for

prevention, suppression or eradication: the importance of mating behavior studies," *Florida Entomologist*, vol. 85, no. 1, pp. 1–13, 2002.

[31] E. F. Knipling, "Sterile insect and parasite augmentation techniques: unexploited solutions for many insect pest problems," *Florida Entomologist*, vol. 81, no. 1, pp. 134–160, 1998.

[32] F. He and R. I. Alfaro, "White pine weevil (Coleoptera: Curculionidae) attack on white spruce: spatial and temporal patterns," *Environmental Entomology*, vol. 26, no. 4, pp. 888–895, 1997.

[33] J. R. Faleiro, "Pheromone technology for the management of red palm weevil Rhynchophorus ferrugineus (Olivier) (Coleoptera: rhynchophoridae) a key pest of coconut," *Technical Bulletin No.4, ICAR Research Complex for Goa*, no. 4, p. 40, 2005.

[34] S.-C. Huang, M. A. Zi-Long, Q. Wi-Quan, L. Chao-Xu, Y. Feng-Yu, and H. Chao-Wen, "The trapping effect of aggregation pheromone for the red palm weevil (rhynchorus ferrugineus (olivier)) and its traps development." *China Forestry Science and Technology*, vol. 3, pp. 1–9, 2008.

[35] D. K. Butani, "Insect pests of fruit crops and their control, sapota-11," *Pesticides Research Journal*, vol. 9, pp. 40–42, 1975.

[36] H. S. Salama, F. N. Zaki, and A. S. Abdel-Razek, "Ecological and biological studies on the red palm weevil Rhynchophorus ferrugineus (Olivier)," *Archives of Phytopathology and Plant Protection*, vol. 42, pp. 392–399, 2009.

[37] A. Martin and S. Ruan, "Predator-prey models with delay and prey harvesting," *Journal of Mathematical Biology*, vol. 43, no. 3, pp. 247–267, 2001.

[38] N. MacDonald, "Time lags in biological models," *volume 27 of Lecture Notes in Biomathematics*, Springer, Berlin, Germany, 1978.